IN-SITU ASSESSMENT OF LINEAR AND NONLINEAR DYNAMIC PROPERTIES OF MUNICIPAL SOLID WASTE

by

Andhika Sahadewa

A dissertation submitted in partial fulfillment
of the requirements for the degree of
Doctor of Philosophy
(Civil Engineering)
in the University of Michigan
2014

Doctoral Committee:

Assistant Professor Dimitrios Zekkos, Chairman
Assistant Professor Adda Athanasopoulos-Zekkos
Professor Roman Hryciw
Emeritus Professor Richard D. Woods
Associate Professor Yin Lu Young

DEDICATION

To my father, bapak Suharno

ACKNOWLEDGEMENTS

I would like to thank to my advisor, Prof. Dimitrios Zekkos, who supported me throughout my Ph.D journey by offering me motivation and encouragement. I would like to thank to the other committee members, Prof. Adda Athanasopoulos-Zekkos, Prof. Roman Hryciw, Prof. Richard Woods, and Prof. Yin Lu Young for their invaluable advice. I am also grateful to Mr. Rick Burch and Mr. Bob Fischer for their help on design and construction of field and laboratory devices. I also would like to acknowledge other members in geotechnical engineering group at the University of Michigan, including Prof. Radoslaw Michalowski, Prof. Donald Gray, and my geotechnical colleagues for sharing their expertise and friendship.

I dedicate special thanks to my parents, bu Esti, bu Dewi, and pak Aji who always pray for me. With all my heart, never enough thanks to my beloved wife, Vava, and my dear daughters Andra and Aya. Without their support and prayer, I would not have been able to finish my Ph.D study. These few words alone cannot adequately express my love and gratitude for them. Finally, I would like to say endless thanks to Allah who always helps, protects, and loves me unconditionally.

TABLE OF CONTENTS

LIST OF FIGURES

LIST OF TABLES

LIST OF APPENDICES

APPENDIX

ABSTRACT

Dynamic properties of solid waste are critical to reliably evaluate the seismic response of landfills. In this study, the dynamic properties of solid waste including shear wave velocity (V_s), small-strain shear modulus (G_{max}), and normalized shear modulus (G/G_{max}) reduction curve, were investigated in situ.

Semi-empirical and empirical models for the V_s of municipal solid waste (MSW) were developed. The semi-empirical model is a more comprehensive model that aims to separately capture the effect of waste density and confining stress on the shear wave velocity of MSW. It was formulated using data generated from large-scale laboratory studies on reconstituted MSW. The empirical model has a simpler mathematical expression that is a function of depth only. The parameters of both models were derived by calibrating them against a total of 49 shear wave velocity profiles, including 13 V_s profiles that were generated in this study. The models can be used to estimate the V_s of MSW and to evaluate the seismic response of landfills.

A field testing method to investigate the dynamic properties of solid waste was implemented in four landfills using the George E. Brown, Jr. Network for Earthquake Engineering Simulation (NEES) facilities. Field investigations were performed at three MSW landfills, namely Austin Community Landfill (Texas), Lamb Canyon Sanitary Landfill (California), and Los Reales Landfill (Arizona). Field investigation was also conducted in a class I hazardous landfill, namely BKK Landfill. The field method was primarily aimed at evaluating shear wave and primary wave velocities as well as, for the first time, the shear modulus reduction curve of solid waste. The relationship between

shear modulus and shearing strain was investigated by applying dynamic horizontal loads at the waste surface in a staged-loading sequence generated by a NEES mobile field shaker. The solid waste response was measured with buried arrays of three-component geophones. The testing method also allowed an assessment of the effect of confining stress and waste variability on the dynamic properties of solid waste. A model for normalized shear modulus reduction curves of solid waste was recommended based on field testing results.

CHAPTER 1. INTRODUCTION

1.1 Problem Statement

Municipal Solid Waste (MSW) generally refers to typical household and office waste, including tires, furniture, newspapers, plastic, containers, and food. Despite the waste recycling action program, the volume of MSW generated in the U.S. tends to increase and its disposal is a growing concern as reported by US Environmental Protection Agency (EPA) in Figure 1.1. More than 50% of generated waste is disposed of in landfills. The demand for placement of more waste in existing landfills will increase as long as no other attractive methods for large volume waste management (Zekkos 2005).

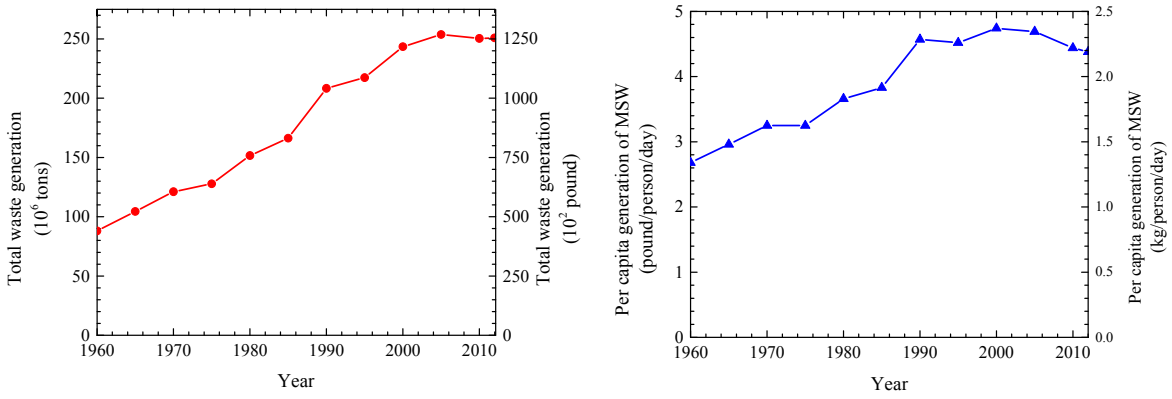

Figure 1.1 MSW generation rates in the US, 1960-2012 (data source: US EPA, 2014).

The consequences of landfill failures under static or seismic conditions are significant. As shown in Fig. 1.2, Leuwigajah landfill failure in Bandung, Indonesia has caused significant loss of life (Koelsh et al. 2005). Merry et al. (2005) reported that Payatas landfill failure, which collapsed after heavy monsoonal rain, in Manila, Philippines led to loss of life as well as major public health consequences as the failed waste masses overwhelmed a residential area (Fig. 1.3).

Additionally, significant expenses are made for subsequent investigations, mitigations, and repairs of a failed landfill (e.g. Rumpke landfill, Ohio, Eid et al. 2000).

Figure 1.2 Leuwi Gajah Landfill failure (Koelsh et al. 2005).

Figure 1.3 Payatas Landfill failure (Merry et al. 2005).

The promulgation of Federal Subtitle D in 1993 has transformed MSW landfills from unregulated waste disposal areas of small to moderate size, to more efficient, regulated, and sophisticated large-size facilities. These subtitle D or modern landfills have to be stable under static and seismic conditions. Subtitle D regulation requires the seismic design and analysis of landfills in areas of modest to high seismicity. The 1994 Northridge Earthquake provided the

first opportunity to garner data on the seismic performance of Subtitle D and pre-Subtitle D landfills. The seismic performance of 21 landfills during this earthquake was reported by Matasovic et al. (1995). Although the majority of landfills were subjected to estimated rock peak horizontal accelerations that were less than 0.2 g, 13 landfills experienced various levels of damage ranging from minor (e.g. cover instabilities) to significant damage (e.g. impairment of the containment system). This study demonstrated that the seismic susceptibility of MSW landfills and the need for more vigorous seismic design guidelines. The seismic response of modern MSW landfills is still poorly understood and cannot be reliably predicted unless reliable and representative linear and nonlinear dynamic properties of MSW are used. The lack of such data is a major challenge to reliably evaluate the seismic performance of landfills.

In recent years, dynamic properties of MSW have been investigated extensively in the laboratory. However, laboratory tests can be very challenging and have several disadvantages. Laboratory testing always involves reconstitution of MSW specimens since recovering "undisturbed" samples of MSW is not feasible. Testing apparatus and samples also need to be relatively large to accommodate large waste particles (Zekkos et al. 2008), that are not widely available. Thus, a field testing method to evaluate dynamic properties of MSW is very attractive and promising.

The Network for Earthquake Engineering Simulation at the University of Texas at Austin (NEES@UT) mobile shakers (i.e. T-Rex and Thumper) provide a new approach and appealing opportunity to study the dynamic properties of MSW in situ. Using these facilities, the first in-situ data on the nonlinear dynamic properties of MSW is generated in this study.

1.2 **Research Objective**

The main objective of the research is the assessment of the in-situ dynamic properties of MSW in the linear and non-linear strain range using NEES@UT equipment. In particular, the proposed field investigation is aimed to achieve the following objectives:

1. To evaluate the P-wave and S-wave velocities of MSW in situ and their variation with depth.
2. To measure the effect of stress state on wave propagation velocity of MSW in situ.
3. To investigate the relationship between shear modulus and shearing strain level in situ.
4. To develop a model for shear wave velocity of MSW.
5. To develop a model for normalized shear modulus reduction relationship with shearing strain for MSW.

1.3 **Organization of Dissertation**

Chapter 1 is an introduction of this thesis. The overall scope of the research program is introduced by describing the need to evaluate linear and nonlinear dynamic properties of MSW in situ, the objectives of this research, and the organization of this dissertation.

Chapter 2 presents the literature review. In this chapter, the fundamentals of dynamic properties of MSW are presented. A review of previous studies on field measurements of nonlinear dynamic properties of geomaterials and MSW is also presented.

Chapter 3 presents the development of a model for shear wave velocity of MSW. In this chapter, surface wave testing in four Michigan landfills are also presented. This chapter resulted in several papers including Sahadewa et al. (2011), Sahadewa et al. (2013), and Zekkos et al. (2013).

In Chapter 4, test equipment, field test setup, test procedure, and data analysis in NEES field testing are described in a generalized fashion. Examples of data analysis are also presented. Uncertainties and limitations from the field testing program are described in this chapter.

Chapters 5, 6, 7, and 8 present field test activities at the Austin Community Landfill (Texas), Lamb Canyon Sanitary Landfill (California), Los Reales Landfill (Arizona), and BKK Hazardous Landfill (California), respectively. In these chapters, testing results from each landfill are reported.

In Chapter 9, field investigation results using the mobile shakers are summarized and synthesized. In particular, this chapter presents an evaluation on anisotropy of solid waste, a synthesis of downhole and crosshole seismic test results, an evaluation of Poisson's ratio of solid waste, and the development of recommended normalized shear modulus reduction curves for solid waste.

Chapter 10 contains the summary, conclusions, and recommendations of this research. General contents of this research are summarized. Conclusions regarding the evaluation of the linear and nonlinear shear moduli of the solid waste from field testing are then presented. In addition, experience from surface wave testing in Michigan landfills and conclusions from the development of model for shear wave velocity of MSW are presented. Recommendations for future research are also listed.

CHAPTER 2. LITERATURE REVIEW

2.1 Introduction

Seismic analysis and design of a landfill, including site response analysis and seismic displacement estimation, need representative properties of municipal solid waste (MSW). In this analysis, critical input parameters include the dynamic properties of MSW, namely:

- The shear wave velocity (V_s) or small-strain shear modulus (G_{max});
- The shear modulus reduction (G/G_{max}) versus shearing strain (γ);
- Material damping ratio (D) versus γ.

Other important input parameters for this analysis are MSW unit weight (γ_{MSW}), Poisson's ratio, and the seismic or dynamic shear strength.

The aforementioned properties can significantly influence the site-specific seismic response of landfills. They are needed to reliably perform seismic response analyses and slope stability analyses of MSW landfills. It is thus crucial to appropriately characterize and understand the dynamic properties of solid waste.

The dynamic properties of soil deposits and rocks have been documented and characterized. A great number of investigators have evaluated these properties using a variety of methods, including laboratory testing (e.g. Hardin-Richart 1963, Hardin and Black 1968, Peacock and Seed 1968, Seed and Idriss 1970, Drnevich 1977, Drnevich et al. 1977, Kokusho et al. 1982, Dyvik and Madshus 1985, Vucetic and Dobry 1991, and Darendeli 2001) and in-situ field testing (Stokoe and Woods 1972, Woods 1978, Nazarian and Stokoe 1984, Axtell et al. 2002, Cox 2006, Rosenblad et al. 2007). Laboratory testing has the advantage that boundary

conditions are well-defined and testing parameters can be controlled. But, disturbance during sampling, issues related to how representative the sample is, inconsistency of stress state between laboratory sample and the material in the field, and testing device compliance frequently become major drawbacks of this method. Figure 2.1 shows the available laboratory testing devices to measure dynamic properties and their corresponding shearing strain capacities. In-situ field testing has advantages over the laboratory testing. Field testing is not affected by sample disturbance and test results incorporate the complexity of the actual stress state. In addition, field testing may occasionally be considered as full-scale testing. Nevertheless, this method is costly, time consuming, incapable of controlling some test parameters (e.g. drainage control and boundary conditions), and demands a comprehensive understanding of the testing methodologies. Although both laboratory and field methods have been used extensively to evaluate the dynamic properties of MSW, to the author's knowledge, very few extensive studies have been performed to evaluate the nonlinear dynamic properties of MSW. There is also very limited in-situ testing performed to evaluate the nonlinear dynamic properties of MSW study. The only available study is test study conducted in preparation for this study (i.e. Zalachoris 2010 and Stokoe et al. 2011).

2.2 Physical Characterization of MSW

Waste composition is one of the most important factors that influence engineering properties of MSW. Physical characterization of MSW requires a procedure to qualitatively and quantitatively evaluate waste composition.

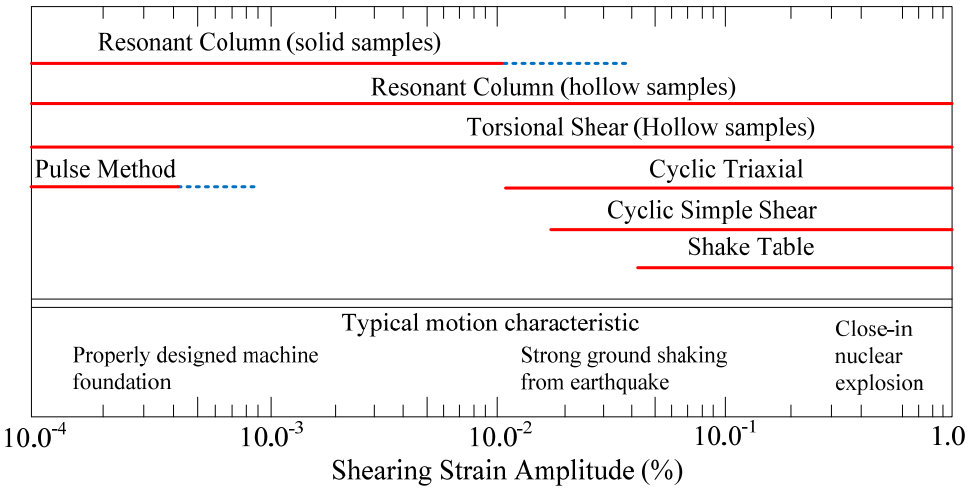

Figure 2.1 Capacities of laboratory devices in inducing shearing strain amplitudes (Woods 1978).

Waste characterization procedures have been developed for a variety of applications, including geochemical characterization, waste stream characterization, and geotechnical characterization. Several MSW characterization procedures for geotechnical purposes have been proposed since the early 1990s (e.g. Landva and Clark 1990; Grisolia et al. 1995). The development of these procedures was intended to collect relevant information about the waste with respect to its geotechnical response, such as shear strength, hydraulic conductivity, stiffness, and compressibility. Essentially, the basis of the earliest MSW classification systems for geotechnical purposes was a distinction between degradable and non-degradable waste constituents. Dixon and Langer (2006) found that none of the existing waste classification systems fulfilled the requirements of a thorough classification scheme and proposed their own classification framework. Also the Dixon and Langer (2006) classification system requires a significant level of effort and was intended mainly for research purposes. Accordingly, this approach may be too time consuming for use in practice.

Zekkos et al. (2010) proposed a MSW physical characterization procedure for geotechnical purposes based on experiences garnered from waste characterization at the

Operating Industries, Inc. (OII) landfill, Monterey Park, California (Geosyntec 1996) and the Tri-Cities landfill, Freemont, California (Zekkos 2005) as well as recommendations from previous waste characterization systems. The proposed recommendation is designed to capture the characteristic of MSW that may have a major influence on its mechanical properties. This procedure consists of four phases, namely: 1) Collection and review of available information, 2) Field characterization, 3) Primary geotechnical characterization, and 4) Secondary geotechnical characterization. At the earlier phases more qualitative information is collected for large volume of MSW progressing to more quantitative information for small amount of MSW. This characterization system requires the segregation of waste constituents to material larger than 20 mm fraction (largely waste materials) and smaller than 20 mm fraction (mostly soil-like materials), which is performed in phase 3. In phase 4, the waste constituents are characterized in more detail to evaluate the waste composition (i.e. percentage by weight of paper, soft plastics, etc) and measurements such as the moisture and organic content are performed.

2.3 MSW Unit Weight

The unit weight of MSW (γ_{MSW}) is a critical material property in landfill engineering. Most engineering analyses of landfill systems, including static and dynamic slope stability, requires an estimate of the MSW unit weight. Indeed, MSW unit weight was the only material property that was important to all different types of landfill analyses listed in Dixon and Jones (2005). Improper selection of MSW unit weight distribution with depth (i.e. unit weight profile) may lead to unreliable engineering analysis results. For instances, Zekkos (2005) showed that the use of two different MSW unit weight profiles that have the same average unit weight of 10.5 kN/m^3 leads to significant differences in the calculated seismic landfill cover displacements. In addition,

γ_{MSW} is also required to evaluate the small-strain shear modulus value when shear wave velocity is available.

Zekkos (2005) summarized the methods used to evaluate MSW unit weight, namely; landfill records with a topographic survey, unit weight of "undisturbed" specimens, and in-situ large-scale samples. Landfill records allow an assessment of the weight of material received by the landfill, whereas topographic survey permits calculation of the volume of landfill. Thus, the MSW unit weight can be estimated. Unfortunately, this method is not reliable for assessing the unit weight profile (i.e. variation of γ_{MSW} with depth). If an "undisturbed" sample of MSW is recoverable, MSW unit weight can be evaluated easily. But, this method is questionable due to inadequate methods of sampling of large specimens and unavoidable sample disturbance. Alternatively, an in-situ large scale method that is essentially a large-scale version of the standard sand-cone density test (ASTM D1556-07) has been proposed. In this method, a large-scale pit is excavated and the excavated material is weighed. Calibrated geomaterial (e.g. pea gravel) with known unit weight is used to fill the pit so that the volume of the pit can be estimated. By knowing the weight and the volume of excavated MSW, its average unit weight can be evaluated. Among the three methods, the in-situ large-scale method is considered to be the most reliable in-situ assessment method of MSW unit weight (Zekkos 2005).

In-situ large-scale MSW unit weight measurements from 11 independent studies (Cowland et al. 1993, Geosyntec 2003, Gomes et al. 2002, Kavazanjian et al. 1996, Landva and Clark 1986, Matasovic and Kavazanjian 1998, Oweis and Khera 1998, Pereira et al. 2002, Richardson and Reynolds 1991, and Zekkos et al. 2006a) were summarized in Zekkos et al. (2006a) and are showed in Fig. 2.2. Additionally, this figure shows the Kavazanjian et al. (1995) MSW unit weight profile. Despite considerable scatter in Fig. 2.2, consistent trends of unit

weight increasing with depth are observed if each landfill is evaluated independently. These trends suggest the existence of a landfill-specific unit weight profile. Relatively uniform waste streams, with wastes of similar composition, organic content, and moisture content, or waste streams that evolve gradually over time, and standard waste disposal operating procedures in modern landfills may support and justify the existence of a landfill-specific unit weight profile (Zekkos et al. 2006a).

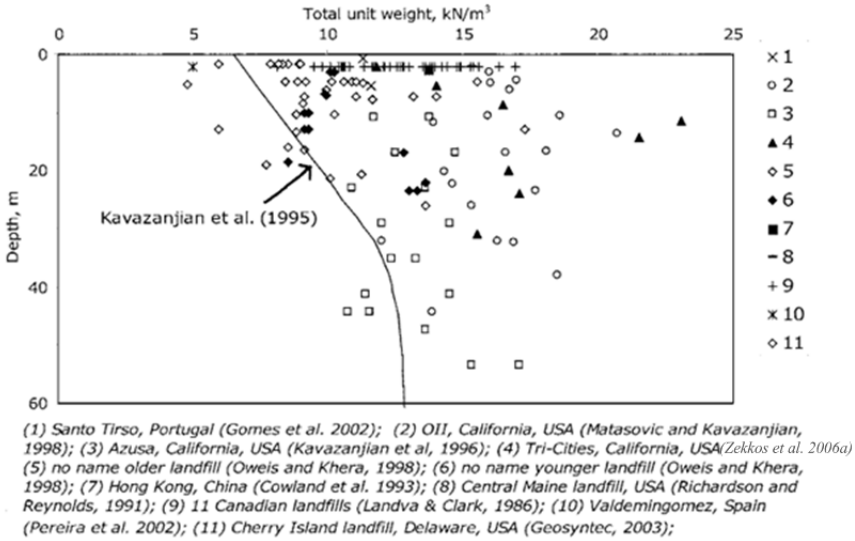

Figure 2.2 Unit weight values of MSW from in-situ measurements (Zekkos et al. 2006a).

Zekkos (2005) reported factors that affect MSW unit weight based on large-scale laboratory testing, such as confining stress and time under confinement. The relationship between MSW unit weight and confining stress level can be described by a hyperbolic equation. In addition, the effect of time under confinement on MSW unit weight is practically not significant. As only considering mechanical compression, there is less than 10% increase in MSW unit weight due to time under confinement for 50 years.

Zekkos et al. (2006a) proposed a unit weight profile model in the form of hyperbolic function which is expressed by Eq. 2.1. Values of α_γ and β_γ in this equation can be estimated

using Fig. 2.3. In addition, Fig. 2.4 shows the unit weight model with typical values of γ_{MSW}-$_i$, α_γ and β_γ shown in Table 2.1. In the absence of a geotechnical investigation, unit weight profiles like those in Fig. 2.4 can be used as guidance. Zekkos et al. (2006a) stressed that when using this recommendation the representative profile should be selected based on the expected near-surface in-situ unit weight. Furthermore, conservatism or a sensitivity analysis is suggested when using this recommendation.

$$\gamma_{MSW-z} = \gamma_{MSW-i} + \frac{z}{\alpha_\gamma + \beta_\gamma \cdot z} \tag{2.1}$$

where:

γ_{MSW-z} = Unit weight at depth z (kN/m^3)

γ_{MSW-i} = Unit weight at near surface (kN/m^3)

α_γ = Modeling parameter 1(m^4/kN)

β_γ = Modeling parameter 2 (m^3/kN)

Table 2.1 Parameters for different compaction effort and amount of soil cover (Zekkos et al. 2006a).

Compaction Effort and Soil Amount	γ_{MSW-i} (kN/m^3)	α_γ (m^4/kN)	β_γ (m^3/kN)
Low	5	2	0.1
Typical	10	3	0.2
High	15.5	6	0.9

Zekkos et al. (2006a) provides recommendations for selecting an appropriate landfill-specific characteristic unit weight profile for three situations: 1) Analysis or design based on a comprehensive geotechnical investigation, 2) analysis or design based on a limited investigation, and 3) analysis or design of a future landfill (i.e. with no investigation). In general, the evaluation of MSW unit weight is performed using test pits (i.e. for near-surface) and large diameter

boreholes (i.e. for greater depth). The weight of the excavated waste material can be measured using the landfill scales. Simultaneously, the volume of the excavated material can be estimated using survey measurements or using a "calibrated" backfill material or water replacement technique.

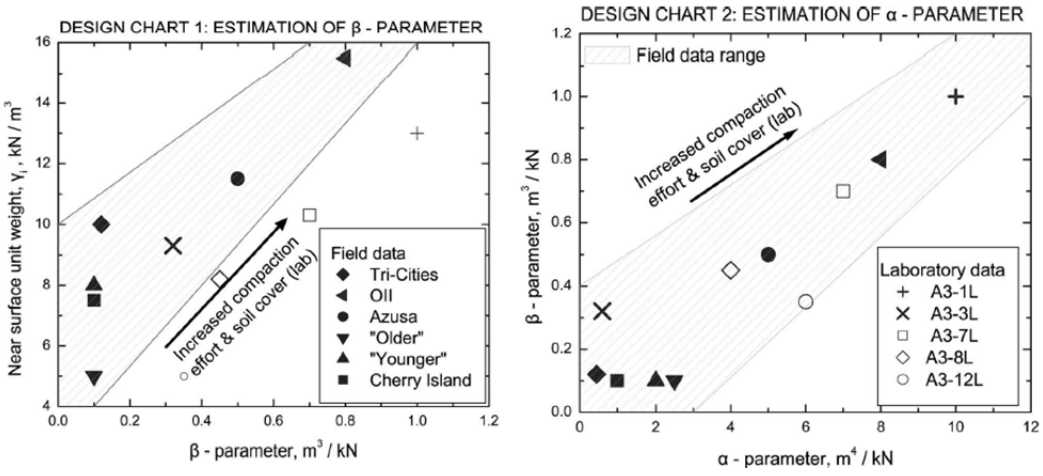

Figure 2.3 Design charts for the estimation of the α_γ and β_γ parameters from the near-surface unit weight (Zekkos et al. 2006a).

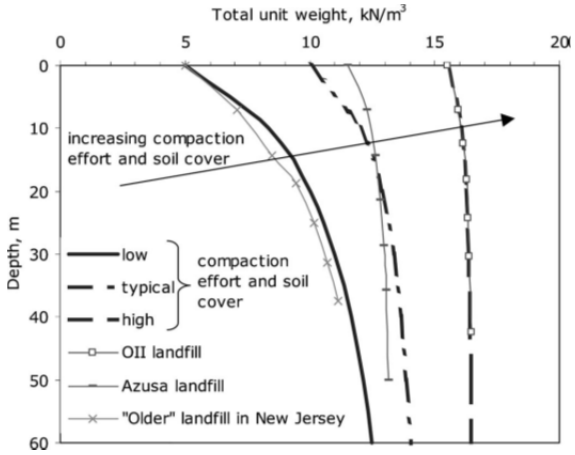

Figure 2.4 Recommended unit weight profiles for conventional municipal solid-waste landfills (Zekkos et al. 2006a).

2.4 Stress Wave Propagation

Stress waves are generated by natural and human activities on the ground surface or at depth. These mechanical wave motions are a mechanism of energy transfer or movement. The velocities of wave propagation in a medium are strongly related to the mechanical properties of the medium. It is important to distinguish between wave propagation velocity and particle velocity. Particle velocity represents how individual particles of the material move around their equilibrium points as the stress wave travels. This following briefly describes the fundamentals of wave propagation as well as some surface wave tests to measure wave propagation velocities.

In general, stress waves can be categorized into two groups: body wave and surface wave. Body waves travel through the interior of the medium and can be distinguished as the following:

- P-wave also known as compression wave, primary wave, dilatational wave, or irrotational wave
- S-wave also known as shear wave, secondary wave, distortional wave, or equivoluminal wave

The propagation characteristic of these body waves is illustrated in Fig. 2.5. Particle displacements/oscillations associated with the P-wave are in the same direction in which the wave is traveling. P-waves are capable of traveling through solid and fluid media. In a P-wave, particle displacements consist of rarefraction and compression. Particle displacements associated with S-waves are in a plane perpendicular to the direction of wave travel and only capable of traveling through solid media. P- and S-waves propagate with velocities of V_p and V_s, respectively and V_p is always faster than V_s by definition.

It is often convenient to separate particle motion associated with the shear wave into two components at right angles to each other. For example, in Fig. 2.6, it could be convenient to describe motion associated with a shear wave propagating in the same direction as the P-wave by two components; SV-wave in the vertical plane and SH-wave in the horizontal plane. This separation of S-wave components is convenient also when describing an anisotropic material where the SV-wave velocity and SH-wave velocity are different. SV-, VH-, and P-waves form a three-dimensional plane wave system that is capable of describing more complex types of waves (Rio 2006).

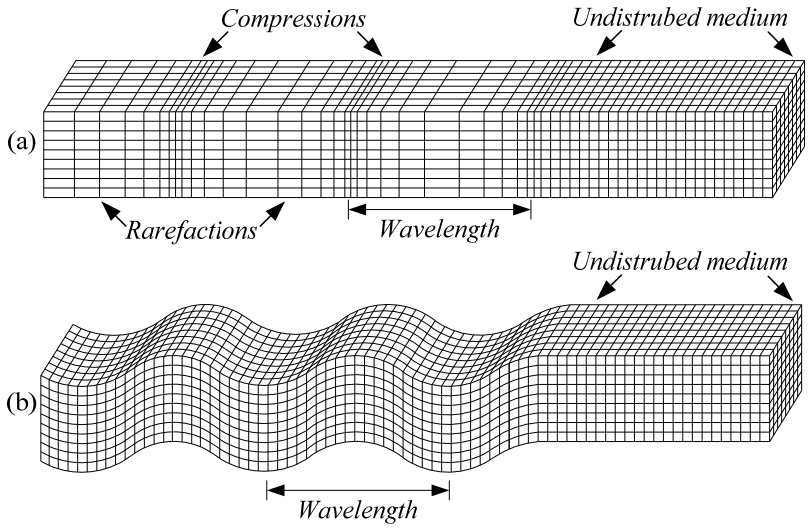

Figure 2.5 Propagation characteristic of (a) P-wave and (b) S-wave (Bolt, 1976).

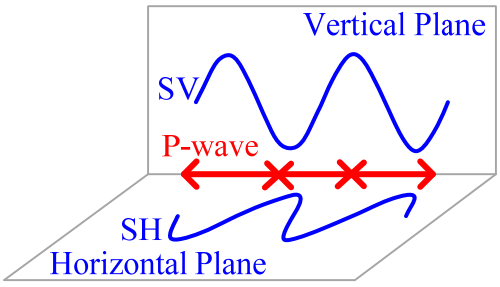

Figure 2.6 P-wave, SV, and SH

Surface waves occur at the interface between two different media and result from the interaction between body wave stresses at the boundary. Figure 2.7 illustrates the most important surface waves, Rayleigh-waves (Rayleigh 1885) and Love-waves (Love 1911). Particle motion associated with Rayleigh waves (R-waves) consists of combined to and fro motion in the direction of wave travel and vertical motion perpendicular to direction of wave travel. The combination of these particle motions is a retrograde ellipse at the surface. Love waves are created from the interaction between SH-waves with a soft near-surface layer. The influence of the surface waves decrease with depth.

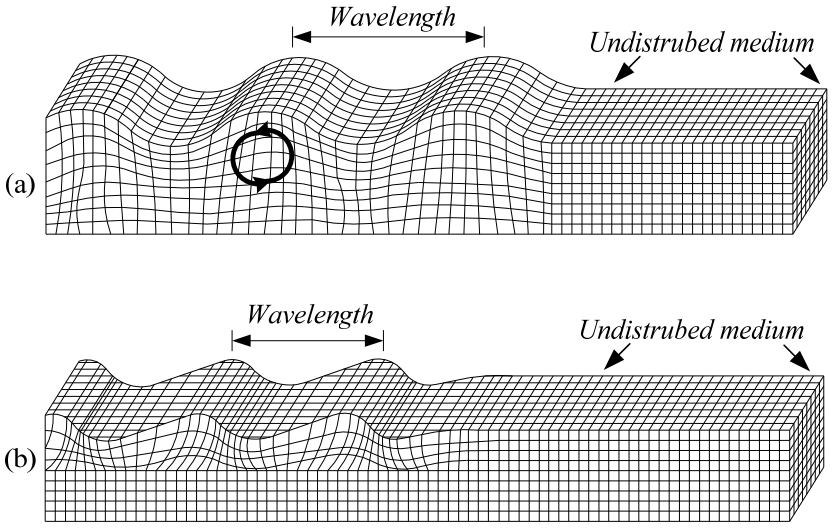

Figure 2.7 Propagation characteristic of (a) Rayleigh and (b) Love waves (Bolt, 1976).

When elastic waves propagate away from their sources, they progressively diminish in amplitude due to attenuation or damping. Damping can be separated into two types: material and geometrical (radiation) damping. In material damping, elastic energy is dissipated by means of energy conversion to another form, such as heat and is often called hysteretic damping. In geometrical damping, energy diminishes due to spreading of energy over a greater volume of material as the wave propagates farther away from its source. Figure 2.8 illustrates stress wave

propagation and characteristic geometrical damping laws. The geometrical damping for body waves that propagate along the free surface of a uniform halfspace is proportional to r^{-2}, where r is the radius from the wave source. Inside a semi-infinite body, the geometrical damping for body waves is proportional to r^{-1}. Rayleigh waves that propagate along the surface have geometrical damping proportional to $r^{-0.5}$. Thus, the farther the stress waves propagate from the source, the greater the amplitude ratio between Rayleigh wave and body waves. Accordingly, R-waves is the most significant disturbance along the surface.

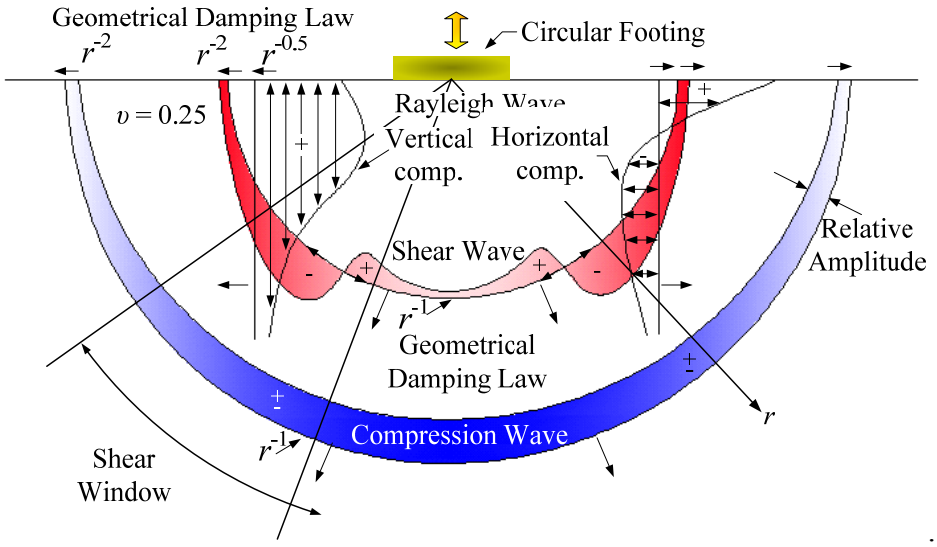

Figure 2.8 Far field displacement field for dynamically loading circular footing on an elastic half space (Woods 1968).

2.4.1 Surface Wave Testing

In the last couple decades, surface wave testing has gained attention for measuring shear wave velocity in the field. Surface wave testing offers a fast, reliable, and non-invasive. In downhole, crosshole, reflection, and refraction seismic testing, shear wave velocity is measured directly. Surface wave testing is an alternative to these techniques where surface wave velocity is used as a proxy to measure shear wave velocity. Most often the Rayleigh wave or ground roll is used in

the surface wave testing, but less frequently the Love wave has also been used (e.g. Mari 1984, Song et al. 1989, and Turner 1990).

In general, surface wave testing involves three steps, data acquisition in the field, dispersion curve extraction, and the inversion process. In the data acquisition stage, surface waves can be generated using either active or passive sources. In active testing, the wave source is relatively well-controlled. Examples of active sources are sledge hammers, explosives, vibroseises, drop weights, and bulldozers. The active testing with small wave source energy, such as a sledge hammer, usually provides a surface wave with high frequency content. The high frequency surface waves are generally suitable for near-surface investigation. In passive testing, the surface wave source is ambient noise, such as cultural noise (e.g. highway traffic), construction activities, or natural noises (e.g. wind movement and ocean waves). These types of wave sources are relatively uncontrolled and special techniques are used in reducing the passive data. Nevertheless, passive testing creates surface waves with low frequency content that provide information for deeper investigation when an active source with high energy and low frequency is not readily available. Field data is commonly acquired using geophones or accelerometers.

Field data can be processed using a simplified method or an advanced integral transformation to obtain an experimental or measured dispersion curve. This dispersion curve describes the relationship between surface wave velocity and frequency or wavelength in the field. In a layered subsurface, surface wave exhibit dispersive nature, i.e. wave propagating at different velocities for different frequencies or wavelengths. In an isotropic single layer material, such as a halfspace, this dispersive nature does not occur as the surface wave travels at a specific velocity, independent of frequency or wavelength.

In inversion process or forward-modeling, an assumed shear wave velocity profile is used to calculate the theoretical dispersion curve. Subsequently, the theoretical dispersion curve is compared with the measured dispersion curve. Iteration process is performed by modifying the shear wave velocity profile. A solution is obtained when a shear wave velocity profile has theoretical dispersion curve that matches with the measured dispersion curve.

There are several surface wave testing techniques, namely Continuous Surface Wave testing, Spectral-Analysis-of-Surface-Wave testing, Multi-channel Analysis of Surface Wave testing, and Microtremor Analysis Method testing. In this section, Continuous Surface Wave testing and Spectral-Analysis-of-Surface-Wave testing are described. The other two techniques are described in another chapter.

2.4.1.1 Continuous Surface Wave Testing

The pioneering works in surface wave testing stem from Van der Pool (1951) and Jones (1955, 1962) and led to the development of the methodology known as continuous surface wave (CSW) or steady-state surface wave. Figure 2.9 illustrates the testing setup for steady-state surface wave testing. An electromechanical vibrator is used as an active wave source at variable frequencies and two vertically oriented geophones are used as receivers. Subsequently, the second geophone is relocated progressively away from the vibrator to measure wavelengths on the surface. The spacing between two geophones that shows the steady-state in phase waveform is considered as one wavelength (λ). Several wavelengths are determined at each frequency. Then this step is repeated with different frequencies to find another wavelengths. Finally, the relationship between surface wave velocity (V_{ph}) and frequency (f) (i.e. dispersion curve) can be extracted using Eq. 2.2.

$$V_{ph} = \lambda \cdot f \tag{2.2}$$

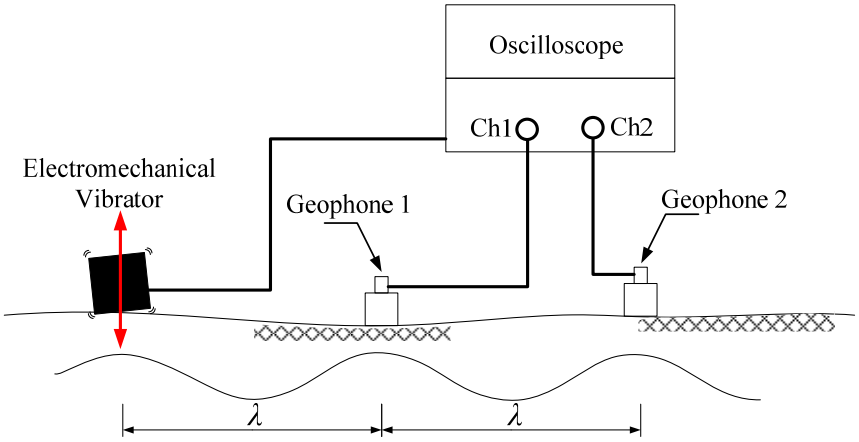

Figure 2.9 Continuous surface wave testing.

The shear wave velocity profile is developed using the following equations.

$$V_s = 1.1 \cdot V_{ph} \tag{2.3}$$

$$z = 0.5 \cdot \lambda \tag{2.4}$$

where z is depth of investigation. Eq. 2.4 was based on field investigations reported by Ballard (1964).

Equations 2.3 and 2.4 show that shear wave velocity profile in the CSW method is obtained in a simple way. The CSW method may provide a reliable estimate for a profile that shear wave velocity increases with depth. For an irregular shear wave velocity profile, such as profile with high contrast shear wave velocity and profile with shear wave velocity decreases with depth, the CSW method may not be able to provide a reliable solution of shear wave velocity profile.

2.4.1.2 Spectral-Analysis-of-Surface-Wave Testing

Spectral-Analysis-of-Surface-Wave (SASW) testing is an advanced surface wave testing that was developed at the University of Texas at Austin in 1980s (Nazarian and Stokoe 1984).

Compared to CSW, SASW is more effective and efficient as there is no need to relocate the geophones to measure wavelength. In SASW, impact or random wave sources are used as they are capable of generating multi-frequencies or wavelengths. Portable electronic devices with capability to perform signal processing analysis offer frequency or wavelength measurement of the recorded surface waves in the field. Similar to other surface wave testing, SASW involves data acquisition in the field, dispersion curve analysis, and inversion or forward-modeling of shear wave velocity profile.

A general testing setup for the SASW is presented in Fig. 2.10. According to Stokoe et al. (1994), SASW field testing is performed by generating surface waves at a point and recording the generated surface waveform using two vertically oriented geophones. The spacing between two geophones is progressively increased to measure longer wavelengths. The spacing between the geophones (s) remains equal to the spacing between the source and the first geophone. SASW testing is conducted with several sets of spacings that are called as an SASW array.

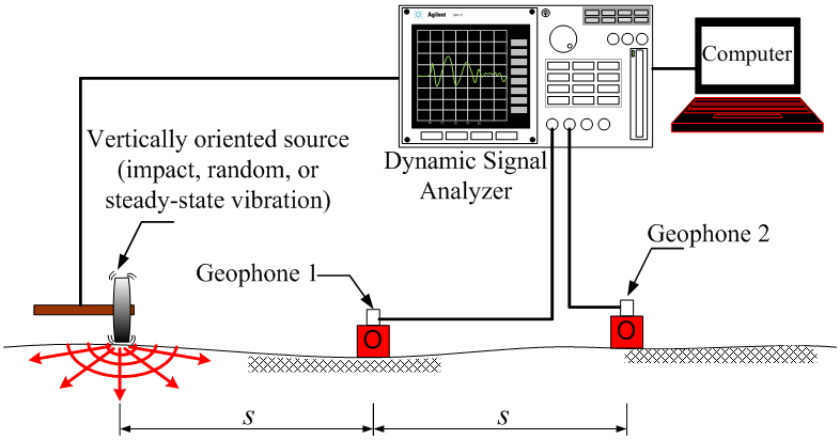

Figure 2.10 General testing setup of Spectral-Analysis-of-Surface-Wave.

The phase velocity of the surface wave can be calculated at each frequency (f) using the following equation:

$$V_{ph} = f \cdot \left(\frac{360}{\phi} \right) \cdot s \tag{2.5}$$

where ϕ is phase angle between geophones that can be calculated using integral transformation of the recorded surface wave at two geophones. Thus, a measured or field dispersion curve can be constructed. Subsequently, an iterative forward modeling or inversion process is performed to construct a theoretical dispersion curve that matches the field dispersion curve. A variety of algorithms can be used to perform the forward-modeling iteration (e.g. Pezeshk and Zarrabi 2005). Stokoe et al. 1994 describe the SASW method in more detail.

2.5 Small-strain Shear Modulus of MSW

Small-strain shear modulus and shear wave velocity are among the most important properties for dynamic analyses as well as seismic response analyses. They are related using elasticity theory through the following equation:

$$G_{\max} = \rho V_s^2 \tag{2.6}$$

where ρ is the density of MSW (equal to the total unit weight of the material divided by the gravitational acceleration). These properties as well as small-strain damping ($D_{\min}$) represents to the dynamic properties in the linear shearing strain range. In addition, the small-strain shear modulus ($G_{\max}$) should not be confused with other shear moduli, such as tangent shear modulus and secant shear modulus (Fig. 2.11).

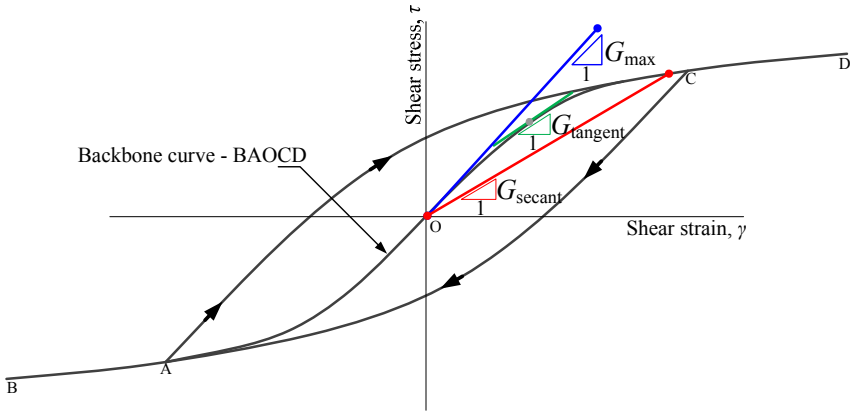

Figure 2.11 Illustration of G_{max}, G_{secant}, and $G_{tangent}$ (after Idriss et al. 1978).

2.5.1 Laboratory Evaluation of Dynamic Properties of MSW in the Small-strain Range

Dynamic properties of MSW have been evaluated extensively in the laboratory by a collaborative research among several institutions, namely the University of California at Berkeley, the University of Texas at Austin, Arizona State University, and Geosyntec Consultants. Evaluations of the small-strain characteristic of MSW from this collaboration can be found in Zekkos 2005, Zekkos et al. 2008, Lee 2007, and Yuan et al. 2011. In these studies, MSW specimens were collected from the Tri-Cities landfill in Fremont, California. In this section, a summary of these comprehensive studies on the linear dynamic properties are presented. Findings on the nonlinear dynamic properties of MSW are discussed in the next section.

Zekkos et al. (2008) performed extensive large-scale stress-controlled cyclic triaxial testing under a wide range of confining pressure to evaluate the small-strain behavior of MSW. In this study, 25 large-scale remolded MSW specimens (d = 300 mm, h = 630 mm) were used in more than 90 cyclic triaxial test series. The small-strain shear modulus was measured in the laboratory and the corresponding shear wave velocity was compared with field test results (Fig. 2.12). Specimens that included 100% < 20 mm material (i.e. 100% soil like material) yielded

slightly higher shear wave velocities than those measured in the field. Specimens that included 62-75% soil-like fractions had similar or slightly lower V_s compared to the field. Specimens with 8-25% soil like-fractions have lower values than V_s in the field. Differences in time under confinement, waste composition, aging, and bonding between laboratory and in-situ condition could justify differences in test results. In addition, sample reconstitution and waste anisotropy may be other explanations for these differences.

Zekkos et al. (2008) evaluated a variety of factors affecting the small-strain behavior of MSW, namely confining stress, unit weight, loading frequency, composition, and time under confinement. Figure 2.13 shows that specimens including only soil-like particles tend to have considerably higher G_{max} than that of specimens with less soil-like fractions at the same confining stress. In terms of unit weight, specimens of varying composition with lower unit weight have lower G_{max} (Fig. 2.14). This result also suggested that unit weight could be an index for waste composition. Zekkos et al. (2008) also found strong relationship between loading frequency and G_{max}, that was G_{max} increased with the loading frequency. Additionally, Zekkos et al. (2008) concluded that G_{max} increased with time under confinement (Fig. 2.15). Table 2.2 sumarizes the effect of these parameters on the G_{max} of MSW. Description about G/G_{max} and D in this table will be presented later in section 2.6.

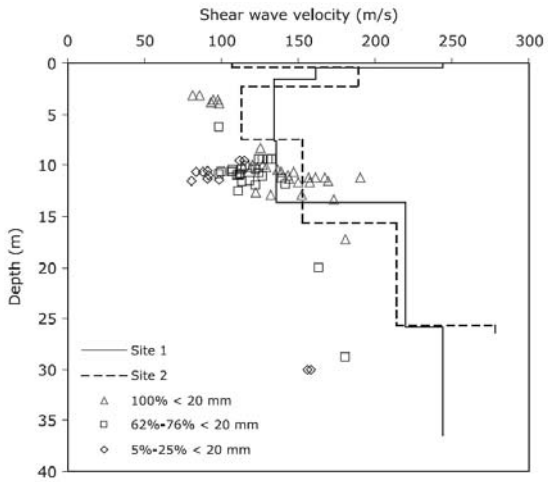

Figure 2.12 Comparison of shear wave velocity of MSW measured in the laboratory and in the field (Zekkos et al. 2008).

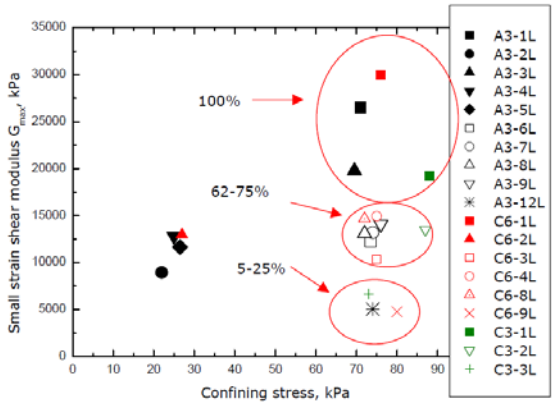

Figure 2.13 Effect of confining stress and composition on the small strain shear modulus. Percentages indicate composition by weight of smaller than 20 mm fraction (Zekkos 2005).

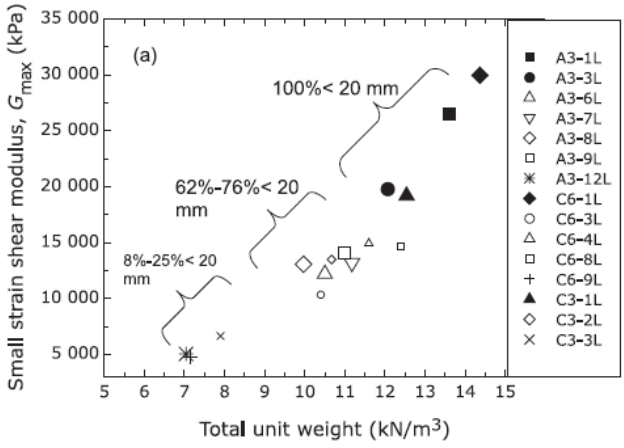

Figure 2.14 Effect of unit weight on the small strain shear modulus. Percentages indicate composition by weight of smaller than 20 mm fraction (Zekkos et al. 2008).

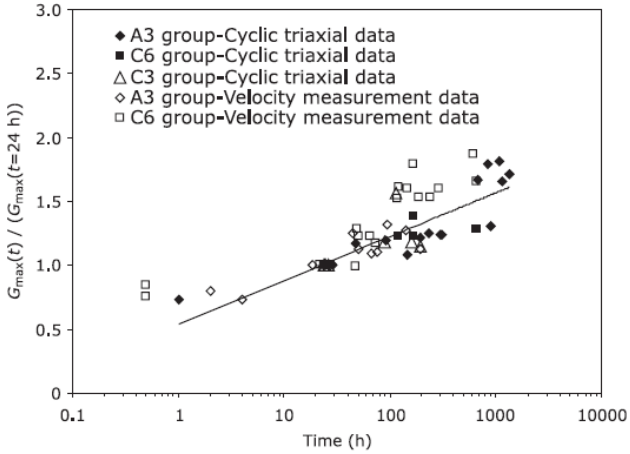

Figure 2.15 Effect of time under confinement on small-strain shear modulus (Zekkos et al. 2008).

Table 2.2 Effect of different parameters on the G_{max} of MSW (Zekkos et al. 2008).

Effect of: \ Property:	G_{max}
Composition	Very important
Confining stress	Important
Unit weight	Important
Loading frequency	Important
Time under confinement	Important

Lee (2007) evaluated the effect of various parameters on G_{max} using resonant column and torsional shear (RCTS) tests and large scale free-free resonant column (LSRC) tests on remolded specimens with diameter of 2.8" and 6", respectively. These devices were used to perform low amplitude resonant column (LARC) in which the shear strains were kept below 0.002% and 0.001 % in RCTS and LSRC, respectively. The parameters studied were duration of confinement, confining pressure, loading frequency, specimen size, waste composition, water content, unit weight, and particle size. This research showed that: 1) G_{max} increased with duration of confinement, 2) G_{max} increased significantly with confining pressure, 3) frequency of

excitation had a moderate effect on G_{max}, 4) the waste composition had a moderate effect on G_{max}, 5) water content increase had small effect on G_{max}, and 6) the effects of variation of total unit weight on G_{max} was small for the same waste composition.

Yuan et al. (2011) performed large-scale cyclic simple shear test on reconstituted rectangular specimens of MSW with dimensions of 304 mm x 406 mm. Specimens were reconstituted using three different compositions of waste: 100%, 65%, and 35% by weight of soil-like constituents (i.e. smaller than 20 mm) and four different levels of compaction effort. All specimens were consolidated under a normal stress of 75 kPa prior to testing. The extrapolated linear trends for the three composition ratios show closely-spaced and nearly parallel patterns (Fig. 2.16). This pattern suggested a dependence of V_s and G_{max} on composition ratio, with a greater amount of soil-like material resulting in G_{max} and higher V_s for the same total unit weight. In addition, the test results show a very strong dependence of V_s and G_{max} on unit weight (Fig. 2.17).

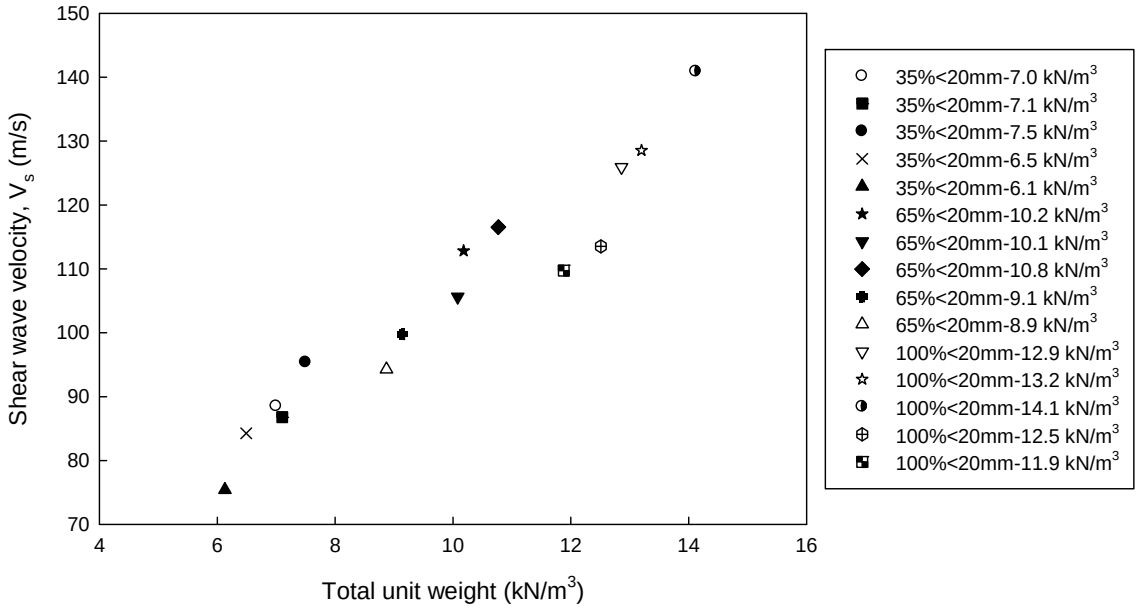

Figure 2.16 Shear wave velocity versus total unit weight (Yuan et al. 2011).

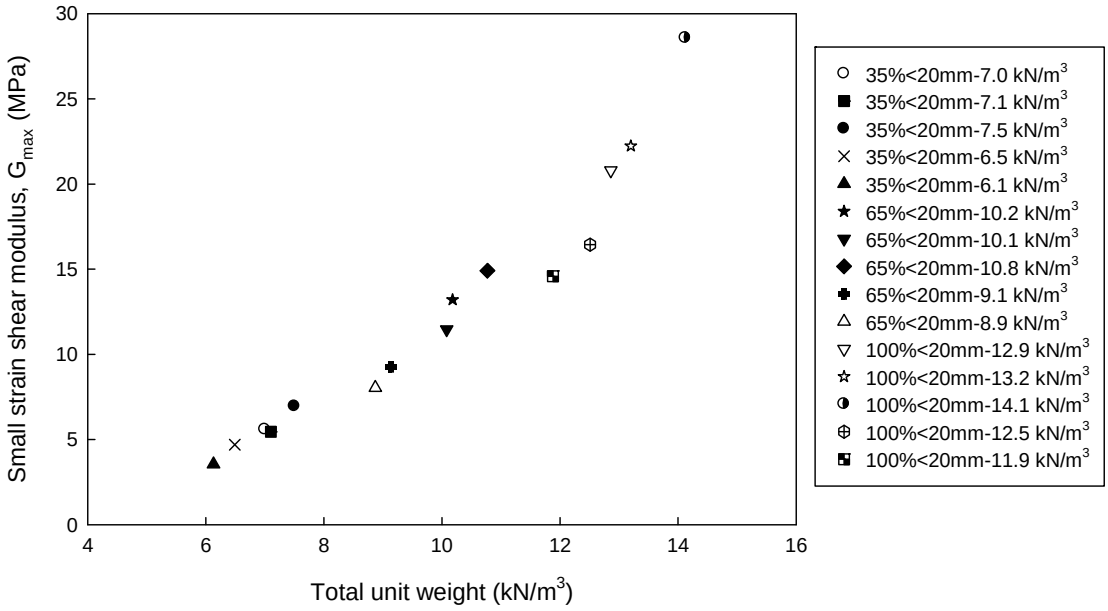

Figure 2.17 Small-strain shear modulus versus total unit weight (Yuan et al. 2011).

2.5.2 Field Investigation of Dynamic Properties of MSW in the Small-strain Range

A number of investigators have evaluated V_s of MSW in the field using seismic techniques, such as refraction, seismic downhole, seismic crosshole, suspension logging and surface wave methods. In particular, surface wave methods are very attractive in measuring V_s of MSW in-situ as they are non-intrusive (i.e. they do not require drilling), efficient, and reliable (Zekkos and Flanagan 2011). The SASW method (Stokoe et al. 1994) has been used widely at various landfills including in California, Georgia, Spain and elsewhere. Additionally, the Multichannel Analysis of Surface Waves (MASW) technique (Park et al. 1999a) and passive Microtremor Analysis Method or MAM (Okada 2003) have been used recently at modern landfills in Michigan (Sahadewa et al. 2011 and Sahadewa et al. 2012).

A great number of field V_s measurements in California landfills have been reported in literature. Sharma et al. (1990) performed seismic downhole tests in a landfill located at City of Richmond, California to evaluate Poisson's ratio of refuse material. They reported an average V_s

of about 198 m/sec for a depth of 0 to 15.3 m. Kavazanjian et al. (1994) reported V_s profiles at eight landfills in Southern California using the SASW and Controlled Surface Wave (CSW)/Steady State Surface Wave (SSSW) surveys. This study reported that shear wave velocities were as low as 80 m/sec near the surface to over 300 m/sec at a depth of 30 m. Kavazanjian et al. (1995) developed a recommended V_s profile for use in practice for site seismic response analysis of California landfills (Fig. 2.18). This recommendation was developed based on a series of investigations using CSSW and SASW in OII landfill. Kavazanjian et al. (1996) proposed a recommended range of shear wave velocity profiles for landfills in Southern California (Fig. 2.18). This recommendation was developed based on the results of CSW and SASW surveys in 6 landfills: OII landfill, Azusa landfill, Sunshine Canyon landfill, Lopez Canyon landfill, Toyon Canyon landfill, and a landfill designated as Landfill A. Matasovic and Kavazanjian (1998) performed downhole seismic test and SASW surveys in OII landfill. In the SASW surveys, a vibroseis truck was utilized to generate the dynamic force. The result of this study is also presented in Fig. 2.18. Morochnik et al. (1998) also investigated the shear wave velocity at the OII landfill. In this study, two locations (SS1 and SS2) at the OII landfill were investigated using the suspension logging method and SASW surveys (Fig. 2.19). Lin et al. (2004) investigated shear wave velocities at 14 locations in the Tri-Cities landfill, the Altamont landfill, and Redwood landfill in northern California. In this study, SASW method was performed using different sources: 1) a hand-held hammer and 2) a D9R or D6 tractor. The results from this investigation are shown in Fig. 2.20.

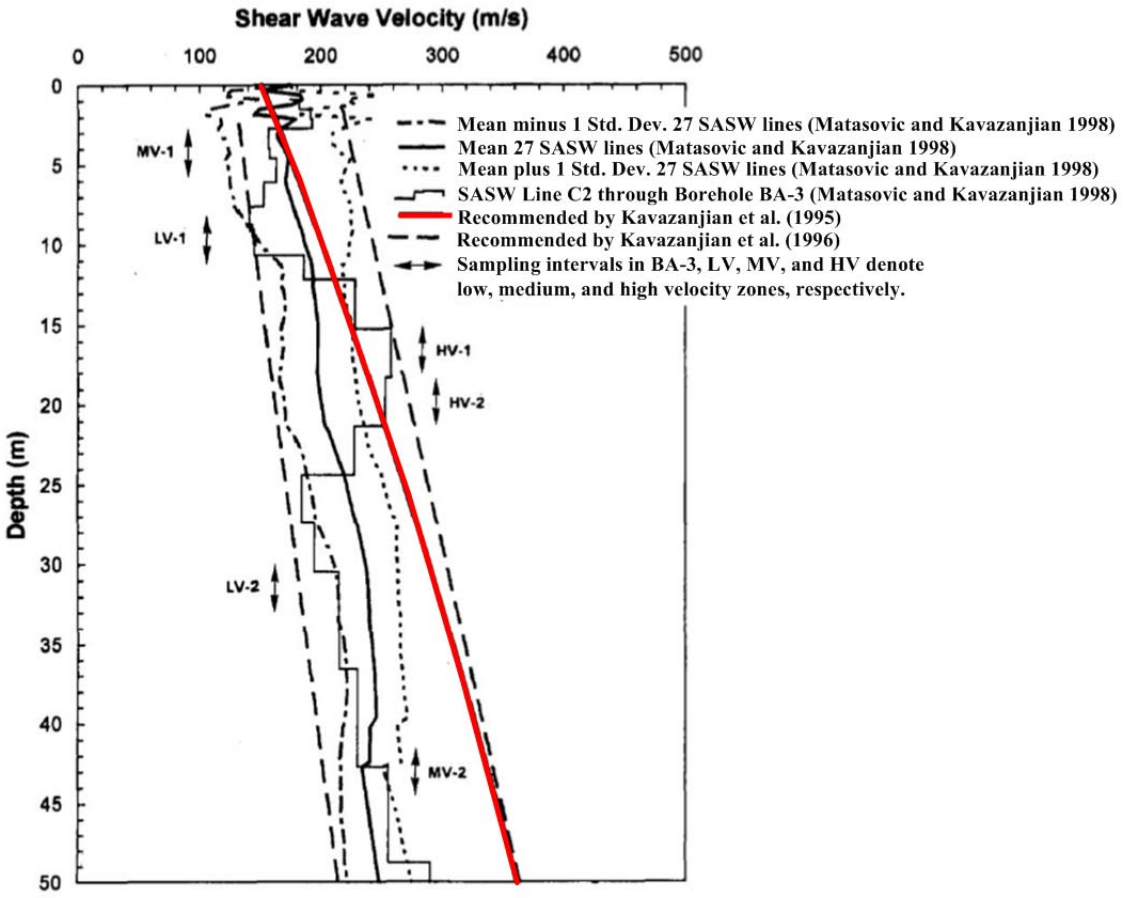

Figure 2.18 Shear wave velocity profiles at the OII landfill (Matasovic and Kavazanjian 1998).

Houston et al. (1995) developed V_s and V_p profiles using surface profiling and seismic downhole test in the Northwest Regional Landfill Facility (NWRLF), Maricopa County, Arizona. Figure 2.21 shows the V_s and V_p profiles of NWRLF. The soil cover in the tested location had higher shear and compression wave velocity than the solid waste material.

Rix et al. (1998) investigated the shear wave velocity at Sanifill and Bolton landfill in Atlanta, Georgia using a simultaneous inversion of surface wave velocity and damping measurements. Thus, the authors were able to estimate both the V_s profiles as well as the small-strain damping profiles for both landfills. The V_s profiles from these landfills are presented in Fig. 2.22.

Shear wave velocity field investigations have also been reported for landfills in Spain. Cuellar et al. (1998) evaluate the shear wave velocity in Villalba waste dump, near Madrid, using the SASW technique. Pereira et al. (2002) measured the shear wave velocity using the SASW method in Valdemingomez landfill near Madrid. Shear wave velocity profiles of Villalba and Valdemingomez landfill are shown in Fig. 2.23.

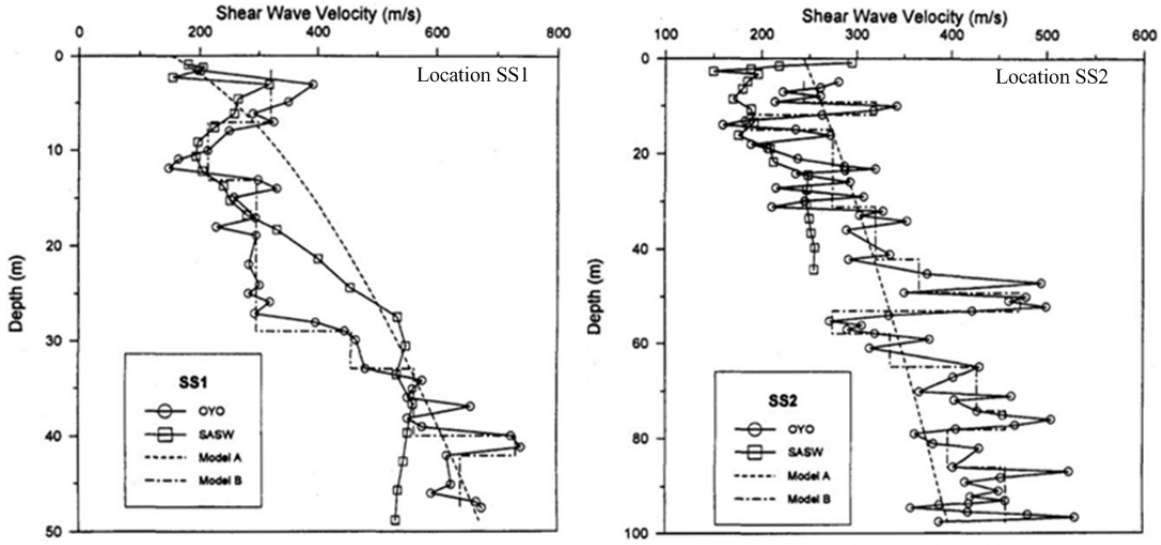

Figure 2.19 Shear wave velocity profiles in two locations at the OII landfill (Morochnik et al. 1998).

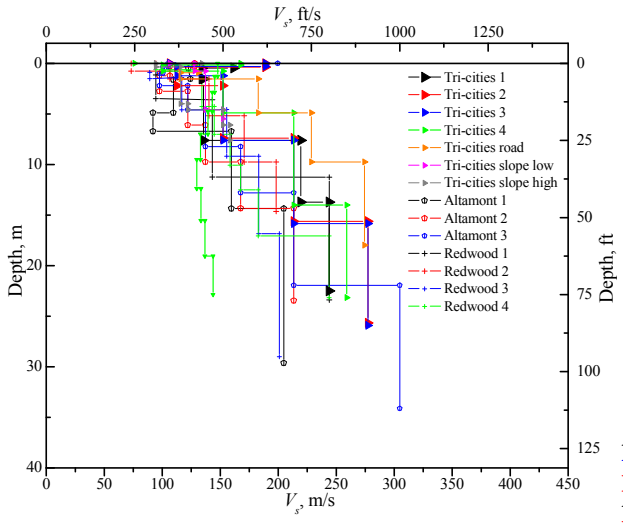

Figure 2.20 Shear wave velocity profiles at 3 landfills in northern California (data from Lin et al. 2004).

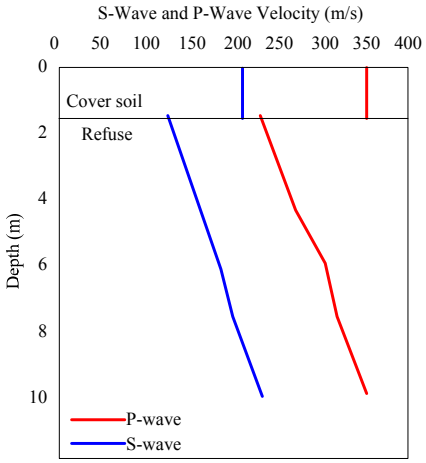

Figure 2.21 Body wave velocity profiles at the NWRLF (after Houston et al. 1995).

In-situ V_s measurements have also been performed in a number of landfills in southeast Michigan (Sahadewa et al. 2011). Figure 2.24 shows V_S profiles from Sauk Trail Hill landfill, Oakland Heights landfill, Carleton Farms landfill, and Arbor Hills landfill. Field investigations in these landfills and test results are presented in more detail in a chapter in this thesis.

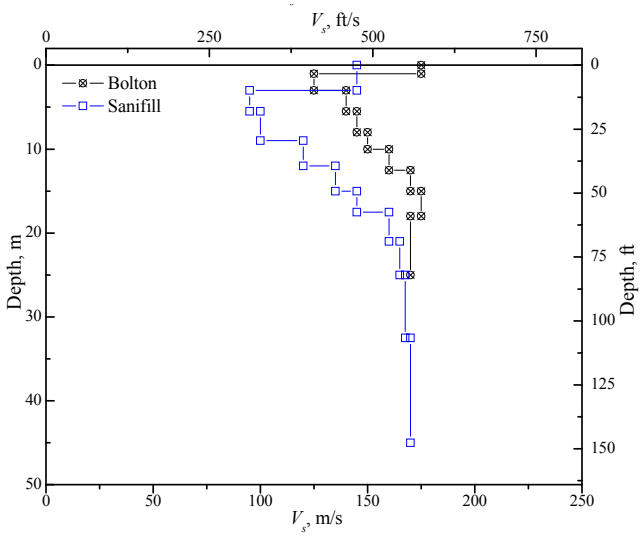

Figure 2.22 Shear wave velocity profiles at Sanifill and Bolton landfill (data from Rix et al. 1998).

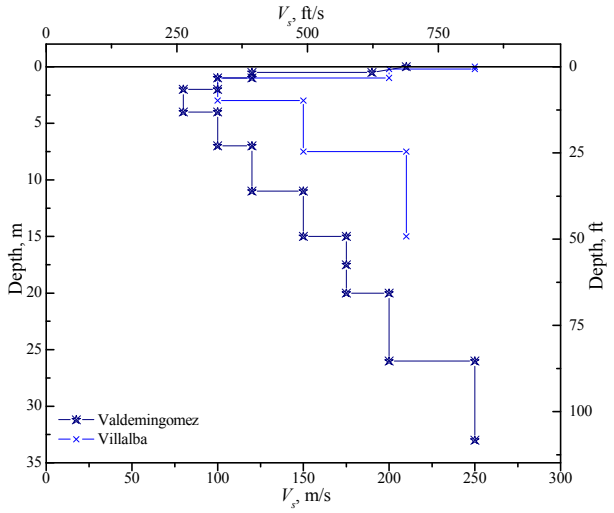

Figure 2.23 Shear wave velocity profiles at Villalba and Valdemingomez landfill (data from Cuellar et al. 1998 and Pereira et al. 2002).

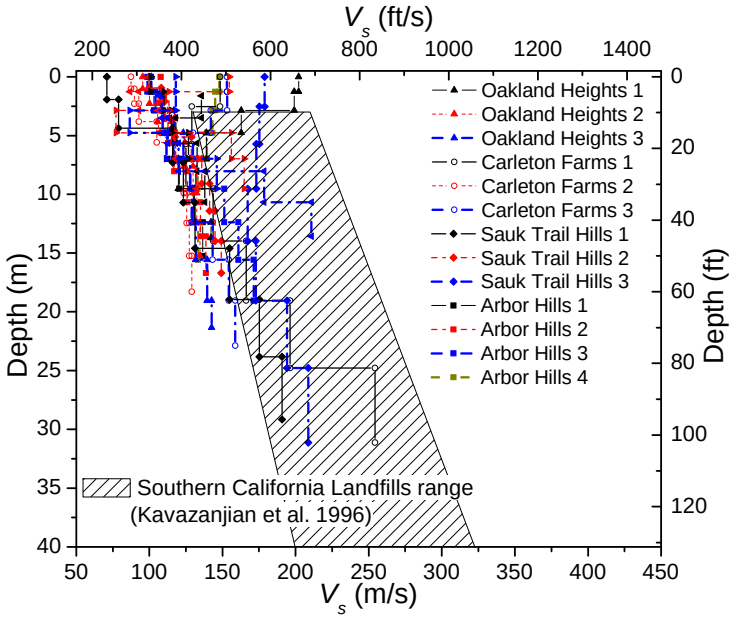

Figure 2.24 Shear wave profiles at 4 landfills in Michigan (Sahadewa et al. 2011).

2.6 Dynamic Properties of MSW in the Nonlinear Shear Strain Range

The stress-strain relationships of geomaterials, including MSW, are nonlinear beyond a certain level of shearing strain under large-amplitude dynamic loading. The dynamic properties in the nonlinear shear strain range are associated with the relationship of G/G_{max} or D with shear strain (Fig. 2.25). These nonlinear dynamic properties are amongst the most important parameters for

any site response analysis as they have the largest overall effect on the calculated response (Augello et al. 1998a).

A number of studies evaluating these nonlinear dynamic properties of waste material are summarized in this section. In general, investigation of nonlinear dynamic properties of geomaterial can be performed using back calculation from earthquake records (e.g. Zeghal et al. 1995; Chang et al. 1996; Ghayangmghamian and Kawakami 2000; and Kokusho et al. 2005), laboratory testing (e.g. Vucetic and Dobry 1991 and Darendeli 2001), and in-situ testing (e.g. Henke and Henke 1993 and 2002; Salgado 1997; Roblee and Riemer 1998; Phillips 2000; Stokoe et al. 2001, 2006, 2011; Axtell et al. 2002; Cox 2006; Kurtulus 2006; Safaqah and Riemer 2006, Park 2010). The emphasize in the next section is on MSW studies.

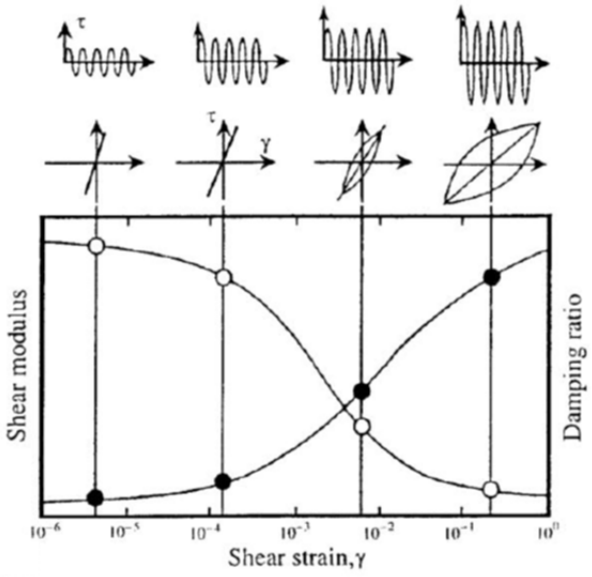

Figure 2.25 General relationship of shear modulus and damping ratio with shear strain (Ishihara 1976).

2.6.1 Early Investigations of Dynamic Properties of MSW in the Nonlinear Strain Range

Singh and Murphy (1990) provided an early recommendation of G/S_u (i.e. equivalent to G/G_{max}) or D versus shear strain curves for MSW by averaging corresponding curves from clay and peat

(Fig. 2.26). These recommended curves were developed with the assumption that the material strength properties of waste were more cohesive than frictional. Thus, the recommended G/S_u or D versus shear strain curves is similar to those of peat and clay. It should be noted that at the time of this publication, laboratory dynamic testing data or field observations of the response of landfills were not available.

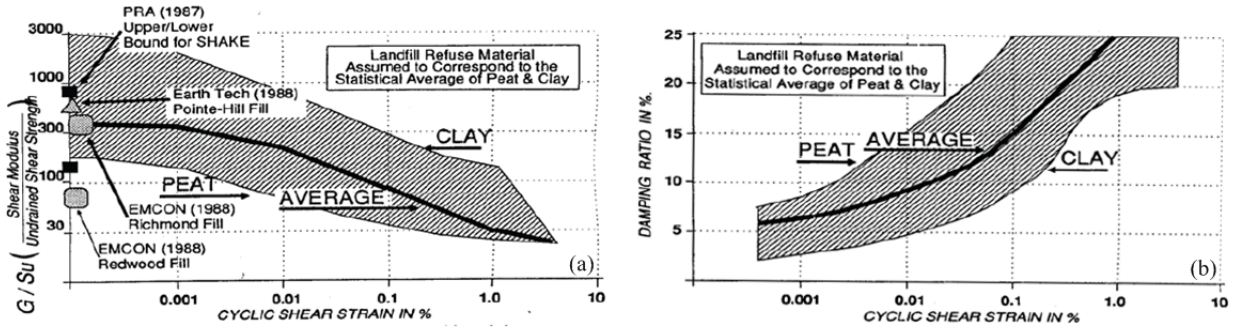

Figure 2.26 (a) Normalized shear modulus reduction and (b) material damping curves from a number of studies (Sing and Murphy 1990).

2.6.2 Back Calculation Using Earthquake Records in Investigations of Dynamic Properties of MSW in the Nonlinear Strain Range

To the author's knowledge, the overwhelming majority of back calculation of dynamic properties of MSW in the nonlinear shear strain range involved numerical analyses using strong motion station records in OII landfill, California. Accelerometers have been installed since 1987 at the crest and near the toe of this landfill and have recorded the ground motions from a series of earthquakes, including the 1994 Northridge earthquake.

Kavazanjian et al. (1995) derived shear modulus reduction and material damping curves for MSW by back-calculating the response of the OII landfill using the Northridge and Landers earthquake records from OII landfill (Fig. 2.27). These curves are developed using the modified Kondner and Zelasko (MKZ) model parameters described in Matasovic and Vucetic (1993).

Using these nonlinear dynamic properties as well as MSW unit weight and shear wave velocity profiles recommended in the same paper, Kavazanjian et al. (1995) performed two site response analyses, namely 1-D equivalent linear analysis and truly nonlinear analysis using SHAKE and D-MOD, respectively. These analyses showed good agreement.

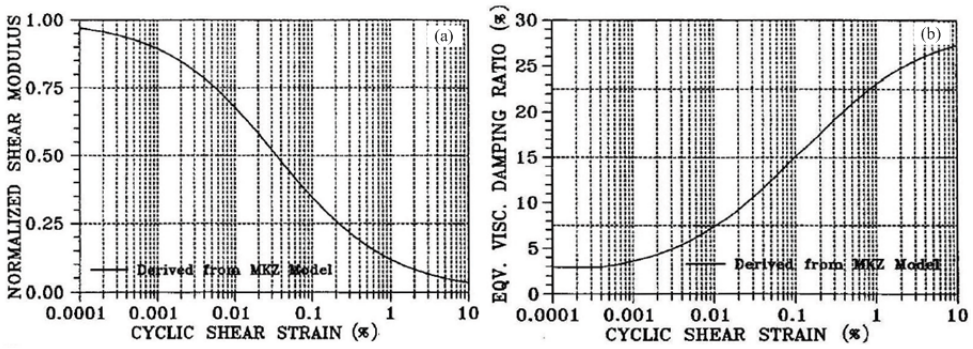

Figure 2.27 (a) Normalized shear modulus reduction and (b) material damping curves of solid waste (Kavazanjian et al. 1995).

Idriss et al. (1995) developed shear modulus reduction and material damping curves for the OII landfill using the strong motion records from four earthquakes (Fig. 2.28). Back-calculation of both nonlinear dynamic properties of MSW was performed using 1-D and 2-D equivalent-linear finite element analyses of a single cross-section in this landfill. In addition, Idriss et al. (1995) also reported that the shear modulus reduction curve of MSW is similar to that of high plasticity clay.

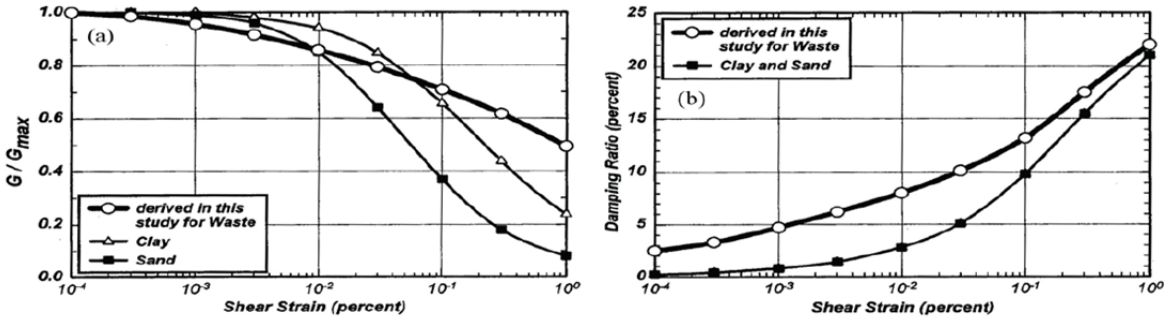

Figure 2.28 (a) Normalized shear modulus reduction and (b) material damping curves of solid waste from Idriss et al. (1995).

Matasovic and Kavazanjian (1998) proposed recommendations for shear modulus reduction and material damping curves (Fig. 2.29). These curves were developed using a combination of back-calculation of time-history records of the OII landfill and results from large-scale cyclic simple shear testing on 9 large-diameter (450 mm) specimens collected from the same landfill. In this study, 2-D equivalent-linear analysis was performed using QUAD4M and acceleration from east-west component of 5 earthquakes recorded by OII's accelerometers. Best-estimate geometry, unit weight, shear wave velocity profile, and Poisson's ratio were used in the analysis and yielded shearing strains up to 0.1%. In addition, shearing strains from 0.1 % up to 7% was generated from cyclic simple shear testing. Consistency between the back calculation analysis and cyclic simple shear testing was checked using Masing criteria (Masing 1926) to propose "internally consistent" curves. They recommended that the upper bound shear modulus reduction and the lower bound of damping ratio curve should be used for site response analyses. This suggestion was proposed for several reasons: 1) the upper bound shear modulus curve was more consistent with that of back-calculation analysis, 2) the upper bound shear modulus reduction and the lower bound of damping ratio curves are considered to be conservative in term of acceleration response at the landfill surface, and 3) samples for laboratory testing may experience disturbances that may have yielded higher shear modulus reduction.

Augello et al. (1998a) generated shear modulus reduction and damping ratio curves for OII landfill (Fig. 2.30). In this study, 2-D equivalent-linear analysis of two perpendicular horizontal cross-sections was performed using strong motion records from 5 different earthquake events with calculated shearing strain up to 0.15%. Comparisons between the calculated and observed motions were conducted using objective statistical analysis technique that allowed the

authors to derive recommended modulus reduction and damping curves. The results of this study were compared with recommended clay curves from Vucetic and Dobry (1991). The conclusion from the comparison was that the best fit to the recorded response in OII landfill was obtained for the nonlinear dynamic property curves that fell between the clay curves for PI = 30 and 100 at small strain and closer to PI = 30 at larger strain.

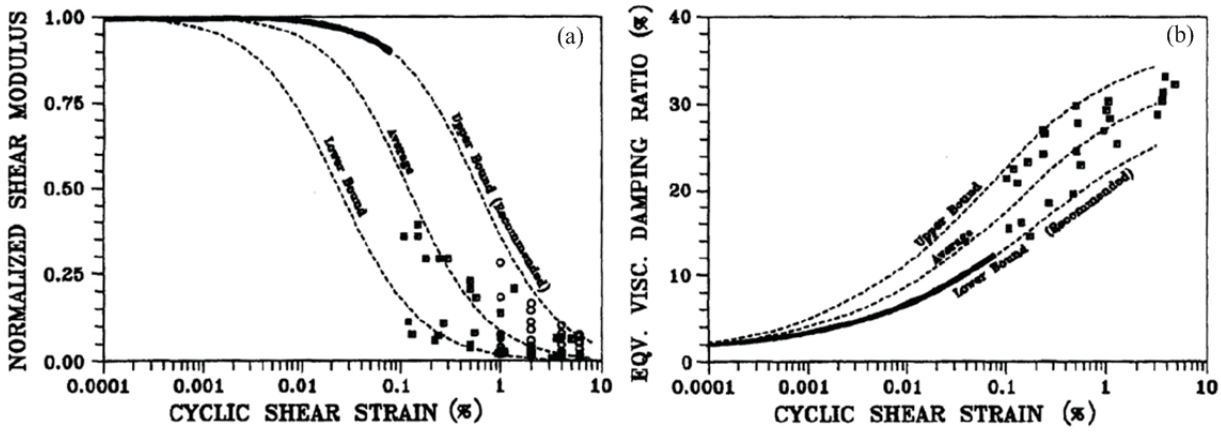

Figure 2.29 (a) Normalized shear modulus reduction and (b) material damping curves of solid waste from Matasovic and Kavazanjian (1998).

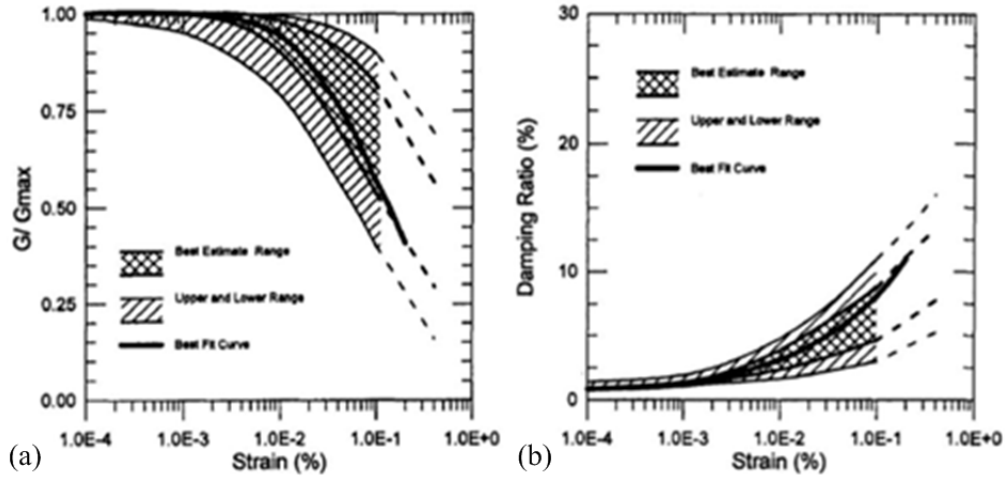

Figure 2.30 Recommended (a) normalized shear modulus reduction and (b) material damping curves from Augelo et al. (1998a).

Morochnik et al. (1998) evaluated the nonlinear dynamic properties of OII landfill using time-history records of 10 earthquake events, field investigation results, and a simplified physical model. In addition, system identification techniques were used to study the nonlinear dynamic properties of MSW. This study showed that the materials behaved as a linear viscoelastic material with insignificant reduction in shear modulus for shear strain amplitude up to 0.08%. Additionally, material damping was frequency dependent in the frequency range of 0.1 to 10 Hz. Figure 2.31 shows the results of this study.

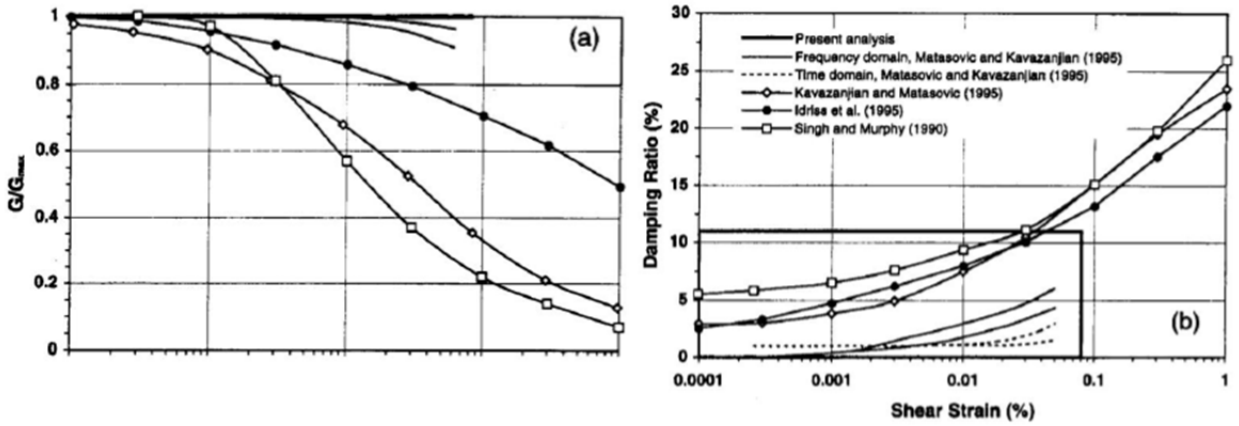

Figure 2.31 Recommended (a) normalized shear modulus reduction and (b) material damping curves from Morochnik et al. (1998).

Elgamal et al. (2004) investigated the shear modulus reduction and material damping ratio curves using system identification techniques. Six earthquake events, which were recorded by strong motion station in OII landfill, were involved in this study. The results of this investigation suggested that the shear modulus was not reduced for strains between 0.001 to 0.2 %. The average constant damping ratio of approximately 5.4% was suggested by this study. Figure 2.32 presents shear modulus reduction and damping curves from Elgamal et al. (2004) and other studies.

Despite numerous evaluations on the nonlinear dynamic properties of solid waste in OII landfill, there remain two important issues:

1. OII landfill is not considered as a typical modern MSW landfill because this also landfill included significant quantities of soil, industrial waste, and liquid waste. Accordingly, the dynamic properties evaluated at this landfill may not be suitable for Subtitle D landfills
2. The evaluations from researchers yielded different recommended shear modulus reduction and damping curves (Fig. 2.32). This variability may stem from different assumptions made by these investigators, such as differences in idealization of lateral response, waste layering, acceleration variation between measurement locations, time window selection of earthquake record, etc.

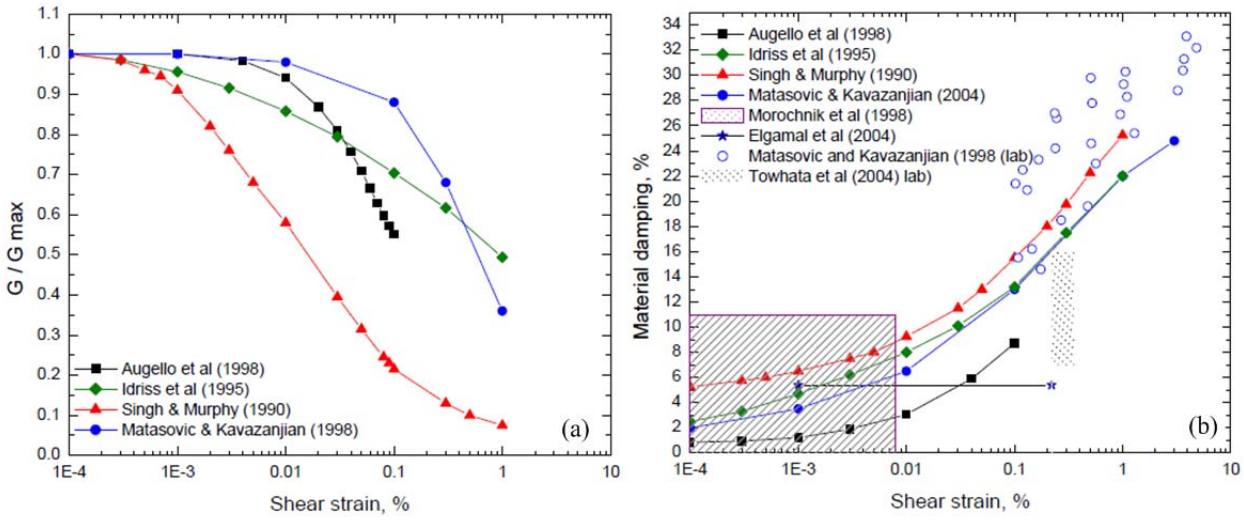

Figure 2.32 Recommended (a) normalized shear modulus reduction and (b) material damping curves from a variety of investigators (Zekkos 2005).

2.6.3 Laboratory Evaluation of Dynamic Properties of MSW in the Nonlinear Strain Range

In the following paragraphs, laboratory evaluations of nonlinear dynamic properties of MSW are presented.

Towhata et al. (2004) studied the nonlinear dynamic properties of MSW using laboratory testing to support the development of an artificial island made of municipal waste. In this research, cyclic triaxial tests under a confining stress of 40 kPa and a frequency excitation of 0.01 to 0.1 Hz were performed on MSW specimens with a dry unit weight of approximately 0.75 gr/cm^3. The results of these tests suggested that the damping ratio of waste is higher than that of soil. Accordingly, the earthquake shaking may be attenuated during wave propagation in a MSW landfill. In addition, higher values of material damping were observed for the specimens without plastic fibers. The authors also conducted a series of small-size shaking table tests using waste compacted by human feet. The results of the shaking table tests confirmed the results of cylic triaxial tests and are shown in Fig. 2.33. Additionally, Fig. 2.34 shows the range of material damping ratio from this study.

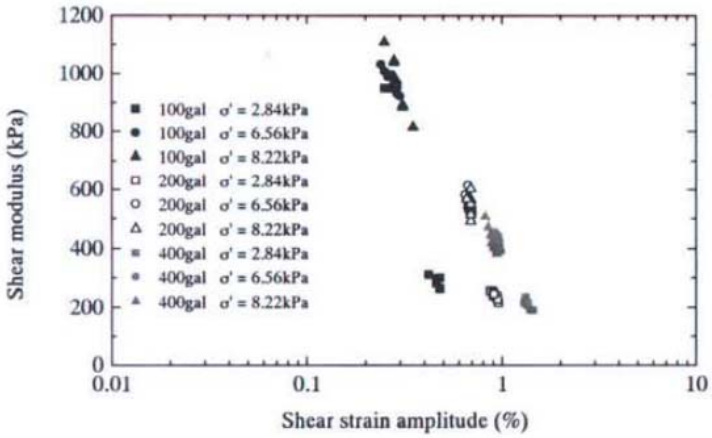

Figure 2.33 Variation of shear modulus with shear strain amplitude in shaking table tests (Towhata et al. 2004)

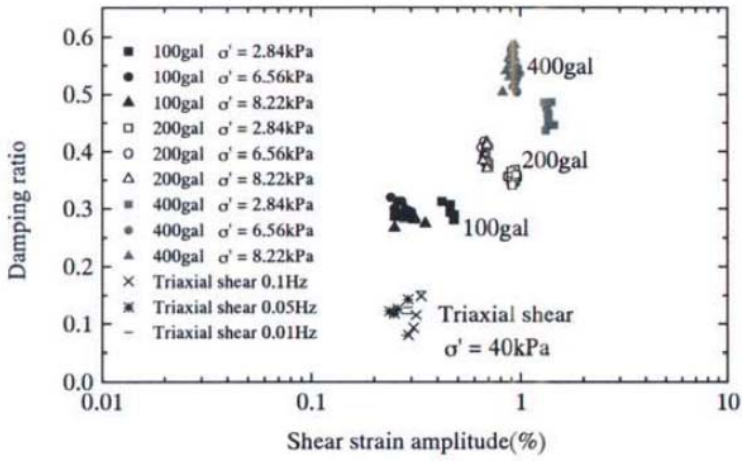

Figure 2.34 Variation of damping ratio with shear strain amplitude in shaking table tests (Towhata et al. 2004).

Zekkos (2005) and Zekkos et al. (2006b, 2008) carried out extensive large-scale cyclic triaxial tests to evaluate the effects of waste composition, confining stress, unit weight, loading frequency, and time under confinement on the nonlinear dynamic properties of MSW. In developing the normalized shear modulus reduction and material damping ratio curves, Zekkos (2005) reconstituted samples into several groups of waste compositions by means of weight percentages of fractions smaller than 20 mm (i.e. soil-like material): 100%, 62–76%, and 8–25%. This study found that the nonlinear dynamic properties of MSW are significantly affected by the waste composition. The effect of waste composition on material damping was particularly pronounced at large strains. Specimens that included more fibrous constituents showed smaller increase in damping than that of specimens with less fibrous constituents. Additionally, this study shows that confining stress also impacts significantly the shear modulus reduction, but has smaller influences in the material damping ratio curve. In summary, the qualitative importance of various parameters on shear modulus reduction and material damping of MSW are presented in Table 2.3. The recommended shear modulus reduction and material damping curves from Zekkos (2005) and Zekkos et al. (2008) are presented in Fig. 2.35. The curves shown correspond

with near surface condition as they were developed using confining stress range of 25 – 125 kPa. Recommended curves for higher confining stresses are also presented in Zekkos et al. (2008). The results of this study showed that increasing confining pressure shear modulus reduction curve moved slightly to higher strain and the damping ratio curve shifted downward.

Table 2.3 Effect of different parameters on the MSW dynamic properties (Zekkos et al. 2008).

Property: / Effect of:	G/G_{max} vs γ	D vs γ
Composition	Very important at large strains	Very important at large strains
Confining stress	Important	Likely important
Unit weight	Not important	Not important
Loading frequency	Not important	Not important
Time under confinement	Not important	Not important

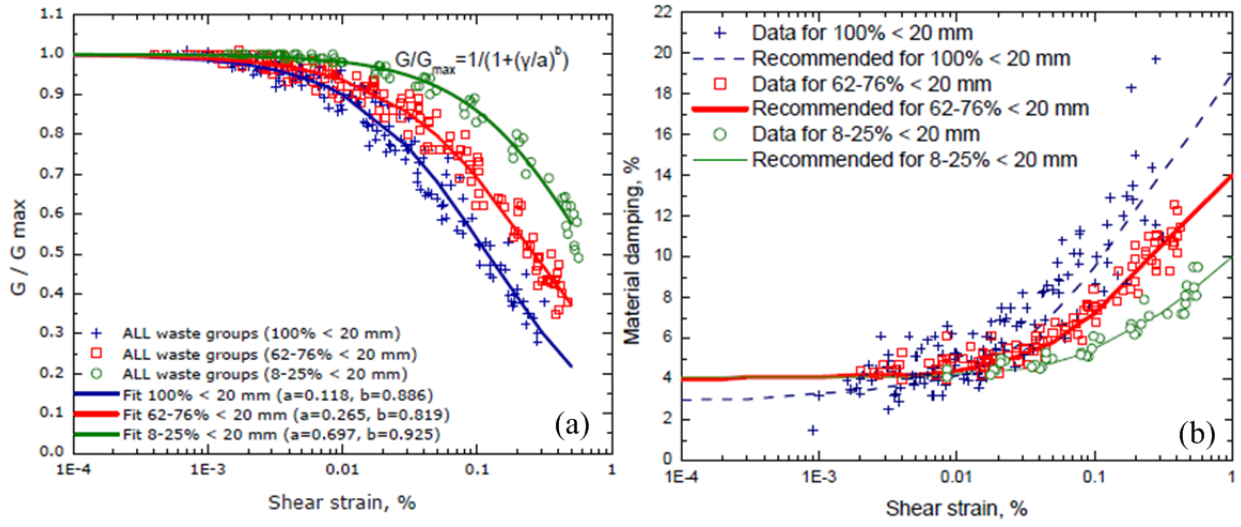

Figure 2.35 (a) Normalized shear modulus and (b) material damping curves for confining stress < 125 kPa (Zekkos 2005).

Lee (2007) performed laboratory testing using RCTS and LSRC in high-amplitude strain range to investigate parameters affecting the nonlinear dynamic properties. Both RCTS and LRSC were used to study shearing strain amplitude, isotropic confining stress, overconsolidation

ratio (OCR) effects on nonlinear dynamic properties of MSW. In addition, RCTS was also used to investigate number of loading cycles and excitation frequency effects. In term of material parameters, both laboratory devices were used to evaluate influences of waste composition and particle size on the nonlinear dynamic properties. Effects of water content and total unit weight on the nonlinear dynamic properties of MSW were only evaluated using RCTS. Similar with Zekkos et al. (2008), this study showed that increasing confining pressure shear modulus reduction curve moved slightly to higher strain and the damping ratio curve shifted downward. Loading frequency, OCR, water content, and unit weight had minor influence on the nonlinear dynamic properties of MSW. Shear modulus reduction and material damping ratio curves of this study are presented in Fig. 2.36. In this figure, the variation in these curves was fitted using the Darendeli model (2001) for different weight percentages of soil size material.

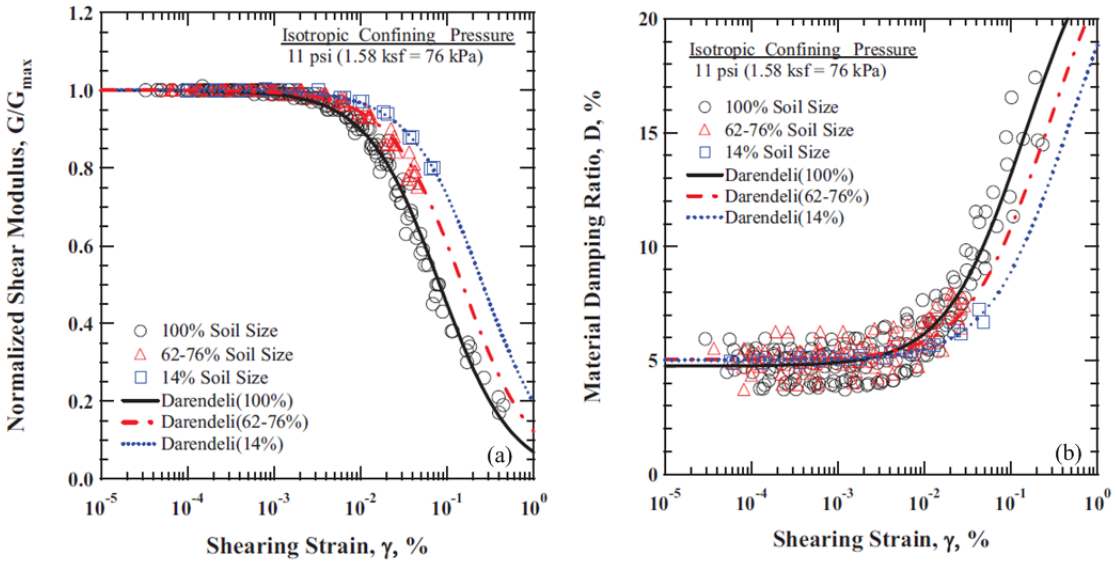

Figure 2.36 (a) Normalized shear modulus reduction and (b) material damping ratio (Lee 2007).

Yuan et al. (2011) evaluated the nonlinear dynamic curves of MSW over a strain range of 0.01% to 3% using large-scale cyclic simple shear testing. The outcomes of this study suggested that normalized shear modulus reduction and damping ratio depended on unit weight.

Additionally, waste composition had a very significant impact on damping and a somewhat lesser influence on normalized shear modulus reduction. The normalized shear modulus reduction data from this study along with fitted curves from Zekkos et al. (2008) is shown in Fig. 2.37. Excellent agreement between these two studies is observed in this figure. The material damping ratio data from Yuan et al. (2011) and fitted curves from Zekkos et al. (2008) are shown in Fig. 2.38**.** For similar composition ratio, the material damping ratio from this study is about 50% higher than that of Zekkos et al. (2008). Nevertheless, the damping ratio trends from both studies are consistent in term of unit weight and waste composition.

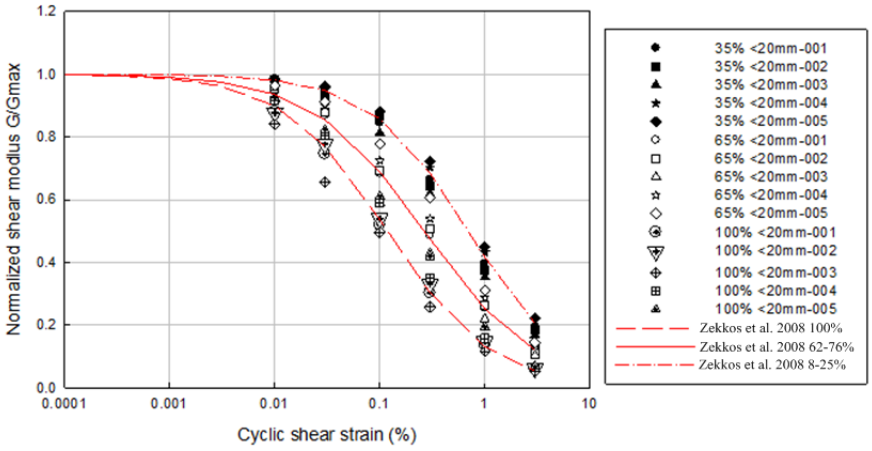

Figure 2.37 Normalized shear modulus reduction values (Yuan et al. 2011).

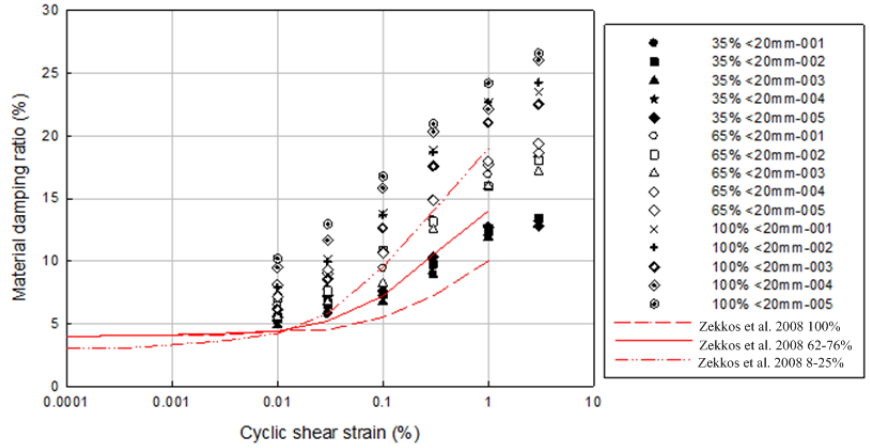

Figure 2.38 Material damping ratio values (Yuan et al. 2011).

2.6.4 Field Investigation of Dynamic Properties of Geomaterials in the Nonlinear Strain Range

Several investigators have attempted to evaluate the nonlinear dynamic properties in-situ during the last 30 years. One of the challenging tasks in this testing is generating large shearing strains in situ that can be properly analyzed. Investigators generate shear strain in the ground using a variety of vibration sources. In the following paragraphs, in-situ evaluations of dynamic properties of geomaterials are briefly reviewed. In addition, a proof-of-concept study for this present study conducted by Zalachoris (2010) is also presented.

Henke and Henke (1993 and 2002) developed a torsional cylindrical impulse shear test (TCIST) to investigate nonlinear dynamic properties of geomaterial in situ. TCIST is performed by drilling hole with a hollow-stem auger, probing an open-ended cylinder to apply impulsive torque from small to large magnitude, and recording the soil responses in term of angular acceleration and torque of the cylinder head (Fig. 2.39). The hollow-stem auger and cylindrical probe can advance to investigate deeper soil stratum. Independently, they analytically calculated the angular acceleration from TCIST. This calculation is performed based on Ramsberg-Osgood equation and Massing's criterion to describe the shear modulus reduction and damping behavior, respectively. Iterations were made by changing calculation parameters to find the least-square difference between the calculated and measured angular accelerations. The calculation parameters from the last iteration are used to develop shear modulus reduction and material damping curves. Henke and Henke (2002) reported that shear modulus reduction curves from the in-situ testing were consistent with direct simple shear test in the laboratory. Nevertheless, the material damping curves from TCIST were higher than those evaluated in laboratory testing. On the contrary, TCIST results underestimated the damping curve from laboratory testing at low

shear strain. Low material damping value from TCIST may be the result of modeling soil behavior using the Masing criterion.

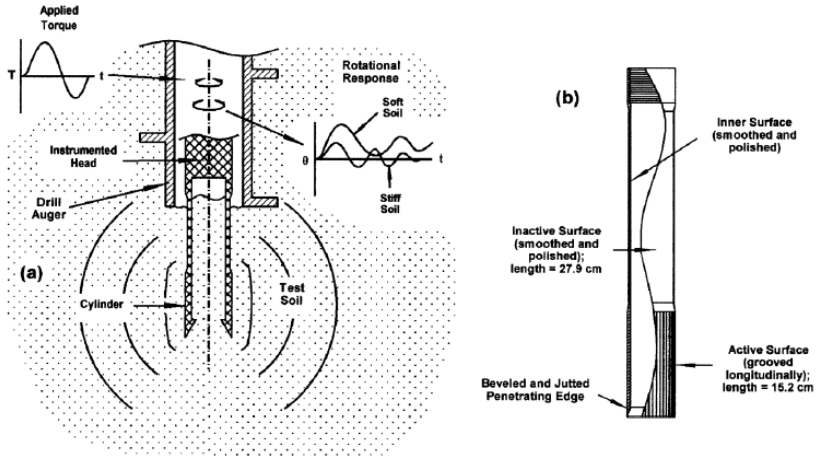

Figure 2.39 (a) General testing configuration and concept of torsional cylindrical impulse shear test and (b) design of cylindrical probe (Henke and Henke 2002).

Salgado et al. (1997) devised a Large-strain Seismic Crosshole Test (LSCT) to study the nonlinear behavior of geomaterial. Figure 2.40 illustrates the testing setup of LSCT. Essentially, LSCT is similar to conventional crosshole seismic testing. The main difference is that LSCT is performed by dropping hammer of varying weight from various heights. Thus, small to large magnitude shearing strain in the soil mass can be induced. The generated waves are recorded using geophones at each sensor hole. Using three geophones, the relationship between travel time and distance is developed (Fig. 2.41). Then, a least-square fitting method is used to find the regression parameters (i.e. t_0, V_s, and c). Shear wave velocity is defined as the inverse of the slope of the regression line at this distance. Finally, shear modulus is calculated using Eq. 2.7. By assuming one dimensional (1-D) plane wave propagation, shearing strain can be calculated from the ratio of particle velocity ($\acute{u}$) and shear wave velocity (Eq. 2.8).

$$G = \rho V_s^2 \tag{2.7}$$

$$\gamma = \dot{u}/V_s \tag{2.8}$$

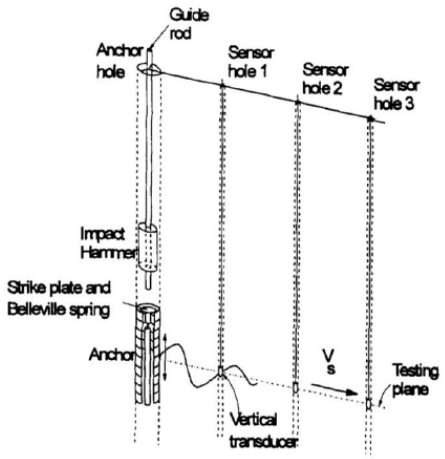

Figure 2.40 General testing configuration of Large-Strain Seismic Crosshole Test (Salgado et al. 1997).

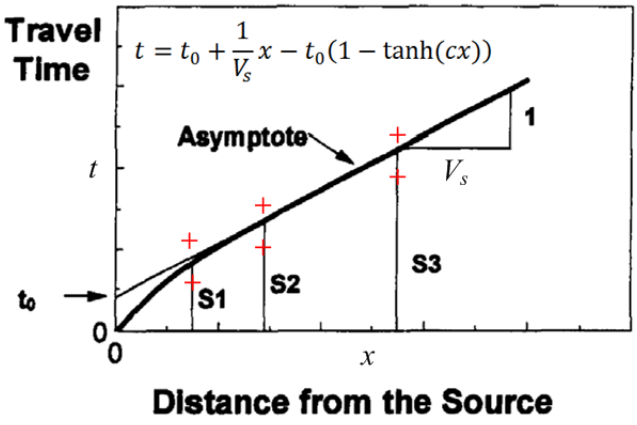

Figure 2.41 Travel-time curve (after Salgado et al. 1997).

Roblee and Riemer (1998) developed a Downhole Freestanding Shear Device (DFSD). Subsequently, Safaqah and Riemer (2006) used the DFSD to investigate the nonlinear dynamic properties of geomaterial insitu. The test is performed by pushing the DFSD cylinder into the ground and applying a torque so that cyclic torsional shear is imposed on the soil column (Fig. 2.42). Torque magnitude and shear deformation are recorded using a sensing system and strain gages. DFSD has been successfully implemented in clayey soil and induced shear strains ranging

from 10^{-4}% to about 1%. Shear modulus at small shear strain from DFSD and crosshole seismic testing was consistent. Shear modulus reduction curve from the DFSD showed good agreement with recommended curves from Vucetic and Dobry (1991). Nevertheless, damping curve from the DFSD overestimated those of Vucetic and Dobry (1991)

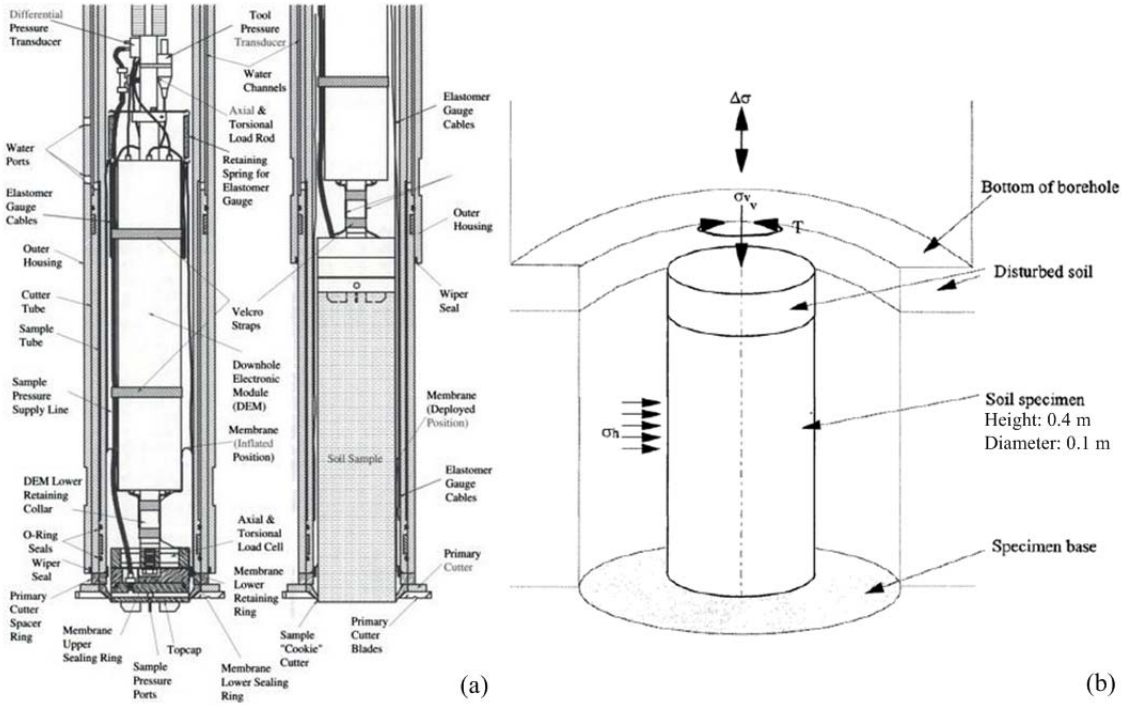

Figure 2.42 (a) Design and (b) concept of Downhole Freestanding Shear Device (Safaqah et al. 2003, Safaqah and Riemer 2006).

The geotechnical engineering group at the University of Texas at Austin has been developing and enhancing an in situ method to study the nonlinear dynamic properties of soils over the past 10 years. The basic testing setup is illustrated in Fig. 2.43. In general, their method utilizes a large-scale vibroseis truck as the wave source. The vibration is applied on a surface footing (e.g. Phillips 2000, Axtell et al. 2002, Park 2010), on a drilled concrete shaft (e.g. Kurtulus 2006), or directly on the ground surface (e.g. Chang 2002, Cox et al. 2009, LeBlanc 2013). An array of geophones or accelerometers is installed in the ground. From these

transducers, particle velocity, displacement, and wave propagation velocity can be calculated. Additionally, this testing configuration permits convenient performance of small-strain crosshole and downhole seismic testing.

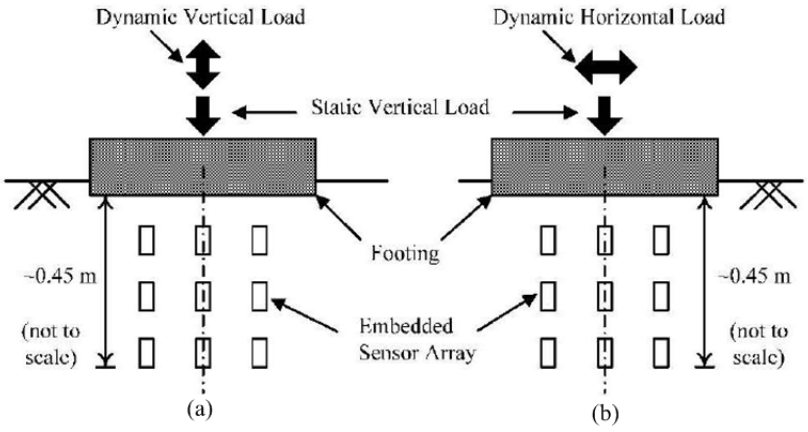

Figure 2.43 General testing setup for (a) compressional and (b) shear wave measurements (Stokoe et al. 2006).

Axtell et al. (2002) mainly investigated the relationship between constrained modulus (M) with axial strain (ε_p) in an unsaturated sand deposit. In achieving this objective, Axtell et al. (2002) used vibrosesis truck to apply static vertical load and dynamic vertical loads [Fig. 2.44(a)]. M and ε_p were calculated using the following equations.

$$M = \rho \cdot V_p^2 \tag{2.9}$$

$$\varepsilon_p = \dot{u}/V_p \tag{2.10}$$

Additionally, Axtell et al. (2002) attempted to evaluate to shear modulus reduction with shear strain in situ. As the vibroseis truck could not generate a dynamic horizontal load, a large pendulum hammer was used for horizontal loading [Fig. 2.44(b)]. Using this method, strain ranged from $2\text{x}10^{-4}$ % to 10^{-2} % were achieved. The results from this study encouraged the

following investigators to employ a similar method in order to evaluate the nonlinear dynamic properties of soils in situ.

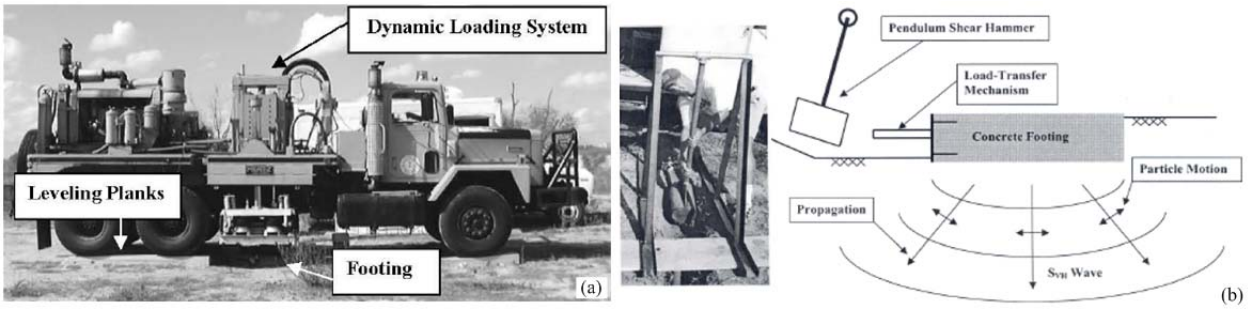

Figure 2.44 General testing setup to evaluate (a) constrained compression modulus and (b) shear modulus relationship with strains (Axtell 2002).

Kurtulus (2006) performed an in situ evaluation of the relationship between shear modulus and shear strain of soil. In this investigation, 6 to 12 feet deep drilled shafts with diameter of 1.5 feet were installed and instrumented with vertically oriented geophones (Fig. 2.45). Geophones were also installed in four boreholes surrounding the shaft. Waves at small strain were generated by hitting the shaft with a handheld hammer. For larger strain, waves were generated by shaking the shaft vertically with a vibroseis truck. Two vibroseis trucks of the Network for Earthquake Engineering Simulation at the University of Texas at Austin (NEES@UT), Thumper and T-Rex, were used in this investigation. Detailed information about these vibroseis is presented in Stokoe et al. (2004 and 2008) and Menq et al. (2008). Using this testing configuration, the velocity propagation of SH waves with particle displacement in vertical direction can be calculated and used to estimate the shear modulus. Shearing strain was evaluated using the following equation.

$$\gamma = (u_1 - u_2)/\Delta x \tag{2.11}$$

where u_i is the particle displacement at geophone i and Δx is the spacing between two adjacent geophones.

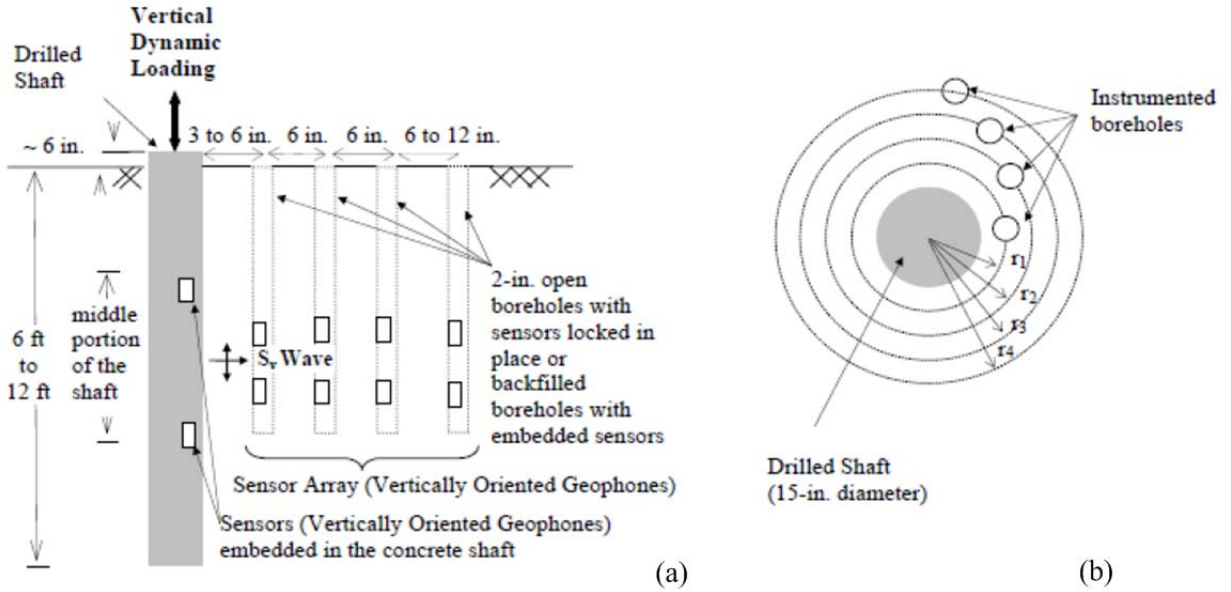

Figure 2.45 Field testing configuration to evaluate nonlinear shear modulus using a drilled shaft (Kurtulus 2006).

Cox et al. (2009) proposed a new in-situ test to investigate liquefaction resistance by evaluating the coupled response between excess porewater pressure generation and nonlinear shear modulus curve. Figure 2.46 shows the testing configuration and customized sensor used by Cox et al. (2009). Four type sensors were pushed in the ground until they reached a liquefiable layer. Each sensor is capable of simultaneously measuring soil particle motion and excess pore water pressure using a three dimensional micro-electrical-mechanical-system (MEMS) accelerometer and a miniature pore pressure transducer, respectively. T-Rex, was used to apply 10 or 20-Hz dynamic horizontal load up to 100 cycles. The magnitude of dynamic horizontal load was increased to induce larger shear strain. The evaluation of shear modulus was performed in a similar way to that of Kurtulus (2006). The shear strain was calculated using a four-node, isoparametric, finite element procedure. The description about this finite element procedure is presented in Chapter 4 of this manuscript. Thus, excess pore pressure generation and shear

modulus reduction curve can be evaluated from small to large shear strain. In addition, small-scale crosshole seismic testing was also included in the testing procedure to evaluate V_p and V_s.

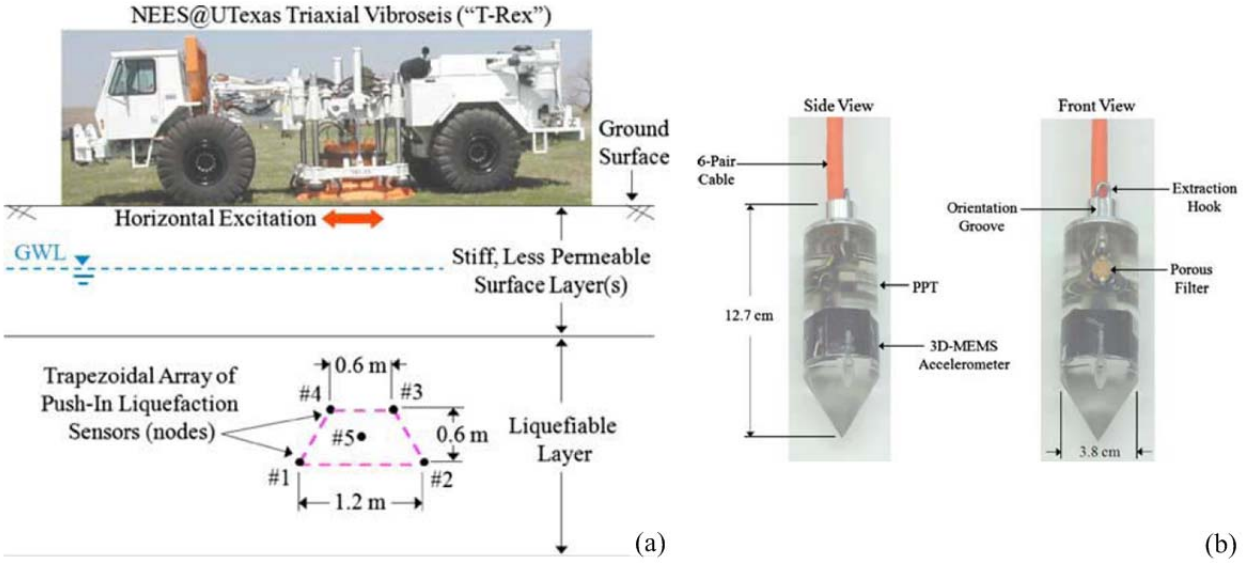

Figure 2.46 (a) Field testing configuration to evaluate liquefaction resistance and (b) in situ liquefaction sensor (Cox et al. 2009).

Park (2010) evaluated in-situ the dynamic properties of cemented alluvium. The general testing setup is illustrated in Fig. 2.47. Two vertical arrays of 3-D geophones were installed in the ground and a concrete foundation was placed on the ground. Small-scale downhole and crosshole seismic testing were performed to evaluate V_p and V_s. Downhole seismic testing was performed by hitting the foundation with hammer. A drilled hole at 1 ft distance from the foundation was used for a wave source in crosshole seismic testing (i.e. impact knob and air bladder). The steady-state dynamic testing was performed using Thumper and T-Rex. These shakers were used to apply static vertical and dynamic horizontal loads on the foundation. SV wave propagation velocity was used to evaluate shear modulus (Eq. 2.7). Shearing strain was evaluated using the two-node displacement based method (Rathje et al. 2004). Static vertical load on the foundation was varied during small-scale downhole and crosshole seismic testing as

well as the steady-state dynamic testing. Thus, the effect of confining pressure on the dynamic properties of cemented alluvium was studied. The in-situ evaluation of dynamic properties of MSW in the current study follows, in general, the procedure and testing setup of Park (2010).

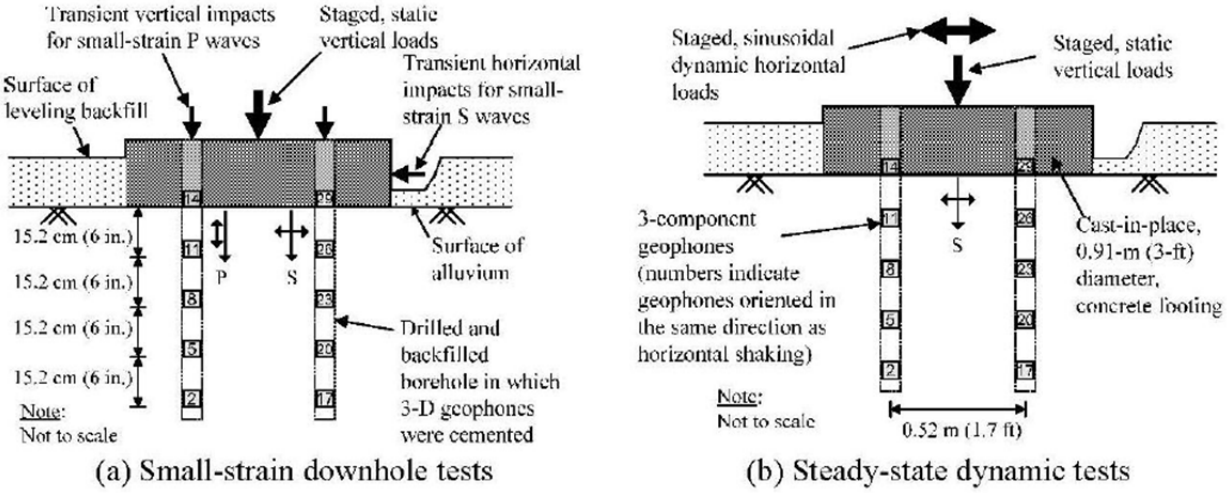

Figure 2.47 General testing setup for (a) small strain downhole seismic testing and (b) steady-state dynamic testing (Park 2010).

Zalachoris (2010) study was a proof concept trial for this present study to demonstrate that the mobile shakers of NEES@UT are capable of inducing moderate to large shear strain in MSW. Illustration of the testing setup in Zalachoris (2010) is presented in Fig. 2.48. Two arrays of 2-D geophone sensors were installed in the waste mass to record particle displacements due to dynamic loading. The dynamic force was incremented by the mobile shaker to obtain small to large shear strain levels. Shearing strains was calculated using two-node displacement based method. The shear modulus reduction data from this study and Zekkos et al. (2008) are shown in Fig. 2.49.

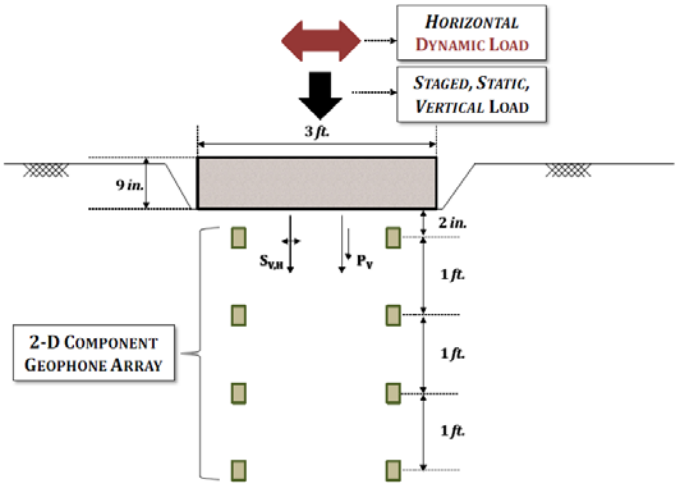

Figure 2.48 In-situ field testing setup to measure nonlinear compression and shear wave propagation in situ with a dynamically loaded footing (Zalachoris 2010).

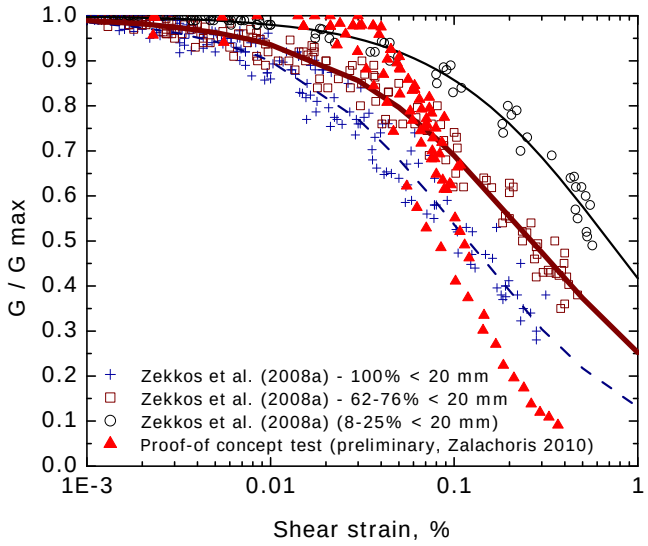

Figure 2.49 Normalized shear modulus reduction curve.

2.7 Poisson's Ratio and Lateral Earth Pressure Coefficient at Rest of MSW

Poisson's ratio (v) and lateral earth pressure coefficient at rest (K_0) are important material properties in engineering practice. Poisson's ratio relates the compressibility of a solid material in perpendicular directions. It is used in the relationship between elastic modulus, such as bulk modulus (K), Young's modulus (E), Lamé's first parameter (λ), shear modulus (G), and P-wave velocity or constrained modulus (M). Lateral earth pressure coefficient at rest describes the ratio

between in-situ horizontal and vertical stresses. Based on elasticity theory, the relationship between ν and K_0 is shown by Eq. 2.12.

$$K_0 = \frac{\nu}{1-\nu} \tag{2.12}$$

To investigate this property, laboratory tests and in-situ geophysical methods have been used. In laboratory, Poisson's ratio is commonly calculated by measuring radial strain and axial strain. In the geophysical field testing, small-strain Poisson's ratio for homogeneous, isotropic, linearly elastic solid materials can be calculated from the relationship between P-wave (V_p) and S-wave (V_s) velocities (Eq. 2.13).

$$\nu = \frac{0.5 \cdot \left(V_s / V_p\right)^2 - 1}{\left(V_s / V_p\right)^2 - 1} \tag{2.13}$$

Lateral earth pressure coefficient at rest has also been investigated in the laboratory and in situ. In the laboratory, K_0 can be measured by applying a vertical pressure value in a laterally constrained sample and measuring the induced horizontal or hoop stress. In the field, pressuremeter or dilatometer testing can be used to evaluate K_0.

Sharma et al. (1990) conducted downhole seismic test in Richmond landfill, California. In this study, Poisson's ratio of refuse material was estimated to be 0.49. Houston et al. (1995) performed seismic downhole test in the Northwest Regional Landfill Facility (NWRLF), Arizona. Houston et al. (1995) reported the Possion's ratio values decrease from 0.3 at near surface (approximately 1.5 m) to 0.11 at 10 m. Carvalho and Vilar (1998) performed crosshole seismic test in the Bandeirantes landfill, Brazil. They reported Poisson's ratio value ranging from 0.25 to 0.35. Matasovic and Kavazanjian (1998) reported a Poisson's ratio profile of OII landfill

based on downhole seismic test results (Fig. 2.50). A Poisson's ratio value of 0.33 was selected for the OII landfill at low shear strain levels.

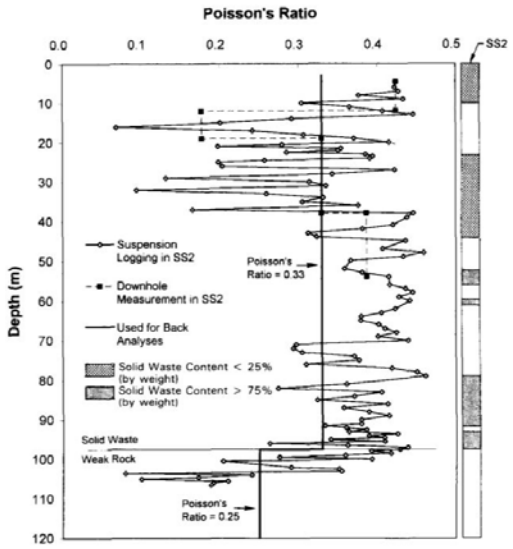

Figure 2.50 Poisson's ratio profile of OII landfill (Matasovic and Kavajanzian, 1998).

Jessberger and Kockel (1995) studied Poisson's ratio using a series of triaxial compression test under different confining pressures. They reported that Poisson's ratio was about zero at low axial strain and increased linearly up to 0.35 as axial strain reached about 20%.

Zekkos (2005) carried out a series of cyclic triaxial tests at mean confining stresses of 25 to 90 kPa using MSW specimens from Tri-Cities landfill. In this investigation, elastometer gauges and a linear voltage displacement transducers (LVDT) were used to measure the radial and axial deformation of the samples, respectively. Figure 2.51 shows the results from this study. Practically, Poisson's ratio remains constant at shearing strain level of 0.01% to 1% (Zekkos 2005). He reported v values ranging from 0.28 to 0.4 for soil-like specimens (i.e. smaller than 20 mm fraction), whereas v values ranging from 0.05 to 0.31 for specimens that include particles larger than 20 mm (mostly fibrous materials).

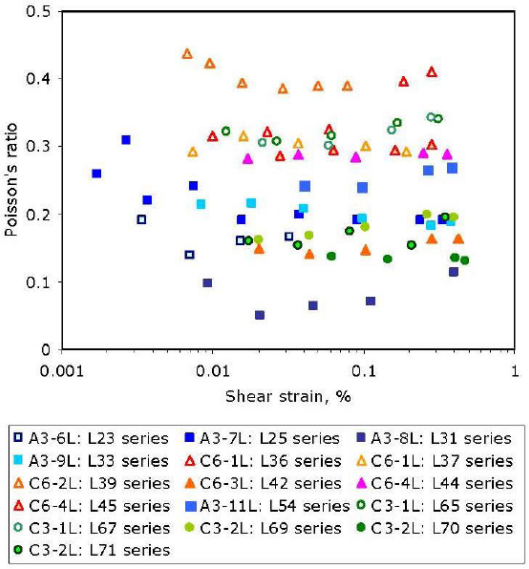

Figure 2.51 Effect of shear strain amplitude on Poisson's ratio (Zekkos 2005).

Dixon et al. (1999) employed a 1.2 m long self-boring pressuremeter in a pre-drilled borehole to evaluate lateral earth pressure coefficient at rest of MSW in situ. In this study, K_0 values ranging from about 0.14 to 1 were reported. These K_0 values were evaluated using strain induced in the borehole by the pressuremeter.

Landva et al. (2000) tested 5 different specimens from Spruce Lake Refuse landfill, Saint John, New Brunswick, Canada to investigate K_0 and compressibility index of MSW. This study was performed using a large split-ring apparatus (d = 600 mm, h = 460 mm), equipped with dial gauges, LVDT, and load cells. The K_0 values ranging from 0.26 to 0.4 were reported from this study. Using elasticity theory in Eq. 2.12, the corresponding υ values range from 0.21 to 0.29.

Towhata et al. (2004) investigated K_0 using a triaxial test. This testing was performed by increasing the axial stress at a constant rate and simultaneously changing the radial stress to maintain small radial deformations. As the axial stresses increase, the K_0 decreased and became constant with values between 0.25 and 0.4 at axial stresses larger than 100 kPa.

Dixon et al. (2004) investigated in situ K_0 of MSW using pressure cells (hydraulic devices 300 mm in diameter) in a United Kingdom MSW landfill. The authors reported K_0 ranged from 0.4 to 0.8 for shallow depth. At depth of 6 to 20 m, K_0 is approximately constant at 0.8.

Poisson's ratio and lateral earth pressure coefficient at rest from the aforementioned laboratory testing is summarized by Zekkos (2005) and is presented in Fig. 2.52. These properties from the field testing are shown in Fig. 2.53. In these figures, solid points represent the original data, whereas the hollow points represent the derived data calculated using Eq. 2.12.

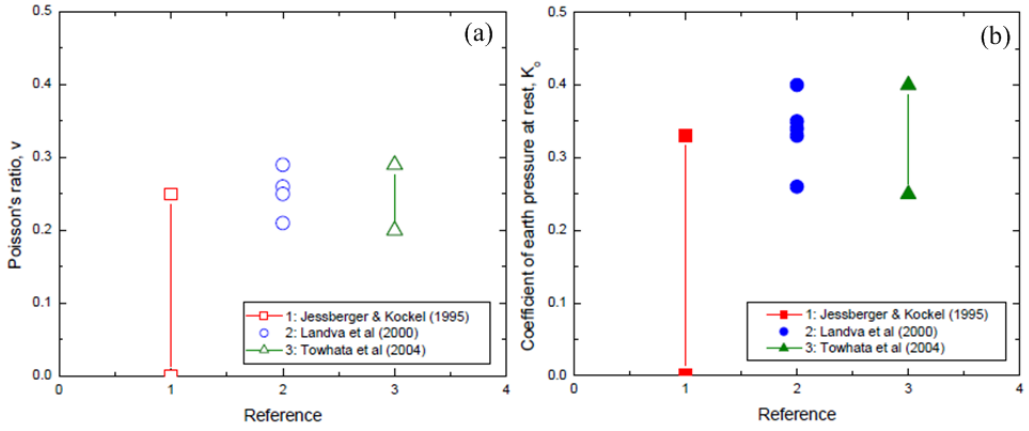

Figure 2.52 (a) Poisson's ratio and (b) lateral pressure coefficient at rest of MSW from laboratory testing (Zekkos, 2005).

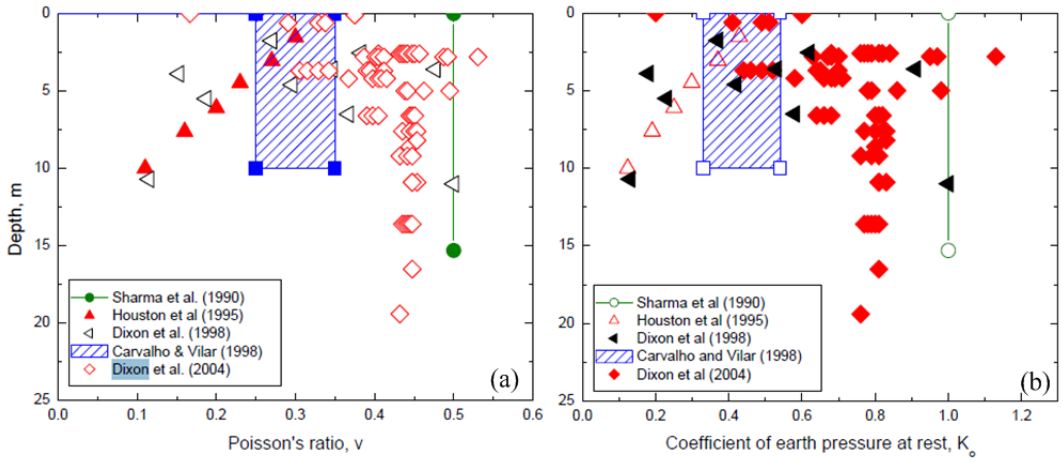

Figure 2.53 (a) Poisson's ratio and (b) lateral pressure coefficient at rest of MSW versus depth from in-situ testing (Zekkos, 2005).

2.8 Seismic Performance of MSW Landfills

Seismic performance of MSW landfills can be assessed by observing modes of damage in MSW landfills after earthquakes. Matasovic et al. (1998) reported comprehensive observations on the seismic performance of MSW landfills. The observational data were mostly gained from Californian canyon fill type landfills during strong earthquakes from 1965 to 1994. The 1969 Santa Rosa and 1971 San Fernando earthquakes provided the earliest reports on the seismic performance of MSW landfills (e.g. Anderson 1995, Barrows 1975, and Oakeshoff 1975). Nevertheless, it was not until the 1994 Northridge earthquake that the performance of Subtitle D landfill during strong shaking could be observed and assessed comprehensively.

Redwood landfill in Marin county, California experienced an estimated peak horizontal ground acceleration (PHGA) in bedrock about 0.05 g during the 1969 Santa Rosa earthquake (Anderson 1995). Seismic-induced damage reported in this pre-subtitle D landfill included failures of a few interior clay cell walls. The damage may have occurred due to the amplification of the shaking by underlying soft sediments. Interestingly, the perimeter berm surrounding the landfill was not damaged.

During the 1971 San Fernando earthquake, 11 major landfills were located within a radius of 60-km from the epicenter. The Russel Moe Landfill was directly on the hanging wall of the fault rupture and experienced an estimated PHGA as high as 0.9 g. In this landfill, cracking was observed around the boundaries of landfill (Barrows 1975). Sunshine canyon Landfill (i.e. North Valley Landfill) and School Canyon Landfill were located about 13 km and 23 km from the fault rupture plane, respectively. These landfills experienced an estimated PHGA of about 0.19 g to 0.3 g. At these landfills, cracking of soil covers was identified as the main mode of damage.

Reports on the seismic performance of 5 MSW landfills are available during the 1987 Whittier-Narrows earthquake. PHGA at the OII landfill during the Whittier-Narrows event was estimated to be about 0.24 to 0.29 g. Siegel et al. (1990) reported 25 to 50 mm wide discontinuous ground cracking on soil cover at the north bench. In addition, multiple ground surface cracks 15 mm to 40 mm wide and as long as 90 m in the top deck soil cover. This damage resulted in the installation of strong motion instruments at the base and top deck of the OII landfill. In the other four landfills, namely Puente Hills, Savage Canyon, BKK, and Azusa Landfills, no damage was observed.

The 1989 Loma Prieta earthquake provided opportunity in assessing the performance of 15 MSW landfills. Post-earthquake surveys were reported by Orr and Finch 1990, Johnson et al. 1991, and Buranek and Prasad 1991. The estimated bedrock PHGA at the base of landfills during this event ranged from 0.1 g to 0.5 g. The common post-earthquake damage was soil cover cracking on the slope and transitions between waste and native ground.

In the 1994 Northridge earthquake, the seismic performance of Subtitle D landfills was assessed in Bradley Avenue, Lopez Canyon, and Chiquita Canyon Landfills. The estimated bedrock PHGA at the Bradley Avenue and the Lopez Canyon landfills was estimated at 0.36 g and 0.42 g, respectively. There was no significant damage observed in the liner system of these landfills. Local tears that were found in the geotextile overlying the side slope liner were not attributed to the earthquake (Augello et al. 1995). The Chiquita Canyon Landfill was subjected to an estimated bedrock PHGA of 0.33 g and some limited damage was identified. A single tear in geomembrane liner with a length of about 4 m and three parallel tears with a total length of about 23 m were found in Area C and D, respectively. In addition to these Subtitle D landfills, post-earthquake investigations were also performed in pre-subtitle D landfills located within 100 km

of the epicenter. At the OII landfill, Hushmand (1994) reported a recorded PHGA of 0.26 g and 0.25 g at the base and the top deck, respectively. An estimated bedrock PHGA of 0.10 g at this landfill was reported by Matasovic et al. (1995). In this landfill, earthquake-induced cracks up to 30 m long with a typical width of 5 mm were observed in the north slope. Additionally, cracks ranging from 30 to 90 m long with 50 to 150 mm wide were identified in the bench road.

The most common damage in the 1994 Northridge earthquake was a cracking of soil cover which was consistent observed the damage following the Loma Prieta earthquake. Cracking was found either on the waste fill and native ground contact or at the changes in slope geometry (Augello et al. 1995). The soil cover cracking can be attributed to: (1) difference in stiffness between soil cover and ductile waste, (2) difference in stiffness of waste fill and adjacent natural ground, (3) uneven waste fill settlement from earthquake shaking, (4) limited down-slope movement, and (5) cracking by rapid gas release due to shaking and/or temporary loss of gas extraction system (Augello et al. 1995).

Matasovic et al. (1995) proposed five-level landfill damage categorization scheme based on their study of landfill damage after the 1994 Northridge earthquake. This damage categorization scheme is presented in Table 2.4. It should be noted that neither the damage categories III and IV imply a release of contaminants to the environment or impairment of the waste containment system.

Table 2.4 Damage categories for solid waste landfills (Matasovic et al. 1995).

Damage category	Description
V. Major damage	General instability with significant deformations. Integrity of the waste containment system compromised.
IV. Significant damage	Waste containment system impaired, but no release of contaminants. Damage cannot be repaired within 48 hours. Specialty contractor needed to repair the damage.
III. Moderate damage	Damage repaired by landfill staff within 48 hours. No compromise of the waste containment system integrity.
II. Minor damage	Damage repaired without interruption to regular landfill operations.
I. Little or no damage	No damage or slight damage but no immediate repair needed.

CHAPTER 3. DEVELOPMENT OF MODEL FOR SHEAR WAVE VELOCITY OF MUNICIPAL SOLID WASTE

3.1 **Introduction**

Shear wave velocity (V_s) and small-strain shear modulus (G_{max}) are important parameters in a broad spectrum of geotechnical engineering analyses, such as seismic response analysis, machine foundation analysis, and soil-structure interaction analysis. These properties can also be used as an index of material characterization and are related to settlement parameter (e.g. Sheehan et al. 2010). Equation 3.1 presents the relationship between the shear wave velocity and the small-strain shear modulus.

$$G_{\max} = V_s^2 \rho \tag{3.1}$$

where ρ is the mass density of material of interest.

Shear wave velocity of municipal solid waste (MSW) has been evaluated in-situ using a variety of methods, including downhole seismic test (e.g. Sharma 1990, Houston et al. 1995, and ESI 1995), crosshole seismic test (e.g. Singh and Murphy 1990), and surface wave based test (e.g. Rix et al. 1998, Cuellar et al. 1995, and Lin et al. 2004). As part of this study, shear wave velocity of MSW was investigated in-situ using a combination of active and passive surface wave based methodologies. Active testing was performed using the Multichannel Analysis of Surface Waves (MASW) technique (Park et al. 1999a). Passive testing was conducted using Microtremor Analysis Method or MAM (Okada 2003). These methods were implemented at 4 Michigan landfills.

Two shear wave velocity models for MSW have been developed using V_s profile data from 4 Michigan landfills as well as data from 15 landfills that is available in literature. A semi empirical V_s model was formulated based on large-scale laboratory data on reconstituted MSW. In addition, an empirical model was also developed simply by fitting it to the measured V_s profiles of MSW and deriving the model parameters. The models are intended to be used in preliminary assessment of the shear wave velocity for design purpose.

The field measurements of V_s in Michigan landfills have been reported by Sahadewa et al. 2011 and Sahadewa et al. 2012. The development of model for V_s of MSW has been presented in Zekkos et al. 2013.

3.2 **Field Measurements of Shear Wave Velocities in Michigan Landfills**

Shear wave velocity of MSW was evaluated using MASW and MAM techniques in 4 Michigan landfills, namely Arbor Hills, Carleton Farms, Sauk Trail Hills, and the Oakland Heights Landfills. Similar to the other surface wave testing, the MASW and the MAM techniques consist of 3 stages: field data acquisition, dispersion curve analysis, and the inversion process. The procedures used in the implementation of the combined MASW and MAM methodologies are presented below.

3.2.1 MASW or Active Measurement

A schematic of general MASW testing setup is shown in Fig. 3.1. Commonly, a sledge hammer is utilized to generate surface waves or ground roll (i.e. Rayleigh wave). Other wave sources, such as an electromechanical vibrator, can also be used. The wave source is located at a source offset of x_s from the closest geophone. The propagating surface waves are captured by a linear

array of geophones that has spacing of *dx* and spread length of *D*. Outputs from geophones are collected by a seismograph and are stored in a PC for further analysis.

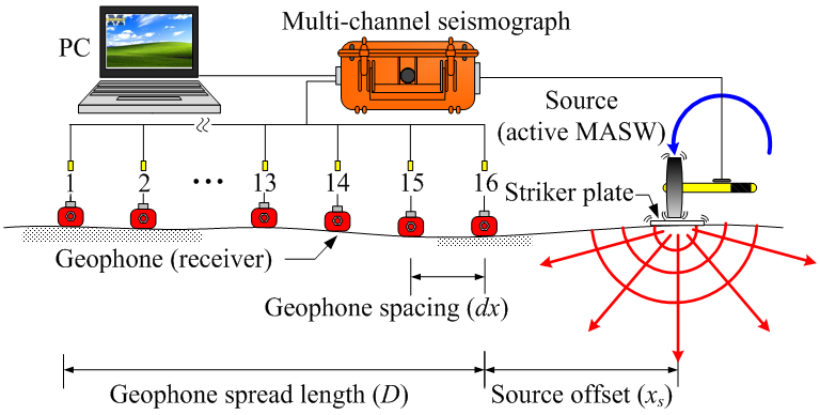

Figure 3.1 General testing setup for MASW.

The geophones and multi-channel seismograph that were used in this study are shown in Fig. 3.2. Surface wave testing was performed using 16 GS-11 D, 4.5-Hz, geophones (Geospace Technologies Corp.). The geophone can be mounted to a cone rod, a cylindrical plate, or a tripod base. These interchangeable geophone bases allow adaption to most field surface conditions. These geophones were connected to an ES-3000 multi-channel seismograph (Geometrics Inc.) that was powered by a 12 VDC external battery. This seismograph is equipped with 24-bit Analog to Digital Conversion and is capable of recording up to 4096 samples/channel with selectable sampling intervals ranging from 0.0625 to 2 milliseconds. The seismograph was connected to a PC via an Ethernet CAT5 cable and was controlled using Seismodule Controller Software (Geometrics Inc.).

In this study, a geophone spacing of 3 m (10 ft) and spread length of 45 m (150 ft) was selected for most locations based on evaluation of initial measurements. A measuring tape was used as a spacing reference during geophone installation (Fig. 3.3). The geophone spacing was selected to prevent aliasing and maximize the depth of investigation for the purposes of

characterizing the MSW material. Geophone spacing and spread length are related to reliable minimum and maximum wavelengths (λ) of surface wave that can be captured in this testing. The magnitude of wavelength greatly affects the depth of investigation (Fig. 3.4). But, it should be noted that a very large spread length (i.e. > 100 m) may increase the risk of higher-mode domination and may reduce signal to noise ratio (SNR) for the fundamental mode (Park et al. 2002). In general, higher-modes may occur in a landfill because it has softer and stiffer zones throughout the waste thickness. SNR, particularly at the far geophones, may be very low as MSW has high material damping (Zekkos et al. 2008). Thus, it should be verified that the surface wave propagation is recorded from the closest to the farthest geophone. In addition, record length has also to be adjusted so that the surface wave of interest is captured.

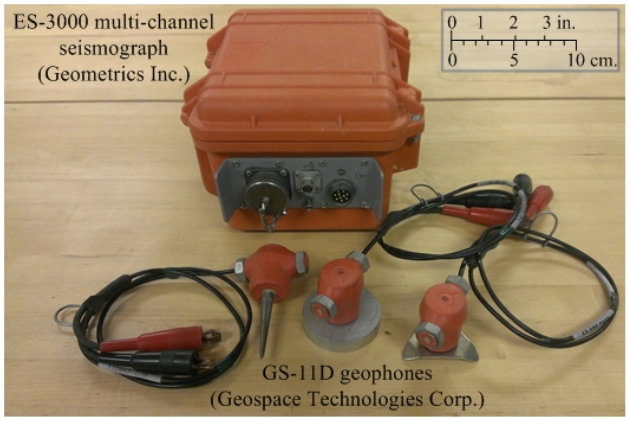

Figure 3.2 Geophones and multi-channel seismograph for field investigation.

A 4.5-kg (10-lb) sledge hammer was used as a wave source at the near offset of 4.5 m (15 ft). This hammer was instrumented with an accelerometer to trigger record time. In general, 5-8 stacks were performed to improve the SNR and generated one active MASW record. An example of a MASW dataset of five stacked records from location 1 at the Carleton Farms Landfill is presented in Fig. 3.5(a).

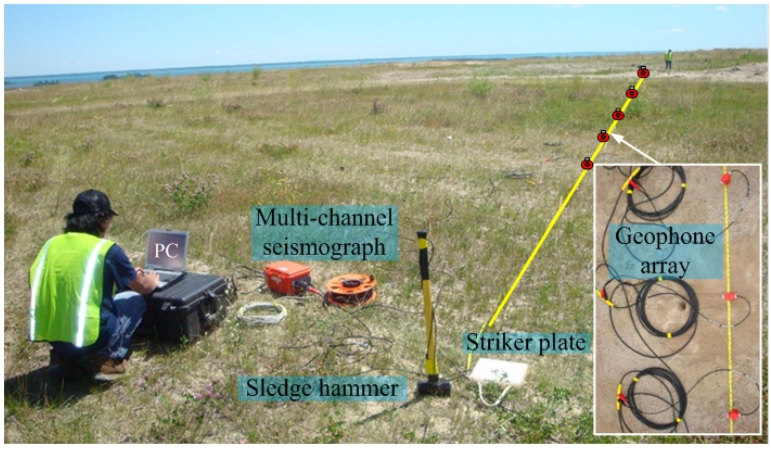

Figure 3.3 Surface wave testing preparation.

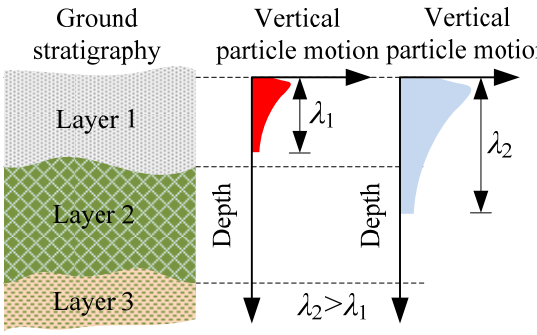

Figure 3.4 Surface wave with different wavelengths sampling different depths (after Stokoe et al. 1994).

3.2.2 MAM or Passive Measurement

In MAM measurement, ambient activities, such as cultural noise (e.g. highway traffic and construction activities), and natural noise (e.g. ocean waves, wind movement, and microseismics) are used as the surface wave sources. In general, these surface waves are rich in low frequency content or long wavelengths. In passive measurements, commonly a circular, triangular, or L-shaped geometric configuration (2-D arrays) is recommended to ensure that the collected data is not affected by directionality of the background noise. However, re-configuring the geophones from the linear array used in MASW, requires significant effort in the field, needs careful surveying, may cover a wide area that can disturb landfill operations, and reduces the

efficiency of the technique. In this investigation, MAM data were collected with the same linear geophone array used in the MASW tests. Use of a linear array for passive measurements has been previously attempted by Louie (2001) and Park and Miller (2008). However, the reliability of the MAM data using a linear array has been questioned (Cox and Beekman 2011). In landfills, it is commonly easy to identify the predominant vibration passive sources. The impact of background noise directionality on the reliability of the results is presented in this chapter.

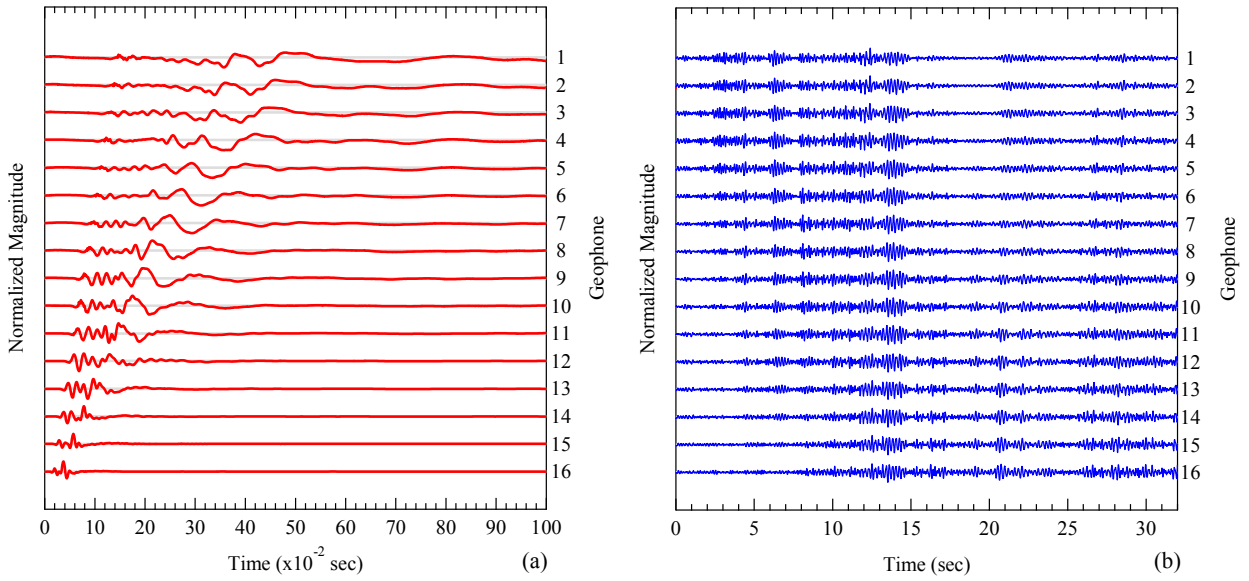

Figure 3.5 Example of surface wave propagation-time histories from location 1 at the Carleton Farms Landfill: (a) active MASW and (b) passive MAM tests.

In this study, surface waves that were generated by cultural activities and other sources were recorded for 32 seconds. An example of a 32- second passive record is shown in Fig. 3.5(b). At least 20 recordings were collected from each location to accommodate temporal variation of background noises.

3.2.3 Dispersion Curve Analysis

The field measurements record was transformed into a dispersion curve using PickWin software (Geometrics Inc.). The dispersion curve shows the variation of phase velocity (V_{ph}) with

frequency (f) of MSW beneath the geophone spread. Phase velocity and Rayleigh wave velocity (V_R) are similar and are commonly used interchangeably (Nazarian 1984). Alternatively, the dispersion curve can also be presented in wavelength and phase velocity space (Equation 3.2).

$$\lambda = V_{ph} / f \tag{3.2}$$

Dispersion curve analysis allows the identification of unwanted waves, such as body waves, higher-mode Rayleigh waves, and other noises (Park et al. 1999a). In general, the dispersion curve is extracted from the fundamental mode of the Rayleigh waves, unless lower V_s layers underlying higher V_s layers are identified (Tokimatsu et al. 1992 and Hayashi 2012).

MASW and MAM records were transformed to a dispersion curve in a frequency-phase velocity space using different signal-processing methodologies. In MASW, the transformation could be performed using f-k transform, f-p transform, Park et al. (1999b) transform, or cylindrical beamformer (Zywicki 1999). In this study, the dispersion curve analyses were performed using the Park et al. (1999b) transform. Figure 3.6**(**a) shows a frequency-phase velocity space of MASW data from Fig. 3.5(a). Blue color gradation at frequencies of 5 to 22 Hz represented the highest Fourier amplitude in this space and was identified as the fundamental mode. The phase velocities with the highest amplitude at each frequency were selected to generate the fundamental dispersion curve.

In MAM, the twenty 32-second recordings were transformed to a single dispersion curve using the Spatial Autocorrelation (SPAC) method (Aki 1957). An example of the resulting dispersion curve (highlighted in white line) generated from the MAM data from Fig. 3.5(b) is presented in Fig. 3.6**(**b). The MASW signal is typically rich in high frequency (short wavelength) content, whereas the MAM signal is richer in low frequency content (long wavelength), providing information at greater depths. MAM data may also include high frequency content,

depending on the generating source and distance. Although signals with frequencies below the geophone's natural frequency are damped according to the geophone's calibration curve, industry-standard geophones are still capable of sensing the seismic waves with frequencies lower than its natural frequency (Park et al. 2002).

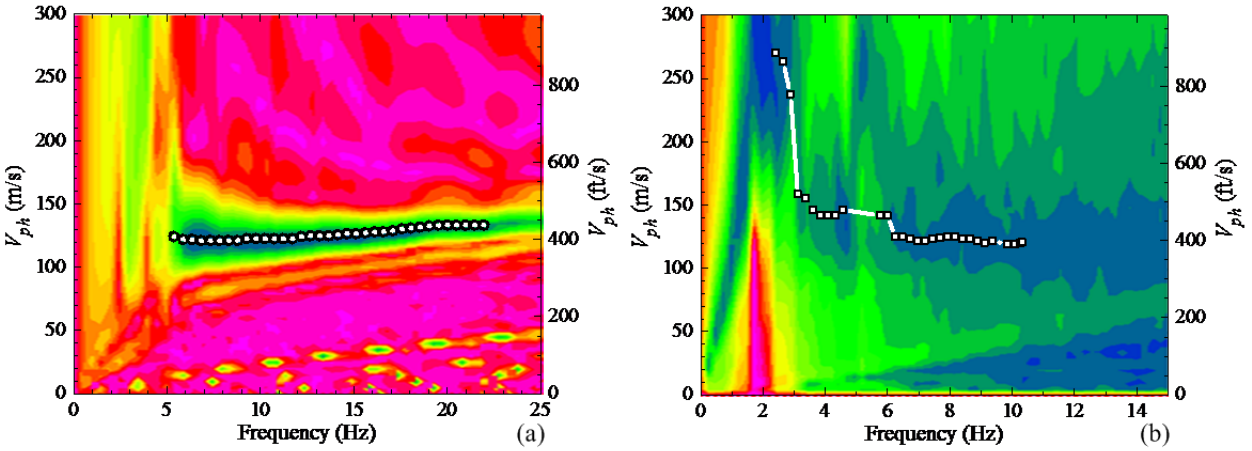

Figure 3.6 Dispersion curves from Carleton landfill location 1: (a) MASW and (b) MAM testing.

The independently developed dispersion curves from the MASW and the MAM data were then compared. In some cases, the passive dispersion curve agreed well with the active dispersion curve and provided additional information on frequencies that were not available from the MASW data. In this study, generally active dispersion curves contain high frequency data (10-30 Hz), whereas the passive curve contains lower frequency data (< 15 Hz). An example of such case is shown in Fig. 3.7, which illustrates the dispersion curves from the active and passive data in Fig. 3.6. In such cases, a smoothed combined dispersion curve was generated from the active and passive data and used in the inversion process. In other cases, the MAM data did not agree well with the MASW data. This discrepancy may be attributed to the method of analysis of the passive data (SPAC method) and the use of a linear array the presence of strong directionality of background noise. The SPAC method assumes that the signal is stable and omnidirectional

(Aki 1957 and Okada 2003). A linear geophone array does not accommodate the omnidirectionality assumption when a passive noise originates primarily from one direction. When active and passive dispersion curves were not consistent for the overlapping frequencies, the inversion process was performed using the active dispersion curve only. The combination of dispersion curves from active and passive records is often valuable. It broadens the frequency range of the dispersion curve. Additionally, it helps differentiate modes of Rayleigh waves in the dispersion curve (Park et al. 2005).

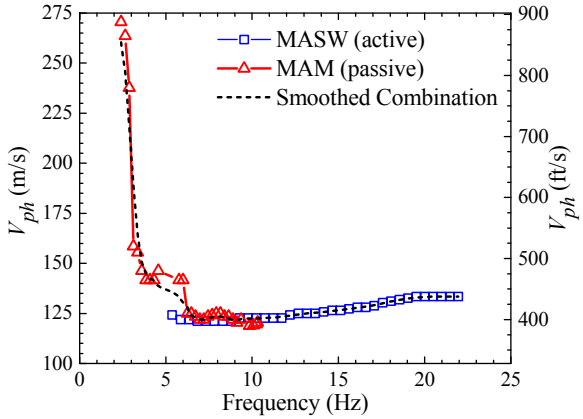

Figure 3.7 Combination of MASW and MAM dispersion curves at location 1 in the Carleton Farms Landfill.

3.2.4 Inversion Process

The measured dispersion curve from the MASW or the combined MASW/MAM data was used in the last stage of the analyses to obtain the V_s profile through an inversion process. An assumed V_s profile, compression wave velocity (V_p) profile, and mass density (ρ) profile were used to perform direct or forward modelling to obtain a theoretical dispersion curve (Lai and Rix 1998). The theoretical curve was compared against the measured one, and changes in the assumed profile were made iteratively until the two curves closely match. In this study, WaveEq software (Geometrics Inc.) was utlized in the inversion process. A non-linear least squares method was

implemented to evaluate the fitness between the theoretical dispersion curve and its measured counterpart (Xia et al. 1999).

It is important to note that as part of the inversion process, the V_s at shallow layers affected the inversed V_s at deeper layers. For this investigation, as shown in the following sections, the highest frequencies recorded were in the order of 25-30 Hz with phase velocities of 100-160 m/sec. Assuming the depth of investigation was about one-third of the wavelength (Eq. 3.2), the shortest wavelengths for which data was recorded were in the order of 2.4-5 m resulting in uncertainty in the V_s for approximately the top 0.8-1.7 m, which was considered acceptable since the objective of this study was to characterize the change in V_s with depth. The V_s profiles shown in subsequent figures include only the V_s of MSW material and not of the foundation soils.

3.2.5 Landfill Descriptions and Surface Wave Testing Results

3.2.5.1 Arbor Hills Landfill

The Arbor Hills Landfill is located in Northville, Michigan and has been receiving MSW from southeast Michigan since 1991. According to the owner, the unit weight of waste is about 14.5 kN/m^3 (2267 lbs/yd^3) based on an average estimate for all disposed waste including MSW as well as construction and demolition debris (C&D). The maximum thickness of waste is 61 m (200 ft).

Surface wave testing in Arbor Hills landfill was performed by Dr. Dimitrios Zekkos, Mr. Adam Lobbestael, and Ms. Stephanie Guisbert on June 12, 2009. Four testing locations in this landfill are shown in Figs. 3.8 and 3.9.

Figure 3.8 Surface wave testing locations in the Arbor Hills Landfill.

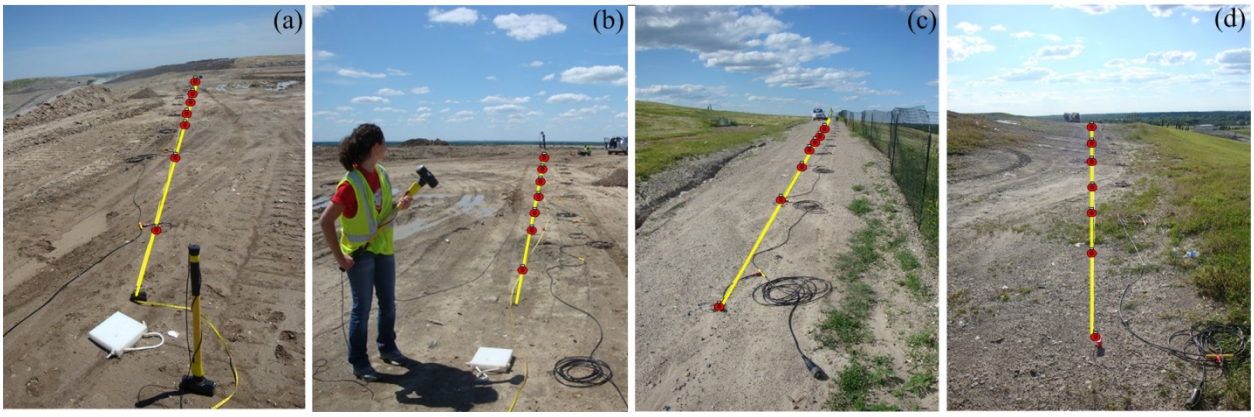

Figure 3.9 Surface wave testing at the Arbor Hills Landfill: (a) location 1, (b) location 2, (c) location 3, and (d) location 4.

Figure 3.10(a) presents the dispersion curves generated from data collected at the Arbor Hills Landfill. Dispersion curves at locations 1 and 4 were developed using the MASW data only. Dispersion curves at locations 2 and 3 were obtained by combining their corresponding MASW and MAM dispersion curves. The majority of the dispersion curves indicate that V_{ph} decreases with increasing frequency, implying a "normal" site with V_s increasing with depth. In some cases, V_{ph} may increase with frequency as shown by location 4 in the Arbor Hills Landfill. This indicates the presence of a high velocity layer over a low velocity layer. In these "irregular"

sites, a consideration of higher modes of Rayleigh waves is recommended in the inversion stage (Tokimatsu et al. 1992 and Hayashi 2012). Thus, the V_s profile at location 4 was calculated by taking into account the higher modes of Rayleigh waves.

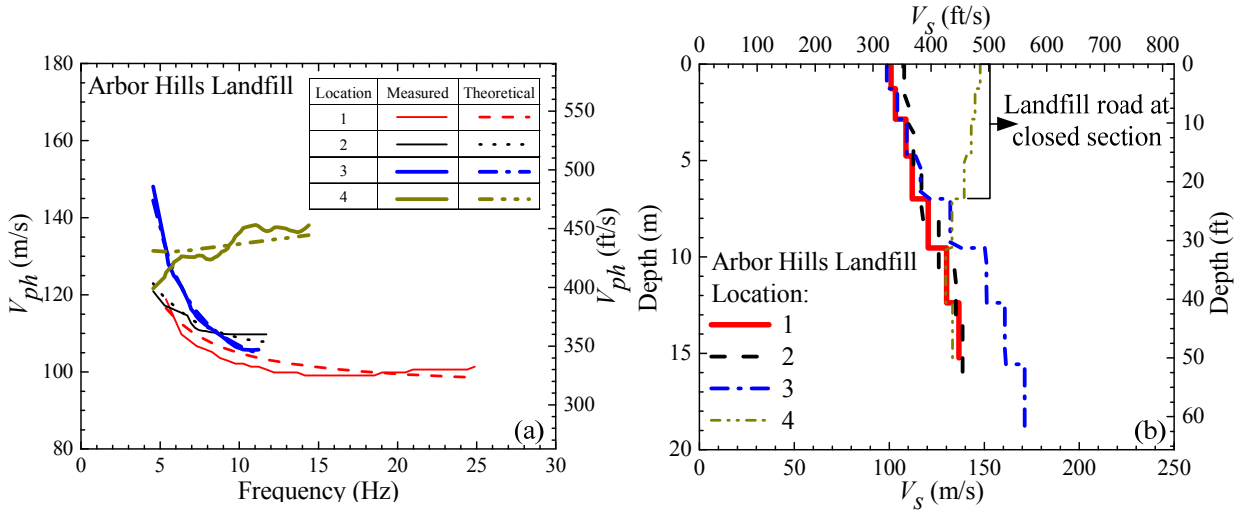

Figure 3.10 (a) Dispersion curves and (b) V_s profiles from the Arbor Hills Landfill.

The V_s profiles at the Arbor Hills Landfill are presented in Fig. 3.10(b). The uncertainty in the V_s profiles for locations 2, 3 and 4 was higher than the uncertainty in the V_s profile for location 1 because the reliable dispersion data were fewer. For example of the worst case, reliable data was collected only for frequencies ranging from 5 Hz to 12 Hz in location 2. This frequency range was equivalent to wavelengths between 9 m and 24 m. In such cases, although the inversion process could be completed, the reliability of this inversed V_s profile was lower than in the case of location 1 where reliable data was collected for wavelengths varying from 4 m to 24 m. The V_s profiles from location 1 and 2 were similar. The V_s profile at location 3 was also consistent for depths up to 10 m and appeared to increase with depth faster at greater depths than in locations 1 and 2. Location 4 was on top of an unpaved landfill road at a closed section of the landfill with older waste. Although, the V_s appeared to be similar to locations 1 and 2 for depths

greater than 7 m, at shallower depths the V_s was much higher, probably due to the cover soils and the fill material used for the landfill access road.

3.2.5.2 Carleton Farms Landfill

The Carleton Farms Landfill is located in New Boston, Michigan. This landfill has been receiving MSW from southeast Michigan and Toronto (Canada) since 1993. Currently, this landfill does not receive waste from Toronto. The owner estimated MSW unit weight of this landfill as high as 13.7 kN/m^3 (2300 lbs/yd^3). Soil cover is 7% by volume on the exterior slopes with auto shredder residue being used throughout the landfill with the exception of the exterior permanent slopes. Auto fluff consists of non-metallic shredded pieces of vehicles, typically soft and stiff plastics, cushions, foam and other parts of the interior of vehicles that are typically light in weight as shown in Fig. 3.11. Caterpillar model 836 compactors are used for the compaction of the waste.

The surface wave testing in the Carleton Farms Landfill was conducted in 3 locations. On June 25, 2010, the author, Dr. Dimitrios Zekkos, and Ms. Sarah Chronister performed testing in location 1 and 2. Location 3 was tested on July 1, 2010 by the author, Dr. Dimitrios Zekkos, and Ms. Anna James. Testing locations in the Carleton Farms Landfill is shown in Figs. 3.12 and 3.13. Location 1 was on a bench of the landfill. The thickness of waste in locations 1, 2 and 3 was 30 m (100 ft), 73 m (215 ft) and 40 m (130 ft). Locations 1 and 3 received borrow soil as daily cover. Location 2 was at the crest of the landfill where auto shredder residue was used as daily cover. Locations 1 and 3 were at a MSW and sludge combined-disposal area. Sludge was placed in trenches excavated in the MSW and then was covered with MSW.

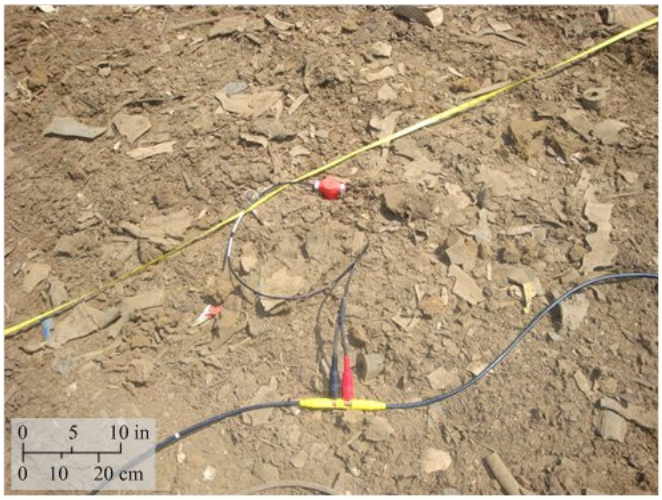

Figure 3.11 Auto fluff in location 2 Carleton Farms landfill.

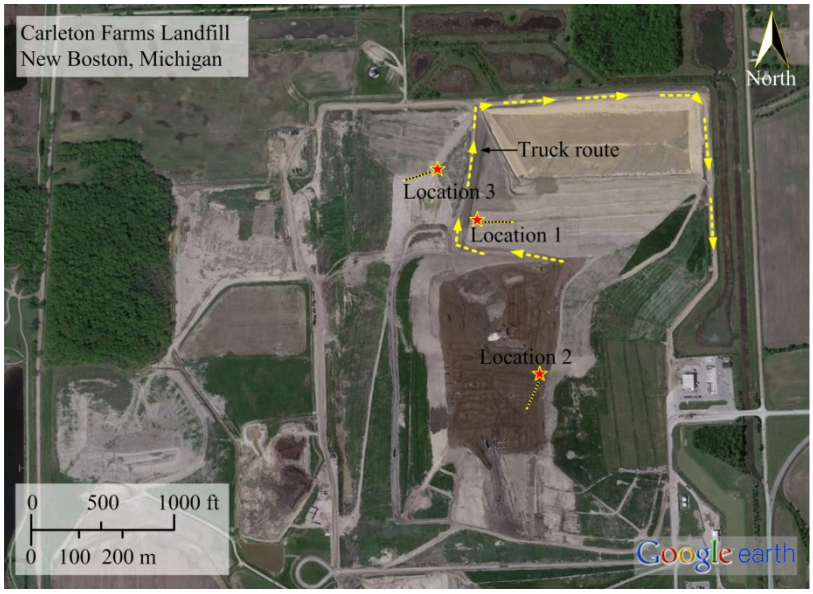

Figure 3.12 Surface wave testing location in the Carleton Farms Landfill.

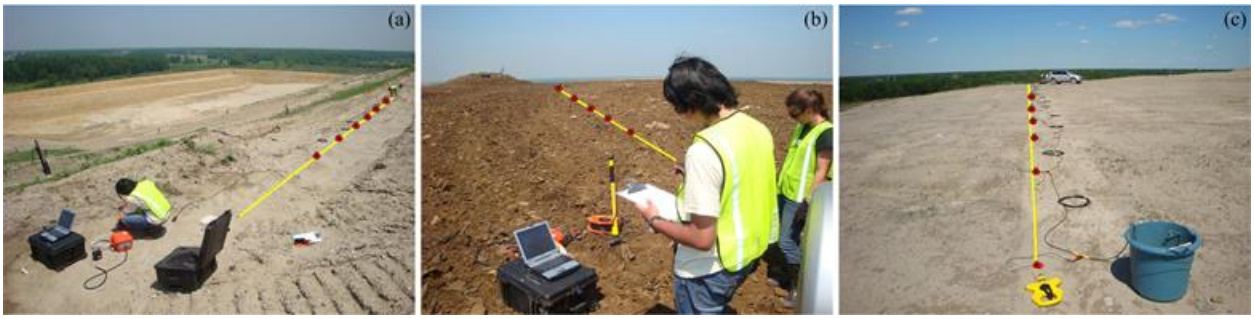

Figure 3.13 Surface wave testing at the Carleton Farms Landfill: (a) location 1, (b) location 2, and (c) location 3.

Surface wave testing at location 1 provided an opportunity to evaluate the reliability of a MAM test with a linear geophone array where trucks were following a route that essentially surrounded the geophone array (Fig. 3.12). The geophones were installed along the slope contour on a bench of a temporary landfill slope. The fundamental dispersion curve of active testing was extracted from frequency of 5 to 22 Hz and is presented in Fig. 3.6(a). The major surface wave sources in MAM passive records were the waste transportation trucks (Fig. 3.12). The other sources in this landfill were likely minor as they were located at significantly greater distances. MAM data acquisition was performed during truck traffic. Fig. 3.6**(**b) shows dispersion curve of passive testing with frequency range between 2.5 and 10 Hz. At frequencies between 6 and 10 Hz, the MASW and MAM dispersion curves yielded consistent results and were combined to generate the "measured" curve, which was used in the inversion process. It appeared that the surrounding truck traffic yielded passive data that were reliable and consistent with the active data. However, this may be possibly attributed to the fact that the closest distance along the truck route that yielded the dominant surface waves was in-line with the geophone array contributing the most to the dispersion image.

Dispersion curves at the Carleton Farms Landfill are presented in Fig. 3.14(a). Dispersion curves at locations 1 and 3 were derived using their MASW and MAM dispersion curves. The dispersion curve of location 2 was generated using MASW data only. Figure. 3.14(b) shows V_s profiles at the Carleton Farms Landfill. Inversion at location 3 was conducted by taking into account the higher-mode of Rayleigh waves. The near surface shear wave velocity of location 2 was significantly lower than those of the other two testing locations. In location 1, the auto fluff was used as alternative daily cover. In general, the V_s profiles at depth of 6 to 20 m were similar.

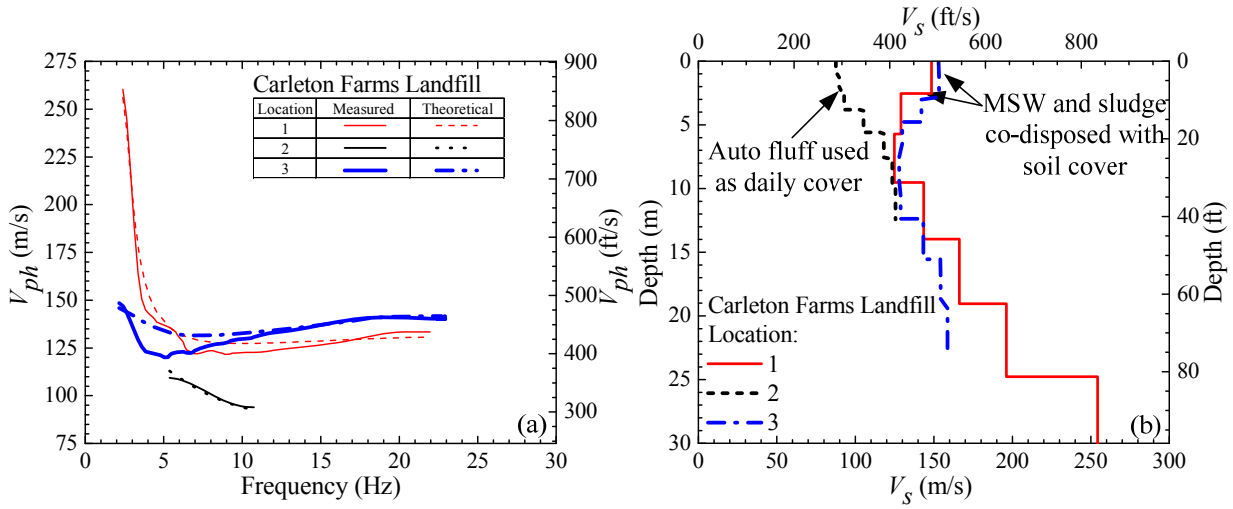

Figure 3.14 (a) Dispersion curves and (b) V_s profiles in the Carleton Farms Landfill.

3.2.5.3 Sauk Trail Hills Landfill

The Sauk Trail Hills Landfill is located in Canton, Michigan. It has been receiving MSW from southeast Michigan since 1974. The estimated MSW unit weight is approximately 13.7 kN/m^3 (2300 lbs/yd^3). Approximately 7% by volume soil is used for daily soil cover operations. Large compactors are also used for the compaction of the waste in this landfill.

Surface wave testing in the Sauk Trail Hills Landfill was performed by the author, Dr. Dimitrios Zekkos, and Mr. Xunchang Fei on July 8, 2010. Three testing locations in this landfill are shown in Figs. 3.15 and 3.16. The thickness of waste was 30 m (100 ft), 70 m (230 ft) and 37 m (120 ft) in locations 1, 2, and 3, respectively. Auto shredder residue was used as daily cover for the top 3 lifts in location 1. Local soil was used as daily cover in locations 2 and 3.

Landfill operation activities (e.g. transportation, placement, and compaction of waste) were ongoing nearby location 1 during MASW and MAM tests (Fig. 3.17). At this location, two MASW tests using the same geophone array yielded essentially the same dispersion curve as shown in Fig. 3.18. The major wave sources in MAM passive record at this location were

construction equipment operating as part of regular landfill operations and included Caterpillar model 836 compactors. The construction machinery was essentially aligned with the linear geophone array at a distance of approximately 90 m (300 ft) as shown in Fig. 3.17. The Rayleigh waves can be treated as horizontally traveling plane waves after they have propagated at certain distance (source offset of x_s) from the source point (Richart et al. 1970). The plane-wave propagation of surface waves does not occur in most cases until x_s is greater than half the maximum desired wavelength (Stokoe et al. 1994). The dispersion curve from MAM testing was extracted at frequencies between 2.5 and 7.5 Hz. The dispersion curves from the two active and the passive soundings were consistent, with similar phase velocities overlapping in the frequency range between 5 and 10 Hz. The dispersion curves were combined to extend the frequency range of the measured dispersion curve and the resulting curve was used in the inversion process.

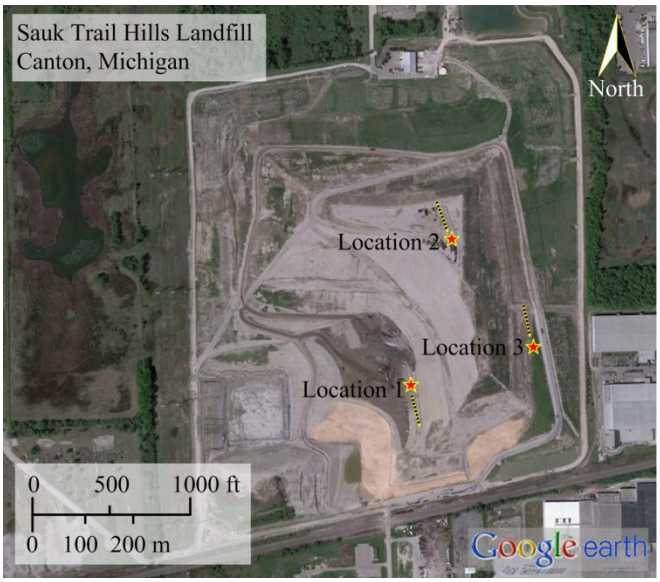

Figure 3.15 Surface wave testing location in the Sauk Trail Hills Landfill.

Figure 3.16 Surface wave testing at the Sauk Trail Hills Landfill: (a) location 1, (b) location 2, and (c) location 3.

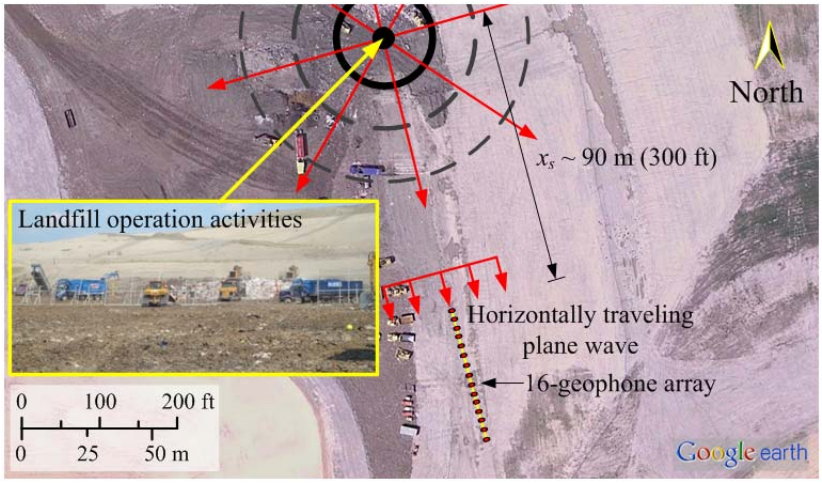

Figure 3.17 Illustration of the location of surface wave sources with respect to the 16-geophone array at location 1 in the Sauk Trail Hills Landfill.

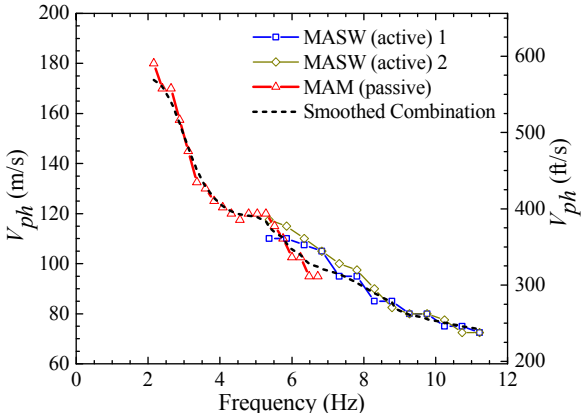

Figure 3.18 Combination of MASW and MAM dispersion curves from location 1 in the Sauk Trail Hills Landfill.

The results indicate that when background noise propagation direction is aligned with the linear geophone array, the resulting dispersion curve is consistent with its active counterpart. Indeed, this particular passive testing configuration resembled an active source type of configuration with the construction machinery being the main MAM sources, compared to the 4.5-kg sledge hammer in the MASW. These sources generated longer wavelengths (lower frequencies) than that of the sledge hammer. As the analyzing depth range is proportional to the range of the analyzable wavelengths, a greater depth of investigation is achieved using the combined MAM and MASW data.

Figure 3.19(a) shows dispersion curves at the Sauk Trail Hills Landfill. Dispersion curves at locations 1 and 3 were generated by combining the MASW and MAM dispersion curves. The dispersion curve at location 2 was only obtained from the MASW data. V_s profiles at the Sauk Trail Hills Landfill are presented in Fig. 3.19(b). Significant variations in V_s were observed between the three profiles at the Sauk Trail Hills Landfill. At location 1, where auto fluff was used, the V_s of the waste was significantly lower than the V_s in locations where local soils were used. An abrupt increase in the V_s values was observed below depths of 4.5 m. This increase was consistent with the thickness of the waste that was covered with auto fluff as opposed to daily soil cover. The V_s for the top 20 m in location 3 was higher than the V_s in locations 1 and 2, probably because of the co-disposal of contaminated soils. According to the landfill operator, contaminated soil may represent as high as 40% of the total volume of waste disposal in the summer months.

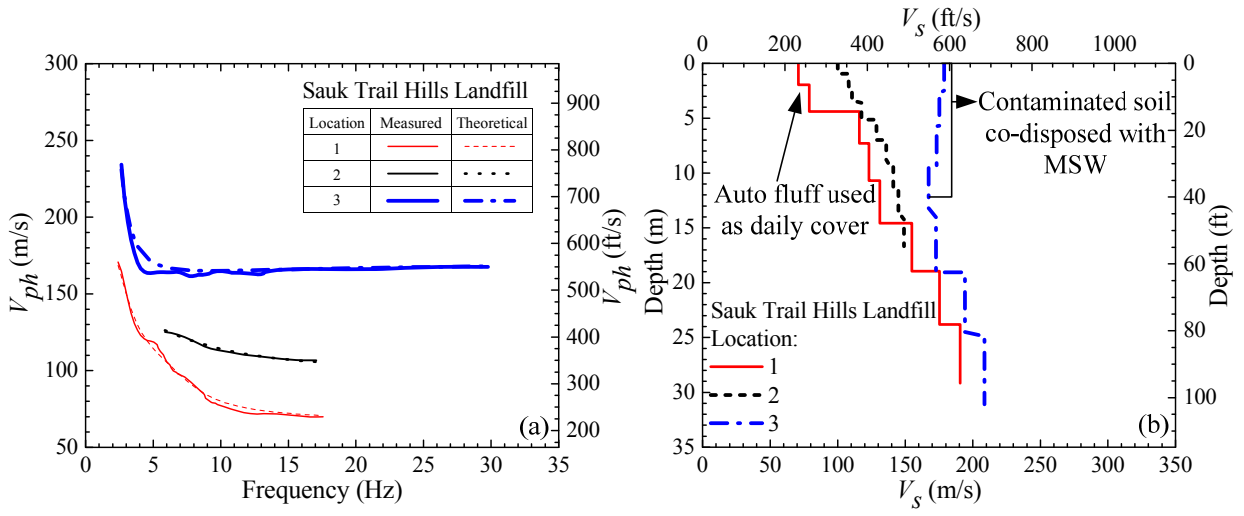

Figure 3.19 (a) Dispersion curves and (b) V_s profiles in the Sauk Trail Hills Landfill.

3.2.5.4 Oakland Heights Landfill

The Oakland Heights Landfill is located in Auburn Hills, Michigan and has been receiving MSW from Macomb and Oakland Counties, Michigan since the 1980s. The MSW unit weight, estimated by the landfill owner, is 11.8-14.7 kN/m^3 (2000-2600 lbs/yd^3). Approximately 12% by volume soil is used for daily cover operations and the waste is compacted with Caterpillar model 836. Operations and maintenances in this landfill are performed by the same operator as in Carleton Farms and Sauk Trail Hills landfill.

Field investigation was performed by the author, Dr. Dimitrios Zekkos, and Ms. Anna James on July 13, 2010. Figures 3.20 and 3.21 show 3 testing locations in the Oakland Heights Landfill. The geophone array in location 1 was situated along a bench of the landfill that was underlain by at least 2 m of soil as observed by a trial test pit followed by MSW from the 1980s. Locations 2 and 3 were at the crest of the landfill on waste placed since 1994. The thickness of waste was 30 m (100 ft) in location 1 and 49 m (160 ft) in locations 2 and 3.

Figure 3.20 Surface wave testing location in the Oakland Heights Landfill.

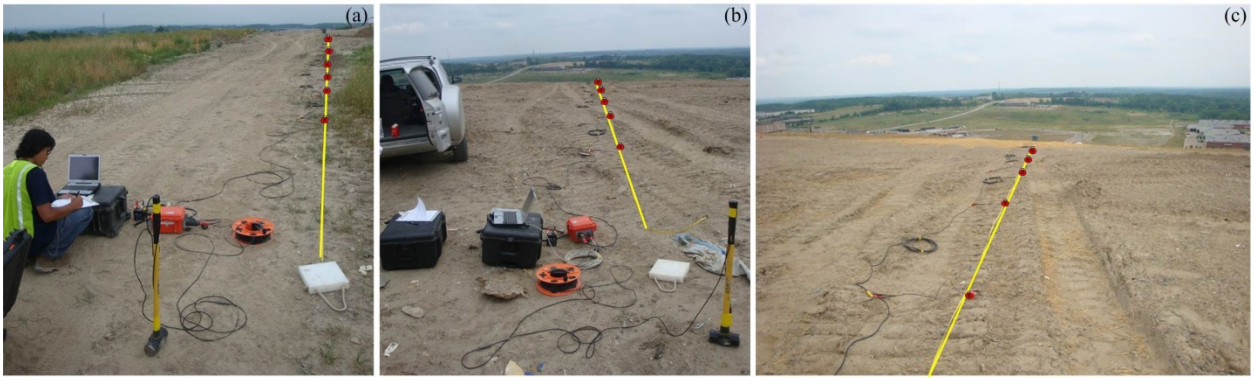

Figure 3.21 Surface wave testing at the Oakland Heights Landfill: (a) location 1, (b) location 2, and (c) location 3.

During surface wave tests at locations 2 and 3, a Caterpillar D8R crawler tractor was constructing a temporary berm. Two linear geophone arrays were positioned so that the movement of the tractor was moving parallel to the geophone array on one side (location 2) and in-line with the geophone array (location 3) as shown in Fig. 3.22. MASW data were collected using the sledge hammer as a source, when the tractor was not in operation. MAM data were collected when the tractor was in operation.

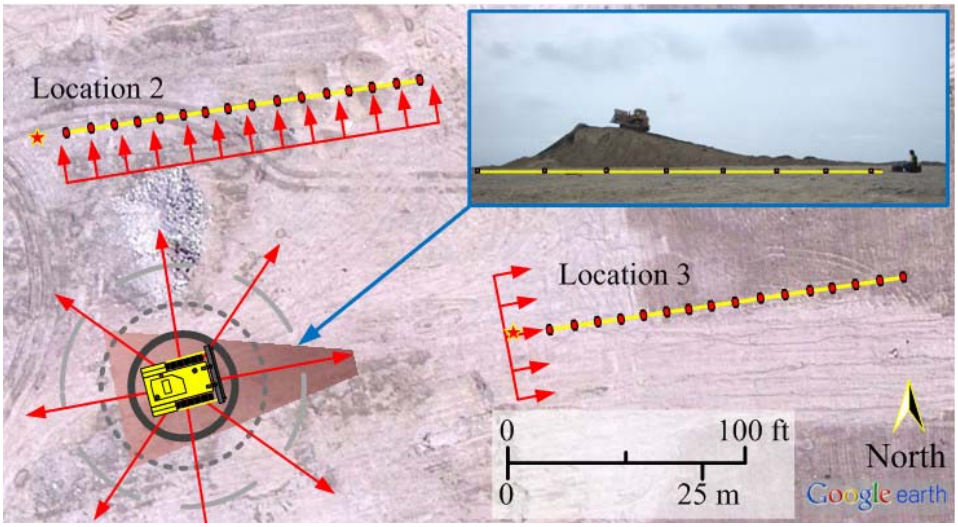

Figure 3.22 Illustration of MASW and MAM testing at locations 2 and 3 in the Oakland Heights Landfill.

Figure 3.23(a) presents the results of MASW test in location 2, whereas the results in location 3 are shown in Fig. 3.23(b). The MASW dispersion curves from both locations were similar. Using the tractor as the major passive surface wave source, twenty 32-second records were collected for each location. An example of time history record from location 2 is presented in Fig. 3.24(a). The time history record shows relatively similar signal amplitude from trace-to-trace at 0 to 5 seconds, an indication of disturbances from the tractor arrived at all geophones at the same time. Figure 3.23(a) presents the dispersion curve of passive testing in location 2. The dispersion curve pattern was not very clear, but data was extracted for frequencies between 2.5 and 15 Hz. Figure 3.24(b) show an example of time history record from location 3. This time history record indicates that the surface waves arrived first at the closest geophone to the crawler tractor (i.e. geophone #16). The dispersion curve of passive testing in this location is presented in Fig. 3.23(b).

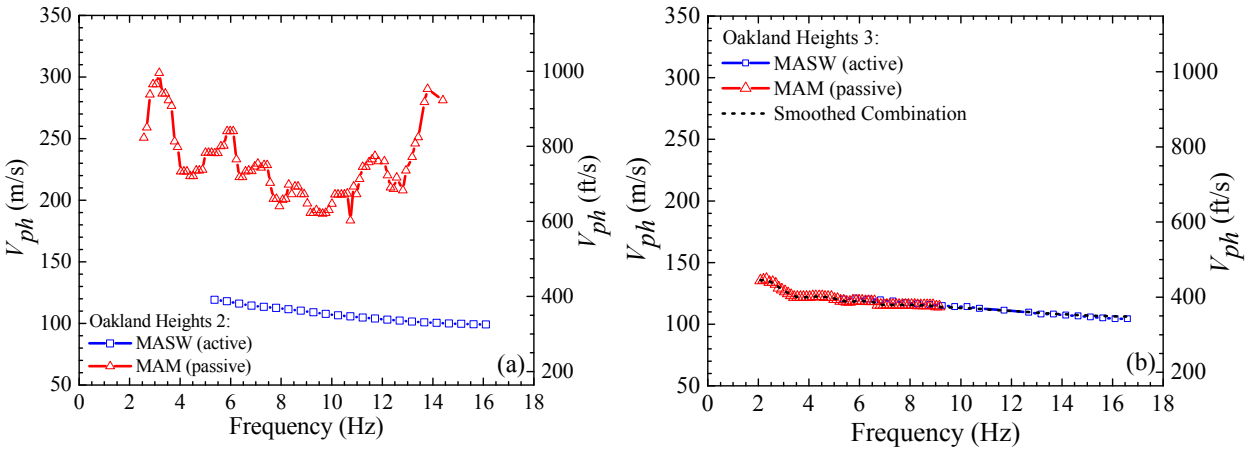

Figure 3.23 Combination of MASW and MAM dispersion curves at (a) location 2 and (b) location 3 in the Oakland Heights Landfill.

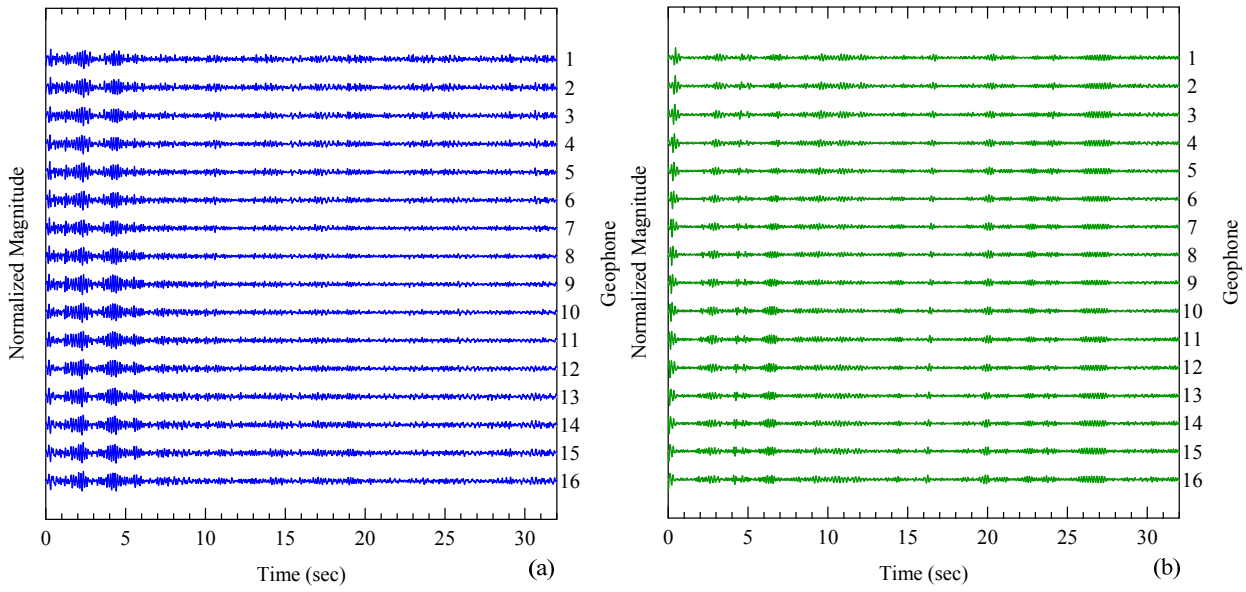

Figure 3.24 Examples of time history record from (a) location 2 and (b) location 3 in the Oakland Heights Landfill.

The measured dispersion curves from MASW and MAM from locations 2 and 3 are presented in Fig. 3.23. The MASW and MAM dispersion curves in location 2 were not consistent, with the MAM dispersion curve yielding significantly higher apparent phase velocities. The MASW and MAM dispersion curves were consistent for location 3 and were overlapping for frequencies between 5 and 9 Hz. The inconsistency in the results of the MAM

test in location 2 was attributed to the relative position of the tractor with respect to the linear geophone array. When the tractor was moving parallel to the geophone array (location 2) the surface waves arrived at all geophones at the same time, yielding high apparent phase velocities that were not reliable. Also SPAC's requirement for omni-directional background noise was not satisfied (Aki 1957 and Asten 1983). The MAM test in location 3 yielded a good result and was consistent with observations at location 1 in the Sauk Trail Hills Landfill.

Dispersion curves from the Oakland Heights Landfill are presented in Fig. 3.25(a). Dispersion curves at locations 1 and 2 were generated using the MASW data only, whereas the dispersion curve at location 3 was derived by combining MASW with MAM. The inversion process of the dispersion curve at location 1 considered higher modes of Rayleigh waves and MAM data. Figure 3.25(b) shows V_s profiles at the Oakland Heights Landfill. The V_s profiles were similar in locations 2 and 3. A high V_s layer was observed in location 1 overlying the MSW which had approximately the same V_s at a depth of 7 m in locations 2 and 3.

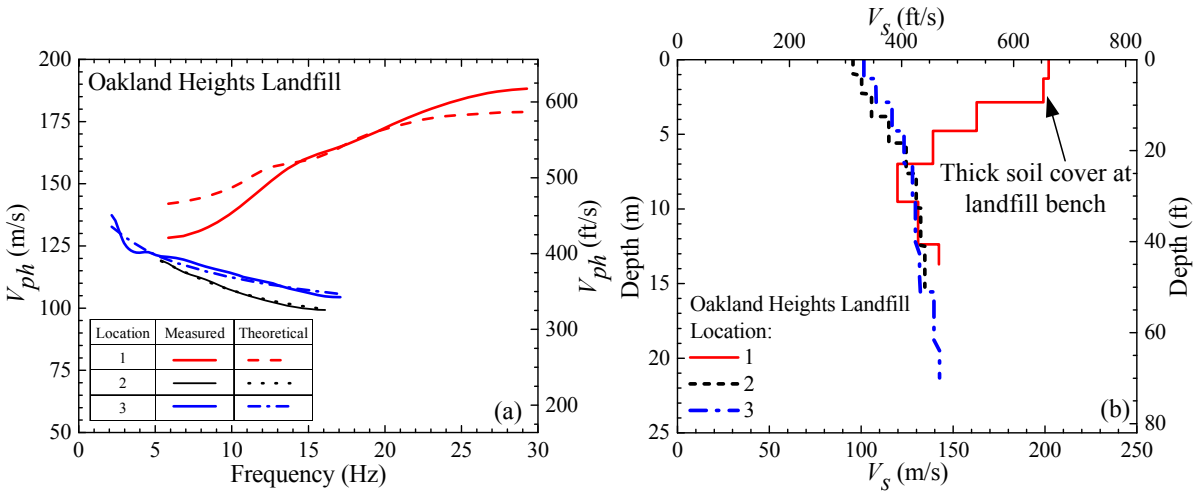

Figure 3.25 (a) Dispersion curves and (b) V_s profiles in the Oakland Heights Landfill.

3.2.6 Statistical Analysis of V_s Profiles from Michigan Landfills

Figure 3.26 presents the statistical analysis results of V_s profiles of four Michigan landfills in this study. This statistical analysis was performed by excluding soil cover, auto fluff cover, and crust layer that occurred in the V_s profiles. On average, V_s was about 100 m/s at the surface and increased to 218 m/s at depth of 29 m. The coefficient of variance (COV) ranges from 0.01 to 0.15 with an average of 0.08.

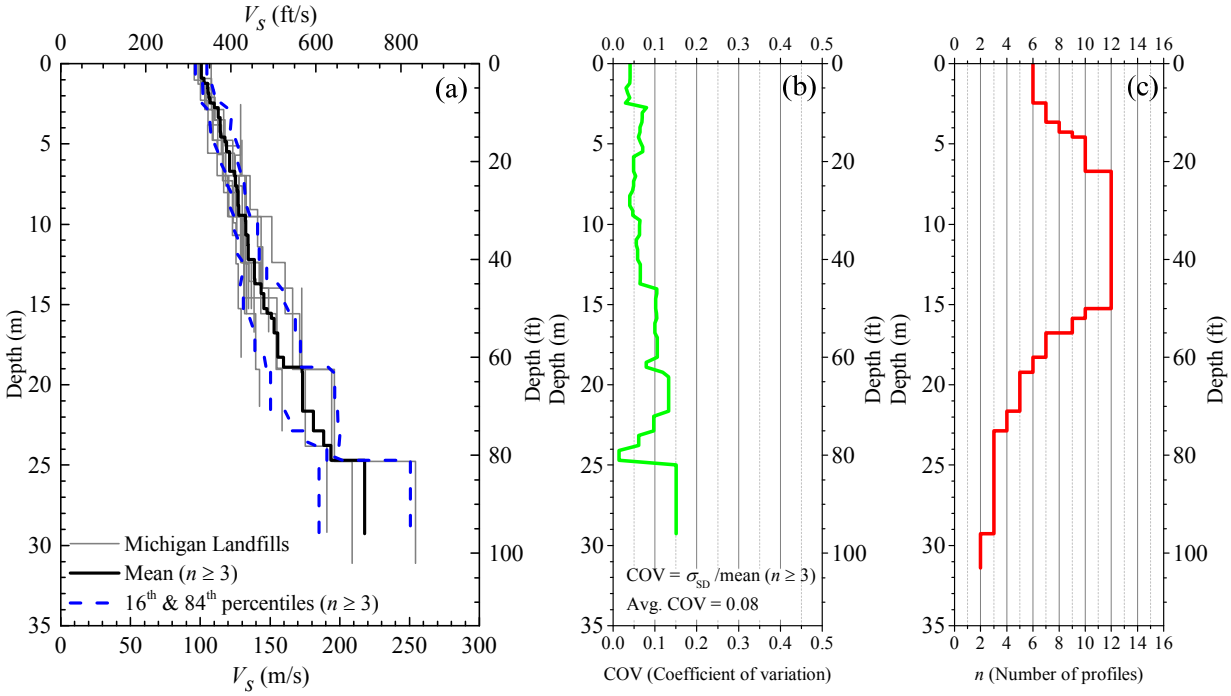

Figure 3.26 Statistical analysis of V_s profiles from 4 Michigan landfills: (a) mean and mean ± standard deviation (b) coefficient of variation, and (c) number of profiles.

The V_s profiles from the landfills in Michigan are compared against the V_s profile data from southern California (Kavazanjian et al. 1996) and northern California (Lin et al. 2004) as shown in Fig. 3.27. The average V_s profiles from Michigan landfills were lower than those of California landfills, particularly the southern California landfills. Nevertheless, at depth greater than 22 m, these V_s profiles were more consistent. The differences may be attributed to a number

of factors, such as differences in operation practices, waste streams, and waste compositions. In addition, differences in climate may affect the degradation of MSW and its composition. Southeast Michigan has a continental climate with much higher seasonal temperature fluctuations (warm summers and cold winters) and greater precipitation (in the order of 750-1000 mm), compared to south California that has a Mediterranean climate with much lower precipitation (in the order of 250-380 mm).

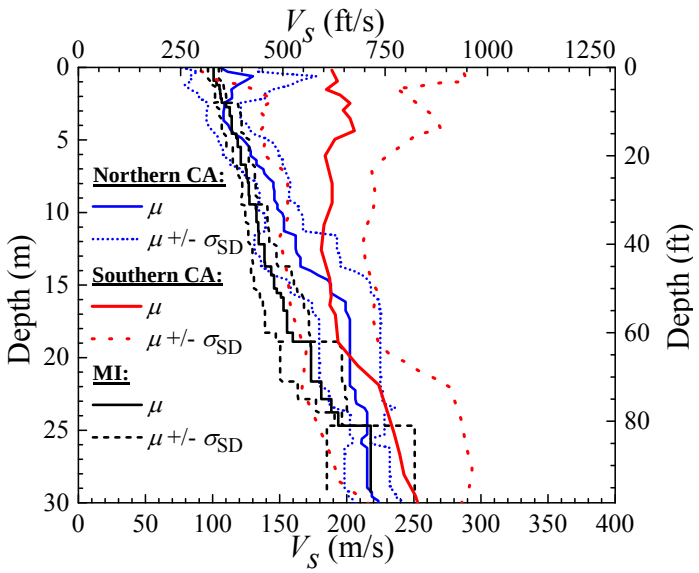

Figure 3.27 Statistical analysis of V_s profiles from Michigan, southern California, and northern California landfills.

3.3 **Models for Shear Wave Velocity of MSW**

The V_s and G_{max} of geomaterials have been studied comprehensively for many years (e.g., Hardin and Drnevich 1972, Seed and Idriss 1970, Richart 1975, Hardin 1978, Kokusho et al 1982, Dobry and Vucetic 1987, Stokoe and Santamarina 2000, and Menq 2003). The general expressions describing V_s and G_{max} are presented in the following equations.

$$V_s = A_{VS} \cdot p(e) \cdot \sigma_0'^{r} \tag{3.3}$$

$$G_{max} = A_G \cdot f(e) \cdot \sigma_0'^{m} \tag{3.4}$$

where A_G and A_{VS} are material parameters affected by various factors, such as soil type, overconsolidation ratio, strain rate, and other factors; $f(e)$ and $p(e)$ are mathematical functions describing the effect of void ratio (e) on V_s and G_{max}, respectively, σ_0' is the effective confining stress; and m and r are the exponents of confining stress with $r = m/2$. Commonly σ_0' represents isotropic confining stress because specimens in laboratory dynamic testing equipment are subjected to an isotropic stress state. Subsequent studies have shown that an anisotropic stress state, either in the laboratory or in the field, induces anisotropy in wave propagation velocities (Belloti et al. 1996, Stokoe et al. 1991). As noted in Eq. 3.4, G_{max} is related to the isotropic stress by a power function with a stress exponent m. Many studies have shown that this exponents may range from 0.13 to 0.65 (Hardin and Richart 1963, Hardin and Black 1968, Iwasaki and Tatsuoka 1977, Hryciw and Thomman 1993, Stokoe et al. 1995, Tatsuoka et al. 1995, Zhuo and Chen 2005, Khosravi and McCartney 2009).

Semi-empirical and empirical models were developed for V_s of MSW based on parallel models developed for soils. The semi-empirical model is a comprehensive model that aims in separating the influence of waste density and confining stress on the *Vs* of MSW. The semi-empirical model involves more variables and its mathematical expression is more complex. This model was mathematically formulated on the basis of laboratory experimental data. After the equation form was derived from laboratory testing, it was utilized to match measured field V_s profile data by adjusting model parameters. The empirical model has a simpler mathematical form that only expresses the relationship between depth and the shear wave velocity. It is calibrated simply by fitting it to the field measurements of the *Vs* of MSW and empirically deriving the model parameters.

3.3.1 Formulation of the Semi-empirical Model from Laboratory Data

The generic form of the V_s model and its corresponding $G_{\max}$ model are presented in Eqs. 3.5 and 3.6.

$$V_s = g\left(\frac{\gamma_t}{\gamma_w}\right) \cdot h\left(\frac{\sigma_0'}{P_a}\right) \tag{3.5}$$

$$G_{max} = k\left(\frac{\gamma}{\gamma_w}\right) \cdot l\left(\frac{\sigma_0'}{P_a}\right) \tag{3.6}$$

where $g(\gamma_t/\gamma_w)$ and $k(\gamma_t/\gamma_w)$ are functions describing the relationship of V_s and G_{max} to the normalized total unit weight of the MSW; $h(\sigma_0')$ and $l(\sigma_0')$ are functions expressing the relationship of V_s and G_{max} with the normalized effective isotropic confining stress; γ_w is unit weight of water; and P_a is atmospheric pressure. To avoid dimension or unit problems, the γ_t and σ_0' in these functions are normalized with γ_w and P_a, respectively.

Most equations for V_s and G_{max} for soils use void ratio or relative density to express the compactness of soils. But, it is impractical to use these properties for MSW. Thus, total unit weight is used. Unit weight, as reported by Zekkos et al. (2006a), is an indicator of waste compactness and waste composition. For the same depth (or confining stress), lower unit weights are correlated with waste-rich MSW, and higher unit weights with soil-rich MSW. Thus, the $g(\gamma_t/\gamma_w)$ function also essentially represents variation in waste composition.

Results from the large-scale laboratory testing generated by Zekkos et al. (2008) and Lee (2007) were used to derive the mathematical form of functions g, h, k, and l in Eq. 3.5 and 3.6. Zekkos et al. (2008) data were generated from a cyclic triaxial testing that measured G_{max}, whereas Lee (2007) data were obtained from a resonant column testing that measured V_s. As the mass densities of MSW specimens were always reported, the transition between G_{max} and V_s could be reliably made (Eq. 3.1). Figure 3.28(a) presents the Zekkos et al. (2008) $G_{\max}$ data for

all MSW triaxial specimens from different waste samples (A3, C3 and C6 as described by Zekkos et al. 2008), tested at at a confining stress of 75 kPa and at 24-hour time under isotropic confinement. The dataset includes specimens that consist entirely of <20 mm material, specimens of intermediate waste composition (62-76%<20 mm by weight), and specimens that consist almost entirely of the coarse waste fraction (17%<20 mm by weight). Figure 3.28(b) shows the corresponding relationship between normalized total unit weight and V_s. A general relationship between the normalized total unit weight and $G_{\max}$ [Fig. 3.28(a)] or V_s [Fig. 3.28(b)] at constant effective confining stress was derived for all MSW specimens from this study and expressed by the following equations.

$$G_{max} = B_G \left(\frac{\gamma_t}{\gamma_w}\right)^{n_\gamma} \tag{3.7}$$

$$V_s = B_{Vs} \left(\frac{\gamma_t}{\gamma_w}\right)^{r_\gamma} \tag{3.8}$$

At effective confining stress of 75 kPa, regression analyses showed that B_G is equal to 10150 kPa and n_γ is equal to 2.74, with a coefficient of determination of 0.94. Similarly, B_{VS} is equal to 103 m/sec and r_γ is equal to 0.74, with a coefficient of determination of 0.87.

Shear wave velocity data from Lee (2007) were obtained from different confining stresses ranging from 8 kPa to 276 kPa. The relationship between G_{max} or V_s with the normalized total unit weight is presented in Figs. 3.29 (a and b), respectively. These figures show that B_G and $B_{VS}$are variables that are a function of the confining stress. The scatter in the Lee (2007) data is somewhat higher than in the Zekkos et al. (2008) data. That may be attributed to the fact that the Lee (2007) data were not collected at the same time under confinement (24-48 hours) as was the case for the Zekkos et al. (2008) data (24 hours).

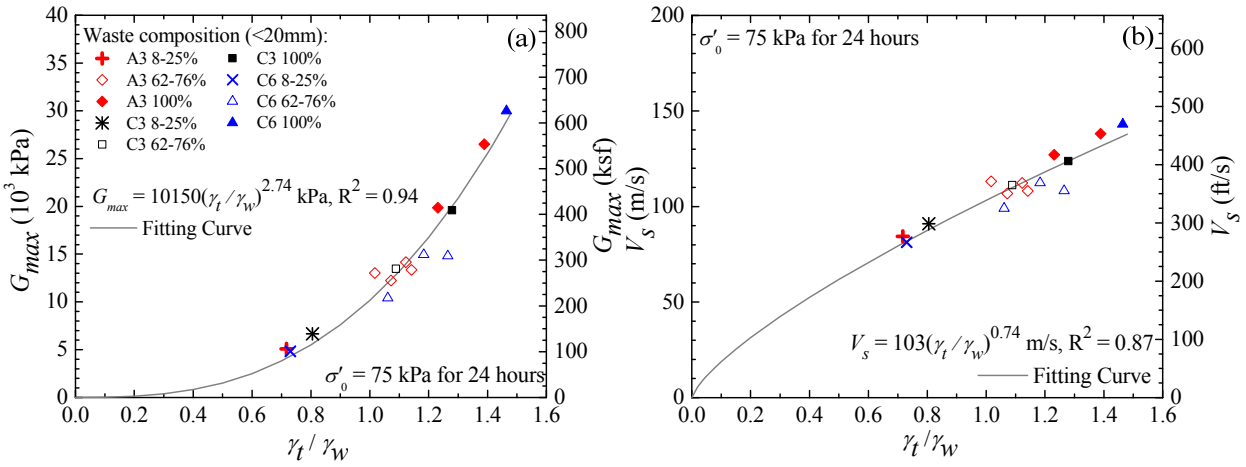

Figure 3.28 Relationship between (a) G_{max} or (b) V_s and the normalized total unit weight of MSW from the Zekkos et al. (2008) laboratory data.

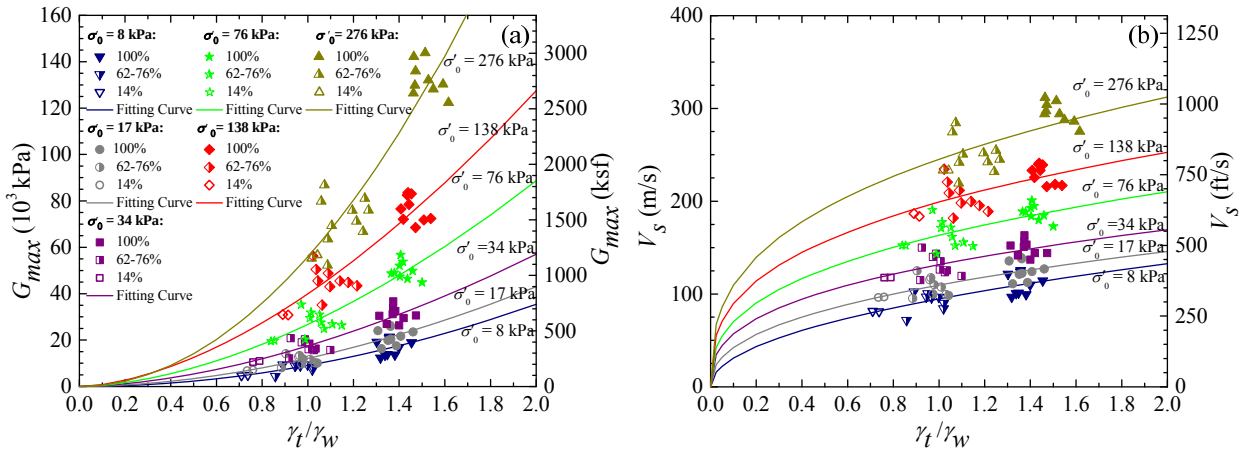

Figure 3.29 Relationship between (a) G_{max} or (b) V_s and the normalized total unit weight of MSW from the Lee (2007) laboratory data.

The resulting B_G, B_{VS}, n_γ, and r_γ values for the Lee (2007) data and Zekkos et al. (2008) data are presented in Table 3.1**.** The value of n_γ parameter varied from 1.7 to 2.0 for the Lee (2007) data. Most of the data appear to indicate a small reduction of the n_γ parameter with confining stress with exception of n_γ value at a confining stress level of 276 kPa. However, a variation between 1.7 and 2.0 is not significant for practical purposes. The n_γ parameter for the Zekkos et al. (2008) data had higher values than those of Lee (2007) data. Differences in the B_G and n_γ value for the Zekkos et al. (2008) and the Lee (2007) data may be attributed to several

differences in testing variables, including variations in testing frequency, time under confinement, specimen size, particle size, specimen preparation and compaction methods, and type of testing apparatus. However, waste variability may not be a contributor to this variability as the source of the waste material was the same for the two studies. Although the values of the n_γ parameter for the Lee (2007) data were lower, they also fit the Zekkos et al. (2008) data with high coefficients of determination.

Table 3.1 Regressed B_G, B_{Vs} , n_γ, and r_γ values and associated R^2 coefficients for the Lee (2007) and Zekkos et al. (2008) Laboratory Data.

Dataset	σ_0 (kPa)	B_G (kPa)	n_γ	R^2	B_{Vs} (m/s)	r_γ	R^2
Lee (2007)	8	9,080	1.97	0.79	95	0.49	0.55
	17	12,080	1.83	0.81	110	0.41	0.51
	34	17,500	1.70	0.84	132	0.36	0.5
	76	26,750	1.73	0.84	163	0.37	0.46
	138	39,930	1.67	0.82	199	0.35	0.43
	276	55,950	1.99	0.84	245	0.35	0.5
Zekkos et al. (2008)	75	10150	2.74	0.94	103	0.74	0.87

Using the Lee (2007) laboratory data, relationships between B_G, B_{Vs} and confining stress were established and are shown in Figs. 3.30(a and b). In general, the B_G and B_{Vs} increased with confining stress. The B_G and B_{Vs} can be related to confining stress using power or hyperbolic functions. Power functions for B_G and B_{Vs} are shown in Eqs. 3.9 and 3.10, respectively. Hyperbolic functions for B_G and B_{Vs} are presented in Eqs. 3.11 and 3.12, respectively.

$$B_G = 32580\left(\frac{\sigma_o'}{P_a}\right)^{0.55} \text{ (kPa)} \tag{3.9}$$

$$B_{Vs} = 179\left(\frac{\sigma_o'}{P_a}\right)^{0.27} \text{ (m/s)} \tag{3.10}$$

$$B_G = 6390 + \frac{101500\times\frac{\sigma_o'}{P_a}}{2.8+\frac{\sigma_o'}{P_a}} \tag{3.11}$$

$$B_{Vs} = 83 + \frac{224 \times \frac{\sigma'_o}{p_a}}{1.3 + \frac{\sigma'_o}{p_\alpha}} \tag{3.12}$$

where B_G is in kPa and B_{Vs} is in m/sec. The stress exponents in Eqs. (3.9-3.10) were consistent with values for soils (e.g. Hardin and Richart 1963, Hardin and Black 1968). Both the power and hyperbolic functions closely fit the data with very high R^2 values (R^2=0.999). Although a power function has been frequently used to express the relationship between V_s and G_{max} with confining stress in geomaterial, the power function indicates that the B_G and B_{Vs} parameters yielded a zero value of G_{max} and V_s at zero confining stress. Zero effective stiffness at zero confining stress (e.g. at the landfill surface) is not a realistic assumption for MSW that has variable waste constituents, particles with large sizes in at least one or two directions, and capillary stresses. The hyperbolic function accommodates that aspect of MSW behavior and allows for a finite stiffness of the MSW at the landfill surface.

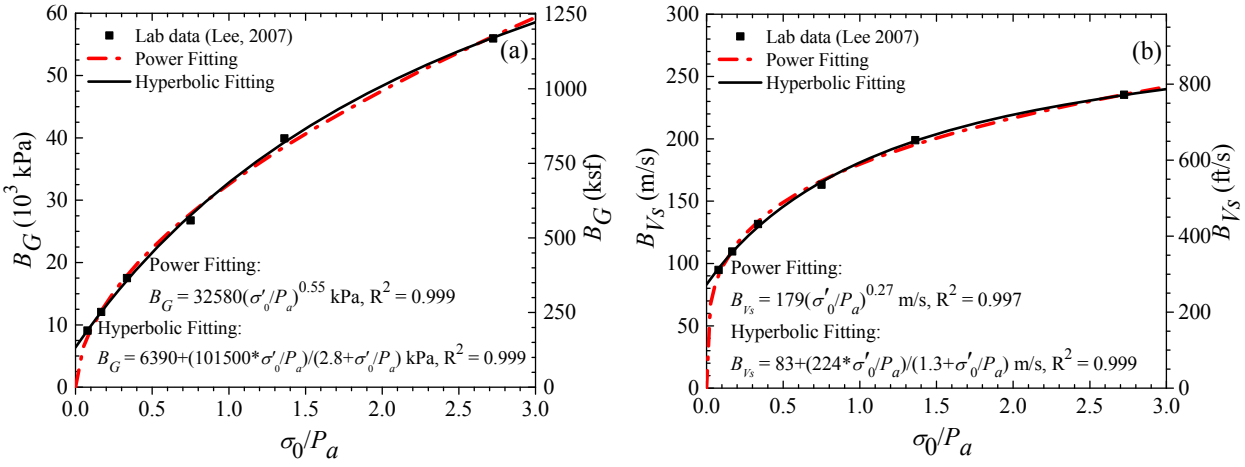

Figure 3.30 Relationship between the (a) B_G or (b) B_{Vs} function and the normalized isotropic confining stress based on the laboratory data from Lee (2007).

The laboratory-based values for the *B*-parameters are not as critical because they are representative of reconstituted laboratory specimens that have been under isotropic confining stress for a relatively short amount of time. However, the mathematical expression of the

equation should capture the relationship of G_{max} and V_s with unit weight and effective confining stress in the field and can be used to calibrate the relationship against field data.

3.3.2 Model Calibration against Shear Wave Velocity Data

3.3.2.1 Semi-empirical Model

The mathematical expression of the semi-empirical V_s model is presented in the following equation.

$$V_s = \left(A_L + \frac{B_L \times \frac{\sigma_o'}{P_a}}{C_L + \frac{\sigma_o'}{P_a}} \right) \left(\frac{\gamma_t}{\gamma_w} \right)^{r_\gamma} \tag{3.13}$$

where A_L, B_L, C_L and r_γ are model fitting parameters based on the laboratory data. A_L is directly related to the value of V_s at zero confining stress. Low A_L values are indicative of low V_s at zero effective confining stress. High A_L values are indicative of high V_s at zero effective confining stress. B_L and C_L are both directly related to the rate of increase of V_s with confining stress. A similar form of this equation for field conditions can be formulated in Eq. (3.14).

$$V_s = \left(A_F + \frac{B_F \times \frac{\sigma_v'}{P_a}}{C_F + \frac{\sigma_v'}{P_a}} \right) \left(\frac{\gamma_t}{\gamma_w} \right)^{r_\gamma} \tag{3.14}$$

where A_F, B_F, C_F and r_γ are model fitting parameters based on field data. Equation 3.13 for laboratory data is also a function of effective confining stress and total unit weight of MSW, but in Eq. 3.14 from field data, MSW is under anisotropic stress conditions. Because of uncertainties associated with calculating the lateral earth pressure at rest coefficient, K_0, for MSW (Zekkos 2005), it is more convenient to formulate the model as a function of vertical effective stress. Vertical effective stress is equal to the product of the effective unit weight of MSW and depth. For "dry tomb" landfills, such as Subtitle D landfills, that are designed to minimize the

introduction of liquids in the waste mass, the waste remains unsaturated. Thus, the effective stress may be higher than the total stress due to suction forces, and if suction forces are insignificant, total stress and effective stress are equal. This assumption was made because capillary stresses in the unsaturated MSW regime are still unknown.

The semi-empirical shear wave velocity model for MSW in Eq. (3.14) requires total unit weight of the MSW. Zekkos et al. (2006a) described the procedures to perform in-situ unit weight measurements. Alternatively, a hyperbolic model relating depth and the unit weight of MSW as a function of depth was proposed as shown in Eq. (3.15).

$$\gamma_{\mathrm{MSW}-z} = \gamma_{\mathrm{MSW}-i} + \frac{z}{\alpha_\gamma + \beta_\gamma \cdot z} \tag{3.15}$$

where $\gamma_{\mathrm{MSW}\text{-}i}$ is the in-place total unit weight (kN/m^3) at the surface, z is the depth (m) at which the MSW unit weight $\gamma_{\mathrm{MSW}\text{-}z}$ is to be estimated, and α_γ and β_γ are modeling parameters with units of m^4/kN and m^3/kN, respectively. Calibration of the model using field test data yielded values for $\gamma_{\mathrm{MSW}\text{-}i}$, α_γ, and β_γ that are a function of compaction effort and amount of soil (particle size < 20mm) and are shown in Table 3.2. Incorporating Eq. (3.15) into Eq. (3.14) allows the formulation of a model for V_s that is only a function of depth z. The mathematical expression of this model is shown by Eq. (3.16).

$$V_s = \left(A_F + \frac{B_F \left(z\left(1/\beta_\gamma + \gamma_{MSW-i}\right) + \dfrac{\alpha_\gamma \ln\left(\alpha_\gamma / \left(\alpha_\gamma + \beta_\gamma z\right)\right)}{\beta^2} \right)}{C_F P_a + \left(z\left(1/\beta_\gamma + \gamma_{MSW-i}\right) + \dfrac{\alpha_\gamma \ln\left(\alpha_\gamma / \left(\alpha_\gamma + \beta_\gamma z\right)\right)}{\beta_\gamma^{\,2}} \right)} \right) \left(\frac{\gamma_{MSW-i} + \dfrac{z}{\alpha_\gamma + \beta_\gamma z}}{\gamma_w} \right)^{r_\gamma} \tag{3.16}$$

Table 3.2 Parameters for different compaction effort and amount of soil cover (Zekkos et al. 2006a).

Compaction Effort and Soil Amount	$\gamma_{MSW\text{-}i}$ (kN/m^3)	α_γ (m^4/kN)	β_γ (m^3/kN)
Low	5	2	0.1
Typical	10	3	0.2
High	15.5	6	0.9

The model (Eq. 3.16) was calibrated against 36 soundings at 15 landfills available in the literature, as well as, the 13 soundings at 4 Michigan landfills generated as part of this study (Table 3.3). For the OII landfill, the model was calibrated against the mean (μ) as well as the mean plus or minus one standard deviation ($\mu \pm \sigma_{SD}$) V_s profiles of the set of 27 V_s profiles. For the Lopez canyon landfill, only the mean V_s profile was used in the calibration process. As part of the calibration process, the model was fitted as closely as possible to each sounding and the values for the parameters A_F and B_F were derived. Model fits to each V_s profile were not made using a least-squares or other regression scheme, but visually, so that the overall shape of the modeled profile followed the measured V_s profile. Although the value of C_F could also be calibrated against the field data, this was not deemed necessary since calibrating the B_F parameter has similar effect on the model. The C_F parameter was set equal to 1.3 based on the value obtained from the Lee (2007) and Zekkos et al. (2008) data. The laboratory data from Lee (2007) suggest r_γ values between 0.35 and 0.50 for confining stresses ranging from 8 kPa to 276 kPa. The larger size triaxial data by Zekkos et al. (2008) at a confining stress of 75 kPa indicate a value of 0.74. The model was calibrated using values of 0.5 and 0.6. An r_γ value of 0.6 was found to result in smaller variability in the B_F field-calibrated values. Since this value also weighs evenly the available laboratory datasets, r_γ equal to 0.6 was used for model regressions.

Table 3.3 Summary of field shear wave measurements at MSW landfills from the literature and this study.

Landfill	Location	No of Soundings	Method(s)	Reference
Azusa	California (USA)	6	SASW	Kavazanjian et al. 1996
Lopez canyon	California (USA)	4	SASW	Kavazanjian et al. 1996
Toyon canyon	California (USA)	1	SASW	Kavazanjian et al. 1996
Sunshine canyon	California (USA)	1	SASW	Kavazanjian et al. 1996
Landfill A	California (USA)	2	SASW	Kavazanjian et al. 1996
Operating Industries, Inc. (OII)	California (USA)	27*	SASW	Kavazanjian et al. 1996
Villalba	Madrid (Spain)	1	SASW	Cuellar et al. 1998
Bolton	Georgia (USA)	1	SASW	Rix et al. 1998
Sanifill	Georgia (USA)	1	SASW	Rix et al. 1998
Valdemingomez	Madrid (Spain)	1	SASW	Pereira et al. 2002
Altamont	California (USA)	3	SASW	Lin et al. 2004
Redwood	California (USA)	4	SASW	Lin et al. 2004
Tri-Cities	California (USA)	7	SASW	Lin et al. 2004
Olympic View Sanitary (OVSL)	Washington (USA)	3	SASW	Matasovic and Kavazanjian 2006
Austin Community	Texas (USA)	1	SASW	Zalachoris 2010
Oakland Heights	Michigan (USA)	3	MASW & MAM	This study
Arbor Hills	Michigan (USA)	4	MASW & MAM	This study
Sauk Trail Hills	Michigan (USA)	3	MASW & MAM	This study
Carleton Farms	Michigan (USA)	3	MASW & MAM	This study

*Mean (μ) and mean +/- standard deviation ($\mu \pm \sigma_{SD}$) profiles were only analyzed as reported by Kavazanjian et al. (1996).

A unit weight variation with depth for each landfill in the database is needed for calibrating the semi-empirical model parameters for V_s (Eq. 3.14). For three landfills (OII, Azusa, and Tri-Cities) in-situ unit weight data is available (Zekkos et al. 2006a), and was used for calibrations. For the remaining landfills, the recommendations by Zekkos et al. (2006a) were followed to select a representative unit weight profile. Through that process, the "typical" unit weight profile was used for 27 soundings and the "high" unit weight profile was used for six soundings only.

Figure 3.31 shows examples of the calibrations of semi-empirical model against the field V_s data at various landfills from the literature and this study. The calibrations were used to derive the semi-empirical (A_F *and* B_F) for each site. For the majority of locations (27 out of 49), V_s is increasing with depth and the models nicely capture this behavior. Examples of such locations are shown in Figs. 3.31(a-c). At some locations (15 out of 49), such as the one shown in Fig. 3.31(d), a layer of higher V_s (or landfill "crust") is observed at the surface, with V_s values of 150 to 250 m/sec. This layer is typically the result of a compacted daily soil cover or a final composite cover and has varying thicknesses that may reach 3-4 m (Matasovic and Kavazanjian 2006, Rix et al. 1998). In a few locations (7 out of 49), such as these shown in Figs. 3.31(e and f), a high V_s layer is identified near the surface or at some depth underlain by lower V_s layers at depths below. For example, in the case of Oakland Heights 1 [Fig. 3.31(e)], as confirmed by trial test pits, a significant amount of soil cover was used to construct a landfill bench that is accessible to traffic. The reason for the high V_s layer at a depth of 30 m in Sunshine Canyon remains unknown to the authors [Fig. 3.31(f)]. Such irregularities may be attributed to major changes in waste composition, and possibly the presence of different waste materials, such as construction and demolition debris. Note that the presence of these layers creates significant challenges in data interpretation during the application of surface wave-based methodologies. The proposed model is not suited to capture such irregularities, which can only be verified via site-specific in situ measurements, typically with boreholes or some other types of penetration testing.

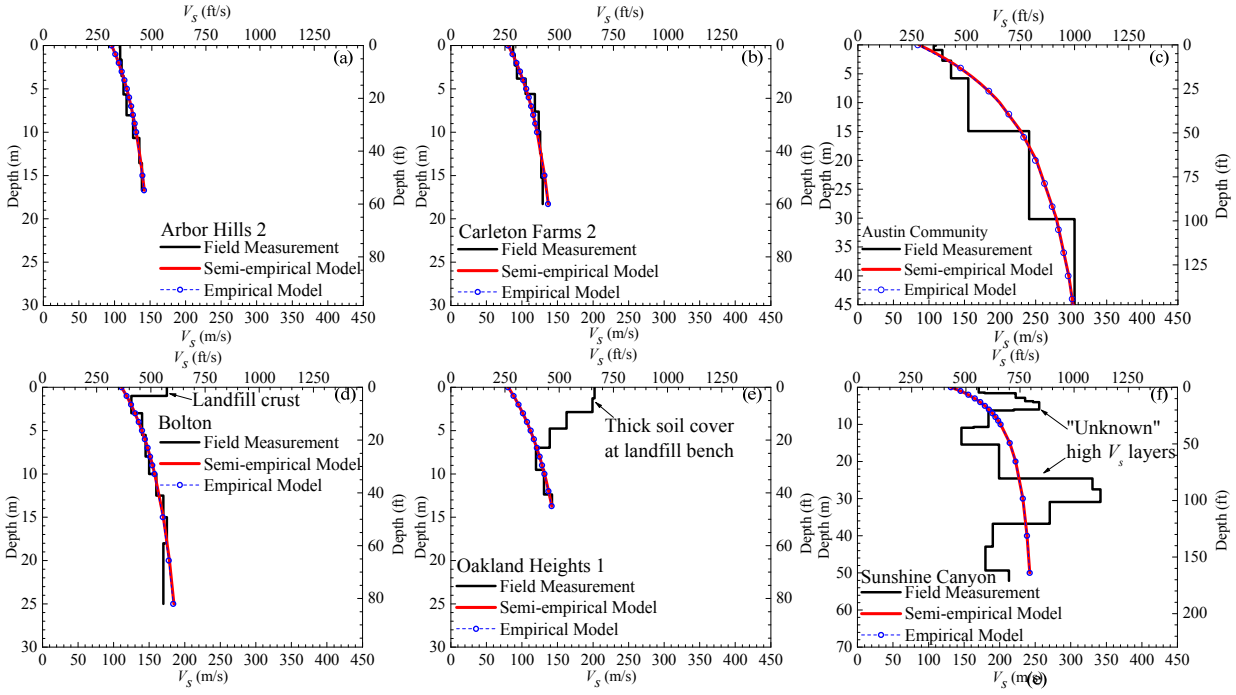

Figure 3.31 Examples of measured V_s and modeled V_s profiles at various sounding locations from the literature and this study: (a–c) good model fits; (d and e) model fits with the misfit as a result of thin or thick crust; (f) poor model fit at several depths.

Figures 3.32(a and b) illustrate the results of the calibration of the model against the field data in terms of the A_F and B_F parameters. The statistical analysis of the calibrated parameters indicates that the A_F and B_F parameters have normal distributions with a pronounced mode. Table 3.4 shows the μ, σ_{SD}, and other statistics of these parameters. The A_F and B_F parameters are not independent, but weakly negatively correlated, as shown in Fig. 3.33 by a low R^2 value of 0.48. Theoretically, higher B_F parameters would be expected to be correlated with lower A_F parameters meaning that when the V_s near the surface is low (i.e., A_F takes low values, in the order of 50-75 m/s), the increase in V_s with depth is significant (i.e., B_F is high).

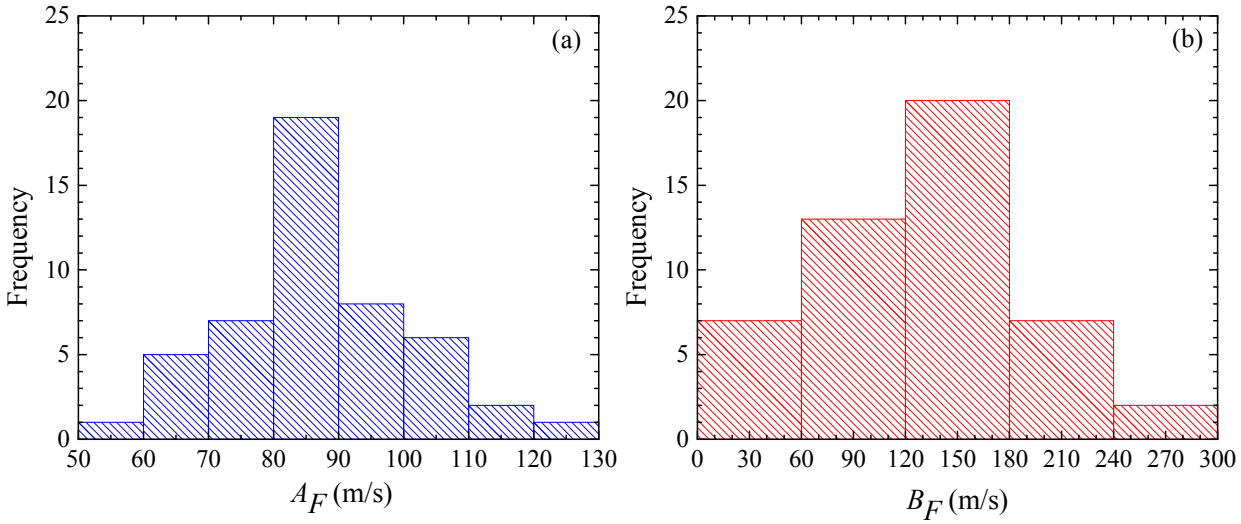

Figure 3.32 Statistics for the (a) A_F and (b) B_F calibration parameters.

Table 3.4 Statistics of regressed A_F, B_F, C_F, r_γ, V_{si}, α_{Vs}, and β_{Vs} parameters based on regression of field data.

Model	Parameter	Mean (μ)	Median	Standard Deviation (σ_{SD})	Max	Min
Semi-empirical (Eq. 3.14)	A_F (m/s)	83	80	15	120	50
	B_F (m/s)	124	130	56	255	40
	C_F [1]	1.3				
	r_γ^2	0.6				
Fully empirical (Eq. 3.17)	V_{si} (m/s)	89	85	21	158	48
	α_{Vs} (s)	0.08	0.07	0.04	0.19	0.04
	β_{Vs} (s/m)	0.006	0.005	0.003	0.012	0.003

[1] C_F was determined based on laboratory data
[2] r_γ was determined based on regression analysis results

3.3.2.2 Empirical Model

A purely empirical model for the variation of V_s with depth can be expressed in a hyperbolic form. This empirical model does not require an estimate of the unit weight [Eq. (3.17)].

$$V_S = V_{si} + \frac{z}{\alpha_{Vs}+\beta_{Vs}\times z} \tag{3.17}$$

where V_{si} is the shear wave velocity at the surface (without considering the presence of the "crust") and α_{Vs} and β_{Vs} are hyperbolic model parameters.

Examples of the calibrations of empirical model against the field V_s data at various landfills from the literature and this study are shown in Figure 3.31. For each site, V_{si}, α_{Vs} and β_{Vs} were adjusted to fit the empirical model with the field data. The statistics of the empirical V_{si}, α_{Vs} and β_{Vs} parameters are also shown in Table 3.4.

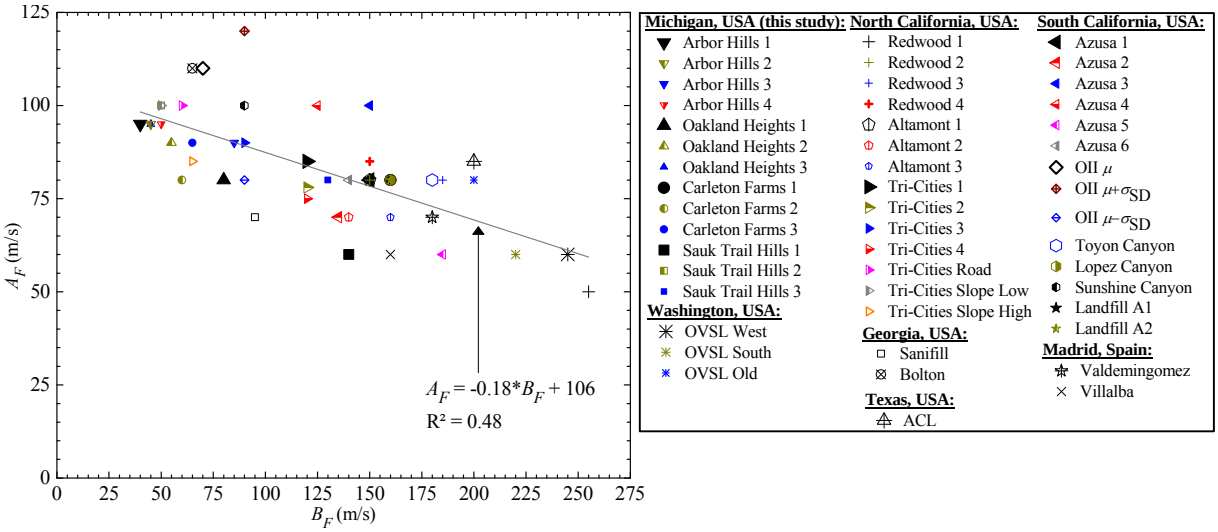

Figure 3.33 Relationship between A_F and B_F based on field data.

3.3.3 Model Recommendation and Limitation

A semi-empirical model for MSW V_s profile is developed using Eq. (3.14) with C_F and r_γ are set to 1.3 and 0.6, respectively. A_F and B_F parameters are listed in Table 3.4. In utilizing this model, an in-situ measurement for the variation of unit weight with depth can be made per Zekkos et al. (2006a) procedures. In the absence of site specific data, Eq. (3.16) and the recommendations for "low", "typical" and "high" unit weight profiles (Table 3.2) can be used.

The recommended V_s profiles with depth are shown in Fig. 3.34 along with all field V_s profiles. Curves are shown for a typical unit weight profile, as well as the "high" and "low" unit weight profiles, as recommended by Zekkos et al. (2006a). Use of the "typical" unit weight profile with the $\mu \pm \sigma_{SD}$ values for the A_F and B_F parameters generally bounds most of the field

data with the exception of the V_s in the top 5 m. When site specific-data indicates that the unit weight of the MSW is higher or lower than the "typical" unit weight, a V_s profile can be developed considering the site-specific variation in unit weight. Note that the present database does not include any sites with V_s profiles where the low unit weight profile was used. However, the V_s estimates of the semi-empirical model for low unit weight profiles are shown and represent the lower bound of the data.

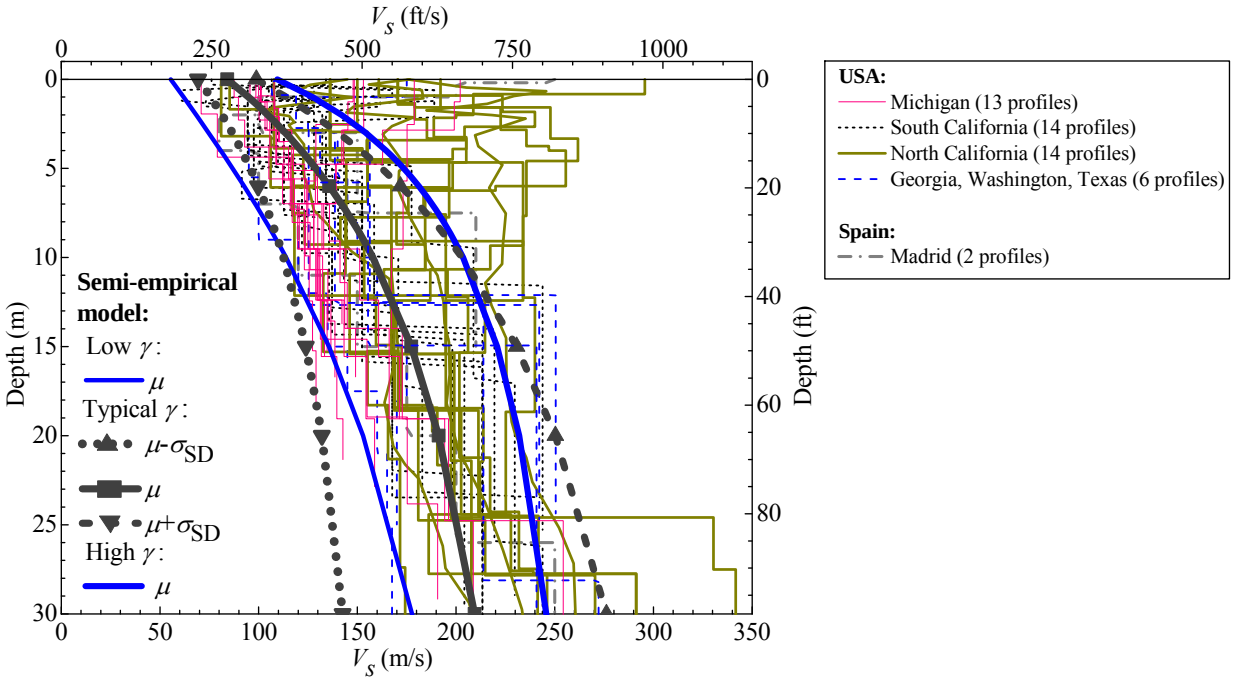

Figure 3.34 V_s profiles from the literature and recommended V_s profiles from this study.

Figure 3.34 is only shown to a depth of 30 m where the majority of field V_s data on MSW is available. Limited field data (e.g. V_s profiles from OII landfill) extend deeper. Because the mathematical expression of the semi-empirical model was developed based on laboratory data for a range of confining stresses and the analyses confirmed that the derived A_F and B_F values are not depth/stress dependent, one would expect that the semi-empirical model estimates will be appropriate at greater depths as well.

An empirical model that is only relating shear wave velocity and depth may be developed according to Eq. (3.17) and V_{si}, α_{Vs}, and β_{Vs} parameters in Table 3.4. Figure 3.35 shows that the mean, lower and upper bound ($\mu \pm \sigma_{SD}$) V_s profiles for the empirical model are very similar to the mean and $\mu \pm \sigma_{SD}$ profiles of the semi-empirical model for the "typical" unit weight profile case.

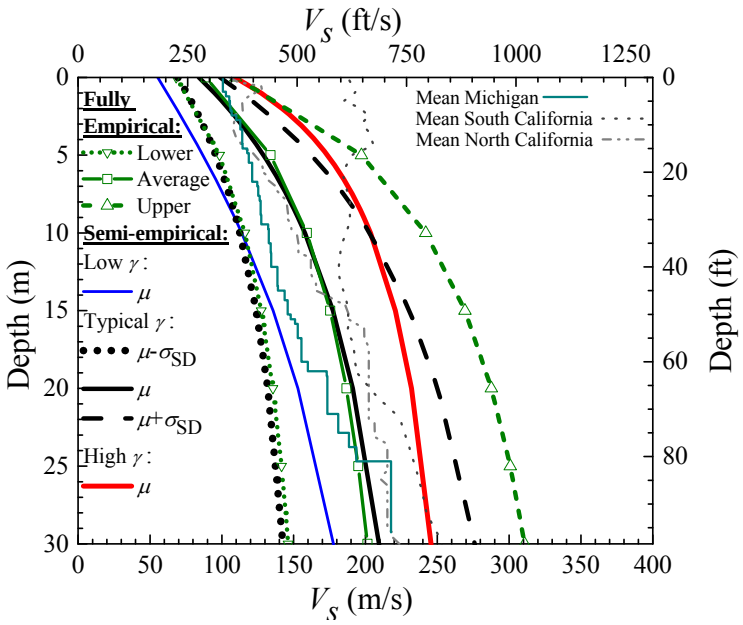

Figure 3.35 Semi-empirical and fully empirical V_s profile models.

The models were not developed to predict large, abrupt, changes in V_s that are caused by disposal of different waste or soil materials. In addition, the models were not aimed to capture the "crust" or other "special" fill and soil materials disposed of at some landfill locations. Based on the available field data, the crust may vary in thickness up to approximately 4 m and has V_s values on the order of 150 to 250 m/sec. However, its presence and extent is site specific and a function of a number of factors, including, type of soil, moisture content (and its fluctuation), and compaction effort. The presence of this high velocity layer at the surface may impact the near-surface seismic response of the landfill. In this case, the semi-empirical model can be adjusted by inserting this high velocity layer at the surface.

The proposed models are also not intended to replace field measurements. As shown in Fig. 3.35, there are differences in the mean V_s profiles of MSW landfills from different regions (e.g. Michigan, southern California, northern California). These geographic differences may be attributed to differences in waste streams, waste composition, climatic conditions (temperature, precipitation), as well as landfill operation practices, such as amount of compaction effort and daily soil cover used, as well as the type of soil used for daily soil cover. In the absence of any site-specific information, the models can be used as a basis for preliminary assessments of V_s and G_{max} of MSW. As indicated by the standard deviations of the A_F and B_F parameters, there is scatter in the recommended A_F and B_F parameters. These differences can have a significant effect on the seismic response and seismic stability of the MSW landfill.

The validity of the semi-empirical and empircal models has to be evaluated for Pre-Subtitle D and bioreactor landfill. The majority of landfills included in the database and used to calibrate the model are modern "dry tomb" landfills and thus, the waste is not saturated. At old, abandoned landfills or bioreactor landfills, the waste may be in a saturated condition.

3.4 **Summary**

The V_s and G_{max} of MSW is an important engineering parameter for the seismic response of landfills and to characterize MSW. Using insights gained from large-scale laboratory tests on reconstituted MSW specimens, a model for V_s (and the associated G_{max}) was developed. A hyperbolic function (or power function) is used to describe the relationship of V_s with effective confining stress (isotropic for the laboratory, vertical for field data for simplicity) and a power function is used to describe the relationship of V_s with the unit weight of MSW. Based on results from previous research studies, the unit weight of MSW is used to capture the effects of waste compactness as well as waste composition. The model is subsequently simplified so that a

relationship between G_{max} and depth can be developed. The model is calibrated against a total of 49 in situ V_s profiles in MSW. Thirty nine V_s profiles from 15 landfills in Georgia, southern California, northern California, Washington, Texas, and Spain that are available in the literature were used. The literature database was expanded with 13 additional profiles generated as part of this study from 4 landfills in Michigan using a combined active and passive surface wave-based methodology. The semi-empirical relationship is described by Eqs. 3.14 and 3.16, and a simplified empirical relationship that is a function of depth only is provided in Eq. 3.17, with the A_F and B_F semi-empirical parameters and the empirical V_{si}, α_{Vs}, and β_{Vs} listed in Table 3.4. To develop a V_s profile, the mean and mean ± σ_{SD} of A_F and B_F parameters are presented and an assumption for the unit weight profile needs to be made, according to recommendations by Zekkos et al. (2006a) for the semi-empirical model. No assumption for unit weight is necessary for the empirical model.

CHAPTER 4. GENERALIZED TEST EQUIPMENT, FIELD TEST SETUP, TEST PROCEDURE, AND DATA ANALYSIS

4.1 **Introduction**

In this chapter, the implementation of a field testing program for in-situ evaluation of dynamic properties of solid waste is described. The work expanded on previous relevant studies (e.g. Axtel et al. 2002, Stokoe et al. 2006 and 2011, and Park 2010). This testing method included small-scale crosshole and downhole seismic testing in the small-strain range combined with steady-state dynamic testing in the nonlinear strain range. In addition, load-settlement tests and in-situ unit weight measurements were performed.

4.2 **General Testing Methodology**

Field testing in the linear range (i.e. small-strain testing) involved small-scale crosshole and downhole seismic testing using source rods and a handheld hammer. The term "small-scale" is used to differentiate the crosshole and downhole seismic tests performed in this study from conventional crosshole and downhole seismic tests which are typically performed at greater depths and larger borehole spacings. The nonlinear dynamic testing consisted of steady-state dynamic testing in a staged loading sequence using mobile field shakers. Embedded three-component (3-D) geophones were used to measure particle velocity time-histories in the solid waste. The general testing configuration is illustrated in Fig. 4.1. The dimensions shown are for testing executed at the Los Reales Landfill, Tucson, Arizona. At each instrumented site, these dimensions varied so that the test could be tailored to the existing conditions. The collected data were used to calculate shear wave velocity (V_s), primary wave velocity (V_p), shear modulus (G),

and shearing strain (γ) at each instrumented site. A load-settlement curve was also generated for the footing by monitoring the vertical displacement during application of static vertical loads by the mobile shaker. Unit weight was also evaluated in-situ using procedure proposed by Zekkos et al. (2006).

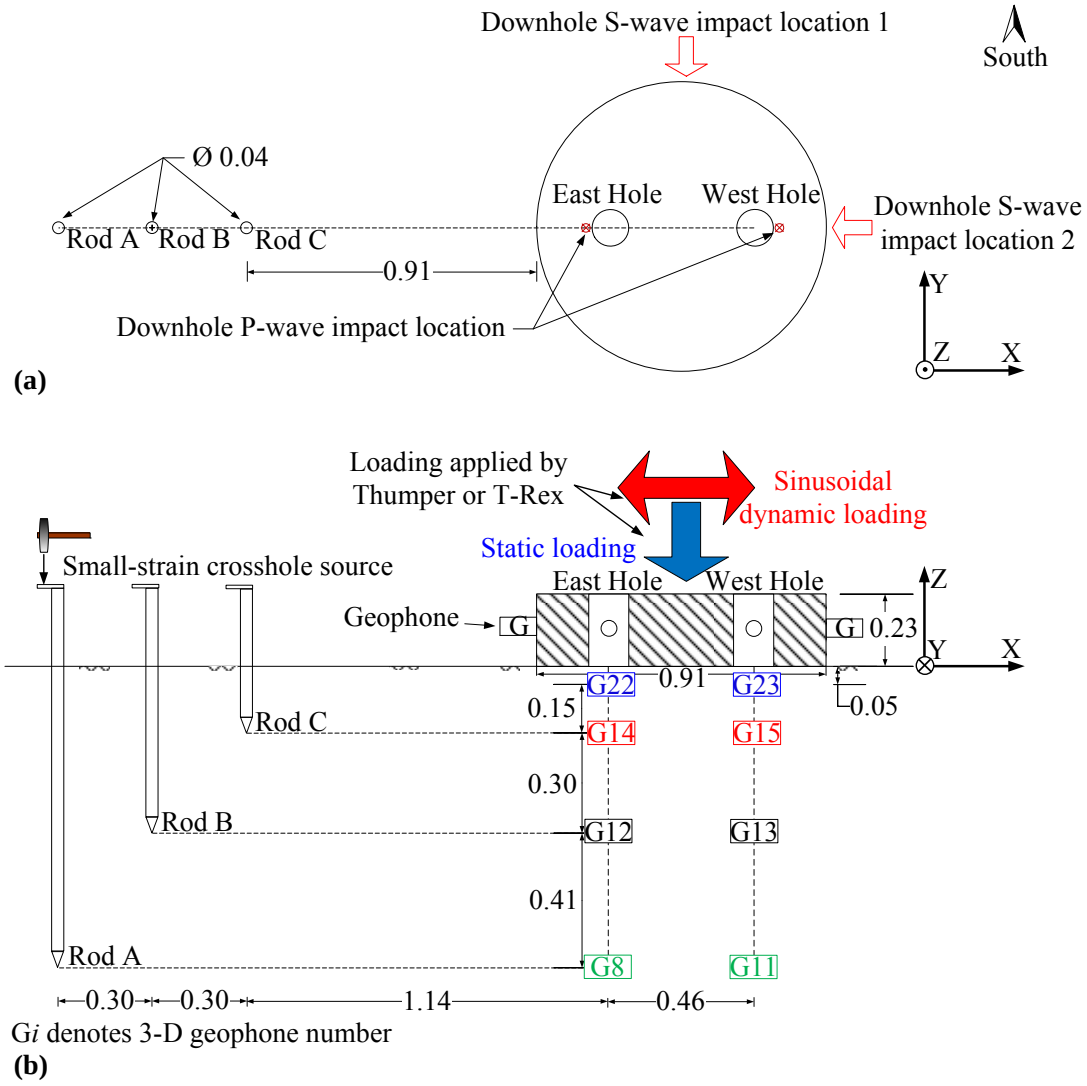

Figure 4.1 Field testing setup: (a) plan and (b) cross-section views (dimensions in meters).

4.3 **Equipment and Instrumentation**

4.3.1 Mobile Field Shakers

Steady-state dynamic testing required a well-controlled dynamic loading source. Thumper and T-Rex (Fig. 4.2), mobile field shakers of the George E. Brown, Jr. Network for Earthquake Engineering Simulation at the University of Texas at Austin (NEES@UT), were used. These mobile field shakers are equipped with a mounted servo-hydraulic vibrator that applies dynamic loads with adjustable frequency, amplitude, number of cycles, and shaking direction. Thumper and T-Rex are capable of generating dynamic loads up to 27 kN and 133 kN, respectively. In addition, Thumper and T-Rex can be used to apply vertical hold-down forces up to 36 kN and 267 kN, respectively. Thumper is equipped with a crane for performing heavy load lifting during field test preparation. T-Rex has a CPT-type hydraulic cylinder that can be used to push a sampler or sensors into the ground. Summary of the general specification of Thumper and T-Rex is presented in Table 4.1. Detailed technical specifications on these mobile field shakers can be found in Stokoe et al. (2004 and 2008) and Menq et al. (2008).

Figure 4.2 Mobile field shakers: Thumper and T-Rex.

Table 4.1 General specification of Thumper and T-Rex (after Stokoe et al. 2004).

Shaker	Thumper	T-Rex
Vehicle type	Build ofn Ford F650 Truck	Buggy-mounted shaker, articulated body
Driving speed	Highway speed	Hydraulic drive system (<24 km/h)
Total weight	9980 kg	29030 kg
Length	7.1 m	9.8 m
Width	2.4 m	2.4 m
Height	2.4 m	3.2 m
Hydraulic pressure system	47.6 MPa	20.7 MPa
Vibrator pump flow	151 l/m	757 l/m
Vibration orientations	Vertical, horizontal in-line, and horizontal cross-line	
Shaking orientation transformation	Field transformable in 4 hours	Push-button transformation
Maximum output force	27 kN (vertical) and 27 kN (horizontal)	267 kN (vertical), 133 kN (horizontal)
Base plate area	0.698 m^2	4.11 m^2
Moving mass	140 kg (vertical) and 140 kg (horizontal)	3670 kg (vertical) and 2200 kg (horizontal)
Stroke (peak to peak)	7.6 cm (vertical and horizontal)	8.9 cm (vertical) and 17.8 cm (horizontal)

4.3.2 3-D Geophone Sensor

A view of a 3-D geophone sensor that was used in these tests is shown in Fig. 4.3. Basically, the 3-D geophone sensor is a cylindrical acrylic case containing 3 independent single-degree-of-freedom geophones installed on 3 perpendicular axes. Slow-set epoxy resin was used to fill the acrylic case and to hold the geophones in place. A counterweight was installed so that the center of gravity (c.g.) of the whole unit coincided with the c.g. of the cylindrical acrylic case in an

effort to minimize rocking along the horizontal axis. A square shaped acrylic neck was also installed at the top of the case for attaching a guide rod to ensure proper sensor orientation during installation in a borehole.

The use of geophones has several advantages. First, the coil-magnet sensor portion of a geophone requires no power, reducing the required wiring and the size of the embedded instrumentation relative to other sensors. In addition, a geophone is a rugged and economical transducer. Geophones with a natural frequency lower than the frequencies of interest in the field testing were selected. Specifically, 28-Hz geophones (GS-14-L9 of Geospace Technologies Corp.) were used as the sensing element. A 1.870 kilo-Ohm resistor, equivalent to 50% critical damping in the geophone, was installed to create a well-damped output response curve. Each geophone was calibrated independently to obtain calibration curves that show the relationship between calibration factor and frequency. Geophone calibrations were performed by Dr. Changyoung Kim in the Soil and Rock Dynamics Laboratory at the University of Texas, Austin. Calibration was performed using a proximitor (Bently-Nevada 19049) as the calibration reference in the frequency range of 5 to 100 Hz. Example of geophone calibration curves from a 3-D geophone sensor is shown in Fig 4.4.

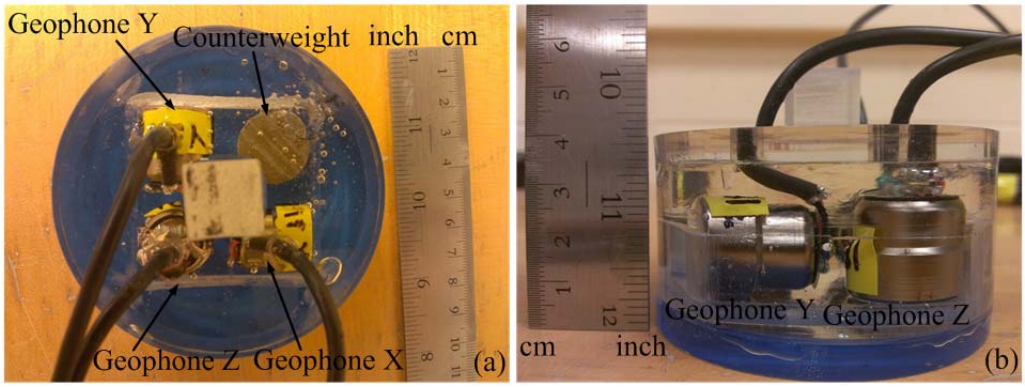

Figure 4.3 3-D geophone sensor: (a) top and (b) side views.

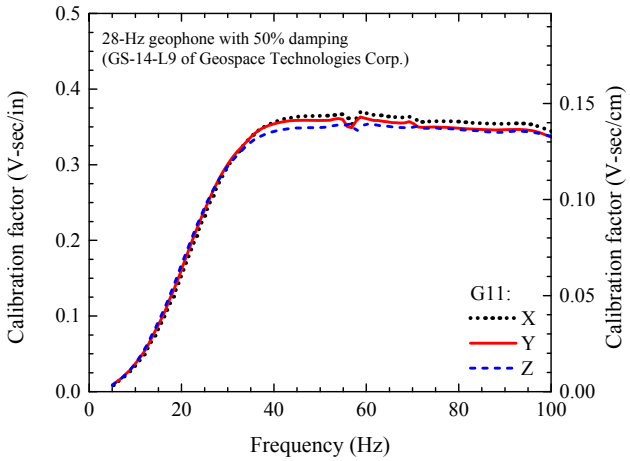

Figure 4.4 Example of geophone calibration curve from G11.

4.3.3 Load Cell, Linear Potentiometer, and Power Supply

A load cell and three identical linear potentiometers were used to measure load versus surface settlement during application of vertical static loads [Fig. 4.5(a, b, c)]. Two 1020 series Interface load cells with maximum capacity of 111 kN (25 kips) and 222 kN (50 kips) were used. The larger capacity load cell was used in vertical load application up to 133 kN (30 kips). The linear potentiometers (CLPR 13-50 Megatron Elektronik GmbH & Co. KG) that were used have a full-scale capacity of 0 to 5.1 cm (0 - 2 inches) with a measurement precision of ± 0.005 cm. The load cells and potentiometers were powered by a 10-VDC Agilent model E3620 power supply.

Figure 4.5 (a) Load cell, (b) linear potentiometer, (c) power supply and function generator, and (d) dynamic signal analyzer used in the field test.

4.3.4 Function Generator and Data Acquisition System

An Agilent model 33120A function generator was used to drive the shaking mechanism of Thumper and T-Rex with a sinusoidal signal at a specified amplitude and frequency for a given number of cycles [Fig. 4.5(c)]. A VXI-technology multichannel Dynamic Signal Analyzer (DSA) was used to record output signals from the 3-D geophones, load cell, linear potentiometers, driving signal from the function generator, and ground force acceleration from the loading plate of the mobile shakers [Fig. 4.5(d)]. This DSA is equipped with 16-bit A/D modules that are capable of recording up to 72 channels with maximum sampling frequency of 51.2 kHz per channel. This DSA has high resolution and high sampling frequency and was needed to ensure adequate sensor output recording.

4.4 **Testing Procedure**

In general, the in-situ testing procedure involved site preparation, geophone installation, load-settlement testing in conjunction with crosshole and downhole seismic testing, steady-state dynamic testing, solid waste sampling, and in-situ unit weight measurements. Each step is discussed in detail below.

4.4.1 Site Preparation and Geophone Installation

Field testing was performed on locations where solid waste was typically covered by daily soil cover. Because shearing strains attenuate with depth during dynamic loading, removing the soil cover entirely and working directly on top of solid waste would be ideal. However, this approach was generally impractical because of uncertain waste support capacity and the need to contain waste gas. As shown in Fig. 4.6, a grader or dozer was used to minimize the thickness of soil cover so that its thickness below the foundation ranged from 0 to 2.5 (1 in.). This thin soil cover permitted generation of the largest shearing strain in the solid waste, hence, inducing pronounced nonlinear behavior.

Figure 4.6 A road grader removing soil cover at Los Reales Landfill.

After the excess soil cover was removed, nylon ropes and nails were used to create grid lines on the ground as references and marks to designate the locations of sensor boreholes, concrete footing or the shaker load plate, and crosshole source rods. In addition, an elevation reference for borehole drilling and 3-D geophone installation was established and the contact area of the concrete footing or mobile field shaker load plate was leveled by hand. In the steady-state dynamic testing, a flat horizontal contact between the loading mechanism and ground is important to generate strong wave propagation, reduce the probability of footing rocking, and ensure axisymmetric mean confining stress and axial strain distributions under the contact area.

Two boreholes were generally prepared for geophone installation. A core barrel with an outside diameter of 10.2 cm (4 in.) and length of 60.9 cm (24 in.) was used to excavate the boreholes. The core barrel was pushed into the solid waste using the CPT-type hydraulic cylinder at the back of T-Rex (Fig. 4.7). Important considerations in creating the geophone boreholes were: (1) minimizing disturbances in the solid waste and (2) maintaining verticality. The solid waste recovered from inside the core barrel was visually assessed and collected in sealed bags. The fine fraction of the collected solid waste was used to backfill the borehole during geophone installation. After the target depth was reached, a thin-walled PVC pipe was used as a casing in each borehole to prevent the boreholes from collapsing. During geophone installation, a portable gas detector was used to assure that gas levels remained below a safety limit.

Figure 4.7 (a) Pushing core barrel to the waste mass and (b) recovered solid waste in the core barrel.

Geophone units were installed using an aluminum hollow rod with a square cross-section (Fig. 4.8). This rod was attached to the geophone square neck on the case (Fig. 4.3**)**. A compass and a mark on the square rod were used as references to properly orient the geophones and to place them at the desired depth. Correct orientation and depth of the geophones were key in the sensor installation stage. The rod and geophone were lowered into the borehole by hand to the desired depth. Subsequently, a small amount of soil was used to fill the gap between the geophone and borehole wall so that good coupling was obtained. Additional soil was also used to bury the geophones. The soil was lightly compacted using 1-cm (0.4-in.) and 2-cm (0.8-in.) diameter steel rods.

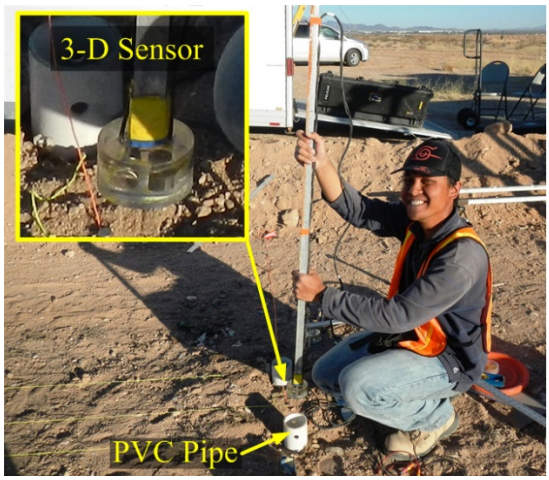

Figure 4.8 A 3-D sensor installation.

Two 1-cm (0.4-in.) diameter steel rods were pushed through the soil to the top cap to hold the geophone in place while the square hollow rod was carefully decoupled from the geophone so that there was no change in geophone orientation. The steel rods were then retracted from the borehole. The finer fraction of the solid waste was used to fill the borehole in lifts and the waste was compacted by tamping with a 2.5-cm (1-in.) diameter wooden rod (Fig. 4.9). In this fashion, the geophone at the deepest elevation was installed. Subsequently, the deepest geophone in the second borehole was placed using the same procedure. After the two deepest geophones have been installed, two more geophones at the shallower depths were similarly installed.

Figure 4.9 (a) Filling the borehole with fine fraction of solid waste, (b) tamping with wooden rod, and (c) checking the depth of borehole.

After all geophones have been installed, a precast reinforced concrete footing was placed on the ground using Thumper's crane. The footing was needed to ensure the contact area of the shaker's loading plate and ground surface was the same. The size of concrete footing, diameter of 91.4 cm (36 in.) and thickness of 22.9 cm (9 in.), was designed based on recommendations from Park (2010). The footprint of the concrete footing needed to be large enough relative to the instrumented area so that plane wave propagation over the instrumented ground was reasonably approximated. The footing needed to be thick enough so that it was considered rigid, but not too thick to avoid rocking motions during steady-state dynamic testing. A circular footing shape was selected so that axisymmetry could be assumed in analyzing mean confining stress and axial strain distributions beneath the footing. Geophone wires were routed through cable access holes in the footing. A hammer tap on the footing was used as source of wave propagation in the downhole testing; vertical tap for primary wave (P-wave) generation and horizontal tap for shear wave (S-wave) generation.

Figure 4.10 Installation of concrete footing.

Three crosshole source rods were installed outside the test pad using the CPT-type hydraulic cylinder at the back of T-Rex (Fig. 4.11). The distance between the source rods and the

footing was selected to be as short as possible, but also long enough to allow the mobile field shakers to straddle the footing and not interfere with the rods.

Figure 4.11 Installation of crosshole source rod.

4.4.2 Staged Load Testing

Field testing was performed in a staged loading sequence as illustrated in Fig. 4.12. First, crosshole and downhole seismic testing were performed without application of a static vertical load on the footing. Subsequently, a predetermined static vertical load was applied to the footing to perform load-settlement testing. The crosshole and downhole seismic testing were performed again at this vertical static load. The vertical static load was released, then reapplied and a steady-state horizontal excitation was applied to the footing using the mobile field shaker. These steps were repeated for different static vertical loads in an increasing load-level sequence as illustrated in Fig. 4.12.

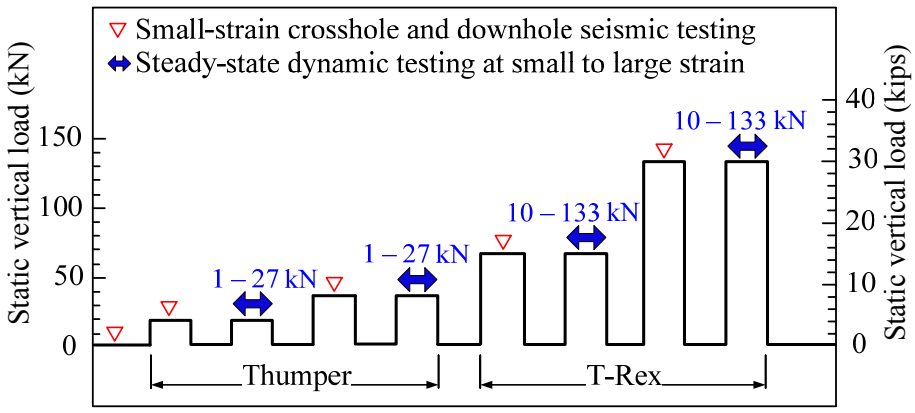

Figure 4.12 General testing sequence.

4.4.2.1 Small-scale Crosshole and Downhole Seismic Testing

Small-scale crosshole and downhole seismic testing were performed to investigate small-strain velocities of primary waves and shear waves (Fig. 4.13). These tests were performed at different levels of static vertical load so that the effect of mean confining stress on these properties could be evaluated.

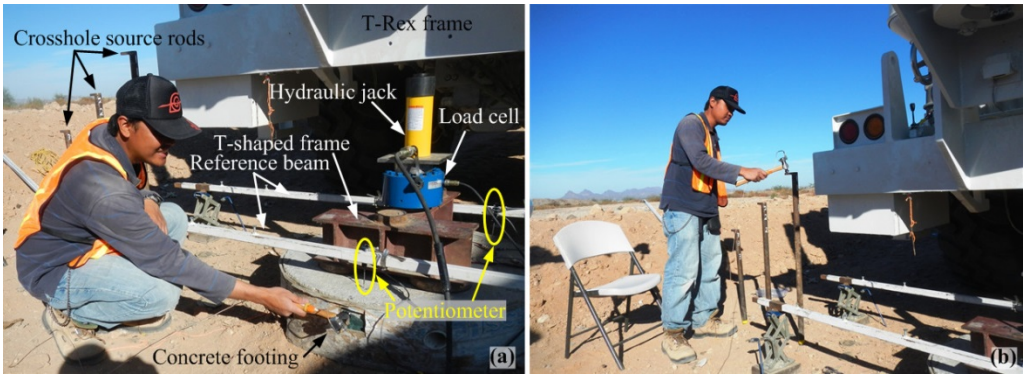

Figure 4.13 (a) Downhole and (b) crosshole seismic test.

The source for the crosshole seismic tests consisted of hitting the crosshole source rods vertically using a hand-held hammer [Fig. 4.13(b)]. Horizontally propagating primary wave velocities ($V_{p\text{-}X}$) and horizontally propagating shear wave velocities with vertical particle motion ($V_{s\text{-}XZ}$) were simultaneously generated. The seismic waves generated by this impact were captured by a pair of 3-D geophones that were located at the same depth as the corresponding

source rod tip. The handheld hammer was instrumented with an accelerometer that was used to trigger the time record and also supplied a time zero on the record by using a pre-trigger capture mode. Ten hits were stacked to increase the signal-to-noise ratio of the recorded waveforms. Data were recorded at a sampling frequency of 51.2 kHz and a pre-trigger time of 7.5 milliseconds.

Small-scale downhole testing was performed by hitting several impact points on concrete footing [Figs. 4.1 and 4.13(a)]. Vertically propagating primary wave velocities ($V_{p\text{-}Z}$) were generated by hitting the top surface of the concrete footing with the handheld hammer. P-wave propagation was captured by the vertically oriented geophones. Vertically propagating shear wave velocities with horizontal particle motion in the X ($V_{s\text{-}ZX}$) and Y ($V_{s\text{-}ZY}$) axes were generated by hitting the sides of the concrete footing. The horizontally oriented geophones captured these shear waves. Ten-hit stacking was also used with a sampling frequency of 51.2 kHz and a pre-trigger time of 7.5 milliseconds.

4.4.2.2 Load-settlement Testing

Load-settlement testing was performed to evaluate footing settlement due to the application of the static vertical load. The testing procedure was based on experiences and recommendations from previous studies (e.g. Sheehan 2005, Park 2010, and Zalachoris 2010). A T-shaped frame was used to distribute a vertical load from the hydraulic jack uniformly across the concrete footing as shown in Fig. 4.13(a). Reference beams spanning the footing supported potentiometers at three equilaterally positioned locations on the footing. The hydraulic jack, reacting against the weight of T-Rex, was used to apply a vertical force through the load cell to the footing while load cell and potentiometers were monitored continuously by the recording system. The jack was hand pumped to achieve a predetermined load, then the load was kept

constant while small-strain crosshole and downhole seismic tests were performed. Additional stages of loading were added to complete the testing sequence. The static loading and displacement measuring equipment must be removed from the footing before the steady-state dynamic testing could be performed.

4.4.2.3 Steady-state Dynamic Testing

Low-to-high-amplitude steady-state dynamic testing was performed to investigate the shear modulus reduction of solid waste. Testing was initiated by placing the vibrator plate of the mobile field shaker on top of the concrete footing (Fig. 4.14). The hydraulic pressure system of the shaker was used to impose a hold-down static force. Concurrently, the servo-hydraulic vibrator was used to apply a sinusoidal horizontal dynamic force at a specified amplitude, frequency, and number of cycles. This sinusoidal horizontal load generated vertically propagating shear waves that induced dynamic shearing strain in the solid waste. The geophones measured particle velocity time-histories at various depths in the solid waste. At a constant static hold-down force, the amplitude of dynamic horizontal loads was incrementally increased so that larger shearing strains were induced in the solid waste. This procedure was also repeated at increasing levels of static hold-down force so that the effect of mean confining stress on shear modulus and normalized shear modulus could be investigated.

Prior to beginning the dynamic staged loading, a frequency sweep was performed at a low load level to find frequencies of dynamic horizontal loads that yielded the best shape of the sinusoidal waveforms recorded by the geophones. Frequencies of 30 Hz and 50 Hz generally created good sinusoidal output signals. However, the optimum excitation frequency is site dependent. For example, a frequency of 100 Hz yielded the best sinusoidal waveforms at an unsaturated silty sand site (Stokoe et al. 2011). The number of dynamic horizontal load cycles

was generally selected to be 8 to 10. Eight to ten cycles were considered sufficient to achieve steady-state motion without degrading the solid waste material. Steady-state testing was performed with a sampling frequency of 20.48 kHz.

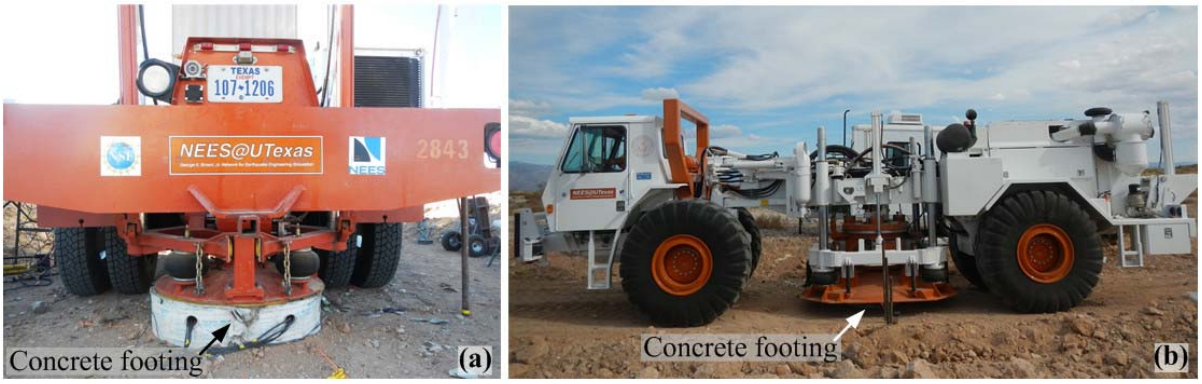

Figure 4.14 Steady-state dynamic test using (a) Thumper and (b) T-Rex.

4.4.3 Solid Waste Sampling and In-situ Unit Weight Measurement

After completion of staged load testing, the test location was excavated to characterize in situ the solid waste, perform in-situ unit weight measurements, collect bulk solid waste samples, and retrieve the 3-D geophones (Fig. 4.15). Characterization of solid waste and in-situ unit weight measurement were performed using procedures proposed by Zekkos et al. (2010) and Zekkos et al. (2006a), respectively. A portable gas detector was used to monitor that gas levels did not exceed a safety threshold.

The in-situ large scale unit weight measurement resembled the ASTM D1556-07 standard sand-cone density. A trench was excavated at the testing location using a small backhoe excavator [Fig. 4.15(a)]. The excavated solid waste was collected in a pre-weighed dump truck or wheel loader. To measure the weight of the excavated solid waste, the total weight of the truck or loader with the loaded solid waste was weighed at scales available at the landfill. Bulk solid waste samples were collected from the trench and are stored in 55-gallon sealed HDPE drums for

further characterization and laboratory testing. Uniform clean gravel was used to estimate the trench volume. The unit weight of this gravel was obtained from the average of measurement using two 55-gallon HDPE drums. The uniform gravel was loaded into the dump truck or the wheel loader. The truck or the loader with the gravel was weighed. The trench was backfilled with the gravel and truck with remaining gravel was re-weighed so that the weigth of gravel that was placed in the trench could be calculated [Fig. 4.15(d)]. The trench volume could be estimated by dividing the weight of calibrated gravel in the trench by its unit weight. The unit weight of solid waste was calculated by dividing the measured weight of the excavated waste by the calculated trench volume.

Figure 4.15 (a) Pit excavation, (b) in-situ waste characterization, (c) exposed 3-D geophone, (d) gravel backfilling, and (e) pit with gravel.

In-situ waste characterization included qualitative description of composition, age, degradation state, and moisture content. Waste composition described the materials that were contained in the excavated solid waste, such as plastic, paper, wood, household garbage, rugs,

tires, clothing etc. Waste age could be estimated using dates on magazines, newspapers, receipts, weekly advertisements, and other documents found in the waste. Waste degradation was approximated using four different levels of degradation based on illegibility and discoloration of newspaper per Zekkos et al. (2010). Moisture content in the solid waste could be visually described as dry, damp, wet, or standing water.

4.5 **Data Analysis**

The analytical techniques used to reduce the raw data were presented below using data from testing location #3 at the Los Reales Landfill, Tucson, Arizona. The testing setup at this location is shown in Fig. 4.1.

4.5.1 Load-settlement Test

Using calibration factors of the load cell and three linear potentiometers, raw data output from the load cell and linear potentiometers were converted to load and displacement, respectively. The displacement-time histories from three linear potentiometers were averaged and plotted versus load. The load-settlement evaluated at the Los Reales Landfill is presented in Fig. 4.16.

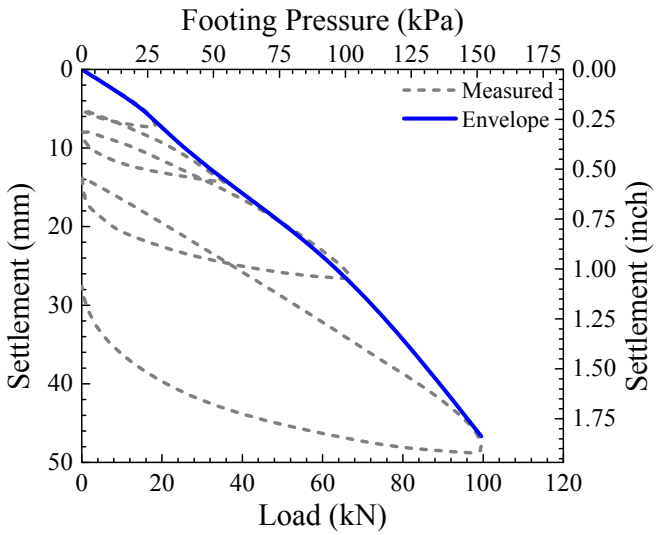

Figure 4.16 Load-settlement curve in location 3 at the Los Reales Landfill, Arizona.

4.5.2 Estimation of Stress and Axial Strain Distributions

The stress state in the solid waste influences its dynamic properties (e.g. Zekkos et al. 2008). In the field tests, the static stress is equal to the stress induced by the static vertical load on the concrete footing plus the geostatic stress. The vertical (σ_z) and radial (σ_r) stresses induced by the static vertical load were approximated using the Foster and Ahlvin (1954) method. This method calculates stresses due to a uniform circular load on a homogeneous, isotropic, semi-infinite, and elastic material. Because Foster and Ahlvin (1954) solution is for weightless material, the geostatic vertical stress (σ_g) was calculated independently as the in-situ unit weight times the depth. The vertical stress (σ_v) was calculated as the sum of σ_g and σ_z. The weight of concrete footing was also considered in calculating the vertical stress. The horizontal stress (σ_h) represented the combination of σ_r and the estimated coefficient lateral pressure at rest (K_0) times σ_g. The mean confining stress (σ_0) was calculated using the following equation:

$$\sigma_0 = \frac{\sigma_v + 2\cdot\sigma_h}{3} = \frac{(\sigma_z + \sigma_g) + 2\cdot(\sigma_r + K_0\cdot\sigma_g)}{3} \quad (4.1)$$

The small-strain Poisson's ratio (v) calculated from the crosshole and downhole seismic tests were evaluated and used to estimate a representative K_0 value using Eq. 4.2.

$$K_0 = \frac{\nu}{1-\nu} \tag{4.2}$$

Sensitivity analysis on the effect of Poisson's ratio on the calculated stress distribution showed that reasonable variations of Poisson's ratio lead to only 10% changes in the calculated mean stress values. It must be noted that the use of the elasticity equation to estimate K_0 may not be appropriate. Nevertheless, this calculation provided at least an estimate of the K_0 value. Figures 4.17, 4.18, and 4.19 show distribution of vertical, horizontal, and mean confining stresses calculated for Los Reales landfill in test location 3.

The Ahlvin and Foster (1954) method was also used to calculate the axial strain distribution in the solid waste that was induced by the application of vertical static load on the concrete footing. The axial strain profile between 3-D geophones at two different depths was used to estimate the change in the vertical spacing between the geophones.

The state of stress and axial strain distribution in the solid waste was estimated using the procedure describe above. The state of stress and axial strain in the solid waste may be more complicated and likely varies from the result shown because solid waste is not homogenous or isotropic material. Nevertheless, simplifications of homogeneity and isotropy assumptions were used in the analysis.

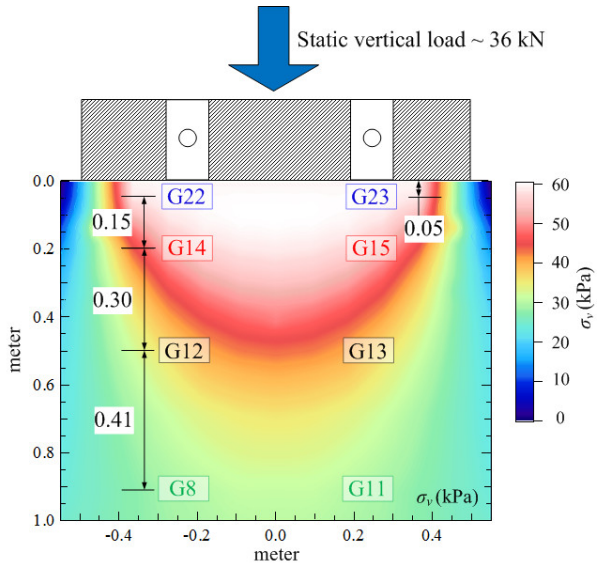

Figure 4.17 Vertical stress distribution with static vertical load of 36 kN.

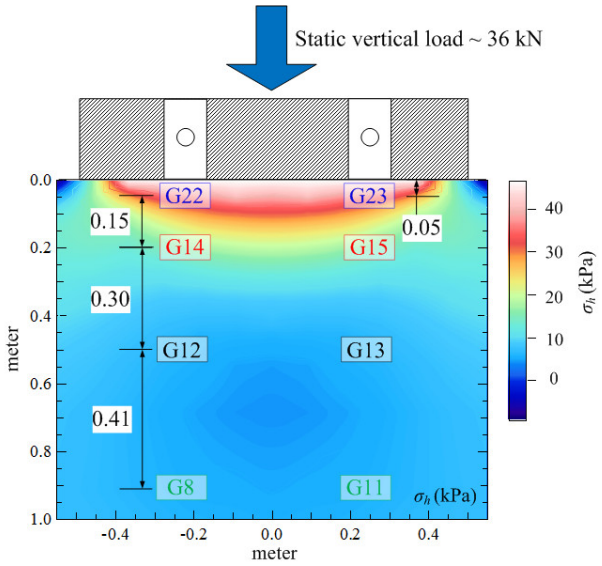

Figure 4.18 Horizontal stress distribution with static vertical load of 36 kN.

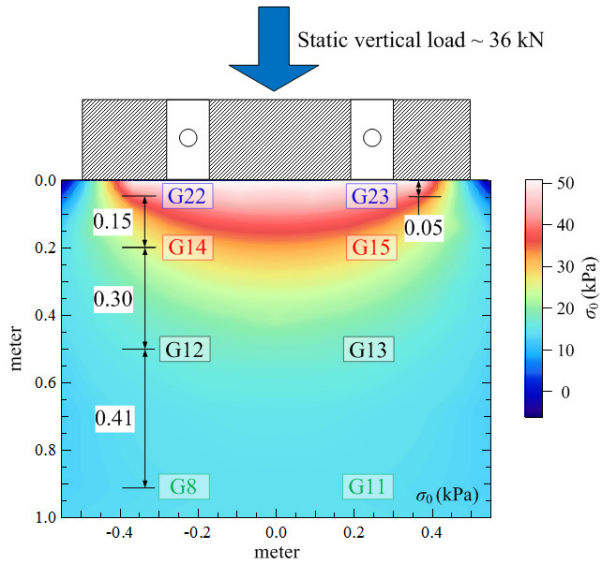

Figure 4.19 Mean confining stress distribution with static vertical load of 36 kN.

4.5.3 Crosshole and Downhole Seismic Tests

A key part in the analysis of the crosshole and downhole seismic tests is evaluating the travel time of the seismic waves. Two techniques that are widely used in measuring travel time were implemented in this work: (1) direct time resolution (e.g. Stokoe and Woods 1972, and Woods and Stokoe 1985) and (2) the cross-correlation method (e.g. Roesler 1977, Woods 1978, Woods and Stokoe 1985, and Sully and Campanella 1995). Direct travel time resolution was performed by visually picking certain points (i.e. first arrival or first trough/peak) in the waveforms. Even though there is some subjectivity in the selection of the arrival times, this technique provides repeatable velocity measurements if the waveforms are of high quality. In the cross-correlation method, all points in the waveforms are used to measure the travel time between sensors. Basically, cross-correlation between two waveforms is calculated by shifting the waveform from the first sensor relative to the waveform from the second sensor in a step increment equal to the sampling interval. At each step increment, the cross-correlation magnitude is calculated by integrating the product of these waveforms. The cross-correlation magnitude reaches a maximum

value when these waveforms match. The time shift corresponding to the maximum value can be used as the travel time. The advantage of the cross-correlation method is that it can be automated to expedite the analysis process. However, it also has several limitations. First, the cross-correlation method provides an "average" velocity, not a phase velocity that is needed to calculate G_{max} and constrained modulus (M_{max}). Second, the cross-correlation requires clean waveforms without strong near-field terms.

In crosshole seismic testing, $V_{p\text{-}X}$ measurements were performed using time records from the X-axis component in two geophones located at the same depth (Fig. 4.1). Propagation velocity was calculated by dividing the horizontal spacing by the wave travel time between these geophones. Example of a $V_{p\text{-}X}$ measurement from crosshole seimic testing is presented in Fig. 4.20(a). The travel time between the geophones was measured by picking the first arrivals, as indicated by blue and red triangles in both waveforms.

$V_{s\text{-}XZ}$ measurements were performed using the time records from the Z-axis component in 3-D geophones located at the same depth. Figure 4.20(b) shows an example of a $V_{s\text{-}XZ}$ measurement from crosshole seismic testing. The travel time between 3-D geophones was measured by picking the first arrivals as denoted by blue and red triangles in both waveforms. Alternatively, it could be measured by picking the first peak or trough as indicated by blue and red circles in both waveforms. The two travel time picks yielded similar results.

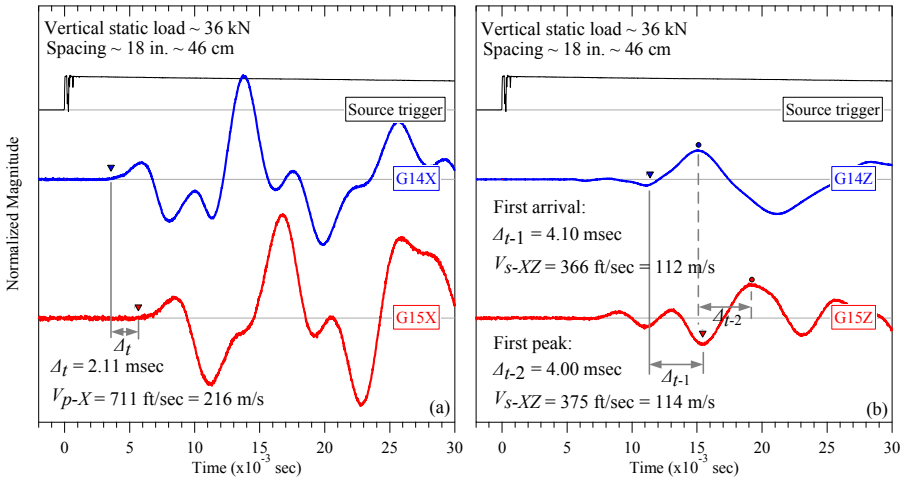

Figure 4.20 Crosshole seismic test records: (a) $V_{p\text{-}X}$ and (b) $V_{s\text{-}XZ}$.

In downhole seismic testing, vertically propagating waves were used to measure time delays between the waveforms monitored by two geophones in each backfilled borehole. $V_{p\text{-}Z}$, $V_{s\text{-}ZX}$, and $V_{s\text{-}ZY}$ were measured using signal records from geophone components in Z, X, and Y direction, respectively. An example of $V_{p\text{-}Z}$ measurements is shown in Fig. 4.21(a). The points indicated by two triangles were used to measure the travel time between the 3-D geophones. Examples of $V_{s\text{-}ZX}$ and $V_{s\text{-}ZY}$ measurements are presented in Fig. 4.21(b and c). The travel times from these shear waves could be estimated by picking the first arrivals as well as the first troughs/peaks. These two travel time picks yielded similar shear wave velocity values.

Figure 4.22(a) shows an example of the use of the cross-correlation method to measure $V_{p\text{-}Z}$ using waveforms from geophones G15 and G13 in the Z direction [Fig. 4.21(a)]. In this example, $V_{p\text{-}Z}$ estimated from the cross-correlation method yielded a value that was about 18% higher than the value of $V_{p\text{-}Z}$ measured from the direct time resolution. The application of cross-correlation method for measuring $V_{s\text{-}ZX}$ using waveforms in geophone G15 and G13 in the X direction [Fig. 4.21(b)] is presented in Fig. 4.22(b). The $V_{s\text{-}ZX}$ measured from cross-correlation was about 3% higher than the $V_{s\text{-}ZX}$ measured from the direct time resolution method. Figure

4.22(c) presents the application of cross-correlation method for evaluating $V_{s\text{-}ZY}$ using waveforms in geophone G15 and G13 in the Y direction [Fig. 4.21(c)]. The $V_{s\text{-}ZY}$ measured from cross-correlation was about 5% higher than the $V_{s\text{-}ZY}$ measured from the direct time resolution method. In the crosshole seismic testing, the $V_{p\text{-}X}$ measured using the cross-correlation method also yielded different $V_{p\text{-}X}$ values compared to those measured from the direct time resolution method. On the other hand, the $V_{s\text{-}XZ}$ measured using the cross-correlation method was similar to $V_{s\text{-}XZ}$ measured using the direct time method. In this study, V_p was measured using the direct time resolution and V_s was measured by direct time resolution method as well as the cross-correlation method.

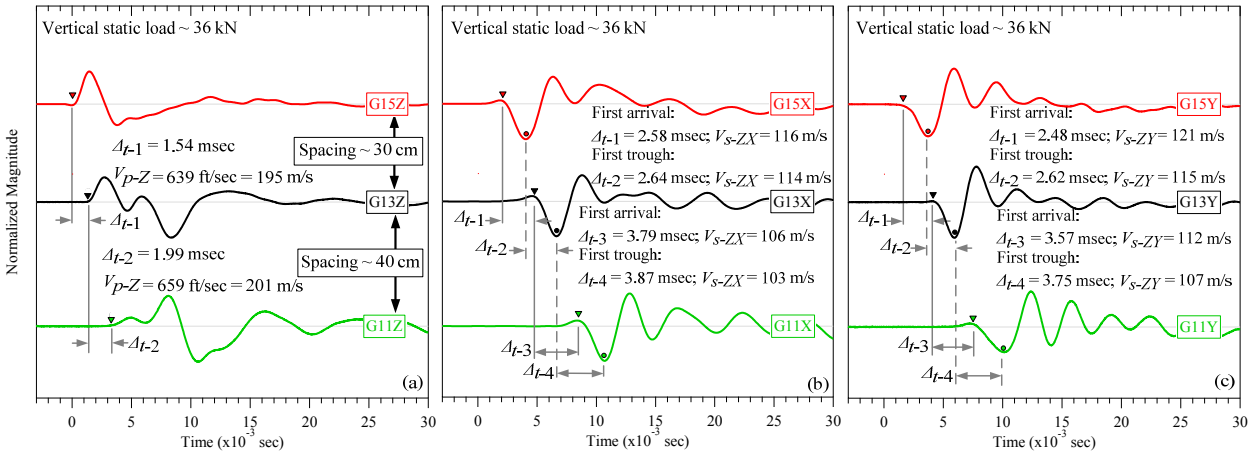

Figure 4.21 Downhole seismic test records: (a) $V_{p\text{-}Z}$, (b) $V_{s\text{-}ZX}$, and (c) $V_{s\text{-}ZY}$.

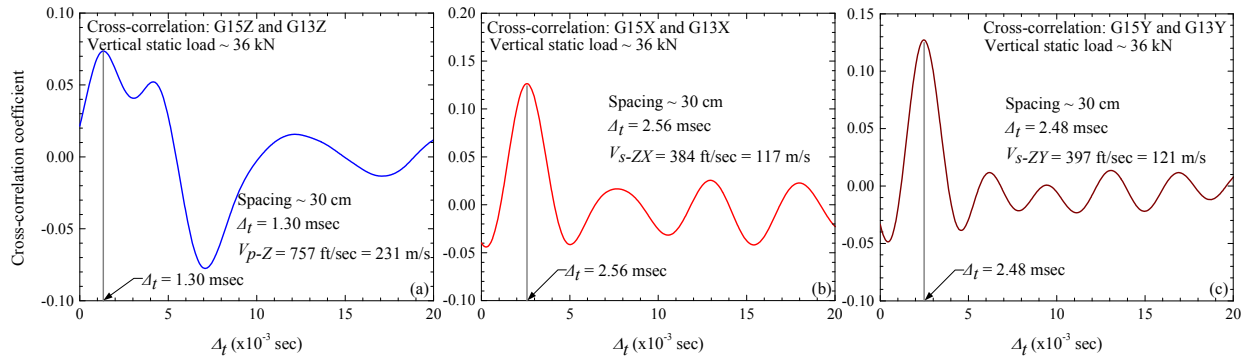

Figure 4.22 Cross-correlation analysis used to evaluate: (a) $V_{p\text{-}Z}$, (b) $V_{s\text{-}ZX}$, and (c) $V_{s\text{-}ZY}$.

4.5.4 Steady-state Dynamic Testing

The steady-state dynamic testing was performed to investigate the nonlinear stress-strain response of solid waste. This stress-strain response is commonly characterized by the relationship between shear modulus and induced shearing strain. Data analysis to calculate shear modulus and shearing strain is presented in detail below.

4.5.4.1 Shear Modulus Calculation

In nonlinear field testing, the loading plate of the mobile field shaker vibrates in the horizontal X direction which generated vertically propagating shear waves with horizontal particle motion in the X direction. Figure 4.23(a) shows the raw output time records of the X-component geophones in west hole array (shown in Fig. 4.1). The shear wave velocities were calculated by dividing the vertical spacing by the associated time intervals between the 3-D geophones. The time intervals are determined using time lags between waveforms in the steady-state portion as indicated in the records.

Shear modulus were calculated from the measured shear wave velocities and the mass density of solid waste (ρ) as:

$$G = \rho \cdot V_s^2 \tag{4.3}$$

The unit weight of the solid waste from the large-scale in-situ measurement was used to obtain the corresponding mass density. Shear moduli calculated using geophone pairs in the west hole array was then averaged with their counterpart geophone pairs in the east hole array to determine the average shear modulus of the solid waste over each depth interval.

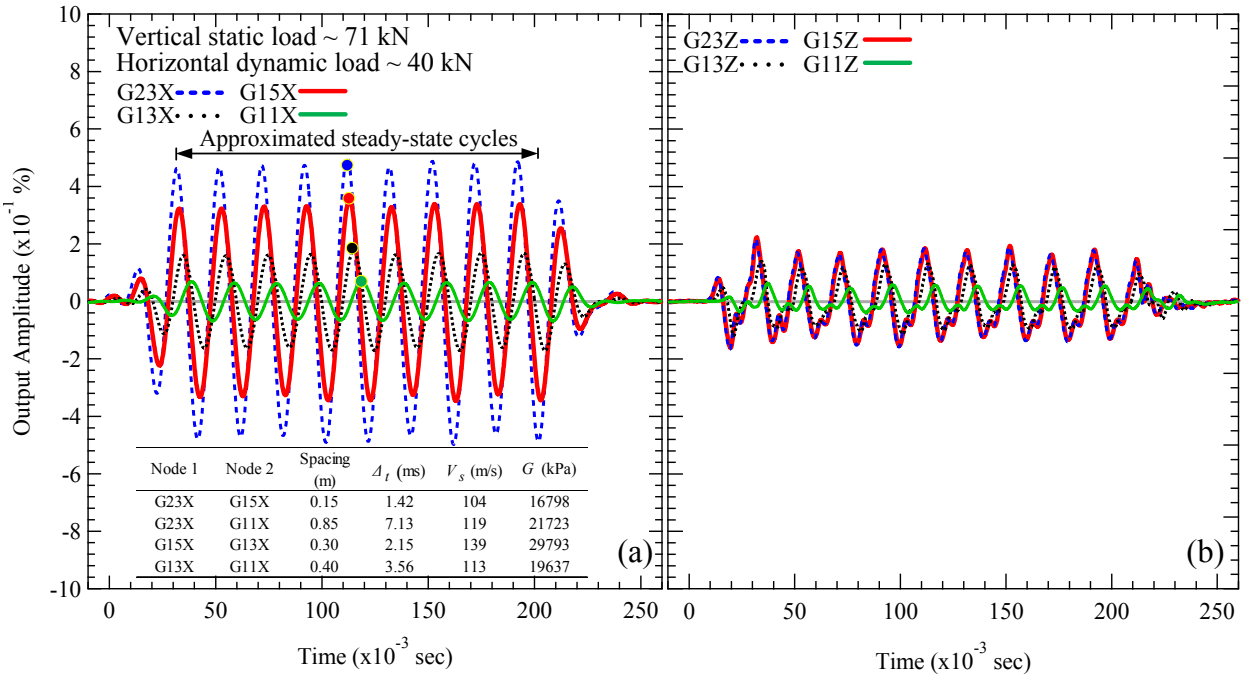

Figure 4.23 Example of steady-state testing result: (a) X-component geophone output time records and (b) Z-component geophone output time records.

4.5.4.2 Shearing Strain Calculation

Shearing strain induced in the waste can be calculated using four different analytical methods, namely the displacement based method, the plane shear wave method, the plane Rayleigh wave method, and the apparent wave method (Rathje et al. 2005). The displacement based (DB) method most represents the correct measured motions and does not require knowledge of the wave propagation velocities. The DB method is described herein. The other shearing strain calculation methods and their comparison with DB method are discussed in more detail in Chang (2002), Rathje et al. (2005), and Cox (2006).

A schematic for the 2-node DB method is presented in Fig. 4.24(a). In this method, a 3-D geophone is considered as a node with single-degree of freedom in the X direction. Shearing strain in the 2-node DB method is calculated using:

$$\gamma = \frac{u_{X1} - u_{X2}}{2b} = \frac{\Delta u_{X1-2}}{2b} \tag{4.4}$$

where u_{Xi} is the horizontal displacement of node-i and b is half of the vertical spacing between two nodes.

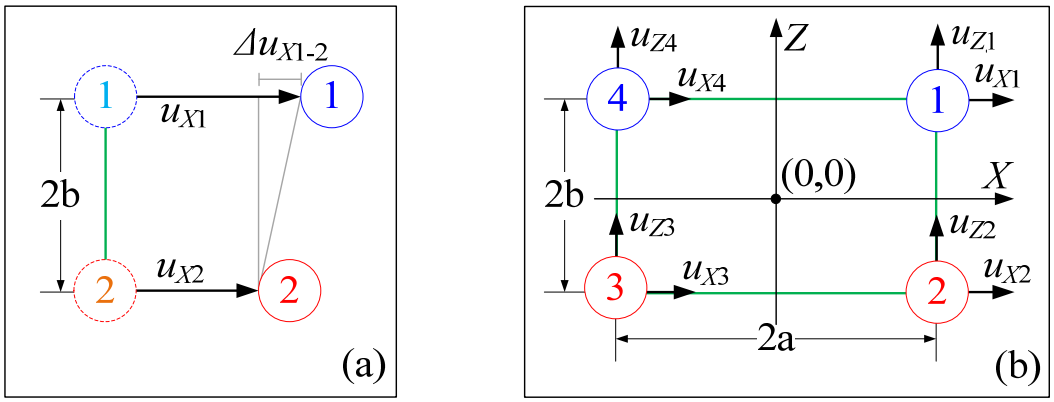

Figure 4.24 Displacement Based (DB) methods for calculation of shearing strain: (a) 2-node and (b) 4-node.

A schematic of the 4-node DB (bilinear quadrilateral) method is presented in Fig. 4.24(b). In this method, a 3-D geophone is considered a node with two-degree of freedom in X and vertical Z directions. Four 3-D geophones form a single quadrilateral element. Shearing strain at any point inside the element can be calculated using (Rathje et al. 2005):

$$\gamma_{XZ}(X,Z) = \frac{1}{4}\left[-\frac{u_{X1}}{b}\left(1-\frac{X}{a}\right) - \frac{u_{Z1}}{a}\left(1-\frac{Z}{b}\right) - \frac{u_{X2}}{b}\left(1+\frac{X}{a}\right) + \frac{u_{Z2}}{a}\left(1-\frac{Z}{b}\right) + \frac{u_{X3}}{b}\left(1+\frac{X}{a}\right) + \frac{u_{Z3}}{a}\left(1+\frac{Z}{b}\right) + \frac{u_{X4}}{b}\left(1-\frac{X}{a}\right) - \frac{u_{Z4}}{a}\left(1+\frac{Z}{b}\right)\right] \tag{4.5}$$

where u_{Zi} is the vertical displacement of node-i and a is half of the horizontal spacing between two nodes.

To use these DB methods, raw output time-history data from the 3-D geophones were converted to particle velocity time-histories using the calibration factor of each geophone.

Displacement time-histories were obtained by numerically integrating the recorded velocity-time histories. In this study, numerical integration was performed using trapezoidal rule. Baseline correction to remove drift in the integrated signals was performed in the frequency domain using high-pass filtering at a cut-off frequency of 5 Hz. Example of shearing strain time-history calculated using 4-node DB is presented in Fig. 4.25.

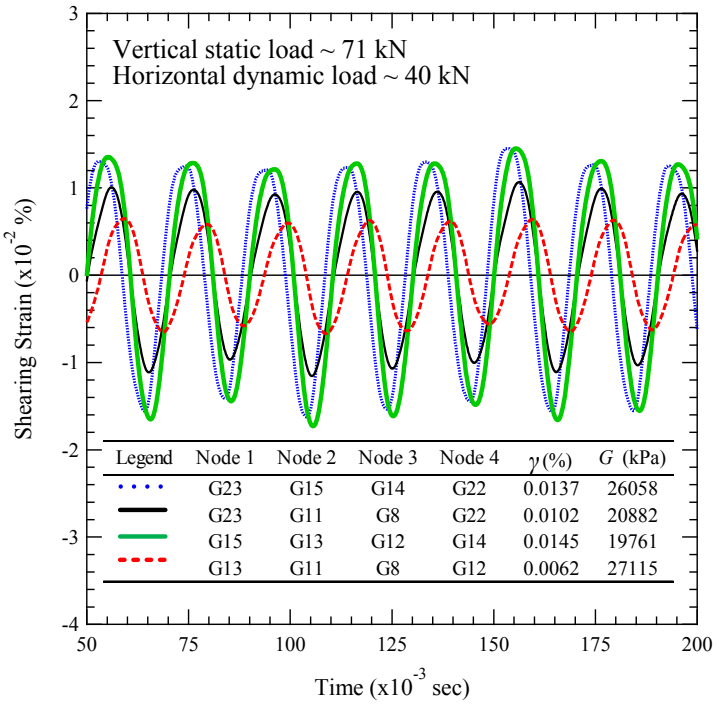

Figure 4.25 Example of shearing strain time-history calculated using 4-node DB

The 2-node DB method is simple and requires fewer sensors. However, as shown in Fig. 4.23(b), the shakers did not generate purely horizontal vibration in field testing, but also induced some rocking which created a small vertical component motion. As a result, the vertical dynamic displacement of the geophones should not be neglected. It contributed to the overall shearing strain induced within the sensor array which could not be addressed by a 2-node DB method.

A comparison between shearing strain calculated using the 2-node and 4-node DB methods is presented in Fig. 4.26(a) for testing at the Los Reales Landfill. Shearing strain calculated using the 2-node and 4-node DB methods tended to be consistent at small shearing strains. As the shearing strain increases, shearing strain calculated using the 2-node method became smaller than that of the 4-node DB method. At shearing strain of about 10^{-3}%, shearing strain calculated using the 2-node method was about 90% of shearing strain calculated using the 4-node method [Fig. 4.26(b)]. At shearing strain of about 10^{-1}%, shearing strain calculated using the 2-node method was less than 60% of shearing strain calculated using the 4-node. The reason for this discrepancy was that the rocking motion created by the combined motions of the shakers' plate increased with the amplitude of dynamic horizontal load (Cox 2006). Thus, the vertical motion induced by rocking of the base plate contributed more to the induced shearing strain at larger horizontal dynamic loads. On the basis of these results, it is recommended that shearing strains at the center of quadrilateral element are calculated using the 4-node DB method. These "average" shearing strains were needed to evaluate the G-log γ as well as G/G_{max}-log γ relationships.

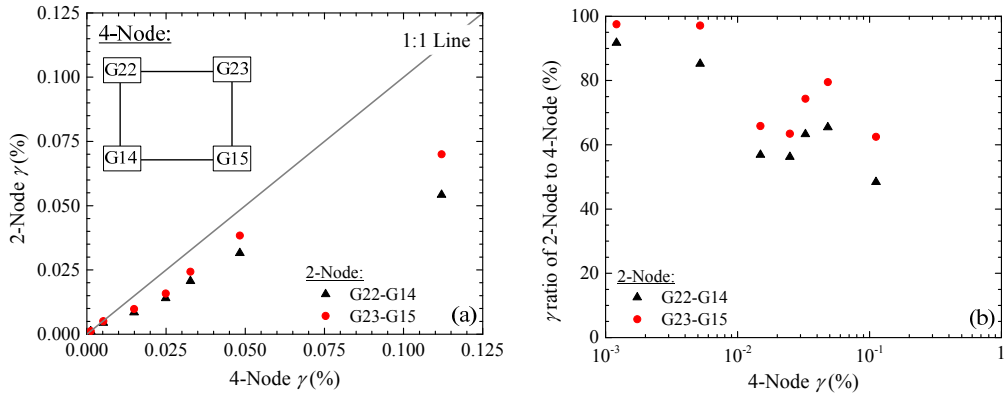

Figure 4.26 Comparison of shearing strains calculated using the 2-node and 4-node displacement-based methods.

4.6 **Example Results**

4.6.1 Wave Propagation Velocities

The crosshole and downhole seismic testing allowed assessment of V_p and V_s with different propagation and polarization directions. As noted earlier, mean confining stress distribution was estimated using the Ahlvin and Foster (1954) method for varying static vertical loads imposed by the shakers. With this information, the relationship between wave propagation velocity and mean confining stress could be investigated under in-situ conditions.

The relationship between $V_{s\text{-}ZX}$ and σ_0 evaluated from downhole seismic testing in the west hole array at the Los Reales Landfill is shown in Fig. 4.27.. The measured $V_{s\text{-}ZX}$ was generated for each of the three pairs of vertically adjacent 3-D geophones. Each V_s represented the shear wave velocity at mid-point between geophones. At each load increment, σ_0 was calculated and its relationship with $V_{s\text{-}ZX}$ was evaluated. A power function was fitted to the data in the form of:

$$V_{s-ZX} = A_{ZX} \cdot \left(\frac{\sigma_0}{P_a} \right)^{n_{ZX}} \tag{4.6}$$

where P_a is atmospheric pressure, and A_{ZX} is V_s at 1 atm, and n_{ZX} is an exponent which represents the effect of confining pressure on $V_{s\text{-}ZX}$. In Fig. 4.27, a bi-linear relationship of $V_{s\text{-}ZX}$ with σ_0 was observed at depths of 0.13 and 0.36 m. At depth of 0.71 m, a linear relationship between $V_{s\text{-}ZX}$ with σ_0 was observed. Bi-linearity relationship indicated that the waste was initially in the overconsolidated (OC) state due to waste compaction (Stokoe et al. 2011). As mean confining stress increased beyond the maximum past mean confining stress of about 30 kPa, the solid waste became normally consolidated (NC). In the OC regime, the stress exponent n_{ZX} was found

to be low, ranging from 0.09 – 0.11. In the NC regime, the n_{ZX} value was significantly higher (n_{ZX} = 0.25 – 0.30). Similar relationship of wave velocities and stresses can also be generated for $V_{s\text{-}ZY}$, $V_{s\text{-}XZ}$, $V_{p\text{-}Z}$, and $V_{p\text{-}X}$.

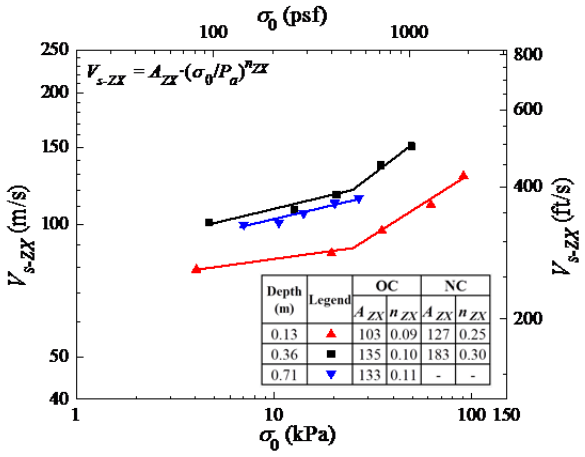

Figure 4.27 Relationship between $V_{s\text{-}ZX}$ and mean confining stress evaluated at the Los Reales Landfill.

4.6.2 Shear Modulus and Normalized Shear Modulus Reduction Curves

The effect of mean confining stress on the shear modulus reduction-log shearing strain (G-log γ) and the normalized shear modulus (G/G_{max}-log γ) relationships are illustrated in Figs. 4.28(a and b), respectively. These curves were obtained from a quadrilateral element that was formed by geophones G13, G12, G14, and G15 (Fig. 4.1). In this example, G_{max} increased from 15 to 28 MPa as mean confining stress increased from 15 to 77 kPa. For this range of mean confining stress, the G-log γ curves moved to the right with increasing σ_0 and showed an increasing linear response [Fig. 4.28(a)]. These trends were similar to trends previously observed in laboratory testing of municipal solid waste (e.g. Lee 2007, Zekkos et al. 2008, and Yuan et al. 2011).

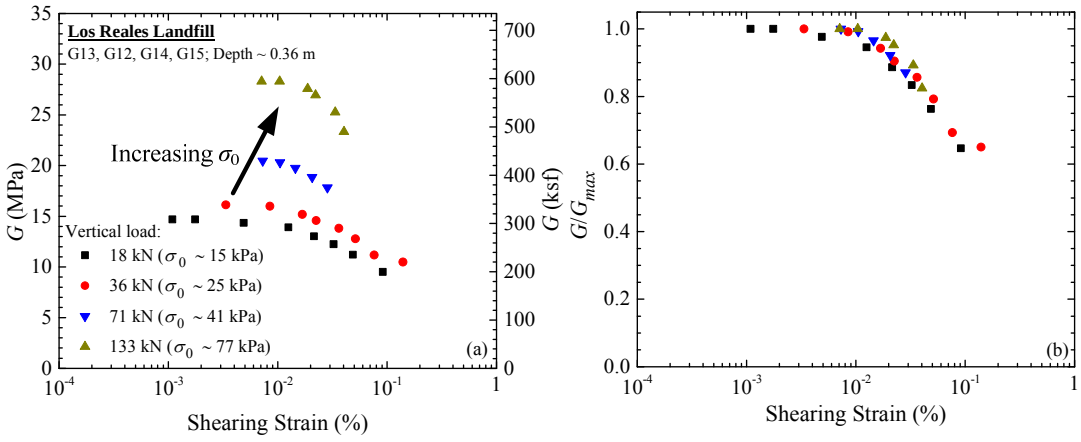

Figure 4.28 Effect of mean confining stress on (a) shear modulus and (b) normalized shear modulus curves

Waste composition is one the most important factors that affects the nonlinear dynamic properties of solid waste (Zekkos et al. 2008). The data collected could also be used to assess the impact of waste variability on G/G_{max}-log γ relationship by examining different quadrilateral elements. Figure 4.29(a) presents examples of G-log γ from three different elements at nearly the same estimated mean confining stresses (12 – 15 kPa). The small-strain shear modulus ranges from 15 to 22 MPa. Differences in G-log γ relationships could be attributed to variability in waste composition. Figure 4.29(b) illustrates the variability in waste composition effect on the G/G_{max}-log γ relationships. For the data shown, the largest shearing strain evaluated in this test was 0.1%.

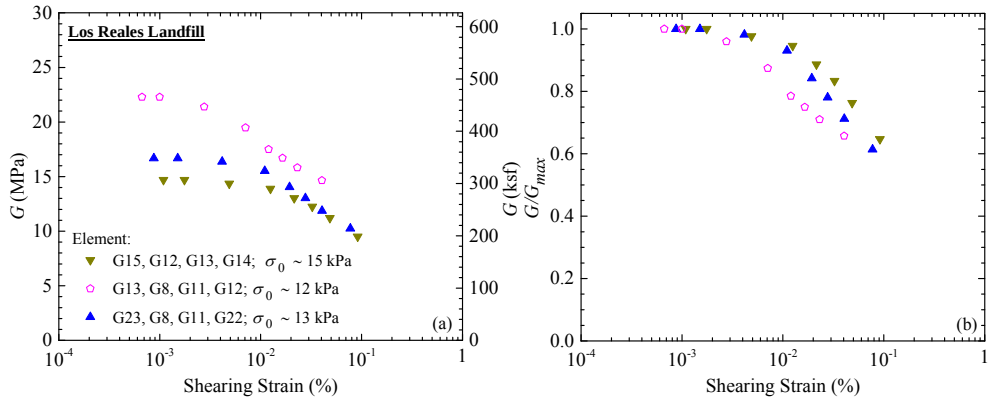

Figure 4.29 Effect of waste variability on (a) shear modulus and (b) normalized shear modulus reduction curves.

4.7 **Uncertainties and Limitations**

In general, crosshole and downhole seismic tests and steady-state tests were performed successfully to evaluate the dynamic properties of solid waste in situ. Nevertheless, there are several uncertainties and limitations associated with these tests that also have been noted in previous studies (e.g. Stokoe et al. 2005, Park 2010, Zalachoris 2010, and LeBlanc 2013). Uncertainties and limitations from this field testing as well as experiences from previous studies include the following:

1. Evaluation of the in-situ stress state was only an approximation (Stokoe et al. 2005, Park 2010, Zalachoris 2010, and LeBlanc 2013). The solid waste is not homogeneous or isotropic. The landfill is layered with the amount of stiff and soft waste constituents varying spatially. These factors were not considered when estimating the stress state in the solid waste.
2. As reported by Park (2010), Zalachoris (2010), and LeBlanc (2013), the wave propagation paths may not be correctly identified. The waves may propagate along some other paths instead of the direct path assumed in the analysis. The vertical and lateral variability in the instrumented zone may cause the waves to propagate along unexpected paths. Zalachoris (2010) reported that this uncertainty may be one of

possibilities resulted in scatters and deviation from the expected trend in the testing results.

3. In small-scale crosshole and downhole seismic tests as well as the steady-state dynamic test, some data could not be analyzed due to several reasons. First, the response of the shallower sensor could be lagged the response of the deeper sensor and resulted in negative wave propagation velocity. Second, the response of the shallower sensor could be in-phase or nearly in-phase with the response of the deeper sensor resulted in infinite or very high wave propagation velocity. Mostly, this problem occurred at the shallowest 3-D sensor pair. Although the origin of this problem is still not clear, it may be attributed to the possibility that the waves followed wave path that was different from the assumed wave path. LeBlanc (2013) also reported similar experience. In addition, poor waveforms in small-scale crosshole and downhole seismic tests, such as ringing and weak signals, resulted in difficulty in estimating the wave arrival points.
4. The sensitivity and resolution of the measuring devices, equipment control in the field, and proper used of the equipment could also be the sources of uncertainties and limitations (Park 2010). In addition, uncertainties could also be attributed to combination of measurement accuracy and simplifications of the in-situ conditions for analytical purposes (Stokoe et al. 2005).

These uncertainties and limitations can explain scatters and deviation from the expected trend from the results of small-scale crosshole and downhole seismic tests as well as steady-state dynamic test.

4.8 **Summary**

In this chapter, an experiment method to study the linear and nonlinear dynamic properties of solid waste is described. This experimental method was adopted from previous studies (e.g. Axtell et al. 2002, Stokoe et al. 2006 and 2011, Park 2010). Detailed descriptions of field setup, main instruments, field procedure, and examples of data analysis have also been presented in this chapter. Uncertainties and limitations from this testing method as well as experiences from previous studies have been described.

This testing method included small-scale crosshole and downhole seismic testing and steady-state dynamic testing. In addition, load-settlement tests and in-situ unit weight measurements were performed. The main results from this field testing method were: (1) wave propagation velocities in varying propagation and polarization directions as well as their variation with confining stress, and (2) shear modulus-log shearing strain and normalized shear modulus-log shearing strain relationships as well as their variation with confining stress. Steady-state dynamic testing was performed using mobile field shakers of NEES@UT and 3-D geophone units embedded in the solid waste were used to capture the waste response. This field method offered the in-situ evaluation of the impact of mean confining stress and variability of waste composition on dynamic properties of solid waste.

CHAPTER 5. FIELD EVALUATION OF DYNAMIC PROPERTIES OF MUNICIPAL SOLID WASTE AT THE AUSTIN COMMUNITY LANDFILL

5.1 **Introduction**

As part of this study, the dynamic properties of municipal solid waste (MSW) were evaluated in situ at the Austin Community Landfill (ACL) in Austin, Texas from June 20 to July 1, 2011. This chapter describes test locations, field test execution, and test results. The field investigation was performed using the procedures described in Chapter 4, and included downhole and crosshole seismic tests, spectral analysis of surface wave (SASW) testing, and steady-state dynamic tests. In addition, load-settlement tests and in-situ unit weight measurements were performed.

5.2 **Field Investigation at the Austin Community Landfill**

The field investigation at the Austin Community Landfill was mainly performed to evaluate the linear and nonlinear dynamic properties of MSW in situ. In the linear range, small-scale crosshole and downhole seismic tests were conducted to investigate shear wave (S-wave) velocity (V_s) and primary wave (P-wave) velocity (V_p) of MSW. The combination of these seismic methods allowed an assessment of anisotropy and Poisson's ratio of MSW. In the nonlinear range, steady-state dynamic testing was performed to evaluate in situ the variation of shear modulus (G) and normalized shear modulus (G/G_{max}) as a function of shearing strain (γ).

The ACL is a MSW landfill operated by the Waste Management of Texas, Inc. under the regulations of the Texas Commission on Environmental Quality (TCEQ) and the U.S. Environmental Protection Agency (EPA). The ACL is located at 9900 Giles Road, Austin, Texas

which is approximately 16 km northeast of downtown Austin (Fig. 5.1). This landfill receives municipal solid waste such as household, commercial, and non-hazardous industrial waste. In addition, this landfill also receives construction and demolition debris. In general, the majority of MSW at the ACL comes from businesses and residents of Travis County, Texas.

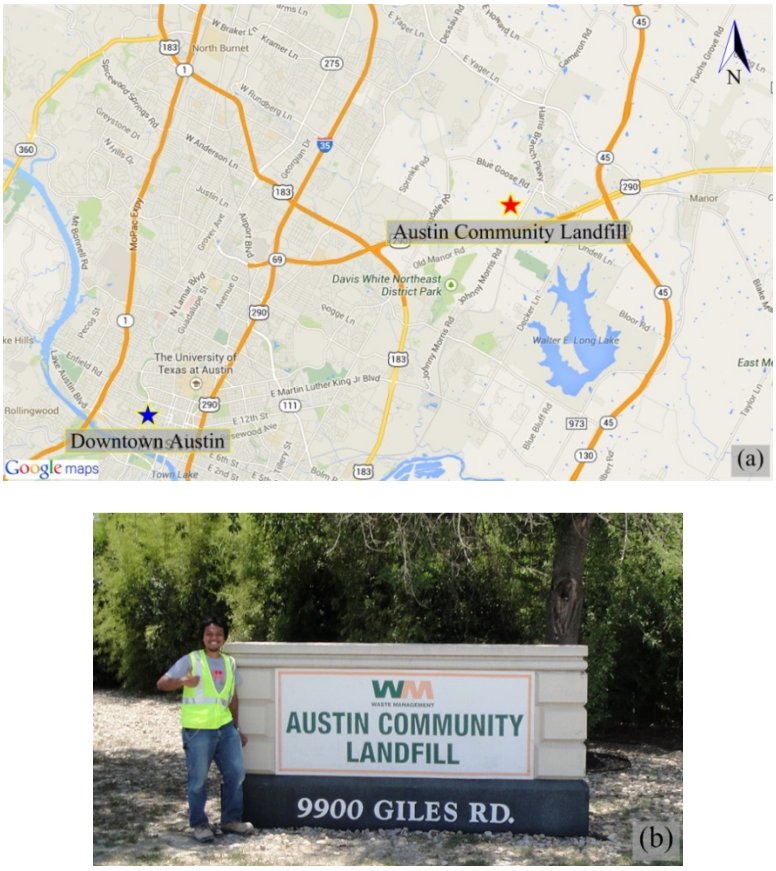

Figure 5.1 The Austin Community Landfill: (a) location and (b) entrance.

The field investigation at the ACL was performed by the author and Dr. Dimitrios Zekkos (University of Michigan); Mr. Cecil G. Hoffpauir, Mr. Curtis Mullins, Dr. Farn-Yuh Menq, and Dr. Changyoung Kim (NEES@UT); and Ms. Lindsay O'Leary (Geosyntec). In addition, test logistics was accommodated by the Waste Management of Texas Inc.

5.2.1 Test Locations

The field investigation was performed in three locations at the ACL (Fig. 5.2). Locations 1 and 3 were located in waste disposal cell 10 (WD-10) area [Fig. 5.3(a)]. This cell was constructed in 2008. Field testing in location 1 was performed from June 20 to 24, 2011. The field investigation in location 3 was conducted on June 24, 2011. According to the landfill operator, MSW age in these locations was estimated to be about 3-year old. During site preparation at location 1, a trial scrapping of soil cover showed that a layer rich in large-waste-particle was found at about 5 – 10 cm below the surface [Fig. 5.3(b)].

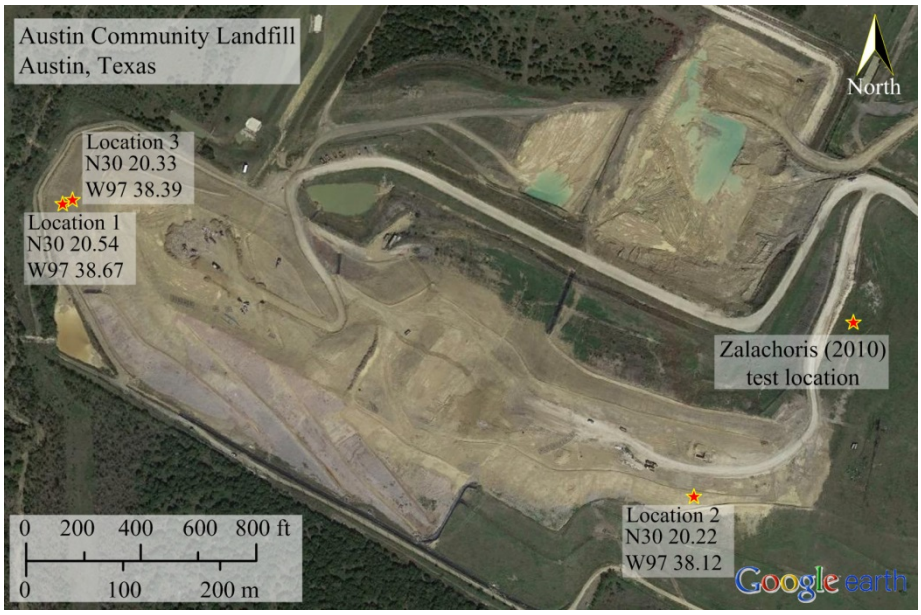

Figure 5.2 Test locations at the Austin Community Landfill.

Location 2 was located in waste disposal cell 6 (WD-6) area (Figs. 5.2 and 5.4). This cell was close to the pre-Subtitle D landfill part of ACL that was constructed in 1980s. In this pre-Subtitle D landfill, Zalachoris (2010) performed proof of concept trial for this present study (Fig. 5.2). Field investigation at location 2 was conducted on June 27 to July 1, 2011. This cell was

constructed from 2003 to 2009. The tested waste age at this location was estimated to be 2 years based on information on excavated newspaper and documents.

Figure 5.3 (a) Site view and (b) layer with large-waste-particle in location 1 at the ACL.

Figure 5.4 (a) Southwest and (b) south views of location 2 at the ACL.

5.2.2 Field Instrumentation and Testing Setup

Figure 5.5 shows activities during the field instrumentation and testing setup at the ACL. In this landfill, sensor holes were created using a low capacity power auger and hand auger [Fig. 5.5(c and d)]. The power auger was used for pre-drilling when hard layers were encountered. Drilling using a power auger and a hand auger was time consuming. In subsequent field testing at the other landfills, drilling was performed by pushing a core barrel.

Testing setups in locations 1, 2, and 3 are shown in Figs. 5.6, 5.7, and 5.8, respectively. Testing setup at locations 1 and 2 were prepared for the load-settlement test; the small-scale downhole and crosshole seismic tests; and the steady-state dynamic test. The deepest 3-D geophone pair at locations 1 and 2 was located at a depth of 1.05 m and 0.56 m, respectively. Testing setup at location 3 was only prepared for steady-state dynamic test without a footing. In this location, the deepest 3-D geophone was installed at a depth of 0.65 m. Having only a single vertical 3-D geophone array, the testing setup at location 3 only offered a 2-node approach to calculate shearing strain. As explained in Chapter 4, the 2-node method underestimates shearing strain as it does not take into account the vertical displacement component. In addition, testing at this location resulted in irregular waveforms with response of the shallower sensor lagging the response of the deeper sensor resulting in negative wave propagation velocities. Results from this location are excluded from this manuscript.

Figure 5.5 Field instrumentation and testing setup at the ACL: (a) removing soil cover, (b) elevation survey, (c) power auger pre-drilling, (d) hand auger drilling, (e) hole depth measurement, (f) sensor installation, (g) hole compaction, and (h) footing placement.

5.2.3 Field Testing Sequence for Evaluation of Dynamic Properties of MSW at the ACL

Investigation of the dynamic properties of MSW in locations 1 and 2 at the ACL were performed according to the staged loading sequence shown in Figs. 5.9 and 5.10, respectively. In location 1, small-scale crosshole and downhole seismic tests were performed at externally applied vertical static loads of 0 kN, 4 kN, 9 kN, 18 kN, 67 kN, and 133 kN. Steady-state dynamic tests were performed using a 18 kN, 67 kN, 133 kN, and 165 kN static hold-down force. These vertical static load levels were kept constant while applying horizontal dynamic loads. Thumper was used to apply static vertical loads up to 18 kN and T-Rex was used to impose the larger vertical static load levels. In location 2, the small-scale crosshole and downhole seismic tests were performed at externally applied vertical static loads of 0 kN, 9 kN, 18 kN, 36 kN, 67 kN, and 133 kN. The steady-state dynamic tests were performed using a 18 kN, 36 kN, 67 kN, and 133 kN static hold-down force. Thumper was used to apply static vertical loads up to 36 kN. At both locations, load-settlement data were collected during vertical static load application for the crosshole and downhole seismic tests.

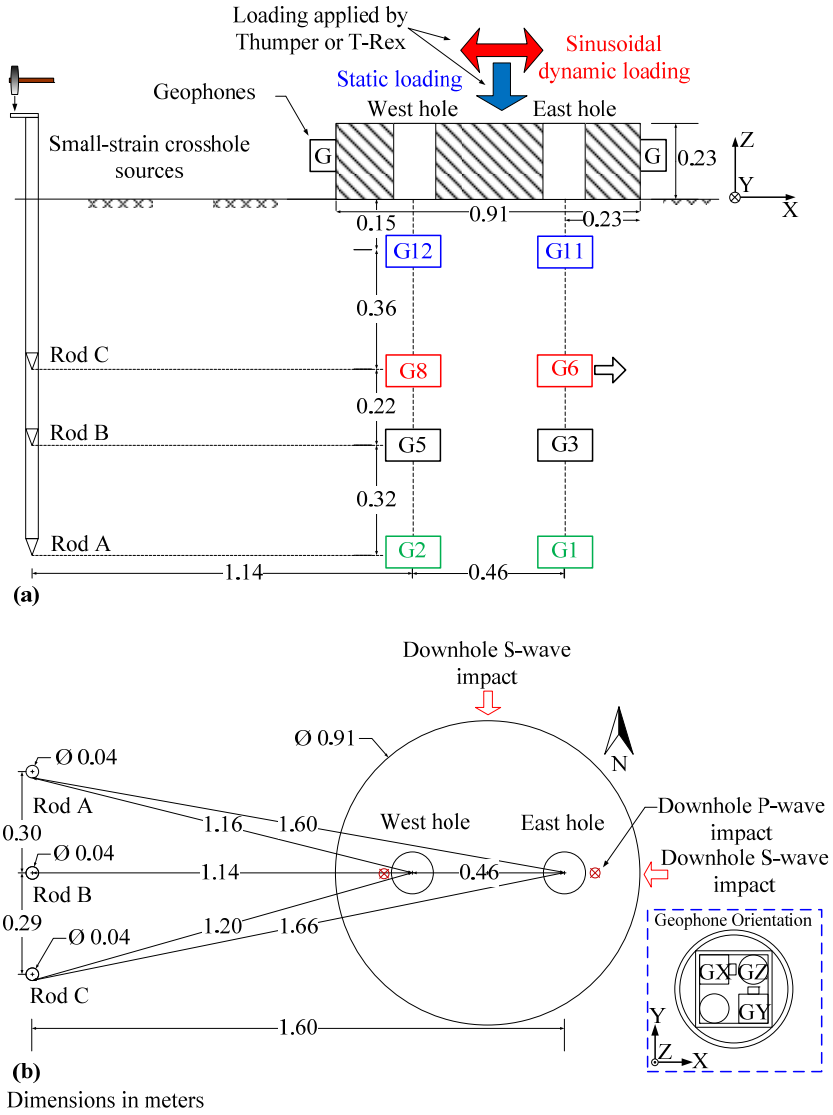

Figure 5.6 Testing setup in location 1 at the ACL.

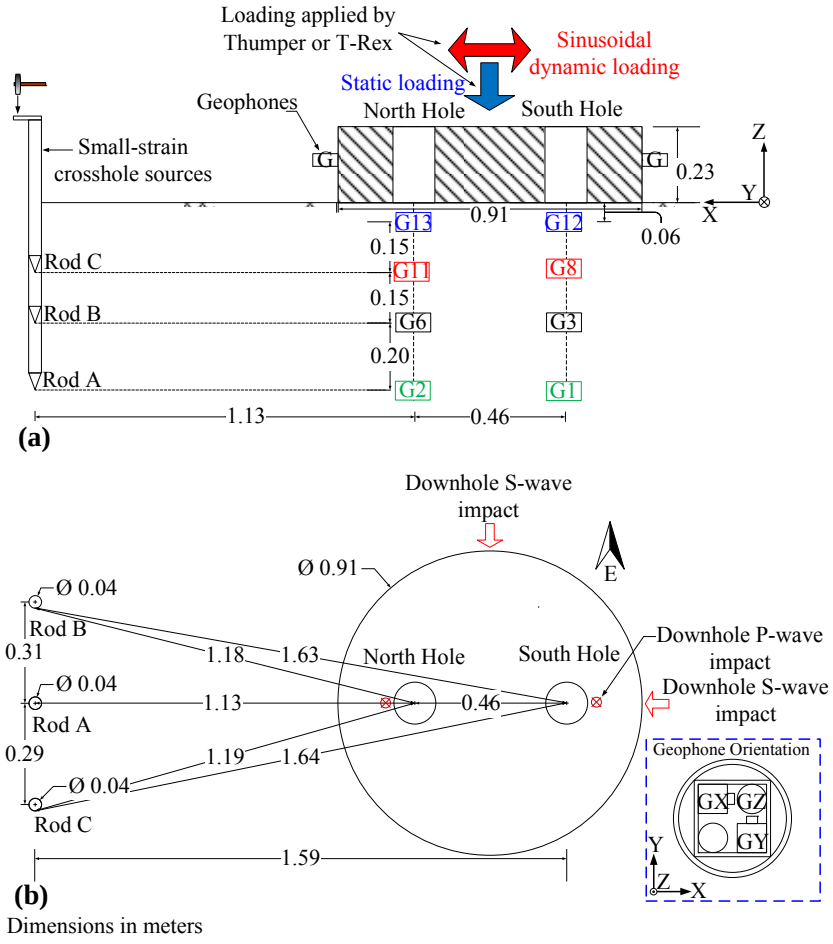

Figure 5.7 Testing setup in location 2 at the ACL.

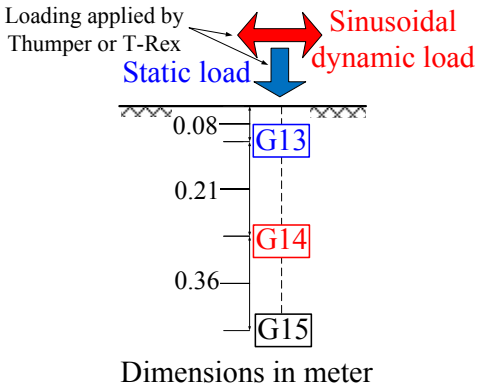

Figure 5.8 Testing setup in location 3 at the ACL.

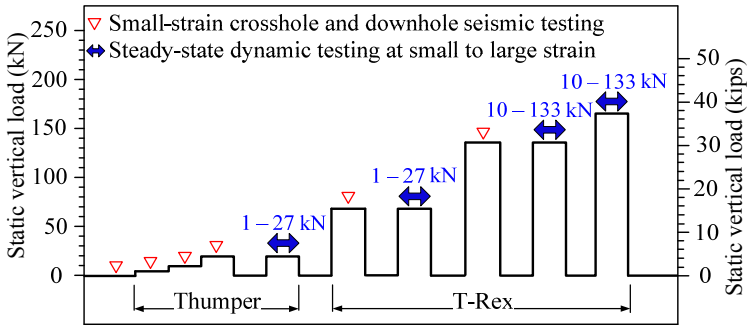

Figure 5.9 Staged loading sequence in location 1 at the ACL.

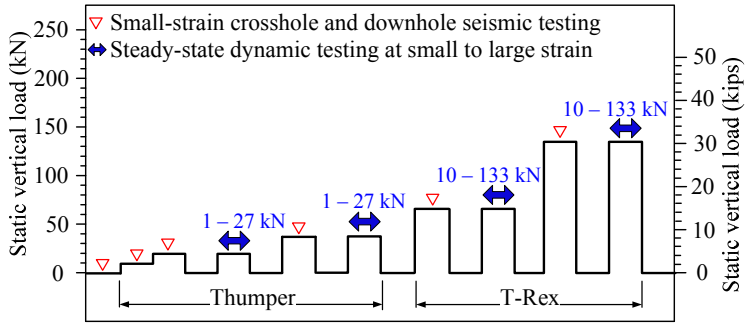

Figure 5.10 Staged loading sequence in location 2 at the ACL.

5.2.4 In-situ Unit Weight Measurements and MSW Sampling

Each test location was excavated to characterize MSW in situ, perform in-situ unit weight measurements, collect bulk solid waste samples, and retrieve 3-D geophones after completion of the staged loading test (Fig. 5.11). Characterization of MSW and in-situ unit weight measurement were performed using procedures proposed by Zekkos et al. (2010) and Zekkos et al. (2006a), respectively. An approximately 1.5 m x 1.5 m x 1.2 m pit was excavated at each location. The volume of the excavation was determined by end dumping calibrated pea gravel with diameter ranging from 0.64 to 0.95 cm (0.25 to 0.375 in.) to fill the pit [Fig. 5.11(d)]. Bulk samples of the excavated MSW were collected in 55-gallon HDPE drums and were transported to the Geoenvironmental Engineering laboratory at the University of Michigan. Four drums were used to store 5.8 kN of MSW in location 1, 2 drums were used to store 2.2 kN of MSW in

location 2, and 2 drums were used to store 2.7 kN of MSW in location 3. Remaining excavated MSW was re-disposed in the landfill.

Table 5.1 presents the results of unit weight measurements and waste characterization for both test locations at the ACL. The gross unit weights were 14.9 kN/m^3, 15.6 kN/m^3, and 17.7 kN/m^3 in locations 1, 2 and 3, respectively. Waste composition was characterized using the collected bulk samples separately for each test location in the Geonvironmental Engineering laboratory at the University of Michigan. It should be noted that although the samples collected from each location involved a significant amount of waste material (i.e. 2.2-5.8 kN), these amounts were still just a portion of the waste mass tested in the field. The collected samples were 25%, 10%, and 16% by weight of the excavated MSW in locations 1, 2 and 3, respectively. Thus, the waste compositions shown are only approximately representative of the tested waste composition and may not be identical to the tested waste composition in the field.

Figure 5.11 (a) Waste excavation, (b) in-situ waste characterization, (c) waste sampling, (d) pea gravel, and (d and e) in-situ unit weight measurement at the ACL.

Table 5.1 Waste composition in locations 1, 2, and 3 at the ACL.

Total Sample Weight (kN)	Unit Weight (kN/m^3)	Composition (% by weight)							
		< 20mm[1]	Paper	Hard Plastic	Soft Plastic	Wood	Metal	Gravel & Glass	Others[2]
5.8	14.9	92.1	3	1.2	1.1	0.9	0.8	0	1
2.2	15.6	79.4	7.4	3.2	3.4	3.2	0	0	3.4
2.7	17.7	88.3	3.3	1.3	1.5	1.5	1.2	0.7	2.2

[1] Soil-like material with organic contents ~ 8%.
[2] Textile, rug, latex, rubber, food remnant, and sponge.

5.3 **Load-settlement Test**

Load-settlement tests were performed in a loading sequence using static vertical loads from 4 kN up to 133 kN in locations 1 and 2 at the ACL. The corresponding average stresses on the footing due to 4 kN to 133 kN static vertical loads were from 6 kPa to 204 kPa, respectively. These static vertical loads were applied using a hydraulic jack that reacted against the mobile field shakers' frame as shown in Fig. 5.12. A T-shaped frame was used to uniformly distribute the load on the footing. The settlements were measured using three linear potentiometers on the footing.

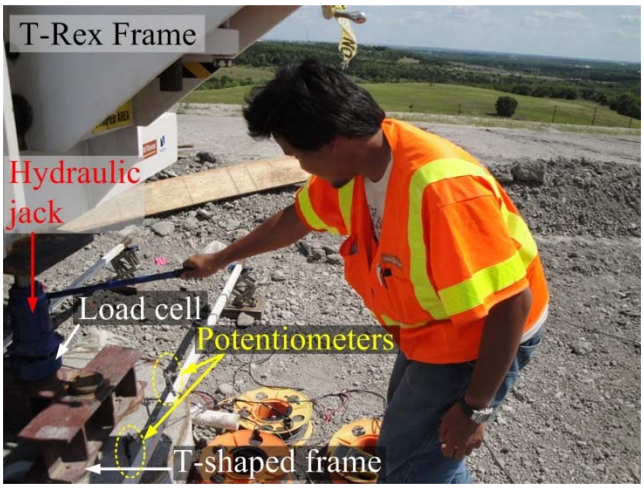

Figure 5.12 Load-settlement test in location 2 at the ACL.

Figure 5.13 shows the load-settlement curves in both testing locations at the ACL. The maximum settlements under static vertical load of 133 kN in locations 1 and 2 were 44 mm and

30 mm, respectively. Location 1 experienced more settlement and showed a more linear response in the load-settlement curve than location 2 where the load-settlement curve showed more pronounced nonlinearity.

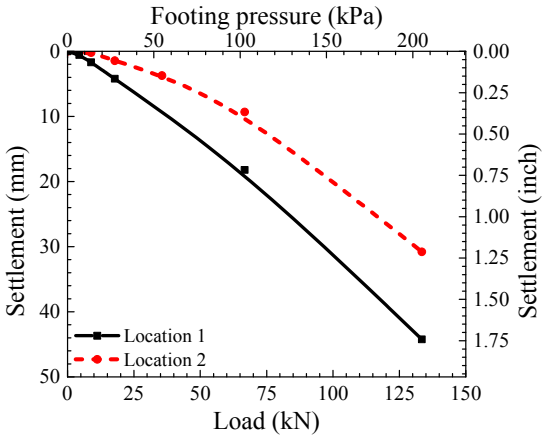

Figure 5.13 Load-settlement test results at the ACL.

5.4 **Small-scale Downhole Seismic Testing**

Small-scale downhole seismic tests were performed to evaluate vertically propagating P-wave velocity ($V_{p\text{-}Z}$), vertically-propagating horizontally-polarized in the X-axis S-wave ($V_{s\text{-}ZX}$), and vertically-propagating horizontally-polarized in the Y-axis S-wave ($V_{s\text{-}ZY}$) at each static vertical load increment (Figs. 5.9 and 5.10). Figures 5.6 and 5.7 illustrate the coordinate orientations. As shown in these figures, this test was conducted by hitting the footing at the sides and at the top with a handheld hammer.

Figure 5.14(a) illustrates the small-scale downhole seismic test without externally applied static vertical load. Testing setup with external static vertical load applied using a hydraulic jack that was reacting against T-Rex is shown in Fig. 5.14(b). The small-scale downhole testing analysis procedure is presented in Chapter 4 in detail.

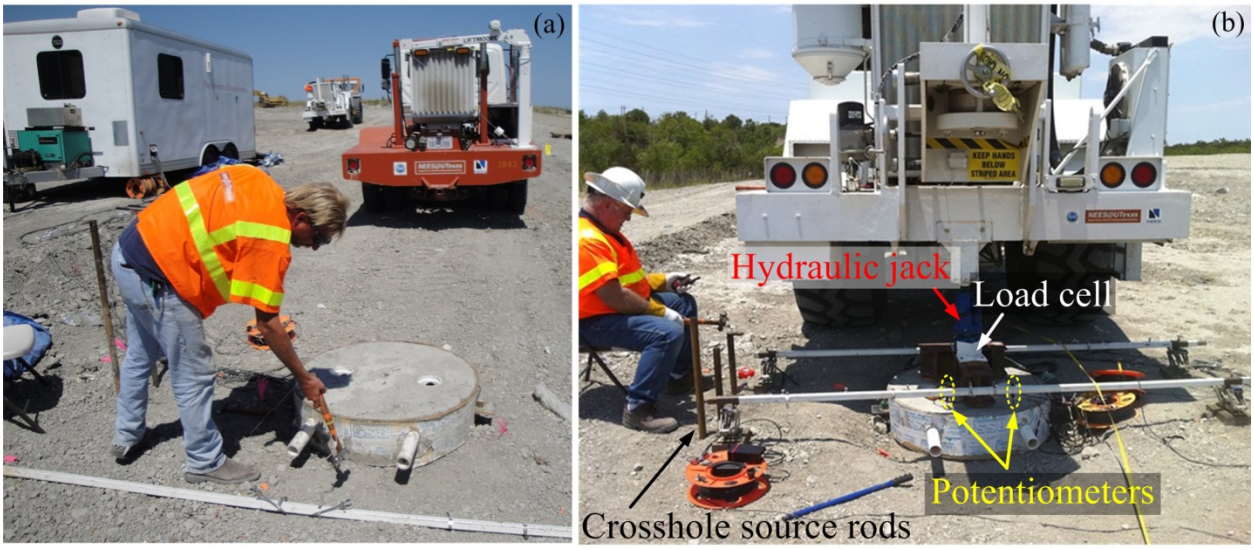

Figure 5.14 (a) Downhole and (b) crosshole seismic testing at the ACL.

Examples of wave train records from downhole seismic test in location 1 are shown in Fig. 5.15. Estimates of wave propagation velocities have been generated for each of the three pairs of downhole sensors. The calculated wave propagation velocity of each 3-D geophone pair was designated at the average depth of each pair.

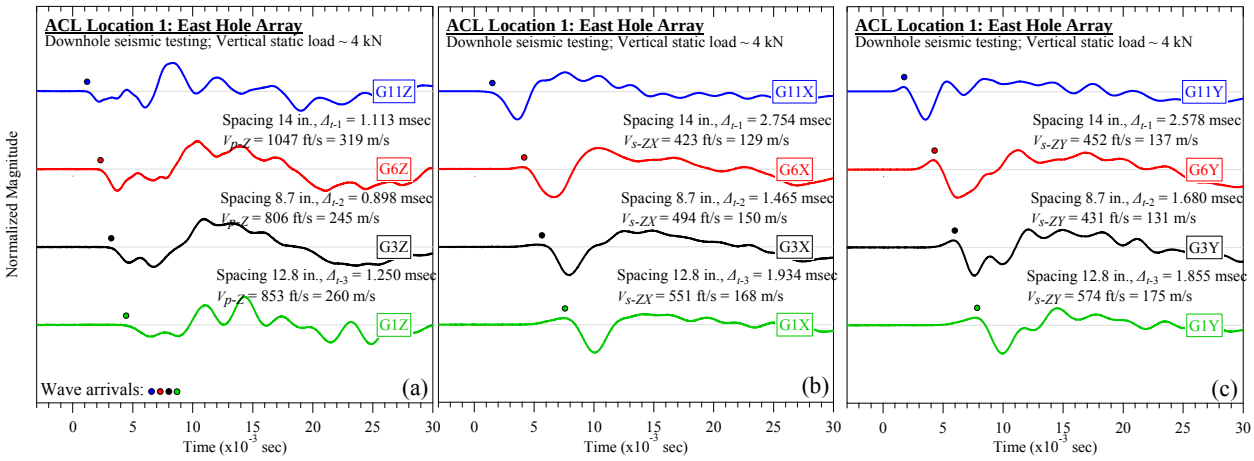

Figure 5.15 Examples of small-scale downhole seismic test wave trains at the ACL: (a) V_{p-Z}, (b) V_{s-ZX}, and (c) V_{s-ZY}.

5.4.1 $V_{s\text{-}ZX}$, $V_{s\text{-}ZY}$, and $V_{p\text{-}X}$ Profiles at Location 1

The $V_{s\text{-}ZX}$ profiles measured from the small-scale downhole seismic tests at location 1 are presented in Fig. 5.16. These profiles were measured for 6 different static vertical loads. Figures 5.16(a) and 5.16(b) present the $V_{s\text{-}ZX}$ profiles from the east and west hole arrays, respectively. As shown in Fig. 5.16(a), the initial $V_{s\text{-}ZX}$ (i.e. with static vertical load of 0 kN) increased from 130 m/s at depth of 0.32 m to 168 m/s at depth of 0.89 m. In the west array, the initial $V_{s\text{-}ZX}$ decreased from 155 m/s at depth of 0.32 m to 95 m/s at depth of 0.61 m and increased to 195 m/s at depth of 0.89 m. Figures 5.16(a) and 5.16(b) also show that the $V_{s\text{-}ZX}$ increased as the static vertical load increased. For example, at depth of 0.32 m in the east hole array, the $V_{s\text{-}ZX}$ increased from 130 m/s to 175 m/s as the static vertical load increased from 0 kN to 133 kN.

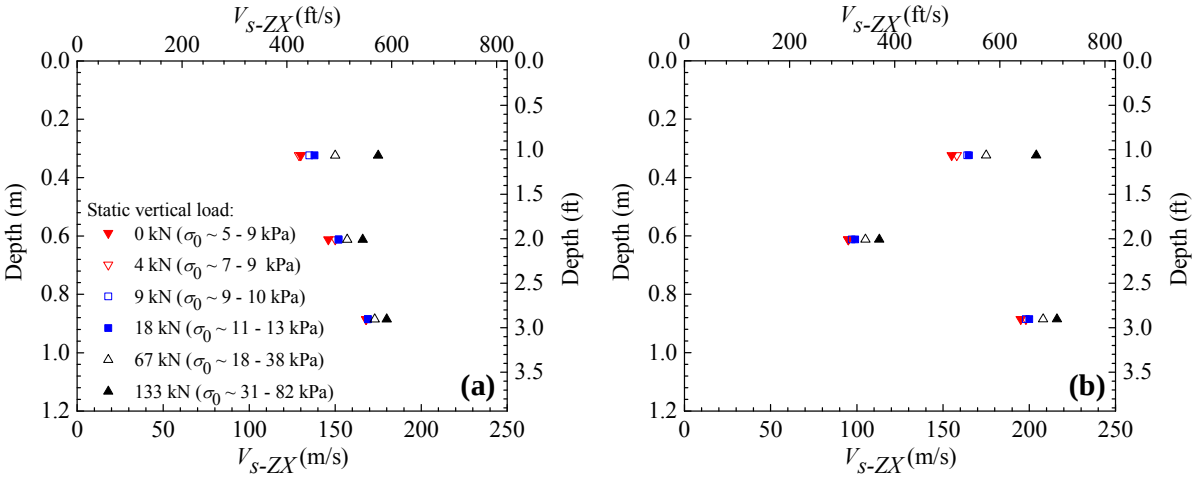

Figure 5.16 $V_{s\text{-}ZX}$ profiles in the (a) east and (b) west hole arrays in location 1 at the ACL.

The variation of $V_{s\text{-}ZY}$ with depth for 6 different static load levels at location 1 is presented in Fig. 5.17. The $V_{s\text{-}ZY}$ profiles from the east array are shown in Fig. 5.17(a). As shown in this figure, the initial $V_{s\text{-}ZY}$ slightly decreased from 138 m/s at depth of 0.32 m to 130 m/s at depth of 0.61 m and increased to 175 m/s at depth of 0.89 m. The variation of $V_{s\text{-}ZY}$ with depth in the west

array can be seen in Fig. 5.17(b). The $V_{s\text{-}ZY}$ decreased from 155 m/s at depth of 0.32 m to 107 m/s at depth of 0.61 m and increased to 231 m/s at depth of 0.89 m.

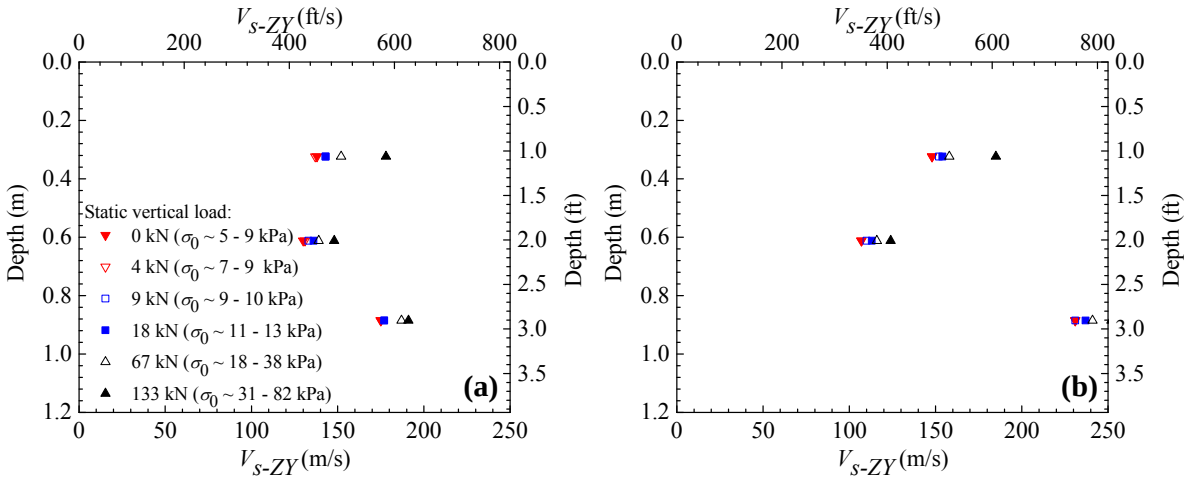

Figure 5.17 $V_{s\text{-}ZY}$ profiles in the (a) east and (b) west hole arrays in location 1 at the ACL.

The $V_{p\text{-}Z}$ profiles measured from the small-scale downhole seismic tests at location 1 are presented in Fig. 5.18. Figures 5.18(a) and 5.18(b) show the $V_{p\text{-}Z}$ profiles from the east and west hole arrays, respectively. In the east array with static vertical load of 0 kN, the initial $V_{p\text{-}Z}$ at depth of 0.32 m was 313 m/s. The $V_{p\text{-}Z}$ in the waste decreased to 240 m/s at depth of 0.61 m and increased to 256 m/s at depth of 0.89 m. In the west array, the $V_{p\text{-}Z}$ were 308 m/s at depth of 0.32 m, 179 m/s at depth of 0.61 m, and 387 m/s at depth of 0.89 m. As observed in Fig. 5.18, the $V_{p\text{-}Z}$ also increased with the static vertical loads.

The overall variations in wave propagation velocities both with depth as well as between holes in Figs. 5.16, 5.17, and 5.18 show significant vertical and lateral variability of MSW in location 1 over short measuring distances. The observed differences in V_s or V_p with depth, including the occasionally "unexpected" reductions or increases of V_s or V_p with depth can be explained when we consider the significant differences in waste composition at the testing scale.

In addition, the increases in wave propagation velocities with static vertical load levels are shown in these figures and are analyzed subsequently.

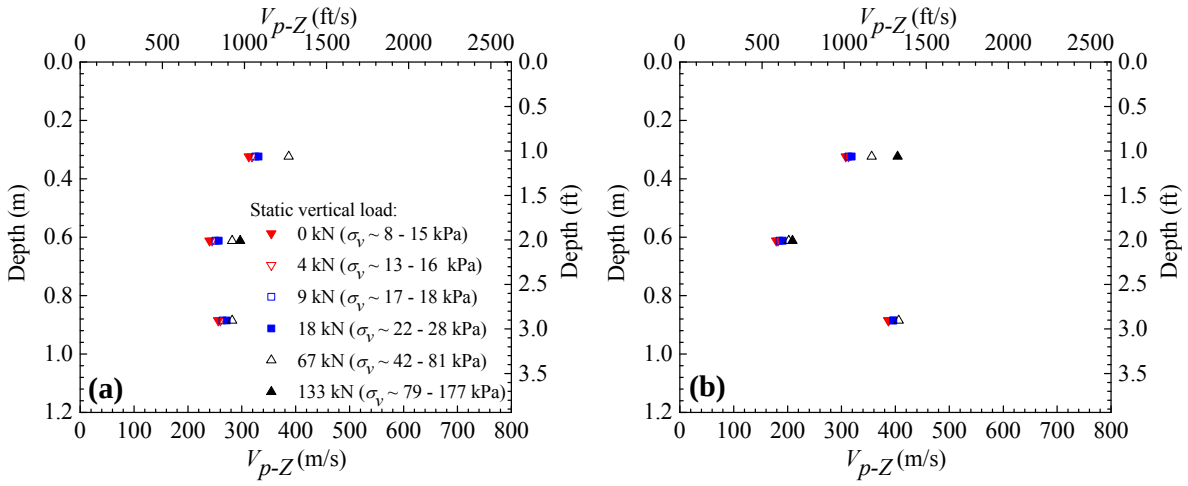

Figure 5.18 $V_{p\text{-}Z}$ profiles in the (a) east and (b) west hole arrays in location 1 at the ACL.

5.4.2 Effect of Stress State on $V_{s\text{-}ZX}$, $V_{s\text{-}ZY}$, and $V_{p\text{-}Z}$ at Location 1

In the small-strain range, the V_s and V_p of MSW depend on the stress state (Zekkos 2005, Lee 2007, Zekkos et al. 2013). To investigate the relationship between wave propagation velocities and the stress state, the vertical (σ_v), horizontal (σ_h), and mean confining (σ_0) stresses were calculated using the Foster and Ahlvin (1954) method as described in Chapter 4. It is known that wave velocity is most affected by stress components aligned with the direction of wave propagation and particle motion (Roesler 1979, Yu and Richart 1984, Stokoe et al. 1985, Stokoe et al. 1995, Fivorante 2000, Stokoe and Santamarina 2000, Wang and Mok 2008). Thus, at each static vertical load increment, σ_v was used as a correlation parameter for $V_{p\text{-}Z}$, whereas σ_0 was used for $V_{s\text{-}ZX}$ and $V_{s\text{-}ZY}$. The relationship between these velocities and stresses was regressed using a power function as commonly done for soils (e.g. Hardin and Richart 1963, Hardin and Black 1968, Hryciw and Thomann 1993, Iwasaki and Tatsuoka 1977). The power functions for

$V_{s\text{-}ZX}$, $V_{s\text{-}ZY}$, and $V_{p\text{-}Z}$ are shown in Eqs. 5.1, 5.2, and 5.3, respectively. Stresses in these equations were normalized with atmospheric pressure (P_a).

$$V_{s-ZX} = A_{ZX} \cdot \left(\frac{\sigma_0}{P_a} \right)^{n_{ZX}} \tag{5.1}$$

$$V_{s-ZY} = A_{ZY} \cdot \left(\frac{\sigma_0}{P_a} \right)^{n_{ZY}} \tag{5.2}$$

$$V_{p-Z} = A_{pZ} \cdot \left(\frac{\sigma_v}{P_a} \right)^{n_{pZ}} \tag{5.3}$$

where A_{ij} is an empirical constant that indicates corresponding wave propagation velocity at 1 atm and n_{ij} is an empirical constant that quantifies the effect of stress on the corresponding wave propagation velocity.

Figures 5.19, 5.20, and 5.21 illustrate the $V_{s\text{-}ZX}$, $V_{s\text{-}ZY}$, and $V_{p\text{-}Z}$ relationships with stresses, respectively. An either linear or bi-linear relationship of wave propagation velocities with stress was observed. Bi-linearity was indicative of the waste being in the overconsolidated (OC) regime due to waste compaction (Stokoe et al. 2011). As stress increased, the MSW reached the normally consolidated (NC) regime. In the OC regime, the stress exponent n_{ZX} for $V_{s\text{-}ZX}$ was found to be low (n_{ZX} = 0.05 – 0.09), while in the NC regime, the n_{ZX} value increased to 0.21. The n_{ZY} value for $V_{s\text{-}ZY}$ ranged from 0.04 to 0.07 in the OC regime and increased up to 0.22 in the NC regime. The n_{pZ} value for $V_{p\text{-}Z}$ ranged from 0.04 to 0.09 in the OC regime and increased up to 0.16 in the NC regime. It should be noted that the regression analysis in the NC regime for $V_{p\text{-}Z}$ at depth of 0.32 m [Fig. 5.21(a)] was not performed due to unavailability of quality data. The interpreted maximum past vertical stress ($\sigma_{v\text{-max}}$) and past mean confining stress ($\sigma_{0\text{-max}}$) at depth

of 0.32 m, as indicated by the change in slope in Figs 5.19, 5.20, and 5.21, were on the order of 51 kPa and 30 – 32 kPa, respectively.

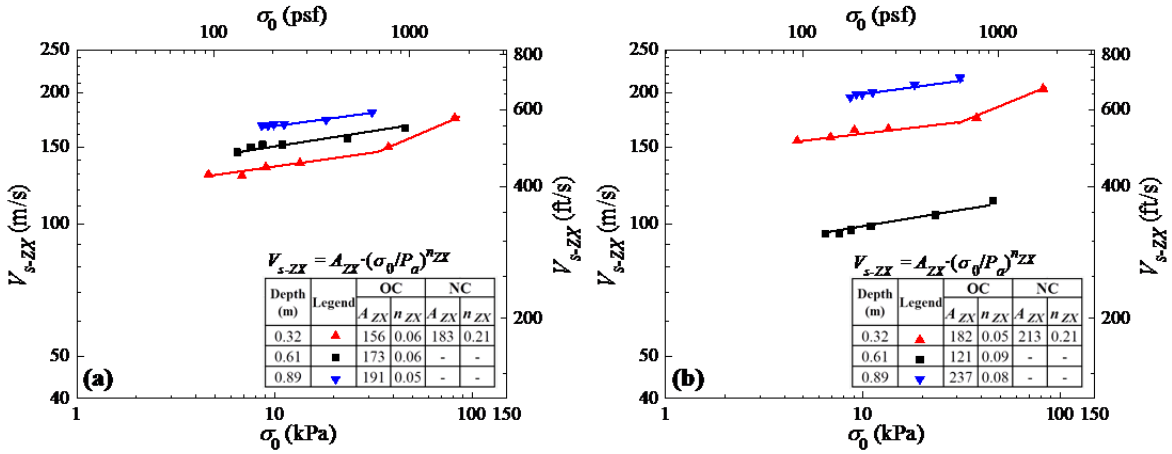

Figure 5.19 Effect of σ_0 on $V_{s\text{-}ZX}$ in the (a) east and (b) west hole arrays in location 1 at the ACL.

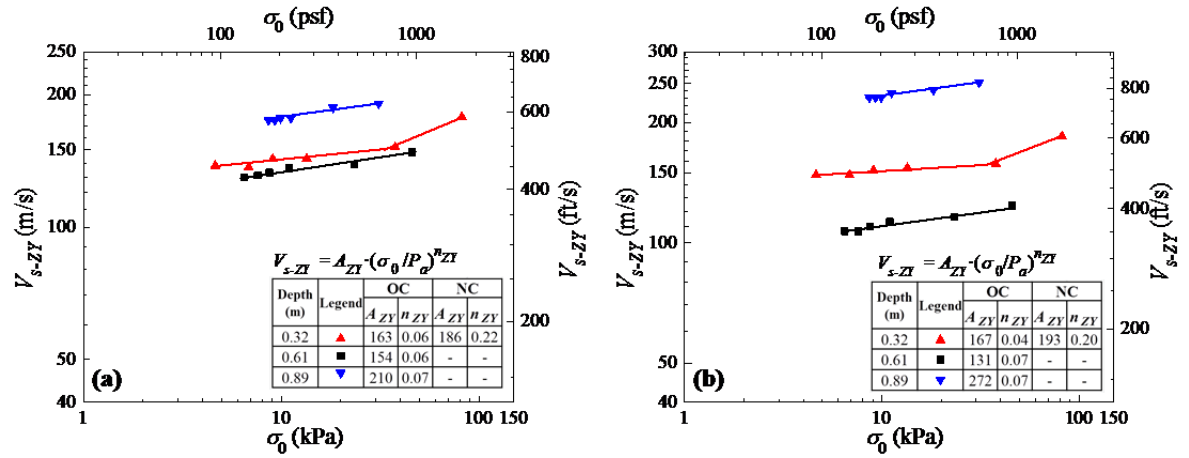

Figure 5.20 Effect of σ_0 on $V_{s\text{-}ZY}$ in the (a) east and (b) west hole arrays in location 1 at the ACL.

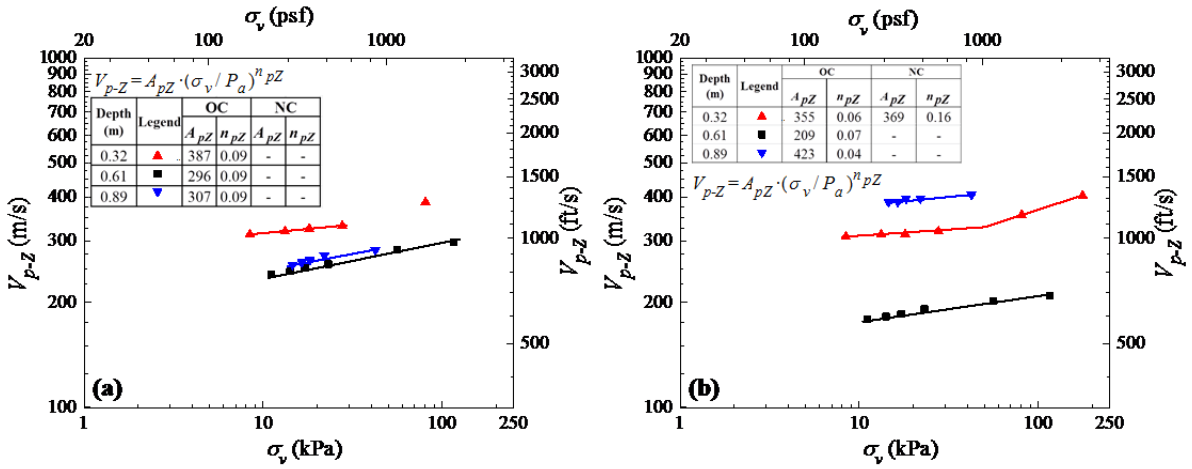

Figure 5.21 Effect of σ_v on $V_{p\text{-}Z}$ in the (a) east and (b) west hole arrays in location 1 at the ACL.

5.4.3 $V_{s\text{-}ZX}$, $V_{s\text{-}ZY}$, and $V_{p\text{-}X}$ Profiles at Location 2

Figure 5.22 shows the variation of $V_{s\text{-}ZX}$ with depth for 6 different static load levels at location 2. As shown in Fig 5.22(a), in the north array, the initial $V_{s\text{-}ZX}$ decreased from 162 m/s at depth of 0.13 m to 106 m/s at depth of 0.29 m and slightly increased to 113 m/s at depth of 0.46 m. The variation of $V_{s\text{-}ZX}$ with depth in the south array is shown in Fig. 5.22(b). The initial $V_{s\text{-}ZX}$ in the south array decreased from 185 m/s at depth of 0.13 m to 105 m/s at depth of 0.46 m. Figure 5.22 also shows that the initial $V_{s\text{-}ZX}$ increased with static vertical load. For example, in the north array at depth of 0.13 m, the initial $V_{s\text{-}ZX}$ increased from 162 m/s to 251 m/s when static vertical load increased from 0 kN to 133 kN.

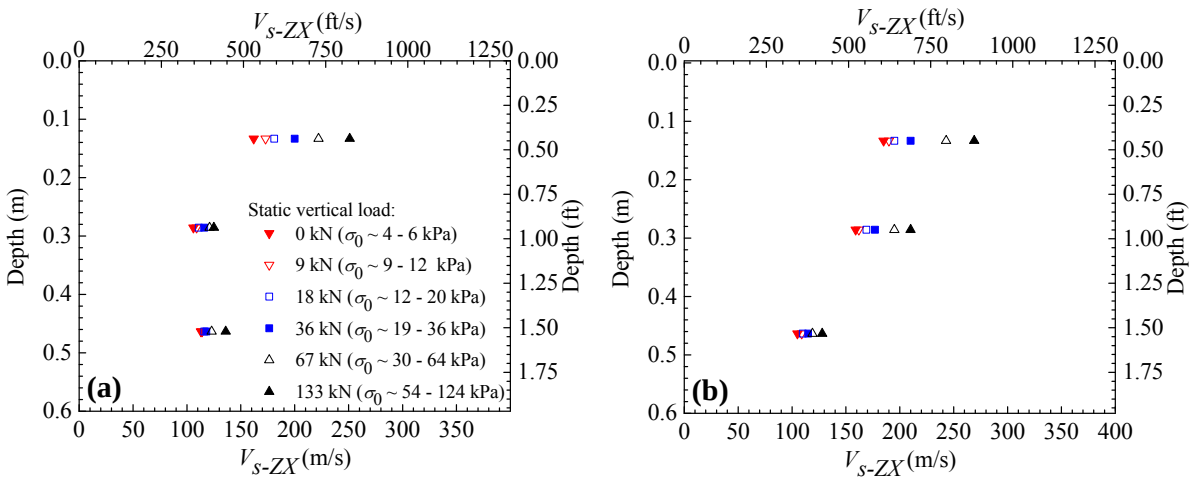

Figure 5.22 $V_{s\text{-}ZX}$ profiles in the (a) north and (b) south hole arrays in location 2 at the ACL.

The $V_{s\text{-}ZY}$ profiles measured from the small-scale downhole seismic tests at location 2 are presented in Fig. 5.23. Figures 5.23(a) and 5.23(b) present the $V_{s\text{-}ZY}$ profiles from the north and south arrays, respectively. In the north array, the initial $V_{s\text{-}ZY}$ decreased from 156 m/s at depth of 0.13 m to 113 m/s at depth of 0.46 m. In the south array, the $V_{s\text{-}ZY}$ initial increased from 136 m/s at depth of 0.13 m to 159 m/s at depth of 0.29 m and decreased to 108 m/s at depth of 0.46 m. The $V_{s\text{-}ZY}$ increased with increasing static vertical load as shown in Fig. 5.23.

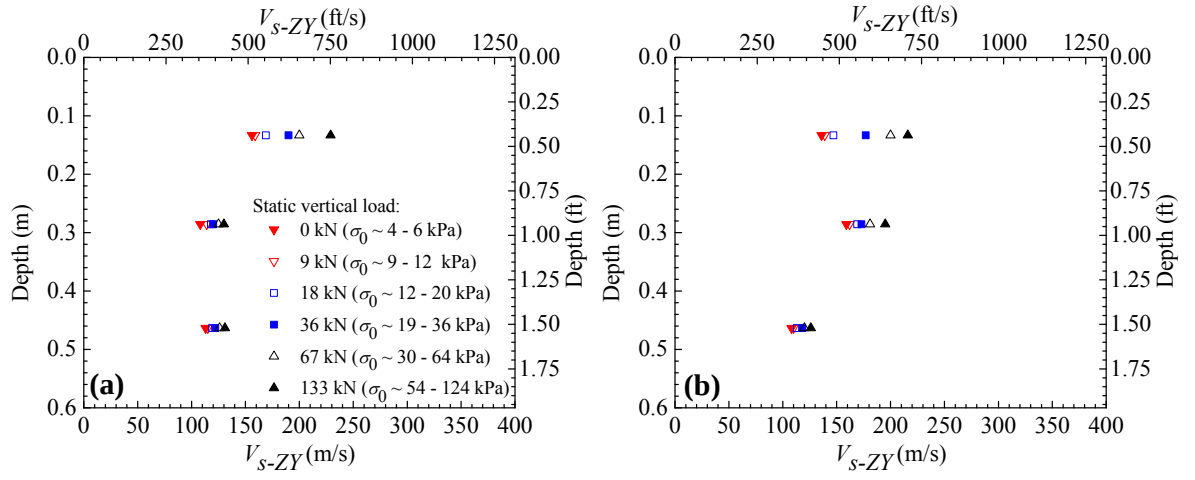

Figure 5.23 $V_{s\text{-}ZY}$ profiles in the (a) north and (b) south hole arrays in location 2 at the ACL.

Figure 5.24 presents the $V_{p\text{-}Z}$ profiles measured from the small-scale downhole seismic tests at location 2. In the north array, the initial $V_{p\text{-}Z}$ at depth of 0.13 m was 390 m/s [Figure 5.24(a)]. The $V_{p\text{-}Z}$ decreased to 269 m/s at depth of 0.29 m and decreased further to 196 m/s at depth of 0.46 m. As shown in Fig. 5.24(b), in the south array, the initial $V_{p\text{-}Z}$ were 312 m/s at depth of 0.13 m, 390 m/s at depth of 0.29 m, and 226 m/s at depth of 0.46m. Figure 5.24 shows that $V_{p\text{-}Z}$ increased with increasing static vertical loads.

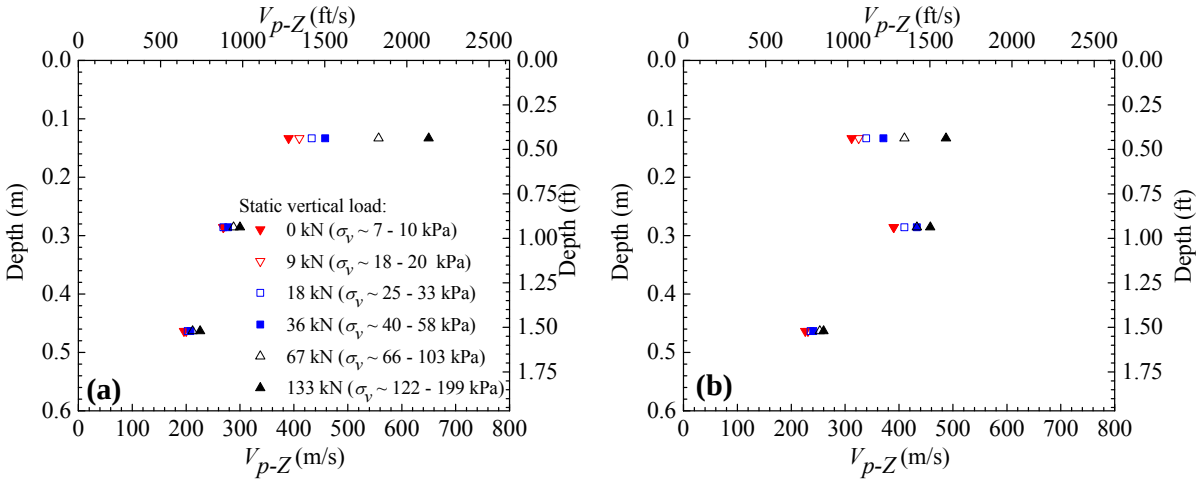

Figure 5.24 $V_{p\text{-}Z}$ profiles in the (a) north and (b) south hole arrays in location 2 at the ACL.

5.4.4 Effect of Stress State on $V_{s\text{-}ZX}$, $V_{s\text{-}ZY}$, and $V_{p\text{-}Z}$ at Location 2

Figures 5.25, 5.26, and 5.27 illustrate the $V_{s\text{-}ZX}$, $V_{s\text{-}ZY}$, and $V_{p\text{-}Z}$ variations with stresses, respectively. In the OC regime, the stress exponent n_{ZX} for $V_{s\text{-}ZX}$ ranged from 0.03 – 0.10, while in the NC regime, the n_{ZX} was on the order of 0.18 to 0.23. The n_{ZY} for $V_{s\text{-}vY}$ varied from 0.05 to 0.07 in the OC regime and increased to 0.21 in the NC regime. The n_{pZ} for $V_{p\text{-}Z}$ ranged from 0.04 to 0.06 in the OC regime and increased to 0.28 in the NC regime. As indicated by the change in slope in Figs 5.25, 5.26, and 5.27, the interpreted maximum $\sigma_{v\text{-max}}$ and $\sigma_{0\text{-max}}$ at depth of 0.29 m were on the order of 55 – 58 kPa and 21 – 32 kPa, respectively.

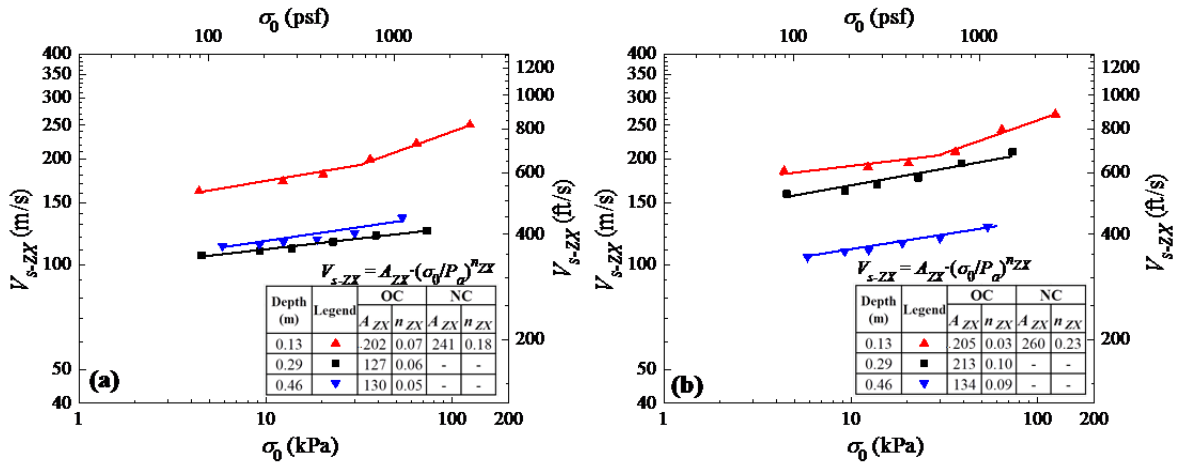

Figure 5.25 Effect of σ_0 on $V_{s\text{-}ZX}$ in the (a) north and (b) south hole arrays in location 2 at the ACL.

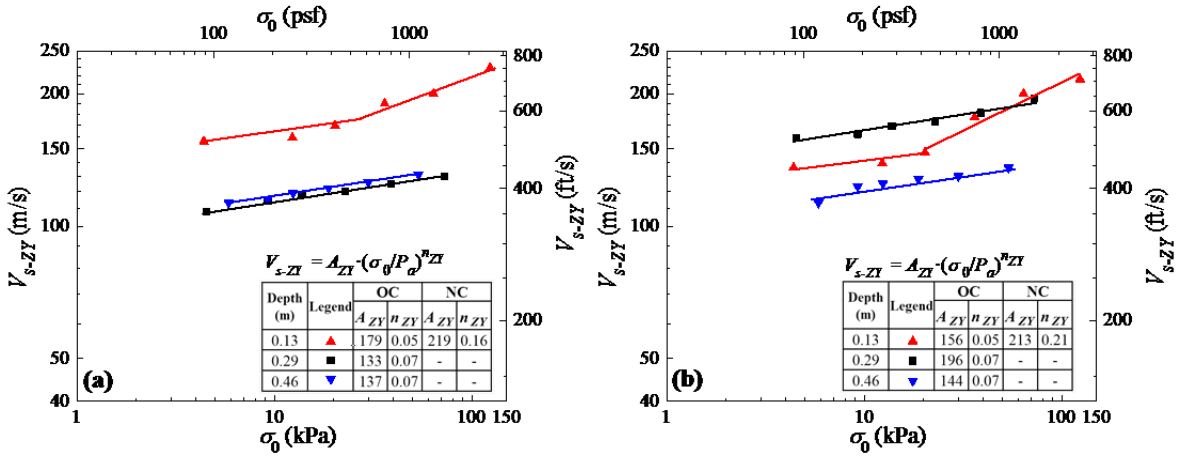

Figure 5.26 Effect of σ_0 on $V_{s\text{-}ZY}$ in the (a) north and (b) south hole arrays in location 2 at the ACL.

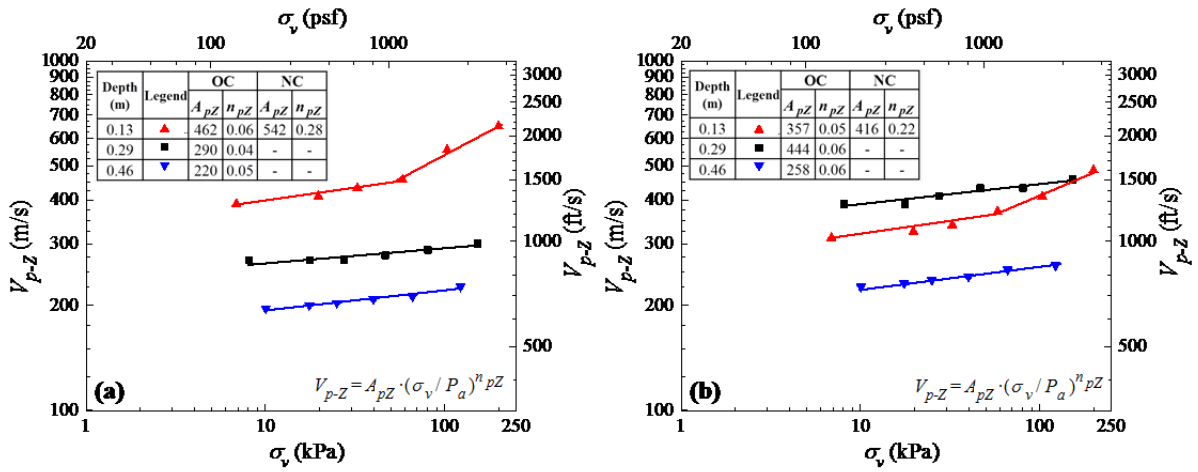

Figure 5.27 Effect of σ_v on $V_{p\text{-}Z}$ in the (a) north and (b) south hole arrays in location 2 at the ACL.

5.5 **Small-scale Crosshole Seismic Testing**

The small-scale crosshole seismic tests were performed at the ACL to evaluate the horizontally propagating P-wave velocity ($V_{p\text{-}X}$) and the vertically-polarized horizontally-propagating S-wave ($V_{s\text{-}XZ}$). As shown in Fig. 5.14(b), this test was performed using three crosshole source rods. Test procedure and analysis for this test are presented in Chapter 4 in more detail. Figure 5.28 shows an example of waveforms from the small-scale crosshole seismic test.

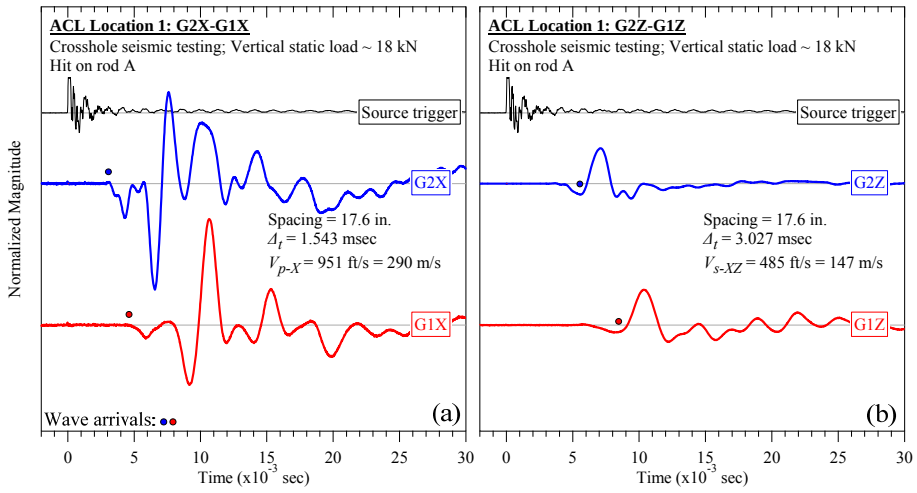

Figure 5.28 Examples of small-scale crosshole seismic test wave trains at the ACL: (a) $V_{p\text{-}X}$ and (b) $V_{s\text{-}XZ}$.

Similarly to downhole seismic testing, the relationship between V_p and V_s and stress was regressed using a power function. In this case, σ_h and σ_0 were used as correlation parameters for $V_{p\text{-}X}$ and $V_{s\text{-}XZ}$, respectively. Relationships between wave propagation velocity and stress component were fitted using the following equations.

$$V_{p-X} = A_{pX} \cdot \left(\frac{\sigma_h}{P_a} \right)^{n_{pX}} \tag{5.4}$$

$$V_{s-XZ} = A_{XZ} \cdot \left(\frac{\sigma_0}{P_a} \right)^{n_{XZ}} \tag{5.5}$$

Figures 5.29(a) and 5.29(b) show the relationship between $V_{p\text{-}X}$ and $V_{s\text{-}XZ}$ and stress states in location 1, respectively. A linear relationship between wave propagation velocities and stresses indicated that the MSW at these depths was still in the OC regime. The stress exponent n_{pX} for $V_{p\text{-}X}$ was on the order of 0.02 to 0.09. The n_{XZ} value for $V_{s\text{-}XZ}$ ranged from 0.02 to 0.07 in the OC regime.

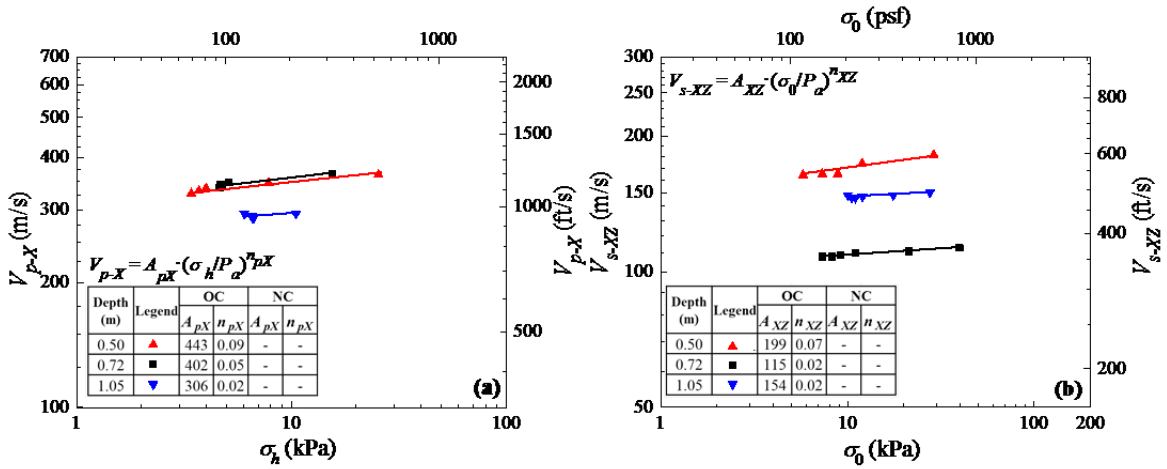

Figure 5.29 Effect of stress states on (a) $V_{p\text{-}X}$ and (b) $V_{s\text{-}XZ}$ in location 1 at the ACL.

The relationship between $V_{p\text{-}X}$ and $V_{s\text{-}XZ}$ and stress states in location 2 are presented in Figures 5.30(a) and 5.30(b), respectively. An either linear or bi-linear relationship between wave propagation velocities and stresses is observed in these figures. In the OC regime, the stress exponent n_{pX} for $V_{p\text{-}X}$ was found to be low (n_{pX} = 0.02 – 0.08), while in the NC regime, the n_{pX} was much higher (n_{pX} = 0.18). The n_{XZ} for $V_{s\text{-}XZ}$ ranged from 0.03 to 0.09 in the OC regime and increased to 0.34 in the NC regime.

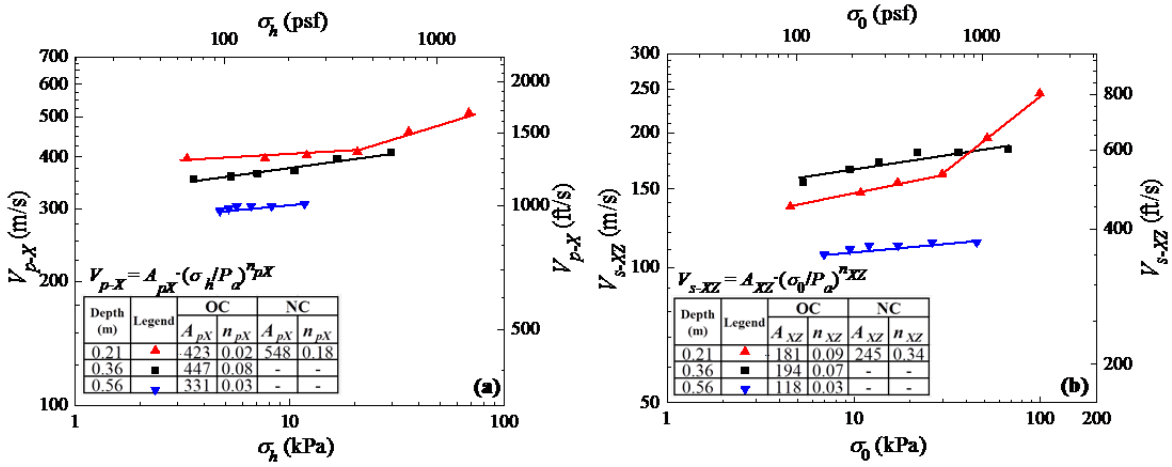

Figure 5.30 Effect of stress states on (a) $V_{p\text{-}X}$ and (b) $V_{s\text{-}XZ}$ in location 2 at the ACL.

5.6 **Evaluation of Anisotropy of Wave Propagation Velocity in MSW at the ACL**

Anisotropy of wave propagation velocity in MSW may have an important role in landfill engineering practice. In seismic response analysis, the seismic wave is commonly considered propagating through isotropic materials. If MSW exhibits a high degree of anisotropy, the actual site response and seismic slope displacement may be different from the analysis results using isotropy assumption. To date, the anisotropy of MSW in term of wave propagation velocities has never been evaluated.

Anisotropy in MSW can be attributed to stress-induced anisotropy and fabric (structural) anisotropy, as discussed in Zekkos (2013). Stress-induced anisotropy results from stress states

that are different in the horizontal and vertical directions. Fabric anisotropy is attributed to preferential orientation of fibrous particles in the MSW. Thus, the MSW can still behave anisotropically even in isotropic stress states. In this study, assessment of the degree of anisotropy in MSW was performed by comparing wave velocities from a variety of propagation and polarization directions.

Figure 5.31(a) shows a comparison between P-wave and S-wave velocities propagating in the vertical direction (i.e. $V_{p\text{-}Z}$ and $V_{s\text{-}ZX}$). In general, the ratios of $V_{s\text{-}ZX}$ to $V_{p\text{-}Z}$ from location 1 were found to be between 0.39 and 0.66. The ratios of $V_{s\text{-}ZX}$ to $V_{p\text{-}Z}$ from location 2 varied from 0.39 to 0.60. The mean of this ratio from both locations was found to be 0.49.

Figure 5.31(b) shows a comparison between the $V_{s\text{-}ZX}$ and the $V_{s\text{-}ZY}$. In location 1, the ratio of $V_{s\text{-}ZY}$ to $V_{s\text{-}ZX}$ varied from 0.87 to 1.19. In location 2, the ratio of $V_{s\text{-}ZY}$ to $V_{s\text{-}ZX}$ ranged from 0.73 to 1.06. The mean of this ratio from both locations was found to be 0.98 indicating minor difference on average between S-wave propagation velocities in the YZ and the XZ plane.

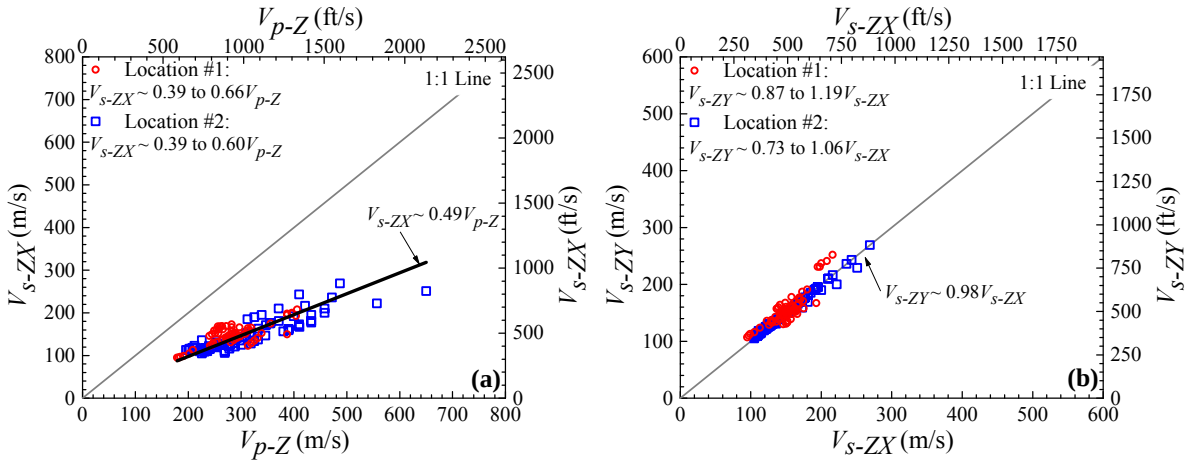

Figure 5.31 Comparison on (a) $V_{p\text{-}Z}$-$V_{s\text{-}ZX}$ and (b) $V_{s\text{-}ZX}$ -$V_{s\text{-}ZY}$ at the ACL.

A comparison between P-wave and S-wave velocities propagating in the horizontal direction (i.e. $V_{p\text{-}X}$ and $V_{s\text{-}XZ}$) is presented in Fig. 5.32. In location 1, the ratio of $V_{s\text{-}XZ}$ to $V_{p\text{-}X}$

ranged from 0.31 to 0.55. In location 2, this ratio varied from 0.35 to 0.49. The mean of this ratio from both locations was found to be 0.42. This ratio was relatively lower than the ratio of V_p and V_s counterparts propagating in the vertical direction.

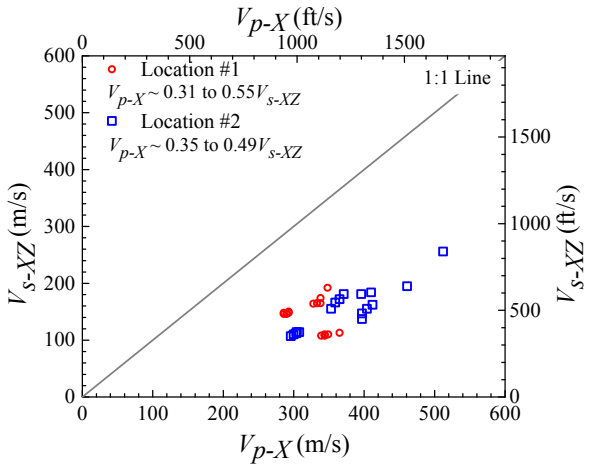

Figure 5.32 Comparison on $V_{p\text{-}X}$ and $V_{s\text{-}XZ}$ at the ACL.

Anisotropy in MSW was also evaluated by comparing wave propagation velocities in the horizontal and vertical directions using results from downhole and crosshole seismic tests. Because the designated measurement points from both small-strain tests were not the same, four $V_{p\text{-}Z}$ values from downhole test were averaged and then compared with a $V_{p\text{-}X}$ value from a crosshole test, as shown in Fig 5.33. The same method was also performed in comparing shear wave velocity propagating in the vertical and horizontal directions.

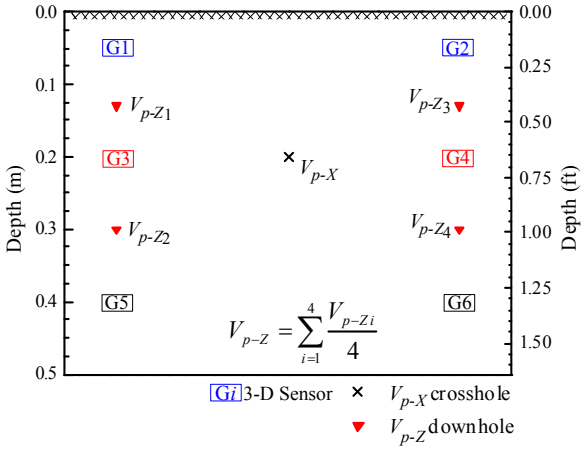

Figure 5.33 Measurement points for comparing wave propagation velocities in the vertical and horizontal directions.

Figure 5.34(a) shows the comparison between V_p propagating in the horizontal ($V_{p\text{-}X}$) and vertical ($V_{p\text{-}Z}$) directions. In location 1, the ratios of $V_{p\text{-}Z}$ to $V_{p\text{-}X}$ varied from 0.69 to 0.89. In location 2, the ratios of $V_{p\text{-}Z}$ to $V_{p\text{-}X}$ varied from 0.74 to 0.88. The mean of this ratio from both locations was 0.78. This ratio indicated that the compressibility of MSW in the horizontal direction was lower than the compressibility in the vertical direction.

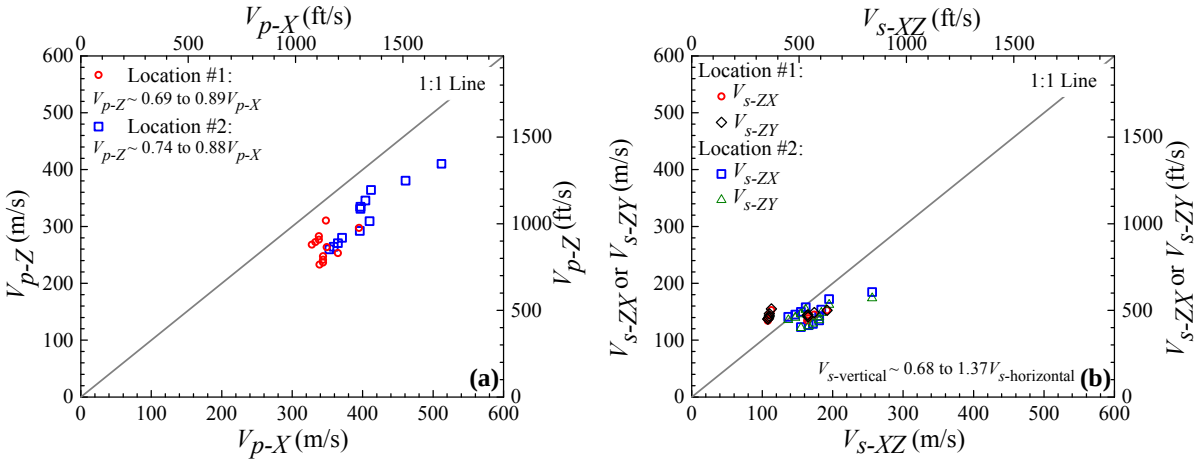

Figure 5.34 (a) Comparison on V_p propagating in the vertical and horizontal directions; and (b) V_s propagating in vertical and horizontal directions.

Figure 5.34(b) illustrates the comparison between V_s propagating in horizontal ($V_{s\text{-}horizontal}$: $V_{s\text{-}XZ}$) and vertical ($V_{s\text{-}vertical}$: $V_{s\text{-}ZX}$ and $V_{s\text{-}ZY}$) directions. The ratio of $V_{s\text{-}vertical}$ to $V_{s\text{-}horizontal}$ was found to be between 0.68 and 1.37 with an average value of 0.88.

In general, the data indicated that wave propagation in the vertical direction was slower than that in the horizontal direction, highlighting that MSW is an anisotropic material. Additionally, the comparison on the ratio of wave propagation velocity of MSW, washed mortar sand, and clay indicates that the range of ratio of wave propagation velocity of MSW is broader than those of washed mortar sand and clay.

5.7 **Evaluation of Poisson's Ratio at the ACL**

In a homogeneous, isotropic, and elastic solid material, small-strain or dynamic Poisson's ratio (v) can be evaluated using Eq. 5.6.

$$v = \frac{0.5 \cdot \left(V_s / V_p\right)^2 - 1}{\left(V_s / V_p\right)^2 - 1} \tag{5.6}$$

MSW is not an isotropic material and the meaning of Poisson's ratio of MSW may be very complex. Nevertheless, Eq. 5.6 was used to evaluate Poisson's ratio of MSW by Sharma et al. (1990), Houston et al. (1995), Matasovic and Kavazanjian (1998), and Zalachoris (2010). In this study, the V_p and V_s values from downhole and crosshole seismic tests were used to evaluate "pseudo" Poisson's ratio. "Pseudo" Poisson's ratios v_{ZX} and v_{ZY} from downhole seismic tests were estimated using Eqs. 5.7 and 5.8.

$$v_{ZX} = \frac{0.5 \cdot \left(V_{s-ZX} / V_{p-Z}\right)^2 - 1}{\left(V_{s-ZX} / V_{p-Z}\right)^2 - 1} \tag{5.7}$$

$$\nu_{ZY} = \frac{0.5 \cdot \left(V_{s-ZY}/V_{p-Z}\right)^2 - 1}{\left(V_{s-ZY}/V_{p-Z}\right)^2 - 1} \tag{5.8}$$

From small-scale crosshole seismic tests, the "pseudo" Poisson's ratio ν_{XZ} was evaluated using Eq. 5.9.

$$\nu_{XZ} = \frac{0.5 \cdot \left(V_{s-XZ}/V_{p-X}\right)^2 - 1}{\left(V_{s-XZ}/V_{p-X}\right)^2 - 1} \tag{5.9}$$

Poisson's ratio variation with depth from all small-strain seismic tests in locations 1 at the ACL is presented in Fig. 5.35(a). In location 1, the ν_{ZX} and ν_{ZY} ranged from 0.31 to 0.41 and 0.34 to 0.40 at depth of 0.32 m, respectively. At depth of 0.61 m, the ν_{ZX} and ν_{ZY} ranged from 0.21 to 0.31 and from 0.22 to 0.34, respectively. At depth of 0.89 m, the ν_{ZX} and ν_{ZY} varied from 0.12 to 0.33 and 0.06 to 0.24, respectively. The ν_{XZ} ranged from 0.31 to 0.45 at depth of 0.5 m to 1.05 m in this location.

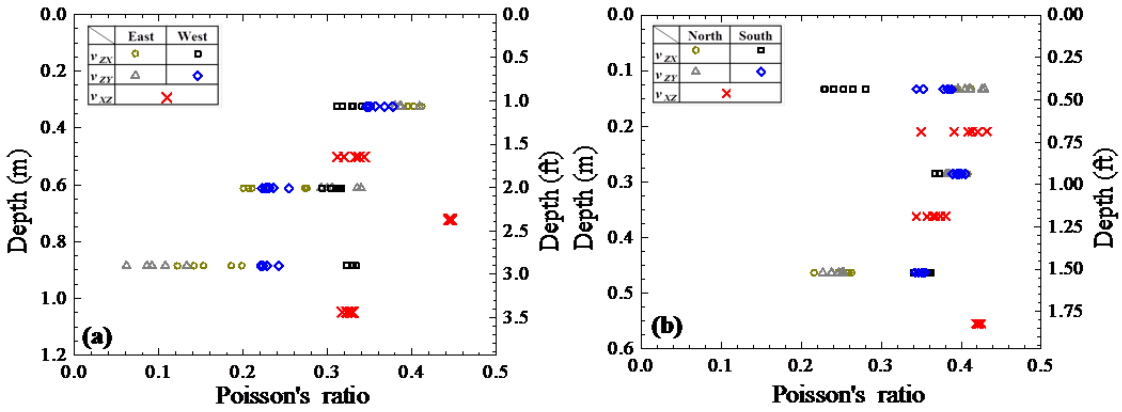

Figure 5.35 Poisson's ratio evaluated using V_s and V_p in (a) location 1 and (b) location 2 at the ACL.

Figure 5.35(b) shows Poisson's ratio variation with depth from all small-strain seismic tests in location 2 at the ACL. In this location, the ν_{ZX} and ν_{ZY} ranged from 0.23 to 0.41 and 0.34 to 0.43 at depth of 0.13 m, respectively. At depth of 0.29 m, the ν_{ZX} and ν_{ZY} varied from 0.36 to

0.41 and from 0.38 to 0.41, respectively. At depth of 0.46 m, the v_{ZX} and v_{ZY} ranged from 0.21 to 0.36 and 0.23 to 0.35, respectively. The v_{XZ} ranged from 0.34 to 0.43 at depth of 0.21 m to 0.56 m.

As shown in Figures 5.35(a) and 5.35(b), the v_{ZX} and v_{ZY} at the same measurement point were in some cases the same and in other cases different. In general, large scatter in Figs 5.35(a) and 5.35(b) could be attributed to the variability of the waste within a test location and the anisotropic nature of the waste.

5.8 **Spectral-Analysis-of-Surface-Wave Test at the ACL**

The Spectral-Analysis-of-Surface-Wave (SASW) tests were conducted in two locations at the ACL (Fig. 5.36) by Dr. Changyoung Kim and the author. At both locations, 4 SASW survey lines were located 1.8 m (6 ft) off footing center (Fig. 5.37). In this test, three 4.5Hz geophones (Geospace GS 11-D) were used. With three geophones, the SASW testing configuration offered 3 combinations of geophone pairs. The spacing between the farthest and the closest geophone to the source ranged from 0.9 m (3 ft) to 9 m (30 ft). A geologic hammer was used as the source for 0.9 m spacing, whereas a sledge hammer was used for longer geophone spacing. Data analysis of the SASW tests was performed by Dr. Yin-Cheng Lin of the University of Texas at Austin.

Figure 5.36 SASW testing in locations (a) 1 and (b) 2 at the ACL.

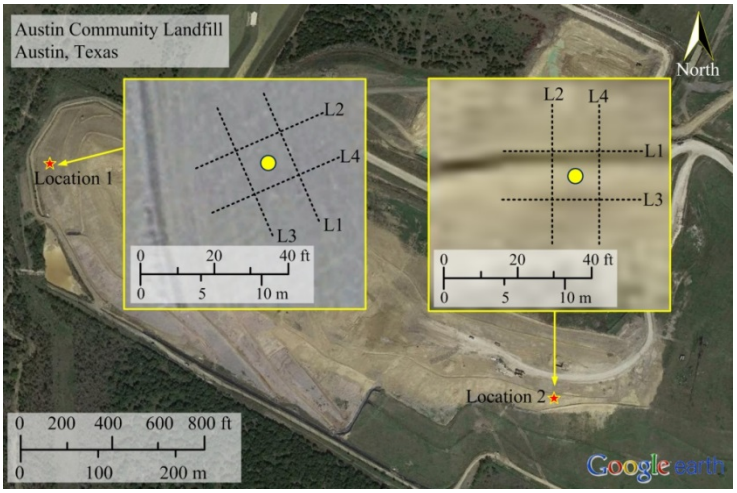

Figure 5.37 SASW survey lines at the ACL.

Figures 5.38, 5.39, 5.40, and 5.41 present the theoretical and field dispersion curves from lines 1, 2, 3, and 4 in location 1 at the ACL, respectively. Dispersion curves from line 1 had wavelengths (λ) ranging from 0.1 m to 10 m that corresponded with Rayleigh wave or phase velocities (V_{ph}) of 20 m/s to 100 m/s. Dispersion curves from line 2 had λ ranging from 0.2 m to 10 m that corresponded with V_{ph} of 50 m/s to 110 m/s. The line 2 dispersion curves showed sharp increase in V_{ph} at wavelength of 0.5 m to 1.2 m. Dispersion curves from line 3 had λ ranging from 0.1 m to 10 m that corresponded with V_{ph} of 30 m/s to 110 m/s. Dispersion curves from line 4 had λ ranging from 0.1 m to 10 m that corresponded with V_{ph} of 50 m/s to 110 m/s. Similar with dispersion curves from line 2, dispersion curves from line 4 exhibited sharp increase in V_{ph} at wavelength of 0.3 m to 1.2 m.

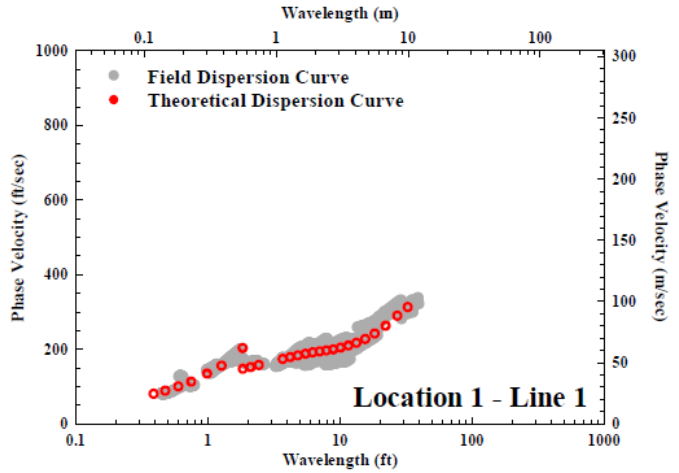

Figure 5.38 Dispersion curves from survey line 1 in location 1 at the ACL.

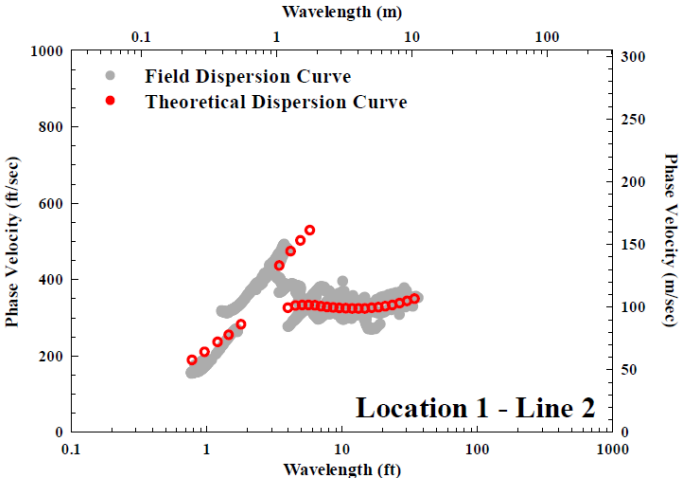

Figure 5.39 Dispersion curves from survey line 2 in location 1 at the ACL.

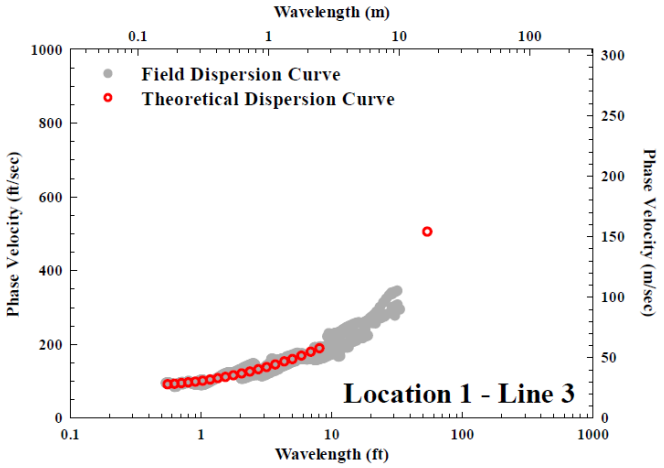

Figure 5.40 Dispersion curves from survey line 3 in location 1 at the ACL.

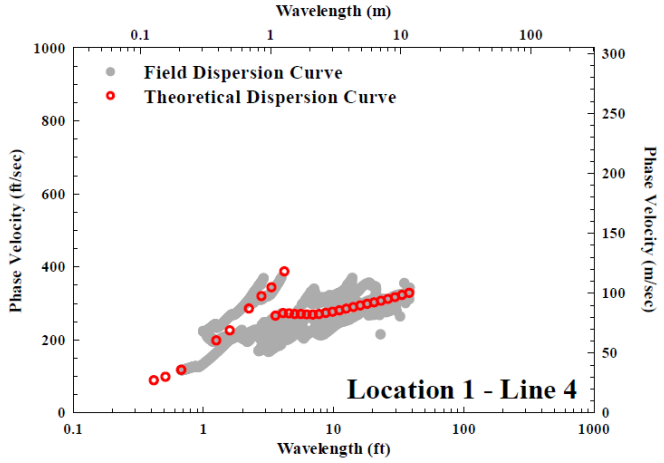

Figure 5.41 Dispersion curves from survey line 4 in location 1 at the ACL.

Figure 5.42 shows the V_s profiles inverted from the dispersion curves in location 1. In general, near surface shear wave velocities from the four lines showed a relatively low V_s ranging from 25 m/s to 80 m/s. Despite the variability in the V_s profiles, lines 1 and 3 yielded similar results. In addition, lines 2 and 4 also had similar V_s profiles. The V_s from lines 1 and 3 were lower than those of lines 2 and 4 from the surface up to depth of 2.5 m. Relatively higher shear wave velocity of about 150 m/s occurred at depth of 0.25 m to 0.75 m in lines 2 and 4. The results from small-scale downhole and crosshole seismic testing are also presented in Fig. 5.42.

In general, the results from downhole and crosshole seismic tests were in good agreement with SASW tests from lines 2 and 4, particularly at depth of about 0.25 m to 0.75 m. At greater depth, shear wave velocities from downhole and crosshole seismic tests were higher than those of SASW tests. It should be noted that the downhole and crosshole seismic tests are more localized measurements in contrast to SASW tests. Thus, different results between those tests may occur, particularly in MSW where waste variability could be high within a small area and at the scale and frequency range of the various methods.

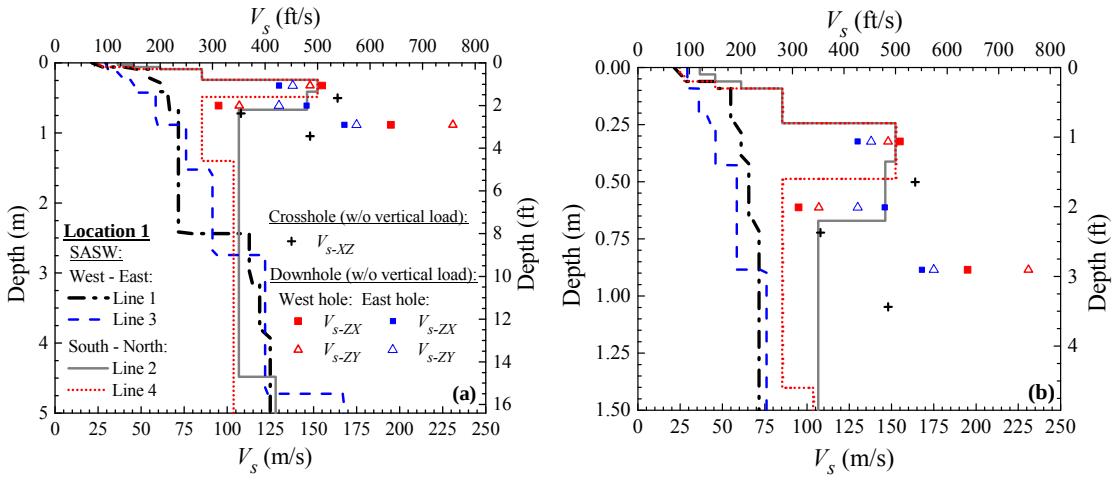

Figure 5.42 Shear wave velocity profile in location 1 at the ACL: (a) up to 5 m and (b) up to 1.5 m.

The theoretical and field dispersion curves from lines 1, 2, 3, and 4 in location 2 at the ACL are presented in Figs. 5.43, 5.44, 5.45, and 5.46, respectively. From survey line 1, the dispersion curves had λ ranging from 0.2 m to 10 m that corresponded with V_{ph} of 110 m/s to 130 m/s. Nevertheless, these dispersion curves had a minimum V_{ph} of 80 m/s at λ of 2.5 m. This indicated that the V_s profile had higher V_s near the surface. Dispersion curves from line 2 had λ ranging from 0.3 m to 10 m that corresponded with V_{ph} of 80 m/s to 100 m/s. Dispersion curves from line 3 had λ ranging from 0.3 m to 10 m that corresponded with V_{ph} of 80 m/s to 115 m/s.

Dispersion curves from line 4 had λ ranging from 0.06 m to 10 m that corresponded with V_{ph} of 40 m/s to 100 m/s.

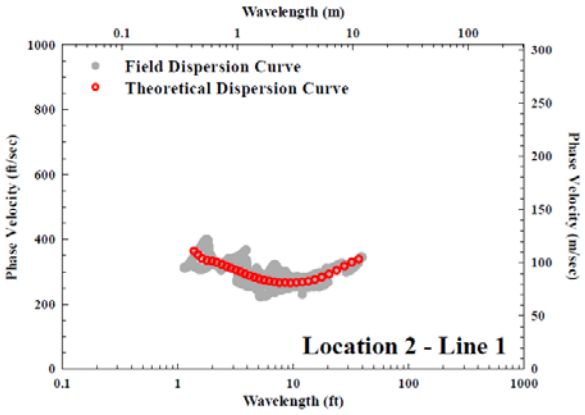

Figure 5.43 Dispersion curves from survey line 1 in location 2 at the ACL.

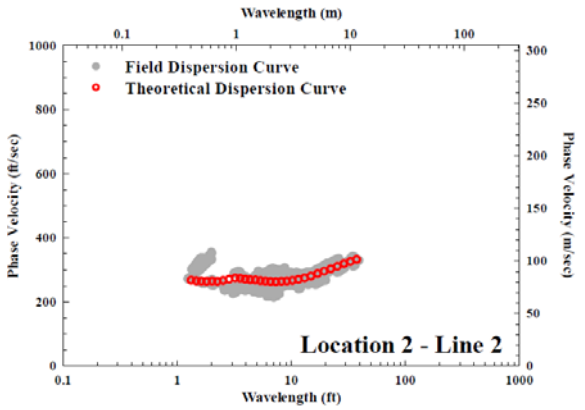

Figure 5.44 Dispersion curves from survey line 2 in location 2 at the ACL.

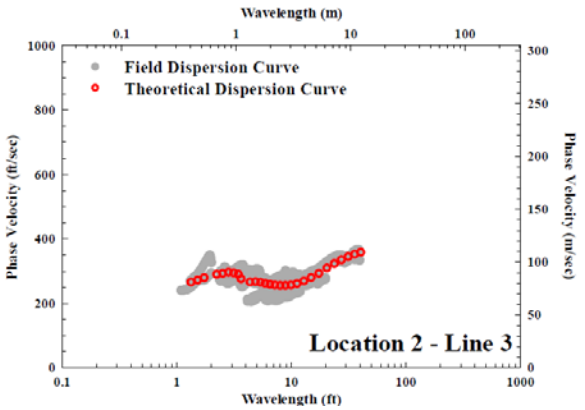

Figure 5.45 Dispersion curves from survey line 3 in location 2 at the ACL.

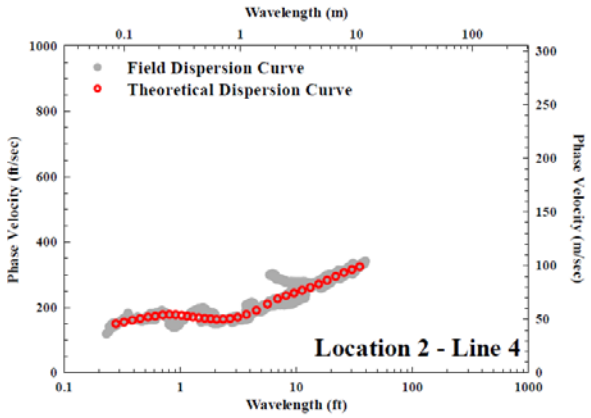

Figure 5.46 Dispersion curves from survey line 4 in location 2 at the ACL.

The V_s profiles in location 2 at the ACL are presented in Fig. 5.47. The shear wave velocity profiles from the surface to depth of 3 m greatly varied from 50 m/s to 145 m/s. At greater depth, the V_s profile variability was lower ranging from 110 m/s to125 m/s. The results from downhole and crosshole seismic testing are also presented in Fig. 5.47. In general, the results from small-scale downhole and crosshole seismic tests were in good agreement with SASW test from lines 1 and 3, particularly at depth of about 0.30 m to 0.50 m. At shallower depth, shear wave velocities from small-scale downhole and crosshole seismic tests were higher than those of SASW tests.

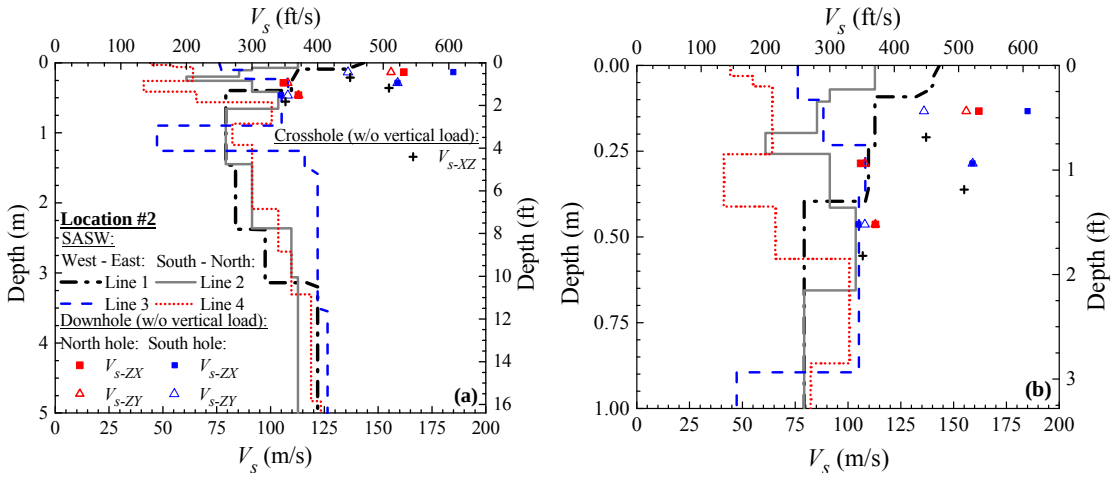

Figure 5.47 Shear wave velocity profile in location 2 at the ACL (a) up to 5 m and (b) up to 1 m.

Figure 5.48 presents the statistical analysis results of V_s profiles from the SASW tests at the ACL. On average, V_s was about 95 m/s at the surface and increased up to 123 m/s at depth of 6 m. Coefficient of variance (COV) ranged from 0.02 to 0.75 with an average of 0.16. The high COV at near surface may be attributed to the fact that thinner layers could be more easily discerned near the surface than at greater depth (Gucunski and Woods 1992). At greater depths, it is only thicker layers that could be clearly identified. It should be noted that the estimated phase velocity represented an estimate of the averaged shear wave velocity of the subsurface.

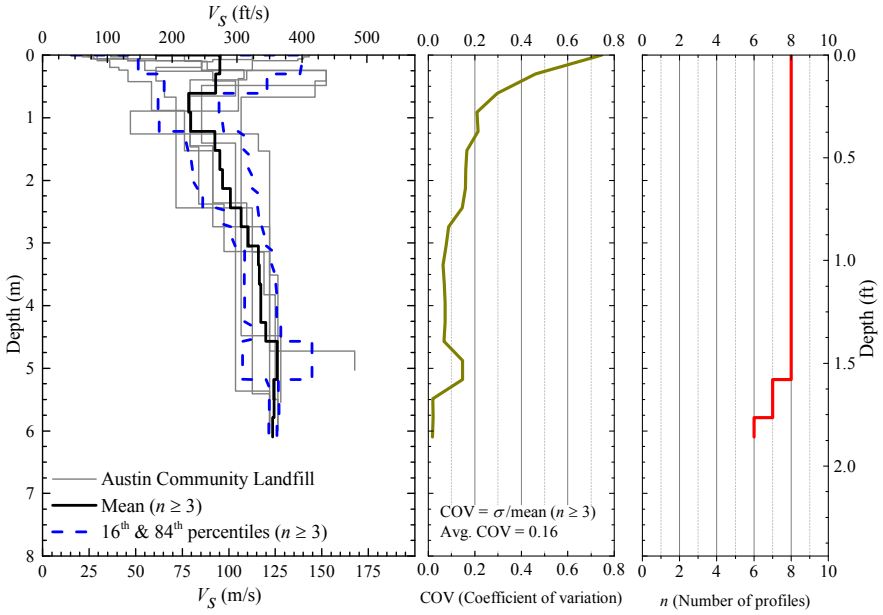

Figure 5.48 Statistical analysis of V_s profiles from SASW testing in both locations at the ACL.

5.9 **Steady-state Dynamic Testing**

Steady-state dynamic tests using Thumper and T-Rex were conducted to study the relationship between shear modulus or normalized shear modulus and shearing strain in the two test locations at the ACL (Fig. 5.49). This test was performed at different static vertical load levels to study the effect of confining stress on the shear modulus and normalized shear modulus reduction curves. In location 1, Thumper or T-Rex was used to impose static vertical loads of 18 kN, 67 kN, 133

kN, and 165 kN as described in Fig. 5.9. In location 2, static vertical loads of 18 kN, 36 kN, 67 kN, and 133 kN were applied (Fig. 5.10). Thumper was used for the steady-state test with static vertical load up to 36 kN. At each vertical static load level, dynamic horizontal loads were applied from small to large amplitude. Chapter 4 presents the testing method of the steady-state dynamic testing as well as the limitations and uncertainties of this method. In this section, the results are presented.

Figure 5.49 Steady-state dynamic testing using (a) Thumper and (b) T-Rex at the ACL.

Figure 5.50 shows the quadrilateral elements in location 1 at the ACL. Elements A, D, and F were formed by four adjacent geophones. Element A was defined by the four sensors closest to the surface, element D is defined by the four intermediate sensors, and element F was defined by the four deepest sensors. Element C was formed by the two deepest and the two shallowest geophones. Figure 5.51 presents the quadrilateral elements for location 2 at the ACL.

Shear modulus was calculated using the shear wave velocity and mass density of MSW. Vertically propagating shear wave velocity was calculated using the phase difference in travel time as shown in Fig. 5.52(a). The mass density was obtained from in-situ unit weight measurements. The average of shear modulus calculated from both arrays was used as the shear

modulus of each element. It should be noted that the mass density may affect the accuracy in shear modulus calculation, but, it does not affect the normalized shear modulus reduction curve. The 4-node displacement based method was used to calculate the shearing strain at the center of quadrilateral elements. Example of shearing strain time history calculated using the 4-node method is shown in Fig. 5.52(b). The analysis method to reduce data from this test is described in detail in Chapter 4. The results of normalized shear modulus reduction curves from this site were used to develop recommended G/G_{max} curves in Chapter 9.

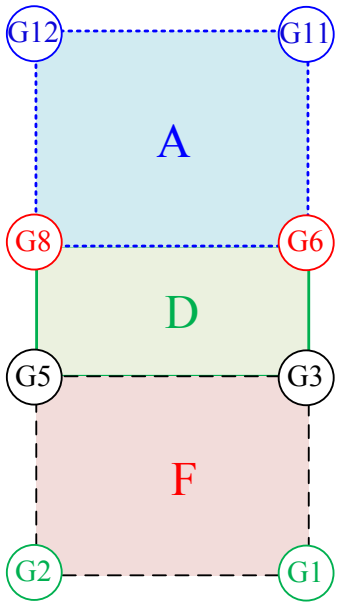

Element	Geophones/Nodes
A	G6, G8, G12, G11
D	G3, G5, G8, G6
F	G1, G2, G5, G3
C = A+D+F	G1, G2, G12, G11

Figure 5.50 Quadrilateral elements for location 1 at the ACL.

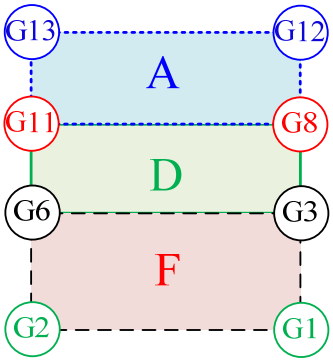

Element	Geophones/Nodes
A	G8, G11, G13, G12
D	G1, G2, G13, G12
F	G3, G6, G11, G8
C = A+D+F	G1, G2, G6, G3

Figure 5.51 Quadrilateral elements for location 2 at the ACL.

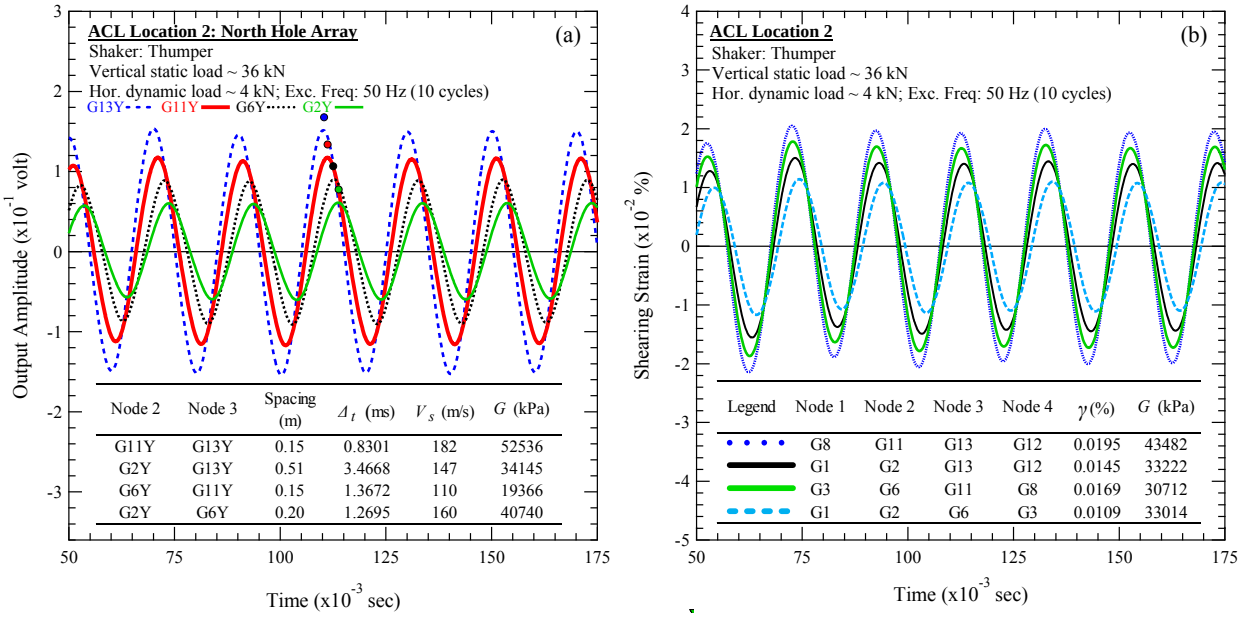

Figure 5.52 Examples of steady-state dynamic testing: (a) shear modulus calculation and (b) shearing strain time history at the ACL.

5.10 **Shear Modulus and Normalized Shear Modulus Reduction Curves in Location 1 at the ACL**

The effect of confining stress on the shear modulus and the normalized shear modulus as a function of shearing strain could be evaluated by examining the same element at different confining stress. Examining the same element isolates the effect of waste composition when investigating the effect of confining stress. Then, by examining different elements at the same confining stress, the effect of waste composition can be investigated.

5.10.1 Effect of Confining Stress on Shear Modulus and Normalized Shear Modulus Reduction Curves in Location 1 at the ACL

The effect of confining stress on the shear modulus and normalized shear modulus as a function of shearing strain could be evaluated by examining the same element at different confining stress. Figures 5.53, 5.54, 5.55, and 5.56 show the effect of confining stress on the shear modulus and normalized shear modulus reduction curves from elements in location 1.

The shear modulus and normalized shear modulus reduction curves for element A in location 1 are presented in Figs. 5.53(a) and 5.53(b), respectively. The center of this element was located at an effective depth of 0.33 m below the footing. The shear modulus was evaluated for shearing strain ranging from 0.0027% up to 0.19%. It should be noted that element A experienced the largest shearing strain due to the proximity of this element to the horizontal dynamic load source. The effect of the confining stress on the shear modulus reduction curve can readily be seen in Fig. 5.53(a). In this case, the small-strain shear modulus (i.e. G_{max}) increased with increasing confining stress. The observed G_{max} increased from 23 MPa to 31 MPa, as mean confining stress increased from 13 kPa to 86 kPa. The normalized shear modulus reduction curves for element A are shown in Fig. 5.53(b). The $G/G_{\max}$ curves systematically moved to the right and exhibited a more linear response with increasing confining stress. These trends in the shear modulus and the normalized shear modulus reduction curves are consistent with laboratory studies on MSW (Lee 2007, Zekkos et al. 2008, and Yuan et al. 2011) as well as on soils (e.g., Darendeli 2001).

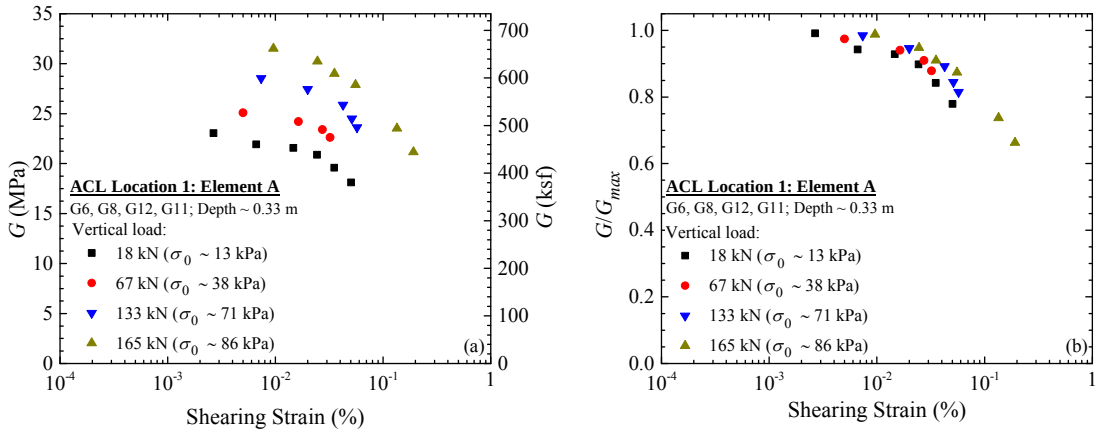

Figure 5.53 (a) Shear modulus and (b) normalized shear modulus reduction curves of element A in location 1 at the ACL.

Figure 5.54(a) presents the G-log γ relationship at different confining stresses for element D in location 1. The center of element D was located at an equivalent depth of 0.61 m below the footing. The nonlinear behavior of element D can readily be seen in Fig. 5.54(a). The steady-state dynamic test for element D was performed over shearing strain ranging from 0.0019% to 0.12%. As shown in Fig. 5.54(a), the small-strain shear modulus increased with increasing confining stress. The small-strain shear modulus increased from 27 MPa to 34 MPa, as mean confining stress increased from 11 kPa to 46 kPa. The G/G_{max}-log γ curves for element D are shown in Fig. 5.54(b). The normalized shear modulus became more linear with increasing confining stress.

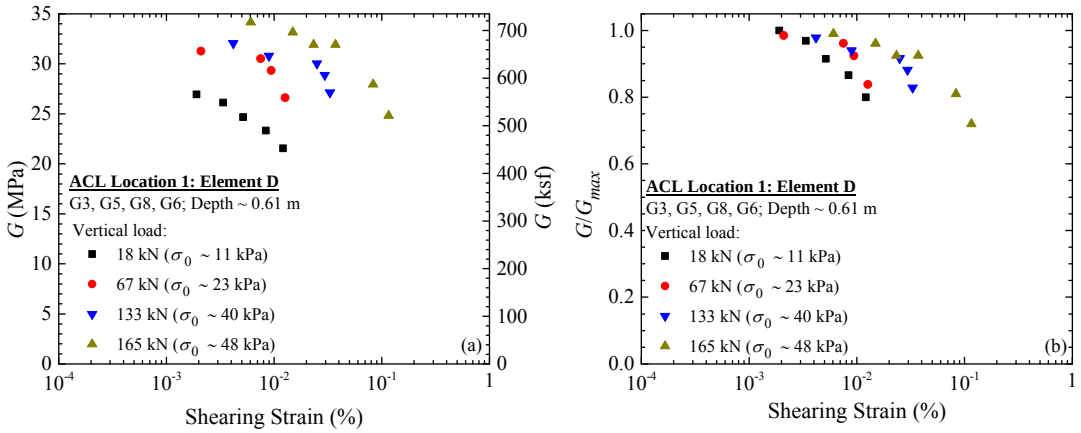

Figure 5.54 (a) Shear modulus and (b) normalized shear modulus reduction curves of element D in location 1 at the ACL.

The variation of shear modulus with shearing strain at different confining stresses for element F in location 1 is presented in Fig. 5.55(a). The center of element F was located at an effective depth of 0.89 m below the footing. As illustrated in Fig. 5.55(a), the shear modulus was successfully obtained from the field measurements over the strain range from 0.0014% to 0.087%. The small-strain shear modulus slightly increased with increasing confining stress. The observed small-strain shear modulus values increased from 43 MPa to 47 MPa, as mean

confining stress increased from 11 kPa to 32 kPa. Figure 5.55(b) presents the normalized shear modulus reduction curves for element F. The normalized shear modulus became slightly more linear with increasing confining stresses from 11 kPa to 30 kPa.

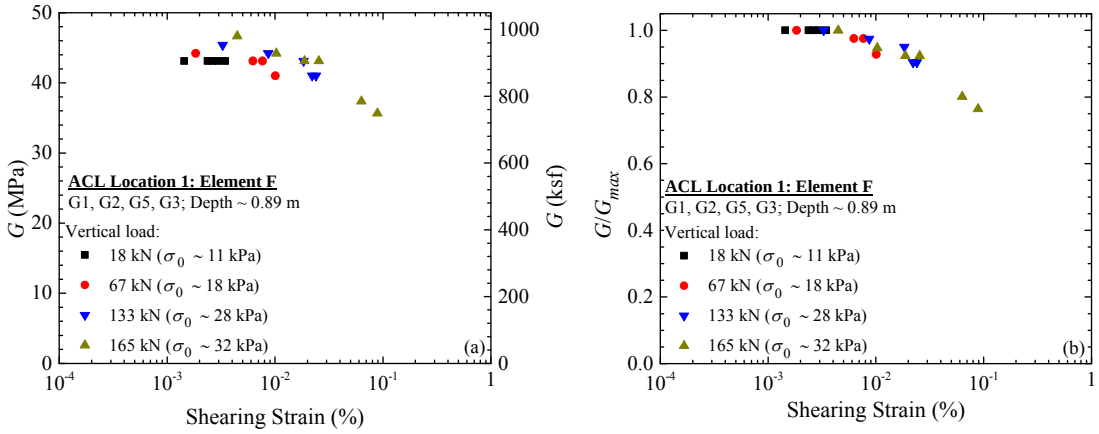

Figure 5.55 (a) Shear modulus and (b) normalized shear modulus reduction curves of element F in location 1 at the ACL.

The shear modulus and normalized shear modulus reduction curves for element C in location 1 are presented in Figs. 5.56(a) and 5.56(b). This element provided an average response of all elements as it was defined by the shallowest and the deepest geophones. The center of this element was located at an effective depth of 0.60 m below the footing. The shear modulus was evaluated for shearing strain ranging from 0.0012% up to 0.13%. As seen in Fig. 5.56(a), the small-strain shear modulus increased with increasing confining stress. The observed G_{max} increased from 29 MPa to 36 MPa, as mean confining stress increased from 11 kPa to 50 kPa. The normalized shear modulus reduction curves for this element are shown in Fig. 5.56(b). With increasing confining stress, the normalized shear modulus reduction curve became more linear.

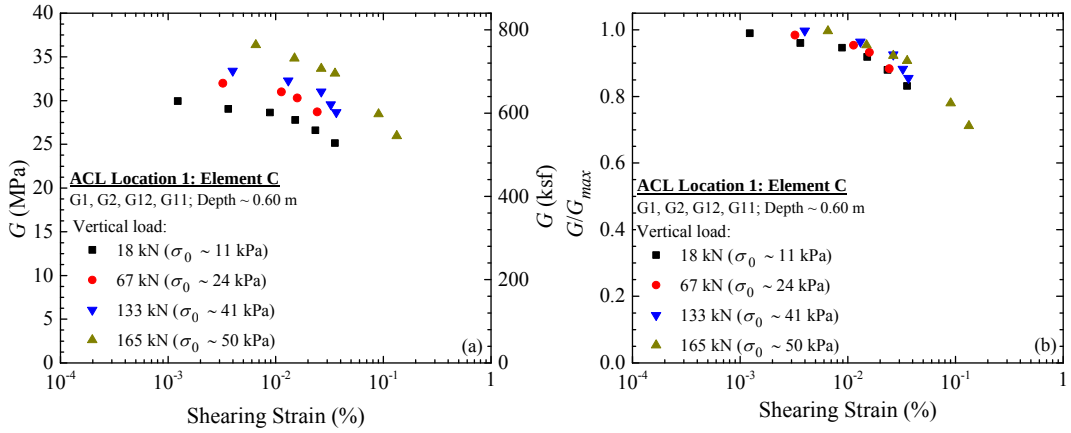

Figure 5.56 (a) Shear modulus and (b) normalized shear modulus reduction curves of element C in location 1 at the ACL.

5.10.2 Effect of Waste Composition on Shear Modulus and Normalized Shear Modulus Reduction Curves in Location 1 at the ACL

The effect of waste composition on the shear modulus and normalized shear modulus reduction as a function of shearing strain could be evaluated using results from different sets of geophones that form elements. Figure 5.57 shows the effect of waste composition on the shear modulus and normalized shear modulus reduction curves from all elements at nearly the same calculated confining stress that varied from 11 kPa to 13 kPa. As shown in Fig. 5.50, elements A, C, D and F were representative of waste at different depths. It should be noted that element C represented the average of the other three elements. Figure 5.57(a) shows differences in shear modulus that are attributed to waste variability. The small-strain shear modulus was 23 MPa, 27 MPa, and 43 MPa for elements A, D and F, respectively. Element C yielded an intermediate shear modulus (~30 MPa). The impact of waste composition on G/G_{max} curves is demonstrated in Fig. 5.57(b).

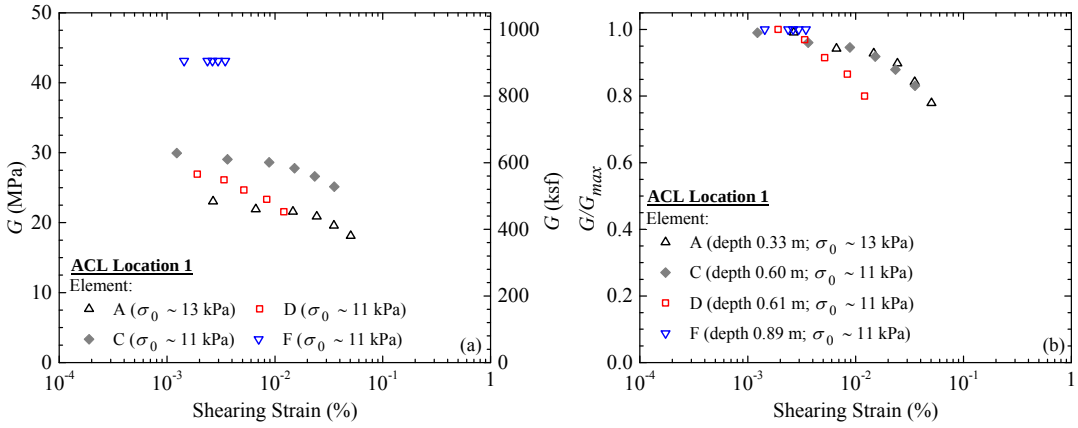

Figure 5.57 Waste composition effect on (a) shear modulus and (b) normalized shear modulus reduction curves in location 1 at the ACL.

5.11 **Shear Modulus and Normalized Shear Modulus Reduction Curves in Location 2 at the ACL**

5.11.1 Effect of Confining Stress on Shear Modulus and Normalized Shear Modulus Reduction Curves in Location 2 at the ACL

The variation of shear modulus with shearing strain at different confining stresses for element A in location 2 is presented in Fig. 5.58(a). The center of this element was located at an effective depth of 0.13 m below the footing. The shear modulus was evaluated for shearing strain ranging from 0.0019% up to 0.16%. Element A was the shallowest element and thus exhibited the largest shearing strain. The nonlinear behavior of element A is shown in Fig. 5.58(a). This figure shows the effect of the confining stress on the shear modulus reduction curves. The small-strain shear modulus increased with increasing confining stress. The observed G_{max} increased from 39 MPa to 84 MPa, as mean confining stress increased from 22 kPa to 138 kPa. The normalized shear modulus reduction curves for element A are shown in Fig. 5.58(b). The $G/G_{\max}$ curves moved to the right and exhibited a more linear response with increasing confining stress.

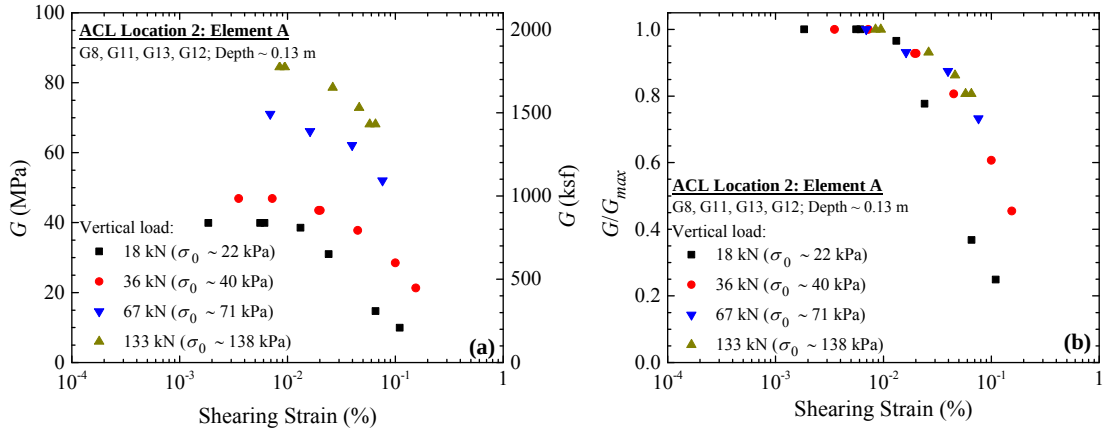

Figure 5.58 (a) Shear modulus and (b) normalized shear modulus reduction curves of element A in location 2 at the ACL.

The variation of shear modulus with shearing strain at different confining stresses for element D in location 2 is presented in Fig. 5.59(a). The center of element D was located at an effective depth of 0.29 m below the footing. The shear modulus was successfully obtained from the field measurements over the shearing strain ranging from 0.0016% to 0.14% as shown in Fig. 5.59(a). In this figure, the small-strain shear modulus increased from 28 MPa to 37 MPa as mean confining stress increased from 17 kPa to 92 kPa. The normalized shear modulus reduction curves for element D are presented in Fig. 5.59(b). The normalized shear modulus reduction curves became more linear with confining stress increase from 17 kPa to 92 kPa.

The G-log γ relationship at different confining stresses for element F in location 2 is shown in Fig. 5.60(a). The center of element F was located at an effective depth of 0.46 m below the footing. The steady-state dynamic test for element F was performed over shearing strain ranging from 0.0011% to 0.064%. The small-strain shear modulus increased with increasing confining stress as shown in Fig. 5.60(a). The small-strain shear modulus increased from 27 MPa to 34 MPa, as mean confining stress increased from 14 kPa to 60 kPa. The G/G_{max}-

log γ curves for element F is shown in Fig. 5.60(b). The normalized shear modulus reduction curves became more linear with increasing confining stress.

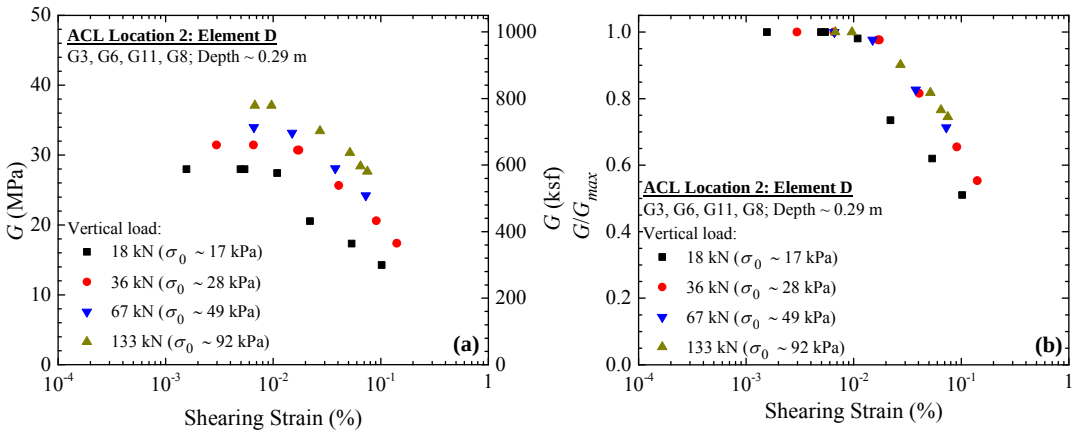

Figure 5.59 (a) Shear modulus and (b) normalized shear modulus reduction curves of element D in location 2 at the ACL.

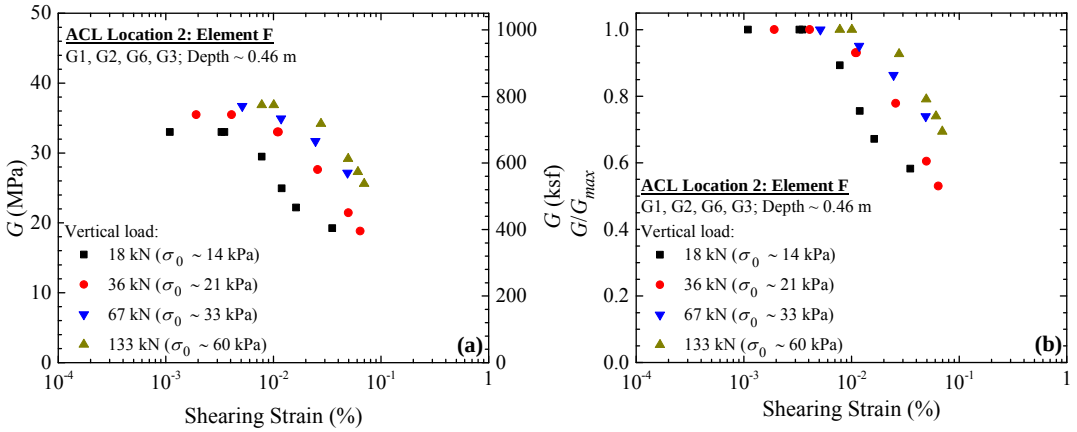

Figure 5.60 (a) Shear modulus and (b) normalized shear modulus reduction curves of element F in location 2 at the ACL.

Figure 5.61(a) presents the shear modulus reduction curves for element C in location 2. Element C provided an average response of the tested waste mass as it was formed by the shallowest and deepest geophones. The center of this element was located at an effective depth of 0.31 m below the footing. The steady-state dynamic tests yielded shearing strain ranging from 0.0013% up to 0.1% for this element. The small-strain shear modulus increased with increasing

confining stress [Fig. 5.61(a)]. The small-strain shear modulus increased from 31 MPa to 43 MPa, as mean confining stress increased from 16 kPa to 86 kPa. Figure 5.61(b) shows the normalized shear modulus reduction curves for this element. The normalized shear modulus reduction curves became more linear with confining stress.

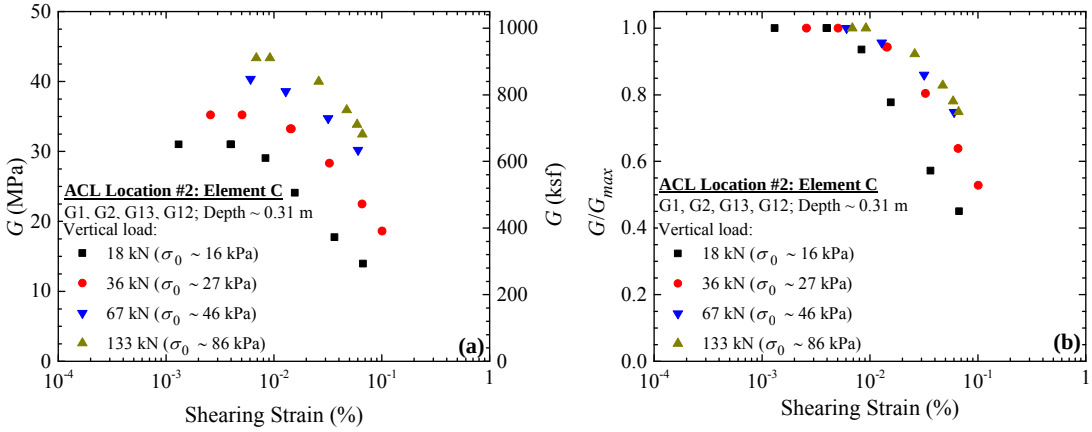

Figure 5.61 (a) Shear modulus and (b) normalized shear modulus reduction curves of element C in location 2 at the ACL.

5.11.2 Effect of Waste Composition on Shear Modulus and Normalized Shear Modulus Reduction Curves in Location 2 at the ACL

The effect of waste composition on G-log γ and G/G_{max}-log γ curves from location 2 at the ACL is presented in Figs. 5.62(a) and 5.62(b). All elements in these figures were at nearly the same calculated confining stress ranging from 14 kPa to 22 kPa. It can be observed that shear modulus from these elements ranging from 27 MPa to 39 MPa [Fig. 5.62(a)]. In this case, element A showed the highest shear modulus and the most nonlinearity in the G-log γ curve. Element D demonstrated the lowest shear modulus and the least nonlinearity in the G-log γ curve. The differences in shear modulus and the degree of nonlinearity could be attributed to the differences in waste composition in each element. The variability in waste composition was also demonstrated by the range of normalized shear modulus reduction curves in Fig. 5.62(b).

According to Zekkos et al. 2008, waste-rich MSW exhibits lower shear modulus and more linear response in G/G_{max} curve compared to waste-poor MSW.

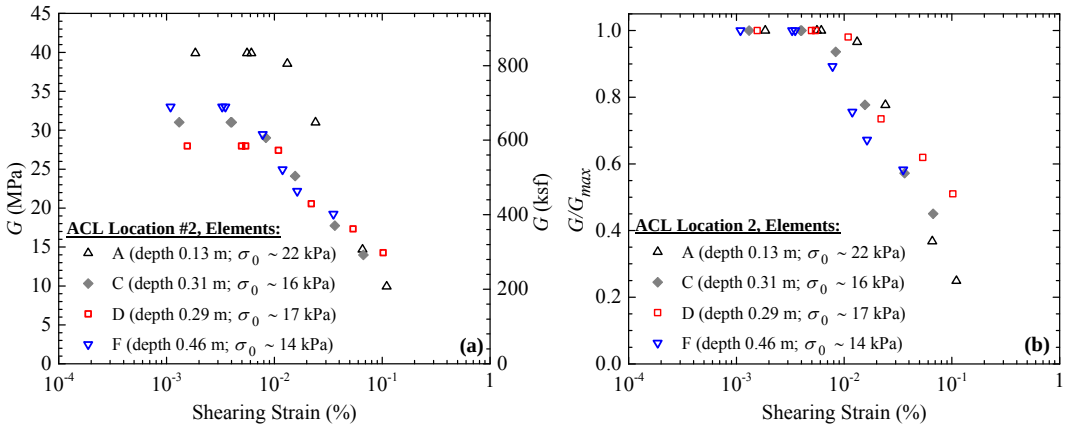

Figure 5.62 Waste composition effect on (a) shear modulus and (b) normalized shear modulus reduction curves in location 2 at the ACL.

5.12 **Comparison of Normalized Shear Modulus Reduction Curves**

In this section, the variation of normalized shear modulus reduction curves as a function of shearing strain from both test locations at the ACL is compared. In addition, the field G/G_{max} data from ACL is also compared with curves proposed by other studies. In this case, the comparison was made with results from other field measurement, laboratory testing, and recorded ground motion back-calculation analysis.

Fig. 5.63 presents results from locations 1 and 2 at the ACL. Dataset from locations 1 and 2 are shown as black squares and red circles, respectively. At location 1, normalized shear modulus reduction curve was evaluated for shearing strains ranging from 0.001% up to 0.2%. At location 2, normalized shear modulus reduction curve was evaluated for shearing strains ranging from 0.001% up to 0.16%. The normalized shear modulus reduction curves were generally consistent, although normalized shear modulus reduction appeared to be more pronounced at larger strains for location 2 compared to location 1. This difference was likely attributed to

variability in waste composition between the two locations as well as differences in confining stresses between quadrilateral elements.

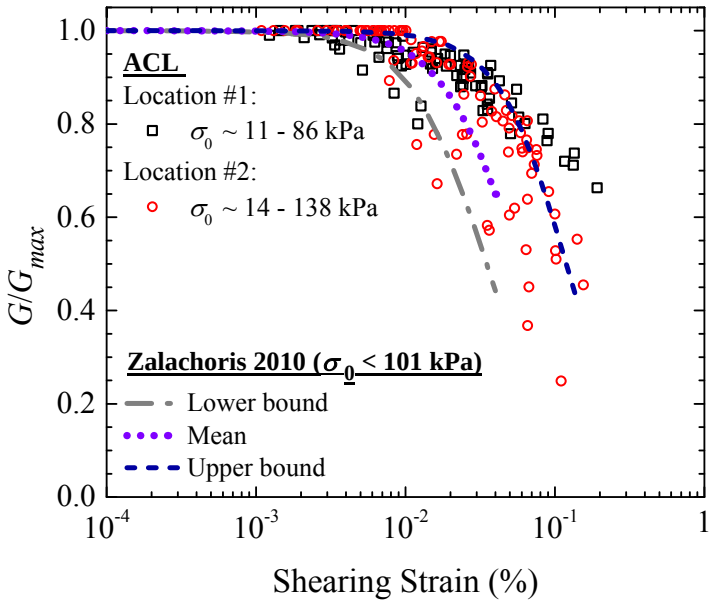

Figure 5.63 The normalized shear modulus reduction curves at the ACL and comparison with Zalachoris (2010) recommended curves.

The field G/G_{max} data from locations 1 and 2 at the ACL is compared with recommended curves from Zalachoris (2010) in Fig. 5.63. Zalachoris performed field measurement in the pre-Subtitle D landfill part at the ACL. It should be noted that Zalachoris analyzed shearing strain using 2-node approach and the data did not separate the results for different confining stress. Most field G/G_{max} data from location 1 was essentially more linear than the upper bound curve of Zalachoris. Most field G/G_{max} data from location 2 was in good agreement with Zalachoris upper bound curve. Zalachoris lower bound curve was slightly to the right of the lower bound field G/G_{max} data from locations 1 and 2.

Figure 5.64 shows the comparison between the field G/G_{max} data from the ACL and Zekkos et al. (2008) curves for mean stress < 125 kPa that were largely developed on the basis of

testing at mean stress of 75 kPa. The field data were generally consistent with the laboratory based curves. The field G/G_{max} data for location 1 with σ_0 in the range of 28 – 86 kPa was in between Zekkos et al. curve for 8 – 25% and 62 – 76% smaller than 20 mm material. The field G/G_{max} data from location 2 with σ_0 in the range of 28 – 138 kPa were generally consistent with curve for 8 – 25% smaller than 20 mm material up to strains of 0.01%. At larger shearing strains and low confining stress, the field G/G_{max} data appeared to drop off more sharply.

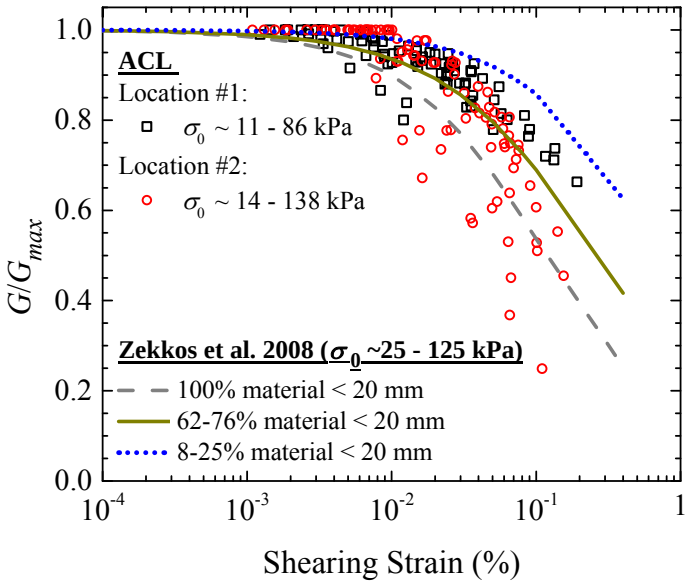

Figure 5.64 Comparison of the normalized shear modulus reduction curves with Zekkos et al. (2008).

Figure 5.65 presents the comparison between the normalized shear modulus reduction curves measured at the ACL with curves for MSW proposed by other researchers. Singh and Murphy (1990) proposed a curve that was developed using the shear modulus reduction curve of peat and clay. The normalized shear modulus reduction curves proposed by Idriss et al. (1995), Matasovic and Kavazanjian (1998), and Augello et al. (1998) were derived from back-calculation analyses using recorded ground motions at the surface of the OII landfill, California. In addition, Matasovic and Kavazanjian (1998) also performed cyclic simple shear testing to

extend their curves to larger strain. The recommended Singh and Murphy curve showed more significant G/G_{max} reduction below shearing strain of 0.001 % than the field G/G_{max} data from the ACL. Idriss et al. curve exhibited a more nonlinear shear modulus reduction curve than the field G/G_{max} data from the ACL. In general, the recommended Singh and Murphy and Idriss et al. curves showed substantial differences from the ACL field G/G_{max} data. The recommended Augello et al. curve essentially provided a median G/G_{max} reduction curve to the field ACL G/G_{max} data. The recommended Matasovic and Kavanzanjian curve was more linear than the upper bound of the field G/G_{max} data from the ACL.

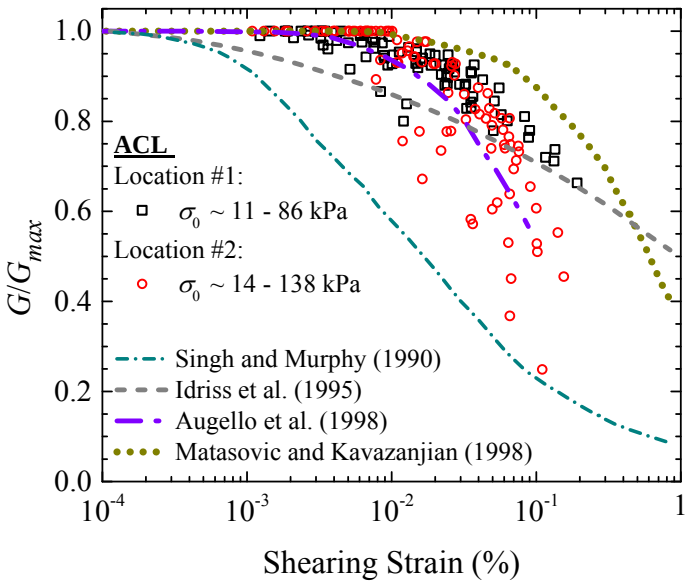

Figure 5.65 Comparison of the normalized shear modulus reduction curves with with curves from other studies in the literature.

5.13 **Summary**

A field experiment program was conducted at three locations in a Subtitle D landfill in Austin, Texas, to investigate dynamic properties of MSW in the linear and nonlinear strain range. Results from two test locations are presented in this chapter. Crosshole and downhole seismic tests at small strains as well as steady-state dynamic testing over a wide shear strain range

(0.001% to 0.2%) was conducted at six different static vertical loads applied using mobile vibroseis shakers of NEES@UTexas. Two arrays of 3-D geophone sensors were embedded in the waste mass and were used to capture the waste response during dynamic testing. The SASW tests were also performed at the ACL. In addition, load-settlement measurements were carried out. Pit excavation was performed at each location to measure the in-situ unit weight, visually assess waste composition, and collect samples for waste characterization and laboratory testing. The outcomes from small-strain testing were the wave propagation velocity-depth relationship and wave propagation velocity-stress relationship. The study also generated in-situ data on shear modulus and normalized shear modulus reduction relationship as a function of shear strain. The results from field testing at the ACL will be synthesized with the results from field testing at the Lamb Canyon Sanitary Landfill and Los Reales Landfill to generate broad conclusions and recommendation in Chapter 9.

Small-scale crosshole and downhole seismic testing allowed for an assessment of $V_{p\text{-}X}$, $V_{p\text{-}Z}$, $V_{s\text{-}XZ}$, $V_{s\text{-}ZX}$, and $V_{s\text{-}ZY}$ as a function of waste composition and confining stress. Small-scale crosshole and downhole seismic testing with different static vertical loads showed that wave propagation velocities increase with stress. In the NC regime, wave propagation velocity increase was more sensitive to stress increase than in the OC regime. The near-surface MSW was overconsolidated due to field compaction at the landfill.

The wave propagation velocity measurements in the ACL were also used to assess waste anisotropy and small-strain Poisson's ratio. For example, the ratio of $V_{p\text{-}Z}$ to $V_{p\text{-}X}$ ranged from 0.69 to 0.89 with a mean value of 0.78. Similarly, the ratio of $V_{s\text{-}vertical}$ to $V_{s\text{-}horizontal}$ was found to be between 0.68 and 1.37 with an average value of 0.88. These average values indicated that the

stiffness in the horizontal direction was generally higher than the stiffness in the vertical direction. The small-strain Poisson's ratio at both test locations varied from 0.06 to 0.45.

The impact of waste variability and confining stress on the shear modulus was also assessed in situ. Shear modulus was found to increase with increasing confining stress, particularly in the normally consolidated regime, and to be affected by waste composition. The normalized shear modulus reduction curves were also affected by waste composition and confining stress. The normalized shear modulus became more linear as confining stress increased similar to soils. At the same confining stress, the shear modulus and normalized shear modulus curves of the MSW at different locations varied indicating the effect of waste composition on these nonlinear dynamic properties of MSW.

CHAPTER 6. FIELD EVALUATION OF DYNAMIC PROPERTIES OF MUNICIPAL SOLID WASTE AT THE LAMB CANYON SANITARY LANDFILL

6.1 **Introduction**

The dynamic properties of municipal solid waste (MSW) were evaluated in situ at the Lamb Canyon Sanitary Landfill (LCSL) in Beaumont, California from June 14 to 26, 2012. In this chapter, testing locations, field test execution, and test results are described. The field investigation in LCSL included downhole and crosshole seismic tests, Multichannel Analysis of Surface Wave (MASW) testing, Microtremor Analysis Method (MAM) testing, and steady-state dynamic testing. Additionally, load-settlement tests and in-situ unit weight measurements were performed. The field testing generally was conducted using the procedures described in Chapter 4.

6.2 **Field Investigation at the Lamb Canyon Sanitary Landfill**

The field investigation at the Lamb Canyon Sanitary Landfill was mainly conducted to evaluate the linear and nonlinear dynamic properties of MSW in situ. In the linear range, shear wave (S-wave) velocity (V_s) and primary wave (P-wave) velocity (V_p) were investigated. In the nonlinear range, variation of shear modulus (G) and normalized shear modulus (G/G_{max}) as a function of shearing strain (γ) was also evaluated.

The LCSL is a MSW landfill operated by the Waste Management Department of Riverside County, California under the regulations of the California Code of Regulations, Title 27 and Air Quality Management District (AQMD) Rule 1150.1. The LCSL is located at 16411

Lamb Canyon Road, Beaumont, California which is approximately 130 km southeast of Los Angeles, California (Fig. 6.1). The LCSL accepts routine refuse, such as MSW from household, furniture, tires, yard trimming, and electronics appliances. In addition, the LCSL receives construction and demolition debris (C&D), asphalt, and clean fill soils.

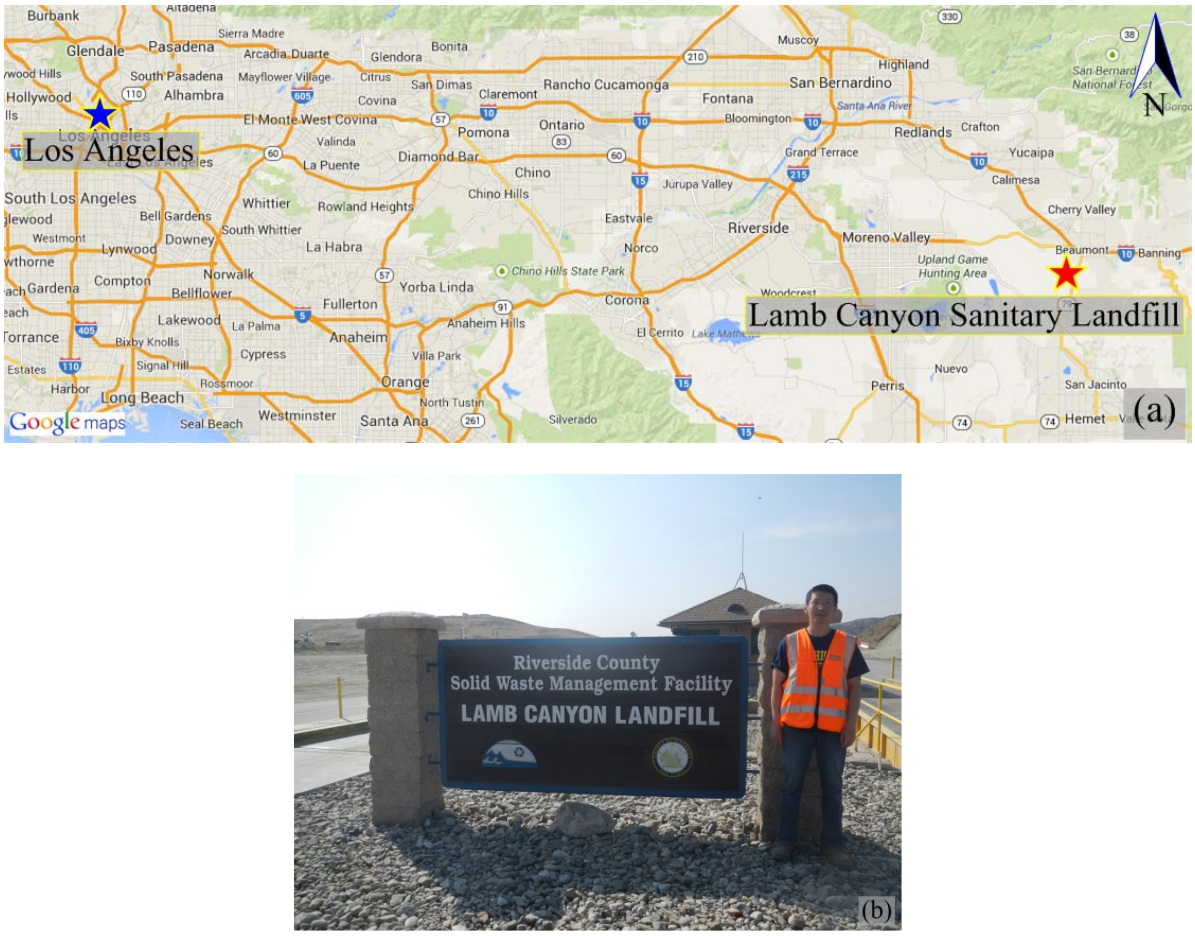

Figure 6.1 The Lamb Canyon Sanitary Landfill: (a) location and (b) entrance.

The field investigation at the LCSL was conducted by the author, Mr. Xunchang Fei, Mr. Clinton Carlson, and Dr. Dimitrios Zekkos (University of Michigan); Mr. Cecil G. Hoffpauir, Mr. Robert Kent, and Dr. Farn-Yuh Menq (NEES@UT); and Mr. Spencer Marcinek (Geosyntec). In addition, testing logistics was accommodated by the Waste Management Department of Riverside County, California.

6.2.1 Testing Locations

The field investigation was performed in three locations at the LCSL (Fig. 6.2). Location 1 was located in waste disposal area B (Fig. 6.3). In this area, field testing was performed from June,14 to 20, 2012. According to the landfill operator, the MSW thickness in this location was about 49 m and was placed from October 2007 to December 2009. Location 2 was located in waste disposal area A (Fig.6.4). In location 2, field investigation was performed from June 20 to 23, 2012. The thickness of MSW was approximated to be 27 m and solid waste was placed from July 2006 to June 2007 in this area. Location 3 was located at waste disposal area C (Fig. 6.5). Field investigation in location 3 was conducted from June 23 to 26, 2012. In this area, solid waste was placed from July 2005 to July 2006. Waste thickness in area C was approximated to be 43 m.

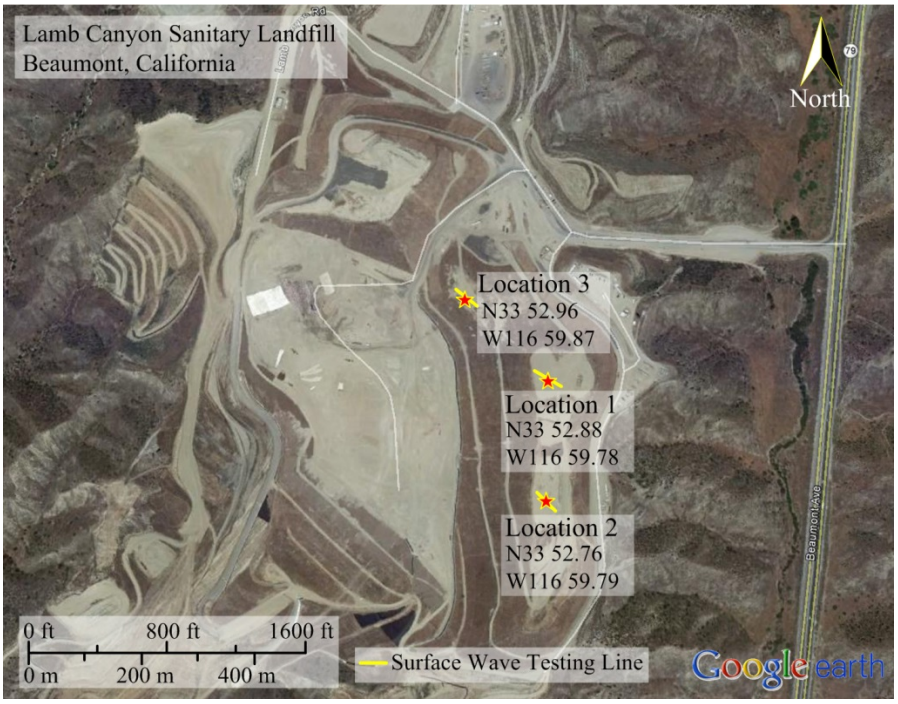

Figure 6.2 Testing locations at the Lamb Canyon Sanitary Landfill.

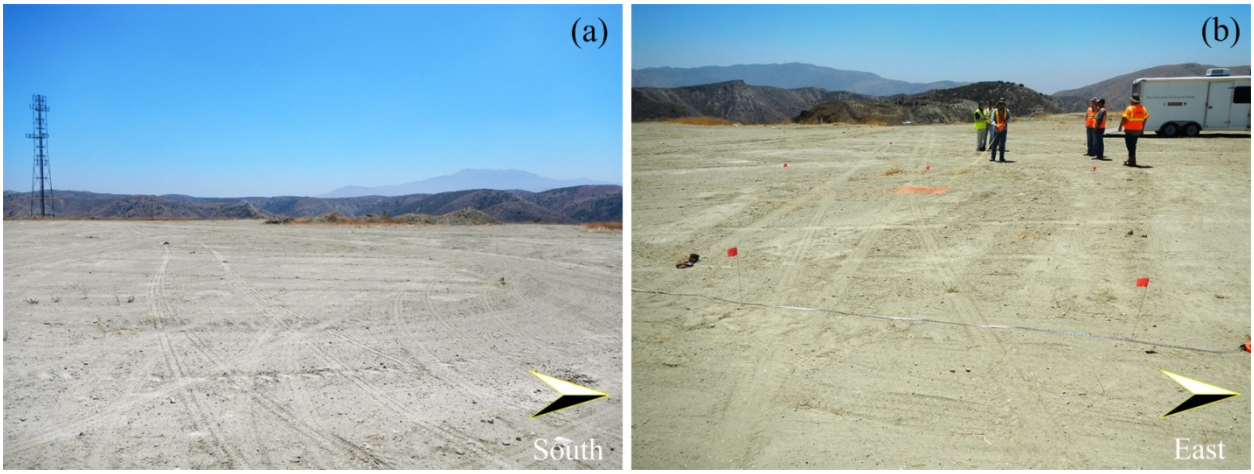

Figure 6.3 (a) East and (b) north views of location 1 at the LCSL.

Figure 6.4 (a) North and (b) northeast views of location 2 at the LCSL.

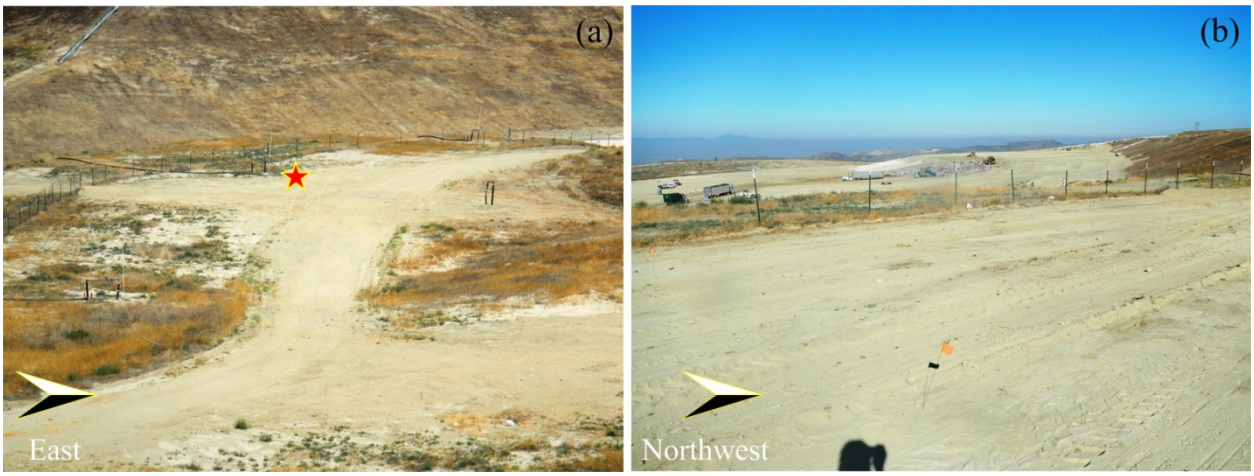

Figure 6.5 (a) North and (b) southwest views of location 3 at the LCSL.

6.2.2 Field Instrumentation and Testing Setup

Activities during the field instrumentation and preparation at the LCSL are shown in Fig. 6.6. Testing setups in locations 1, 2, and 3 are shown in Figs. 6.7, 6.8, and 6.9, respectively. As shown in these figures, testing setup for all locations was identical with the deepest 3-D geophone pair located at a depth of 0.65 m. All test locations were prepared for load-settlement test, downhole and crosshole seismic tests, and steady-state dynamic testing.

Figure 6.6 Field instrumentation and testing setup at the LCSL: (a) removing cover soil, (b) pushing core barrel, (c) removing waste from core barrel, (d) 3-D geophone installation, (e) compaction of sensor hole, (f) crosshole source rod installation, and (g) footing placement.

6.2.3 Field Testing Sequence for Evaluation of Dynamic Properties of MSW at the LCSL

The field investigations in locations 1, 2, and 3 at the LCSL were performed according to the staged loading sequence as shown in Figs. 6.10, 6.11, and 6.12, respectively. In location 1, small-scale crosshole and downhole seismic tests were performed at externally applied vertical static

load of 0 kN, 18 kN, 36 kN, 71 kN, and 111 kN. Steady-state dynamic tests were performed using a 18 kN, 36 kN, 71 kN, and 133 kN static hold-down force. These vertical static load levels were kept constant while applying dynamic horizontal loads. In location 2, crosshole and downhole seismic tests were performed at externally applied vertical static loads of 0 kN, 18 kN, 36 kN, 71 kN, and 107 kN. Steady-state dynamic tests were performed using a 18 kN, 36 kN, 71 kN, and 133 kN static hold-down force. In location 3, crosshole and downhole seismic tests were performed at externally applied vertical static loads of 0 kN, 18 kN, 36 kN, 71 kN, and 98 kN. In this location, steady-state dynamic tests were performed using a 18 kN, 36 kN, 71 kN, and 133 kN static hold-down force. In all locations, load-settlement data were collected during vertical static load application for the crosshole and downhole seismic tests. It should be noted that the highest vertical static load for the downhole and crosshole seismic testing was planned to be 133 kN. However, it was very difficult to reach a static vertical load of 133 kN using a hydraulic jack pump in all locations. In steady-state dynamic testing, Thumper was used to apply static vertical loads up to 36 kN and T-Rex was used to impose larger vertical static load levels.

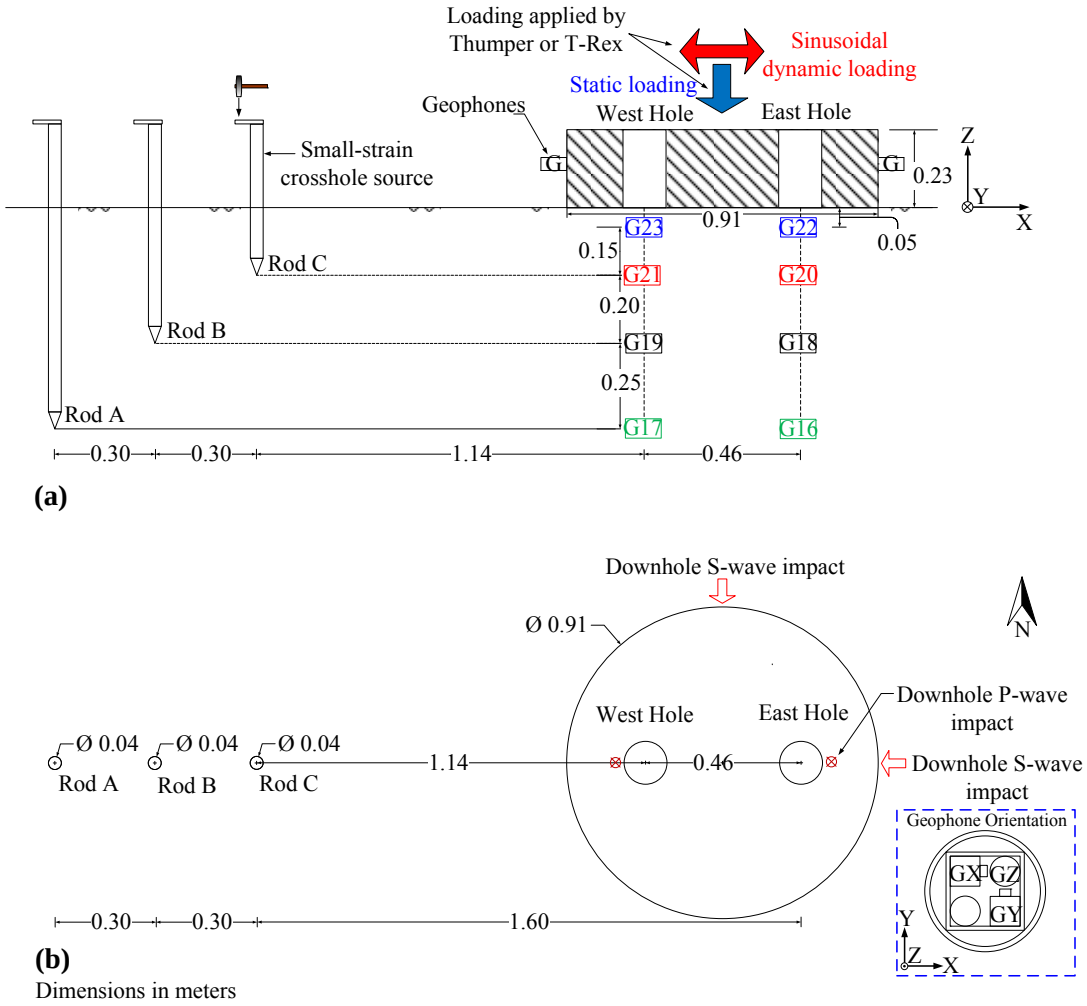

Figure 6.7 Testing setup in location 1 at the LCSL: (a) cross-section and (b) plan views.

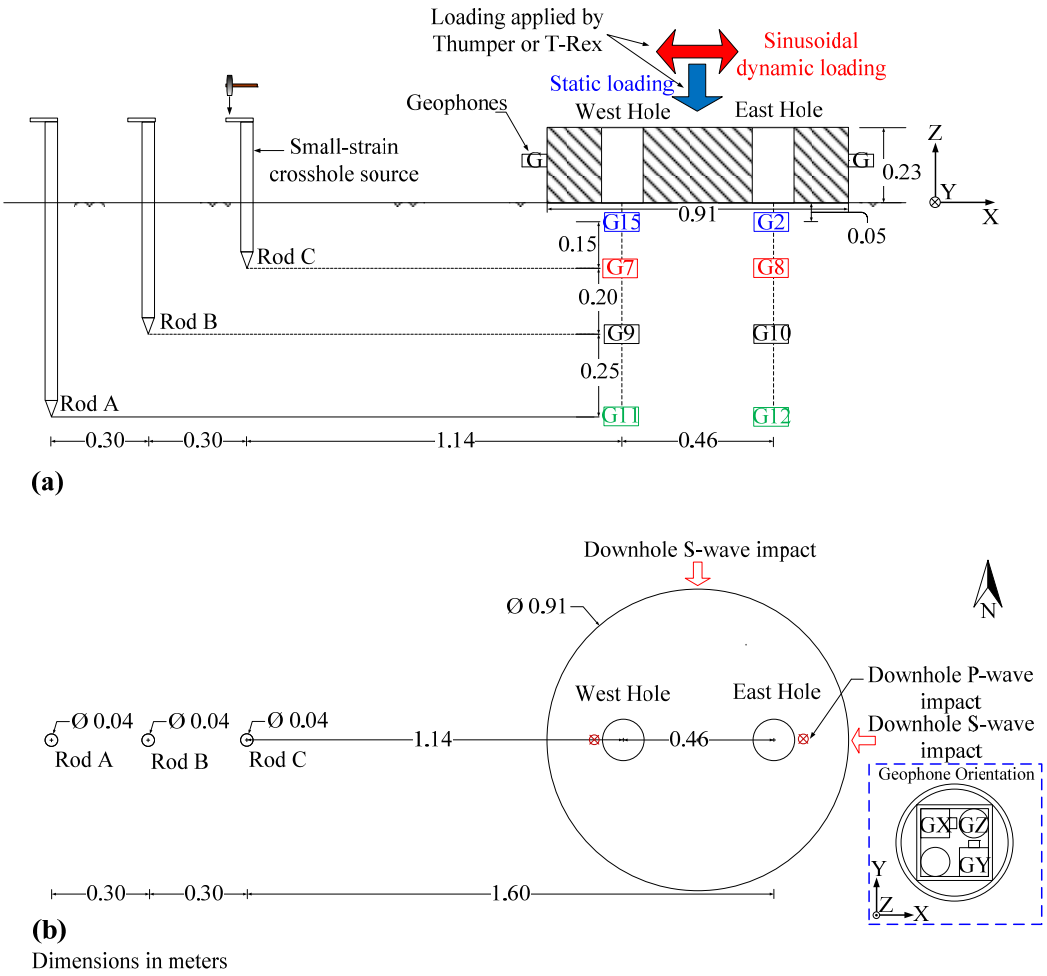

Figure 6.8 Testing setup in location 2 at the LCSL: (a) cross-section and (b) plan views.

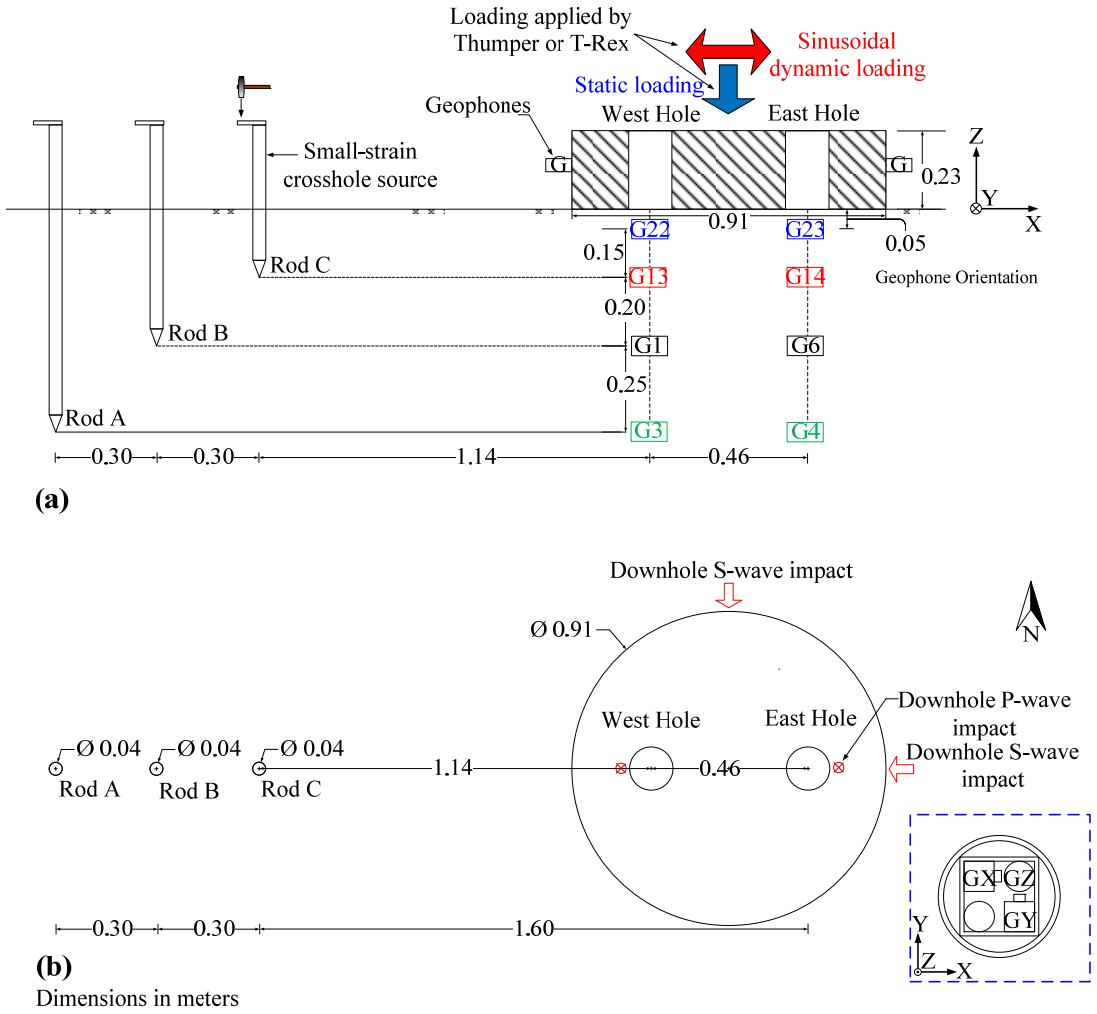

Figure 6.9 Testing setup in location 3 at the LCSL: (a) cross-section and (b) plan views.

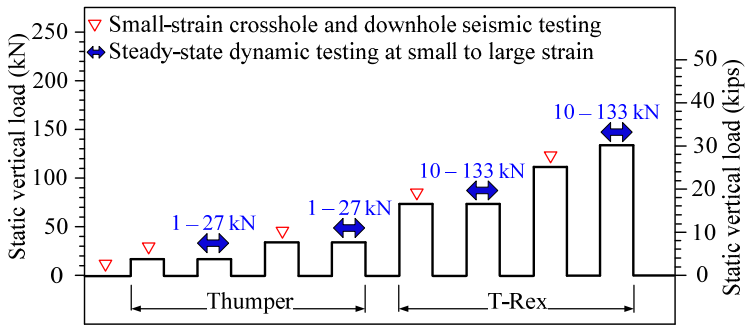

Figure 6.10 Staged loading sequence in location 1 at the LCSL.

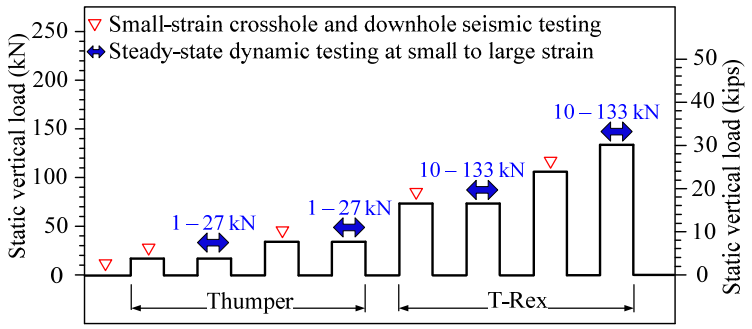

Figure 6.11 Staged loading sequence in location 2 at the LCSL.

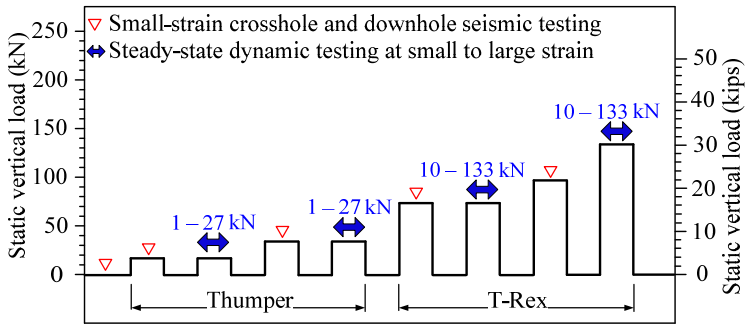

Figure 6.12 Staged loading sequence in location 3 at the LCSL.

6.2.4 In-situ Unit Weight Measurements and MSW Sampling

In-situ unit weight measurements, MSW sampling, in-situ MSW characterization, and sensor recovery were performed after completion of the staged loading test (Fig. 6.13). In-situ unit weight measurement and MSW characterization were performed using procedures proposed by Zekkos et al. (2006a) and Zekkos et al. (2010), respectively. An approximately 2m x 1.5 m x 1 m (depth) pit was excavated in each location. Bulk MSW samples of 2.25 kN, 2.52 kN, and 2.05 kN were collected from locations 1, 2, and 3, respectively. These bulk samples were stored in 55-gallon HDPE drums and were transported to the Geoenvironmental Engineering laboratory at the University of Michigan. Remaining excavated MSW was re-disposed to the landfill. In-situ weight measurements were conducted using gravel with a unit weight of 16.7 kN/m^3.

Table 6.1 shows the unit weight and waste composition for all test locations at the LCSL. The gross unit weights were 13.6 kN/m^3, 14.9 kN/m^3, and 13.3 kN/m^3 in locations 1, 2, and 3,

respectively. Waste composition was characterized using the collected bulk samples independently for each test location in the Geonvironmental Engineering laboratory at the University of Michigan. It should be noted that although the samples collected from each location involved a significant amount of waste material (i.e. 2.05-2.52 kN), these amounts were still just a small portion of the waste mass tested in the field. The collected samples were 4%, 10% and 6% by weight of the excavated MSW in locations 1, 2, and 3, respectively. Thus, the waste compositions shown are only approximately representative of the tested waste composition and may not be identical to the tested waste in the field.

Figure 6.13 (a) Waste excavation, (b) MSW pit, (c) exposed 3-D geophone, (d) placement of MSW into drums, and (e) in-situ unit weight measurement at the LCSL.

Table 6.1 Waste composition in locations 1, 2, and 3 at the LCSL.

Location	Total Sample Weight (kN)	Unit Weight (kN/m^3)	Composition (% by weight)							
			< 20mm[1]	Paper	Hard Plastic	Soft Plastic	Wood	Metal	Gravel & Glass	Others[2]
1	2.25	13.6	79.9	5.2	1.7	2.2	0.8	1.1	6.4	2.7
2	2.52	14.9	67.7	3.4	0.8	1.4	4.9	0.4	19.1	2.3
3	2.05	13.3	71	5.2	3.3	3.3	6.8	0.5	6.3	3.7

[1] Soil-like material.
[2] Textile, rug, leaf, soft rubber, and sponge.

6.3 **Load-settlement Test**

Load-settlement tests were performed in a loading sequence in three test locations at the LCSL. The highest static vertical load in the load-settlement test was 111 kN, 107 kN, and 98 kN for locations 1, 2, and 3, respectively. These highest vertical loads corresponded to maximum stresses on the footing ranging from 150 kPa to 170 kPa. The static vertical loads were applied using a hydraulic jack that reacted against the mobile field shakers' frame as shown in Fig. 6.14. A T-shaped frame was used to uniformly distribute the load on the footing. The settlements were measured using three linear potentiometers on the footing.

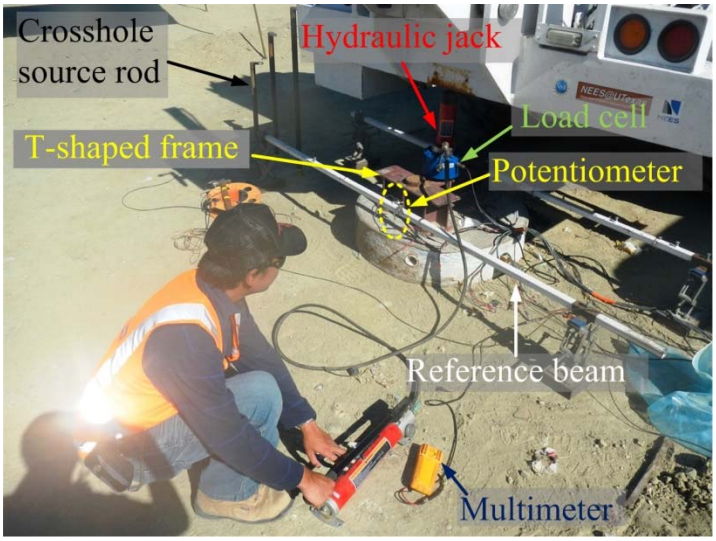

Figure 6.14 Load-settlement test in location 2 at the LCSL.

Figure 6.15 shows the load-settlement curves in three test locations at the LCSL. The maximum settlements under the highest static vertical load in locations 1, 2, and 3 were 13 mm, 18 mm, and 38 mm, respectively.

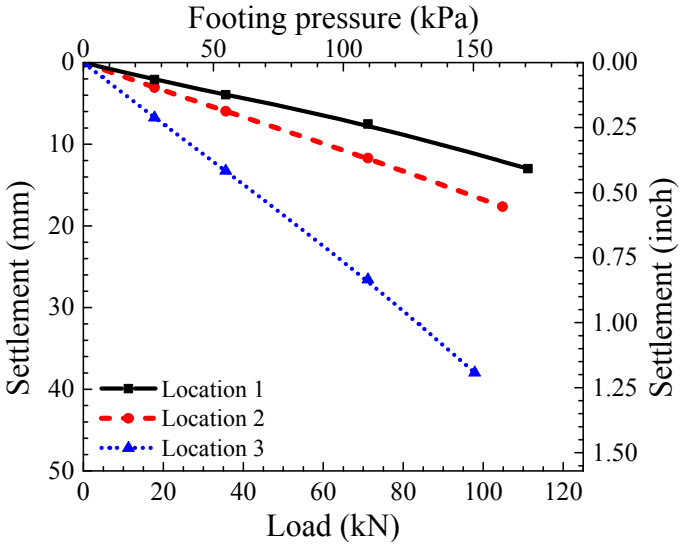

Figure 6.15 Load-settlement test results at the LCSL.

6.4 **Small-scale Downhole Seismic Testing**

As part of field testing at the LCSL, small-scale downhole seismic tests were performed to evaluate vertically propagating P-wave velocity ($V_{p\text{-}Z}$), vertically-propagating horizontally-polarized in the X-axis S-wave ($V_{s\text{-}ZX}$), and vertically-propagating horizontally-polarized in the Y-axis S-wave ($V_{s\text{-}ZY}$) at each load increment (Figs. 6.10, 6.11, and 6.12). The coordinate orientations are presented in Figs. 6.7, 6.8, and 6.9. As shown in these figures, downhole seismic test was conducted by hitting the footing at the sides and at the top with a handheld hammer. Figure 6.16(a) shows the small-scale downhole seismic test with externally applied static vertical load.

Figure 6.16 (a) Downhole and (b) crosshole seismic testing at the LCSL.

Examples of wave train records from downhole seismic test at the LCSL are shown in Fig. 6.17. Estimates of wave propagation velocities have been generated for each of the three pairs of downhole sensors. The measured wave propagation velocity was designated at the average depth between a 3-D geophone pair. As explained in Chapter 4, some wave propagation velocities from downhole seismic tests could not be calculated due to poor or irregular waveforms.

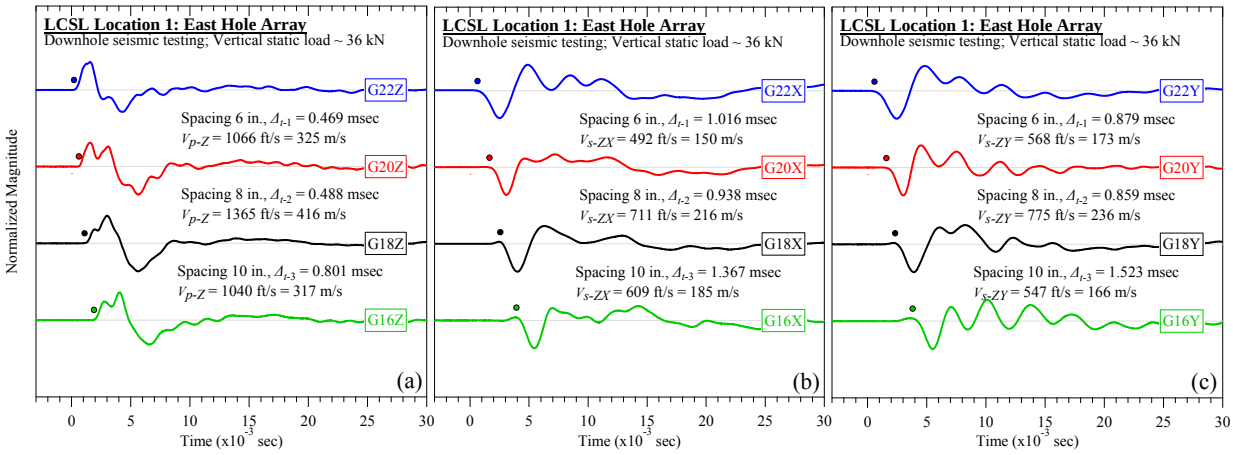

Figure 6.17 Examples of wave trains from small-scale downhole seismic test at the LCSL: (a) V_{p-Z}, (b) V_{s-ZX}, and (c) V_{s-ZY}.

6.4.1 $V_{s\text{-}ZX}$, $V_{s\text{-}ZY}$, and $V_{p\text{-}Z}$ Profiles in Location 1 at the LCSL

The $V_{s\text{-}ZX}$ profiles measured from the small-scale downhole seismic tests in location 1 are presented in Fig. 6.18. These profiles were measured for 5 different static vertical loads. Figures 6.18(a) and 6.18(b) present the $V_{s\text{-}ZX}$ profiles from the east and west hole arrays, respectively. In the east array, the initial $V_{s\text{-}ZX}$ (i.e. at static vertical load of 0 kN) increased from 120 m/s at depth of 0.13 m to 173 m/s at depth of 0.53 m. In the west array, the initial $V_{s\text{-}ZX}$ decreased from 155 m/s at depth of 0.30 m to 147 m/s at depth of 0.53 m. Figures 6.18(a) and 6.18(b) also show that the $V_{s\text{-}ZX}$ increased as the static vertical load increased. For example, at depth of 0.13 m in the east hole array, the $V_{s\text{-}ZX}$ increased from 120 m/s to 190 m/s as the static vertical load increased from 0 kN to 111 kN.

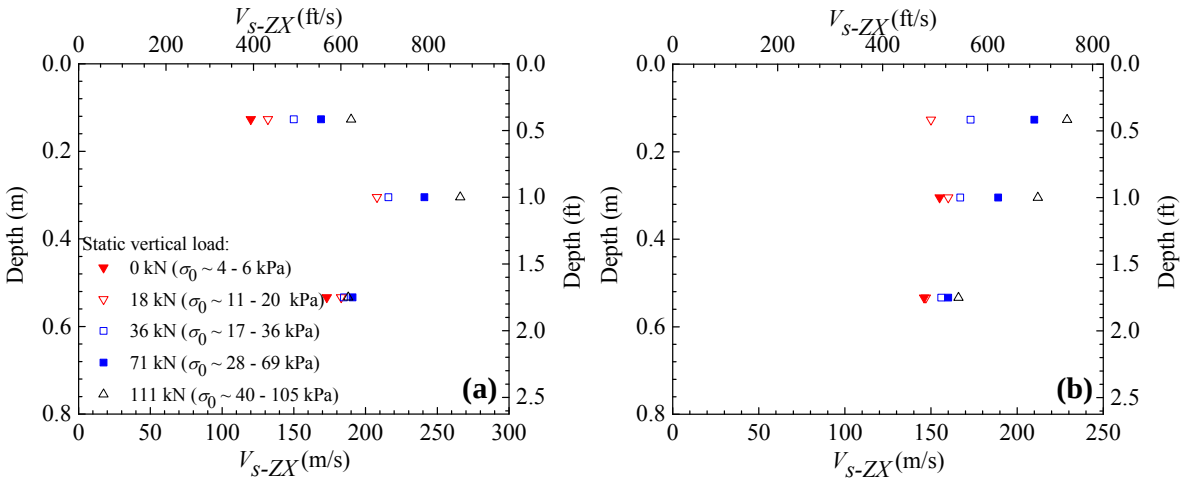

Figure 6.18 $V_{s\text{-}ZX}$ profiles in the (a) east and (b) west hole arrays in location 1 at the LCSL.

The variation of $V_{s\text{-}ZY}$ with depth for 5 different static load levels in location 1 is presented in Fig. 6.19. The $V_{s\text{-}ZY}$ profiles from the east array are shown in Fig. 6.19(a). In this figure, the initial $V_{s\text{-}ZY}$ was 150 m/s at depth of 0.13 m and increased to 216 m/s at depth of 0.30 m and decreased to 160 m/s at depth of 0.53 m. The $V_{s\text{-}ZY}$ profiles from the west array are shown

in Fig. 6.19(b). In the west array, the initial $V_{s\text{-}ZY}$ was 166 m/s at depth of 0.13 m and increased to 182 m/s at depth of 0.30 m and decreased to 146 m/s at depth of 0.53 m.

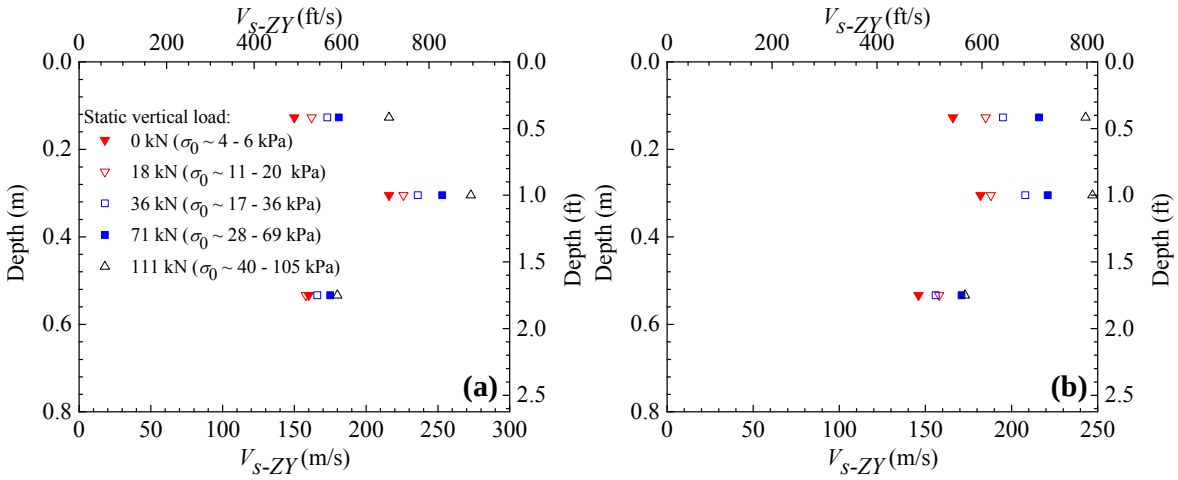

Figure 6.19 $V_{s\text{-}ZY}$ profiles in the (a) east and (b) west hole arrays in location 1 at the LCSL.

The $V_{p\text{-}Z}$ profiles measured from the small-scale downhole seismic tests in location 1 are presented in Fig. 6.20. Figures 6.20(a) and 6.20(b) present the $V_{p\text{-}Z}$ profiles from the east and west hole arrays, respectively. In the east array, the initial $V_{p\text{-}Z}$ at depth of 0.13 m was 269 m/s. The $V_{p\text{-}Z}$ in the waste increased to 358 m/s at depth of 0.30 m and decreased to 295 m/s at depth of 0.53 m. In the west array, the $V_{p\text{-}Z}$ were 278 m/s at depth of 0.13 m, 281 m/s at depth of 0.30 m, and 295 m/s at depth of 0.53 m. As observed in Fig. 6.20, the $V_{p\text{-}Z}$ increased with increasing static vertical load.

The overall variations in wave propagation velocities both with depth as well as between holes in Figs. 6.18, 6.19, and 6.20 show significant vertical and lateral variability of MSW in location 1 over short measuring distances. The observed differences in V_s or V_p with depth, including the occasionally "unexpected" reductions or increases V_s or V_p with depth can be explained when we consider the significant differences in waste composition at the testing scale.

In addition, the increases in wave propagation velocities with static vertical load levels are shown in these figures and are analyzed subsequently.

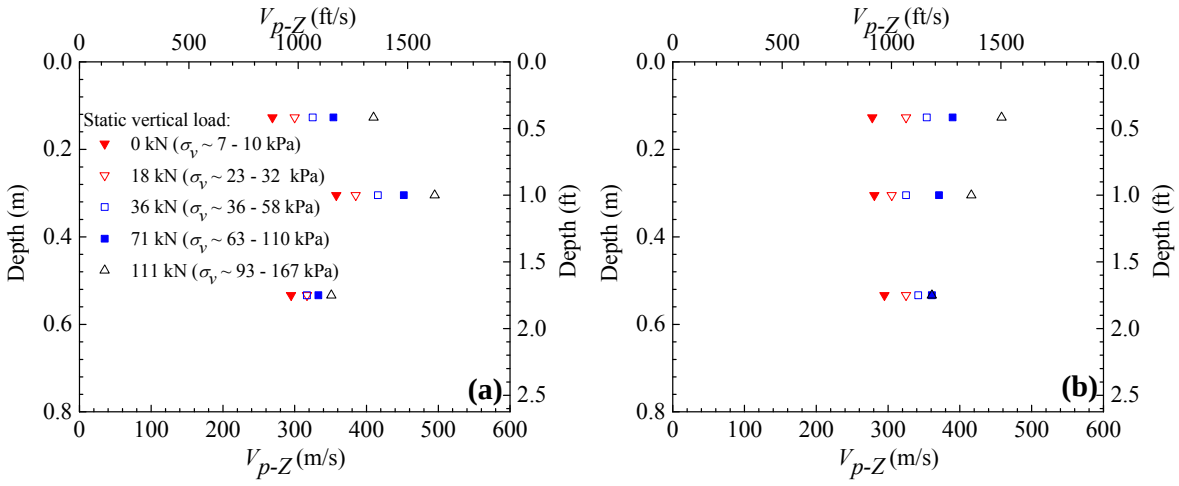

Figure 6.20 $V_{p\text{-}Z}$ profiles in the (a) east and (b) west hole arrays in location 1 at the LCSL.

6.4.2 Effect of Stress State on $V_{s\text{-}ZX}$, $V_{s\text{-}ZY}$, and $V_{p\text{-}Z}$ in Location 1 at the LCSL

As discussed in Chapter 5, wave propagation velocities in MSW depend on the stress state (Zekkos 2005, Lee 2007, Zekkos et al. 2013). To investigate the relationship between wave propagation velocities and the stress state, the vertical (σ_v), horizontal (σ_h), and mean confining (σ_0) stresses were calculated using the Foster and Ahlvin (1954) method as described in Chapter 4. It is known that wave velocity is most affected by stress components aligned with the direction of wave propagation and particle motion (Roesler 1979, Yu and Richart 1984, Stokoe et al. 1985, Fivorante 2000, Stokoe and Santamarina 2000, Wang and Mok 2008). Thus, at each vertical load increment, σ_v was used as correlation parameters for $V_{p\text{-}Z}$, whereas σ_0 was used for and $V_{s\text{-}ZX}$ and $V_{s\text{-}ZY}$. The relationship between these velocities and stresses was regressed using a power function as commonly done for soils (e.g. Hardin and Richart 1963, Hardin and Black 1968, Hryciw and Thomann 1993, Iwasaki and Tatsuoka 1977). For convenience of the reader, the

power functions for $V_{s\text{-}ZX}$, $V_{s\text{-}ZY}$, and $V_{p\text{-}Z}$ are shown again in Eqs. 6.1, 6.2, and 6.3, respectively. Stresses in these equations were normalized with atmospheric pressure (P_a).

$$V_{s-ZX} = A_{vX} \cdot \left(\frac{\sigma_0}{P_a} \right)^{n_{ZX}} \tag{6.1}$$

$$V_{s-ZY} = A_{vY} \cdot \left(\frac{\sigma_0}{P_a} \right)^{n_{ZY}} \tag{6.2}$$

$$V_{p-Z} = A_{pZ} \cdot \left(\frac{\sigma_v}{P_a} \right)^{n_{pZ}} \tag{6.3}$$

where A_{ij} is an empirical constant that indicates corresponding wave propagation velocity at 1 atm and n_{ij} is an empirical constant that quantifies the effect of stress on the corresponding wave propagation velocity.

As mentioned earlier, some wave propagation velocities from downhole seismic tests could not be calculated due to poor or irregular waveforms. The lack of some data points may result in difficulty in performing regression analysis, particularly for shallower depths where the bi-linear relationship between wave propagation velocities and stresses is expected. Thus, some regression analyses were not executed if the lack of data points was considered to have a significant impact on the regression analysis results.

Figures 6.21, 6.22, and 6.23 illustrate the $V_{s\text{-}ZX}$, $V_{s\text{-}ZY}$, and $V_{p\text{-}Z}$ variations with stresses, respectively. A bi-linear relationship of wave propagation velocities with stress was observed. Bi-linearity was indicative of the waste being in the overconsolidated (OC) regime due to waste compaction (Stokoe et al. 2011). As stress increased, the MSW reached the normally consolidated (NC) regime. In the OC regime, the stress exponent n_{ZX} for $V_{s\text{-}ZX}$ was found to range

from 0.05 to 0.07, while in the NC regime, the n_{ZX} increased up to 0.28. The n_{ZY} for $V_{s\text{-}ZY}$ ranged from 0.05 to 0.09 in the OC regime and increased to 0.27 in the NC regime. The n_{pZ} for $V_{p\text{-}Z}$ ranged from 0.07 to 0.10 in the OC regime and varied from 0.21 to 0.28 in the NC regime. The interpreted maximum past vertical stress ($\sigma_{v\text{-max}}$) and past mean confining stress ($\sigma_{0\text{-max}}$), as indicated by the change in slope in Figs 6.21, 6.22, and 6.23, were on the order of 50 – 60 kPa and 30 kPa, respectively.

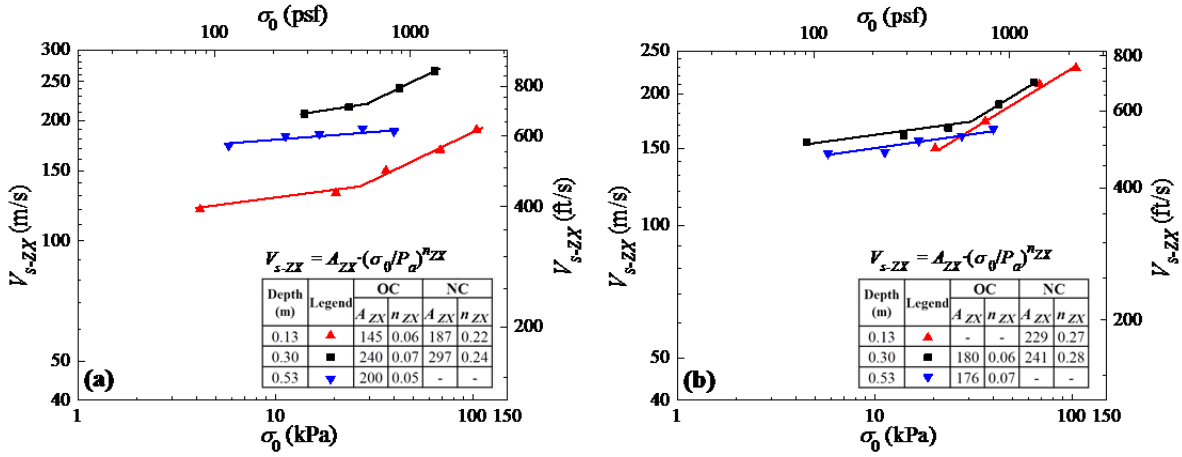

Figure 6.21 Effect of σ_0 on $V_{s\text{-}ZX}$ in the (a) east and (b) west hole arrays in location 1 at the LCSL.

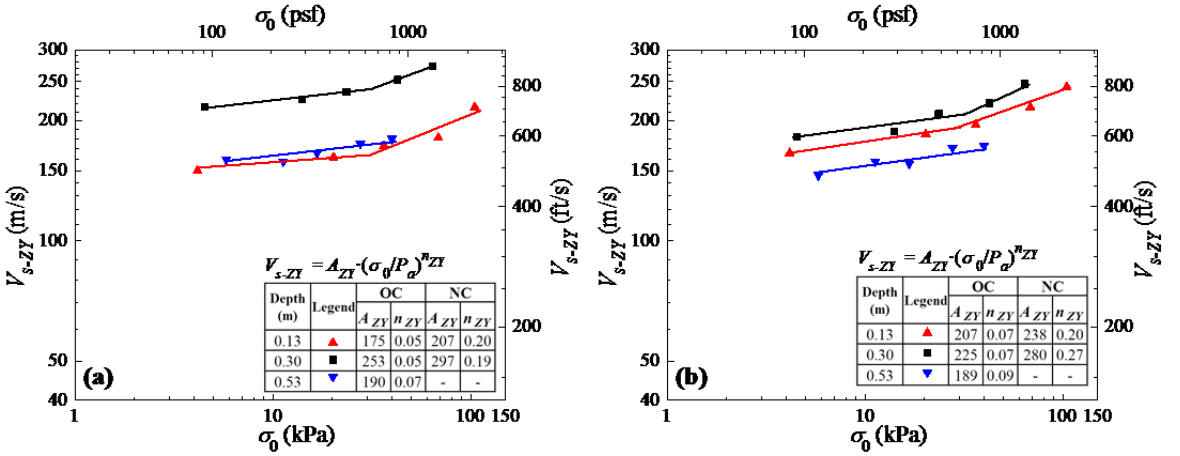

Figure 6.22 Effect of σ_0 on $V_{s\text{-}ZY}$ in the (a) east and (b) west hole arrays in location 1 at the LCSL.

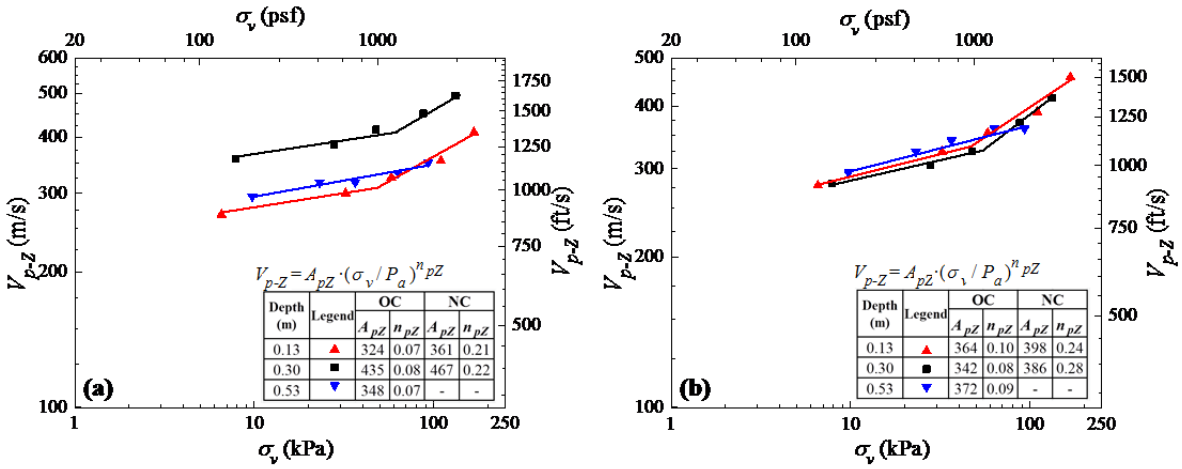

Figure 6.23 Effect of σ_v on $V_{p\text{-}Z}$ in the (a) east and (b) west hole arrays in location 1 at the LCSL.

6.4.3 $V_{s\text{-}ZX}$, $V_{s\text{-}ZY}$, and $V_{p\text{-}Z}$ Profiles in Location 2 at the LCSL

Figure 6.24 shows the variation of $V_{s\text{-}ZX}$ with depth for 5 different static load levels in location 2. Based on Fig 6.24(a), in the east array, the $V_{s\text{-}ZX}$ increased from 106 m/s at depth of 0.13 m to 135 m/ at depth of 0.30 m and increased to 149 m/s at depth of 0.53 m. The variation of $V_{s\text{-}ZX}$ with depth in the west array is shown in Fig. 6.24(b). In the west array, $V_{s\text{-}ZX}$ increased from 125 m/s at depth of 0.13 m to 146 m/ at depth of 0.30 m and decreased to 139 m/s at depth of 0.53 m. As shown in Figure 6.24, $V_{s\text{-}ZX}$ increased with increasing static vertical load.

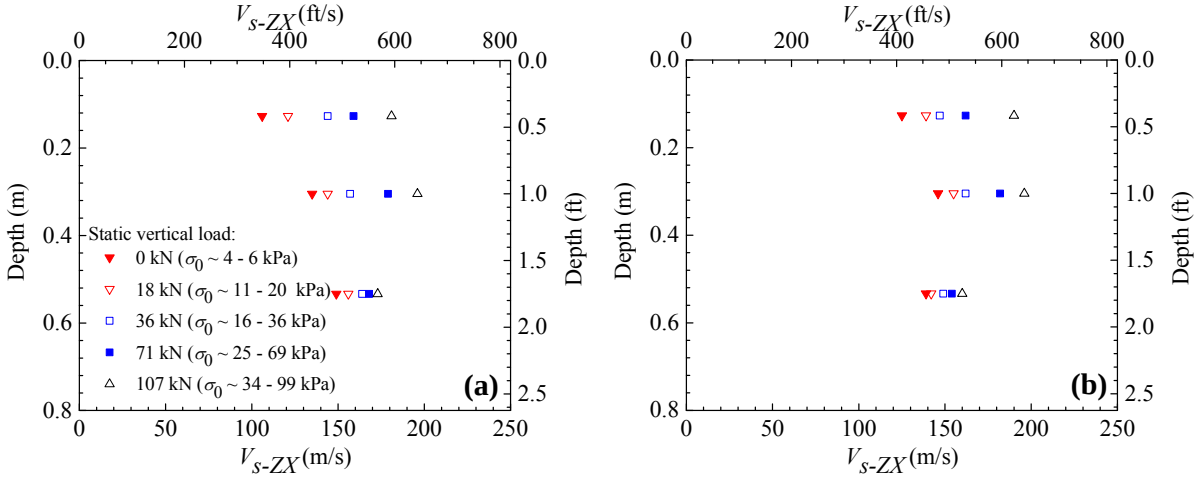

Figure 6.24 $V_{s\text{-}ZX}$ profiles in the (a) east and (b) west hole arrays in location 2 at the LCSL.

The $V_{s\text{-}ZY}$ profiles measured from the small-scale downhole seismic tests at location 2 are presented in Fig. 6.25. Figures 6.25(a) and 6.25(b) present the $V_{s\text{-}ZY}$ profiles from the east and west arrays, respectively. In the east array, the $V_{s\text{-}ZY}$ increased from 130 m/s at depth of 0.13 m to 146 m/s at depth of 0.53 m. In the west array, the $V_{s\text{-}ZY}$ increased from 120 m/s at depth of 0.13 m to 150 m/s at depth of 0.30 m and slightly decreased to 149 m/s at depth of 0.53 m.

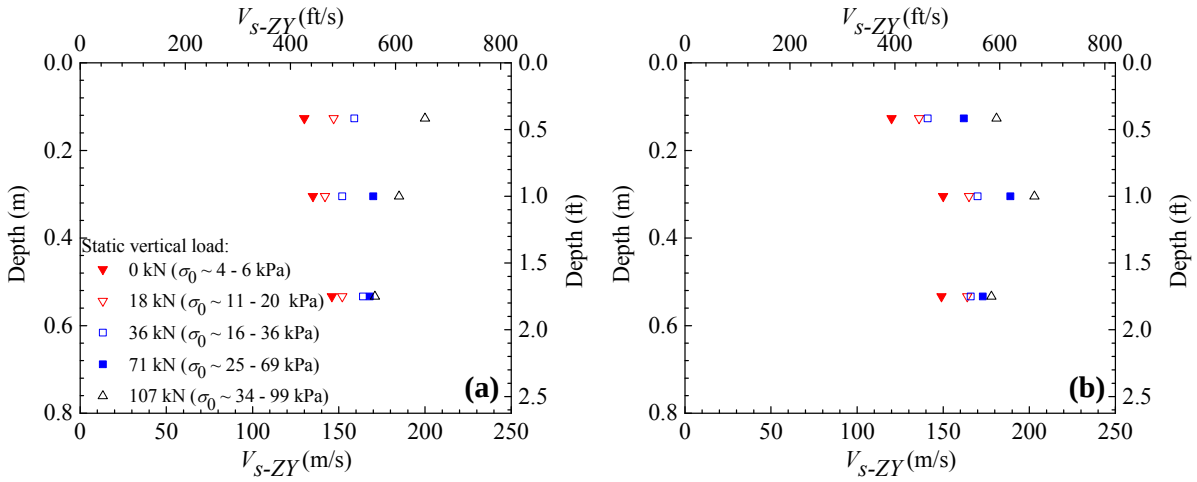

Figure 6.25 $V_{s\text{-}ZY}$ profiles in the (a) east and (b) west hole arrays in location 2 at the LCSL.

Figure 6.26 presents the $V_{p\text{-}Z}$ profiles measured from the small-scale downhole seismic tests at location 2. In the east array [Fig. 6.26(a)], the initial $V_{p\text{-}Z}$ at depth of 0.13 m was 251 m/s. The $V_{p\text{-}Z}$ slightly increased to 266 m/s and 265 m/s at depths of 0.30 m and 0.53 m, respectively. In the west array [Fig. 6.26(b)], the initial $V_{p\text{-}Z}$ were 236 m/s at depth of 0.13 m, 241 m/s at depth of 0.30 m, and 260 m/s at depth of 0.53 m. Figure 6.26 shows that $V_{p\text{-}Z}$ increased with increasing static vertical load.

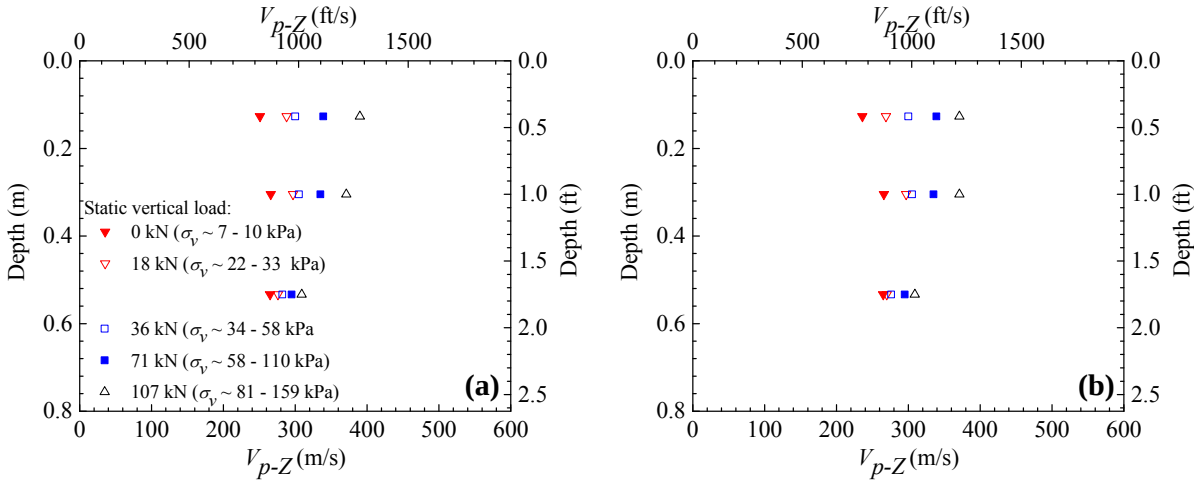

Figure 6.26 $V_{p\text{-}Z}$ profiles in the (a) east and (b) west hole arrays in location 2 at the LCSL.

6.4.4 Effect of Stress State on $V_{s\text{-}ZX}$, $V_{s\text{-}ZY}$, and $V_{p\text{-}Z}$ in Location 2 at the LCSL

Figures 6.27, 6.28, and 6.29 illustrate the $V_{s\text{-}ZX}$, $V_{s\text{-}ZY}$, and $V_{p\text{-}Z}$ variations with stresses in location 2, respectively. In the OC regime, the stress exponent n_{ZX} for $V_{s\text{-}ZX}$ ranged from 0.06 – 0.09, while in the NC regime, the n_{ZX} was on the order of 0.21 to 0.26. The n_{ZY} for $V_{s\text{-}ZY}$ varied from 0.07 to 0.10 in the OC regime and ranged from 0.20 and 0.25 in the NC regime. The n_{pZ} for $V_{p\text{-}Z}$ ranged from 0.07 to 0.09 in the OC regime and varied from 0.21 to 0.29 in the NC regime. As indicated by the change in slope in Figs 6.27, 6.28, and 6.29, the interpreted maximum $\sigma_{v\text{-max}}$ and $\sigma_{0\text{-max}}$ were approximately on the order of 49 – 62 kPa and 26 – 31 kPa, respectively.

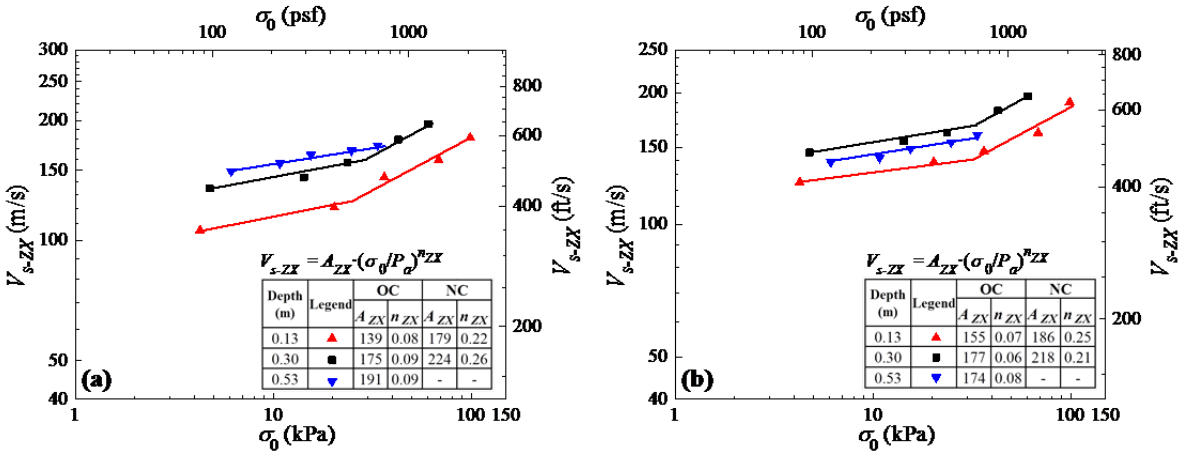

Figure 6.27 Effect of σ_0 on $V_{s\text{-}ZX}$ in the (a) east and (b) west hole arrays in location 2 at the LCSL.

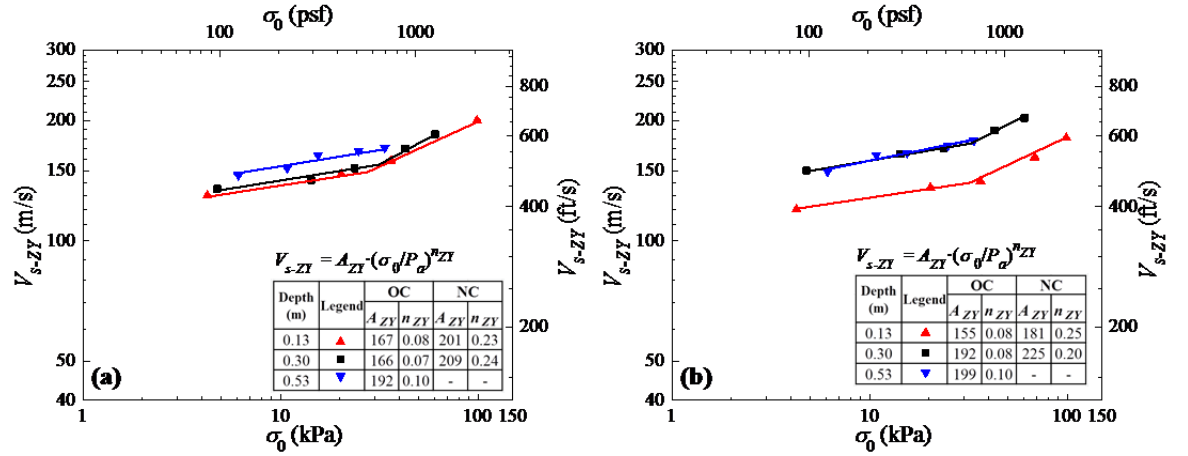

Figure 6.28 Effect of σ_0 on $V_{s\text{-}ZY}$ in the (a) east and (b) west hole arrays in location 2 at the LCSL.

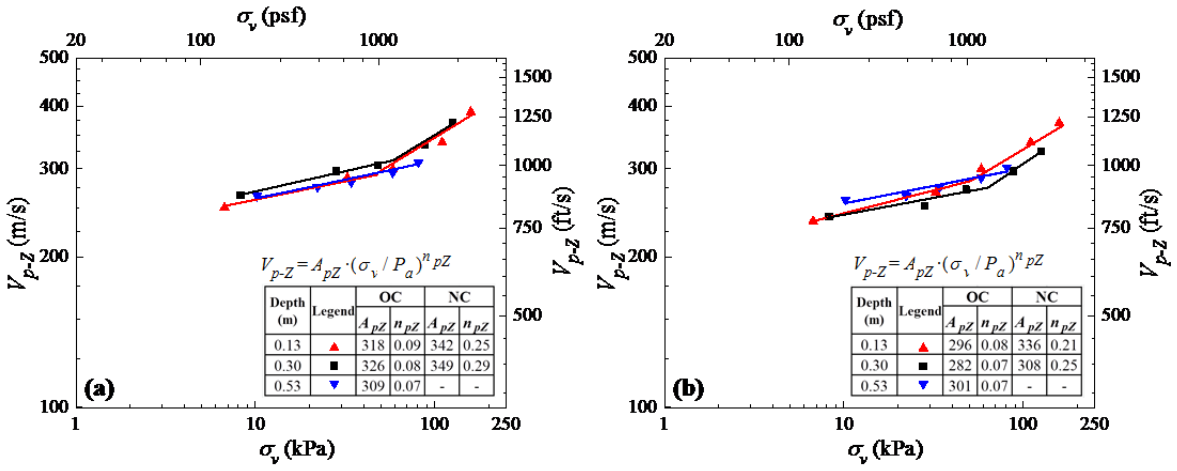

Figure 6.29 Effect of σ_v on $V_{p\text{-}Z}$ in the (a) east and (b) west hole arrays in location 2 at the LCSL.

6.4.5 $V_{s\text{-}ZX}$, $V_{s\text{-}ZY}$, and $V_{p\text{-}Z}$ Profiles in Location 3 at the LCSL

The small-scale downhole seismic tests were performed to investigate $V_{s\text{-}ZX}$ in location 3. Figures 6.30(a) and 6.30(b) present the $V_{s\text{-}ZX}$ profiles from the east and west hole arrays, respectively. These profiles were measured using static vertical load levels ranging from 0 kN to 98 kN. In the east array, the initial $V_{s\text{-}ZX}$ decreased from 125 m/s at depth of 0.13 m to 94 m/s at depth of 0.53 m. In the west array, $V_{s\text{-}ZX}$ decreased from 136 m/s at depth of 0.13 m to 93 m/s at depth of 0.30 m and increased to 106 m/s at depth of 0.53 m. As shown in Figure 6.30, the $V_{s\text{-}ZX}$ increased with increasing vertical static load.

The $V_{s\text{-}ZY}$ profiles measured from the small-scale downhole seismic tests at location 3 are presented in Fig. 6.31. Figures 6.31(a) and 6.31(b) present the $V_{s\text{-}ZY}$ profiles from the east and west arrays, respectively. In the east array, the initial $V_{s\text{-}ZY}$ was generally decreased from 123 m/s at depth of 0.13 m to 96 m/s at depth of 0.53 m. In the west array, the $V_{s\text{-}ZY}$ decreased from 116 m/s at depth of 0.13 m to 108 m/s at depth of 0.53 m.

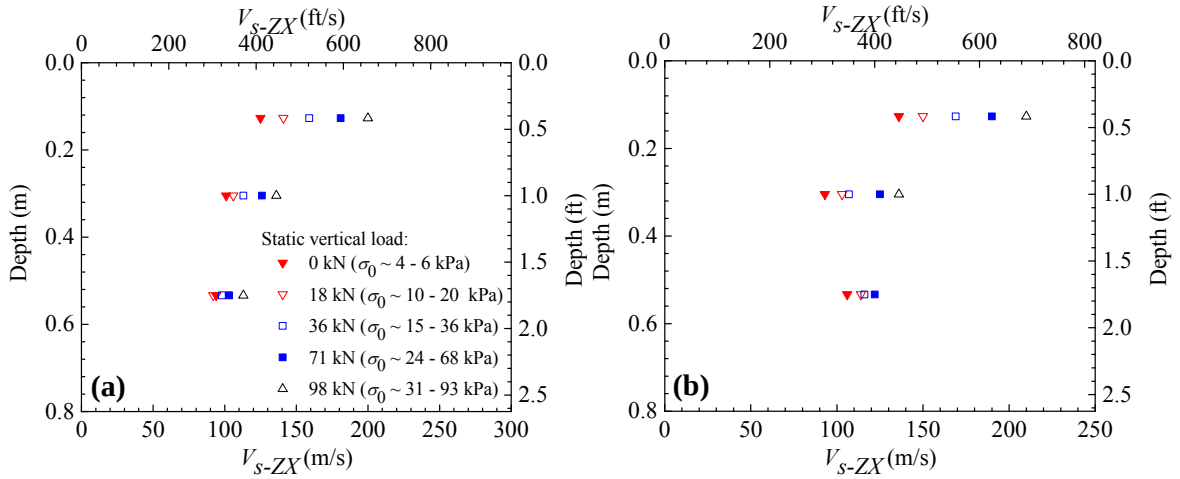

Figure 6.30 $V_{s\text{-}ZX}$ profiles in the (a) east and (b) west hole arrays in location 3 at the LCSL.

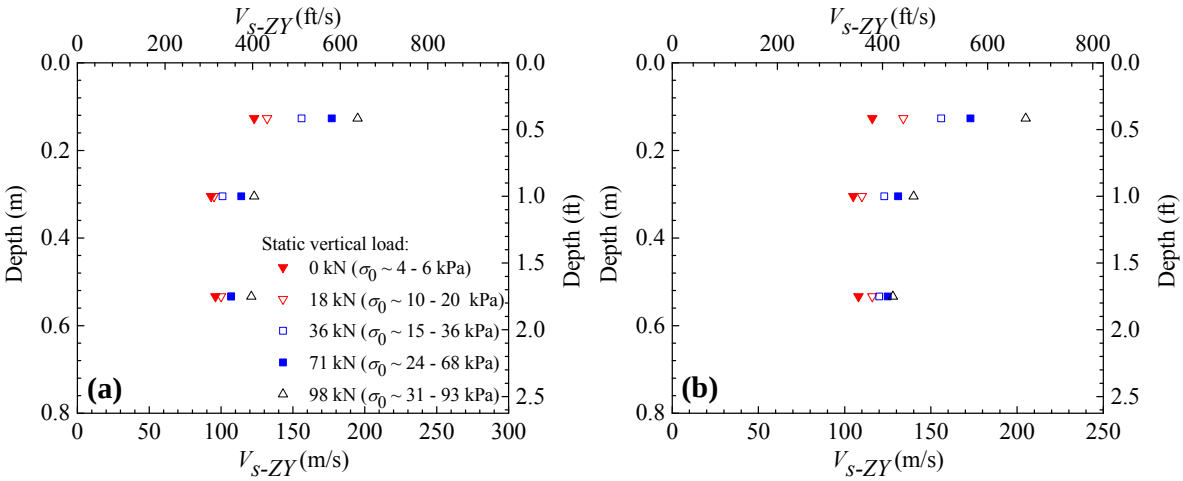

Figure 6.31 $V_{s\text{-}ZY}$ profiles in the (a) east and (b) west hole arrays in location 3 at the LCSL.

The $V_{p\text{-}Z}$ profiles measured from the small-scale downhole seismic tests in location 3 are presented in Fig. 6.32. Figures 6.32(a) and 6.32(b) present the $V_{p\text{-}Z}$ profiles from the east and west hole arrays, respectively. In the east array, the initial $V_{p\text{-}Z}$ at depth of 0.13 m was 251 m/s. The $V_{p\text{-}Z}$ decreased to 170 m/s at depth of 0.30 m and decreased slightly to 168 m/s at depth of 0.53 m. In the west array, the $V_{p\text{-}Z}$ were 251 m/s at depth of 0.13 m, 185 m/s at depth of 0.30 m, and 194 m/s at depth of 0.53 m. As shown in Fig. 6.32, the $V_{p\text{-}Z}$ increased with increasing static vertical load.

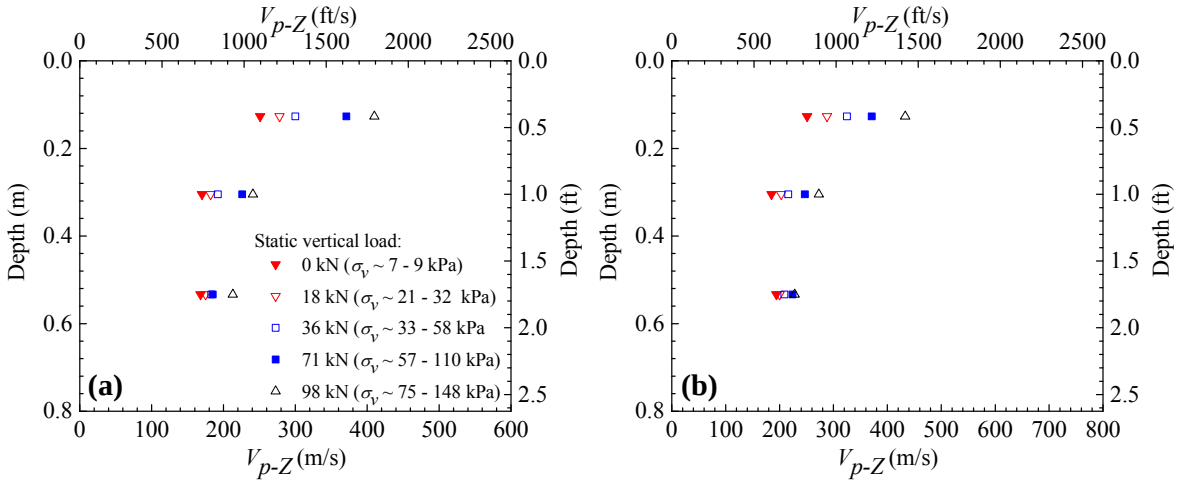

Figure 6.32 $V_{p\text{-}Z}$ profiles in the (a) east and (b) west hole arrays in location 3 at the LCSL.

6.4.6 Effect of Stress State on $V_{s\text{-}ZX}$, $V_{s\text{-}ZY}$, and $V_{p\text{-}Z}$ in Location 3 at the LCSL

The variations of $V_{s\text{-}ZX}$, $V_{s\text{-}ZY}$, and $V_{p\text{-}Z}$ with stresses are presented in Figures 6.33, 6.34, and 6.35, respectively. In the OC regime, the stress exponent n_{ZX} for $V_{s\text{-}ZX}$ ranged from 0.06 – 0.1, while in the NC regime, the n_{ZX} was on the order of 0.22 to 0.29. The n_{ZY} for $V_{s\text{-}ZY}$ varied from 0.04 to 0.09 in the OC regime and increased to 0.23 and 0.27 in the NC regime. The n_{pZ} for $V_{p\text{-}Z}$ ranged from 0.06 to 0.09 in the OC regime and varied from 0.22 to 0.33 in the NC regime. As indicated by the change in slope in Figs 6.33, 6.34, and 6.35, the interpreted maximum $\sigma_{v\text{-max}}$ and $\sigma_{0\text{-max}}$ were approximately on the order of 50 – 61 kPa and 23 – 30 kPa, respectively.

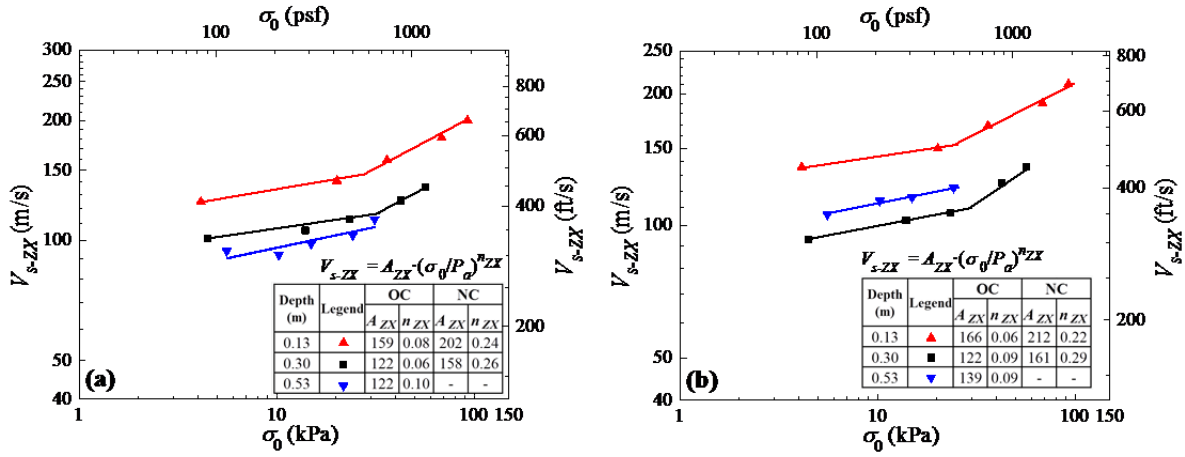

Figure 6.33 Effect of σ_0 on $V_{s\text{-}ZX}$ in the (a) east and (b) west hole arrays in location 3 at the LCSL.

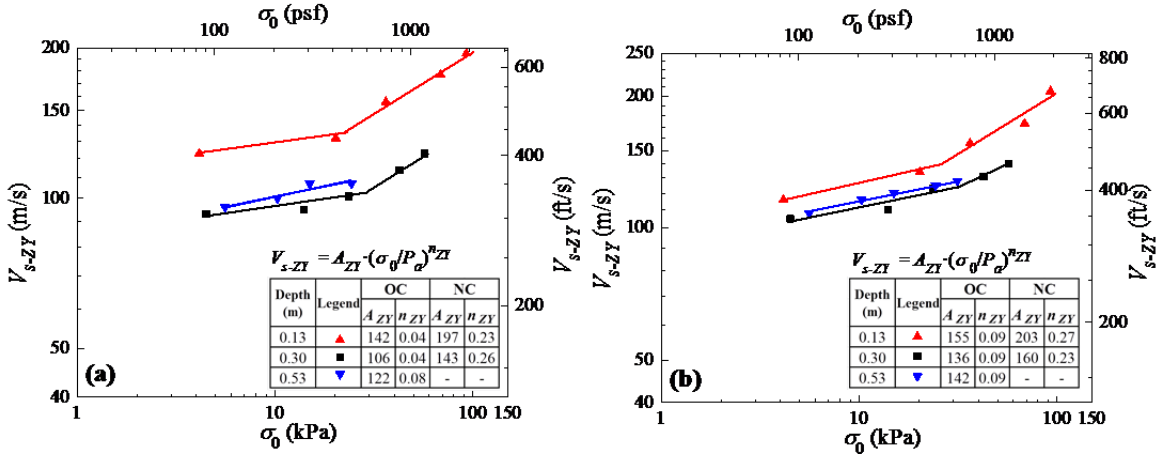

Figure 6.34 Effect of σ_0 on $V_{s\text{-}ZY}$ in the (a) east and (b) west hole arrays in location 3 at the LCSL.

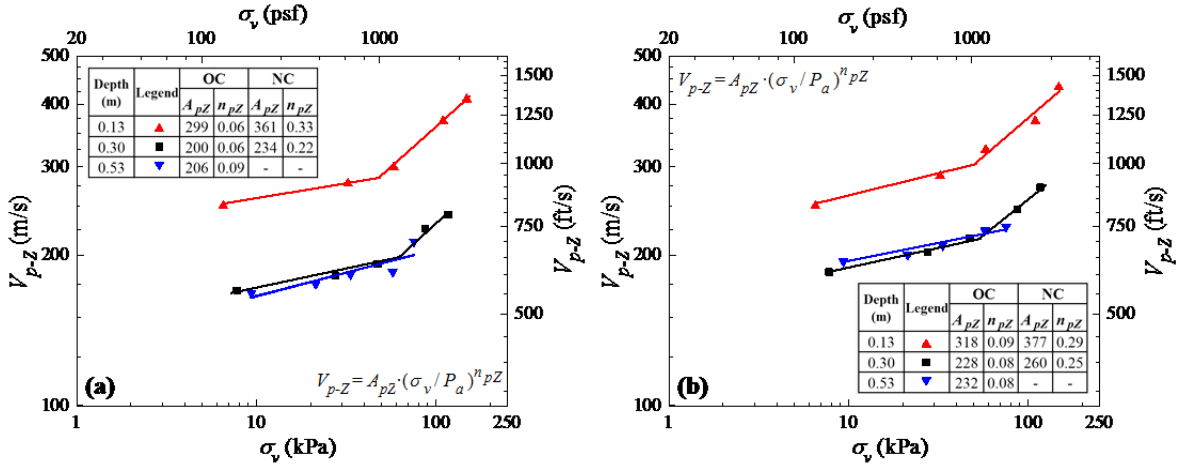

Figure 6.35 Effect of σ_v on $V_{p\text{-}Z}$ in the (a) east and (b) west hole arrays in location 3 at the LCSL.

6.5 **Small-scale Crosshole Seismic Testing**

The small-scale crosshole seismic tests were performed at the LCSL to evaluate horizontally propagating P-wave velocity ($V_{p\text{-}X}$) and horizontally-propagating vertically-polarized in the Z-axis S-wave ($V_{s\text{-}XZ}$). This test was conducted by hitting the crosshole source rods as illustrated in Figure 6.16(b). Figure 6.36 shows an example of wave trains from the small-scale crosshole seismic test.

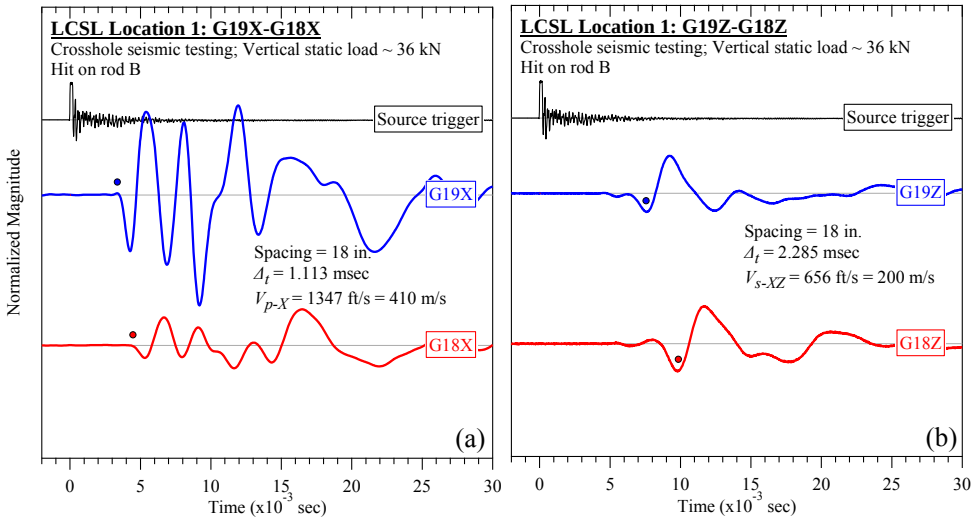

Figure 6.36 Examples of wave trains from small-scale crosshole seismic test at the LCSL: (a) $V_{p\text{-}X}$ and (b) $V_{s\text{-}XZ}$.

Similarly to downhole seismic testing, the relationship between $V_{p\text{-}X}$ and $V_{s\text{-}XZ}$ and stresses was regressed using a power function. In this case, σ_h and σ_0 were used as dependent parameters for $V_{p\text{-}X}$ and $V_{s\text{-}XZ}$, respectively. Relationships between wave propagation velocity and stress component were fitted using the following equations.

$$V_{p-X} = A_{pX} \cdot \left(\frac{\sigma_h}{P_a} \right)^{n_{pX}} \tag{6.4}$$

$$V_{s-XZ} = A_{XZ} \cdot \left(\frac{\sigma_0}{P_a} \right)^{n_{XZ}} \tag{6.5}$$

Some wave propagation velocities from crosshole seismic tests could not be calculated due to poor or irregular waveforms. The lack of some data points may result in difficulty in performing regression analysis, particularly for shallower depths where the bi-linear relationship between wave propagation velocities and stresses is expected. Thus, some regression analyses were not executed if the lack of data points was considered to have a significant impact on the regression analysis results.

Figures 6.37(a) and 6.37(b) show the relationship between $V_{p\text{-}X}$ and $V_{s\text{-}XZ}$ and stress states in location 1, respectively. An either linear or bi-linear relationship between wave propagation velocities and stresses is observed in these figures. In the OC regime, the stress exponent n_{pX} for $V_{p\text{-}X}$ was found to be low (n_{pX} ~ 0.07 – 0.10), while in the NC regime, the n_{pX} increased to 0.18. The n_{XZ} for $V_{s\text{-}XZ}$ ranged from 0.06 to 0.08 in the OC regime and varied from 0.19 to 0.26 in the NC regime.

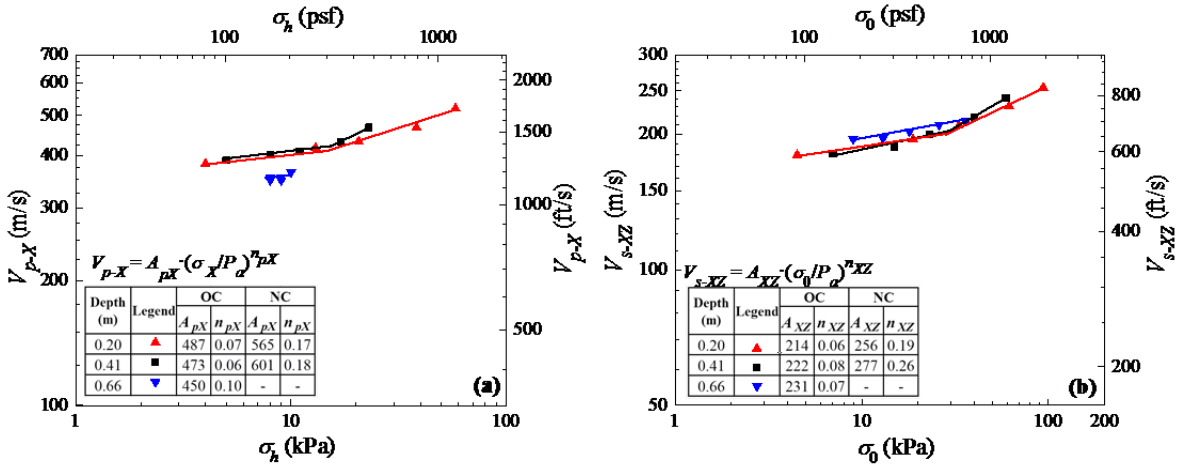

Figure 6.37 Effect of stress states on (a) $V_{p\text{-}X}$ and (b) $V_{s\text{-}XZ}$ in location 1 at the LCSL.

The relationship between $V_{p\text{-}X}$ and $V_{s\text{-}XZ}$ and stress states in location 2 are presented in Figures 6.38(a) and 6.38(b), respectively. An either linear or bi-linear relationship between wave propagation velocities and stresses is observed in these figures. In the OC regime, the stress exponent n_{pX} for $V_{p\text{-}X}$ ranged from 0.08 to 0.10. The n_{XZ} for $V_{s\text{-}XZ}$ ranged from 0.05 to 0.09 in the OC regime. In the NC regime, this exponent varied from 0.21 to 0.29.

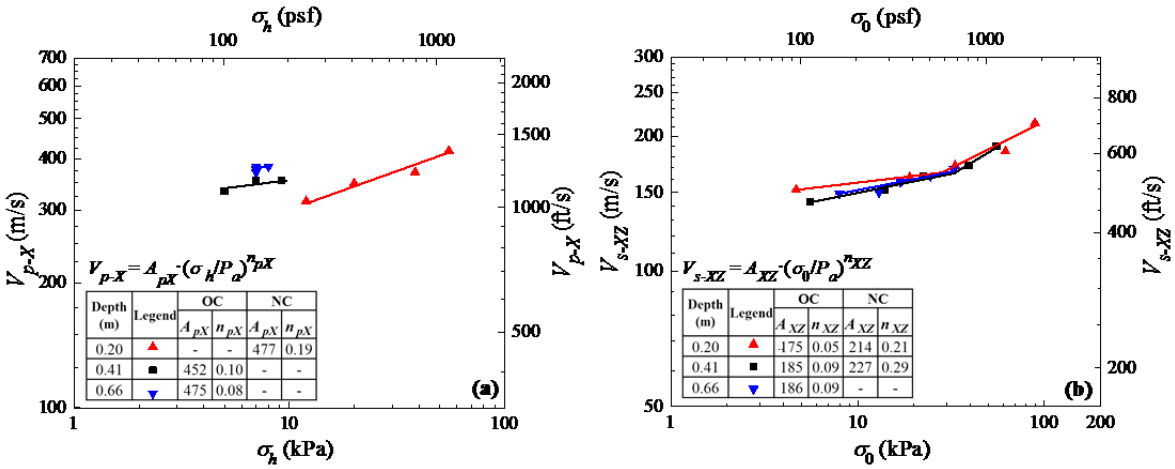

Figure 6.38 Effect of stress states on (a) $V_{p\text{-}X}$ and (b) $V_{s\text{-}XZ}$ in location 2 at the LCSL.

Figures 6.39(a) and 6.39(b) show the relationship between $V_{p\text{-}X}$ and $V_{s\text{-}XZ}$ and stress states in location 3, respectively. The relationship between wave propagation velocities and stresses also exhibited linear or bi-linear form. In the OC regime, the stress exponent n_{pX} for $V_{p\text{-}X}$ ranged from 0.07 – 0.10, while in the NC regime, the n_{pX} was much higher (n_{pX} ~ 0.20 – 0.21). The n_{XZ} for $V_{s\text{-}XZ}$ was 0.08 in the OC regime and increased to 0.25 in the NC regime.

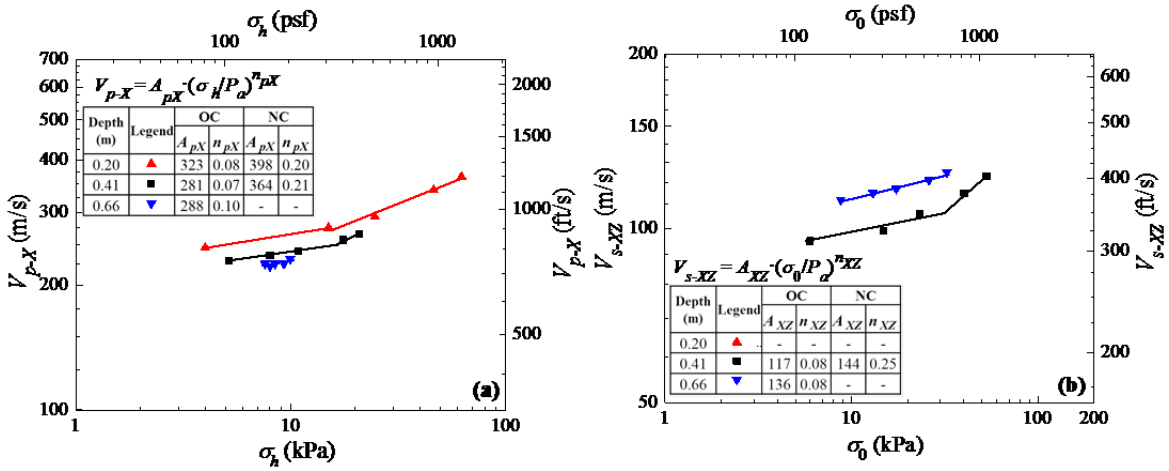

Figure 6.39 Effect of stress states on (a) $V_{p\text{-}X}$ and (b) $V_{s\text{-}XZ}$ in location 3 at the LCSL.

6.6 **Evaluation of Anisotropy of Wave Propagation Velocity in MSW at the LCSL**

As discussed in Chapter 5, anisotropy of wave propagation velocity in MSW may have an important role in landfill engineering practice. To date, the anisotropy of MSW in terms of wave propagation velocities has never been evaluated.

Anisotropy in MSW can be attributed to stress-induced anisotropy and fabric (structural) anisotropy, as discussed in Zekkos (2013). Stress-induced anisotropy is attributed to stress states that are different in the horizontal and vertical directions. Fabric anisotropy is attributed to preferential orientation of fibrous particles in the MSW. Thus, the MSW can still behave anisotropically even in isotropic stress states. In this study, assessment of the degree of anisotropy in MSW was performed by comparing wave velocities from a variety of propagation and polarization directions.

Figure 6.40(a) shows a comparison between P-wave and S-wave velocities propagating in the vertical direction (i.e. $V_{p\text{-}Z}$ and $V_{s\text{-}ZX}$). The ratio of $V_{s\text{-}ZX}$ to $V_{p\text{-}Z}$ in location 1 ranged from 0.44 to 0.59. The ratio of $V_{s\text{-}ZX}$ to $V_{p\text{-}Z}$ in location 2 varied from 0.42 to 0.61. In location 3, the ratio of

$V_{s\text{-}ZX}$ to $V_{p\text{-}Z}$ ranged from 0.48 to 0.59. The mean from three locations shows that the ratio of $V_{s\text{-}ZX}$ to $V_{p\text{-}Z}$ was 0.52.

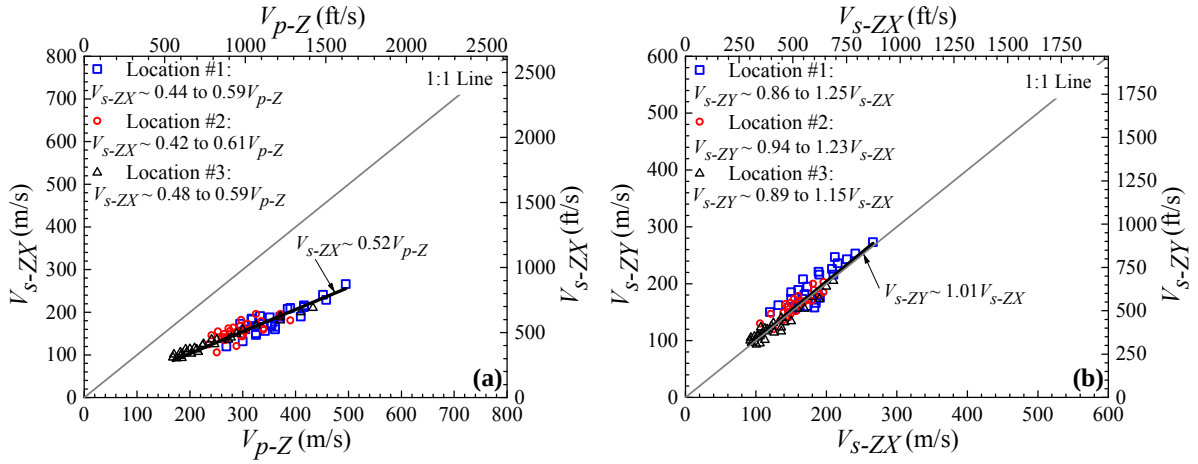

Figure 6.40 Comparison on (a) $V_{p\text{-}Z}$-$V_{s\text{-}ZX}$ and (b) $V_{s\text{-}ZX}$ -$V_{s\text{-}ZY}$ at the LCSL.

Figure 6.40(b) presents a comparison between the $V_{s\text{-}ZX}$ and the $V_{s\text{-}ZY}$. In location 1, the ratio of $V_{s\text{-}ZY}$ to $V_{s\text{-}ZX}$ varied from 0.86 to 1.25. In location 2, the ratio of $V_{s\text{-}ZY}$ to $V_{s\text{-}ZX}$ ranged from 0.94 to 1.23. In location 3, the ratio of $V_{s\text{-}ZY}$ to $V_{s\text{-}ZX}$ varied from 0.89 to 1.15. The average ratio from three locations was found to be 1.01 indicating minor difference on average between S-wave propagation velocities in the YZ and the XZ plane, which is expected.

Figure 6.41 shows a comparison between P-wave and S-wave velocities propagating in the horizontal direction (i.e. $V_{p\text{-}X}$ and $V_{s\text{-}XZ}$). In location 1, the ratio of $V_{s\text{-}XZ}$ to $V_{p\text{-}X}$ ranged from 0.46 to 0.59. In location 2, this ratio varied from 0.40 to 0.51. In location 3, this ratio varied from 0.41 to 0.54. In general, the ratio of $V_{s\text{-}XZ}$ to $V_{p\text{-}X}$ in three test locations at the LCSL ranged from 0.40 to 0.59 with a mean value of 0.48. This ratio was slightly lower than the ratio of V_p and V_s counterparts propagating in the vertical direction.

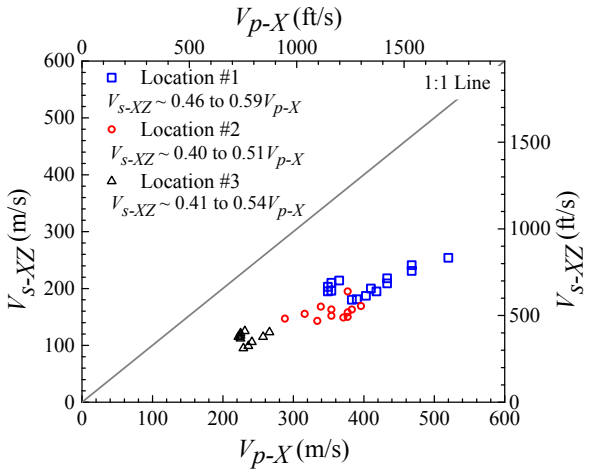

Figure 6.41 Comparison on $V_{p\text{-}X}$ and $V_{s\text{-}XZ}$ at the LCSL.

Anisotropy in MSW was also evaluated by comparing wave propagation velocities in the horizontal and vertical directions. Because the designated measurement points from downhole and crosshole seismic tests were not the same, four $V_{p\text{-}Z}$ values from downhole tests were averaged and then compared with a $V_{p\text{-}X}$ from a crosshole test, as shown in Fig 6.42. The same method was also performed in comparing shear wave velocity propagating in the vertical and horizontal directions.

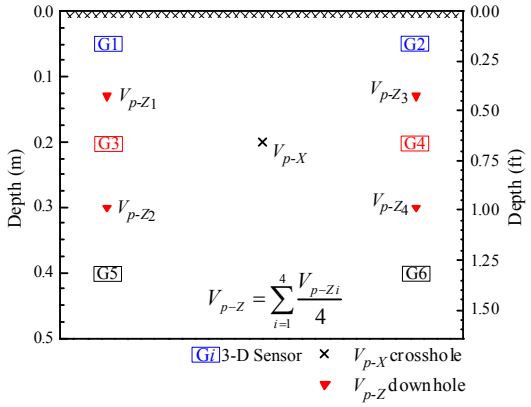

Figure 6.42 Example of measurement points for comparing wave propagation velocities in the vertical and horizontal directions.

Figure 6.43(a) shows a comparison between V_p propagating in the horizontal ($V_{p\text{-}X}$) and vertical ($V_{p\text{-}Z}$) directions. In location 1, the ratios of $V_{p\text{-}Z}$ to $V_{p\text{-}X}$ varied from 0.77 to 0.88. In

location 2, the ratios of $V_{p\text{-}Z}$ to $V_{p\text{-}X}$ varied from 0.77 to 0.88. In location 3, the ratios of $V_{p\text{-}Z}$ to $V_{p\text{-}X}$ varied from 0.78 to 0.93. The ratio of $V_{p\text{-}Z}$ to $V_{p\text{-}X}$ from three locations ranged from 0.77 to 0.93 with a mean value of 0.84. This ratio indicated that the compressibility of MSW in the horizontal direction was lower than the compressibility in the vertical direction.

The relationship between V_s propagating in the horizontal ($V_{s\text{-}horizontal}$: $V_{s\text{-}XZ}$) and vertical ($V_{s\text{-}vertical}$: $V_{s\text{-}ZX}$ and $V_{s\text{-}ZY}$) directions is shown in Figure 6.43(b). The ratio of $V_{s\text{-}vertical}$ and $V_{s\text{-}horizontal}$ were found to be between 0.67 and 1.06 with an average value of 0.92. In general, the data indicated that wave propagation in the vertical direction was slower than that in the horizontal direction, highlighting that MSW is an anisotropic material.

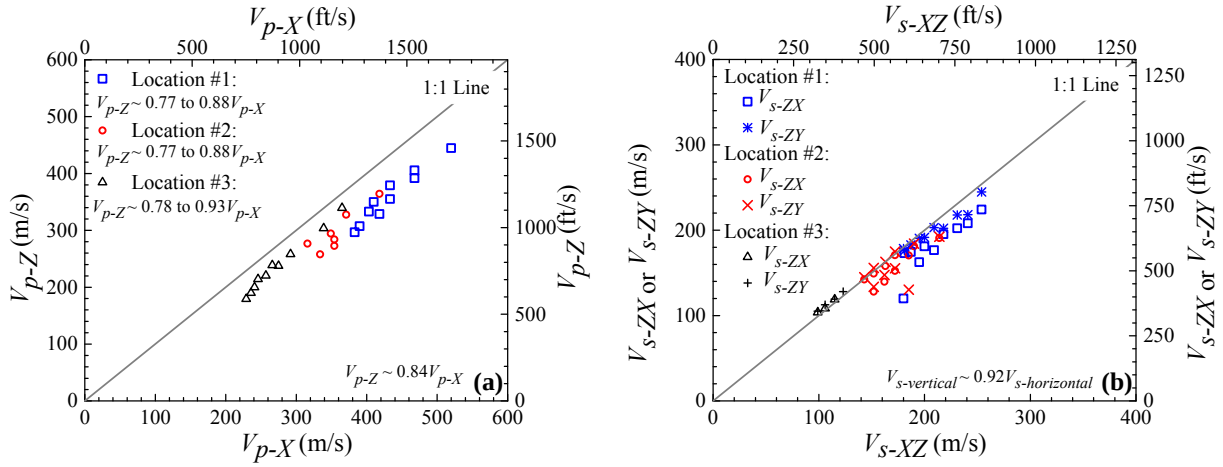

Figure 6.43 (a) Comparison on V_p propagating in the vertical and horizontal directions; and (b) V_s propagating in the vertical and horizontal directions at the LCSL.

6.7 **Evaluation of Poisson's ratio at the LCSL**

The V_p and V_s from small-strain downhole and crosshole seismic tests can be used to evaluate small-strain Poisson's ratio based on elasticity equation (Eq. 2.13). It should be noted that this equation was derived for homogeneous, isotropic, and elastic solid material. For anisotropic material, such as MSW, the meaning of Poisson's ratio can be very complex. Nevertheless, Eq.

2.13 was used to evaluate Poisson's ratio of MSW by Sharma et al. (1990), Houston et al. (1995), Matasovic and Kavazanjian (1998), and Zalachoris (2010). In this study, the V_p and V_s values from downhole and crosshole seismic tests were used to evaluate "pseudo" Poisson's ratio. "Pseudo" Poisson's ratios v_{ZX} and v_{ZY} from downhole seismic testing were estimated using Eqs. 6.6 and 6.7 that have identic expression to Eq. 2.13.

$$\nu_{ZX} = \frac{0.5 \cdot \left(V_{s-ZX} / V_{p-Z}\right)^2 - 1}{\left(V_{s-ZX} / V_{p-Z}\right)^2 - 1} \tag{6.6}$$

$$\nu_{ZY} = \frac{0.5 \cdot \left(V_{s-ZY} / V_{p-Z}\right)^2 - 1}{\left(V_{s-ZY} / V_{p-Z}\right)^2 - 1} \tag{6.7}$$

The "pseudo" Poisson's ratio v_{XZ} was evaluated using small-scale crosshole seismic test results (Eq. 6.8).

$$\nu_{XZ} = \frac{0.5 \cdot \left(V_{s-XZ} / V_{p-X}\right)^2 - 1}{\left(V_{s-XZ} / V_{p-X}\right)^2 - 1} \tag{6.8}$$

Poisson's ratio variation with depth from downhole and crosshole seismic tests in location 1 at the LCSL is presented in Figs. 6.44. In location 1, the v_{ZX} and v_{ZY} ranged from 0.29 to 0.38 and 0.23 to 0.32 at depth of 0.13 m, respectively. At depth of 0.30 m, the v_{ZX} and v_{ZY} ranged from 0.29 to 0.32 and from 0.14 to 0.28, respectively. At depth of 0.53 m, the v_{ZX} and v_{ZY} varied from 0.24 to 0.38 and 0.29 to 0.37, respectively. The v_{XZ} ranged from 0.23 to 0.38.

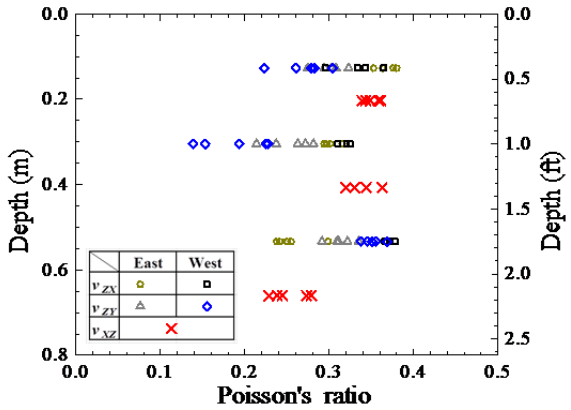

Figure 6.44 Small-strain Poisson's ratio evaluated using V_s and V_p in location 1 at the LCSL.

Poisson's ratio variation with depth from downhole and crosshole seismic tests in location 2 at the LCSL is presented in Fig. 6.45. The v_{ZX} and v_{ZY} ranged from 0.30 to 0.39 and 0.30 to 0.36 at depth of 0.13 m, respectively. At depth of 0.30 m, the v_{ZX} and v_{ZY} varied from 0.20 to 0.35 and from 0.13 to 0.35, respectively. At depth of 0.53 m, the v_{ZX} and v_{ZY} ranged from 0.26 to 0.30 and 0.19 to 0.28, respectively. The v_{XZ} varied from 0.32 to 0.41.

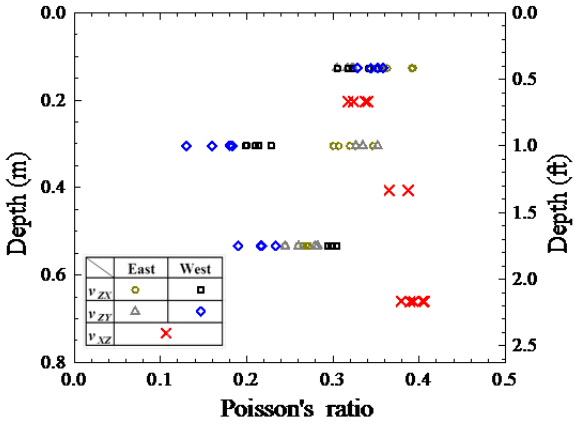

Figure 6.45 Small-strain Poisson's ratio evaluated using V_s and V_p in location 2 at the LCSL.

Figure 6.46 shows the Poisson's ratio variation with depth from downhole and crosshole seismic tests in location 3 at the LCSL. In this location, the v_{ZX} and v_{ZY} varied from 0.29 to 0.34 and 0.31 to 0.36 at depth of 0.13 m, respectively. At depth of 0.30 m, the v_{ZX} and v_{ZY} ranged from

0.23 to 0.34 and from 0.26 to 0.33, respectively. At depth of 0.53 m, the v_{ZX} and v_{ZY} ranged from 0.27 to 0.31 and 0.24 to 0.27, respectively. The v_{XZ} ranged from 0.29 to 0.39.

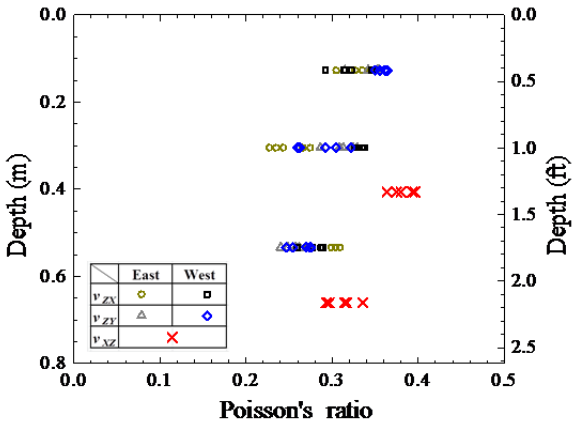

Figure 6.46 Small-strain Poisson's ratio evaluated using V_s and V_p in location 3 at the LCSL.

The v_{ZX} and v_{ZY} at the same measurement point were in some cases the same and in other cases different. In general, large scatter in Figs. 6.44, 6.45, and 6.46 could be attributed to the variability of the waste within a test location as well as the anisotropic nature of the waste.

6.8 **Multichannel Analysis of Surface Wave and Microtremor Analysis Method Tests at the LCSL**

A combination of Multichannel Analysis of Surface Wave (MASW) and Microtremor Analysis Method (MAM) tests was conducted in three locations at the LCSL (Fig. 6.2). Figure 6.47 shows the application of the surface wave testing at the LCSL. In this investigation, sixteen 4.5 Hz geophones (Geospace GS 11-D) were used and were positioned with spacing of 0.91 m (3 ft) and 3 m (10 ft) in a linear array. In the MASW or active method, data acquisition was performed by recording the ground roll generated using a 6.8-kg sledge hammer. In the MAM or passive test, data was acquired by recording background noise. The testing procedure used in the surface wave test is described in Chapter 3 in detail.

Figure 6.47 Surface wave testing at the LCSL: (a) MASW and (b) MAM.

Figure 6.48 presents the theoretical and field combined dispersion curves (i.e. joint MASW and MAM) from location 1 at the LCSL. In this figure, raw dispersion curves from active and passive tests are also presented. Dispersion curve from location 1 had frequency content ranging from 2.3 Hz to 30 Hz that corresponded with Rayleigh wave or phase velocity (V_{ph}) of 243 m/s to 103 m/s. Figure 6.49 shows the V_s profile inverted from the dispersion curves in location 1 at the LCSL. Near surface shear wave velocity was 103 m/s and increased to 225 m/s at depth of 33 m. In general, the shear wave velocities from downhole and crosshole seismic tests were relatively higher than those of surface wave testing test. It should be noted that the downhole and crosshole seismic tests are more localized measurements than surface wave testing. Different results between those tests may occur, particularly in MSW where waste variability could be high within a small area and at the scale and frequency range of the various methods. In location 1, the highest frequency in the dispersion curve corresponded with the shortest wavelength (λ) of 3.4 m. By assuming a wavelength to depth of investigation conversion factor of 0.5 (Ballard 1964), the shallowest reliable depth of investigation was about 1.7 m. This resulted in uncertainty in the shear wave velocity for the top 1.7 m from the surface wave testing.

The downhole and crosshole seismic tests better captured the localized shear wave velocity variability at shallower depth than 1.7 m.

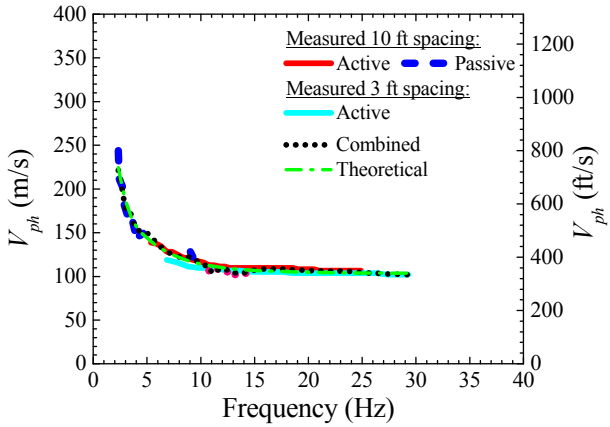

Figure 6.48 Dispersion curves from location 1 at the LCSL.

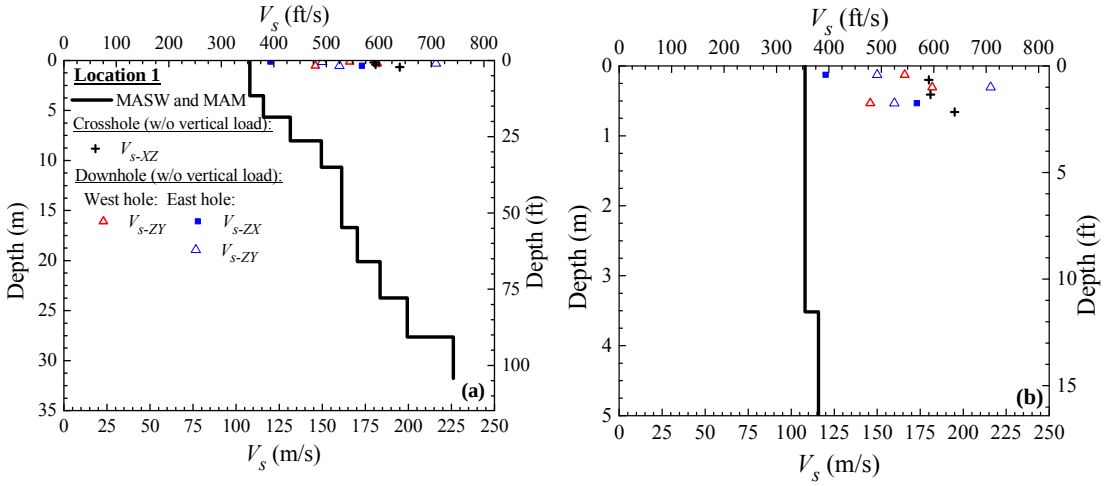

Figure 6.49 Shear wave velocity profile in location 1 at the LCSL: (a) up to 35 m and (b) up to 5 m.

The theoretical and field combined dispersion curves from location 2 at the LCSL are presented in Figs. 6.50. Frequency content of this dispersion curve ranged from 2.3 Hz to 30 Hz that corresponded with V_{ph} of 83 m/s to 333 m/s. The V_s profile in location 2 at the LCSL is presented in Fig. 6.51. The shear wave velocity profiles varied from 90 m/s to 458 m/s from the surface to depth of 45 m. A stiffer layer with shear wave velocity of 186 m/s was observed at

depth of 7 to 13 m. The shear wave velocities from downhole and crosshole seismic testing are presented in Fig. 6.51(b). In general, the shear wave velocities from downhole and crosshole seismic tests were relatively higher than those of surface wave testing. The highest frequency in the dispersion curve corresponded with the shortest λ of 2.8 m. Thus, the shallowest reliable depth of investigation from the surface wave testing was about 1.4 m by assuming a wavelength to depth of investigation conversion factor of 0.5 (Ballard 1964). The downhole and crosshole seismic tests better identified the localized shear wave velocity variability at shallower depth than 1.4 m.

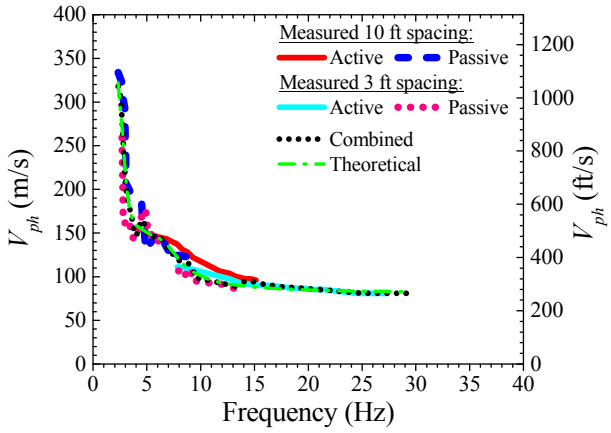

Figure 6.50 Dispersion curves from location 2 at the LCSL.

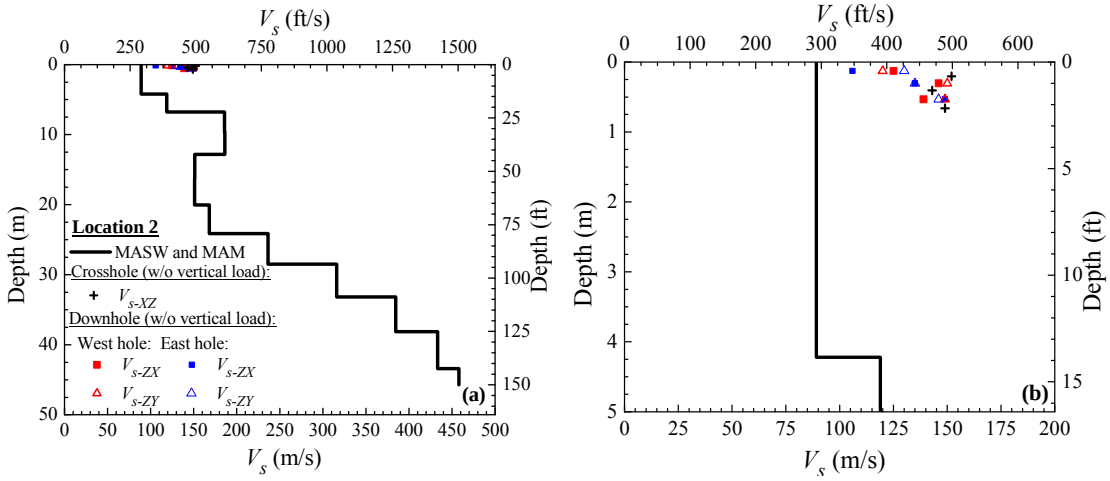

Figure 6.51 Shear wave velocity profile in location 2 at the LCSL: (a) up to 50 m and (b) up to 5 m.

Figure 6.52 presents the theoretical and field combined dispersion curves in location 3 at the LCSL. Raw dispersion curve from active and passive tests are also presented in this figure. Dispersion curve from location 3 had frequency content ranging from 2.7 Hz to 20 Hz that corresponded with Rayleigh wave or phase velocity (V_{ph}) of 204 m/s to 89 m/s. Figure 6.53 shows the V_s profiles in location 3 at the LCSL. In general, near surface shear wave velocity was 83 m/s and increased to 188 m/s at depth of 25 m. The shear wave velocities from downhole and crosshole seismic tests were relatively higher than those of surface wave testing test. But, the differences were not as high as the other two test locations. In location 3, the highest frequency in the dispersion curve corresponded with the shortest λ of 4.5 m. By assuming a wavelength to depth of investigation conversion factor of 0.5 (Ballard 1964), the shallowest reliable depth of investigation was about 2.25 m. This resulted in uncertainty in the shear wave velocity for the top 2.25 m from the surface wave testing.

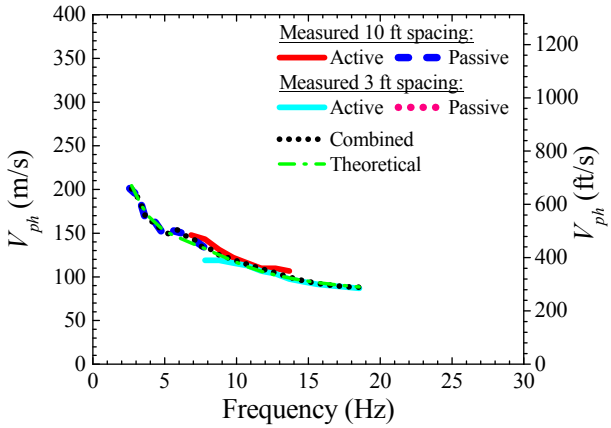

Figure 6.52 Dispersion curves from location 3 at the LCSL.

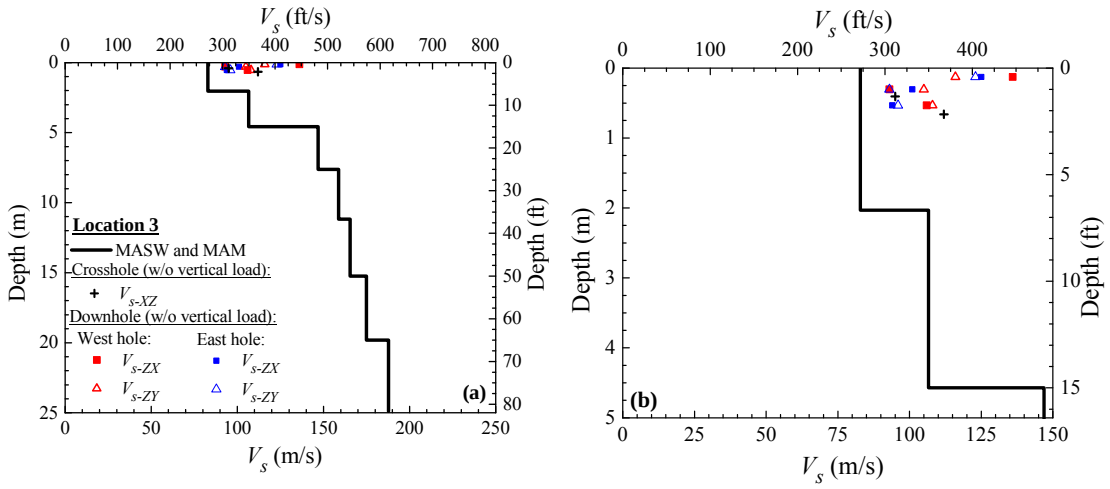

Figure 6.53 Surface wave testing result in location 3 at the LCSL: (a) up to 25 m and (b) up to 5 m.

Figure 6.54 presents the statistical analysis results of V_s profiles from the surface wave test at the LCSL. On average, V_s value was about 93 m/s at the surface and increases up to 208 m/s at depth of 25 m. Coefficient of variance (COV) ranged from 0.05 to 0.18 with an average of 0.09.

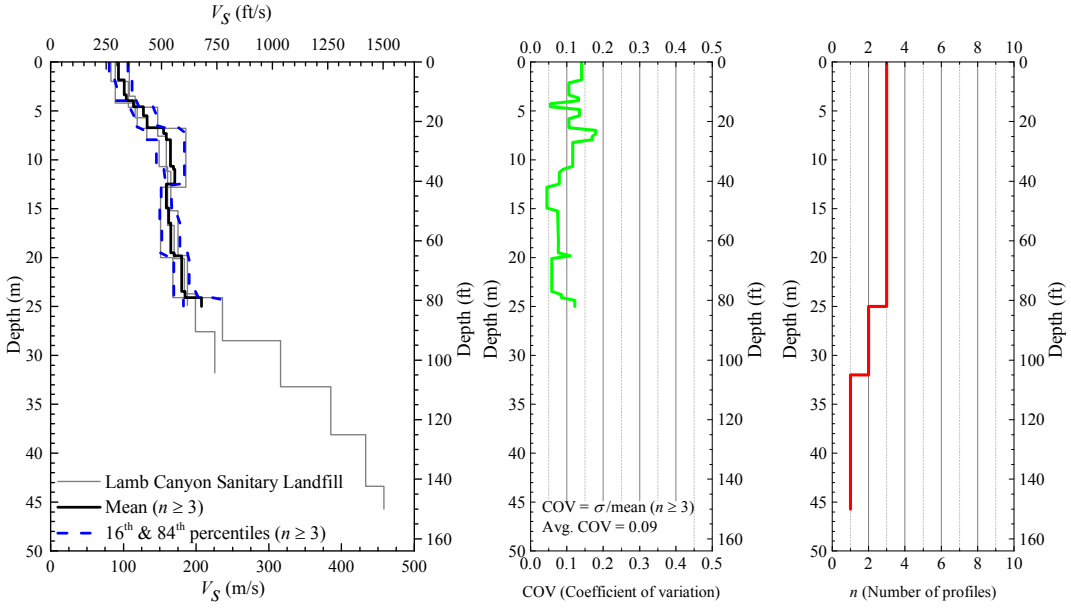

Figure 6.54 Statistical analysis of V_s profiles from surface wave testing at the LCSL.

6.9 **Steady-state Dynamic Testing**

Steady-state dynamic test using Thumper and T-Rex was conducted to study the relationship between shear modulus or normalized shear modulus and shearing strain at the LCSL (Fig. 6.55). This test was performed at different static vertical load levels to study the effect of confining stress on the shear modulus and normalized shear modulus reduction curves. In each test location at the LCSL, Thumper or T-Rex was used to impose static vertical loads of 18 kN, 36 kN, 71 kN, and 133 kN as described in Figs. 6.10, 6.11, and 6.12. Thumper was used for steady-state test with static vertical load up to 36 kN. At each vertical static load level, dynamic horizontal loads were applied from small to large amplitude. Chapter 4 describes the testing method of the steady-state dynamic testing as well as the limitations and uncertainties of this method. In this section, the results are presented.

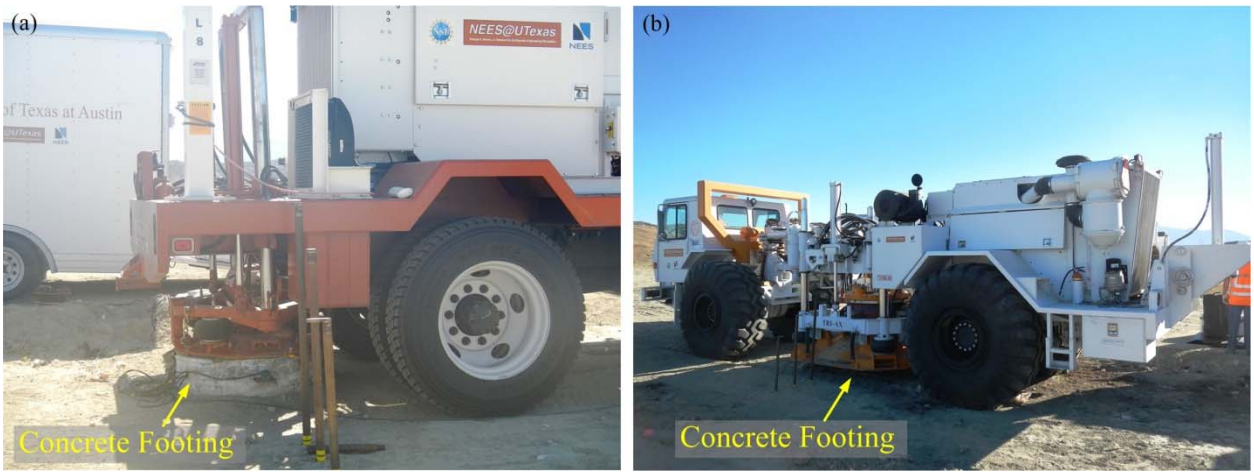

Figure 6.55 Steady-state dynamic testing using (a) Thumper and (b) T-Rex at the LCSL.

Figure 6.56 shows the quadrilateral elements for location 1 at the LCSL. Elements A, D, and F were defined by four adjacent geophones. Element A was defined by the four sensors closest to the surface, element D was defined by the four intermediate sensors, and element F was defined by the four deepest sensors. Element C was defined by the two deepest and the two

shallowest geophones. Figures 6.57 and 6.58 present the quadrilateral elements for locations 2 and 3 at the LCSL, respectively.

Shear modulus was calculated using the shear wave velocity and mass density of MSW. Vertically propagating shear wave velocity was calculated using the phase difference in travel time as shown in Fig. 6.59(a). Mass density was obtained from in-situ unit weight measurements. The average of the shear modulus calculated from both arrays was used as the shear modulus of each element. It should be noted that the mass density may affect the accuracy in shear modulus calculation, but, does not affect the normalized shear modulus reduction curve. The 4-node displacement based method (Rathje et al. 2005) was used to calculate the shearing strain at the center of quadrilateral elements. Example of shearing strain time history calculated using the 4-node method is shown in Fig. 6.59(b). The analysis method to reduce data from the steady-state test is described in detail in Chapter 4. The results of normalized shear modulus reduction curves from this site were used to develop recommended G/G_{max} curves in Chapter 9.

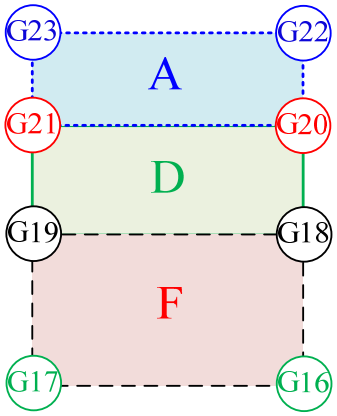

Element	Geophones/Nodes
A	G20, G21, G23, G22
D	G18, G19, G21, G20
F	G16, G17, G19, G18
C = A+D+F	G16, G17, G23, G22

Figure 6.56 Quadrilateral elements for location 1 at the LCSL.

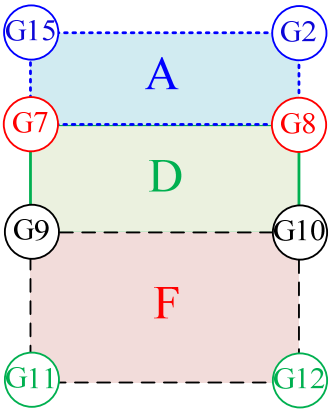

Element	Geophones/Nodes
A	G8, G7, G15, G2
D	G10, G9, G7, G8
F	G12, G11, G9, G10
C = A+D+F	G12, G11, G15, G2

Figure 6.57 Quadrilateral elements for location 2 at the LCSL.

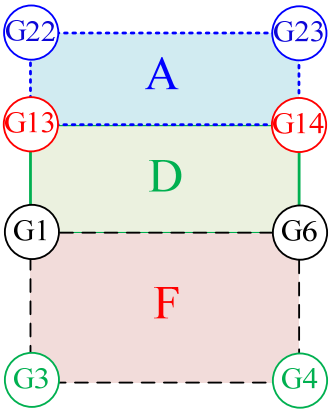

Element	Geophones/Nodes
A	G14, G13, G22, G23
D	G6, G1, G13, G14
F	G4, G3, G22, G23
C = A+D+F	G4, G3, G22, G23

Figure 6.58 Quadrilateral elements for location 3 at the LCSL.

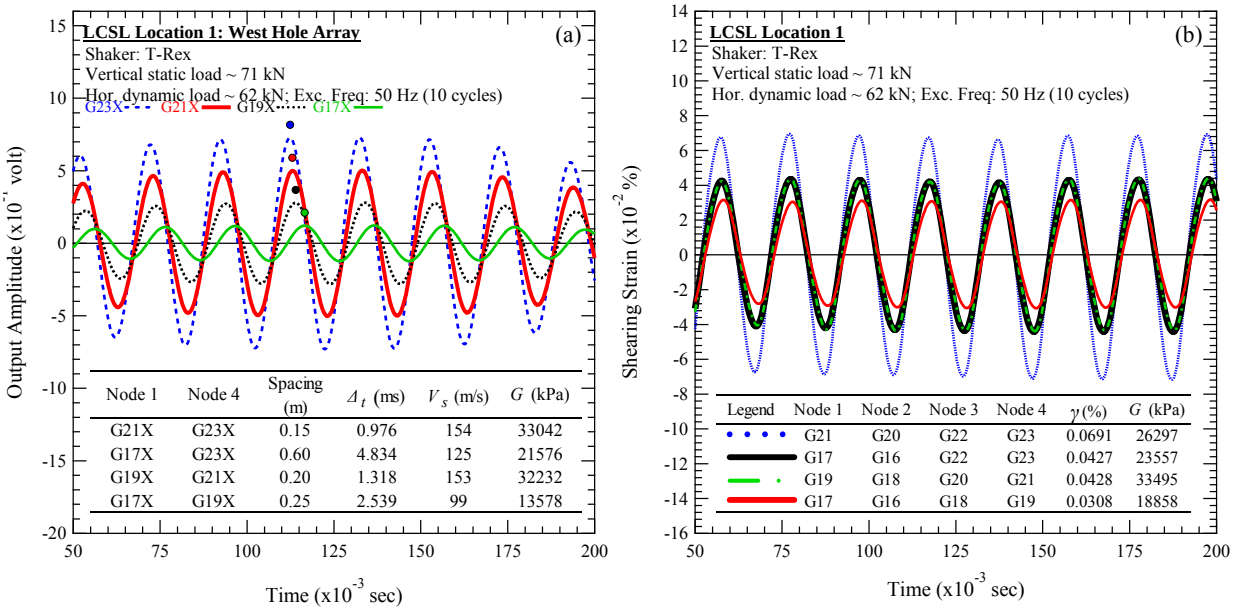

Figure 6.59 Examples of steady-state dynamic testing: (a) shear modulus calculation and (b) shearing strain time history at the LCSL.

6.10 **Shear Modulus and Normalized Shear Modulus Reduction Curves in Location 1 at the LCSL**

The effect of confining stress on the shear modulus and the normalized shear modulus as a function of shearing strain could be evaluated by examining the same element at different confining stress. Examining the same element isolates the effect of waste composition when investigating the effect of confining stress. Then, by examining different elements at the same confining stress, the effect of waste composition can be investigated.

6.10.1 Effect of Confining Stress on Shear Modulus and Normalized Shear Modulus Reduction Curves in Location 1 at the LCSL

The shear modulus and the normalized shear modulus reduction curves for element A in location 1 are presented in Figs. 6.60(a) and 6.60(b), respectively. The center of this element was located at an effective depth of 0.13 m below the footing. The shear modulus was evaluated for shearing

strain ranging from 0.0043% up to 0.14%. It should be noted that Element A was the shallowest element and exhibited the largest shearing strain. The effect of confining stress on the shear modulus curve is shown in Fig. 6.60(a). The G_{max} increased from 21 MPa to 44 MPa, as mean confining stress increased from 22 kPa to 137 kPa. The normalized shear modulus reduction curves for element A are shown in Fig. 6.60(b). The G/G_{max} curves systematically moved to the right and exhibited a more linear response with increasing confining stress. These trends in the shear modulus and the normalized shear modulus reduction curves are consistent with laboratory studies on MSW (Lee 2007, Zekkos et al. 2008, and Yuan et al. 2011) as well as on soils (e.g., Darendeli 2001).

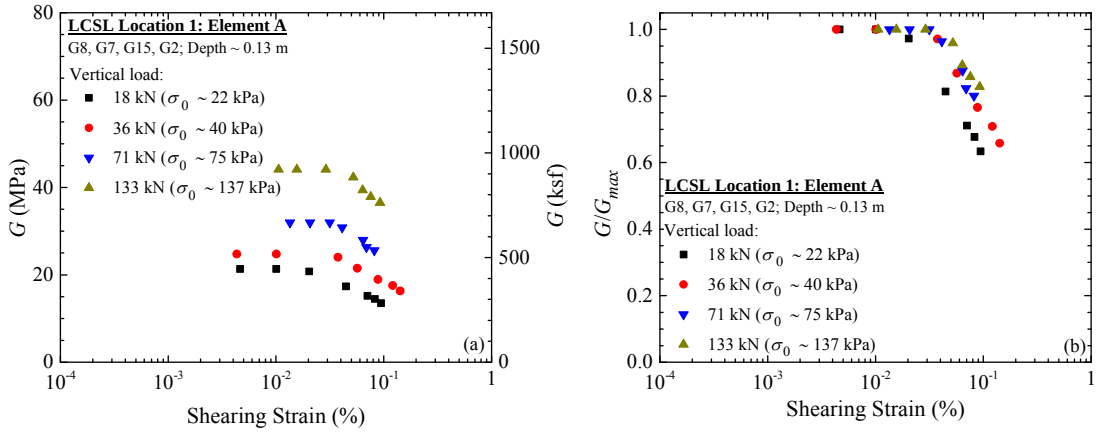

Figure 6.60 (a) Shear modulus and (b) normalized shear modulus reduction curves of element A in location 1 at the LCSL.

Figure 6.61(a) presents the G-log γ relationship at different confining stresses for element D in location 1. The center of element D was located at an effective depth of 0.30 m below the footing. The nonlinear behavior of element D is shown in Fig. 6.61(a). The steady-state dynamic test for element D was performed over shearing strain ranging from 0.0023% to 0.08%. As shown in Fig. 6.61(a), the small-strain shear modulus increased from 32 MPa to 49 MPa, as

mean confining stress increased from 16 kPa to 85 kPa. The G/G_{max}-log γ curves for element D are shown in Fig. 6.61(b). The normalized shear modulus became more linear with increasing confining stress.

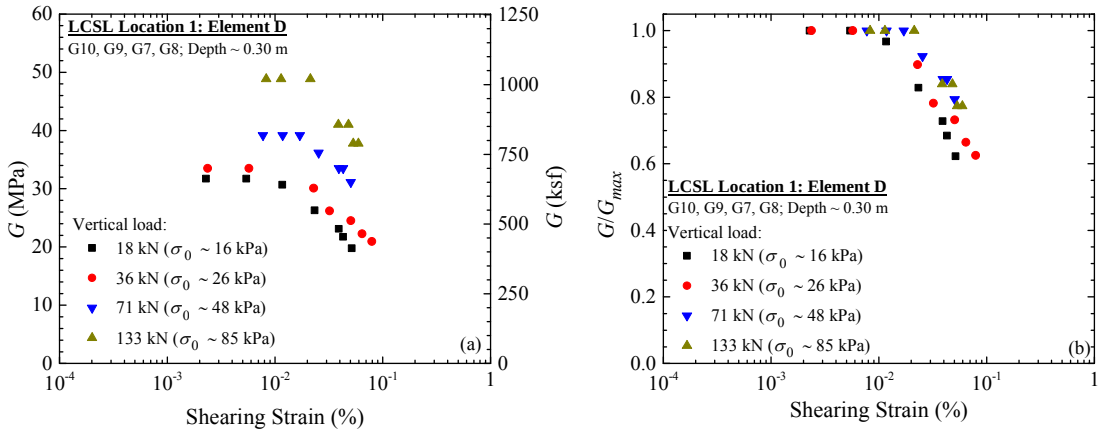

Figure 6.61 (a) Shear modulus and (b) normalized shear modulus reduction curves of element D in location 1 at the LCSL.

The variation of shear modulus with shearing strain at different confining stresses for element F in location 1 is presented in Fig. 6.62(a). The center of element F was located at an effective depth of 0.53 m below the footing. As illustrated in Fig. 6.62(a), the shear modulus was successfully obtained from the field measurements over the strain range from 0.0014% to 0.055%. As shown in this figure, the small-strain shear modulus increased with increasing confining stress. The G_{max} increased from 18 MPa to 24 MPa, as mean confining stress increased from 12 kPa to 50 kPa. Figure 6.62(b) presents the normalized shear modulus reduction curves for element F. The normalized shear modulus became more linear with increasing confining stresses from 12 kPa to 50 kPa.

The shear modulus and the normalized shear modulus reduction curves for element C in location 1 are presented in Figs. 6.63(a) and 6.63(b), respectively. This element provided an average response of the other elements as it was defined by the shallowest and the deepest

geophones. The center of this element was located at an effective depth of 0.35 m below the footing. The shear modulus was evaluated for shearing strain ranging from 0.0022% up to 0.077%. As illustrated in Fig. 6.63(a), the small-strain shear modulus increased with confining stress. The G_{max} increased from 22 MPa to 34 MPa, as mean confining stress increased from 15 kPa to 75 kPa. The normalized shear modulus reduction curves for this element are presented in Fig. 6.63(b). With increasing confining stress, the normalized shear modulus became more linear.

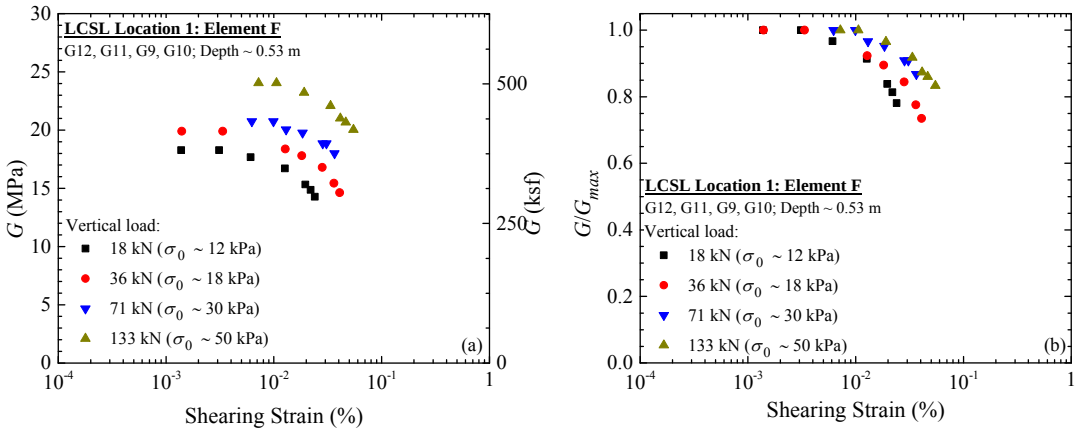

Figure 6.62 (a) Shear modulus and (b) normalized shear modulus reduction curves of element F in location 1 at the LCSL.

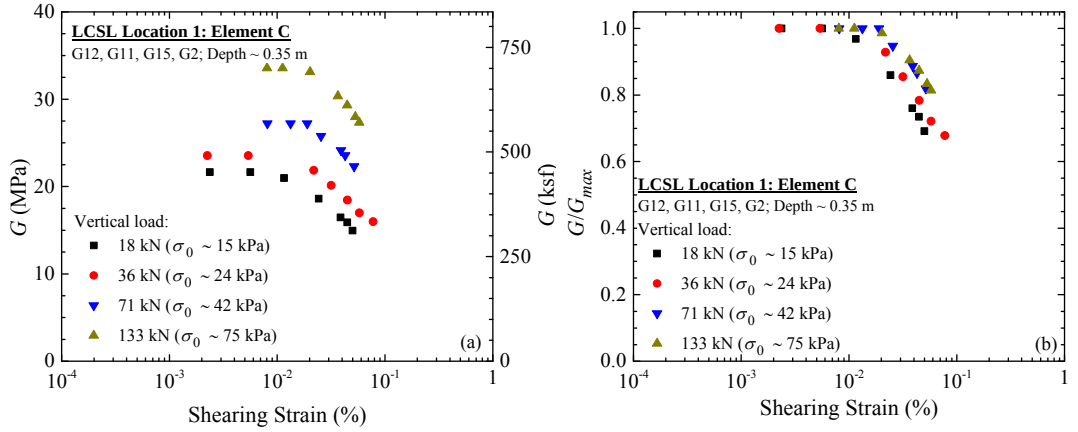

Figure 6.63 (a) Shear modulus and (b) normalized shear modulus reduction curves of element C in location 1 at the LCSL.

6.10.2 Effect of Waste Composition on Shear Modulus and Normalized Shear Modulus Reduction Curves in Location 1 at the LCSL

The effect of waste composition on the shear modulus and the normalized shear modulus reduction as a function of shearing strain could be evaluated using results from different sets of geophones that formed elements. Figure 6.64 shows the effect of waste composition on the shear modulus and the normalized shear modulus curves from elements at nearly the same calculated confining stress that varied from 12 kPa to 14 kPa. As shown in Fig. 6.56, elements C, D and F were representatives of waste at different depths. It should be noted that the element C represented the average of the other three elements. Figure 6.64(a) shows differences in shear modulus that are attributed to waste variability. The small-strain shear modulus was 22 MPa, 32 MPa, and 18 MPa for elements C, D and F, respectively. The corresponding normalized shear modulus reduction curves are shown in Fig. 6.64(b).

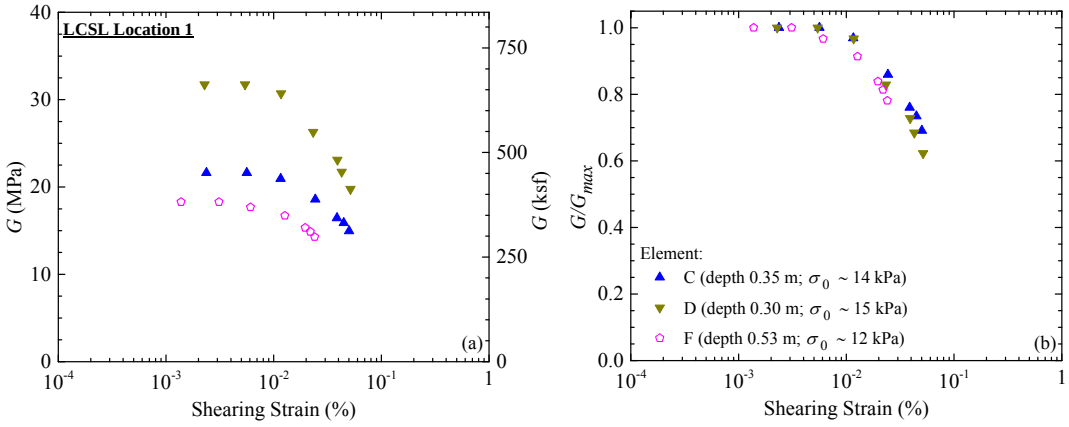

Figure 6.64 Waste composition effect on (a) shear modulus and (b) normalized shear modulus reduction curves in location 1 at the LCSL.

6.11 **Shear Modulus and Normalized Shear Modulus Reduction Curves in Location 2 at the LCSL**

6.11.1 Effect of Confining Stress on Shear Modulus and Normalized Shear Modulus Reduction Curves in Location 2 at the LCSL

The variation of shear modulus with shearing strain at different confining stresses for element A in location 2 is presented in Fig. 6.65(a). The center of this element was located at an effective depth of 0.13 m below the footing. Element A was the shallowest element and exhibited the largest shearing strain. The shear modulus was evaluated for shearing strain ranging from 0.003% up to 0.143%. As shown in Fig. 6.65(a), shear modulus increased as mean confining stress increased from 22 kPa to 137 kPa. It should be noted that the G_{max} values for mean stresses of 75 kPa and 137 kPa were not clearly observed and so G/G_{max} curves are not presented for these stresses. Nevertheless, based on observation from data series for mean stresses of 22 kPa and 40 kPa, the shear modulus data at the lowest shearing strain for mean stresses of 75 kPa and 137 kPa was probably very close to their corresponding G_{max}. The normalized shear modulus reduction curves for element A are shown in Fig. 6.65(b). The $G/G_{\max}$ curves moved to the right and exhibited a more linear response with increasing confining stress.

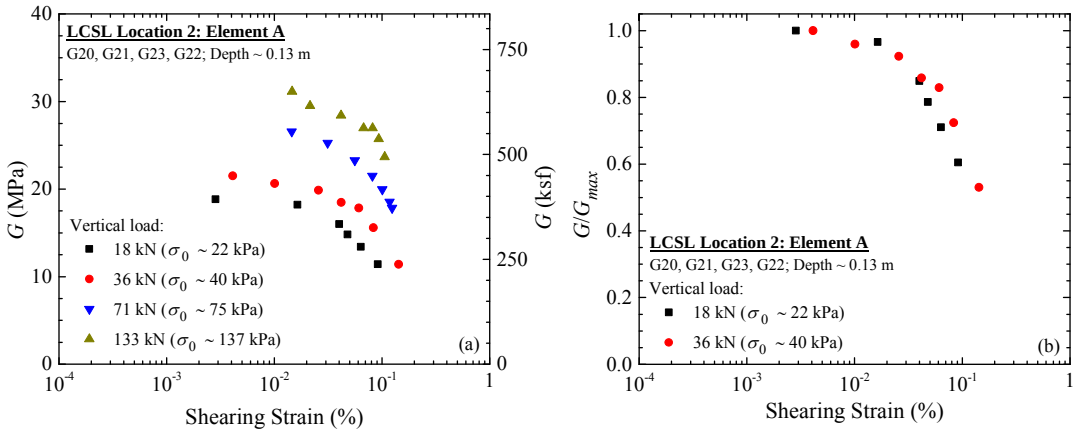

Figure 6.65 (a) Shear modulus and (b) normalized shear modulus reduction curves of element A in location 2 at the LCSL.

The variation of shear modulus with shearing strain at different confining stresses for element D in location 2 is presented in Fig. 6.66(a). The center of element D was located at an effective depth of 0.30 m below the footing. The shear modulus curves were successfully obtained from the field measurements over the shearing strain ranging from 0.0016% to 0.09% as presented in Fig. 6.66(a). It should be noted that the G_{max} values for mean stresses of 48 kPa and 85 kPa were also not clearly observed and the G/G_{max} data for these stresses is excluded in this thesis. Nevertheless, based on observation from data series for mean stresses of 15 kPa and 26 kPa, the shear modulus data at the lowest shearing strain for mean stresses of 48 kPa and 85 kPa was probably close to the G_{max}. The normalized shear modulus reduction curves for element D are presented in Fig. 6.66(b). The normalized shear modulus reduction curves became more linear with confining stress increase from 15 kPa to 26 kPa.

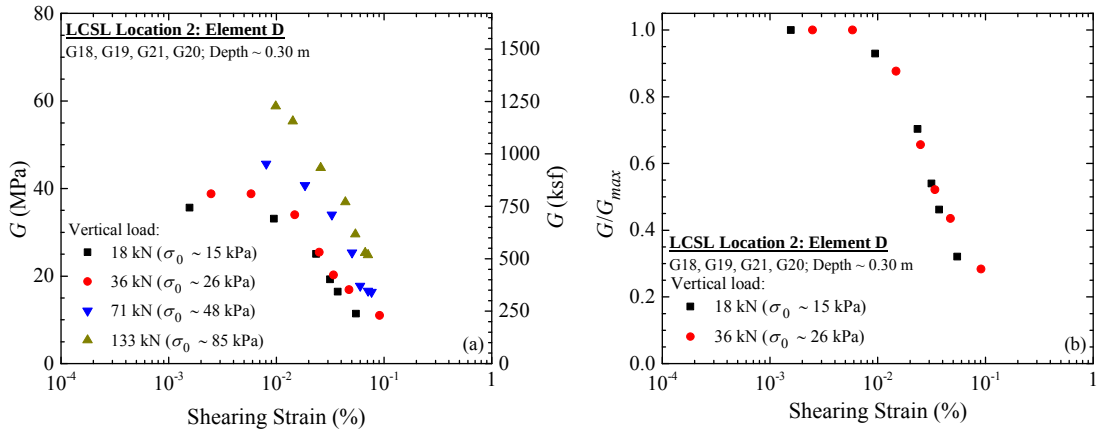

Figure 6.66 (a) Shear modulus and (b) normalized shear modulus reduction curves of element D in location 2 at the LCSL.

The G-log γ relationships at different confining stresses for element F in location 2 are presented in Fig. 6.67(a). The center of element F was located at an effective depth of 0.53 m below the footing. The steady-state dynamic test for element F was performed over shearing strain ranging from 0.001% to 0.052%. As shown in Fig. 6.67(a), the G_{max} values for mean stresses of 29 kPa and 49 kPa were not clearly observed and the G/G_{max} data for these stresses is not presented. Nevertheless, based on observation from data series for mean stresses of 12 kPa and 18 kPa, the shear modulus data at the lowest shearing strain for mean stresses of 29 kPa and 49 kPa was believed to be very close to the G_{max}. As shown in Fig. 6.67(a), the small-strain shear modulus increased from 25 MPa to 28 MPa as mean confining stress increased from 12 kPa to 18 kPa. The $G/G_{\max}$-log γ curves for element F is shown in Fig. 6.67(b). The $G/G_{\max}$-log γ curves became more linear with increasing confining stress.

Figure 6.68(a) presents the shear modulus reduction curves for element C in location 2. Element C provided an average response of the tested waste mass as it was defined by the shallowest and the deepest geophones. The center of this element was located at an effective depth of 0.35 m below the footing. This element experienced shearing strain ranging from

0.0017% to 0.08% during the steady-state dynamic tests. As shown in Fig. 6.68(a), the G_{max} values for mean stresses of 42 kPa and 75 kPa were also not clearly observed and the G/G_{max} data for these stresses is not presented. Nevertheless, the shear modulus data at the lowest shearing strain for mean stresses of 42 kPa and 75 kPa were probably very close to the G_{max}. The G_{max} increased from 25 MPa to 28 MPa, as mean confining stress increased from 14 kPa to 24 kPa [Fig. 6.68(a)]. Figure 6.68(b) shows the normalized shear modulus reduction curves for this element. The normalized shear modulus reduction curves became more linear with confining stress.

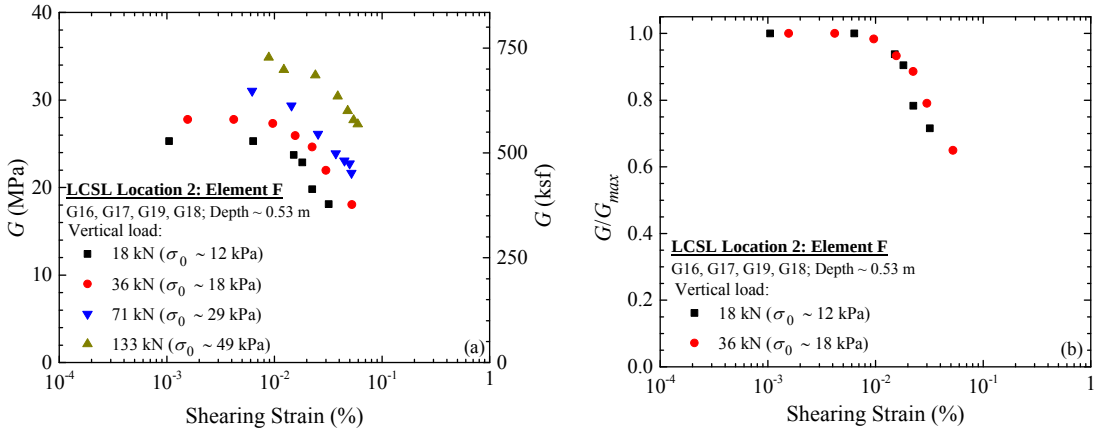

Figure 6.67 (a) Shear modulus and (b) normalized shear modulus curves of element F in location 2 at the LCSL.

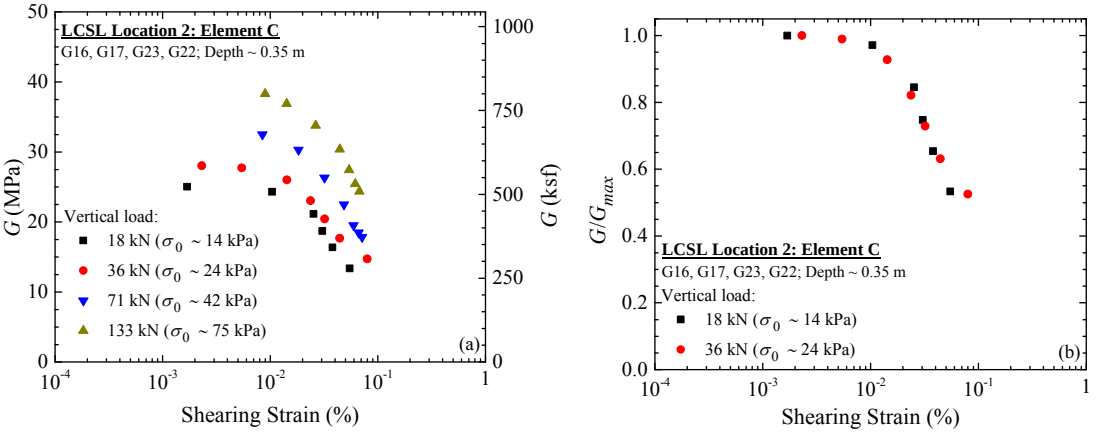

Figure 6.68 (a) Shear modulus and (b) normalized shear modulus reduction curves of element C in location 2 at the LCSL.

6.11.2 Effect of Waste Composition on Shear Modulus and Normalized Shear Modulus Reduction Curves in Location 2 at the LCSL

The effect of waste composition on G-log γ and G/G_{max}-log γ curves from location 2 at the LCSL is presented in Figs. 8.72(a) and 8.72(b). All elements in these figures were at nearly the same calculated confining stress ranging from 12 kPa to 15 kPa. The shear modulus from these elements ranged from 25 MPa to 36 MPa [Fig. 8.72(a)]. In this case, element D showed the highest shear modulus and the most nonlinearity in the G-log γ curve. The differences in shear modulus and the degree of nonlinearity could be attributed to the differences in waste composition in each element. The impact of waste composition on the relationship between G/G_{max} and shearing strain is demonstrated in Fig. 8.72(b). Element C and F showed similarity both in the shear modulus and normalized shear modulus reduction curves. According to Zekkos et al. 2008, waste-rich MSW exhibits lower shear modulus and more linear response in G/G_{max} curve compare to waste-poor MSW.

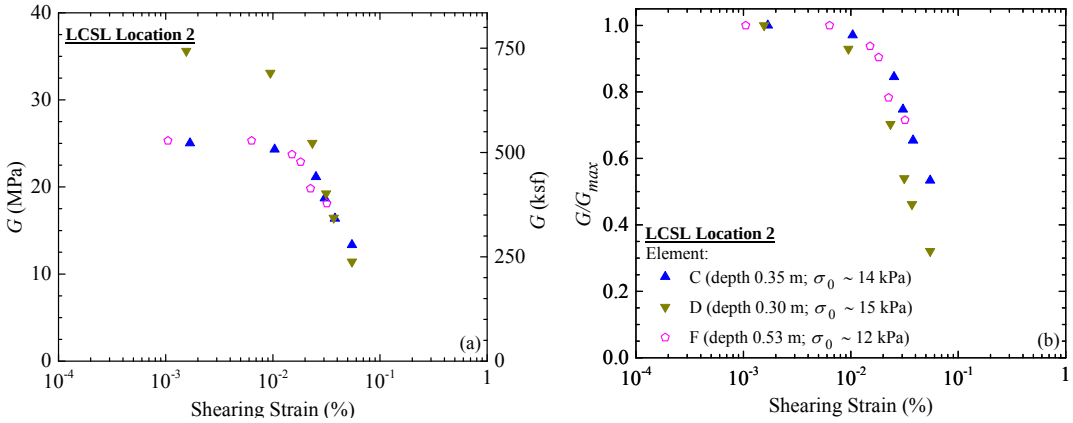

Figure 6.69 Waste composition effect on (a) shear modulus and (b) normalized shear modulus reduction curves in location 2 at the LCSL.

6.12 **Shear Modulus and Normalized Shear Modulus Reduction Curves in Location 3 at the LCSL**

6.12.1 Effect of Confining Stress on Shear Modulus and Normalized Shear Modulus Reduction Curves in Location 3 at the LCSL

The shear modulus and the normalized shear modulus reduction curves for element A in location 3 are presented in Figs. 6.70(a) and 6.70(b). The center of this element was located at an effective depth of 0.13 m below the footing. The shear modulus was evaluated for shearing strain ranging from 0.0022% up to 0.19%. Element A was the shallowest element and exhibited the largest shearing strain. The effect of confining stress on the shear modulus curve is presented in Fig. 6.70(a). The G_{max} increased from 28 MPa to 50 MPa, as mean confining stress increased from 22 kPa to 137 kPa. The normalized shear modulus reduction curves for element A are shown in Fig. 6.70(b). The G/G_{max} curves generally moved to the right and exhibited a more linear response with increasing confining stress

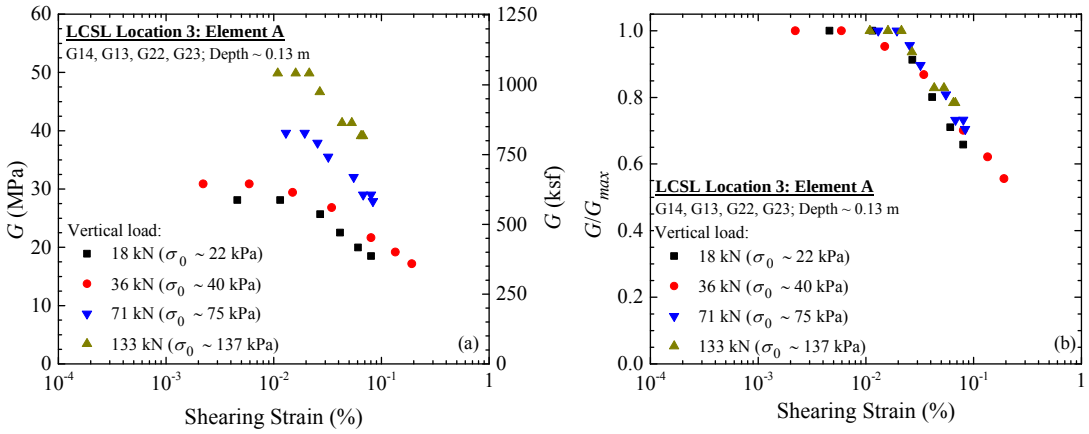

Figure 6.70 (a) Shear modulus and (b) normalized shear modulus reduction curves of element A in location 3 at the LCSL.

Figure 6.71(a) presents the G-log γ relationship at different confining stresses for element D in location 3. The center of element D was located at an effective depth of 0.30 m below the footing. The nonlinear behavior of element D can readily be seen in Fig. 6.71(a). This element experienced shearing strain ranging from 0.0014% to 0.11% during the steady-state dynamic test. As shown in Fig. 6.71(a), the small-strain shear modulus increased from 14 MPa to 21 MPa, as mean confining stress increased from 15 kPa to 85 kPa. The G/G_{max}-log γ curves for element D are shown in Fig. 6.71(b). The G/G_{max}-log γ curves became more linear with increasing confining stress.

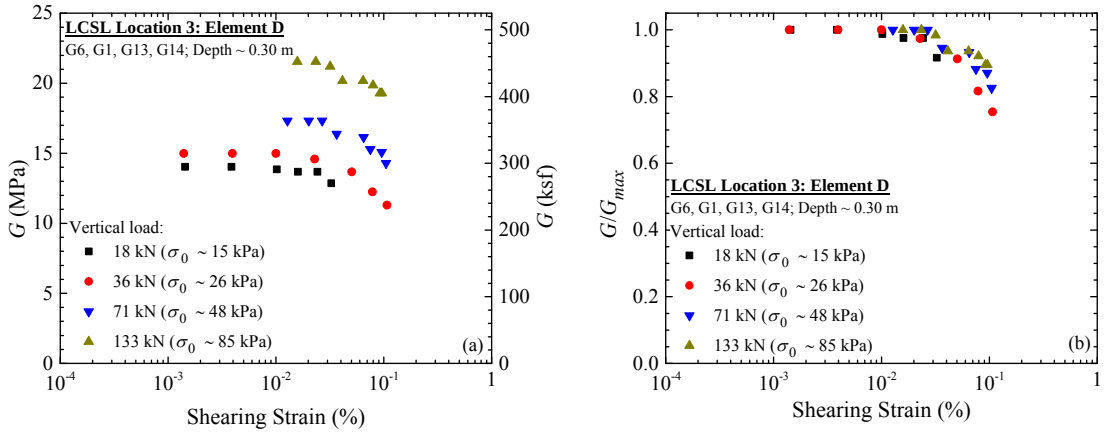

Figure 6.71 (a) Shear modulus and (b) normalized shear modulus curves of element D in location 3 at the LCSL.

The variation of shear modulus with shearing strain at different confining stresses for element F in location 3 is presented in Fig. 6.72(a). The center of element F was located at an effective depth of 0.53 m below the footing. As shown in Fig. 6.72(a), the shear modulus was successfully obtained from the field measurements over the strain range from 0.0008% to 0.064%. As shown in this figure, the G_{max} values for mean stresses of 29 kPa and 49 kPa were not clearly observed and the G/G_{max} data for these stresses is not included in this thesis.

Nevertheless, based on observation from data series for mean stresses of 12 kPa and 17 kPa, the shear modulus data at the lowest shearing strain for mean stresses of 29 kPa and 49 kPa were probably close to their corresponding G_{max}. The observed small-strain shear modulus increased from 14 MPa to 15 MPa as mean confining stress increased from 12 kPa to 17 kPa [Fig. 6.72(a)]. Figure 6.72(b) presents the normalized shear modulus reduction curves for element F. The normalized shear modulus curves became more linear with increasing confining stresses from 12 kPa to 17 kPa.

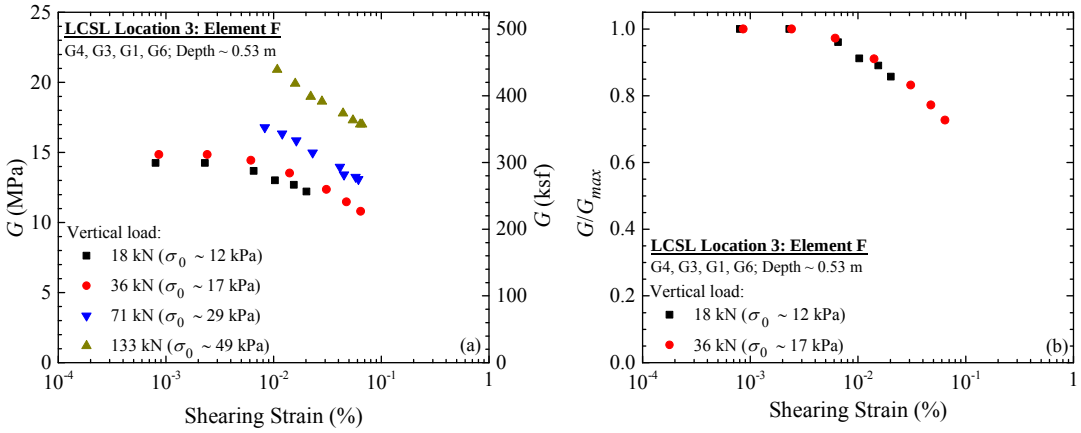

Figure 6.72 (a) Shear modulus and (b) normalized shear modulus reduction curves of element F in location 3 at the LCSL.

The shear modulus and the normalized shear modulus reduction curves for element C in location 3 are presented in Figs. 6.73(a) and 6.73(b). This element provided an average response of the other elements as it was defined by the shallowest and the deepest geophones. The center of this element was located at an effective depth of 0.35 m below the footing. The shear modulus was evaluated for shearing strain ranging from 0.0011% up to 0.088%. As shown in Fig. 6.73(a), the G_{max} for mean stresses of 42 kPa and 75 kPa were not clearly identified and the G/G_{max} data for these stresses is not presented here. However, based on observation from data series for mean stresses of 14 kPa and 23 kPa, the shear modulus data at the lowest shearing strain for mean

stresses of 42 kPa and 75 kPa were believed to be close to their corresponding G_{max}. As shown in Fig. 6.73(a), the G_{max} increased from 15 MPa to 16 MPa, as mean confining stress increased from 14 kPa to 23 kPa. The normalized shear modulus reduction curves for this element are shown in Fig. 6.73(b). With increasing confining stress, the normalized shear modulus reduction curves became more linear.

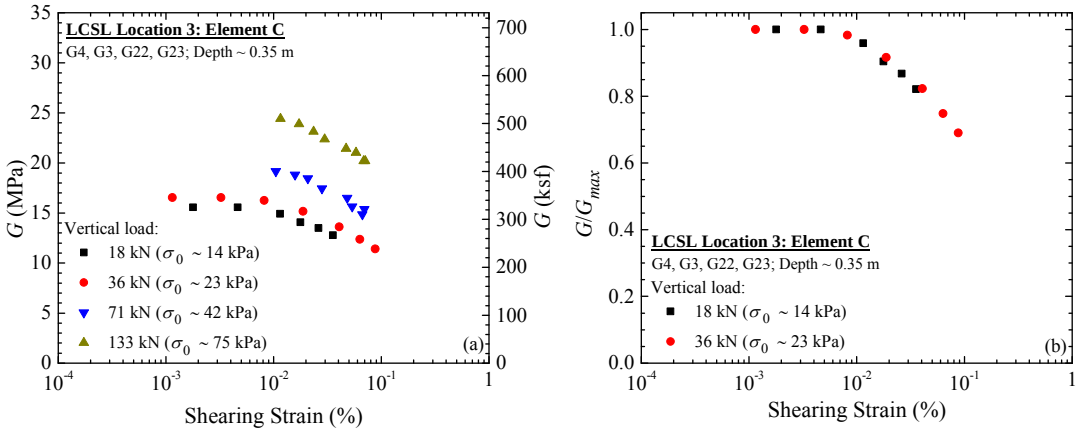

Figure 6.73 (a) Shear modulus and (b) normalized shear modulus reduction curves of element C in location 3 at the LCSL.

6.12.2 Effect of Waste Composition on Shear Modulus and Normalized Shear Modulus Reduction Curves in Location 3 at the LCSL

Figure 6.74 shows the effect of waste composition on the shear modulus and the normalized shear modulus reduction curves from all elements at nearly the same calculated confining stress that varied from 12 kPa to 14 kPa. As shown in Fig. 6.58, elements C, D and F were representatives of waste at different depths. It should be noted that the element C represents the average of the other three elements. Figure 6.74(a) shows differences in shear modulus that could be attributed to waste variability. The small-strain shear modulus was 16 MPa, 14 MPa, and 14 MPa for elements C, D, and F, respectively. The variability in waste composition is also demonstrated by the range of normalized shear modulus reduction curves in Fig. 6.74(b).

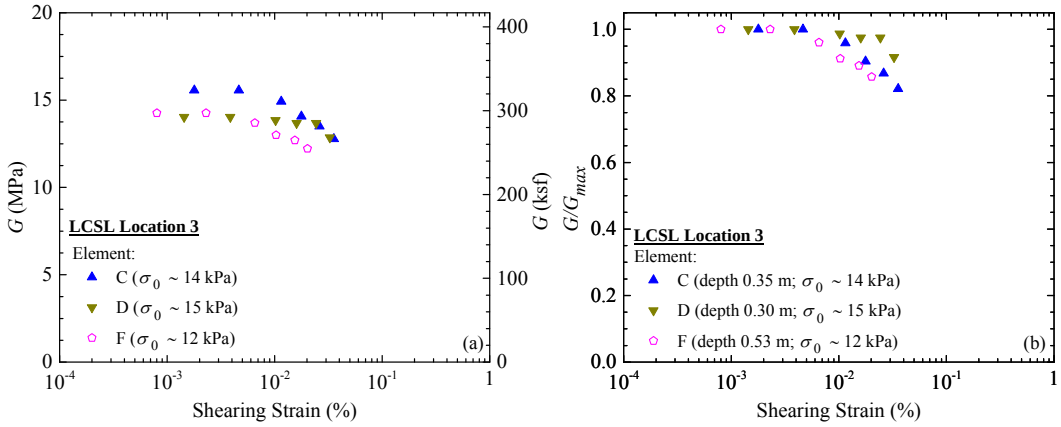

Figure 6.74 Waste composition effect on (a) shear modulus and (b) normalized shear modulus curves in location 3 at the LCSL.

6.13 **Comparison of Normalized Shear Modulus Reduction Curves with Other Studies**

In this section, the variation of normalized shear modulus reduction curves as a function of shearing strain from three test locations at the LCSL was compared. In addition, the field G/G_{max} data from the LCSL was also compared with curves proposed by other studies in the literature. In this case, the comparison was made with results from laboratory testing and recorded ground motion back-calculation analysis.

The steady-state dynamic test results from three test locations at the LCSL are presented in Fig. 6.75. Dataset from locations 1, 2, and 3 are shown as black squares, red circles, and blue triangles, respectively. In location 1, normalized shear modulus reduction curve was evaluated for shearing strains ranging from 0.0014% to 0.14%. In location 2, normalized shear modulus reduction curve was evaluated for shearing strains ranging from 0.001% to 0.14%. Normalized shear modulus reduction curve was evaluated for shearing strains ranging from 0.0008% to 0.19% in location 3. In general, the normalized shear modulus reduction curves were consistent. Nevertheless, normalized shear modulus reduction appeared to be more nonlinear for some of the data series in location 2 compared to field G/G_{max} data from the other test locations at the LCSL.

In addition, some data series in location 3 showed the most linearity in the normalized shear modulus reduction curves. The variation of normalized shear modulus reduction curves as a function of shearing strain can be attributed to variability in waste composition between the three test locations as well as differences in confining stresses between quadrilateral elements.

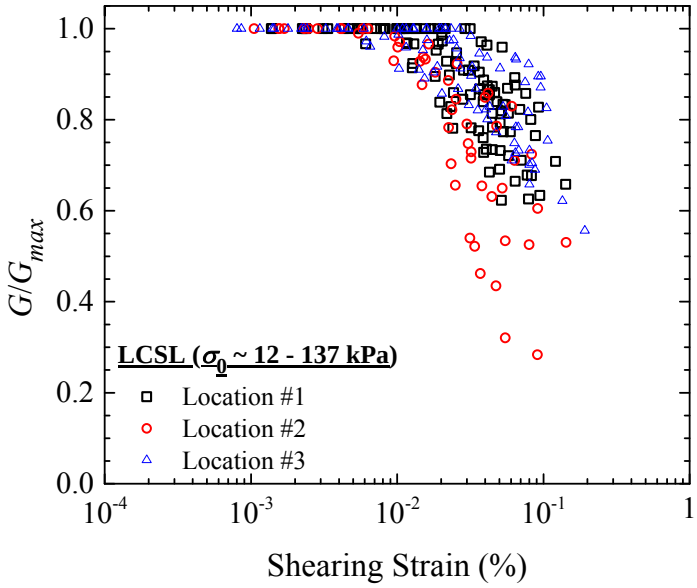

Figure 6.75 The normalized shear modulus reduction curves from 3 testing locations at the LCSL.

Figure 6.76 shows the comparison between the field G/G_{max} data from the LCSL and Zekkos et al. (2008) curves for mean stress < 125 kPa that were largely developed on the basis of testing at mean stress of 75 kPa. The field data was generally consistent with the laboratory based curves. Most field G/G_{max} data for locations 1 and 3 was in between Zekkos et al. curve for 8 – 25% and 100% smaller than 20 mm material. But, some data from these locations were more linear than Zekkos et al. curve for 8 – 25% smaller than 20 mm material. Some G/G_{max} data from location 2 showed more nonlinear behavior than Zekkos et al. curves.

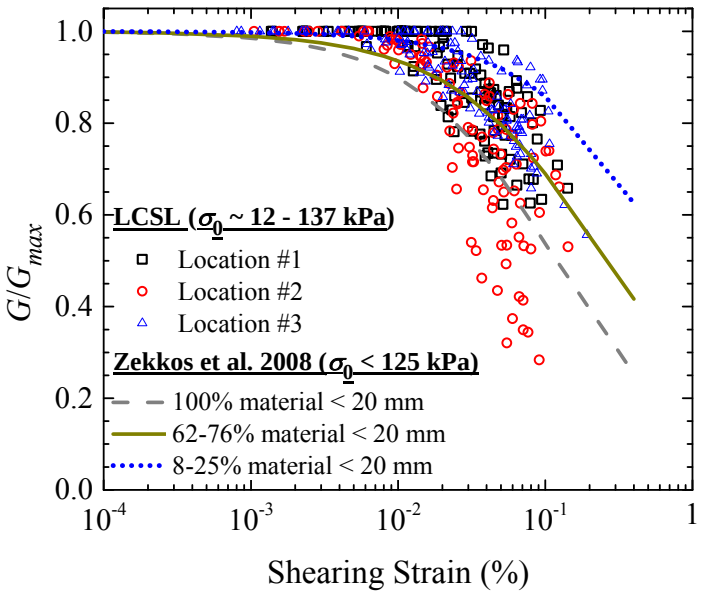

Figure 6.76 Comparison of the normalized shear modulus reduction curves with Zekkos et al. (2008) recommended curves.

Figure 6.77 presents the comparison between the normalized shear modulus reduction curves measured in situ at the LCSL with curves proposed by other researchers. The normalized shear modulus reduction curve proposed by Idriss et al. (1995), Matasovic and Kavazanjian (1998), and Augello et al. (1998) were derived from back-calculation analyses using recorded ground motions at the surface of the OII landfill, California. In addition, Matasovic and Kavazanjian (1998) also performed cyclic simple shear testing to extend their curves to larger strain. Singh and Murphy (1990) proposed a curve that was developed using the shear modulus reduction curve of peat and clay. As shown in Fig. 6.77, the field G/G_{max} data from LCSL shows substantial difference from Singh and Muprhy curve as well as Idriss et al. curve. Singh and Murphy curve showed more significant shear modulus reduction below shearing strain of 0.001 % than the field G/G_{max} data from the LCSL. Idriss et al. curve exhibited a relatively more nonlinear shear modulus reduction than the field G/G_{max} data from the LCSL. Augello et al. curve was closest to the lower bound curve for the field G/G_{max} data in locations 1 and 3 at the

LCSL. In addition, Augello et al. curve approximately close to the median curve for the field G/G_{max} data in location 2. The recommended Matasovic and Kavanzanjian curve provided an approximated upper bound curve for the field G/G_{max} data from the LCSL.

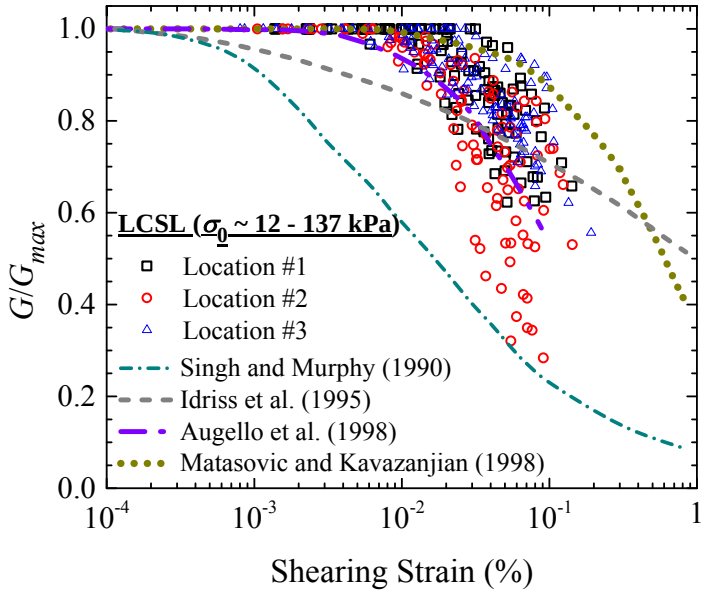

Figure 6.77 Comparison of the normalized shear modulus reduction curves with curves from other studies in the literature.

6.14 **Summary**

A field experiment program was conducted at three locations at the Lamb Canyon Sanitary Landfill, Beaumont, California, to evaluate dynamic properties of MSW in the linear and nonlinear strain range. Crosshole and downhole seismic tests were performed at 5 different static vertical loads. Steady-state dynamic testing over a wide shear strain range (0.0008% to 0.14%) was conducted at four different static vertical loads applied using mobile vibroseis shakers of NEES@UTexas. Two arrays of 3-D geophone sensors were embedded in the waste mass and were used to capture the waste response during dynamic testing. A combined MASW and MAM tests were also performed at the LCSL to measure the shear wave velocity profile in three test locations. In addition, load-settlement measurements were conducted. Pit excavation was

performed at each location to measure the in-situ unit weight, visually assess waste composition, and collect samples for waste characterization and laboratory testing. The outcomes from downhole and crosshole seismic tests were the wave propagation velocity profiles and wave propagation velocity-stress relationship. The study also generated in-situ data on shear modulus and normalized shear modulus reduction relationship as a function of shear strain. The results from field testing at the LCSL will be synthesized with the results from field testing at Austin Community Landfill and Los Reales Landfill to generate broad conclusions and recommendation in Chapter 9.

Small-scale crosshole and downhole seismic testing allowed for an assessment of $V_{p\text{-}X}$, $V_{p\text{-}Z}$, $V_{s\text{-}XZ}$, $V_{s\text{-}ZX}$, and $V_{s\text{-}ZY}$ as a function of waste composition and confining stress. Small-scale crosshole and downhole seismic testing with different static vertical loads showed that wave propagation velocities increase with stress. In the NC regime, wave propagation velocity increase was more sensitive to stress increase than in the OC regime. The near-surface MSW was overconsolidated due to field compaction at the landfill.

The wave propagation velocity measurements at the LCSL were also used to assess waste anisotropy and small-strain Poisson's ratio. For example, the ratio of $V_{p\text{-}Z}$ to $V_{p\text{-}X}$ ranged from 0.77 to 0.93 with a mean value of 0.84. Similarly, the ratio of $V_{s\text{-}vertical}$ to $V_{s\text{-}horizontal}$ was found to be between 0.67 and 1.06 with an average value of 0.92. These average values indicated that the stiffness in the horizontal direction was generally higher than the stiffness in the vertical direction. The small-strain Poisson's ratio at three test locations varied from 0.13 to 0.41.

The impact of waste variability and confining stress on the shear modulus was also assessed in situ. Shear modulus was found to increase with increasing confining stress, particularly in the NC regime, and to be affected by waste composition. The normalized shear

modulus reduction curves were also affected by waste composition and confining stress. The normalized shear modulus became more linear as confining stress increased, similarly to soils. At the same confining stress, the shear modulus and normalized shear modulus curves of MSW at different locations was generally consistent, but varied indicating the effect of waste composition on the nonlinear dynamic properties of MSW.

CHAPTER 7. FIELD EVALUATION OF DYNAMIC PROPERTIES OF MUNICIPAL SOLID WASTE AT THE LOS REALES LANDFILL

7.1 **Introduction**

The dynamic properties of municipal solid waste (MSW) were evaluated in situ at the Los Reales Landfill (LRL) in Tucson, Arizona from October 29 to November 7, 2012. This chapter describes testing locations, field test execution, and test results. The field investigation included downhole and crosshole seismic tests and steady-state dynamic test. Additionally, load-settlement tests and in-situ unit weight measurements were performed. Generally, field testing was performed using the procedures described in Chapter 4.

7.2 **Field Investigation at the Los Reales Landfill**

The field investigation at the Los Reales Landfill was primarily conducted to evaluate the linear and nonlinear dynamic properties of MSW in situ. In the linear range, shear wave (S-wave) velocity (V_s) and primary wave (P-wave) velocity (V_p) were investigated. In the nonlinear range, the variation of shear modulus (G) and normalized shear modulus (G/G_{max}) as a function of shearing strain (γ) was evaluated.

The LRL is a regional MSW landfill owned and managed by the City of Tucson since 1967. The LRL is located at 5300 E. Los Reales Road, Tucson, Arizona which is approximately 15 km from downtown Tucson (Fig. 7.1). This landfill accepts routine refuse, such as household waste, furniture, rugs, wooden pallets, and mattresses. In addition, the LRL also receives construction debris, concrete, and asphalt. The LRL serves businesses and residents of Tucson and Pima County, Arizona.

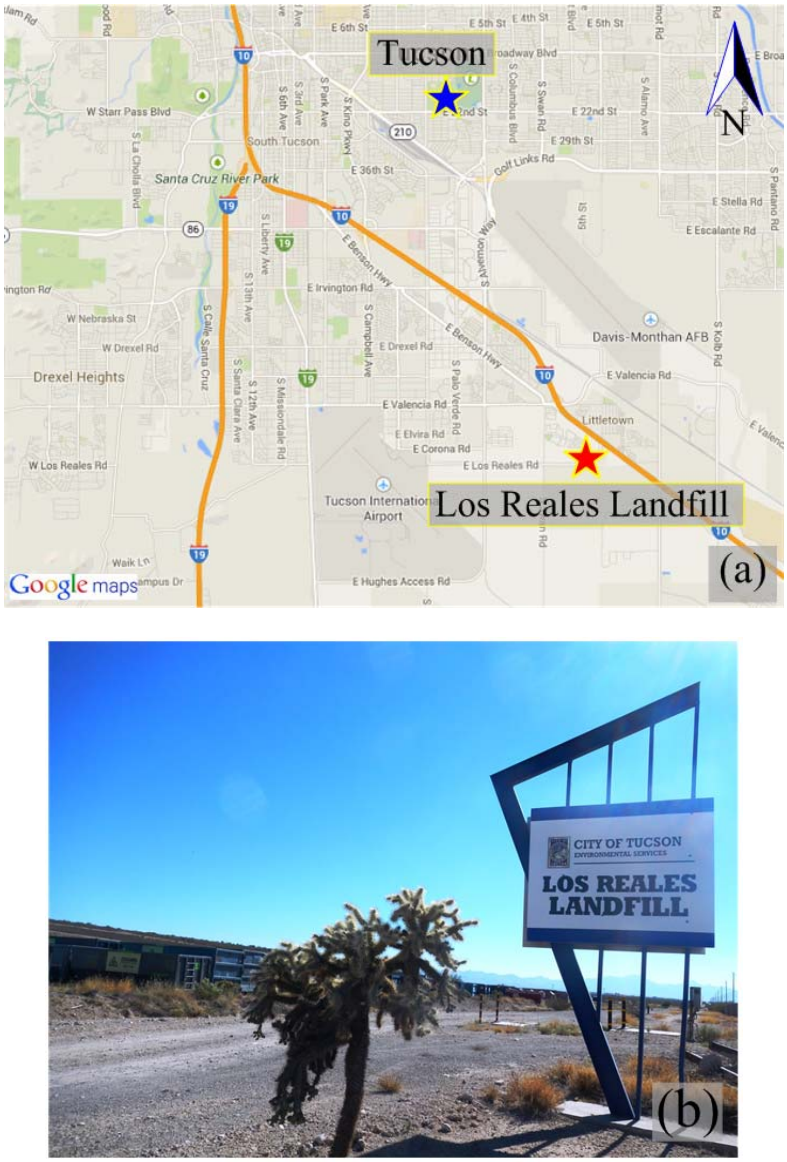

Figure 7.1 The Los Reales Landfill: (a) location and (b) entrance.

The field investigation at the LRL was conducted by the author (University of Michigan), Mr. Cecil G. Hoffpauir and Mr. Andrew Valentine (NEES@UT), and Mr. Spencer Marcinek (Geosyntec). The field investigation was supervised by Dr. Richard D. Woods (University of Michigan).

7.2.1 Test Locations

The field investigation was performed in three locations at the LRL (Fig. 7.2). In location 1 (Fig. 7.3), field testing was performed from October 29 to November 1, 2012. Waste age in this location was estimated to be about 4 years. In location 2 (Fig.7.4), field investigation was conducted from November 1 to 3, 2012. Waste age in this location was approximately 18 years old. In location 3 (Fig. 7.5), field investigation was conducted from November 5 to 7, 2012. Waste age in this location was estimated to be 4 years. It should be noted that the waste age from these testing locations was estimated based on information from excavated and recovered newspapers and documents.

Figure 7.2 Testing locations at the Los Reales Landfill.

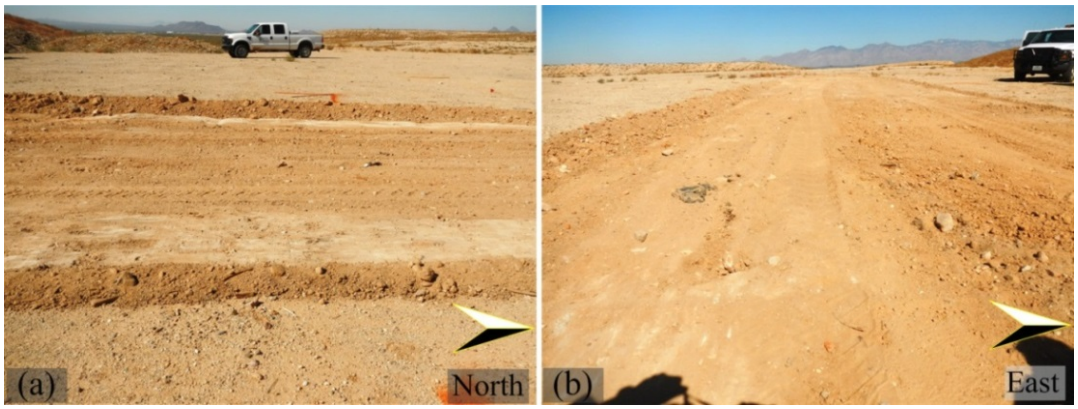

Figure 7.3 (a) East and (b) south views of location 1 at the LRL.

Figure 7.4 South view of location 2 at the LRL.

Figure 7.5 Northwest view of location 3 at the LRL.

7.2.2 Field Instrumentation and Testing Setup

Activities during the field instrumentation and preparation at the LRL are shown in Fig. 7.6. Testing setups in locations 1, 2, and 3 are shown in Figs. 7.7, 7.8, and 7.9, respectively. Initially, the testing setup for all locations was planned to be identical to testing setup in locations 1 and 3. However, it was proven to be very challenging to prepare deeper sensor holes in location 2. Drilling attempts were made using a low capacity power auger in three spots without success. As shown in Fig. 7.8, the deepest 3-D geophone pair in location 2 was located at depth of 0.61 m which was 0.30 m shallower than the deepest geophone pair in the other test locations at the LRL. All test locations were prepared for load-settlement test; downhole and crosshole seismic tests; and steady-state dynamic test.

Figure 7.6 Field instrumentation and testing setup at the LRL: (a) removing cover soil, (b) pushing core barrel, (c) recovered waste from core barrel, (d) 3-D geophone installation, (e) sensor hole, (f) crosshole source rod installation, and (g) footing placement.

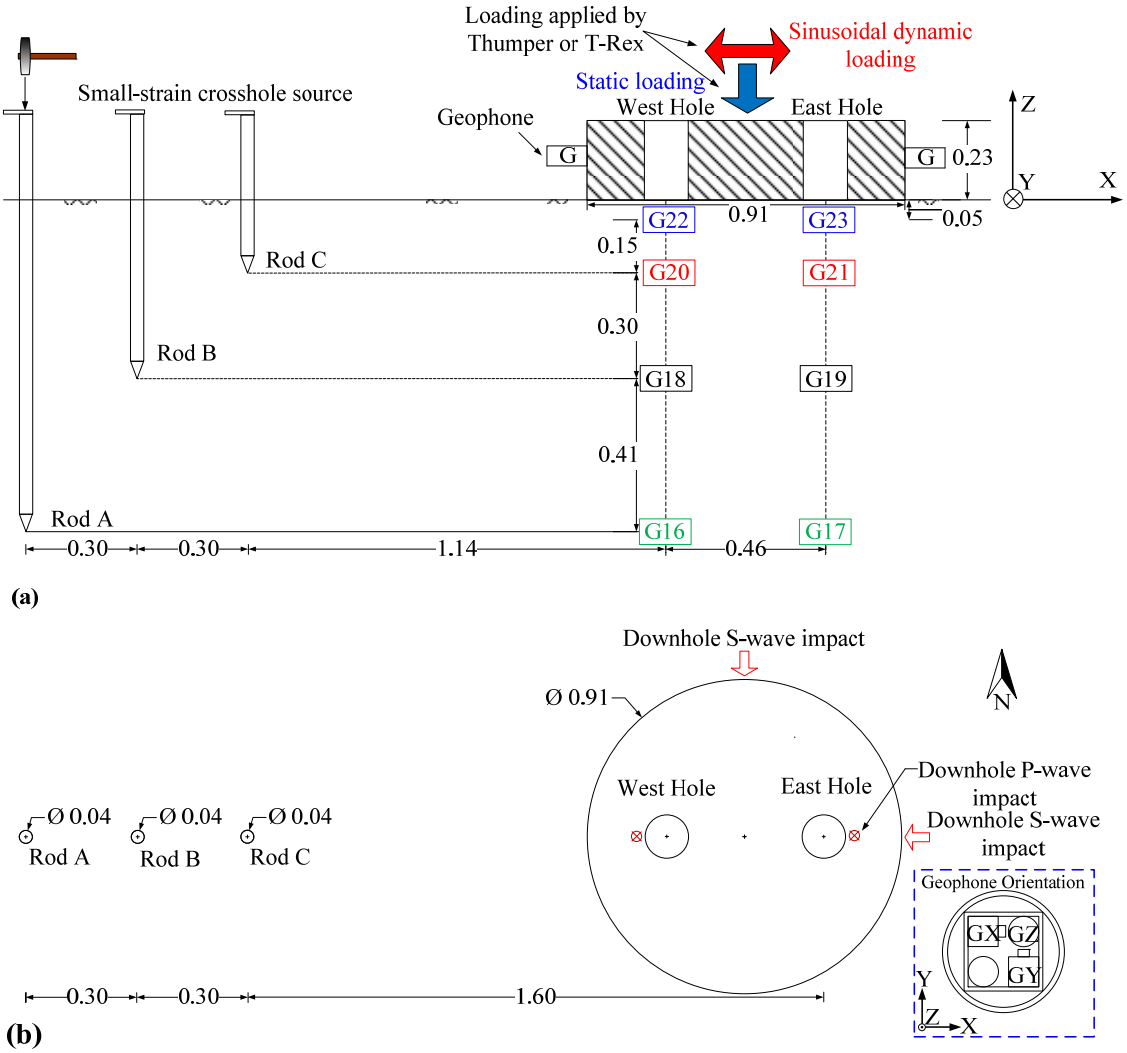

Figure 7.7 Testing setup in location 1 at the LRL: (a) cross-section and (b) plan views.

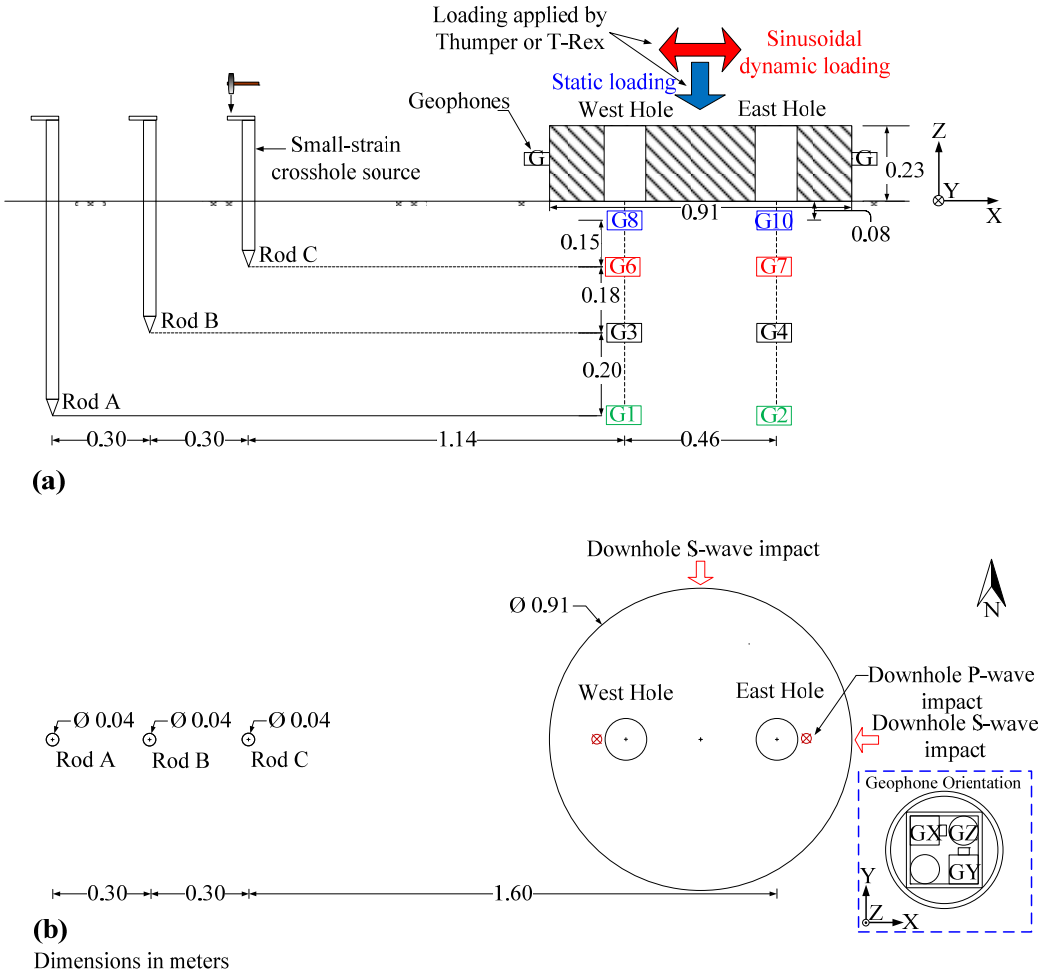

Figure 7.8 Testing setup in location 2 at the LRL: (a) cross-section and (b) plan views.

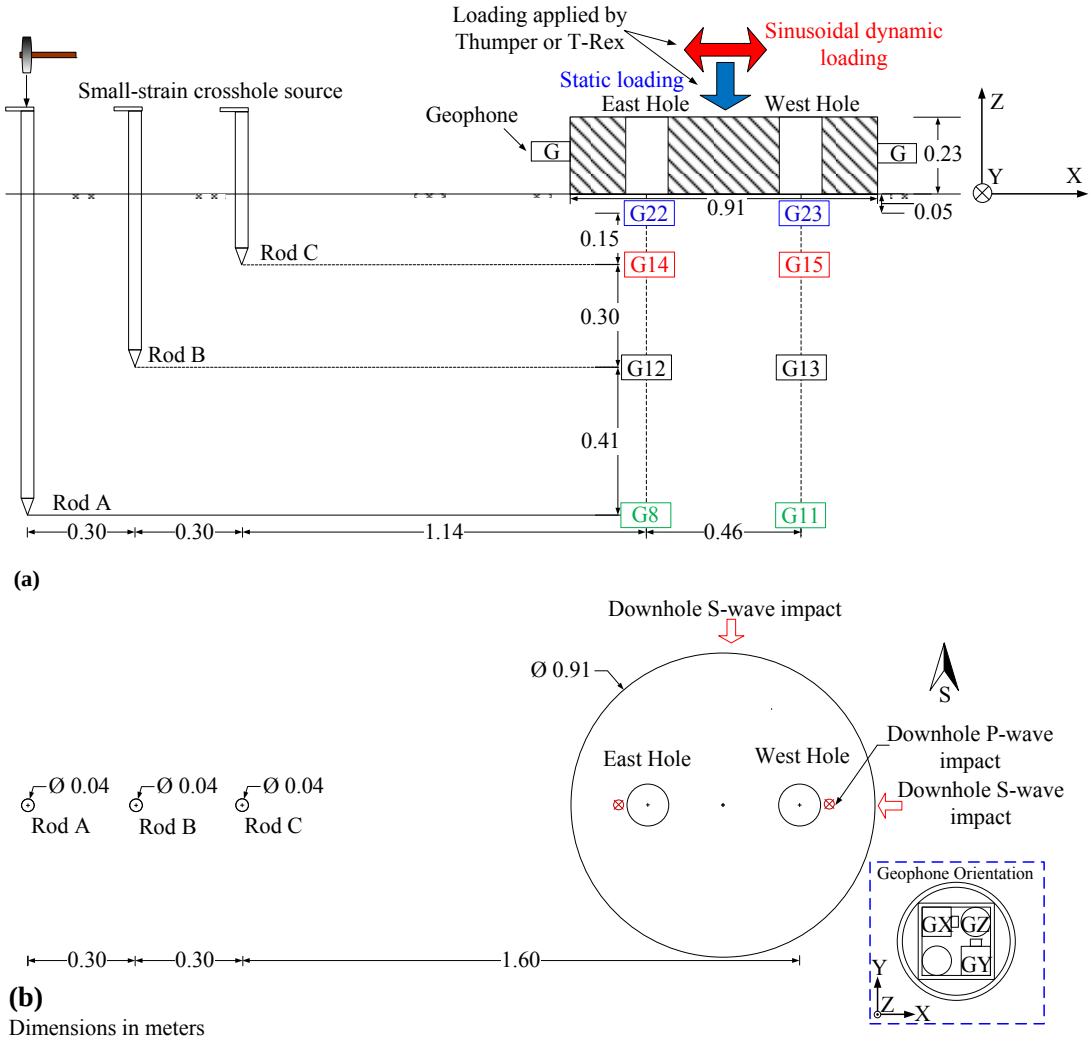

Figure 7.9 Testing setup in location 3 at the LRL: (a) cross-section and (b) plan views.

7.2.3 Field Testing Sequence for Evaluation of Dynamic Properties of MSW at the LRL

The field investigations in locations 1, 2, and 3 at the LRL were performed according to staged loading sequence as shown in Figs. 7.10, 7.11, and 7.12, respectively. In location 1, crosshole and downhole seismic tests were performed at externally applied vertical static loads of 0 kN, 18 kN, 36 kN, 71 kN, and 111 kN. Steady-state dynamic tests were performed using a 18 kN, 36 kN, 71 kN, and 133 kN static hold-down force. These vertical static load levels were kept constant while applying dynamic horizontal loads. In location 2, crosshole and downhole seismic tests were performed at externally applied vertical static load of 0 kN, 18 kN, 36 kN, 67 kN, and

107 kN. Steady-state dynamic tests were performed using a 18 kN, 36 kN, 71 kN, and 133 kN static hold-down force. In location 3, crosshole and downhole seismic tests were performed at externally applied vertical static load of 0 kN, 18 kN, 36 kN, 67 kN, and 102 kN. In this location, steady-state dynamic tests were performed using a 18 kN, 36 kN, 71 kN, and 133 kN static hold-down force. In all locations, load-settlement data were collected during the application of vertical static load for the crosshole and downhole seismic tests. It should be noted that the highest vertical static load for the downhole and crosshole seismic tests was planned to be 133 kN. But, it was very difficult to reach a static vertical load of 133 kN using a hydraulic jack pump in all locations. In steady-state dynamic testing, Thumper was used to apply static vertical load up to 36 kN and T-Rex was used to impose the larger vertical static load levels.

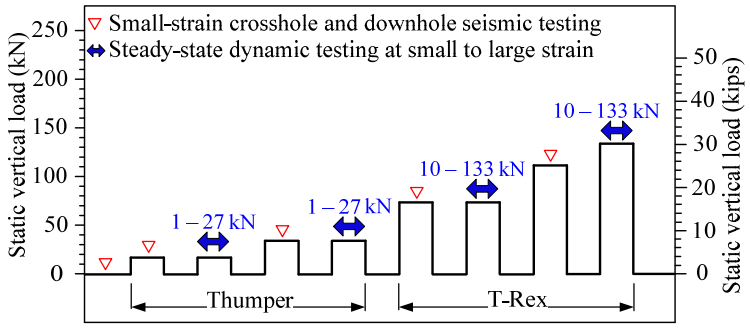

Figure 7.10 Staged loading sequence in location 1 at the LRL.

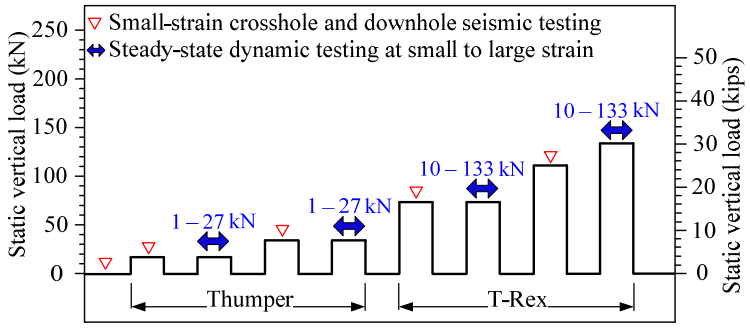

Figure 7.11 Staged loading sequence in location 2 at the LRL.

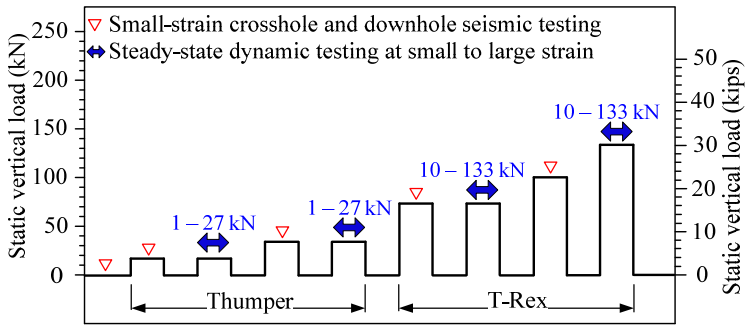

Figure 7.12 Staged loading sequence in location 3 at the LRL.

7.2.4 In-situ Unit Weight Measurements and MSW Sampling

In-situ unit weight measurements, MSW sampling, in-situ MSW characterization, and sensor recovery were performed after completion of the staged loading test (Fig. 7.13). In-situ unit weight measurement and MSW characterization were performed using procedures proposed by Zekkos et al. (2006a) and Zekkos et al. (2010), respectively. A pit with depth of approximately 1 m was excavated in each location. Bulk MSW samples of 1.78 kN, 1.29 kN, and 1.46 kN were collected from locations 1, 2, and 3, respectively. These bulk samples were stored in 55-gallon HDPE drums and were trasnported to the Geoenvironmental Engineering laboratory at the University of Michigan. Remaining excavated MSW was re-disposed to the landfill. In-situ unit weight measurements were performed using gravel that had a grain size varying from 0.63 cm to 0.95 cm with unit weight of 15.2 kN/m^3.

Table 7.1 shows the unit weight and waste composition for all test locations at the LRL. The gross unit weights were 13.5 kN/m^3, 12.6 kN/m^3, and 15.1 kN/m^3 in locations 1, 2, and 3, respectively. Waste composition was characterized using the collected bulk samples independently for each test location in the Geonvironmental Engineering laboratory at the University of Michigan. It should be noted that although the samples collected from each location involved a significant amount of waste material (i.e. 1.29-1.78 kN), these amounts were

still just a portion of the waste mass tested in the field. In each location, the collected samples were approximately 4% by weight of the excavated MSW. Thus, the waste compositions shown are only approximately representative of the tested waste composition and may not be identical to the tested waste in the field.

Figure 7.13 (a) Waste excavation, (b) MSW pit, (c) exposed 3-D geophone, (d) placement of gravel into truck, and (e and f) in-situ unit weight measurement at the LRL.

Table 7.1 Waste composition in locations 1, 2, and 3 at the LRL.

Location	Total Sample Weight (kN)	Unit Weight (kN/m^3)	Composition (% by weight)							
			< 20mm[1]	Paper	Hard Plastic	Soft Plastic	Wood	Metal	Gravel & Glass	Others[2]
1	1.78	13.5	64.4	11.4	4	2.2	5	1.6	5.7	5.7
2	1.29	12.6	56.6	16.6	3.8	3.4	6	2.3	7.1	4.2
3	1.46	15.1	46.6	20.8	5.7	5.4	2.2	6.3	3.3	9.7

[1] Soil-like material.
[2] Textile, leaf, stiff rubber, bones, and ceramics.

7.3 **Load-settlement Test**

Load-settlement tests were performed in a loading sequence in three test locations at the LRL. The highest static vertical load in the load-settlement tests was 111 kN, 111 kN, and 102 kN for locations 1, 2, and 3, respectively. These highest vertical loads corresponded to maximum stresses on the footing ranging from 150 kPa to 170 kPa. The static vertical loads were applied using a hydraulic jack that reacted against the mobile field shakers' frame as shown in Fig. 7.14. A T-shaped frame was used to uniformly distribute the load on the footing. The settlements were measured using three linear potentiometers on the footing.

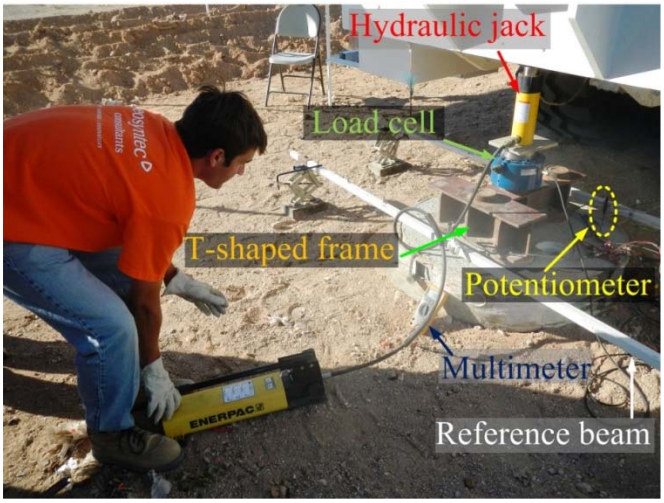

Figure 7.14 Load-settlement test in location 3 at the LRL.

Figure 7.15 shows the load-settlement curves in three test locations at the LRL. The maximum settlements under the highest static vertical load in locations 1, 2, and 3 were 22 mm, 20 mm, and 46 mm, respectively.

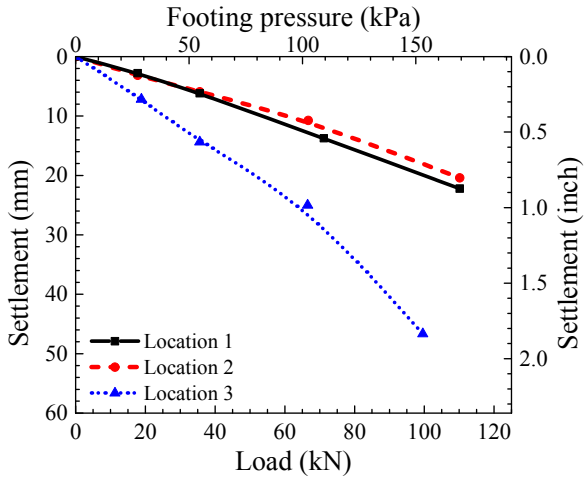

Figure 7.15 Load-settlement test results at the LRL.

7.4 **Small-scale Downhole Seismic Testing**

As part of field testing at the LRL, small-scale downhole seismic tests were performed to evaluate vertically propagating P-wave velocity ($V_{p\text{-}Z}$), vertically-propagating horizontally-polarized in the X-axis S-wave ($V_{s\text{-}ZX}$), and vertically-propagating horizontally-polarized in the Y-axis S-wave ($V_{s\text{-}ZY}$) at each vertical load increment (Figs. 7.10, 7.11, and 7.12). The coordinate orientations are illustrated in Figs. 7.7, 7.8, and 7.9. As presented in these figures, this test was conducted by hitting the footing at the sides and at the top. Figure 7.16(a) shows downhole seismic test with externally applied static vertical load. The small-scale downhole testing and analysis procedures are presented Chapter 4 in detail.

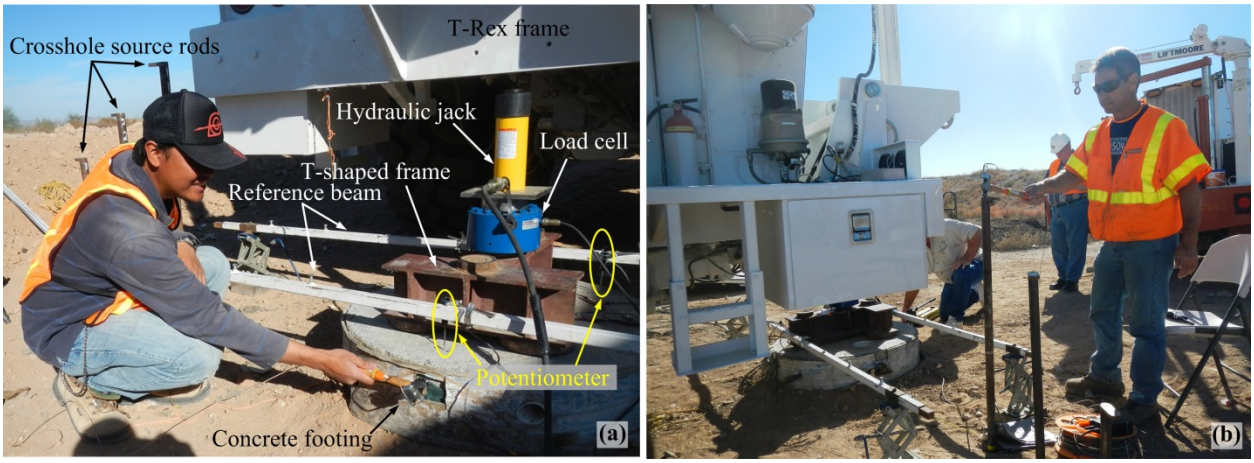

Figure 7.16 Performance of (a) downhole and (b) crosshole seismic testing at the LRL.

Examples of wave train records from downhole seismic test at the LRL are shown in Fig. 7.17. Estimates of wave propagation velocities have been generated for each of the three pairs of downhole sensors. The measured wave propagation velocity was designated at the average depth between a 3-D geophone pair. It should be noted that some wave propagation velocities from downhole seismic tests could not be calculated due to poor or irregular waveforms.

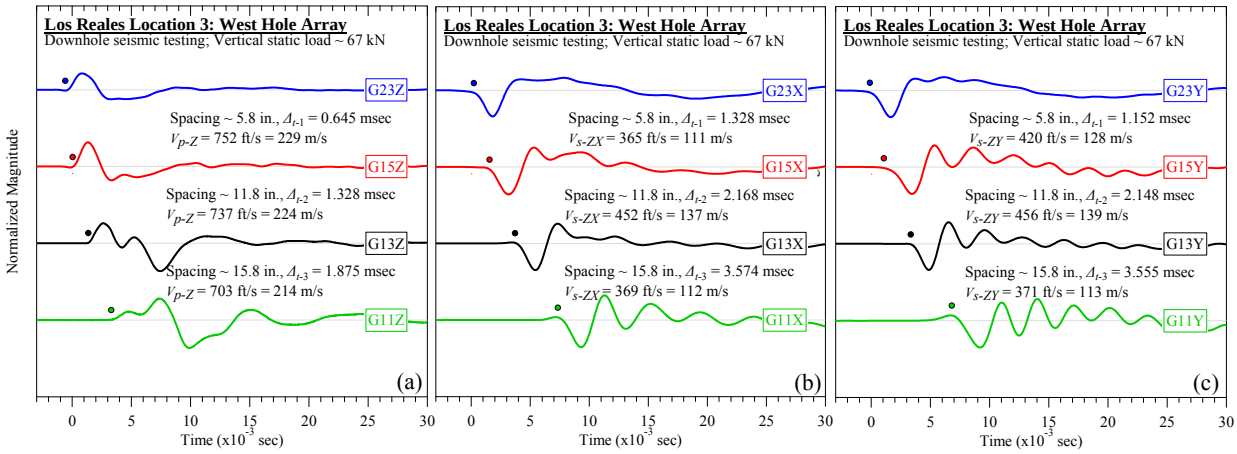

Figure 7.17 Examples of wave trains from downhole seismic test at the LRL: (a) V_{p-Z}, (b) V_{s-ZX}, and (c) V_{s-ZY}.

7.4.1 $V_{s\text{-}ZX}$, $V_{s\text{-}ZY}$, and $V_{p\text{-}Z}$ Profiles in Location 1 at the LRL

The $V_{s\text{-}ZX}$ profiles measured from the small-scale downhole seismic tests in location 1 are presented in Fig. 7.18. These profiles were measured for 5 different static vertical loads. Figures 7.18 (a) and 7.18(b) present the $V_{s\text{-}ZX}$ profiles from the east and west hole arrays, respectively. In the east array, the initial $V_{s\text{-}ZX}$ (i.e. at static vertical load of 0 kN) increased from 109 m/s at depth of 0.36 m to 171 m/s at depth of 0.71 m. In the west array, the initial $V_{s\text{-}ZX}$ decreased from 169 m/s at depth of 0.13 m to 142 m/s at depth of 0.71 m. Figures 7.18(a) and 7.18(b) show that the $V_{s\text{-}ZX}$ increased as the static vertical load increased. For example, at depth of 0.36 m in the east hole array, the $V_{s\text{-}ZX}$ increased from 109 m/s to 138 m/s as the static vertical load increased from 0 kN to 111 kN.

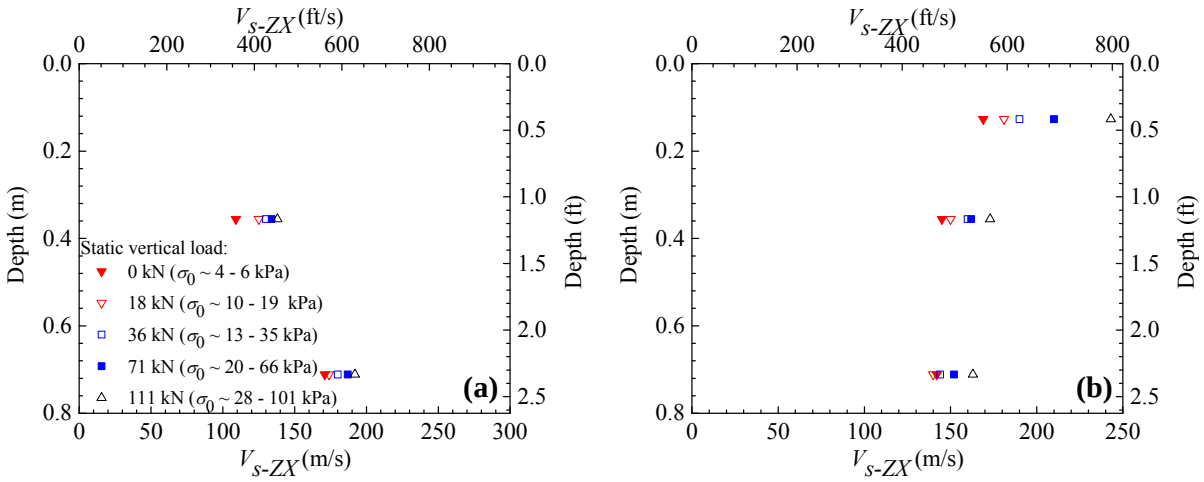

Figure 7.18 $V_{s\text{-}ZX}$ profiles in the (a) east and (b) west hole arrays in location 1 at the LRL.

The variation of $V_{s\text{-}ZY}$ with depth for 5 different static load levels at location 1 is presented in Fig. 7.19. The $V_{s\text{-}ZY}$ profiles from the east array are shown in Fig. 7.19(a). In this figure, the initial $V_{s\text{-}ZY}$ was 104 m/s at depth of 0.36 m and increased to 177 m/s at depth of 0.71 m. The $V_{s\text{-}ZY}$ profiles from the west array are shown in Fig. 7.19(b). In the west array, the initial $V_{s\text{-}ZY}$ was

150 m/s at depth of 0.13 m and increased to 175 m/s at depth of 0.36 m and decreased to 135 m/s at depth of 0.71 m.

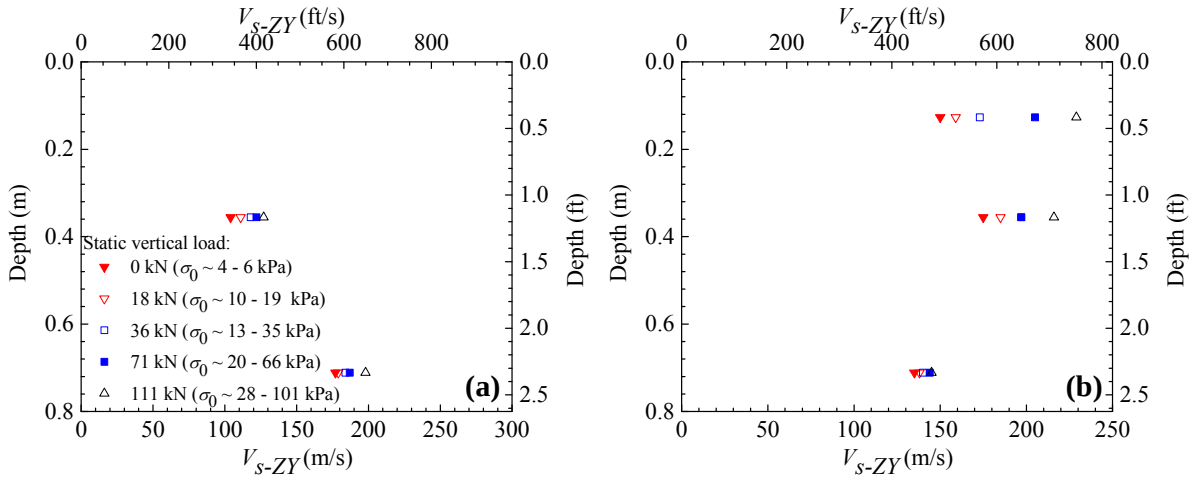

Figure 7.19 $V_{s\text{-}ZY}$ profiles in the (a) east and (b) west hole arrays in location 1 at the LRL.

The $V_{p\text{-}Z}$ profiles measured from the small-scale downhole seismic tests at location 1 are presented in Figs. 7.20(a) and 7.20(b) for the east and west hole arrays, respectively. In the east array with static vertical load of 0 kN, the $V_{p\text{-}Z}$ at depth of 0.36 m was 216 m/s. The $V_{p\text{-}Z}$ in the waste increased to 301 m/s at depth of 0.71 m. In the west array, the initial $V_{p\text{-}Z}$ were 278 m/s at depth of 0.36 m and 247 m/s at depth of 0.71 m. As observed in Fig. 7.20, $V_{p\text{-}Z}$ increased with increasing static vertical load.

The overall variations in wave propagation velocities both with depth as well as between holes in Figs. 7.18, 7.19, and 7.20 show significant vertical and lateral variability of MSW in location 1 over short measuring distances. The observed differences in V_s or V_p with depth, including the occasionally "unexpected" reductions or increases of V_s or V_p with depth can be explained when we consider the significant differences in waste composition at the testing scale. In addition, the increases in wave propagation velocities with static vertical load levels are shown in these figures and are analyzed subsequently.

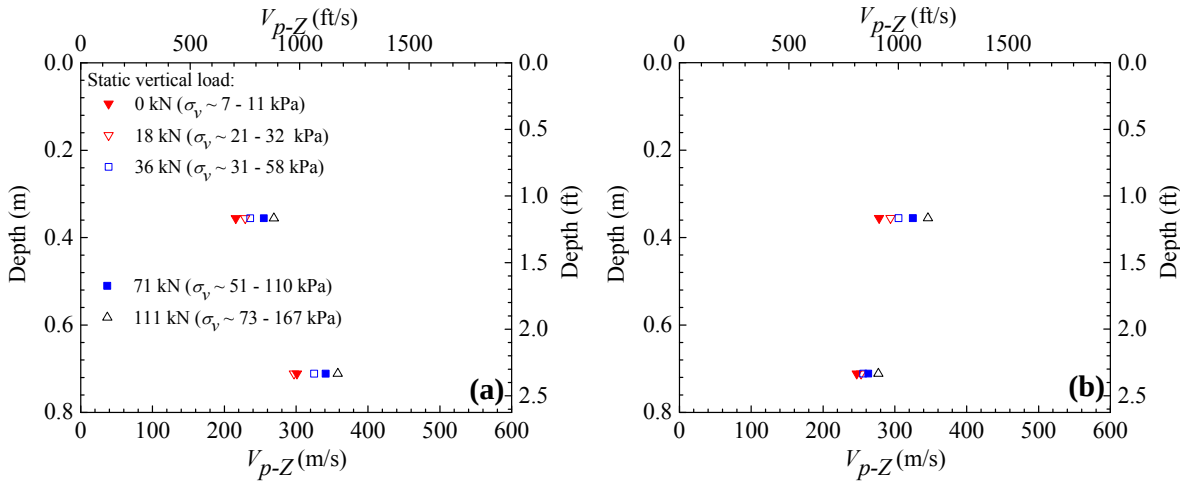

Figure 7.20 $V_{p\text{-}Z}$ profiles in the (a) east and (b) west hole arrays in location 1 at the LRL.

7.4.2 Effect of Stress State on $V_{s\text{-}ZX}$, $V_{s\text{-}ZY}$, and $V_{p\text{-}Z}$ in Location 1 at the LRL

As discussed in Chapter 5, wave propagation velocities in MSW depend on the stress state (Zekkos 2005, Lee 2007, and Zekkos et al. 2013). To investigate the relationship between wave propagation velocities and the stress state, the vertical (σ_v), horizontal (σ_h), and mean confining (σ_0) stresses were calculated using the Foster and Ahlvin (1954) method as described in Chapter 4. It is known that wave velocity is most affected by stress components aligned with the direction of wave propagation and particle motion (Roesler 1979, Yu and Richart 1984, Stokoe et al. 1985, Stokoe and Santamarina 2000, Fivorante 2000, Wang and Mok 2008). Thus, at each vertical load increment, σ_v was used as correlation parameters for $V_{p\text{-}Z}$, whereas σ_0 was used for and $V_{s\text{-}ZX}$ and $V_{s\text{-}ZY}$. The relationship between these velocities and stresses was regressed using a power function as commonly done for soils (e.g. Hardin and Richart 1963, Hardin and Black 1968, Hryciw and Thomann 1993, Iwasaki and Tatsuoka 1977). For convenience of the reader, the power functions for $V_{s\text{-}ZX}$, $V_{s\text{-}ZY}$, and $V_{p\text{-}Z}$ are shown again in Eqs. 7.1, 7.2, and 7.3, respectively. Stresses in these equations were normalized with atmospheric pressure (P_a).

$$V_{s-ZX} = A_{vX} \cdot \left(\frac{\sigma_0}{P_a} \right)^{n_{ZX}} \tag{7.1}$$

$$V_{s-ZY} = A_{vY} \cdot \left(\frac{\sigma_0}{P_a} \right)^{n_{ZY}} \tag{7.2}$$

$$V_{p-Z} = A_{pZ} \cdot \left(\frac{\sigma_v}{P_a} \right)^{n_{pZ}} \tag{7.3}$$

where A_{ij} is an empirical constant that indicates corresponding wave propagation velocity at 1 atm and n_{ij} is an empirical constant that quantifies the effect of stress on the corresponding wave propagation velocity.

Figures 7.21, 7.22, and 7.23 illustrate the $V_{s\text{-}ZX}$, $V_{s\text{-}ZY}$, and $V_{p\text{-}Z}$ variations with stresses, respectively. An either linear or bi-linear relationship of wave propagation velocities with stress was observed. Bi-linearity was indicative of the waste being in the overconsolidated (OC) regime due to waste compaction (Stokoe et al. 2011). As stress increased, the MSW reached the normally consolidated (NC) regime. In the OC regime, the stress exponent n_{ZX} for $V_{s\text{-}ZX}$ was found to be ranging from 0.05 to 0.09, while in the NC regime, the n_{ZX} increased to 0.23. The n_{ZY} for $V_{s\text{-}ZY}$ ranged from 0.05 to 0.08 in the OC regime and increased to 0.26 in the NC regime. The n_{pZ} for $V_{p\text{-}Z}$ ranged from 0.07 to 0.10 in the OC regime. The interpreted maximum past mean confining stress ($\sigma_{0\text{-max}}$), as indicated by the change in slope in Figs 7.21 and 7.22, was on the order of 28 – 31 kPa.

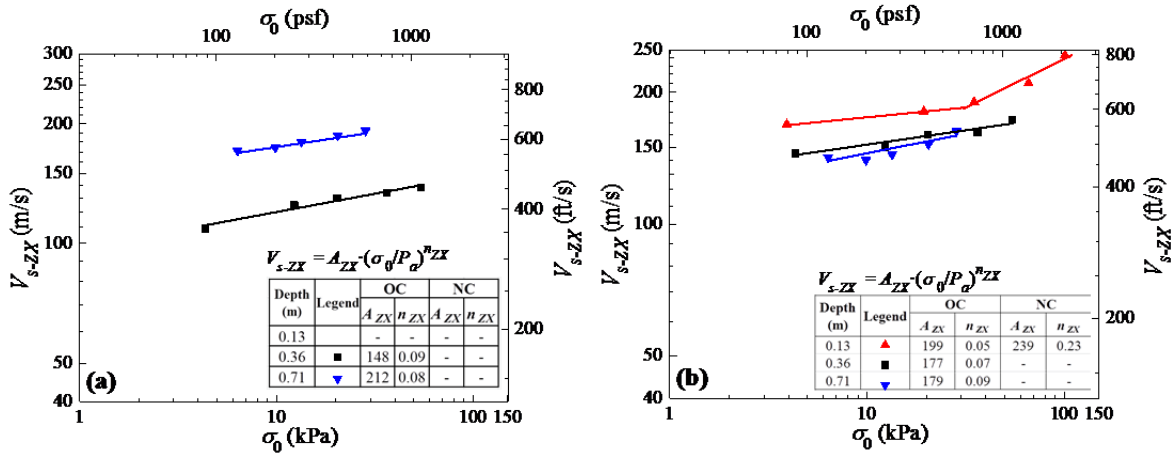

Figure 7.21 Effect of σ_0 on $V_{s\text{-}ZX}$ in the (a) east and (b) west hole arrays in location 1 at the LRL.

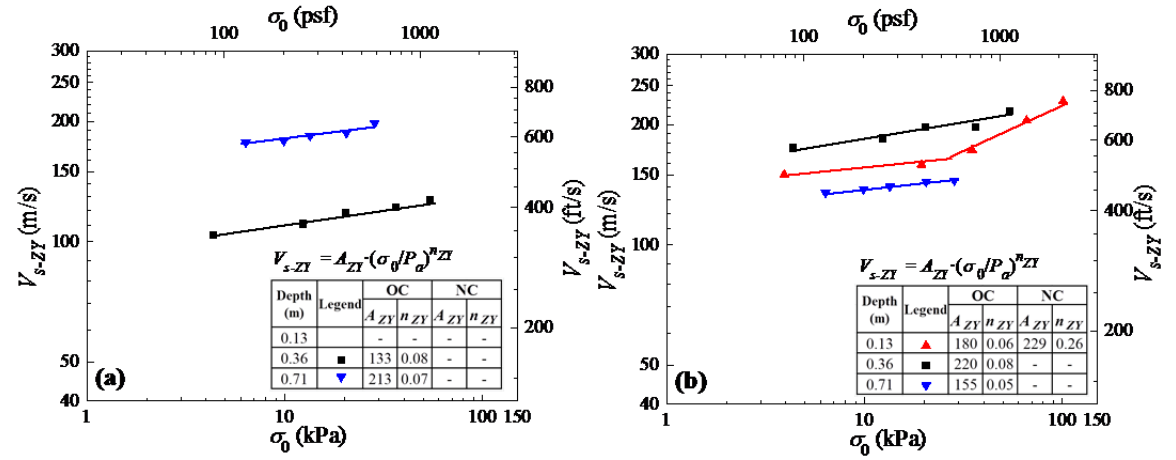

Figure 7.22 Effect of σ_0 on $V_{s\text{-}ZY}$ in the (a) east and (b) west hole arrays in location 1 at the LRL.

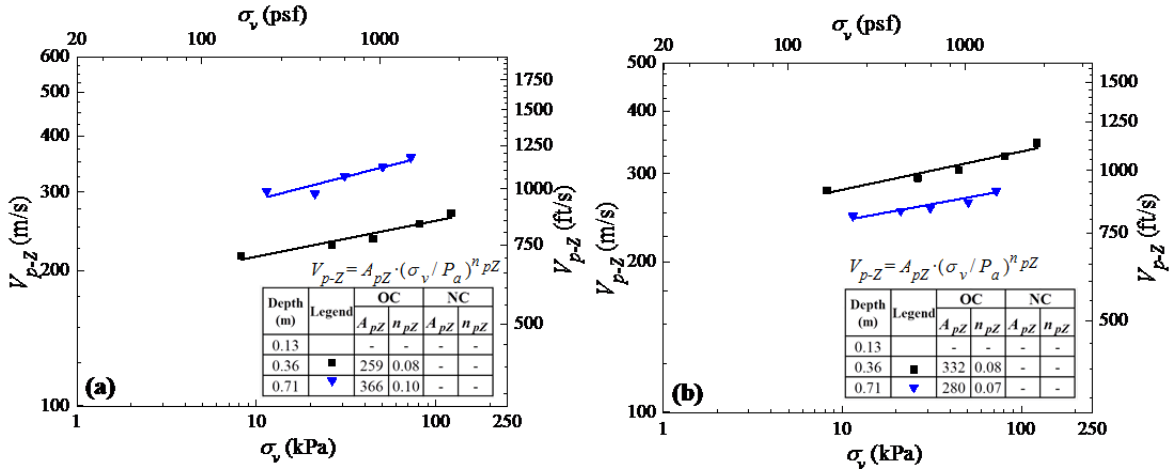

Figure 7.23 Effect of σ_v on $V_{p\text{-}Z}$ in the (a) east and (b) west hole arrays in location 1 at the LRL.

7.4.3 $V_{s\text{-}ZX}$, $V_{s\text{-}ZY}$, and $V_{p\text{-}Z}$ Profiles in Location 2 at the LRL

Figure 7.24 shows the variation of $V_{s\text{-}ZX}$ with depth for 5 different static load levels at location 2. Based on Fig 7.24(a), the initial $V_{s\text{-}ZX}$ in the east array decreased from 150 m/s at depth of 0.15 m to 144 m/ at depth of 0.32 m and decreased to 114 m/s at depth of 0.51 m. The variation of $V_{s\text{-}ZX}$ with depth in the west array is shown in Fig. 7.24(b). In the west array, the initial $V_{s\text{-}ZX}$ were 141 m/s at depth of 0.15 m, 154 m/ at depth of 0.32 m, and 125 m/s at depth of 0.51 m. As shown in Figure 7.24, the $V_{s\text{-}ZX}$ increased with increasing static vertical load.

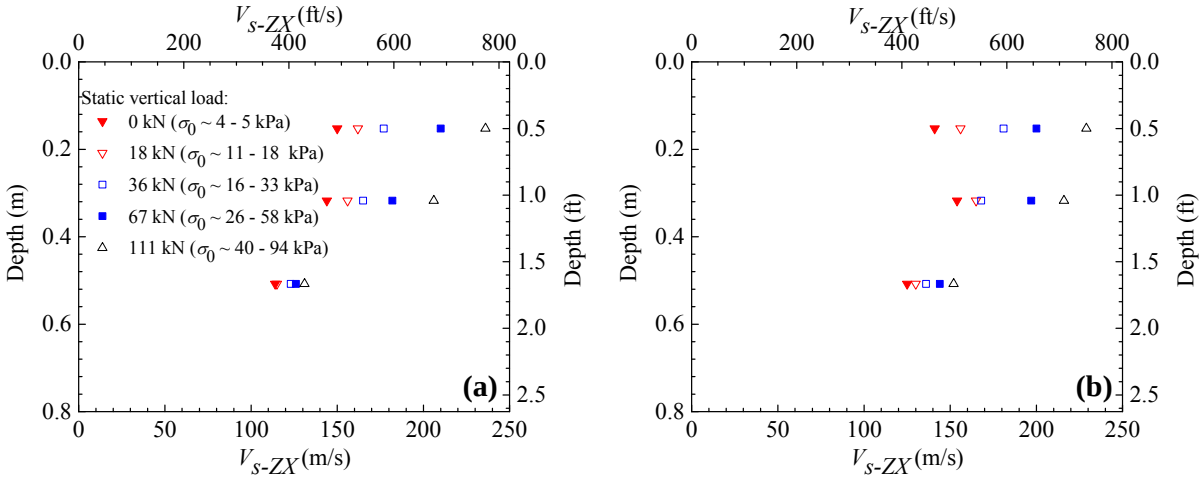

Figure 7.24 $V_{s\text{-}ZX}$ profiles in the (a) east and (b) west hole arrays in location 2 at the LRL.

The $V_{s\text{-}ZY}$ profiles measured from downhole seismic tests at location 2 are presented in Figs. 7.25(a) and 7.25(b) for the east and west arrays, respectively. In the east array, the initial $V_{s\text{-}ZY}$ were 133 m/s at depth of 0.32 m and 118 m/s at depth of 0.51 m. In the west array, the initial $V_{s\text{-}ZY}$ decreased from 144 m/s at depth of 0.15 m to 137 m/s at depth of 0.32 m and slightly increased to 140 m/s at depth of 0.51 m.

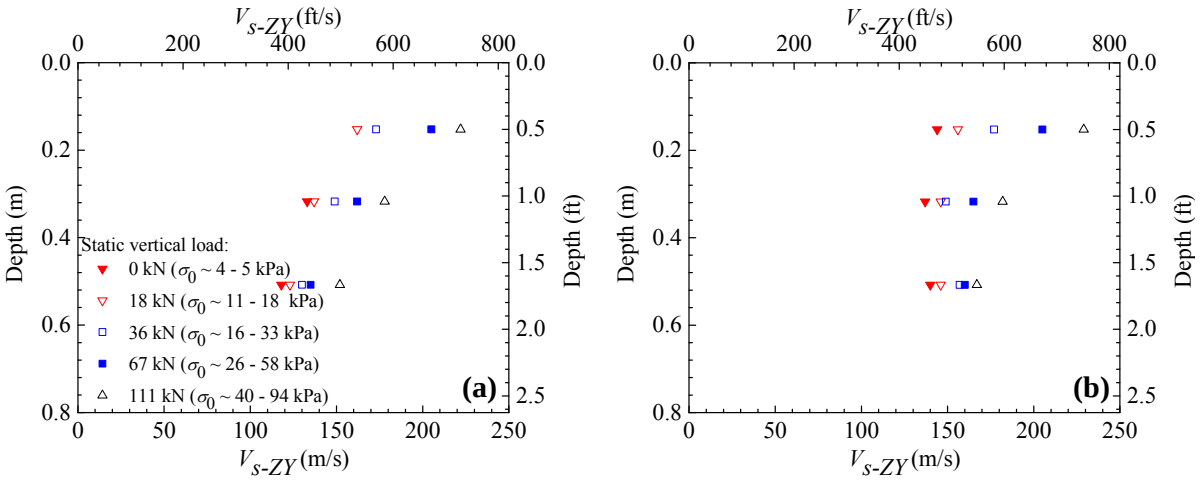

Figure 7.25 $V_{s\text{-}ZY}$ profiles in the (a) east and (b) west hole arrays in location 2 at the LRL.

Figure 7.26 presents the $V_{p\text{-}Z}$ profiles measured from downhole seismic tests at location 2. In the east array with static vertical load of 0 kN [Figure 7.26(a)], the initial $V_{p\text{-}Z}$ at depth of 0.15 m was 312 m/s. The initial $V_{p\text{-}Z}$ decreased to 284 m/s and 241 m/s at depths of 0.32 m and 0.51 m, respectively. In the west array with static vertical load of 0 kN [Figure 7.26(b)], the initial $V_{p\text{-}Z}$ were 278 m/s at depth of 0.15 m, 303 m/s at depth of 0.32 m, and 253 m/s at depth of 0.51 m. Figure 7.26 shows that $V_{p\text{-}Z}$ increased with increasing static vertical load.

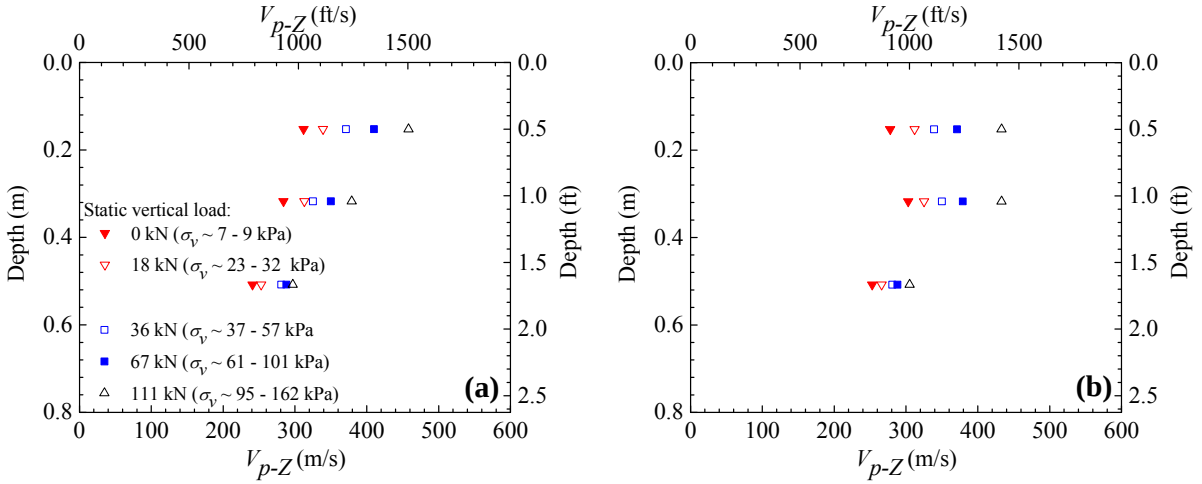

Figure 7.26 $V_{p\text{-}Z}$ profiles in the (a) east and (b) west hole arrays in location 2 at the LRL.

7.4.4 Effect of Stress State on $V_{s\text{-}ZX}$, $V_{s\text{-}ZY}$, and $V_{p\text{-}Z}$ in Location 2 at the LRL

Figures 7.27, 7.28, and 7.29 illustrate the $V_{s\text{-}ZX}$, $V_{s\text{-}ZY}$, and $V_{p\text{-}Z}$ variations with stresses in location 2, respectively. As discussed in earlier, some wave propagation velocities from downhole seismic tests could not be calculated due to poor or irregular waveforms. Unavailable data points may result in difficulty in performing regression analysis, particularly for shallower depths where the bi-linear relationship between wave propagation velocities and stresses occurred. Thus, some regression analyses were not performed if unavailable data points were considered significantly affecting the regression analysis results.

In the OC regime, the stress exponent n_{ZX} for $V_{s\text{-}ZX}$ ranged from 0.05 – 0.10, while in the NC regime, the n_{ZX} was on the order of 0.20 to 0.28. The n_{ZY} for $V_{s\text{-}ZY}$ varied from 0.06 to 0.11 in the OC regime and ranged from 0.21 to 0.25 in the NC regime. The n_{pZ} for $V_{p\text{-}Z}$ ranged from 0.05 to 0.09 in the OC regime and varied from 0.17 to 0.29 in the NC regime. As indicated by the change in slope in Figs 7.27, 7.28, and 7.29, the interpreted maximum vertical stress ($\sigma_{v\text{-max}}$) and $\sigma_{0\text{-max}}$ were approximately on the order of 45 – 59 kPa and 25 – 31 kPa, respectively.

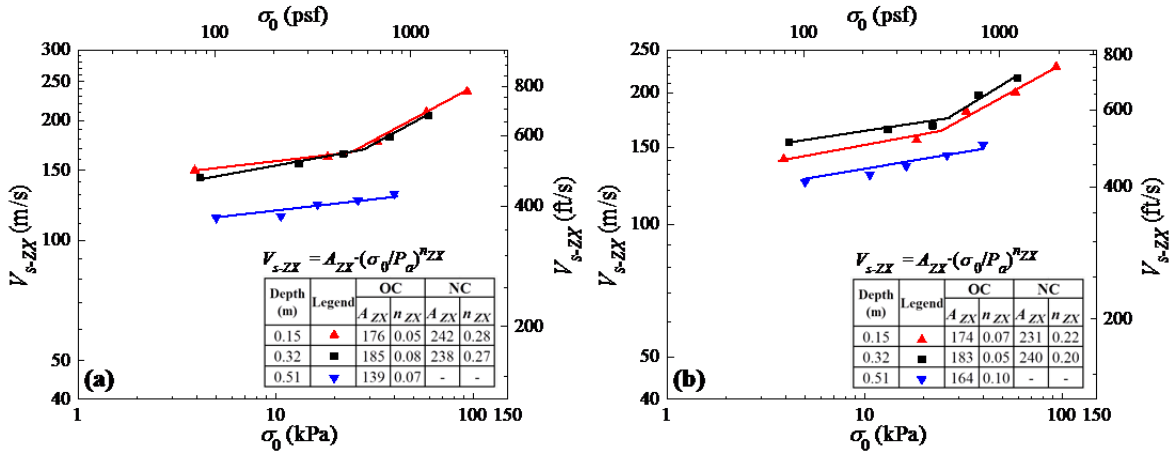

Figure 7.27 Effect of σ_0 on $V_{s\text{-}ZX}$ in the (a) east and (b) west hole arrays in location 2 at the LRL.

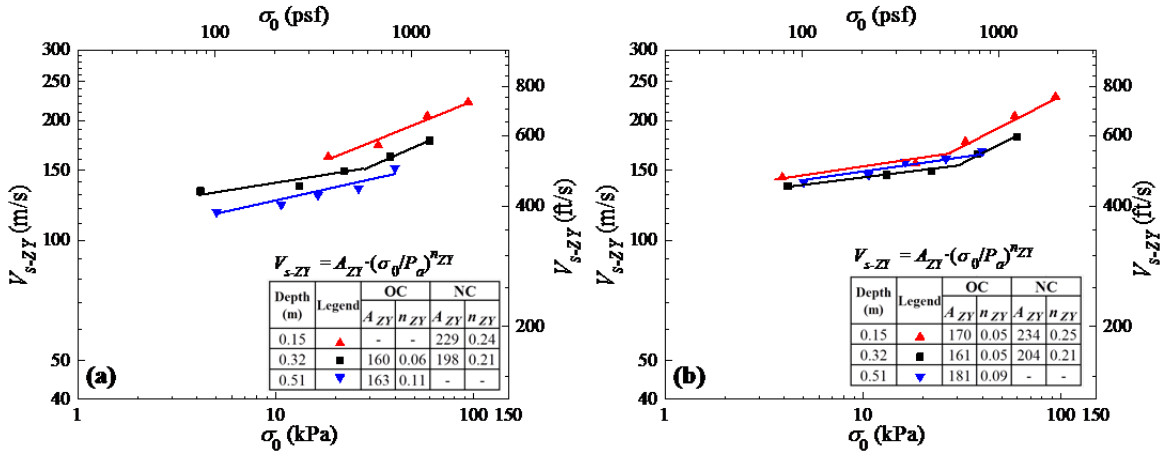

Figure 7.28 Effect of σ_0 on $V_{s\text{-}ZY}$ in the (a) east and (b) west hole arrays in location 2 at the LRL.

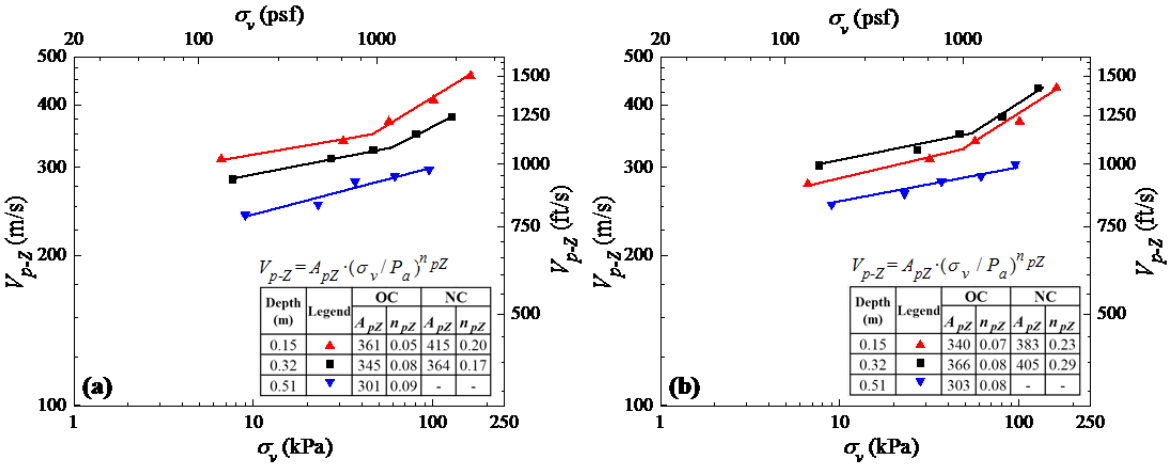

Figure 7.29 Effect of σ_v on $V_{p\text{-}Z}$ in the (a) east and (b) west hole arrays in location 2 at the LRL.

7.4.5 $V_{s\text{-}ZX}$, $V_{s\text{-}ZY}$, and $V_{p\text{-}Z}$ Profiles in Location 3 at the LRL

Downhole seismic tests were performed to investigate $V_{s\text{-}ZX}$ in location 3. Figures 7.30(a) and 7.30(b) present the $V_{s\text{-}ZX}$ profiles from the east and west hole arrays, respectively. These profiles were measured using static vertical load levels ranging from 0 kN to 102 kN. In the east array, the initial $V_{s\text{-}ZX}$ decreased from 123 m/s at depth of 0.13 m to 89 m/s at depth of 0.36 m and increased to 145 m/s at depth of 0.71 m. In the west array, the initial $V_{s\text{-}ZX}$ increased from 79 m/s

at depth of 0.13 m to 101 m/s at depth of 0.36 m and slightly decreased to 100 m/s at depth of 0.71 m. As shown in Figure 7.30, the $V_{s\text{-}ZX}$ increased with increasing vertical static load.

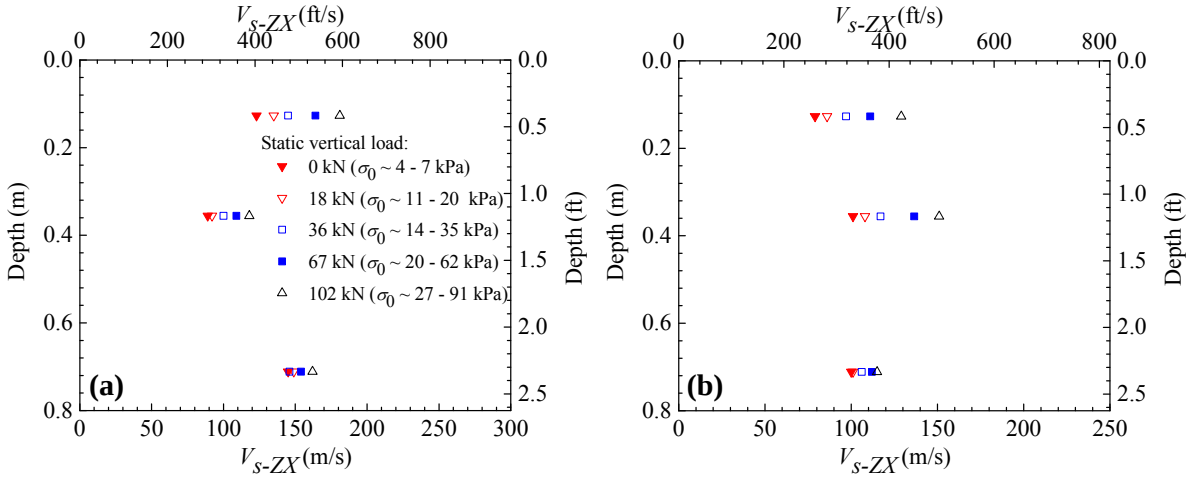

Figure 7.30 $V_{s\text{-}ZX}$ profiles in the (a) east and (b) west hole arrays in location 3 at the LRL.

The $V_{s\text{-}ZY}$ profiles measured from downhole seismic tests at location 3 are presented in Figs. 7.31(a) and 7.31(b) for the east and west arrays, respectively. In the east array, the initial $V_{s\text{-}ZY}$ decreased from 113 m/s at depth of 0.13 m to 90 m/s at depth of 0.36 m and increased to 117 m/s at depth of 0.71 m. In the west array, the initial $V_{s\text{-}ZY}$ increased from 98 m/s at depth of 0.13 m to 106 m/s at depth of 0.36 m and slightly decreased to 105 m/s at depth of 0.71 m.

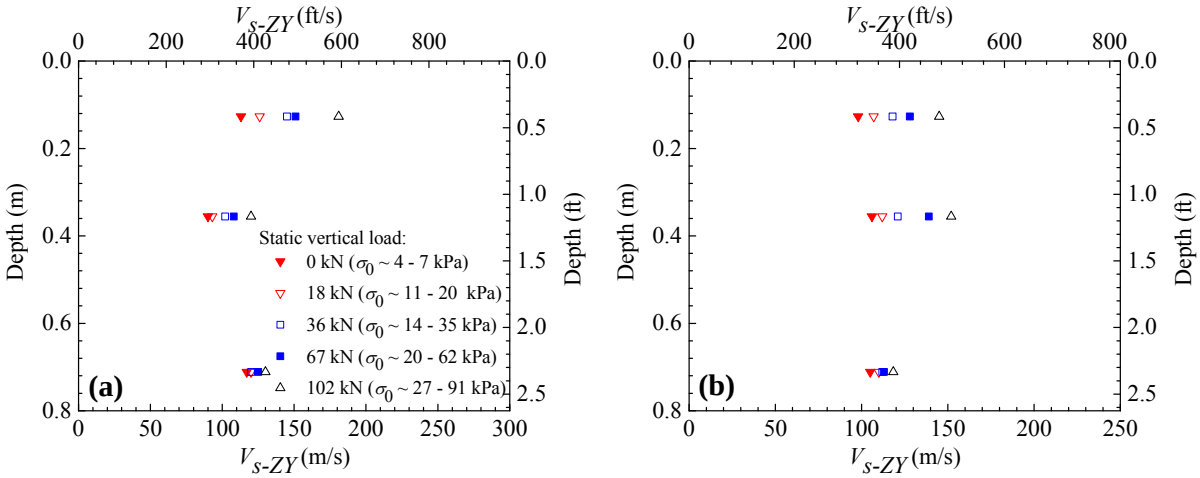

Figure 7.31 $V_{s\text{-}ZY}$ profiles in the (a) east and (b) west hole arrays in location 3 at the LRL.

The $V_{p\text{-}Z}$ profiles measured from downhole seismic tests in location 3 are presented in Figs. 7.32(a) and 7.32(b) for the east and west hole arrays, respectively. In the east array with static vertical load of 0 kN, the $V_{p\text{-}Z}$ at depth of 0.13 m was 216 m/s. The $V_{p\text{-}Z}$ decreased to 179 m/s at depth of 0.36 m and increased to 228 m/s at depth of 0.71 m. In the west array, the initial $V_{p\text{-}Z}$ were 169 m/s at depth of 0.13 m, 173 m/s at depth of 0.36 m, and 194 m/s at depth of 0.71 m. As observed in Fig. 7.32, the $V_{p\text{-}Z}$ increased with increasing static vertical loads.

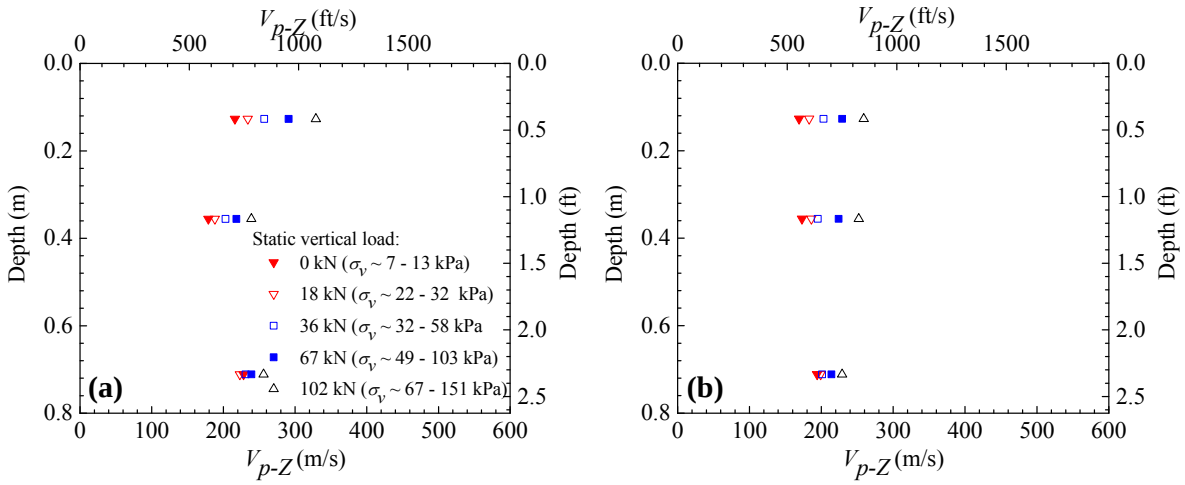

Figure 7.32 $V_{p\text{-}Z}$ profiles in the (a) east and (b) west hole arrays in location 3 at the LRL.

7.4.6 Effect of Stress State on $V_{s\text{-}ZX}$, $V_{s\text{-}ZY}$, and $V_{p\text{-}Z}$ in Location 3 at the LRL

The variations of $V_{s\text{-}ZX}$, $V_{s\text{-}ZY}$, and $V_{p\text{-}Z}$ with stresses are presented in Figures 7.33, 7.34, and 7.35, respectively. In the OC regime, the stress exponent n_{ZX} for $V_{s\text{-}ZX}$ ranged from 0.07 – 0.11, while in the NC regime, the n_{ZX} was on the order of 0.22 to 0.30. The n_{ZY} for $V_{s\text{-}ZY}$ varied from 0.06 to 0.08 in the OC regime and increased to 0.21 and 0.30 in the NC regime. The n_{pZ} for $V_{p\text{-}Z}$ ranged from 0.05 to 0.07 in the OC regime and varied from 0.25 to 0.33 in the NC regime. As indicated by the change in slope in Figs 7.33, 7.34, and 7.35, the interpreted maximum $\sigma_{v\text{-max}}$ and $\sigma_{0\text{-max}}$ were approximately on the order of 45 – 61 kPa and 23 – 31 kPa, respectively.

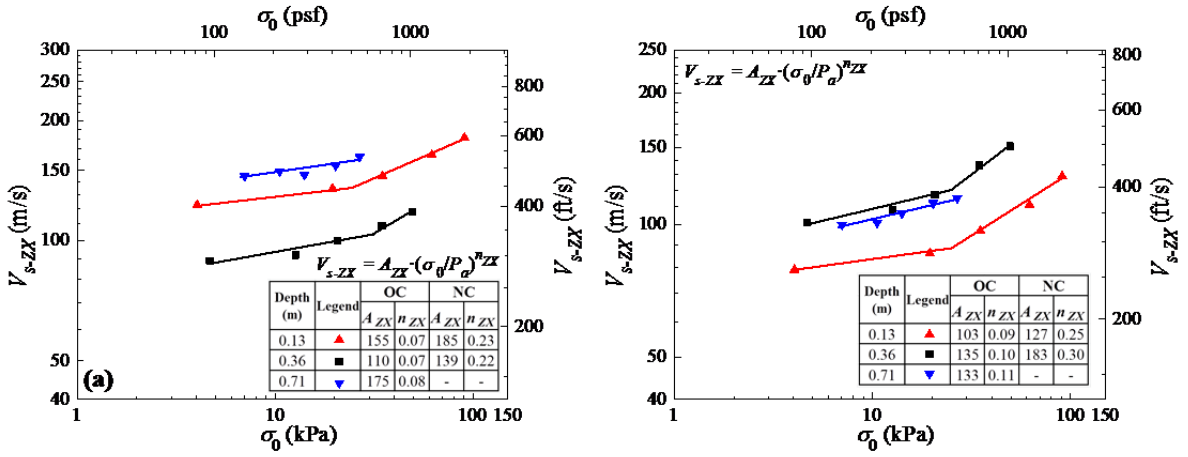

Figure 7.33 Effect of σ_0 on $V_{s\text{-}ZX}$ in the (a) east and (b) west hole arrays in location 3 at the LRL.

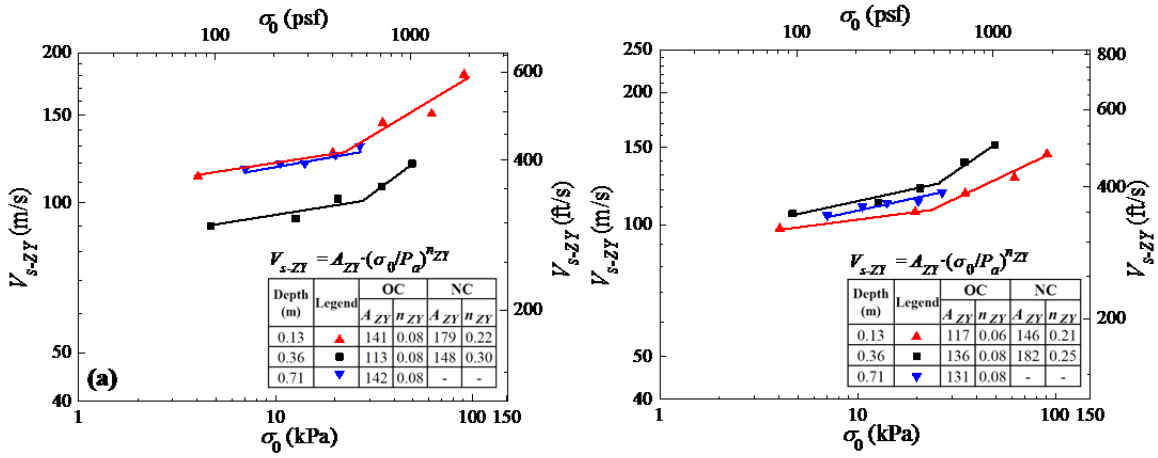

Figure 7.34 Effect of σ_0 on $V_{s\text{-}ZY}$ in the (a) east and (b) west hole arrays in location 3 at the LRL.

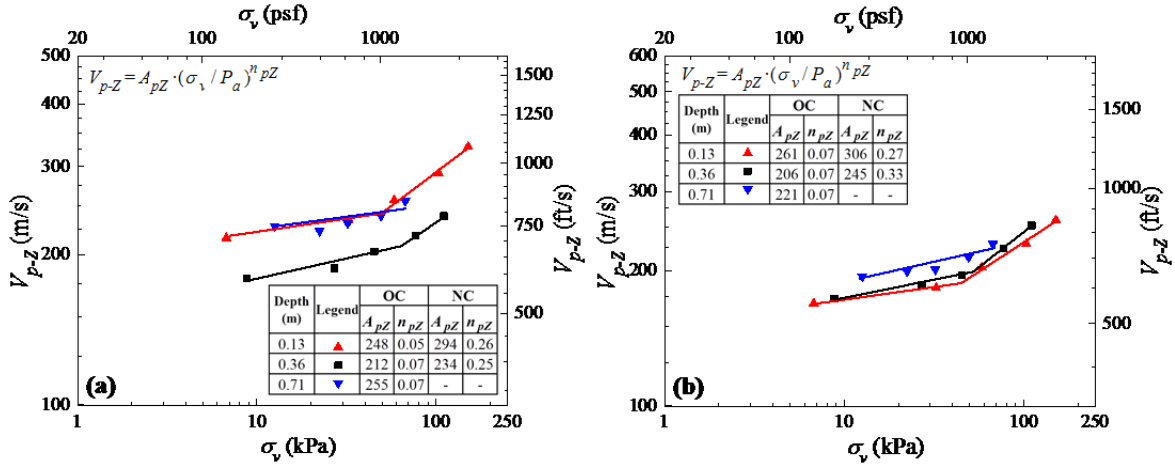

Figure 7.35 Effect of σ_v on $V_{p\text{-}Z}$ in the (a) east and (b) west hole arrays in location 3 at the LRL.

7.5 **Small-scale Crosshole Seismic Testing**

The crosshole seismic tests were performed at the LRL to evaluate horizontally propagating P-wave velocity ($V_{p\text{-}X}$) and horizontally-propagating vertically-polarized in the Z-axis S-wave ($V_{s\text{-}XZ}$). This test was conducted by hitting the crosshole source rods using a handheld hammer as illustrated in Figure 7.16(b). Figure 7.36 shows example of wave trains from crosshole seismic test. It should be noted that some wave propagation velocities from crosshole seismic tests could not be calculated due to poor or irregular waveforms.

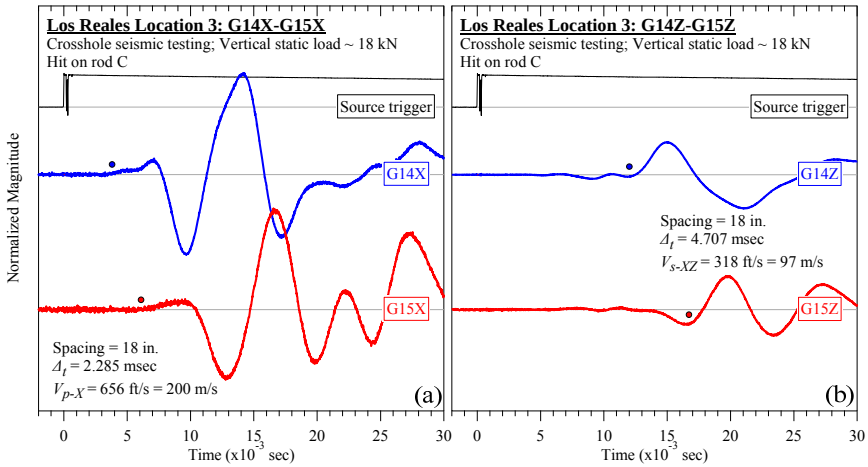

Figure 7.36 Examples of wave trains from crosshole seismic test at the LRL: (a) $V_{p\text{-}X}$ and (b) $V_{s\text{-}XZ}$.

Similarly to the downhole seismic testing, the relationship between $V_{p\text{-}X}$ and $V_{s\text{-}XZ}$ and stress was regressed using a power function. In this case, σ_h and σ_0 were used as correlation parameters for $V_{p\text{-}X}$ and $V_{s\text{-}XZ}$, respectively. Relationships between wave propagation velocity and stress component were fitted using the following equations.

$$V_{p-X} = A_{pX} \cdot \left(\frac{\sigma_h}{P_a} \right)^{n_{pX}} \tag{7.4}$$

$$V_{s-XZ} = A_{XZ} \cdot \left(\frac{\sigma_0}{P_a} \right)^{n_{XZ}} \tag{7.5}$$

Figures 7.37(a) and 7.37(b) show the relationship between $V_{p\text{-}X}$ and $V_{s\text{-}XZ}$ and stress states in location 1, respectively. An either linear or bi-linear relationship between wave propagation velocities and stresses is observed in these figures. In the OC regime, the stress exponent n_{pX} for $V_{p\text{-}X}$ was found to be low (n_{pX} ~ 0.06 – 0.11), while in the NC regime, the n_{pX} increased to 0.21. The n_{XZ} for $V_{s\text{-}XZ}$ ranged from 0.04 to 0.07 in the OC regime.

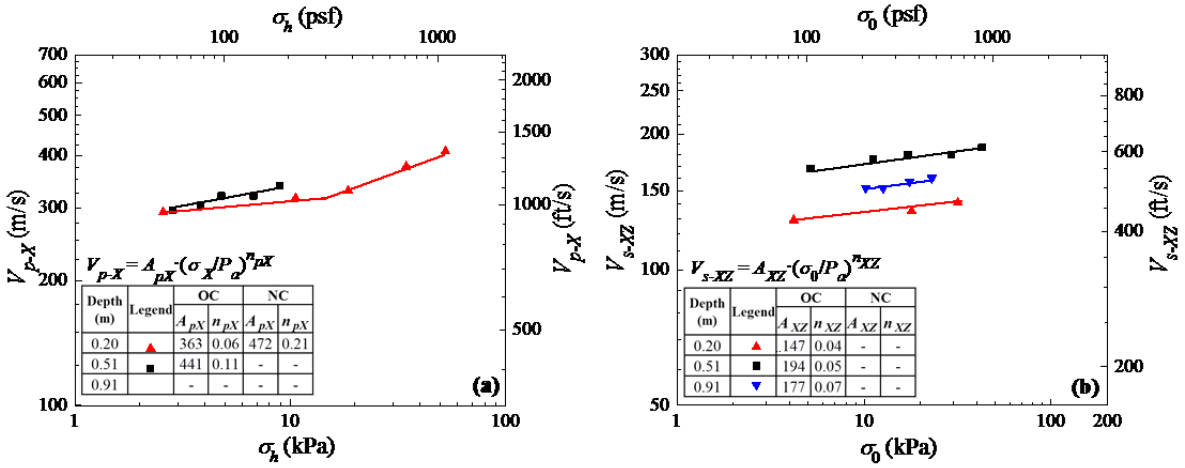

Figure 7.37 Effect of stress states on (a) $V_{p\text{-}X}$ and (b) $V_{s\text{-}XZ}$ in location 1 at the LRL.

The relationship between $V_{p\text{-}X}$ and $V_{s\text{-}XZ}$ and stress states in location 2 are presented in Figures 7.38(a) and 7.38(b), respectively. An either linear or bi-linear relationship between wave propagation velocities and stresses is observed in these figures. In the OC regime, the stress exponent n_{pX} for $V_{p\text{-}X}$ ranged from 0.06 to 0.11. In the NC regime, the n_{pX} for $V_{p\text{-}X}$ increased to 0.20. The n_{XZ} for $V_{s\text{-}XZ}$ ranged from 0.05 to 0.08 in the OC regime. In the NC regime, the n_{XZ} increased to 0.26.

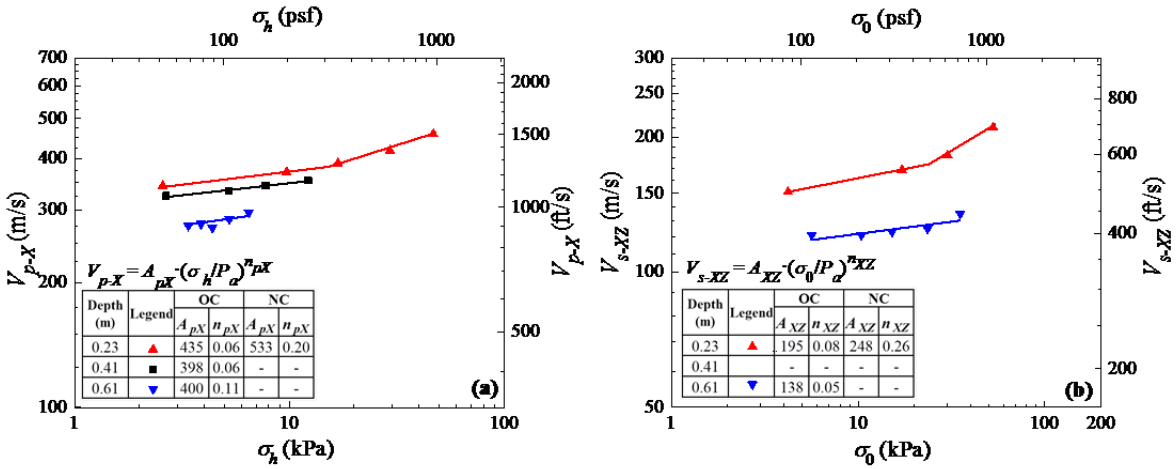

Depth (m)	Legend	OC A_{pX}	OC n_{pX}	NC A_{pX}	NC n_{pX}
0.23	▲	435	0.06	533	0.20
0.41	■	398	0.06	-	-
0.61	▼	400	0.11	-	-

Depth (m)	Legend	OC A_{XZ}	OC n_{XZ}	NC A_{XZ}	NC n_{XZ}
0.23	▲	195	0.08	248	0.26
0.41		-	-	-	-
0.61	▼	138	0.05	-	-

Figure 7.38 Effect of stress states on (a) $V_{p\text{-}X}$ and (b) $V_{s\text{-}XZ}$ in location 2 at the LRL.

Figures 7.39(a) and 7.39(b) show the relationship between $V_{p\text{-}X}$ and $V_{s\text{-}XZ}$ and stress states in location 3, respectively. The relationship between wave propagation velocities and stresses also exhibited linear or bi-linear form. In the OC regime, the n_{pX} for $V_{p\text{-}X}$ ranged from 0.04 – 0.09, while in the NC regime, the n_{pX} increased to 0.28. The n_{XZ} for $V_{s\text{-}XZ}$ varied from 0.08 to 0.10 in the OC regime and increased to 0.20 in the NC regime.

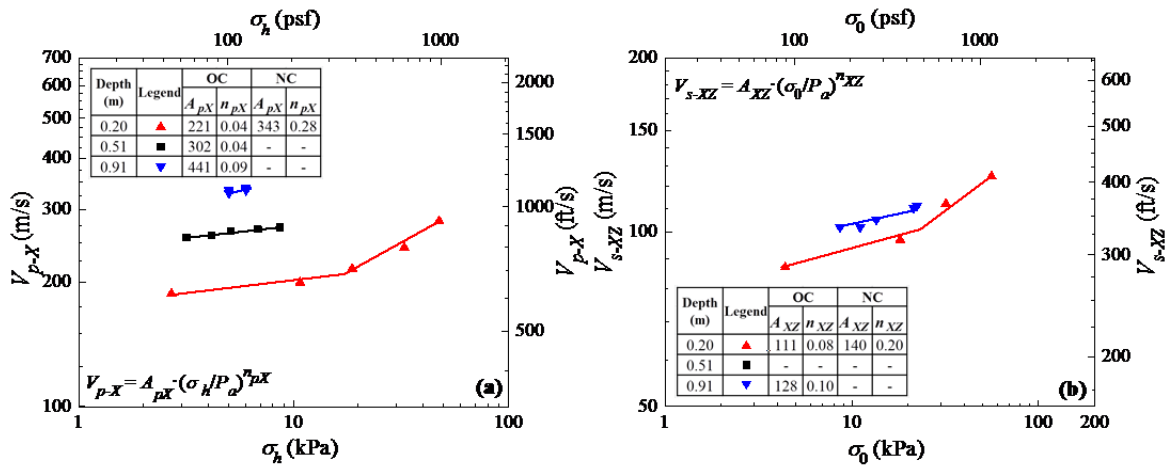

Depth (m)	Legend	OC A_{pX}	OC n_{pX}	NC A_{pX}	NC n_{pX}
0.20	▲	221	0.04	343	0.28
0.51	■	302	0.04	-	-
0.91	▼	441	0.09	-	-

Depth (m)	Legend	OC A_{XZ}	OC n_{XZ}	NC A_{XZ}	NC n_{XZ}
0.20	▲	111	0.08	140	0.20
0.51	■	-	-	-	-
0.91	▼	128	0.10	-	-

Figure 7.39 Effect of stress states on (a) $V_{p\text{-}X}$ and (b) $V_{s\text{-}XZ}$ in location 3 at the LRL.

7.6 **Evaluation of Anisotropy of Wave Propagation Velocity in MSW at the LRL**

As discussed in Chapter 5, anisotropy of wave propagation velocity in MSW may have an important role in landfill engineering practice. To date, the anisotropy of MSW in term of wave propagation velocities has never been evaluated.

Anisotropy in MSW can be attributed to stress-induced anisotropy and fabric (structural) anisotropy, as discussed in Zekkos (2013). Stress-induced anisotropy is attributed to stress states that are different in the horizontal and vertical directions. Fabric anisotropy is attributed to preferential orientation of fibrous particles in the MSW. Thus, the MSW can still behave anisotropically even in isotropic stress states. In this study, assessment of the degree of anisotropy in MSW was performed by comparing wave velocities from a variety of propagation and polarization directions.

Figure 7.40(a) shows a comparison between $V_{p\text{-}Z}$ and $V_{s\text{-}ZX}$. The ratio of $V_{s\text{-}ZX}$ to $V_{p\text{-}Z}$ in location 1 ranged from 0.50 to 0.59. The ratio of $V_{s\text{-}ZX}$ to $V_{p\text{-}Z}$ in location 2 varied from 0.44 to 0.54. In location 3, the ratio of $V_{s\text{-}ZX}$ to $V_{p\text{-}Z}$ ranged from 0.47 to 0.67. On average, the ratio of $V_{s\text{-}ZX}$ to $V_{p\text{-}Z}$ from three locations was 0.51.

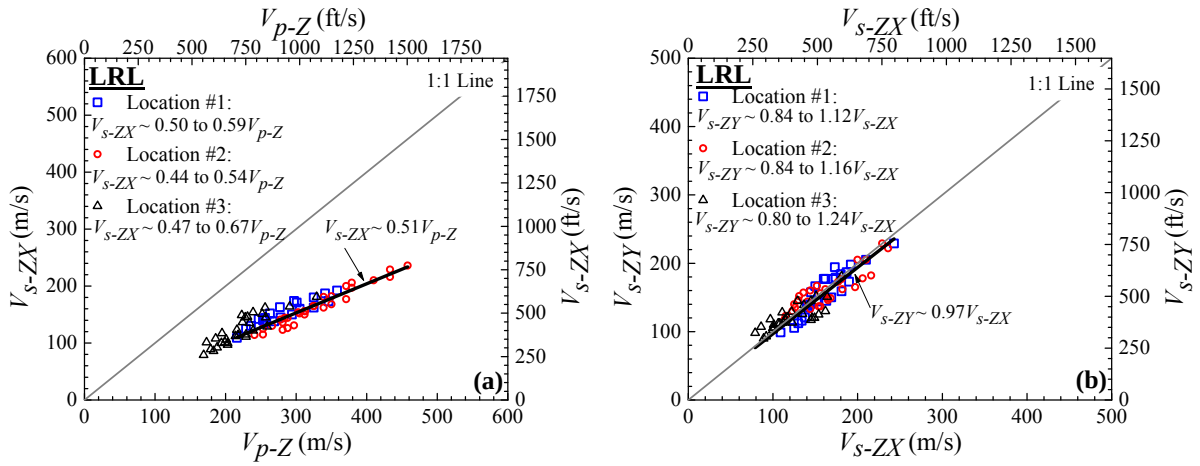

Figure 7.40 Comparison on (a) $V_{p\text{-}Z}$-$V_{s\text{-}ZX}$ and (b) $V_{s\text{-}ZX}$ -$V_{s\text{-}ZY}$ at the LRL.

Figure 7.40(b) presents a comparison between the $V_{s\text{-}ZX}$ and the $V_{s\text{-}ZY}$. In location 1, the ratio of $V_{s\text{-}ZY}$ to $V_{s\text{-}ZX}$ varied from 0.84 to 1.12. In location 2, the ratio of $V_{s\text{-}ZY}$ to $V_{s\text{-}ZX}$ ranged from 0.84 to 1.16. In location 3, the ratio of $V_{s\text{-}ZY}$ to $V_{s\text{-}ZX}$ varied from 0.80 to 1.24. On average, the ratio from three locations was found to be 0.97 indicating minor difference on average between S-wave propagation velocities in the YZ and the XZ plane.

Figure 7.41 shows a comparison between $V_{p\text{-}X}$ and $V_{s\text{-}XZ}$. In location 1, the ratio of $V_{s\text{-}XZ}$ to $V_{p\text{-}X}$ ranged from 0.43 to 0.58. In location 2, this ratio varied from 0.44 to 0.53. In location 3, this ratio varied from 0.31 to 0.52. In general, the ratio of $V_{s\text{-}XZ}$ to $V_{p\text{-}X}$ in three test locations at the LRL ranged from 0.31 to 0.59 with a mean value of 0.45. This ratio was lower than the ratio of V_p and V_s counterparts propagating in the vertical direction.

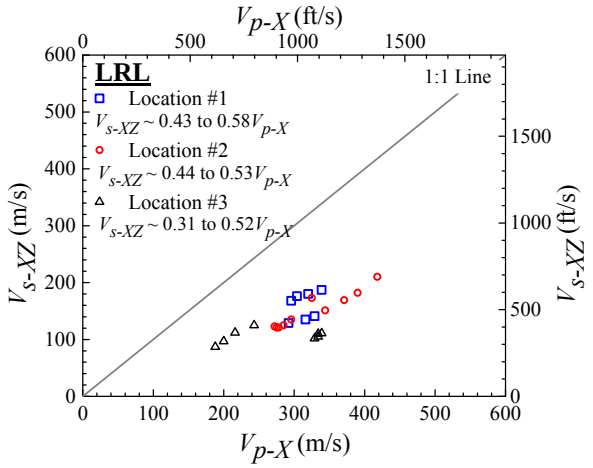

Figure 7.41 Comparison on $V_{p\text{-}X}$ and $V_{s\text{-}XZ}$ at the LRL.

Anisotropy in MSW was also evaluated by comparing wave propagation velocities in the horizontal and vertical directions. Because the designated measurement points from downhole and crosshole seismic tests were not the same, four $V_{p\text{-}Z}$ values from downhole tests were averaged and then compared with a $V_{p\text{-}X}$ from a crosshole test, as shown in Fig 7.42. The same

method was also performed in comparing shear wave velocity propagating in the vertical and horizontal directions.

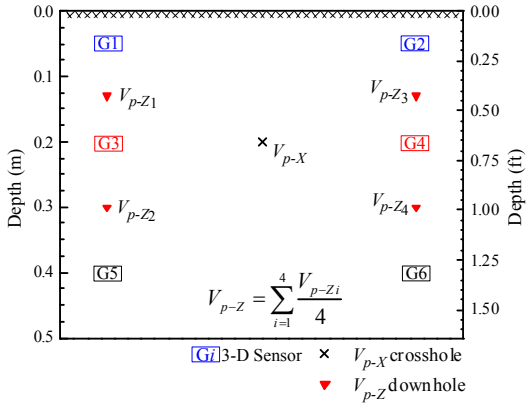

Figure 7.42 Measurement points for comparing wave propagation velocities in the vertical and horizontal directions.

Figure 7.43(a) shows a comparison between V_p propagating in horizontal ($V_{p\text{-}X}$) and vertical ($V_{p\text{-}Z}$) directions. In location 1, the ratios of $V_{p\text{-}Z}$ to $V_{p\text{-}X}$ varied from 0.75 to 0.93. In location 2, the ratios of $V_{p\text{-}Z}$ to $V_{p\text{-}X}$ varied from 0.83 to 0.93. In location 3, the ratios of $V_{p\text{-}Z}$ to $V_{p\text{-}X}$ varied from 0.75 to 0.99. The ratio of $V_{p\text{-}Z}$ to $V_{p\text{-}X}$ from three locations ranged from 0.75 to 0.99 with mean value of 0.86. This ratio indicated that the compressibility of MSW in the horizontal direction was lower than compressibility in the vertical direction.

The relationship between V_s propagating in the horizontal ($V_{s\text{-}horizontal}$: $V_{s\text{-}XZ}$) and vertical ($V_{s\text{-}vertical}$: $V_{s\text{-}ZX}$ and $V_{s\text{-}ZY}$) directions is shown in Figure 7.43(b). The ratio $V_{s\text{-}vertical}$ and $V_{s\text{-}horizontal}$ were found to be between 0.69 and 1.17 with an average value of 0.92. In general, the data indicated that wave propagation in the vertical direction was slower than that in the horizontal direction, highlighting that MSW is an anisotropic material.

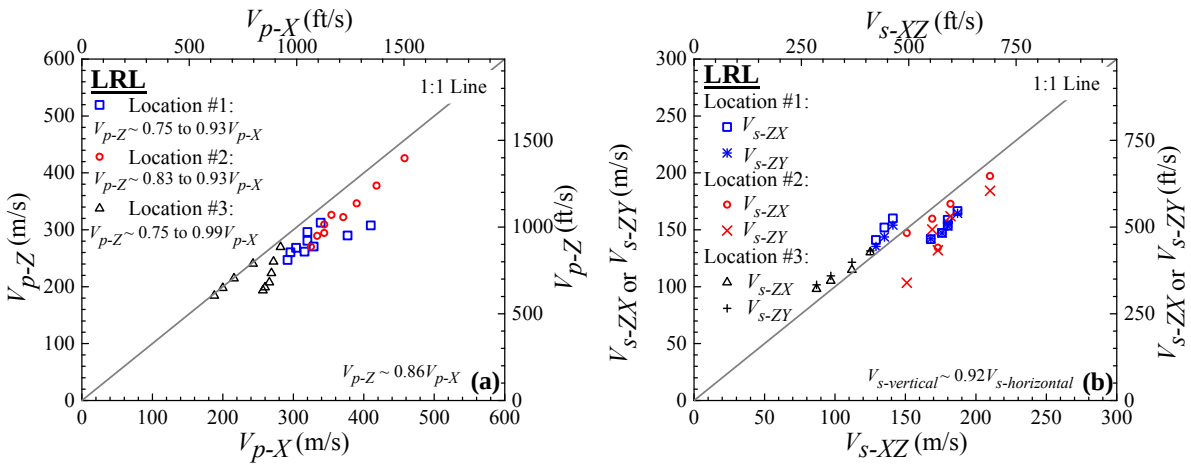

Figure 7.43 (a) Comparison on V_p propagating in the vertical and horizontal directions; and (b) V_s propagating in the vertical and horizontal directions at the LRL.

7.7 **Evaluation of Poisson's ratio at the LRL**

The V_p and V_s from small-strain downhole and crosshole seismic tests can be used to evaluate small-strain Poisson's ratio based on elasticity equation (Eq. 2.13). It should be noted that this equation was derived for homogeneous, isotropic, and elastic solid material. For anisotropic material, such as MSW, the meaning of Poisson's ratio can be very complex. Nevertheless, Eq. 2.13 was used to evaluate Poisson's ratio of MSW by Sharma et al. (1990), Houston et al. (1995), Matasovic and Kavazanjian (1998), and Zalachoris (2010). In this study, the V_p and V_s values from downhole and crosshole seismic tests were used to evaluate "pseudo" Poisson's ratio. "Pseudo" Poisson's ratios v_{ZX} and v_{ZY} from downhole seismic testing were estimated using Eqs. 7.6 and 7.7 that have identic expression to Eq. 2.13.

$$v_{ZX} = \frac{0.5 \cdot \left(V_{s-ZX}/V_{p-Z}\right)^2 - 1}{\left(V_{s-ZX}/V_{p-Z}\right)^2 - 1} \tag{7.6}$$

$$v_{ZY} = \frac{0.5 \cdot \left(V_{s-ZY}/V_{p-Z}\right)^2 - 1}{\left(V_{s-ZY}/V_{p-Z}\right)^2 - 1} \tag{7.7}$$

The "pseudo" Poisson's ratio v_{XZ} was evaluated using crosshole seismic test results (Eq. 7.8).

$$\nu_{XZ} = \frac{0.5 \cdot \left(V_{s-XZ}/V_{p-X}\right)^2 - 1}{\left(V_{s-XZ}/V_{p-X}\right)^2 - 1} \tag{7.8}$$

Poisson's ratio variation with depth from downhole and crosshole seismic tests in location 1 at the LRL is presented in Figs. 7.44. In location 1, the ν_{ZX} and ν_{ZY} ranged from 0.28 to 0.33 and 0.14 to 0.36 at depth of 0.36 m, respectively. At depth of 0.71 m, the ν_{ZX} and ν_{ZY} varied from 0.23 to 0.29 and 0.21 to 0.31, respectively. The ν_{XZ} ranged from 0.24 to 0.37.

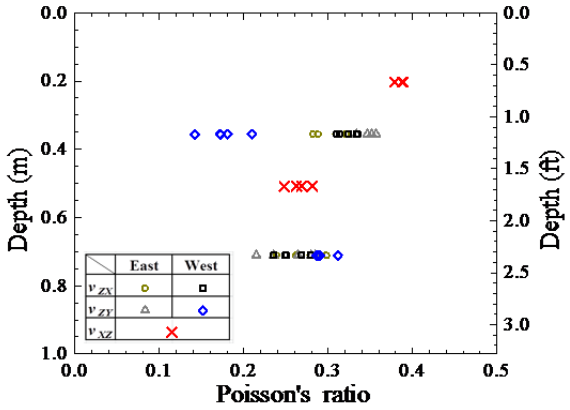

Figure 7.44 Small-strain Poisson's ratio evaluated using V_s and V_p in location 1 at the LRL.

Poisson's ratio variation with depth from downhole and crosshole seismic tests in location 2 at the LRL is presented in Fig. 7.45. The ν_{ZX} and ν_{ZY} ranged from 0.30 to 0.35 and 0.28 to 0.33 at depth of 0.13 m, respectively. At depth of 0.36 m, the ν_{ZX} and ν_{ZY} varied from 0.29 to 0.35 and from 0.36 to 0.39, respectively. At depth of 0.71 m, the ν_{ZX} and ν_{ZY} ranged from 0.33 to 0.38 and 0.27 to 0.38, respectively. The ν_{XZ} varied from 0.33 to 0.38.

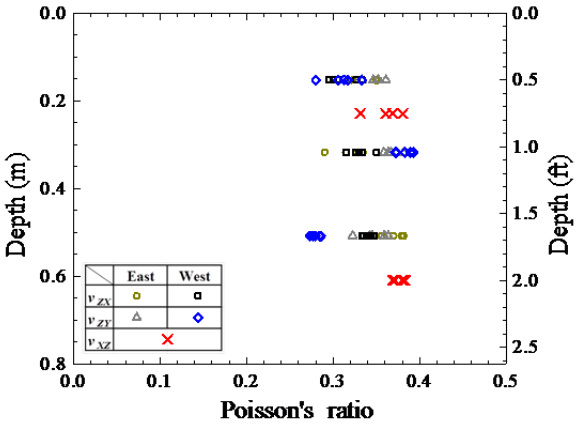

Figure 7.45 Small-strain Poisson's ratio evaluated using V_s and V_p in location 2 at the LRL.

Figure 7.46 shows the Poisson's ratio variation with depth from downhole and crosshole seismic tests in location 3 at the LRL. In this location, the v_{ZX} and v_{ZY} varied from 0.25 to 0.36 and 0.24 to 0.31 at depth of 0.13 m, respectively. At depth of 0.36 m, the v_{ZX} and v_{ZY} ranged from 0.20 to 0.34 and from 0.19 to 0.34, respectively. At depth of 0.71 m, the v_{ZX} and v_{ZY} ranged from 0.10 to 0.33 and 0.27 to 0.33, respectively. The v_{XZ} ranged from 0.32 to 0.45.

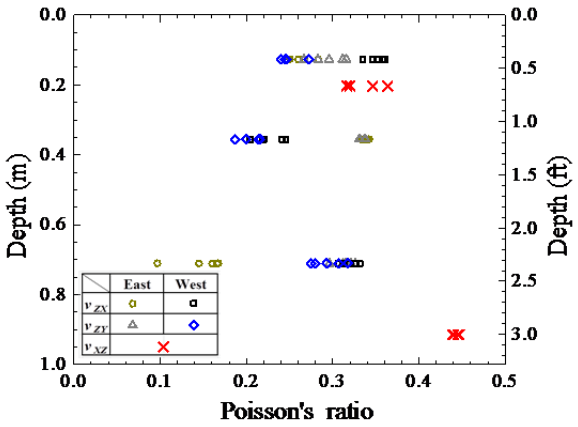

Figure 7.46 Small-strain Poisson's ratio evaluated using V_s and V_p in location 3 at the LRL.

Figures 7.44, 7.45, and 7.46 show large scatter of Poisson's ratio of MSW. In general, large scatter in these figures could be attributed to the variability of the waste within a test location as well as the anisotropic nature of the waste.

7.8 **Steady-state Dynamic Testing**

Steady-state dynamic test using Thumper and T-Rex was conducted to study the relationship between shear modulus or normalized shear modulus and shearing strain at the LRL (Fig. 7.47). This test was performed at different static vertical load levels to study the effect of confining stress on the shear modulus and normalized shear modulus reduction curves. In each test location at the LRL, Thumper or T-Rex was used to impose static vertical loads of 18 kN, 36 kN, 71 kN, and 133 kN as described in Figs. 7.10, 7.11, and 7.12. Thumper was used for steady-state test with static vertical load up to 36 kN. At each vertical static load level, dynamic horizontal loads were applied from small to large amplitude. Chapter 4 describes the testing method of the steady-state dynamic testing as well as the limitations and uncertainties of this method. In this secetion, the results are presented.

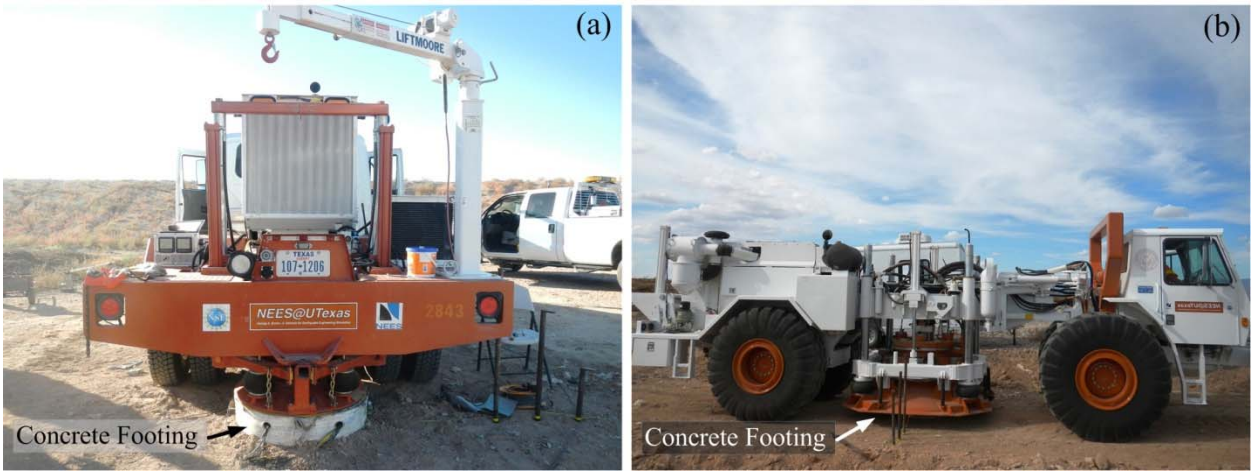

Figure 7.47 Steady-state dynamic testing using (a) Thumper and (b) T-Rex at the LRL.

Figure 7.48 shows the quadrilateral elements for location 1 at the LRL. Elements A, D, and F were defined by four adjacent geophones. Element A was defined by the four sensors closest to the surface, element D was defined by four intermediate sensors, and element F was defined by the four deepest sensors. Element C was defined by the deepest and the shallowest

geophones. It should be noted that sensor# 23 in location 1 exhibited irregular response. The output amplitude of this sensor was very weak and much lower than those of deeper sensors. Thus, elements A and C that included sensor#23 were not analyzed in this location. After field investigation in location 1, sensor# 23 was recovered from the hole and was found to work normally. The problem may be attributed to the extension cable that connected the sensor to the data acquisition system. Figures 7.49 and 7.50 present the quadrilateral elements for locations 2 and 3 at the LRL, respectively.

Shear modulus was calculated using the shear wave velocity and mass density of MSW. Vertically propagating shear wave velocity was calculated using the phase difference in travel time as shown in Fig. 7.51(a). Mass density was obtained from in-situ unit weight measurements. The average of the shear modulus calculated from both arrays was used as the shear modulus of each element. It should be noted that the mass density may affect the accuracy in shear modulus calculation, but, does not affect the normalized shear modulus reduction curve. The 4-node displacement based method (Rathje et al. 2005) was used to calculate the shearing strain at the center of quadrilateral elements. Example of shearing strain time history calculated using the 4-node method is shown in Fig. 7.51(b). The analysis method to reduce data from steady-state dynamic test is described in detail in Chapter 4. The results of normalized shear modulus reduction curves from this site were used to develop recommended G/G_{max} curves in Chapter 9.

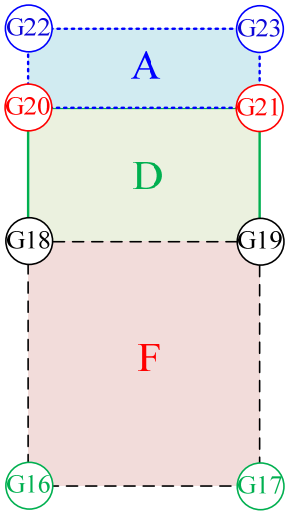

Element	Geophones/Nodes
A	G20, G21, G23, G22
D	G18, G19, G21, G20
F	G16, G17, G19, G18
C = A+D+F	G16, G17, G23, G22

Figure 7.48 Quadrilateral elements for location 1 at the LRL.

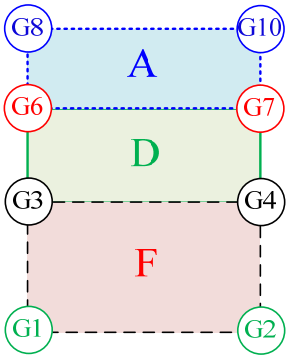

Element	Geophones/Nodes
A	G7, G6, G8, G10
D	G4, G3, G6, G7
F	G2, G1, G3, G4
C = A+D+F	G2, G1, G8, G10

Figure 7.49 Quadrilateral elements for location 2 at the LRL.

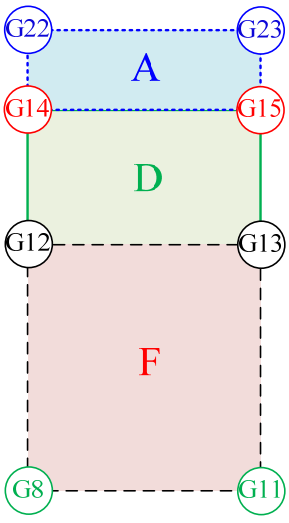

Element	Geophones/Nodes
A	G15, G14, G22, G23
D	G13, G12, G14, G15
F	G11, G8, G12, G13
C = A+D+F	G11, G8, G12, G13

Figure 7.50 Quadrilateral elements for location 3 at the LRL.

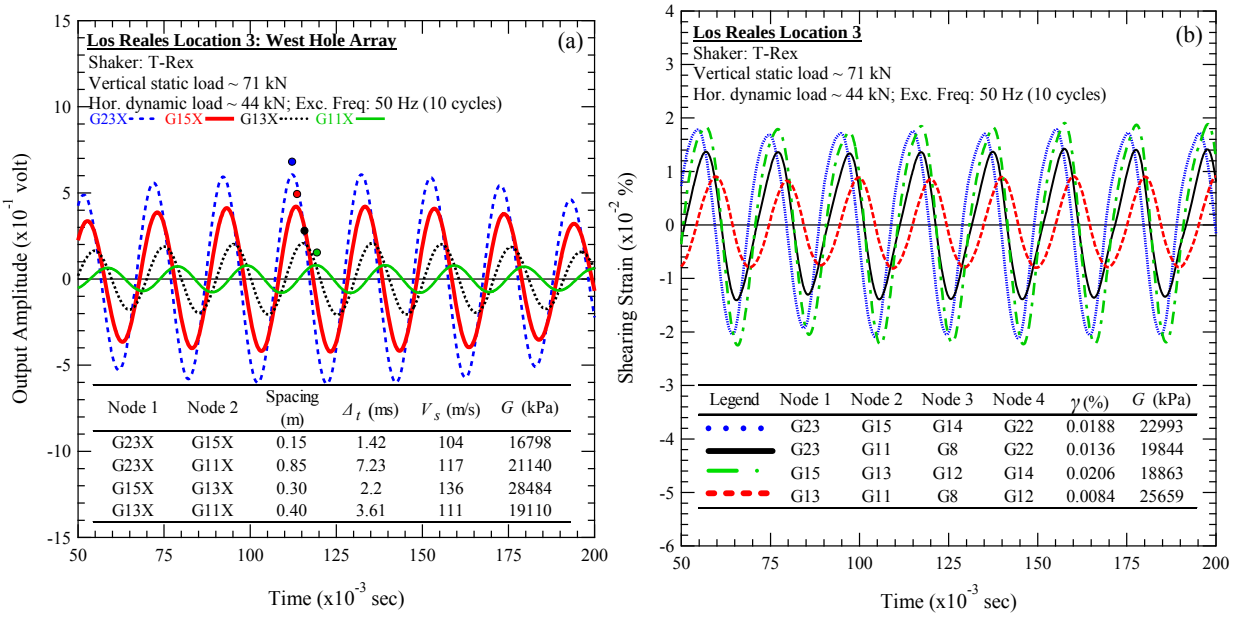

Figure 7.51 Examples of steady-state dynamic testing: (a) shear modulus calculation and (b) shearing strain time history at the LRL.

7.9 **Shear Modulus and Normalized Shear Modulus Reduction Curves in Location 1 at the LRL**

The effect of confining stress on the shear modulus and the normalized shear modulus as a function of shearing strain could be evaluated by examining the same element at different confining stress. Examining the same element isolates the effect of waste composition when investigating the effect of confining stress. Then, by examining different elements at the same confining stress, the effect of waste composition can be investigated.

7.9.1 Effect of Confining Stress on Shear Modulus and Normalized Shear Modulus Reduction Curves in Location 1 at the LRL

Figure 7.52(a) presents the G-log γ relationship at different confining stresses for element D in location 1. The center of element D was located at an effective depth of 0.36 m below the footing. The nonlinear behavior of element D is shown in Fig. 7.52(a). Steady-state dynamic test

for element D was performed over shearing strain ranging from 0.0017% to 0.07%. As shown in Fig. 7.52(a), the small-strain shear modulus increased with increasing confining stress. The observed small-strain shear modulus increased from 23 MPa to 35 MPa, as mean confining stress increased from 15 kPa to 76 kPa. The G/G_{max}-log γ curves for element D are shown in Fig. 7.52(b). The G/G_{max} curves systematically moved to the right and exhibited a more linear response with increasing confining stress. These trends in the shear modulus and the normalized shear modulus reduction curves are consistent with laboratory studies on MSW (Lee 2007, Zekkos et al. 2008, and Yuan et al. 2011) as well as on soils (e.g., Darendeli 2001).

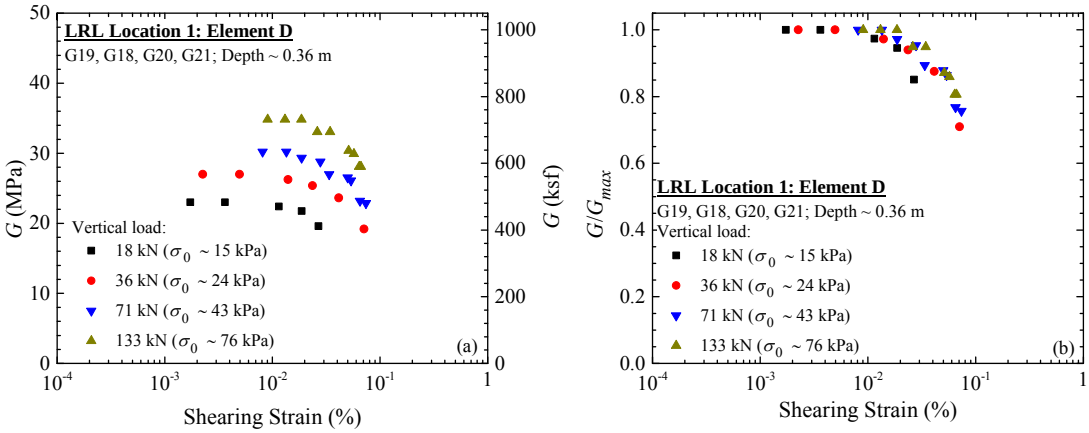

Figure 7.52 (a) Shear modulus and (b) normalized shear modulus reduction curves of element D in location 1 at the LRL.

The variation of shear modulus with shearing strain at different confining stresses for element F in location 1 is presented in Fig. 7.53(a). The center of element F was located at an effective depth of 0.71 m below the footing. As shown in Fig. 7.53(a), the shear modulus was successfully obtained from the field measurements over the shearing strain range from 0.0008% to 0.035%. The G_{max} increased from 38 MPa to 50 MPa, as mean confining stress increased from 11 kPa to 37 kPa. Figure 7.53(b) presents the normalized shear modulus reduction curves for

element F. The normalized shear modulus became more linear with increasing confining stresses from 11 kPa to 37 kPa.

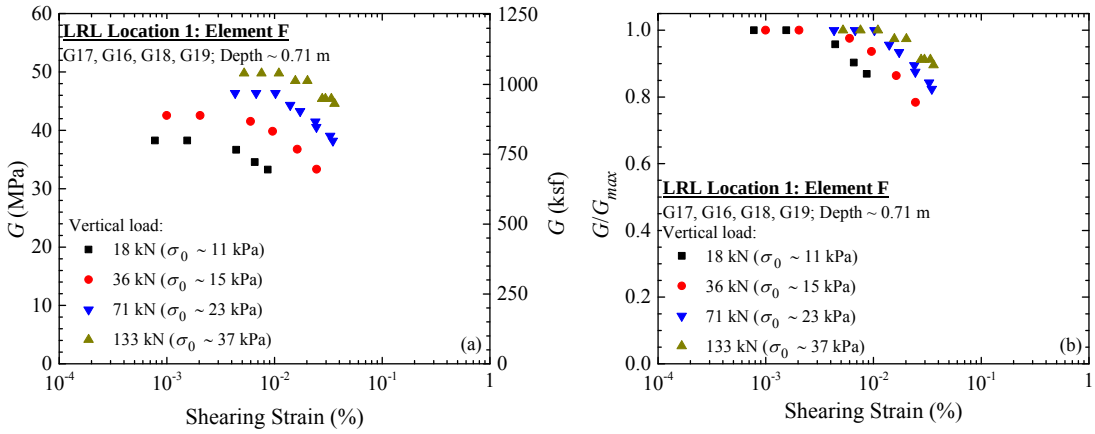

Figure 7.53 (a) Shear modulus and (b) normalized shear modulus reduction curves of element F in location 1 at the LRL.

7.9.2 Effect of Waste Composition on Shear Modulus and Normalized Shear Modulus Reduction Curves in Location 1 at the LRL

The effect of waste composition on the shear modulus and the normalized shear modulus reduction as a function of shearing strain could be evaluated using results from different sets of geophones that form elements. Figure 7.54 shows the effect of waste composition on the shear modulus and the normalized shear modulus curves from elements at nearly the same calculated confining stress that varied from 11 kPa to 15 kPa. As shown in Fig. 7.48, elements D and F were representatives of waste at different depths. Figure 7.54(a) shows differences in shear modulus that could be attributed to waste variability. The small-strain shear modulus was 23 MPa and 38 MPa for elements D and F, respectively. The corresponding normalized shear modulus reduction curves are shown in Fig. 7.54(b).

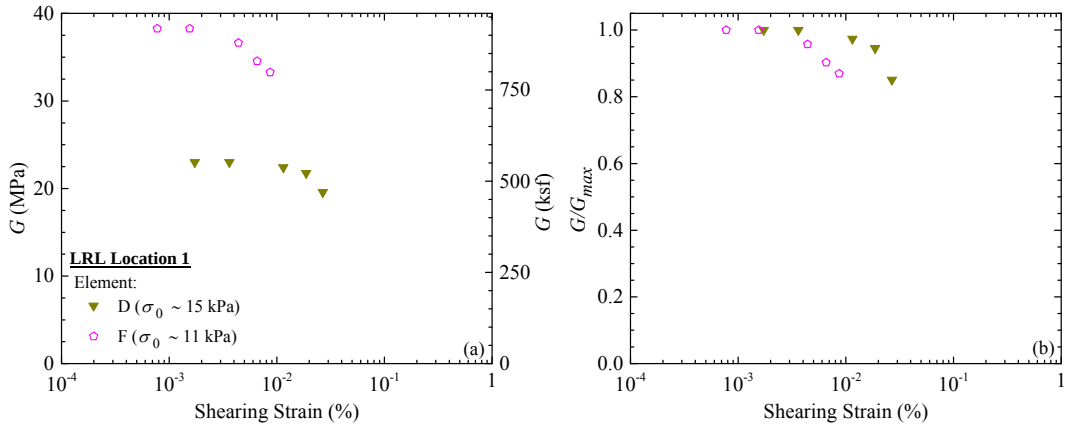

Figure 7.54 Waste composition effect on (a) shear modulus and (b) normalized shear modulus reduction curves in location 1 at the LRL.

2.9 Shear Modulus and Normalized Shear Modulus Reduction Curves in Location 2 at the LRL

7.9.3 Effect of Confining Stress on Shear Modulus and Normalized Shear Modulus Reduction Curves in Location 2 at the LRL

The shear modulus and normalized shear modulus reduction curves from location 2 at the LRL are presented in Figs. 7.55, 7.56, 7.57, 7.58. It should be noted that data from steady-state dynamic test using vertical static load of 71 kN was not included in this manuscript due to relatively poor waveforms observed.

The variation of shear modulus with shearing strain at different confining stresses for element A in location 2 is presented in Fig. 7.55(a). The center of this element was located at an effective depth of 0.15 m below the footing. The shear modulus was evaluated for shearing strain ranging from 0.003% up to 0.21%. Element A was the shallowest element and exhibited the largest shearing strain. As shown in Fig. 7.55(a), the G_{max} increased from 30 MPa to 56 MPa, as mean confining stress increased from 21 kPa to 131 kPa. The normalized shear modulus

reduction curves for element A are shown in Fig. 7.55(b). The G/G_{max} curves moved to the right and exhibited a more linear response with increasing confining stress.

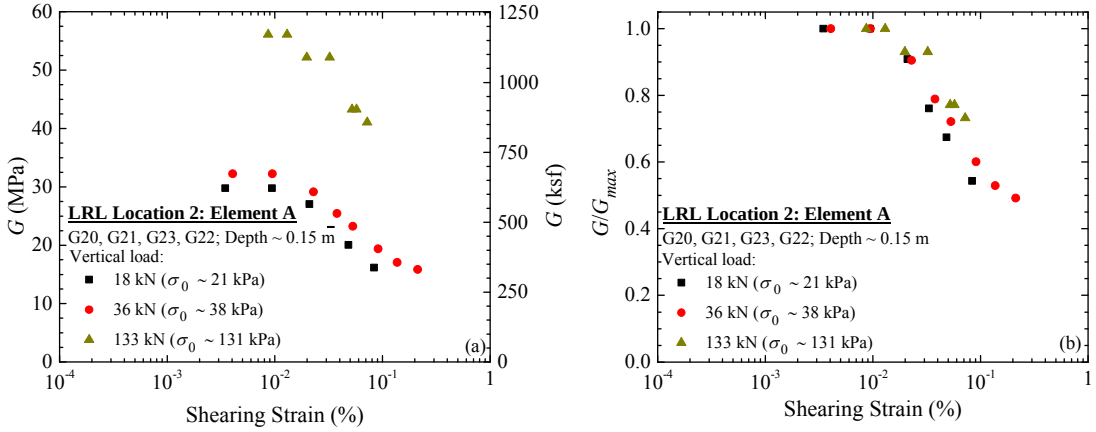

Figure 7.55 (a) Shear modulus and (b) normalized shear modulus reduction curves of element A in location 2 at the LRL.

The variation of shear modulus with shearing strain at different confining stresses for element D in location 2 is presented in Fig. 7.56(a). The center of element D was located at an effective depth of 0.32 m below the footing. The shear modulus curves were successfully obtained from the field measurements over the shearing strain ranging from 0.0025% to 0.14% as presented in Fig. 7.56(a). In this figure, the small-strain shear modulus increased from 38 MPa to 60 MPa, as mean confining stress increased from 15 kPa to 84 kPa. The normalized shear modulus reduction curves for element D are presented in Fig. 7.56(b). The normalized shear modulus reduction curves became more linear with increasing confining stresses from 15 kPa to 84 kPa.

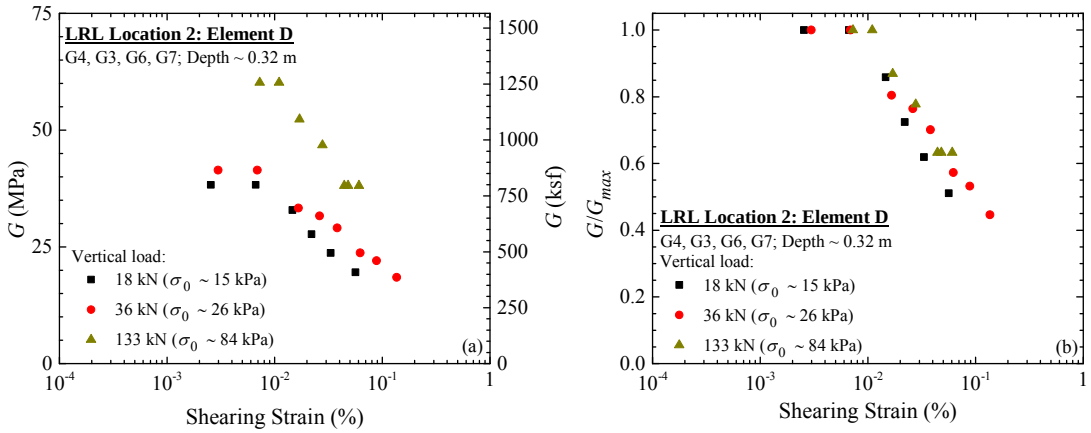

Figure 7.56 (a) Shear modulus and (b) normalized shear modulus reduction curves of element D in location 2 at the LRL.

The G-log γ relationships at different confining stresses for element F in location 2 are presented in Fig. 7.57(a). The center of element F was located at an effective depth of 0.51 m below the footing. The steady-state dynamic test for element F was performed over shearing strain ranging from 0.002% to 0.1%. The small-strain shear modulus increased from 17 MPa to 23 MPa as mean confining stress increased from 12 kPa to 53 kPa [Fig. 7.57(a)]. The G/G_{max}-log γ curves for element F is shown in Fig. 7.57(b). The normalized shear modulus reduction curves became more linear with increasing confining stress.

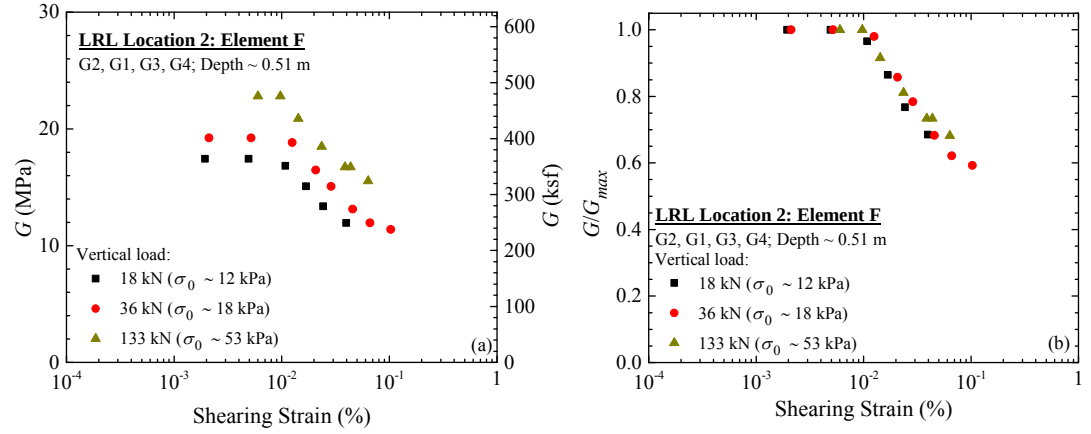

Figure 7.57 (a) Shear modulus and (b) normalized shear modulus curves of element F in location 2 at the LRL.

Figure 7.58(a) presents the shear modulus reduction curves for element C in location 2. Element C provided an average response of the tested waste mass as it was defined by the shallowest and the deepest geophones. The center of this element was located at an effective depth of 0.34 m below the footing. This element experienced shearing strain ranging from 0.002% to 0.14% during the steady-state dynamic tests. The G_{max} increased from 25 MPa to 37 MPa, as mean confining stress increased from 15 kPa to 79 kPa [Fig. 7.58(a)]. Figure 7.58(b) shows the normalized shear modulus reduction curves for this element. The normalized shear modulus reduction curves became more linear with confining stress.

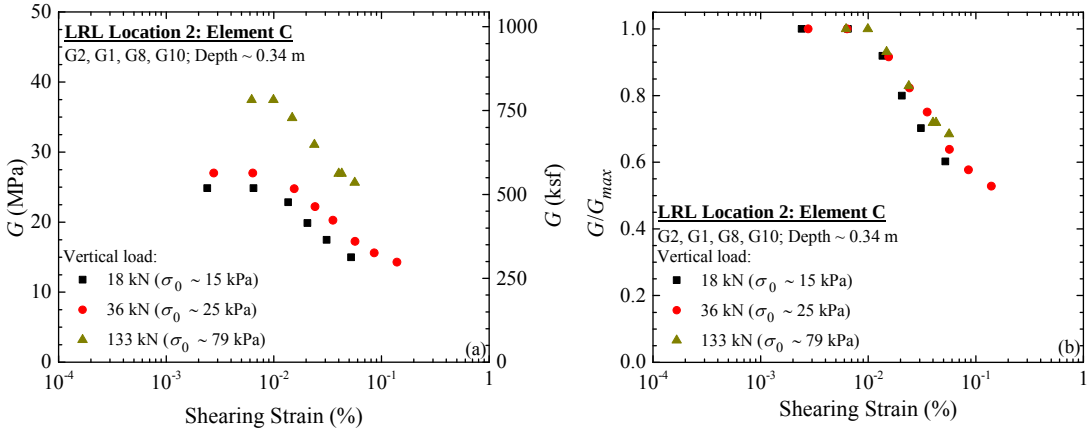

Figure 7.58 (a) Shear modulus and (b) normalized shear modulus reduction curves of element C in location 2 at the LRL.

7.9.4 Effect of Waste Composition on Shear Modulus and Normalized Shear Modulus Reduction Curves in Location 2 at the LRL

The effect of waste composition on G-log γ and G/G_{max}-log γ curves from location 2 at the LRL is presented in Figs. 7.59(a) and 7.59(b). All elements in these figures were at nearly the same calculated confining stress ranging from 12 kPa to 15 kPa. It can be observed that small-strain shear modulus from these elements ranging from 17 MPa to 38 MPa [Fig. 7.59(a)]. In this case, element D showed the highest shear modulus and the most nonlinearity in the G-log γ curve. The

differences in shear modulus and the degree of nonlinearity could be attributed to the differences in waste composition in each element. The corresponding normalized shear modulus reduction curves are shown in Fig.7.59(b).

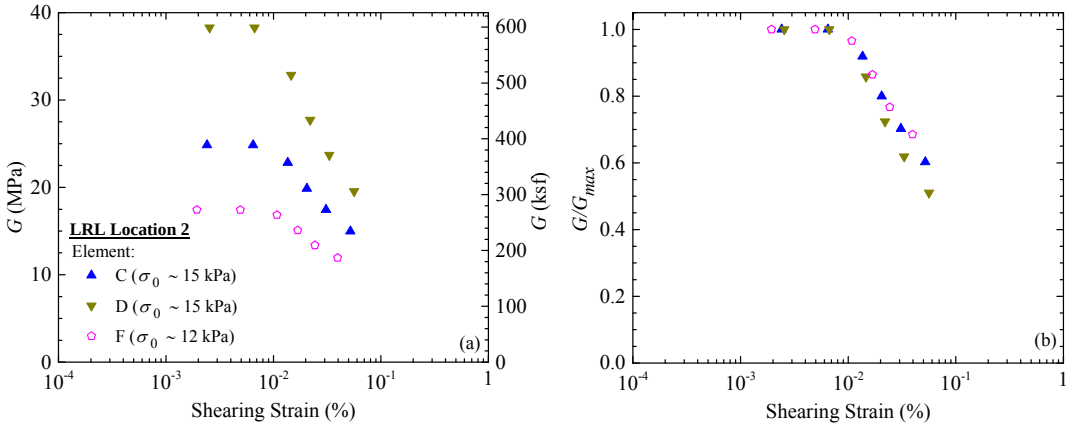

Figure 7.59 Waste composition effect on (a) shear modulus and (b) normalized shear modulus reduction curves in location 2 at the LRL.

7.10 **Shear Modulus and Normalized Shear Modulus Reduction Curves in Location 3 at the LRL**

7.10.1 Effect of Confining Stress on Shear Modulus and Normalized Shear Modulus Reduction Curves in Location 3 at the LRL

The shear modulus and the normalized shear modulus reduction curves for element A in location 3 are presented in Figs. 7.60(a) and 7.60(b). The center of this element was located at an effective depth of 0.13 m below the footing. The shear modulus was evaluated for shearing strain ranging from 0.0012% up to 0.13%. Element A was the shallowest element and exhibited the largest shearing strain. The effect of confining stress on the shear modulus curve is shown in Fig. 7.60(a). The G_{max} increased from 17 MPa to 32 MPa, as mean confining stress increased from 23 kPa to 140 kPa. The normalized shear modulus reduction curves for element A are shown in Fig.

7.60(b). The G/G_{max} curves generally moved to the right although not significantly and exhibited a more linear response with increasing confining stress

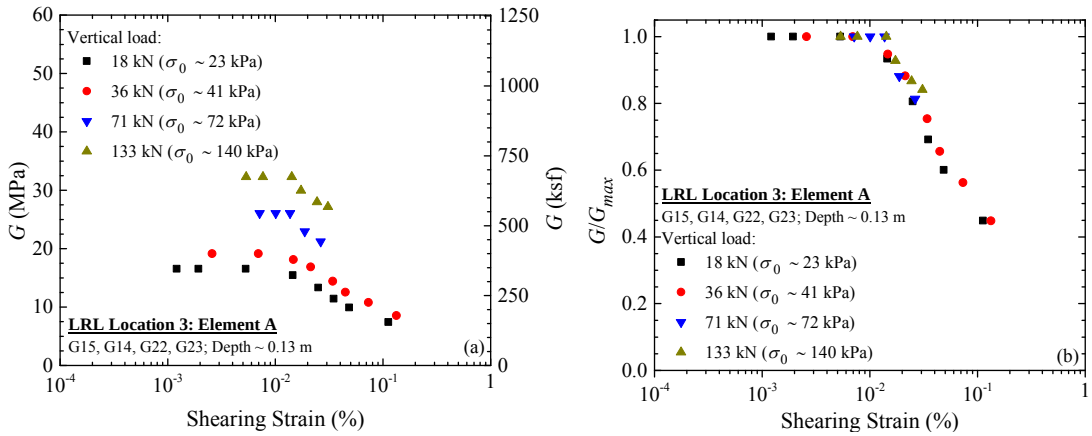

Figure 7.60 (a) Shear modulus and (b) normalized shear modulus reduction curves of element A in location 3 at the LRL.

Figure 7.61(a) presents the G-log γ relationship at different confining stresses for element D in location 3. The center of element D was located at an effective depth of 0.36 m below the footing. The nonlinear behavior of element D is shown in Fig. 7.61(a). This element experienced shearing strain ranging from 0.0011% to 0.14% during the steady-state dynamic test. As shown in Fig. 7.61(a), the small-strain shear modulus increased from 15 MPa to 28 MPa, as mean confining stress increased from 15 kPa to 77 kPa. The G/G_{max}-log γ curves for element D are shown in Fig. 7.61(b). The normalized shear modulus became more linear with increasing confining stress.

The variation of shear modulus with shearing strain at different confining stresses for element F in location 3 is presented in Fig. 7.62(a). The center of element F was located at an effective depth of 0.71 m below the footing. As shown in Fig. 7.62(a), the shear modulus was successfully obtained from the field measurements over the shearing strain range from 0.0008% to 0.14%. The observed small-strain shear modulus increased from 22 MPa to 30 MPa as mean

confining stress increased from 12 kPa to 38 kPa. Although data for σ_0 of 16 kPa may not clearly indicate G_{max}, shear modulus at the lowest shearing strain at σ_0 of 16 kPa was probably very close to its G_{max} based on observation on data for σ_0 of 12 kPa, 23 kPa, and 38 kPa. Figure 7.62(b) presents the normalized shear modulus reduction curves for element F. The normalized shear modulus became more linear with increasing confining stresses from 12 kPa to 38 kPa.

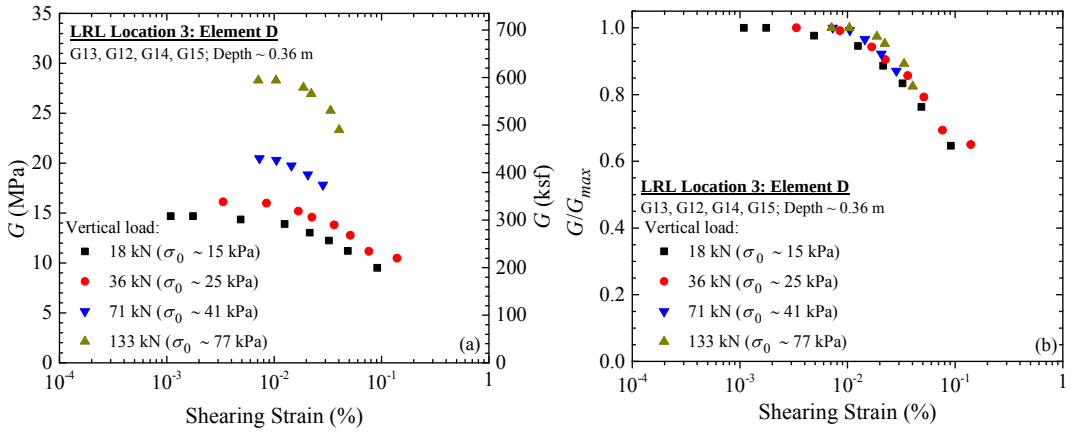

Figure 7.61 (a) Shear modulus and (b) normalized shear modulus curves of element D in location 3 at the LRL.

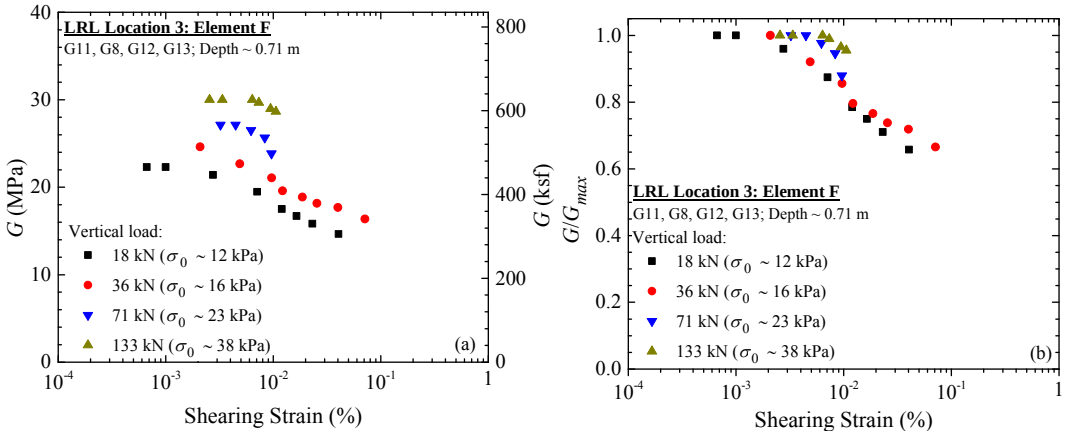

Figure 7.62 (a) Shear modulus and (b) normalized shear modulus reduction curves of element F in location 3 at the LRL.

The shear modulus and the normalized shear modulus reduction curves for element C in location 3 are presented in Figs. 7.63(a) and 7.63(b). This element provided an average response

of the other elements as it was defined by the shallowest and the deepest geophones. The center of this element was located at an effective depth of 0.48 m below the footing. The shear modulus was evaluated for shearing strain ranging from 0.0009% up to 0.088%. As shown in Fig. 7.63(a), the G_{max} increased from 17 MPa to 26 MPa, as mean confining stress increased from 13 kPa to 55 kPa. The normalized shear modulus reduction curves for this element are shown in Fig. 7.63(b). With increasing confining stress, the normalized shear modulus reduction curves became more linear.

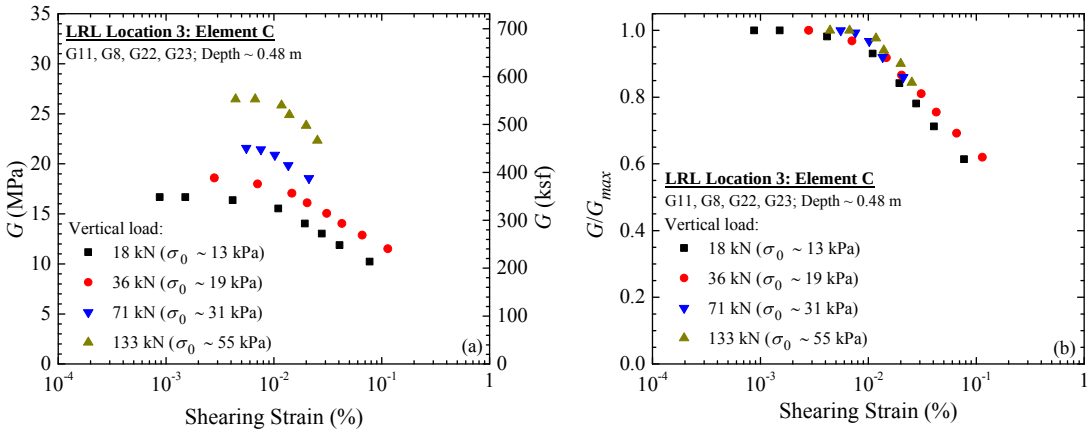

Figure 7.63 (a) Shear modulus and (b) normalized shear modulus reduction curves of element C in location 3 at the LRL.

7.10.2 Effect of Waste Composition on Shear Modulus and Normalized Shear Modulus Reduction Curves in Location 3 at the LRL

The effect of waste composition on the shear modulus and the normalized shear modulus reduction as a function of shearing strain was evaluated using results from different sets of geophones that form elements. Figure 7.64 shows the effect of waste composition on the shear modulus and the normalized shear modulus reduction curves from all elements at nearly the same calculated confining stress that varied from 12 kPa to 15 kPa. As shown in Fig. 7.50, elements C, D and F were representatives of waste at different depths. It should be noted that the

element C represents the average of the other three elements. Figure 7.64(a) shows differences in shear modulus that could be attributed to waste variability. The small-strain shear modulus was 17 MPa, 15 MPa, and 22 MPa for elements C, D, and F, respectively. The impact of waste composition on the normalized shear modulus reduction curve is demonstrated in Fig. 7.64(b).

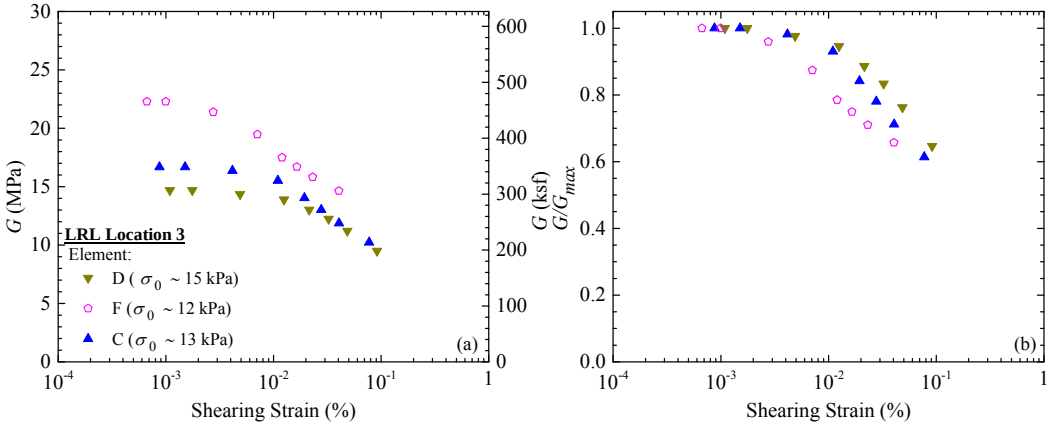

Figure 7.64 Waste composition effect on (a) shear modulus and (b) normalized shear modulus curves in location 3 at the LRL.

7.11 **Comparison of Normalized Shear Modulus Reduction Curves with Other Studies**

In this section, the variation of normalized shear modulus reduction curves as a function of shearing strain from three test locations at the LRL was compared. In addition, the field G/G_{max} data from the LRL was also compared with curves proposed by other studies in the literature. In this case, the comparison was made with results from laboratory testing and recorded ground motion back-calculation analysis.

The steady-state dynamic test results from three test locations at the LRL are presented in Fig. 7.65. Dataset from locations 1, 2, and 3 are shown as black squares, red circles, and blue triangles, respectively. In location 1, normalized shear modulus reduction curve was evaluated for shearing strains ranging from 0.0008% to 0.074%. In location 2, normalized shear modulus reduction curve was evaluated for shearing strains ranging from 0.002% to 0.21%. Normalized

shear modulus reduction curve was evaluated for shearing strains ranging from 0.0007% to 0.14% in location 3. The normalized shear modulus reduction curves were generally consistent. Nevertheless, normalized shear modulus reduction appeared to be more nonlinear for some data series in locations 1 and 3 compared to location 2 at the LRL. In addition, some data series in location 1 showed the most linearity in the normalized shear modulus reduction curves. The variation of normalized shear modulus reduction curves as a function of shearing strain can be attributed to variability in waste composition between the three locations as well as differences in confining stresses between quadrilateral elements.

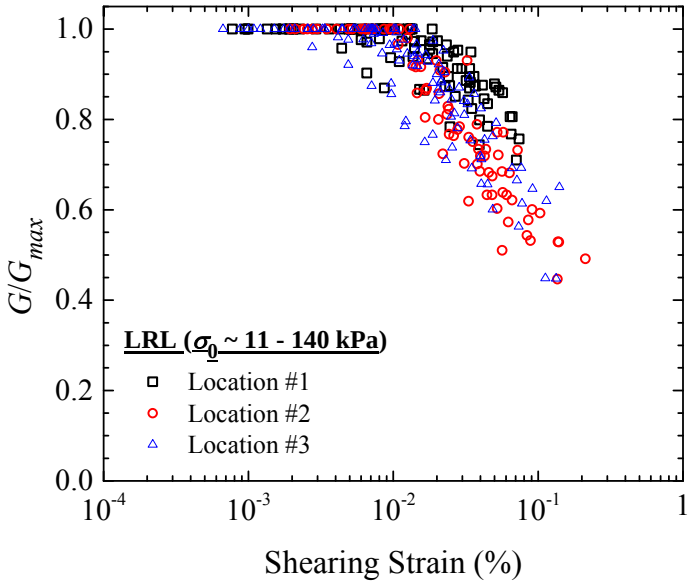

Figure 7.65 The normalized shear modulus reduction curves from 3 testing locations at the LRL.

Figure 7.66 shows the comparison between the field G/G_{max} data from the LRL and Zekkos et al. (2008) curves for mean stress < 125 kPa that were largely developed on the basis of testing at mean stress of 75 kPa. In general, the field data was consistent with the laboratory based curves. Most field G/G_{max} data for locations 1 was in between Zekkos et al. curve for 8 – 25% and 62-76% smaller than 20 mm material. The field G/G_{max} data from locations 2 and 3 was

generally consistent with curve for 8 – 25% smaller than 20 mm material up to strains of 0.01%. At larger shearing strains and low confining stress, the field G/G_{max} data in locations 2 amd 3 was more nonlinear than curve for 8 – 25% smaller than 20 mm material.

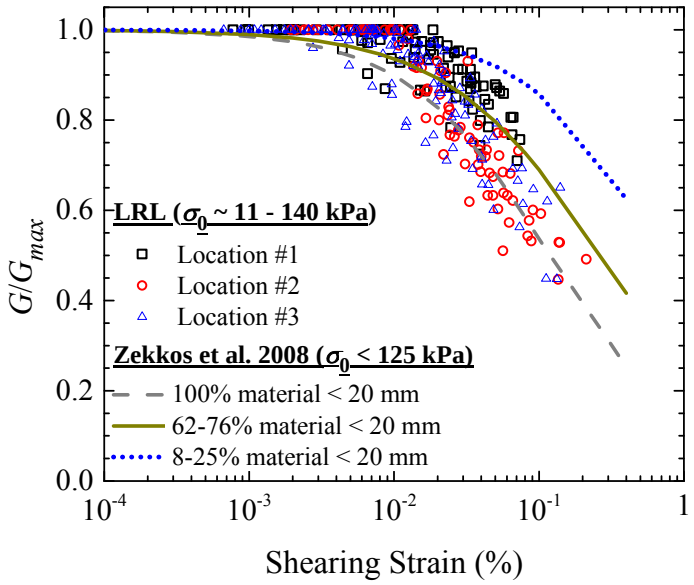

Figure 7.66 Comparison of the normalized shear modulus reduction curves with Zekkos et al. (2008) recommended curves.

Figure 7.67 presents the comparison between the normalized shear modulus reduction curves measured in situ at the LRL with curves proposed by other researchers. The normalized shear modulus reduction curves proposed by Idriss et al. (1995), Matasovic and Kavazanjian (1998), and Augello et al. (1998) were derived from back-calculation analyses using recorded ground motions at the surface of the OII landfill, California. In addition, Matasovic and Kavazanjian (1998) also performed cyclic simple shear testing to extend their curves to larger strain. Singh and Murphy (1990) proposed a curve that was developed using the shear modulus reduction curve of peat and clay. In general, the field G/G_{max} data from LRL shows substantial differences from Singh and Muprhy curve as well as Idriss et al. curve. Singh and Murphy (1990) curve showed more significant shear modulus reduction below shearing strain of 0.001 %

than the field G/G_{max} data from the LRL. Idriss et al. curve exhibited a relatively less linear shear modulus reduction than the field G/G_{max} data from the LRL. Augello et al. curve was closest to the median curve of the field G/G_{max} data from LRL. Matasovic and Kavanzanjian curve was more linear than the field G/G_{max} data from the LRL.

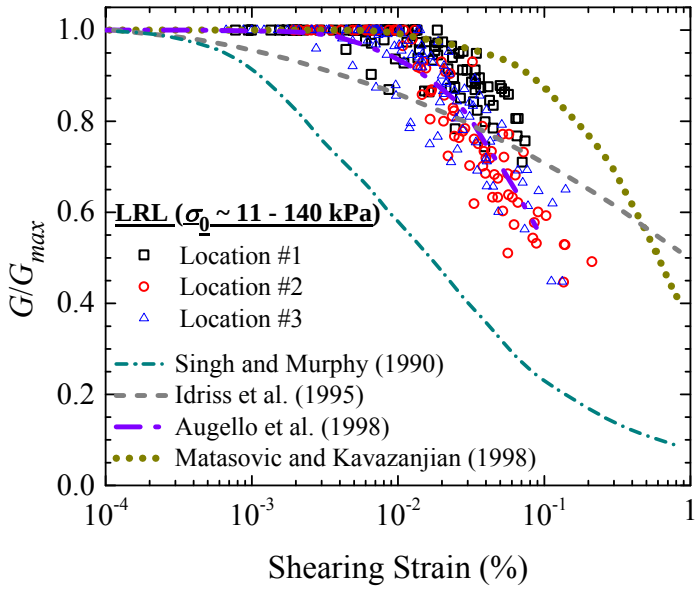

Figure 7.67 Comparison of the normalized shear modulus reduction curves with curves from other studies in the literature.

7.12 **Summary**

A field experiment program was conducted in three locations at the Los Reales Landfill, Tucson, Arizona, to investigate dynamic properties of MSW in the linear and nonlinear strain range. Crosshole and downhole seismic tests were conducted to evaluate dynamic properties of MSW at small strains. Steady-state dynamic testing over a wide shear strain range (0.0008% to 0.21%) was conducted at four different static vertical loads applied using mobile vibroseis shakers of NEES@UTexas. Two arrays of 3-D geophone sensors were embedded in the waste mass and were used to capture the waste response during dynamic testing. Additionally, load-settlement measurements were carried out. Pit excavation was performed at each location to measure the in-

situ unit weight, visually assess waste composition, and collect samples for waste characterization and laboratory testing. The outcomes from small-strain testing were the wave propagation velocity profiles and wave propagation velocity-stress relationship. The study also generated in-situ data on shear modulus and normalized shear modulus reduction relationship as a function of shear strain. The results from field testing at the LRL will be synthesized with the results from field testing at the Austin Community Landfill and Lamb Canyon Sanitary Landfill to generate broad conclusions and recommendation in Chapter 9.

Small-scale crosshole and downhole seismic testing allowed for an assessment of $V_{p\text{-}X}$, $V_{p\text{-}Z}$, $V_{s\text{-}XZ}$, $V_{s\text{-}ZX}$, and $V_{s\text{-}ZY}$ as a function of waste composition and confining stress. Crosshole and downhole seismic testing with different static vertical loads showed that wave propagation velocities increased with stress. In the NC regime, wave propagation velocity increase was more sensitive to stress increase than in the OC regime. The near-surface MSW was overconsolidated due to field compaction at the landfill.

The wave propagation velocity measurements at the LRL were also used to assess waste anisotropy and small-strain Poisson's ratio. For example, the ratio of $V_{p\text{-}Z}$ to $V_{p\text{-}X}$ ranged from 0.75 to 0.99 with a mean value of 0.86. Similarly, the ratio of $V_{s\text{-}vertical}$ to $V_{s\text{-}horizontal}$ was found to be between 0.69 and 1.17 with an average value of 0.92. These average values indicated that the compressibility in the horizontal direction was generally lower than the compressibility in the vertical direction. The small-strain Poisson's ratio at three test locations varied from 0.09 to 0.44.

The impact of waste variability and confining stress on the shear modulus was also assessed in situ. Shear modulus was found to increase with increasing confining stress, particularly in the NC regime, and to be affected by waste composition. The normalized shear modulus reduction curves were also affected by waste composition and confining stress. The

normalized shear modulus became more linear as confining stress increased, similarly to soils. At the same confining stress, the shear modulus and normalized shear modulus curves of the MSW at different locations was generally consistent but varied indicating the effect of waste composition on these nonlinear dynamic properties of MSW.

CHAPTER 8. FIELD EVALUATION OF DYNAMIC PROPERTIES OF SOLID WASTE AND SOIL COVER AT THE BKK HAZARDOUS LANDFILL

8.1 **Introduction**

The dynamic properties of solid waste and soil cover were evaluated in situ at the BKK hazardous landfill in West Covina, California from July 20 to August 1, 2012. This chapter describes testing locations, field test execution, and test results. The field investigation included downhole and crosshole seismic tests, Multichannel Analysis of Surface Wave (MASW) testing, Microtremor Analysis Method (MAM), and steady-state dynamic testing. Additionally, load-settlement tests and in-situ unit weight measurements were performed. The field testing generally was conducted using the procedures described in Chapter 4.

8.2 **Field Investigation at the BKK Landfill**

Field investigation at the BKK Landfill was mainly conducted to evaluate the linear and nonlinear dynamic properties of solid waste and soil cover in situ. In the linear range, shear wave (S-wave) velocity (V_s) and primary wave (P-wave) velocity (V_p) were investigated. In the nonlinear range, the variation of shear modulus (G) and normalized shear modulus (G/G_{max}) as a function of shearing strain (γ) was also evaluated.

The BKK Landfill is a closed 190-acre hazardous waste landfill (Class I Landfill) where hazardous waste and municipal solid wastes were co-disposed of between 1972 and 1987. The BKK Landfill also encompasses an inactive 170-acre municipal solid waste landfill (Class III Landfill) which operated from 1987 to 1996. This landfill is located at 2210 South Azusa Avenue in West Covina, California which is approximately 37 km east of Los Angeles,

California (Fig. 8.1). Approximately 3.4 million tons of liquid and solid hazardous wastes were disposed of in the Class I Landfill between 1972 and 1987. Currently, the Department of Toxic Substances Control (DTSC) regulates the post-closure care and maintenance of the Class I landfill. Regular landfill operations and maintenance of the facility is performed by Remediation Resources Group, Inc. (ERRG).

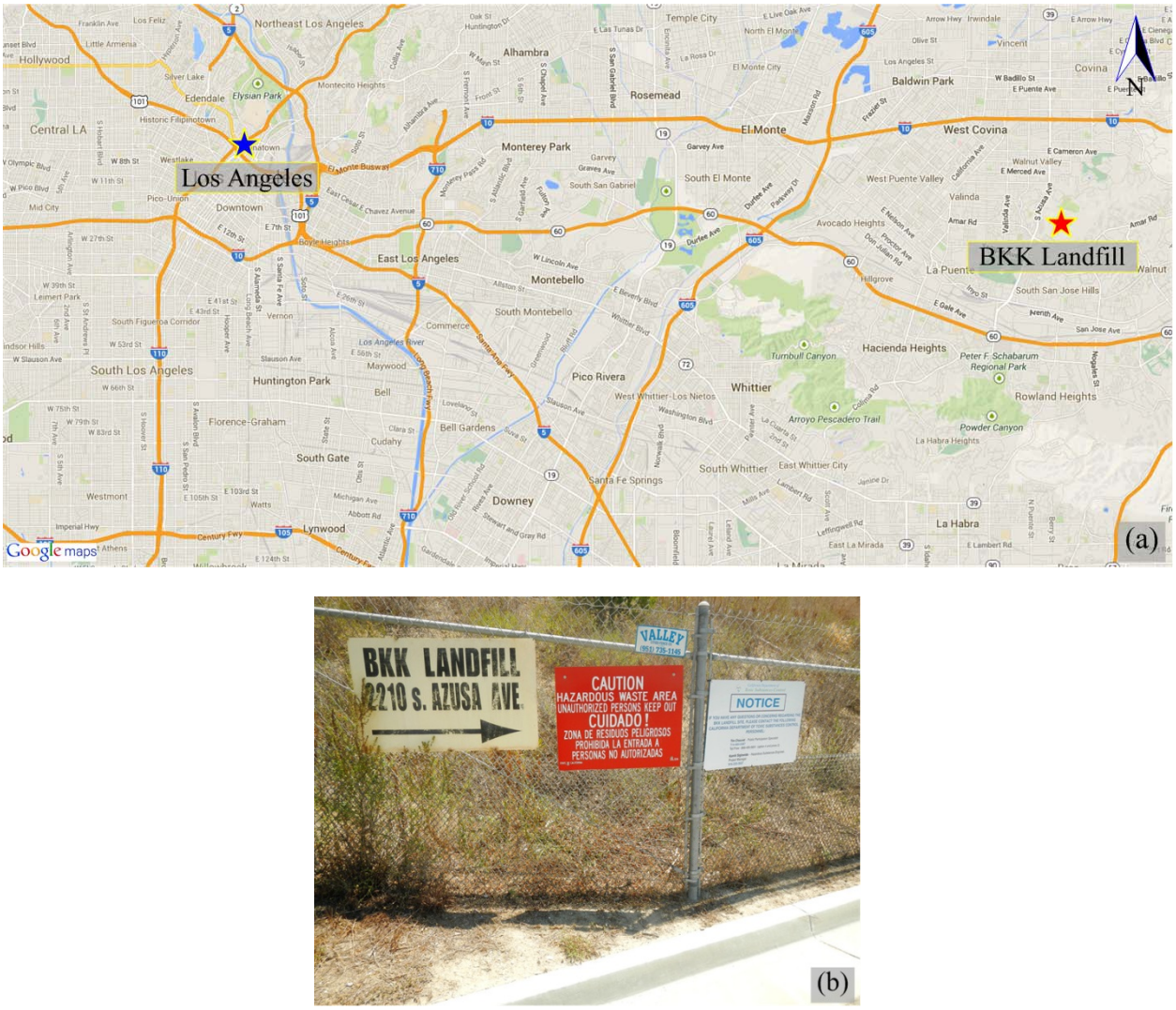

Figure 8.1 The BKK Landfill: (a) location and (b) entrance.

The field investigation at the BKK was conducted by the author, Mr. Clinton Carlson, and Dr. Dimitrios Zekkos (University of Michigan); Mr. Cecil G. Hoffpauir and Mr. Robert Kent

(NEES@UT); and Mr. Spencer Marcinek (Geosyntec). In addition, testing logistics was accommodated by SCS Engineers.

8.2.1 Testing Locations

The field investigation was performed in three locations at the BKK (Fig. 8.2). All testing locations were located at Deck 1040. Field investigation in location 1 (Fig. 8.3) was performed on solid waste from July 20 to 24, 2012. Field investigation in location 2 (Fig.8.4) was also performed on solid waste. In location 2, field investigation was performed from July 25 to 27, 2012. Soil cover of about 4-5 m in thickness was excavated in locations 1 and 2 as a preparation for this field testing. Field testing in location 3 (Fig. 8.5) was performed on soil cover from July 30 to August 1, 2012.

Figure 8.2 Testing locations at the BKK Landfill.

Figure 8.3 (a) West and (b) south views of location 1 at the BKK.

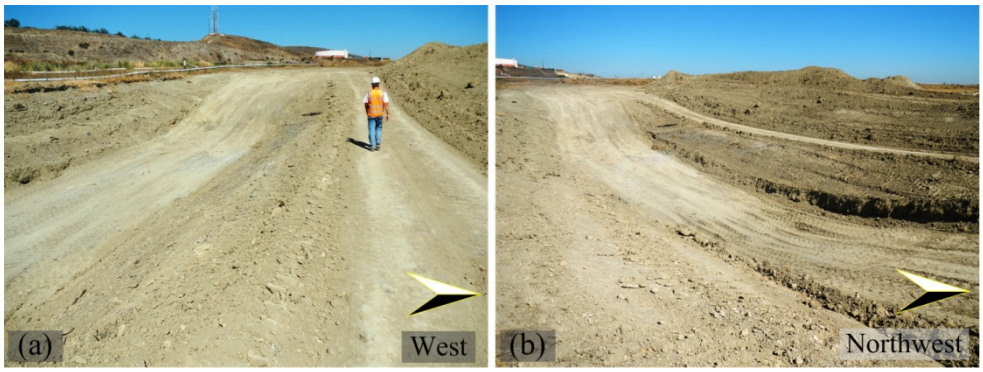

Figure 8.4 (a) South and (b) southwest views of location 2 at the BKK.

Figure 8.5 North view of location 3 at the BKK.

8.2.2 Field Instrumentation and Testing Setup

Figure 8.6 shows activities during the field instrumentation and preparation at the BKK. Testing setups in locations 1, 2, and 3 are shown in Figs. 8.7, 8.8, and 8.9, respectively. As shown in these figures, testing setup for all locations was similar with the deepest 3-D geophone pair

located at a depth of 0.91 m. All test locations were prepared for load-settlement test; downhole and crosshole seismic tests; and steady-state dynamic test.

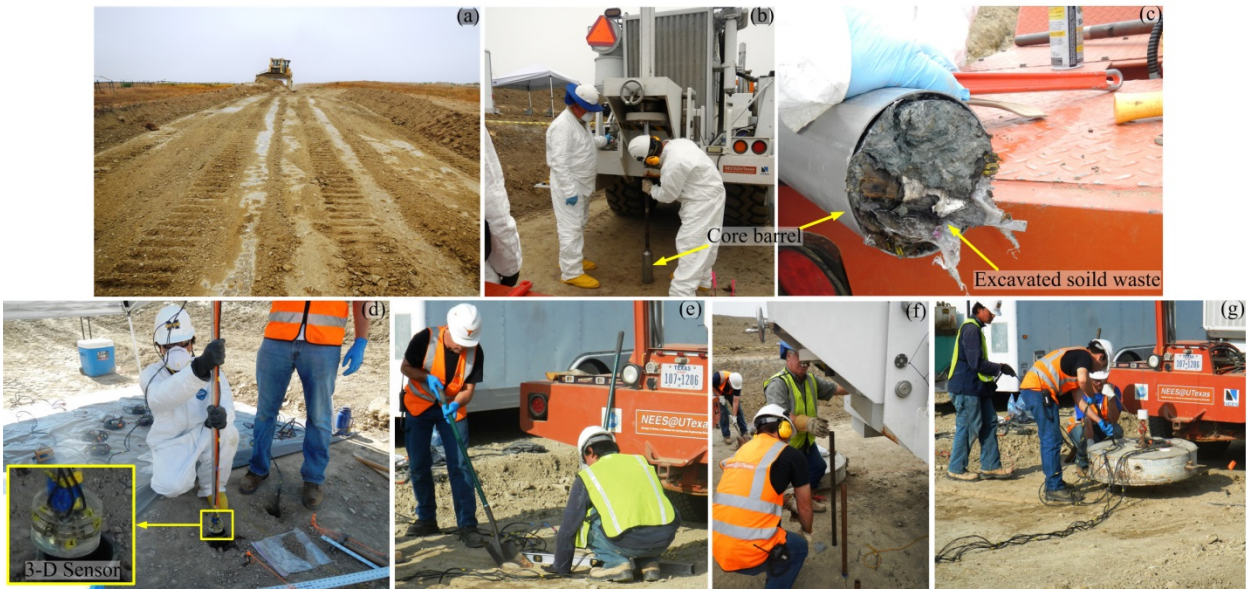

Figure 8.6 Field instrumentation and testing setup at the BKK: (a) removing soil cover, (b) pushing core barrel, (c) removing waste from core barrel, (d) 3-D geophone installation, (e) testing pad levelling, (f) crosshole source rod installation, and (g) footing placement.

8.2.3 Field Testing Sequence for Evaluation of Dynamic Properties of Solid Waste and Soil Cover at the BKK

The field investigations in locations 1, 2, and 3 at the BKK were performed according to the staged loading sequence as shown in Fig. 8.10. In each location, small-scale crosshole and downhole seismic tests were performed at externally applied vertical static loads of 0 kN, 9 kN, 18 kN, 36 kN, 71 kN, and 111 kN. Steady-state dynamic tests were performed using a 18 kN, 36 kN, 71 kN, and 133 kN static hold-down force. These vertical static load levels were kept constant while applying dynamic horizontal loads. In all locations, load-settlement data were collected during vertical static load application for the crosshole and downhole seismic tests. It should be noted that the highest vertical static load for the downhole and crosshole seismic

testing was planned to be 133 kN. However, it was very difficult to reach a static vertical load of 133 kN using a hydraulic jack pump in all locations. In steady-state dynamic testing, Thumper was used to apply static vertical loads up to 36 kN and T-Rex was used to impose larger vertical static load levels.

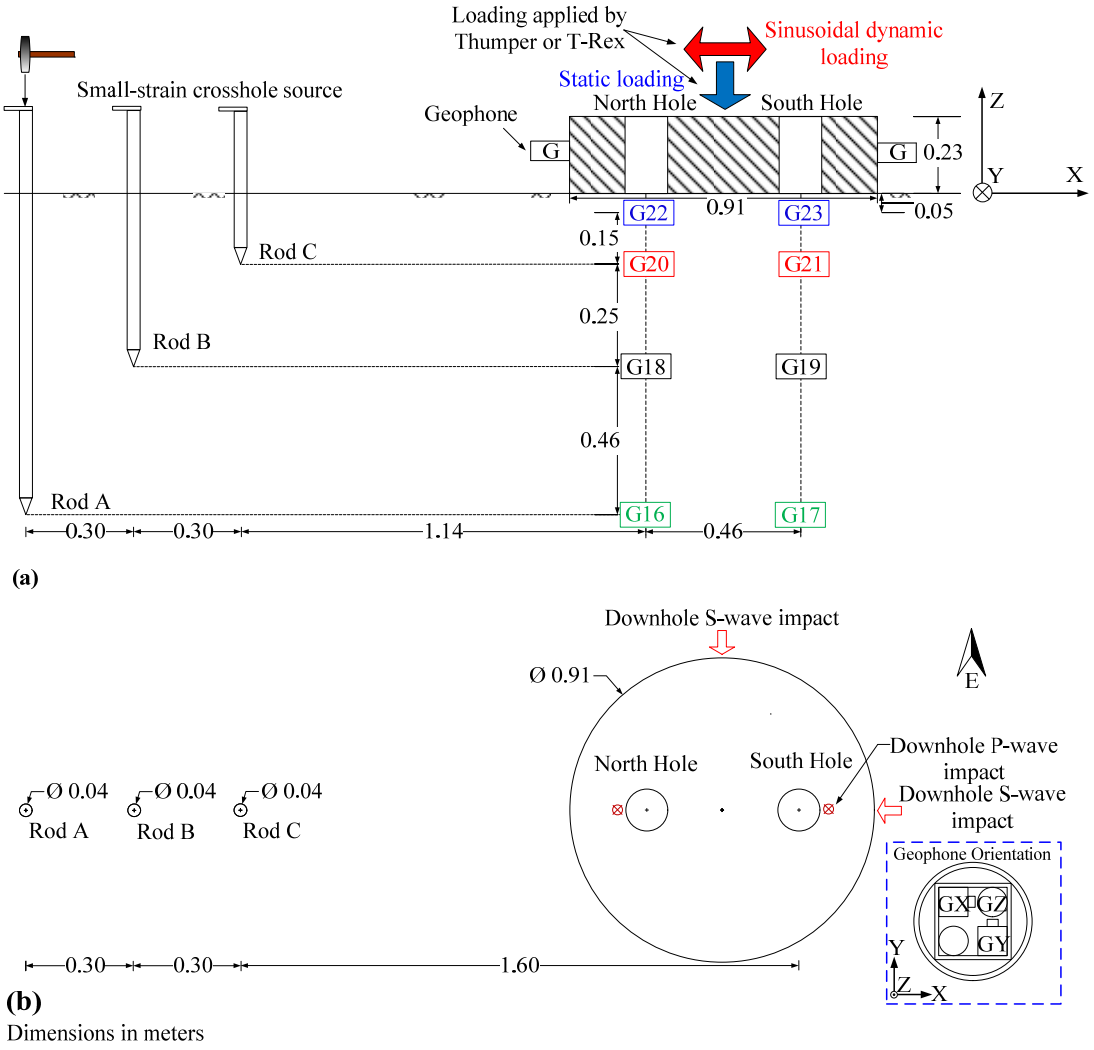

Figure 8.7 Testing setup in location 1 at the BKK: (a) cross-section and (b) plan views.

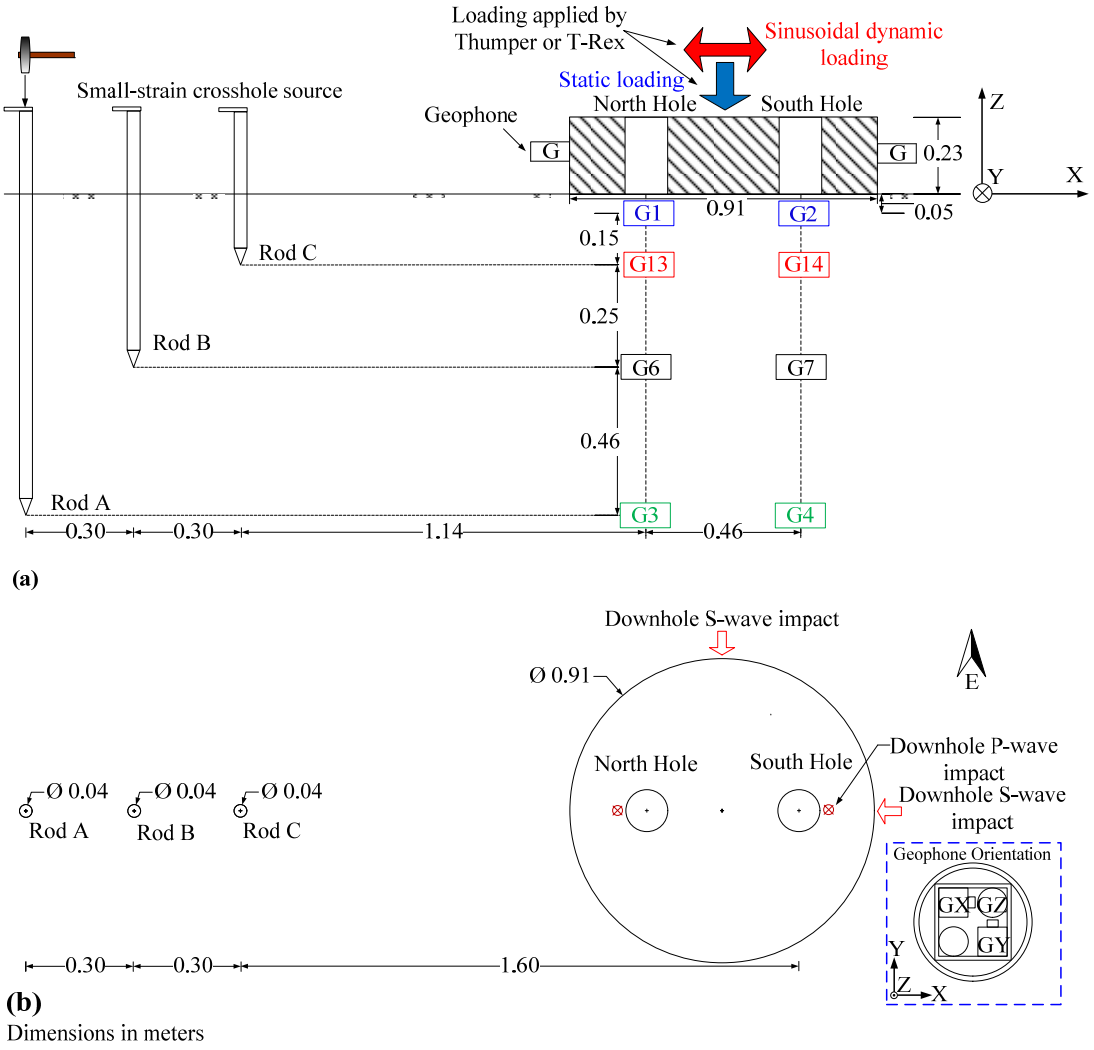

Figure 8.8 Testing setup in location 2 at the BKK: (a) cross-section and (b) plan views.

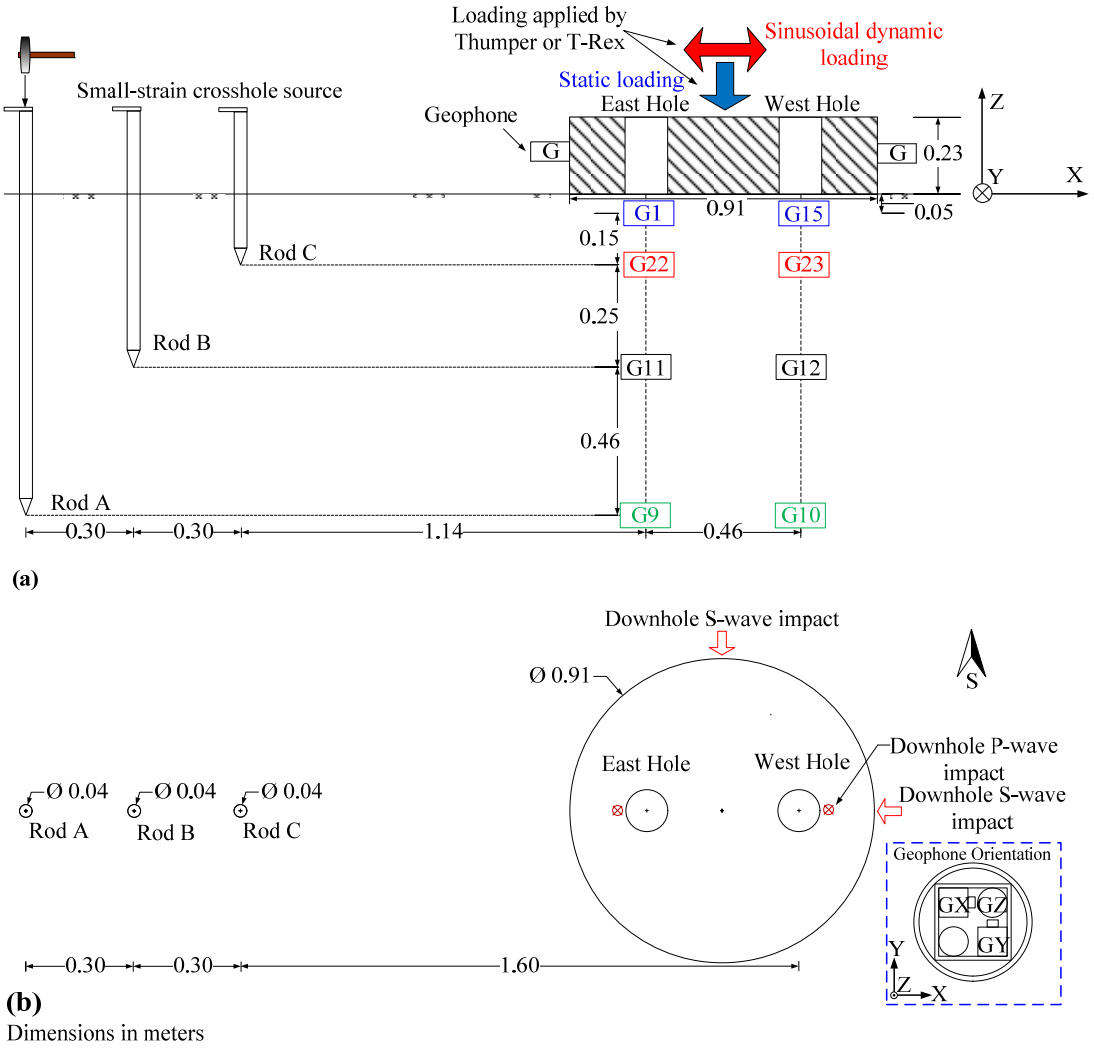

Figure 8.9 Testing setup in location 3 at the BKK: (a) cross-section and (b) plan views.

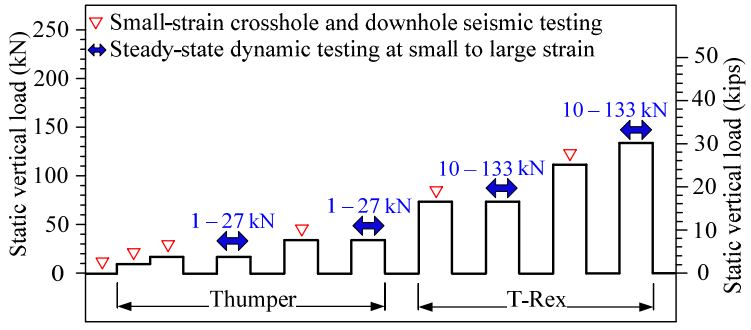

Figure 8.10 Staged loading sequence in each location at the BKK.

8.2.4 In-situ Unit Weight Measurements, Solid Waste and Soil cover Sampling, and Laboratory Soil Index Test on Soil Cover

In-situ unit weight measurements, waste sampling, in-situ solid waste characterization, and sensor recovery were performed after completion of the staged loading test in locations 1 and 2 [Fig. 8.11(a-f)]. In-situ unit weight measurement and solid waste characterization were performed using procedures proposed by Zekkos et al. (2006a) and Zekkos et al. (2010), respectively. An approximately 1.8 m x 1.8 m x 1.2 m (depth) pit was excavated in each location. Bulk solid waste samples were collected from locations 1 and 2. These bulk samples were stored in two 55-gallon HDPE drums for each locations. Remaining excavated solid waste was re-disposed to the landfill. In location 3, a pit was excavated only to recover the 3-D sensors [Fig. 8.11(g)] and collect bulk samples of soil cover. Bulk samples of soil cover were stored in two 5-gallon buckets. In addition, four "undisturbed" samples of soil cover were collected using shelby tubes.

The in-situ unit weights of solid waste were estimated to be 16.1 kN/m^3 and 18.6 kN/m^3 in locations 1 and 2, respectively. Information about representative unit weight of soil cover in location 3 was obtained from Geosyntec Consultants. Unit weight of 18.5 kN/m^3 for soil cover was measured at a depth of 1.5 m in this location and was used in this study. Laboratory waste characterization of BKK solid waste has not been performed yet.

Figure 8.11 (a) Waste excavation, (b) excavated waste in the dump truck, (c) calibrated gravels in a 55-gallon HDPE drum, (d) placement of waste into drums, (e) in-situ unit weight measurement, (f) an exposed 3-D sensor pair, and (g) an exposed 3-D sensor in location 3.

Laboratory soil index tests on soil cover samples were executed by Ms. Jiacheng Li in the geotechnical laboratory at the University of Michigan. Grain-size analysis was performed in accordance with ASTM D422-63(2007) and ASTM D1140-00(2006). The results of the wet sieve and hydrometer analyses indicated that the soil cover near the ground surface at location 3 had more than 60% fine contents as shown in Fig. 8.12. Atterberg Limits tests (ASTM D4318-10) performed on soil cover samples showed that the fines content had plastic limit of 30%, liquid limit of 73%, and plasticity index (PI) of 43%. The soil cover in location 3 was classified as fat clay (CH) based on the Unified Soil Classification System (ASTM D2487-11). As indicated by the high PI, the soil cover in location 3 had high shrink-swell potential and this was consistent with field observations of soil cover cracks (Fig. 8.13).

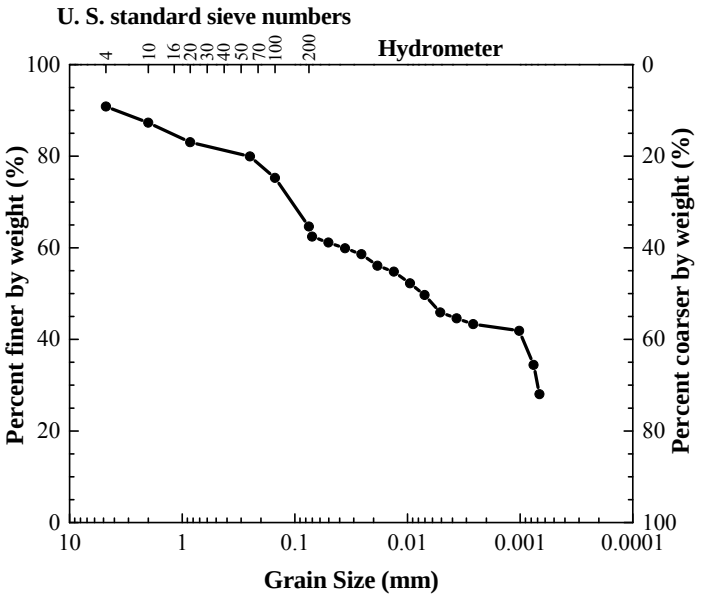

Figure 8.12 Grain size distribution of soil cover in location 3 at the BKK.

Figure 8.13 Soil cover cracks at the BKK.

8.3 **Load-settlement Test**

Load-settlement tests were performed in a loading sequence in three test locations at the BKK. The highest static vertical load in the load-settlement test was 111 kN for each location. These highest vertical loads corresponded to maximum stresses of 170 kPa on the footing. The static vertical loads were applied using a hydraulic jack that reacted against the mobile field shakers' frame as shown in Fig. 8.14. A T-shaped frame was used to uniformly distribute the

load on the footing. The settlements were measured using three linear potentiometers on the footing. Figure 8.15 shows the load-settlement curves in three test locations at the BKK. The maximum settlements under the highest static vertical load in locations 1, 2, and 3 were 10 mm, 8 mm, and 4 mm, respectively.

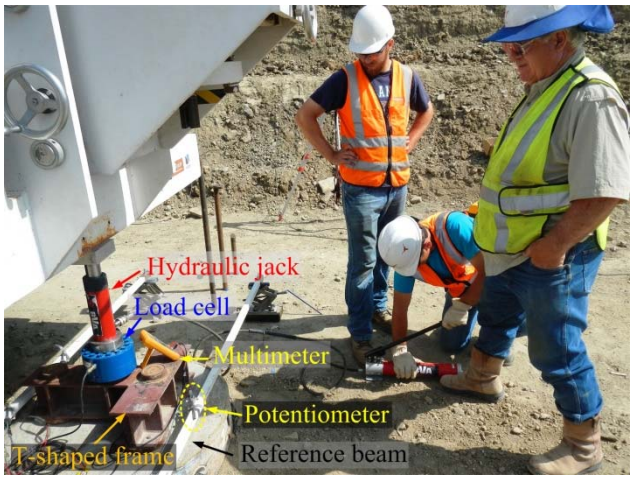

Figure 8.14 Load-settlement test in location 2 at the BKK.

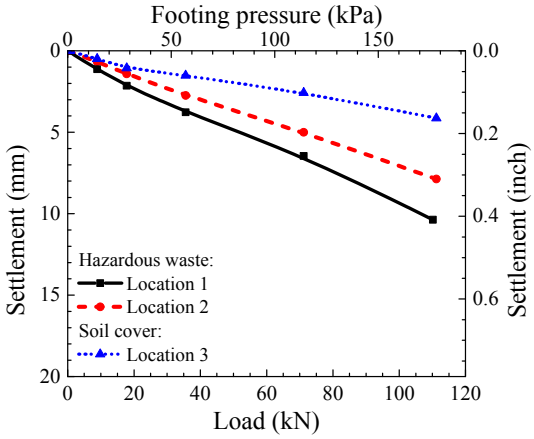

Figure 8.15 Load-settlement test results at the BKK.

8.4 **Small-scale Downhole Seismic Testing**

As part of field testing at the BKK, small-scale downhole seismic tests were performed to evaluate vertically propagating P-wave velocity ($V_{p\text{-}Z}$), vertically-propagating horizontally-

polarized in the X-axis S-wave ($V_{s\text{-}ZX}$), and vertically-propagating horizontally-polarized in the Y-axis S-wave ($V_{s\text{-}ZY}$) at each load increment shown in Fig. 8.10. The coordinate orientations are presented in Figs. 8.7, 8.8, and 8.9. As shown in these figures, this test was conducted by hitting the footing at the sides and at the top with a handheld hammer. Figure 8.16(a) shows the small-scale downhole seismic test with externally applied static vertical load.

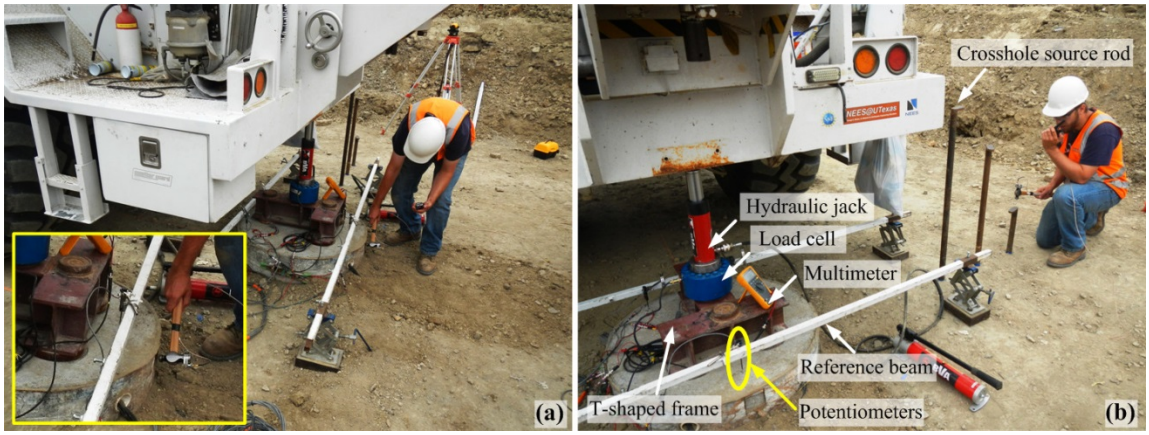

Figure 8.16 (a) Downhole and (b) crosshole seismic testing at the BKK landfill.

Examples of wave train records from downhole seismic test at the BKK are shown in Fig. 8.17. Estimates of wave propagation velocities have been generated for each of the three pairs of downhole sensors. The measured wave propagation velocity was designated at the average depth between a 3-D geophone pair. It should be noted that some wave propagation velocities from downhole seismic tests could not be calculated due to poor or irregular waveforms. In particular, cables from sensor G9 in location 3 were damaged by animals. Even though these cables were repaired, G9 in X axis generated poor waveforms. As a result, data from G9 in X axis could not be used for measuring $V_{s\text{-}ZX}$.

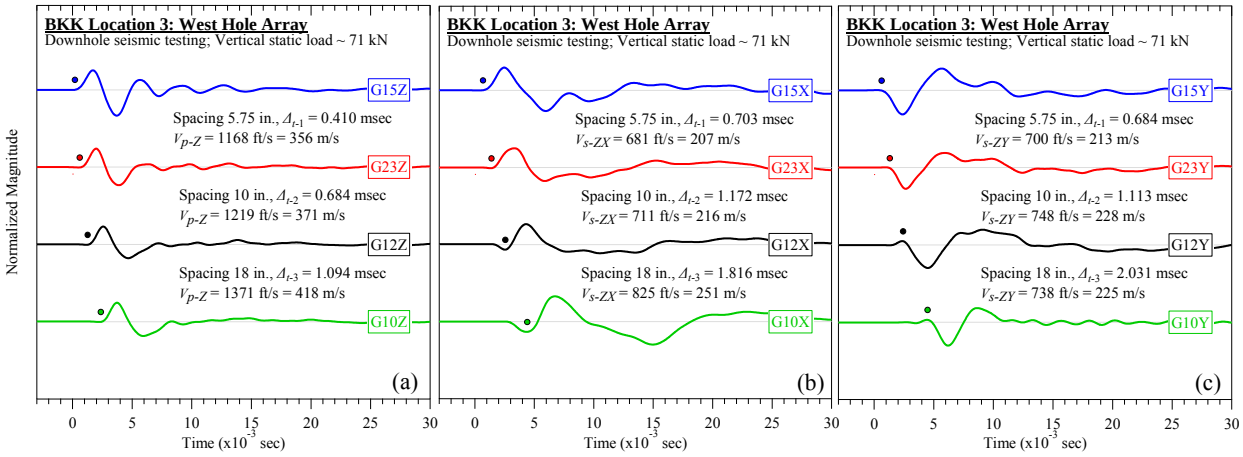

Figure 8.17 Examples of wave trains from small-scale downhole seismic test at the BKK: (a) $V_{p\text{-}Z}$, (b) $V_{s\text{-}ZX}$, and (c) $V_{s\text{-}ZY}$.

8.4.1 $V_{s\text{-}ZX}$, $V_{s\text{-}ZY}$, and $V_{p\text{-}Z}$ Profiles of Solid Waste in Location 1 at the BKK

The $V_{s\text{-}ZX}$ profiles measured from downhole seismic tests in location 1 are presented in Fig. 8.18. These profiles were measured for 6 different static vertical loads. Figures 8.18(a) and 8.18(b) present the $V_{s\text{-}ZX}$ profiles from the north and south hole arrays, respectively. In the north array, the initial $V_{s\text{-}ZX}$ decreased from 178 m/s at depth of 0.33 m to 123 m/s at depth of 0.69 m. In the south array, the initial $V_{s\text{-}ZX}$ increased from 177 m/s at depth of 0.13 m to 191 m/s at depth of 0.33 m and decreased to 159 m/s at depth of 0.69 m. Figures 8.18(a) and 8.18(b) also show that the $V_{s\text{-}ZX}$ increased with increasing static vertical load. For example, at depth of 0.13 m in the south hole array, the $V_{s\text{-}ZX}$ increased from 177 m/s to 216 m/s as the static vertical load increased from 0 kN to 111 kN.

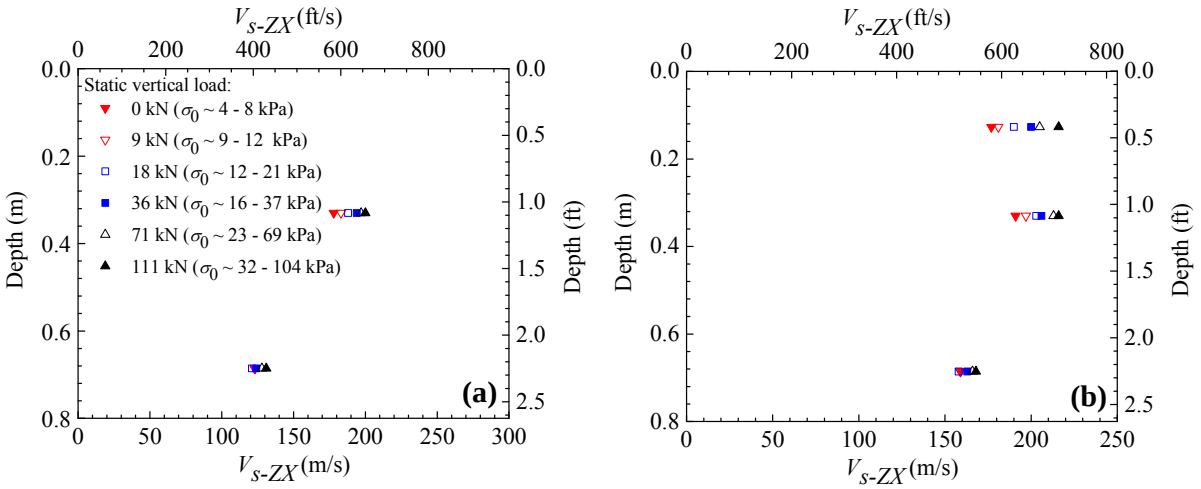

Figure 8.18 $V_{s\text{-}ZX}$ profiles in the (a) north and (b) south hole arrays in location 1 at the BKK.

The variation of $V_{s\text{-}ZY}$ with depth for 6 different static load levels in location 1 is presented in Fig. 8.19. The $V_{s\text{-}ZY}$ profiles from the north array are shown in Fig. 8.19(a). In this figure, the initial $V_{s\text{-}ZY}$ was 175 m/s at depth of 0.33 m and decreased to 125 m/s at depth of 0.69 m. The $V_{s\text{-}ZY}$ profiles from the south array are shown in Fig. 8.19(b). In the south array, the initial $V_{s\text{-}ZY}$ was 180 m/s at depth of 0.33 m and decreased to 131 m/s at depth of 0.69 m.

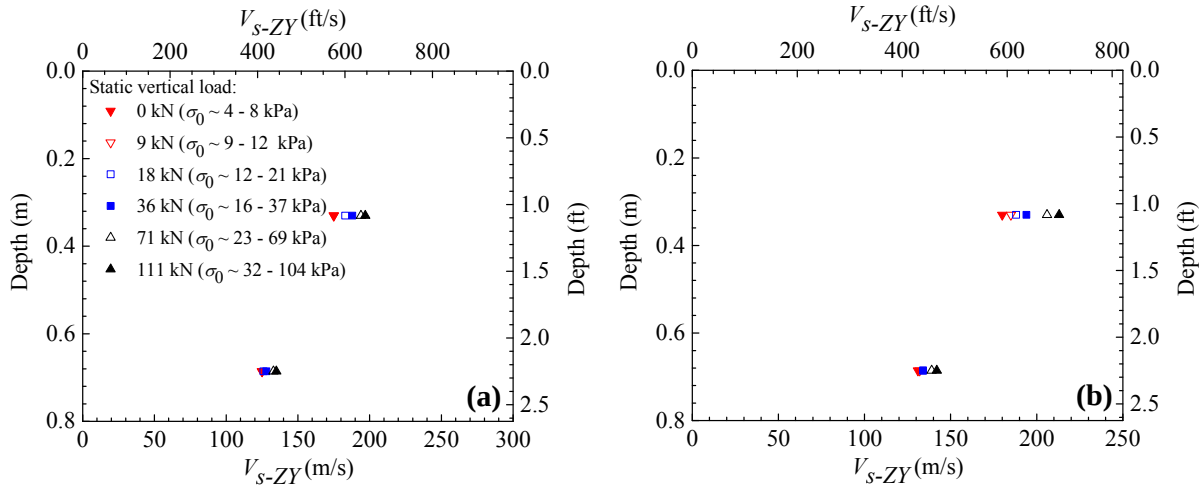

Figure 8.19 $V_{s\text{-}ZY}$ profiles in the (a) north and (b) south hole arrays in location 1 at the BKK.

The $V_{p\text{-}Z}$ profiles measured from downhole seismic tests in location 1 are presented in Fig. 8.20. Figures 8.20(a) and 8.20(b) present the $V_{p\text{-}Z}$ profiles from the north and south hole arrays,

respectively. In the north array with static vertical load of 0 kN, the $V_{p\text{-}Z}$ at depth of 0.33 m was 325 m/s. The $V_{p\text{-}Z}$ in the waste decreased to 225 m/s at depth of 0.69 m. In the south array, the $V_{p\text{-}Z}$ were 312 m/s at depth of 0.13 m, 325 m/s at depth of 0.33 m, and 272 m/s at depth of 0.69 m. As observed in Fig. 8.20, the $V_{p\text{-}Z}$ increased with increasing static vertical load.

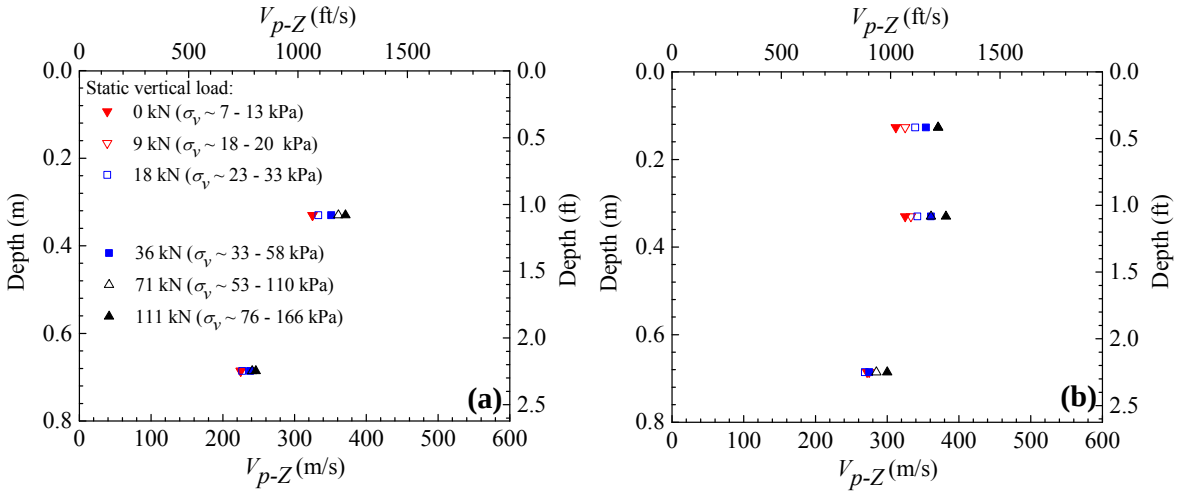

Figure 8.20 $V_{p\text{-}Z}$ profiles in the (a) north and (b) south hole arrays in location 1 at the BKK.

The overall variations in wave propagation velocities both with depth as well as between holes in Figs. 8.18, 8.19, and 8.20 show significant vertical and lateral variability of solid waste in location 1 over short measuring distances. The observed differences in V_s or V_p with depth, including the occasionally "unexpected" reductions or increases V_s or V_p with depth can be explained when we consider the significant differences in waste composition at the testing scale. In addition, the increases in wave propagation velocities with static vertical load levels are shown in these figures and are analyzed subsequently.

8.4.2 Effect of Stress State on $V_{s\text{-}ZX}$, $V_{s\text{-}ZY}$, and $V_{p\text{-}Z}$ of Solid Waste in Location 1 at the BKK

As discussed in Chapter 5, wave propagation velocities in solid waste depend on the stress state (Zekkos 2005, Lee 2007, Zekkos et al. 2013). To investigate the relationship between wave

propagation velocities and the stress state, the vertical (σ_v), horizontal (σ_h), and mean confining (σ_0) stresses were calculated using the Foster and Ahlvin (1954) method as described in Chapter 4. It is known that wave velocity is most affected by stress components aligned with the direction of wave propagation and particle motion (Roesler 1979, Yu and Richart 1984, Stokoe et al. 1985, Stokoe and Santamarina 2000, Fivorante 2000, Wang and Mok 2008). Thus, at each vertical load increment, σ_v was used as correlation parameters for $V_{p\text{-}Z}$, whereas σ_0 was used for and $V_{s\text{-}ZX}$ and $V_{s\text{-}ZY}$. The relationship between these velocities and stresses was regressed using a power function as commonly done for soils (e.g. Hardin and Richart 1963, Hardin and Black 1968, Hryciw and Thomann 1993, Iwasaki and Tatsuoka 1977). For convenience of the reader, the power functions for $V_{s\text{-}ZX}$, $V_{s\text{-}ZY}$, and $V_{p\text{-}Z}$ are shown again in Eqs. 8.1, 8.2, and 8.3, respectively. Stresses in these equations were normalized with atmospheric pressure (P_a).

$$V_{s-ZX} = A_{vX} \cdot \left(\frac{\sigma_0}{P_a} \right)^{n_{ZX}} \tag{8.1}$$

$$V_{s-ZY} = A_{vY} \cdot \left(\frac{\sigma_0}{P_a} \right)^{n_{ZY}} \tag{8.2}$$

$$V_{p-Z} = A_{pZ} \cdot \left(\frac{\sigma_v}{P_a} \right)^{n_{pZ}} \tag{8.3}$$

where A_{ij} is an empirical constant that indicates corresponding wave propagation velocity at 1 atm and n_{ij} is an empirical constant that quantifies the effect of stress on the corresponding wave propagation velocity.

As discussed earlier, some wave propagation velocities from downhole seismic tests could not be calculated due to poor or irregular waveforms. Unavailable data points may result in difficulty in performing some regression analysis.

Figures 8.21, 8.22, and 8.23 illustrate the $V_{s\text{-}ZX}$, $V_{s\text{-}ZY}$, and $V_{p\text{-}Z}$ variations with stresses, respectively. A linear relationship of wave propagation velocities with stress and low n_{ij} were observed. This indicated that waste in the overconsolidated (OC) regime and remained so throughout the course of testing. The stress exponent n_{ZX} for $V_{s\text{-}ZX}$ was found to be ranging from 0.05 to 0.06. The n_{ZY} for $V_{s\text{-}ZY}$ ranged from 0.05 to 0.06 in the OC regime. The n_{pZ} for $V_{p\text{-}Z}$ ranged from 0.05 to 0.06 in the OC regime.

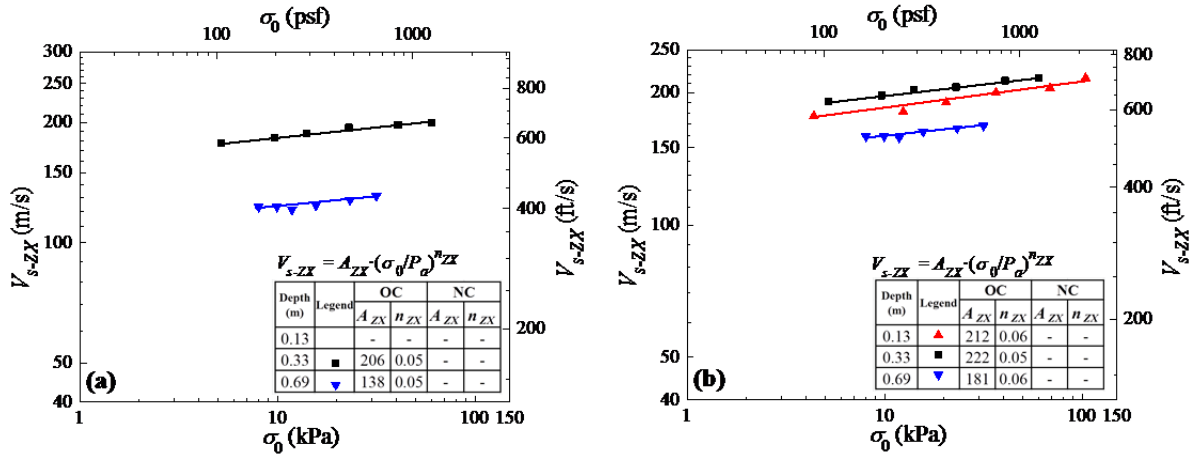

Figure 8.21 Effect of σ_0 on $V_{s\text{-}ZX}$ in the (a) north and (b) south hole arrays in location 1 at the BKK.

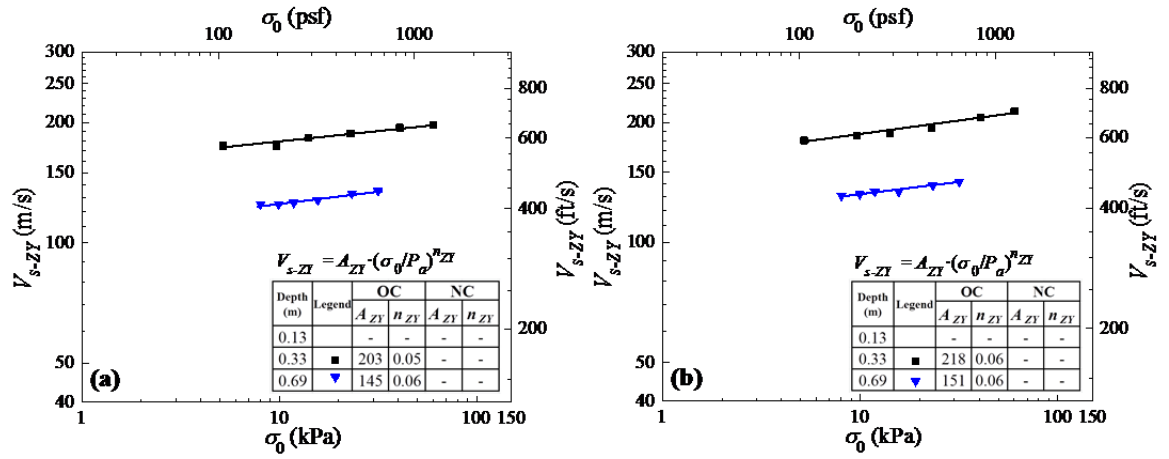

Figure 8.22 Effect of σ_0 on $V_{s\text{-}ZY}$ in the (a) north and (b) south hole arrays in location 1 at the BKK.

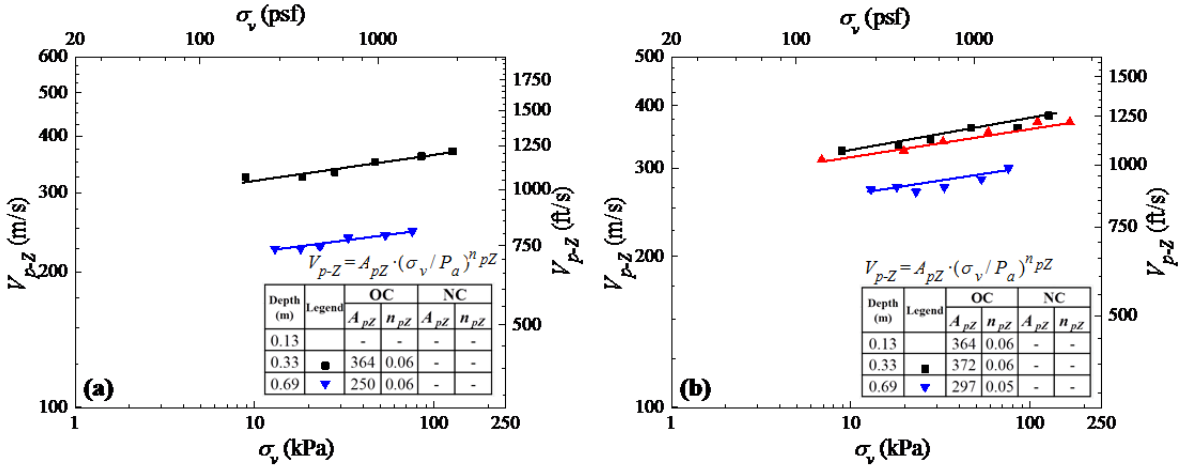

Figure 8.23 Effect of σ_v on $V_{p\text{-}Z}$ in the (a) north and (b) south hole arrays in location 1 at the BKK.

8.4.3 $V_{s\text{-}ZX}$, $V_{s\text{-}ZY}$, and $V_{p\text{-}Z}$ Profiles of Solid Waste in Location 2 at the BKK

Figure 8.24 shows the variation of $V_{s\text{-}ZX}$ with depth for 6 different static load levels in location 2. As shown in Fig 8.24(a), in the north array, the $V_{s\text{-}ZX}$ increased from 183 m/s at depth of 0.33 m to 195 m/ at depth of 0.69 m. The variation of $V_{s\text{-}ZX}$ with depth in the south array is shown in Fig. 8.24(b). In the south array, the $V_{s\text{-}ZX}$ increased from 178 m/s at depth of 0.33 m to 243 m/ at depth of 0.69. As shown in Figure 8.24, $V_{s\text{-}ZX}$ increased with increasing static vertical load.

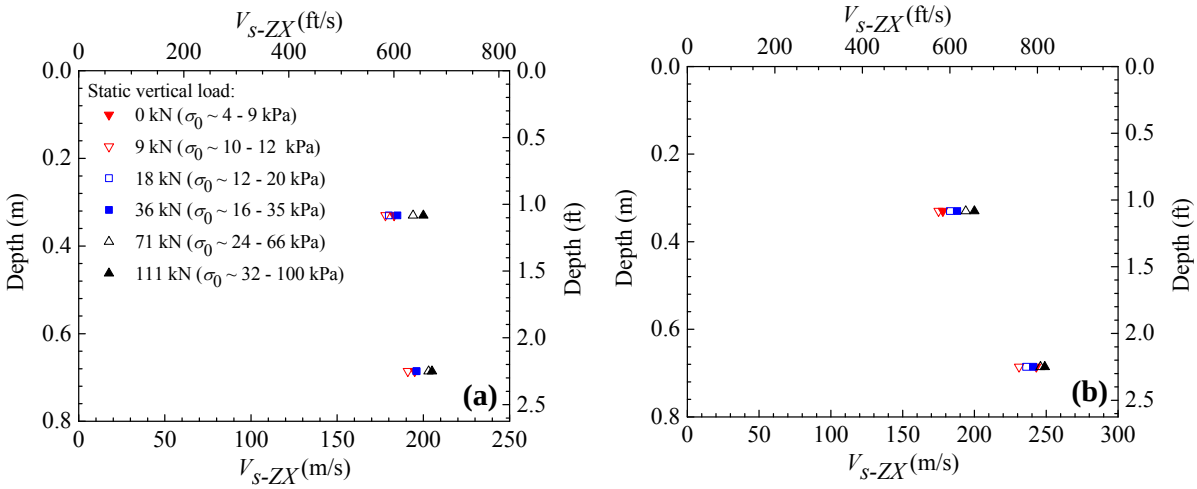

Figure 8.24 $V_{s\text{-}ZX}$ profiles in the (a) north and (b) south hole arrays in location 2 at the BKK.

The $V_{s\text{-}ZY}$ profiles measured from downhole seismic tests in location 2 are presented in Fig. 8.25. Figures 8.25(a) and 8.25(b) present the $V_{s\text{-}ZY}$ profiles from the north and south arrays, respectively. In the north array, the $V_{s\text{-}ZY}$ slightly increased from 197 m/s at depth of 0.33 m to 201 m/s at depth of 0.69 m. In the south array, the $V_{s\text{-}ZY}$ increased from 180 m/s at depth of 0.33 m to 241 m/s at depth of 0.69 m.

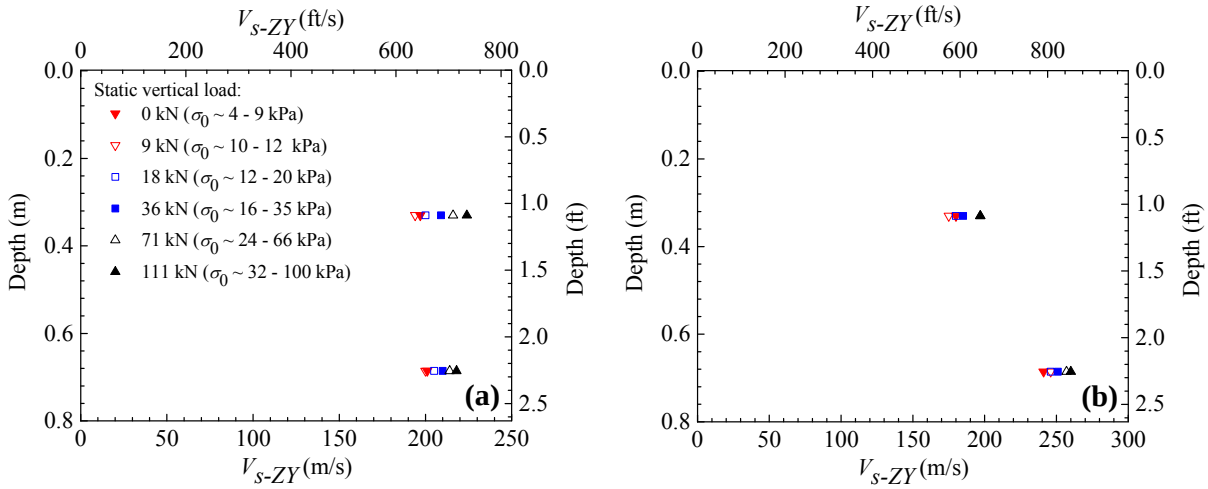

Figure 8.25 $V_{s\text{-}ZY}$ profiles in the (a) north and (b) south hole arrays in location 2 at the BKK.

Figure 8.26 presents the $V_{p\text{-}Z}$ profiles measured from downhole seismic tests in location 2. In the north array [Figure 8.26(a)], the $V_{p\text{-}Z}$ at depth of 0.33 m was 394 m/s during application of

static vertical load of 9 kN. The initial $V_{p\text{-}Z}$ at depth of 0.69 m was as high as 410 m/s. In the south array, the initial $V_{p\text{-}Z}$ were 342 m/s at depth of 0.33 m and 418 m/s at depth of 0.69 m. Figure 8.26 shows that $V_{p\text{-}Z}$ increased with increasing static vertical load.

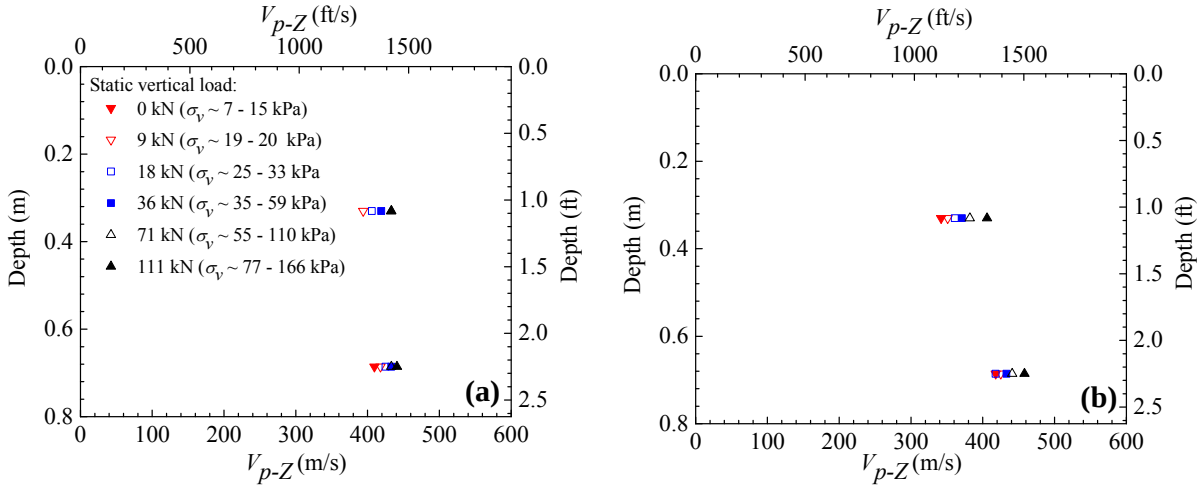

Figure 8.26 $V_{p\text{-}Z}$ profiles in the (a) north and (b) south hole arrays in location 2 at the BKK.

8.4.4 Effect of Stress State on $V_{s\text{-}ZX}$, $V_{s\text{-}ZY}$, and $V_{p\text{-}Z}$ of Solid Waste in Location 2 at the BKK

Figures 8.27, 8.28, and 8.29 illustrate the $V_{s\text{-}ZX}$, $V_{s\text{-}ZY}$, and $V_{p\text{-}Z}$ variations in solid waste with stresses in location 2, respectively. In the OC regime, the stress exponent n_{ZX} for $V_{s\text{-}ZX}$ ranged from 0.04 – 0.06. The n_{ZY} for $V_{s\text{-}ZY}$ varied from 0.05 to 0.06 in the OC regime. The n_{pZ} for $V_{p\text{-}Z}$ ranged from 0.04 to 0.06 in the OC regime.

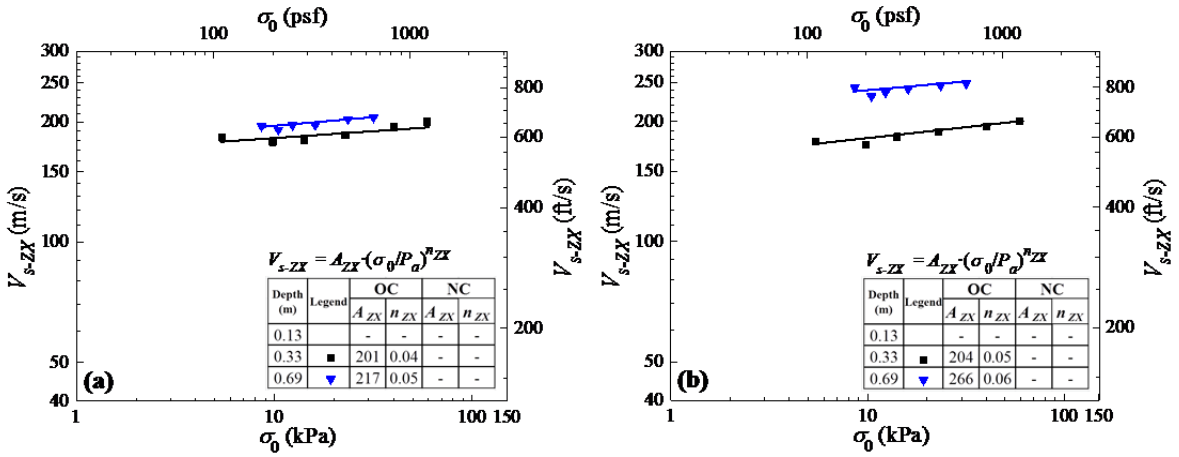

Figure 8.27 Effect of σ_0 on $V_{s\text{-}ZX}$ in the (a) north and (b) south arrays in location 2 at the BKK.

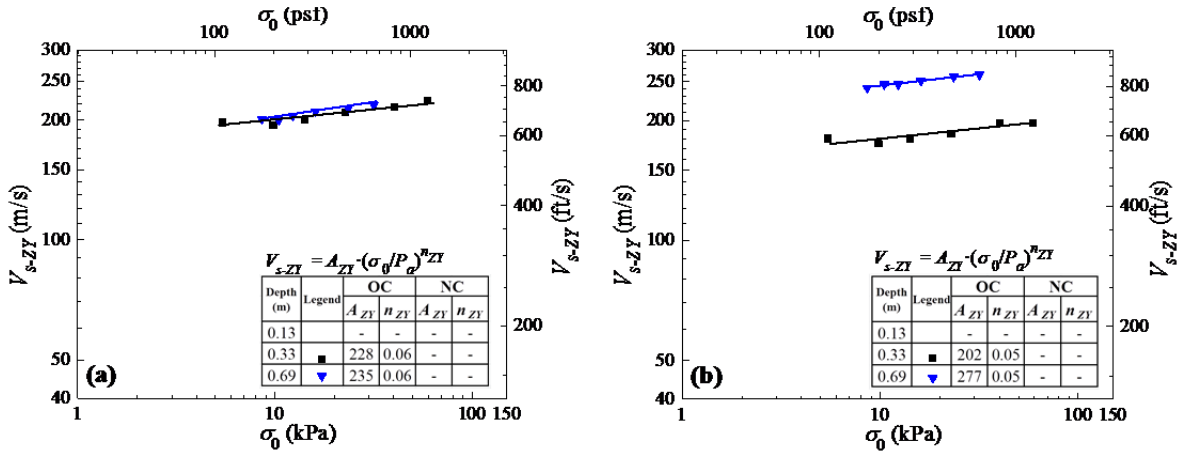

Figure 8.28 Effect of σ_0 on $V_{s\text{-}ZY}$ in the (a) north and (b) south arrays in location 2 at the BKK.

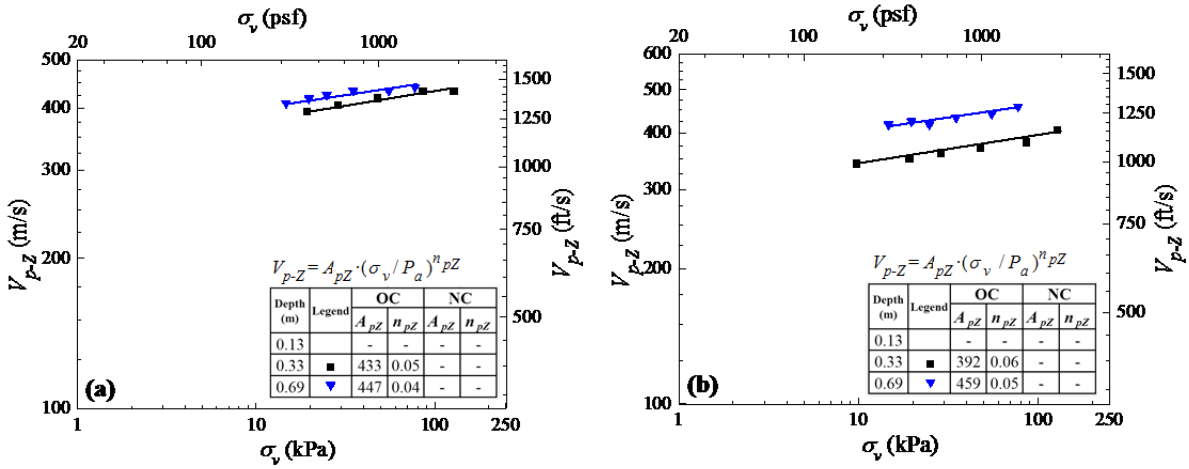

Figure 8.29 Effect of σ_v on $V_{p\text{-}Z}$ in the (a) north and (b) south arrays in location 2 at the BKK.

8.4.5 $V_{s\text{-}ZX}$, $V_{s\text{-}ZY}$, and $V_{p\text{-}Z}$ Profiles of Soil Cover in Location 3 at the BKK

Downhole seismic tests were performed to investigate $V_{s\text{-}ZX}$ of soil cover in location 3. Figures 8.30(a) and 8.30(b) present the $V_{s\text{-}ZX}$ profiles from the east and west hole arrays, respectively. These profiles were measured using static vertical load levels ranging from 0 kN to 111 kN. In the east array, the initial $V_{s\text{-}ZX}$ was 166 m/s at depth of 0.13 m. In the west array, $V_{s\text{-}ZX}$ increased from 149 m/s at depth of 0.13 m to 236 m/s at depth of 0.69 m. As shown in Figure 8.30, the $V_{s\text{-}ZX}$ increased with increasing vertical static load.

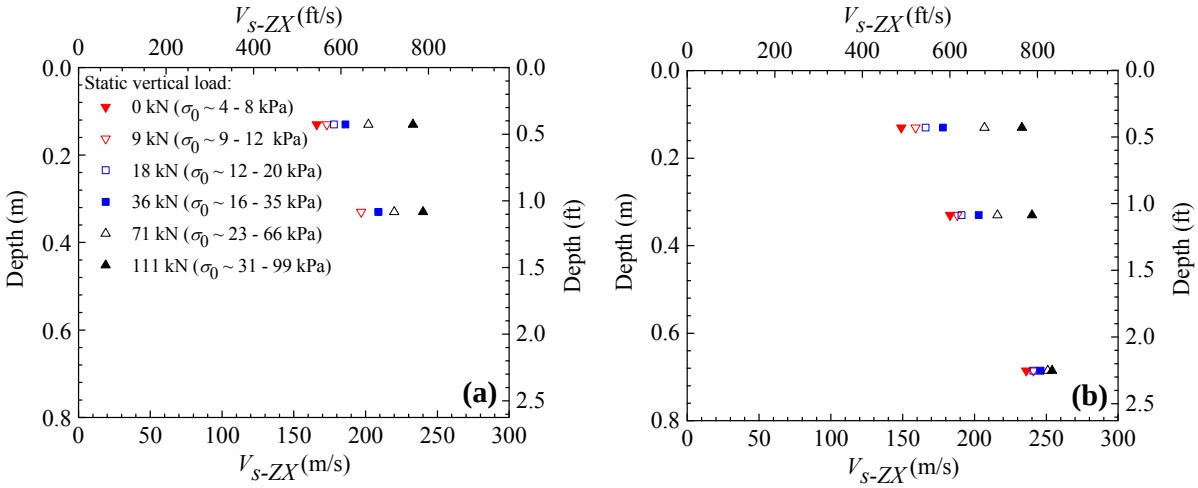

Figure 8.30 $V_{s\text{-}ZX}$ profiles in the (a) east and (b) west hole arrays in location 3 at the BKK.

The $V_{s\text{-}ZY}$ profiles of soil cover measured from downhole seismic tests in location 3 are presented in Fig. 8.31. Figures 8.31(a) and 8.31(b) present the $V_{s\text{-}ZY}$ profiles from the east and west arrays, respectively. In the east array, the $V_{s\text{-}ZY}$ at a static vertical load of 9 kN generally increased from 188 m/s at depth of 0.33 m to 200 m/s at depth of 0.69 m. In the west array, the initial $V_{s\text{-}ZY}$ increased from 169 m/s at depth of 0.13 m to 216 m/s at depth of 0.69 m.

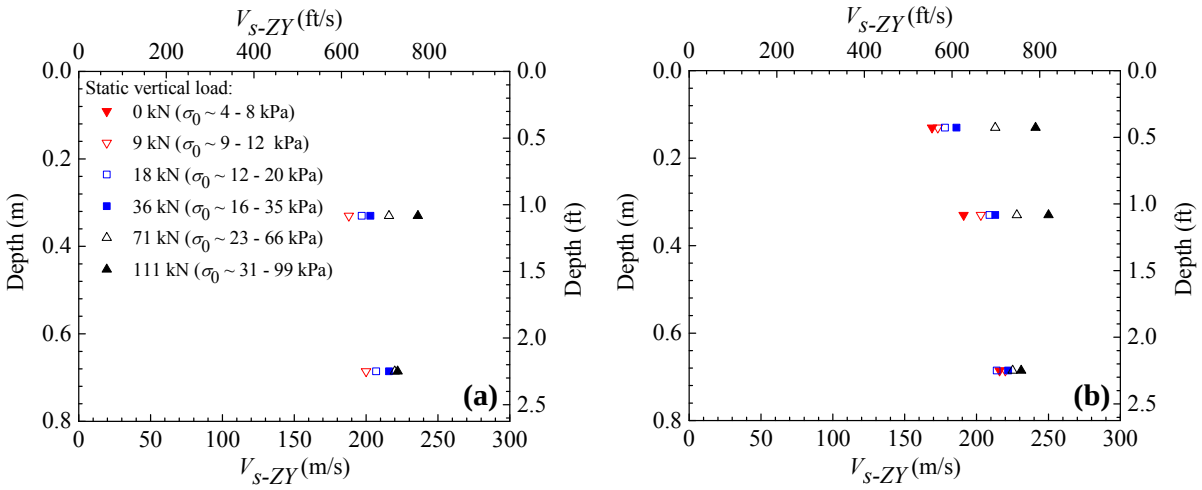

Figure 8.31 $V_{s\text{-}ZY}$ profiles in the (a) east and (b) west hole arrays in location 3 at the BKK.

The $V_{p\text{-}Z}$ profiles of soil cover measured from downhole seismic tests in location 3 are presented in Fig. 8.32. Figures 8.32(a) and 8.32(b) present the $V_{p\text{-}Z}$ profiles from the east and west hole arrays, respectively. In the east array, the initial $V_{p\text{-}Z}$ at depth of 0.13 m was 299 m/s. The $V_{p\text{-}Z}$ increased to 317 m/s at depth of 0.33 m and increased to 371 m/s at depth of 0.69 m. In the west array, the $V_{p\text{-}Z}$ were 276 m/s at depth of 0.13 m, 333 m/s at depth of 0.33 m, and 396 m/s at depth of 0.69 m. As shown in Fig. 8.32, the $V_{p\text{-}Z}$ increased with increasing static vertical load.

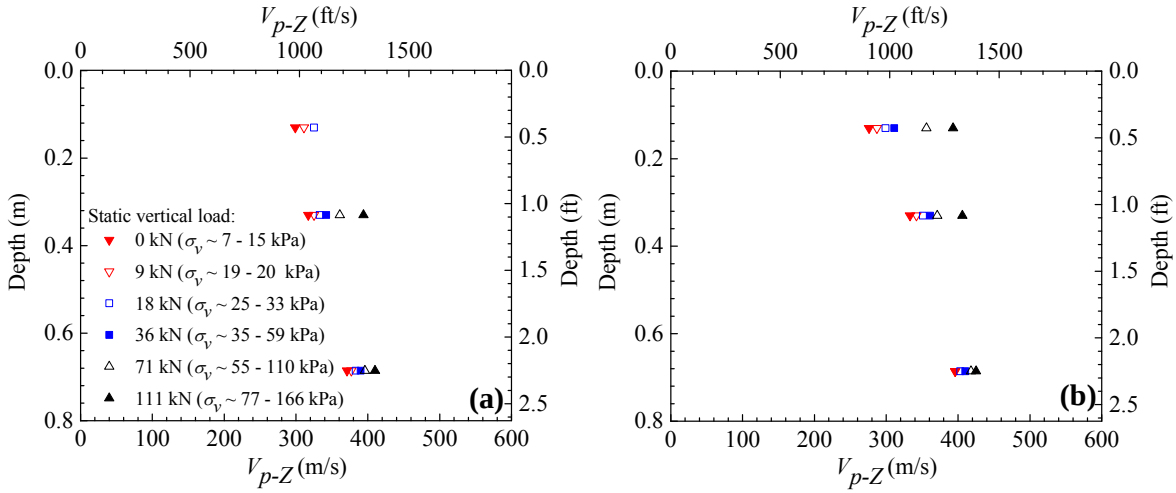

Figure 8.32 $V_{p\text{-}Z}$ profiles in the (a) east and (b) west hole arrays in location 3 at the BKK.

8.4.6 Effect of Stress State on $V_{s\text{-}ZX}$, $V_{s\text{-}ZY}$, and $V_{p\text{-}Z}$ of Soil Cover in Location 3 at the BKK

The variations of $V_{s\text{-}ZX}$, $V_{s\text{-}ZY}$, and $V_{p\text{-}Z}$ with stresses are presented in Figures 8.33, 8.34, and 8.35, respectively. An either linear or bi-linear relationship of wave propagation velocities with stress was observed. Bi-linearity was indicative of the soil cover being in the OC regime due to compaction. As stress increased, the soil cover reached the normally consolidated (NC) regime. In the OC regime, the stress exponent n_{ZX} for $V_{s\text{-}ZX}$ ranged from 0.05 – 0.07, while in the NC regime, the n_{ZX} was on the order of 0.21 to 0.27. The n_{ZY} for $V_{s\text{-}ZY}$ varied from 0.03 to 0.09 in the OC regime and increased to 0.23 and 0.25 in the NC regime. The n_{pZ} for $V_{p\text{-}Z}$ ranged from 0.05 to 0.06 in the OC regime and varied from 0.22 to 0.23 in the NC regime. As indicated by the change in slope in Figs 8.33, 8.34, and 8.35, the interpreted maximum vertical stress ($\sigma_{v\text{-max}}$) and mean stress ($\sigma_{0\text{-max}}$) were approximately on the order of 60 – 80 kPa and 36 – 40 kPa, respectively.

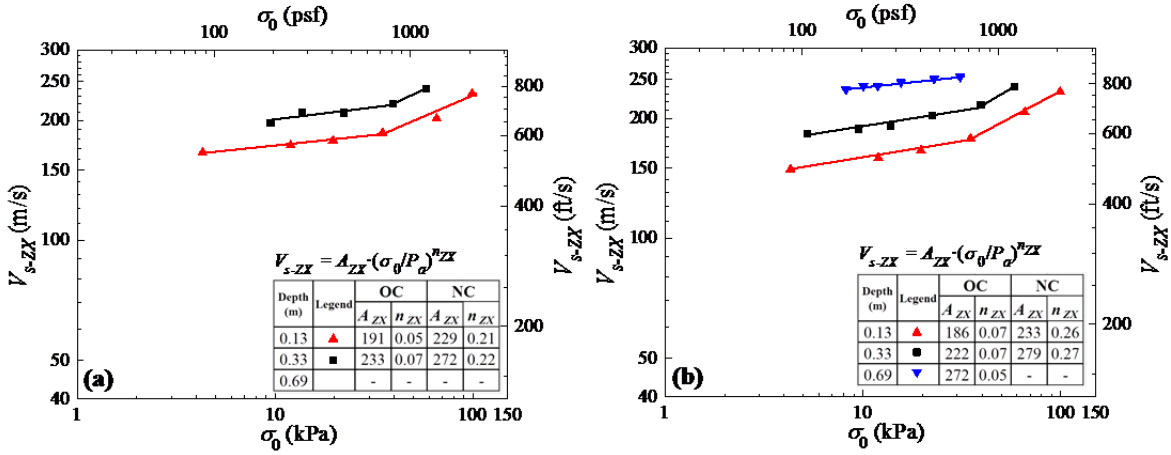

Figure 8.33 Effect of σ_0 on $V_{s\text{-}ZX}$ in the (a) east and (b) west hole arrays in location 3 at the BKK.

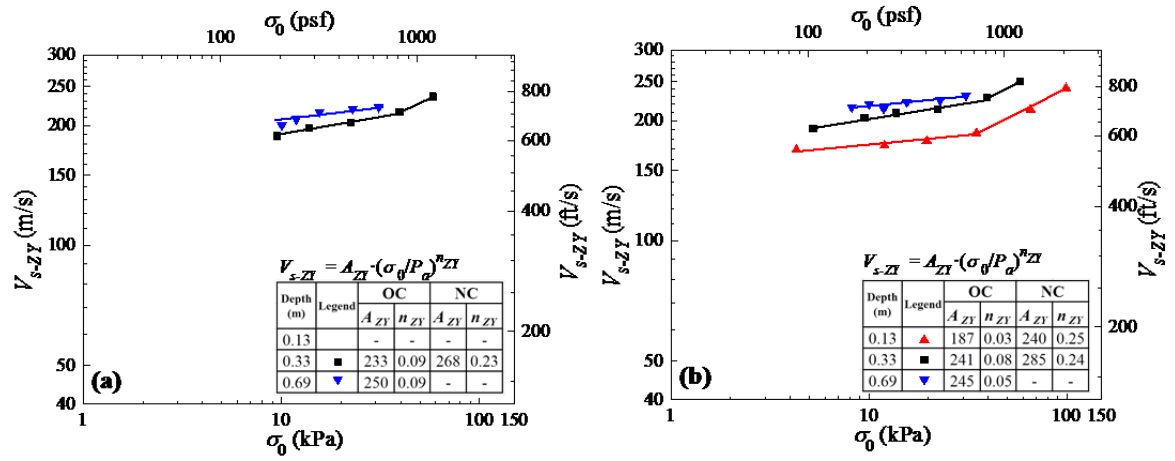

Figure 8.34 Effect of σ_0 on $V_{s\text{-}ZY}$ in the (a) east and (b) west hole arrays in location 3 at the BKK.

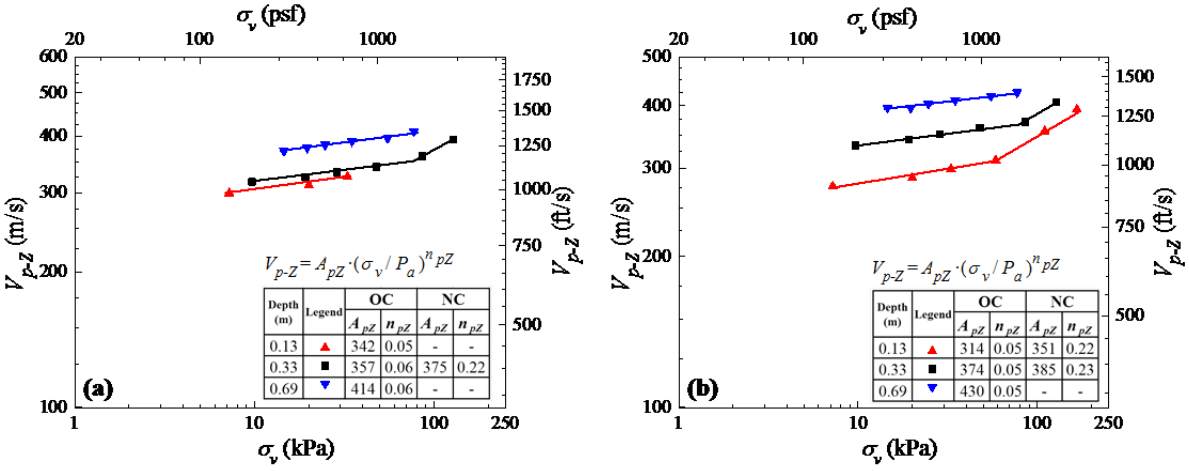

Figure 8.35 Effect of σ_v on $V_{p\text{-}Z}$ in the (a) east and (b) west hole arrays in location 3 at the BKK.

8.5 **Small-scale Crosshole Seismic Testing**

Crosshole seismic tests were performed at the BKK to evaluate horizontally propagating P-wave velocity ($V_{p\text{-}X}$) and horizontally-propagating vertically-polarized in the Z-axis S-wave ($V_{s\text{-}XZ}$). This test was conducted by hitting the crosshole source rods as illustrated in Figure 8.16(b). Figure 8.36 shows an example of wave trains from the small-scale crosshole seismic test.

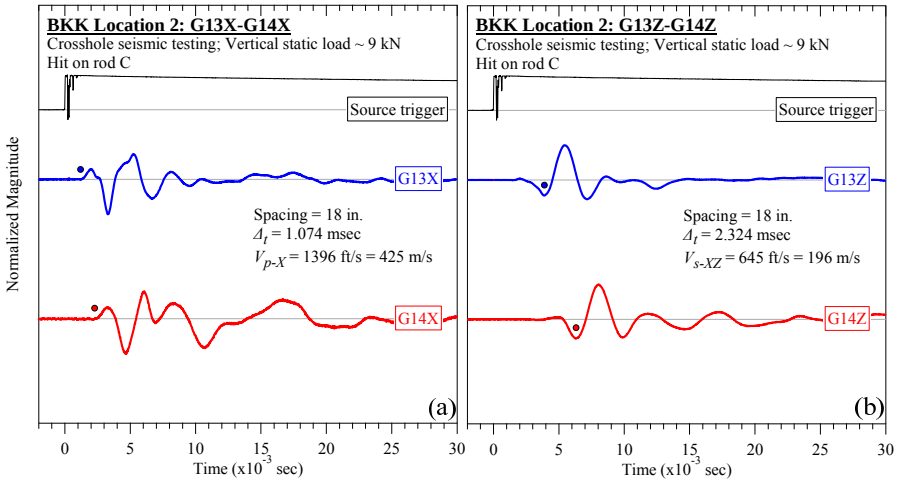

Figure 8.36 Examples of wave trains from crosshole seismic test at the BKK: (a) $V_{p\text{-}X}$ and (b) $V_{s\text{-}XZ}$.

Similarly to downhole seismic testing, the relationship between $V_{p\text{-}X}$ and $V_{s\text{-}XZ}$ and stresses was regressed using a power function. In this case, σ_h and σ_0 were used as correlation parameters for $V_{p\text{-}X}$ and $V_{s\text{-}XZ}$, respectively. Relationships between wave propagation velocity and stress component were fitted using the following equations.

$$V_{p-X} = A_{pX} \cdot \left(\frac{\sigma_h}{P_a} \right)^{n_{pX}} \tag{8.4}$$

$$V_{s-XZ} = A_{XZ} \cdot \left(\frac{\sigma_0}{P_a} \right)^{n_{XZ}} \tag{8.5}$$

Some wave propagation velocities from crosshole seismic tests could not be calculated due to poor or irregular waveforms. Unavailable data points may result in difficulty in performing regression analysis. Some regression analyses were not performed if unavailable data points were considered significantly affecting the regression analysis results.

Figures 8.37(a) and 8.37(b) show the relationship between stress states and $V_{p\text{-}X}$ and $V_{s\text{-}XZ}$ of solid waste in location 1, respectively. A linear relationship between wave propagation

velocities and stresses is observed in these figures. In the OC regime, the stress exponent n_{pX} for $V_{p\text{-}X}$ was found to be low (n_{pX} ~ 0.04 – 0.06). The n_{XZ} for $V_{s\text{-}XZ}$ ranged from 0.05 to 0.06 in the OC regime.

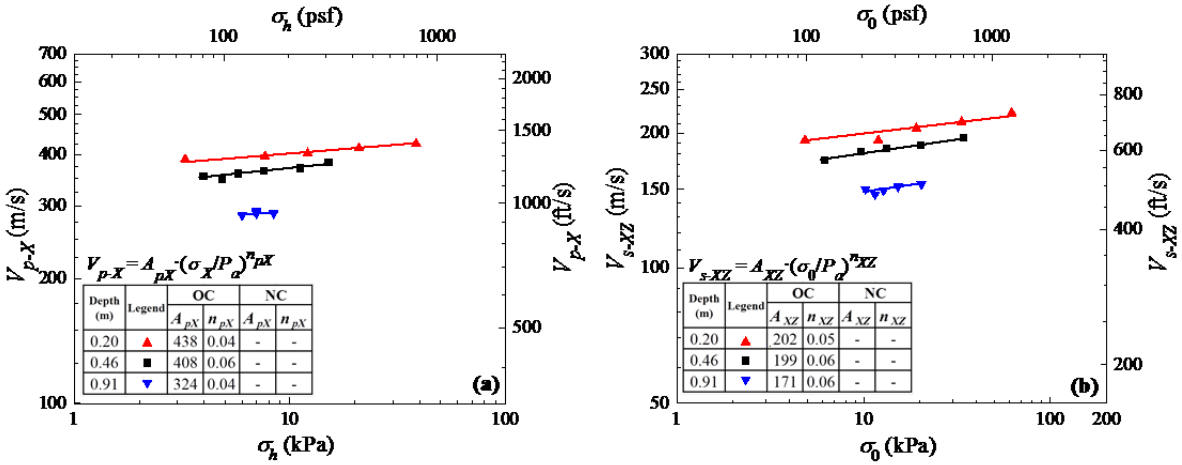

Figure 8.37 Effect of stress states on (a) $V_{p\text{-}X}$ and (b) $V_{s\text{-}XZ}$ of solid waste in location 1 at the BKK.

The relationship between $V_{p\text{-}X}$ and $V_{s\text{-}XZ}$ and stress states in location 2 are presented in Figures 8.38(a) and 8.38(b), respectively. A linear relationship between wave propagation velocities and stresses is observed in these figures. In the OC regime, the stress exponent n_{pX} for $V_{p\text{-}X}$ ranged from 0.04 to 0.06. The n_{XZ} for $V_{s\text{-}XZ}$ ranged from 0.04 to 0.05 in the OC regime.

Figures 8.39(a) and 8.39(b) show the relationship between stress states and $V_{p\text{-}X}$ and $V_{s\text{-}XZ}$ of soil cover in location 3, respectively. The relationship between wave propagation velocities and stresses exhibited linear or bi-linear form. In the OC regime, the stress exponent n_{pX} for $V_{p\text{-}X}$ ranged from 0.04 – 0.05, while in the NC regime, the n_{pX} increased to 0.21. The n_{XZ} for $V_{s\text{-}XZ}$ varied from 0.05 to 0.07 in the OC regime and increased to 0.25 in the NC regime.

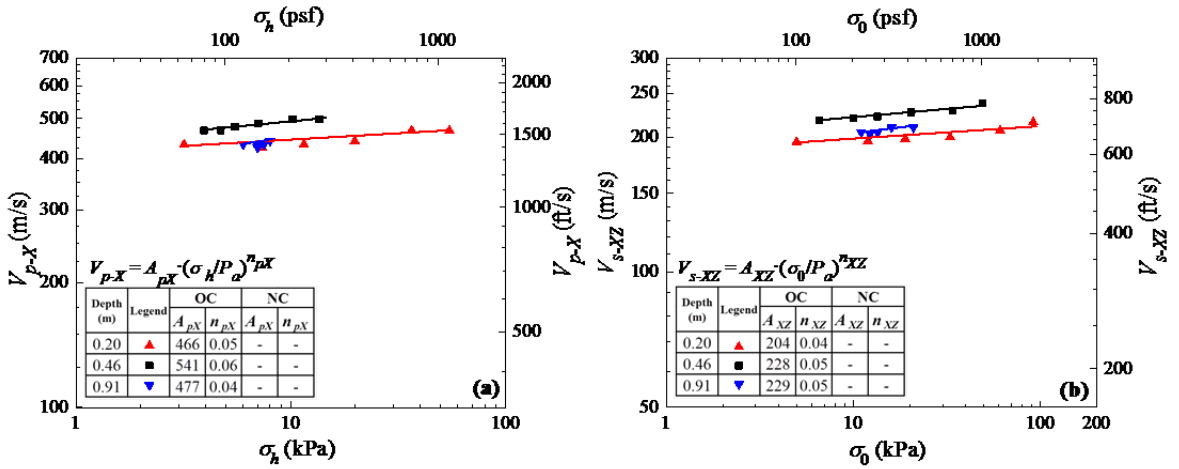

Figure 8.38 Effect of stress states on (a) $V_{p\text{-}X}$ and (b) $V_{s\text{-}XZ}$ in location 2 at the BKK.

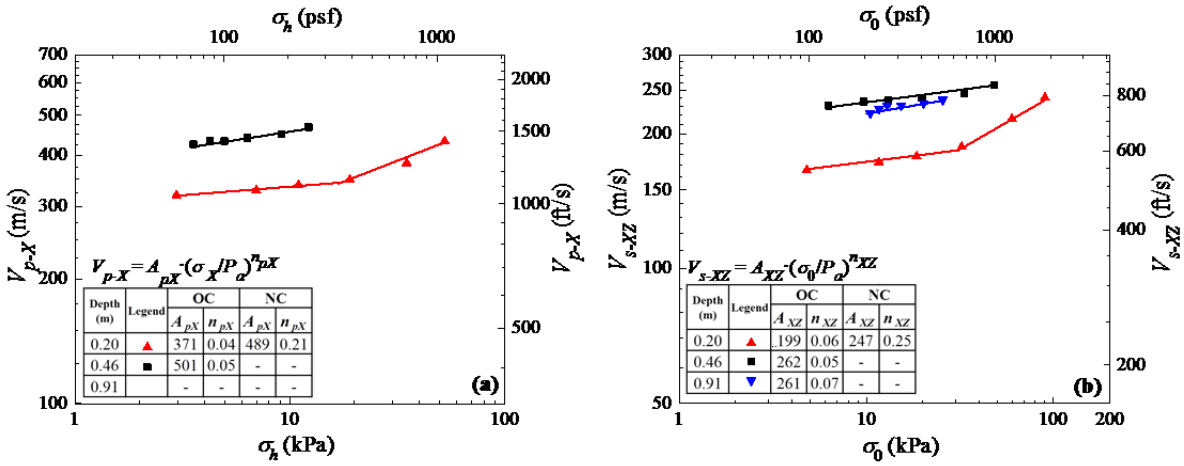

Figure 8.39 Effect of stress states on (a) $V_{p\text{-}X}$ and (b) $V_{s\text{-}XZ}$ in location 3 at the BKK.

8.6 **Evaluation of Anisotropy of Wave Propagation Velocity in Solid Waste and Soil Cover at the BKK**

Anisotropy in solid waste can be attributed to stress-induced anisotropy and fabric (structural) anisotropy, as discussed in Zekkos (2013). Stress-induced anisotropy is attributed to stress states that are different in the horizontal and vertical directions. Fabric anisotropy is attributed to preferential orientation of fibrous particles in the solid waste. Thus, the solid waste can still behave anisotropically even in isotropic stress states. In this study, assessment of the degree of

anisotropy in solid waste and soil cover was performed by comparing wave velocities from a variety of propagation and polarization directions.

8.6.1 Solid Waste in Locations 1 and 2 at the BKK

Figure 8.40(a) shows a comparison between P-wave and S-wave velocities propagating in the vertical direction (i.e. $V_{p\text{-}Z}$ and $V_{s\text{-}ZX}$) in solid waste at the BKK. The ratio of $V_{s\text{-}ZX}$ to $V_{p\text{-}Z}$ in location 1 ranged from 0.52 to 0.59. The ratio of $V_{s\text{-}ZX}$ to $V_{p\text{-}Z}$ in location 2 varied from 0.44 to 0.58. The mean from two locations shows that the ratio of $V_{s\text{-}ZX}$ to $V_{p\text{-}Z}$ was 0.53.

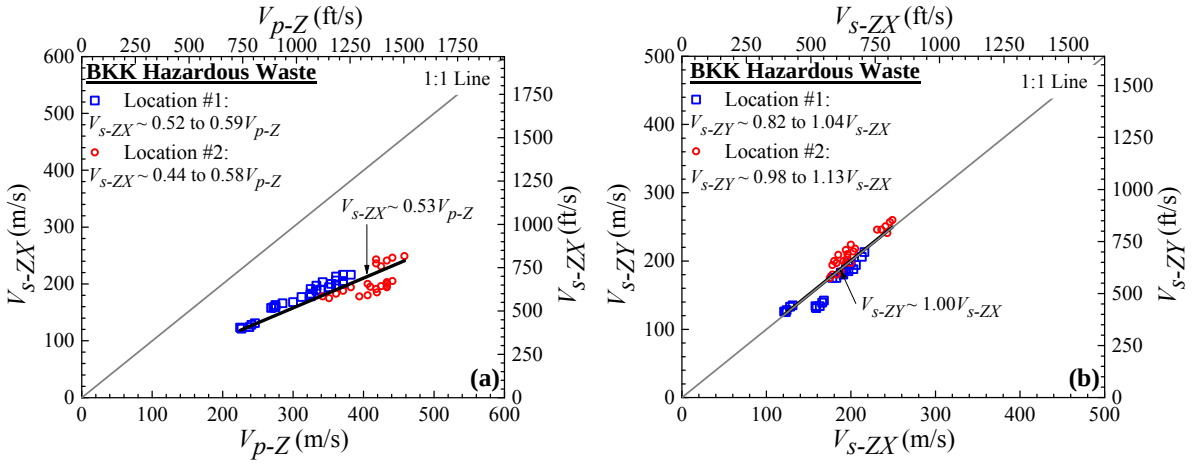

Figure 8.40 Comparison on (a) $V_{p\text{-}Z}$-$V_{s\text{-}ZX}$ and (b) $V_{s\text{-}ZX}$ -$V_{s\text{-}ZY}$ in solid waste testing locations at the BKK.

Figure 8.40(b) presents a comparison between the $V_{s\text{-}ZX}$ and the $V_{s\text{-}ZY}$. In location 1, the ratio of $V_{s\text{-}ZY}$ to $V_{s\text{-}ZX}$ varied from 0.82 to 1.04. In location 2, the ratio of $V_{s\text{-}ZY}$ to $V_{s\text{-}ZX}$ ranged from 0.98 to 1.13. The mean of this ratio from two locations was found to be 1.00 indicating minor difference on average between S-wave propagation velocities in the YZ and the XZ plane.

Figure 8.41 shows a comparison between P-wave and S-wave velocities propagating in the horizontal direction (i.e. $V_{p\text{-}X}$ and $V_{s\text{-}XZ}$). In location 1, the ratio of $V_{s\text{-}XZ}$ to $V_{p\text{-}X}$ ranged from 0.49 to 0.55. In location 2, this ratio varied from 0.44 to 0.49. In general, the ratio of $V_{s\text{-}XZ}$ to $V_{p\text{-}X}$

in solid waste test locations at the BKK ranged from 0.44 to 0.55 with a mean value of 0.48. This ratio was lower than the ratio of V_p and V_s counterparts propagating in the vertical direction.

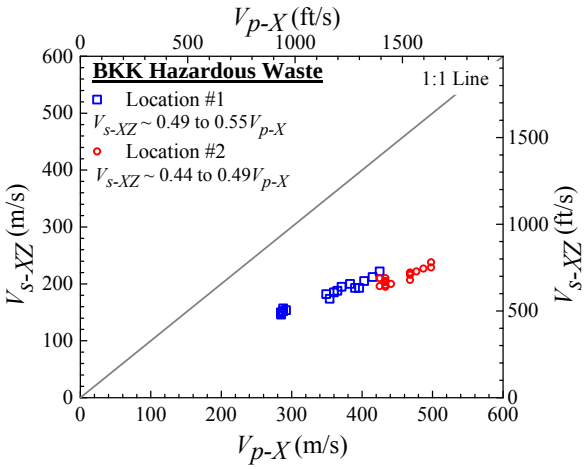

Figure 8.41 Comparison on $V_{p\text{-}X}$ and $V_{s\text{-}XZ}$ in solid waste testing locations at the BKK.

Anisotropy in solid waste was also evaluated by comparing wave propagation velocities in the horizontal and vertical directions. Because the designated measurement points from downhole and crosshole seismic tests were not the same, four $V_{p\text{-}Z}$ values from downhole tests were averaged and then compared with a $V_{p\text{-}X}$ from a crosshole test, as shown in Fig 8.42. The same method was also performed in comparing shear wave velocity propagating in the vertical and horizontal directions.

Figure 8.43(a) shows a comparison between V_p propagating in the horizontal ($V_{p\text{-}X}$) and vertical ($V_{p\text{-}Z}$) directions. In location 1, the ratios of $V_{p\text{-}Z}$ to $V_{p\text{-}X}$ varied from 0.81 to 0.86. In location 2, the ratios of $V_{p\text{-}Z}$ to $V_{p\text{-}X}$ varied from 0.79 to 0.90. The ratio of $V_{p\text{-}Z}$ to $V_{p\text{-}X}$ from solid waste testing locations ranged from 0.79 to 0.90 with a mean value of 0.85. This ratio indicated that the compressibility of solid waste in the horizontal direction was lower than the compressibility in the vertical direction.

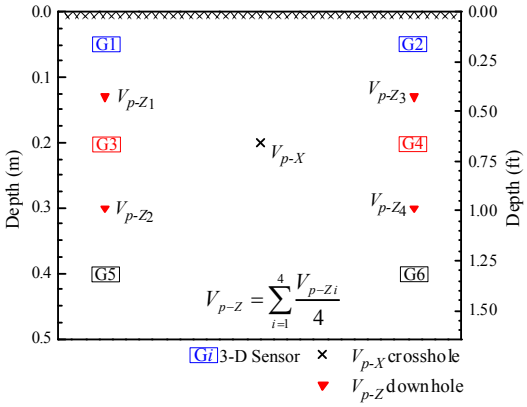

Figure 8.42 Example of measurement points for comparing wave propagation velocities in the vertical and horizontal directions.

The relationship between V_s propagating in the horizontal ($V_{s\text{-}horizontal}$: $V_{s\text{-}XZ}$) and vertical ($V_{s\text{-}vertical}$: $V_{s\text{-}ZX}$ and $V_{s\text{-}ZY}$) directions is shown in Figure 8.43(b). The ratio $V_{s\text{-}vertical}$ and $V_{s\text{-}horizontal}$ were found to be between 0.85 and 1.00 with an average value of 0.92. In general, the data indicated that wave propagation in the vertical direction was slower than that in the horizontal direction, highlighting that solid waste is an anisotropic material.

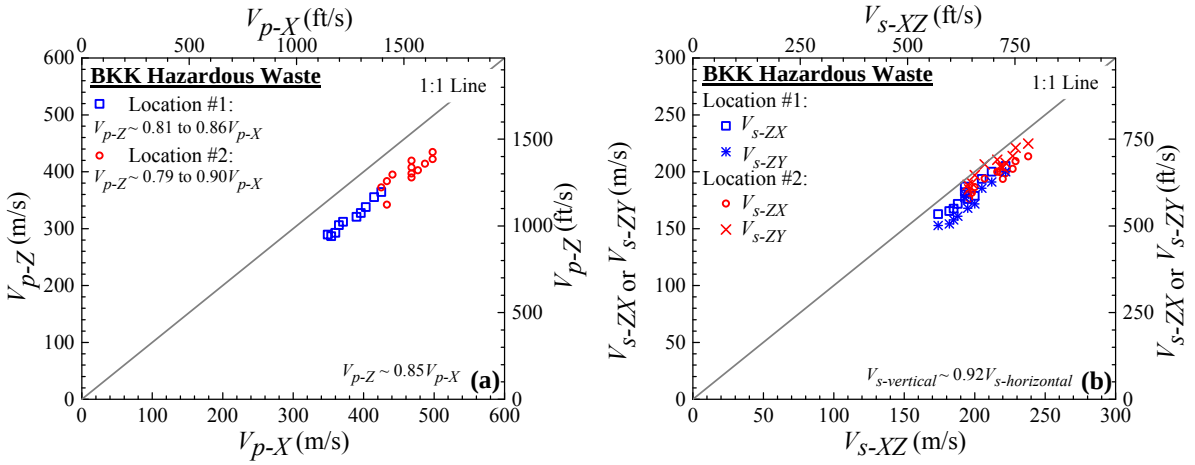

Figure 8.43 (a) Comparison on V_p propagating in the vertical and horizontal directions; and (b) V_s propagating in the vertical and horizontal directions in solid waste testing locations at the BKK.

8.6.2 Soil Cover in Location 3 at the BKK

Figure 8.44(a) shows a comparison between $V_{p\text{-}Z}$ and $V_{s\text{-}ZX}$ in the soil cover test location at the BKK. The ratio of $V_{s\text{-}ZX}$ to $V_{p\text{-}Z}$ in this location ranged from 0.54 to 0.61 with a mean value of 0.58. Figure 8.44(b) presents a comparison between the $V_{s\text{-}ZX}$ and the $V_{s\text{-}ZY}$. The ratio of $V_{s\text{-}ZY}$ to $V_{s\text{-}ZX}$ in soil cover test location varied from 0.89 to 1.13 with a mean value of 0.98.

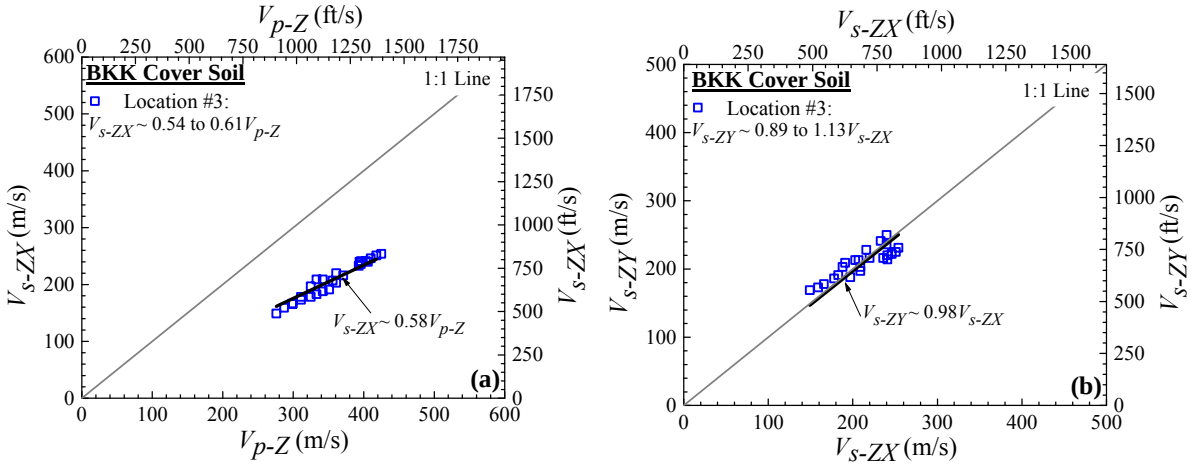

Figure 8.44 Comparison on (a) $V_{p\text{-}Z}$-$V_{s\text{-}ZX}$ and (b) $V_{s\text{-}ZX}$ -$V_{s\text{-}ZY}$ in soil cover testing location at the BKK.

Figure 8.45 shows a comparison between $V_{p\text{-}X}$ and $V_{s\text{-}XZ}$. The ratio of $V_{s\text{-}XZ}$ to $V_{p\text{-}X}$ of soil cover ranged from 0.52 to 0.57 with a mean value of 0.55. This ratio was lower than the ratio of V_p and V_s counterparts propagating in the vertical direction.

Figure 8.46(a) shows a comparison between $V_{p\text{-}X}$ and $V_{p\text{-}Z}$ directions in soil cover testing location. The ratios of $V_{p\text{-}Z}$ to $V_{p\text{-}X}$ varied from 0.83 to 0.97 with a mean value of 0.90. The relationship between $V_{s\text{-}horizontal}$ and $V_{s\text{-}vertical}$ directions is shown in Figure 8.46(b). The ratio $V_{s\text{-}horizontal}$ and $V_{s\text{-}vertical}$ were found to be between 0.86 and 1.09 with an average value of 0.95. In general, the data indicated that wave propagation in the vertical direction was slower than that in the horizontal direction.

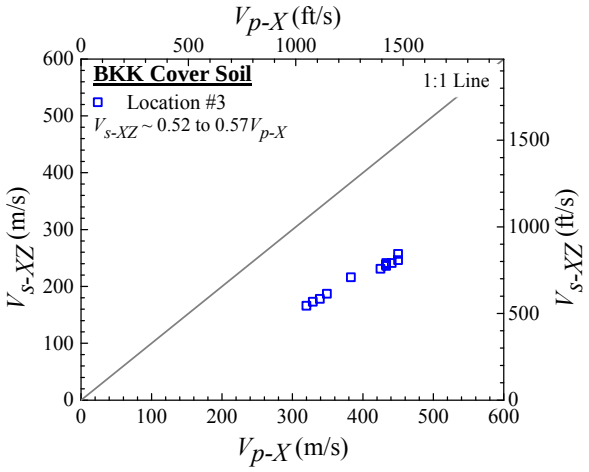

Figure 8.45 Comparison on $V_{p\text{-}X}$ and $V_{s\text{-}XZ}$ in soil cover testing location at the BKK.

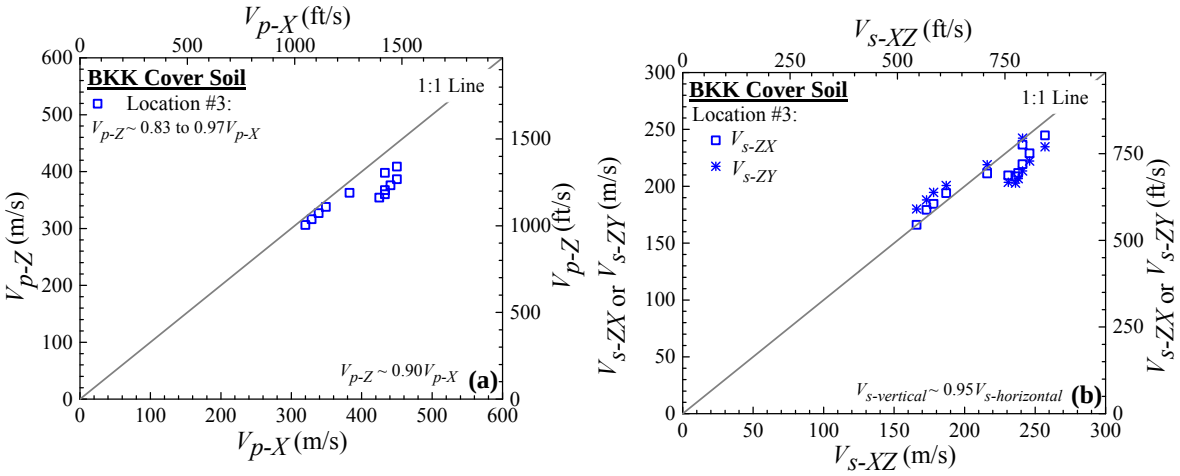

Figure 8.46 (a) Comparison on V_p propagating in the vertical and horizontal directions; and (b) V_s propagating in the vertical and horizontal directions in soil cover testing location at the BKK.

8.7 **Evaluation of Poisson's ratio at the BKK**

The V_p and V_s from small-strain downhole and crosshole seismic tests can be used to evaluate small-strain Poisson's ratio based on elasticity equation (Eq. 2.13). It should be noted that this equation was derived for homogeneous, isotropic, and elastic solid material. For anisotropic material, such as MSW, the meaning of Poisson's ratio can be very complex. Nevertheless, Eq. 2.13 was used to evaluate Poisson's ratio of MSW by Sharma et al. (1990), Houston et al. (1995), and Matasovic and Kavazanjian (1998). In this study, the V_p and V_s values from

downhole and crosshole seismic tests were used to evaluate "pseudo" Poisson's ratio. "Pseudo" Poisson's ratios v_{ZX} and v_{ZY} from downhole seismic testing were estimated using Eqs. 8.6 and 8.7 that have identic expression to Eq. 2.13.

$$\nu_{ZX} = \frac{0.5 \cdot \left(V_{s-ZX} / V_{p-Z}\right)^2 - 1}{\left(V_{s-ZX} / V_{p-Z}\right)^2 - 1} \tag{8.6}$$

$$\nu_{ZY} = \frac{0.5 \cdot \left(V_{s-ZY} / V_{p-Z}\right)^2 - 1}{\left(V_{s-ZY} / V_{p-Z}\right)^2 - 1} \tag{8.7}$$

The "pseudo" Poisson's ratio v_{XZ} was evaluated using crosshole seismic test results (Eq. 8.8).

$$\nu_{XZ} = \frac{0.5 \cdot \left(V_{s-XZ} / V_{p-X}\right)^2 - 1}{\left(V_{s-XZ} / V_{p-X}\right)^2 - 1} \tag{8.8}$$

8.7.1 Poisson's Ratio Profiles of Solid Waste in Locations 1 and 2 at the BKK

Poisson's ratio variation with depth of solid waste from downhole and crosshole seismic tests in location 1 at the BKK is presented in Figs. 8.47. In location 1, the v_{ZX} ranged from 0.24 to 0.28 at depth of 0.13 m. At depth of 0.33 m, the v_{ZX} and v_{ZY} ranged from 0.23 to 0.29 and from 0.26 to 0.30, respectively. At depth of 0.69 m, the v_{ZX} and v_{ZY} varied from 0.23 to 0.31 and 0.28 to 0.36, respectively. The v_{XZ} ranged from 0.29 to 0.34.

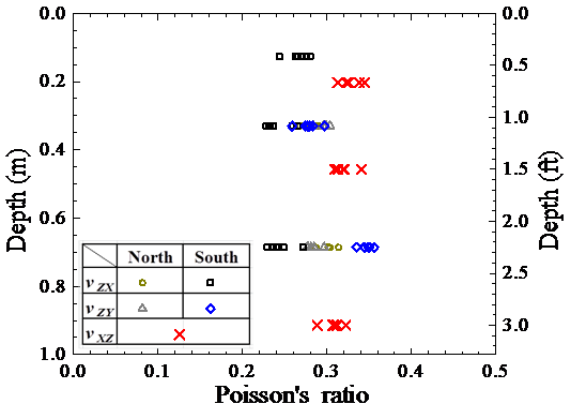

Figure 8.47 Small-strain Poisson's ratio of solid waste evaluated using V_s and V_p in location 1 at the BKK.

Poisson's ratio variation with depth from downhole and crosshole seismic tests in location 2 at the BKK is presented in Fig. 8.48. At depth of 0.33 m, the v_{ZX} and v_{ZY} varied from 0.31 to 0.38 and from 0.31 to 0.35, respectively. At depth of 0.69 m, the v_{ZX} and v_{ZY} ranged from 0.24 to 0.37 and 0.23 to 0.35, respectively. The v_{XZ} varied from 0.34 to 0.38.

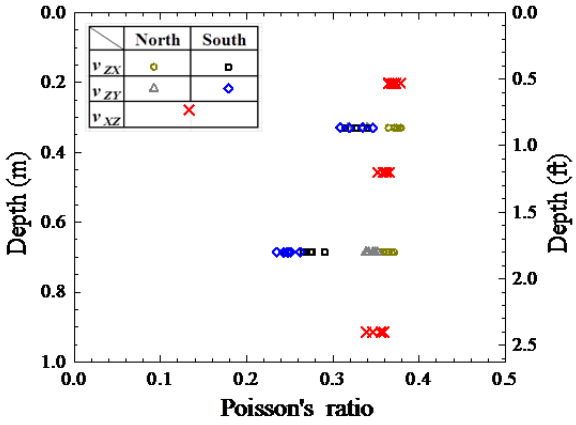

Figure 8.48 Small-strain Poisson's ratio of solid waste evaluated using V_s and V_p in location 2 at the BKK.

The v_{ZX} and v_{ZY} at the same measurement point in solid waste were in some cases the same and in other cases different. In general, scatter in Figs. 8.47 and 8.48 could be attributed to the variability of the waste within a test location as well as the anisotropic nature of the waste.

8.7.2 Poisson's Ratio Profiles of Soil Cover in Location 3 at the BKK

Figure 8.49 shows the Poisson's ratio variation with depth of soil cover from downhole and crosshole seismic tests in location 3 at the BKK. For soil cover, the v_{ZX} and v_{ZY} varied from 0.23 to 0.29 and 0.20 to 0.26 at depth of 0.13 m, respectively. At depth of 0.33 m, the v_{ZX} and v_{ZY} ranged from 0.20 to 0.29 and from 0.20 to 0.25, respectively. At depth of 0.69 m, the v_{ZX} and v_{ZY} ranged from 0.21 to 0.22 and 0.28 to 0.30, respectively. The v_{XZ} ranged from 0.26 to 0.32.

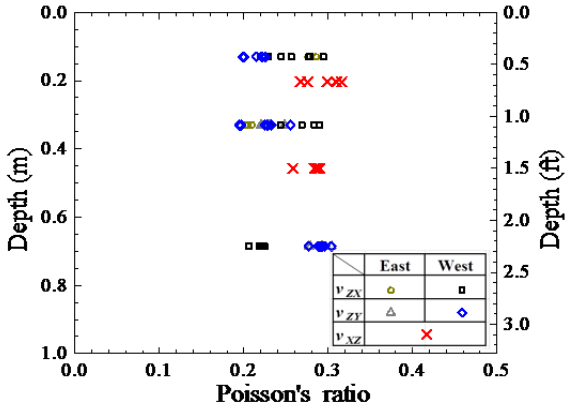

Figure 8.49 Small-strain Poisson's ratio of soil cover evaluated using V_s and V_p in location 3 at the BKK.

8.8 **Multichannel Analysis of Surface Wave and Microtremor Analysis Method Tests at the BKK**

A Combination of Multi-channel Analysis of Surface Wave (MASW) and Microtremor Analysis Method (MAM) tests was conducted in 14 locations at the BKK. In this manuscript, MASW and MAM test results from three testing locations as shown in Fig. 8.2 are presented. The results for all locations are presented in detail in Zekkos et al. (2012). In this thesis, the emphasis is given in three locations were nonlinear dynamic testing was executed. Figure 8.50 shows application of the surface wave testing at the BKK. In this investigation, sixteen 4.5 Hz geophones (Geospace GS 11-D) were used and were positioned with spacing of 0.91 m (3 ft) and 1.52 m (5 ft) in a

linear array. In the MASW or active method, data acquisition was performed by recording the ground roll generated using a 6.8-kg sledge hammer. In the MAM or passive test, data was acquired by recording background noise. The testing procedure used in the surface wave test is described in Chapter 3 in detail.

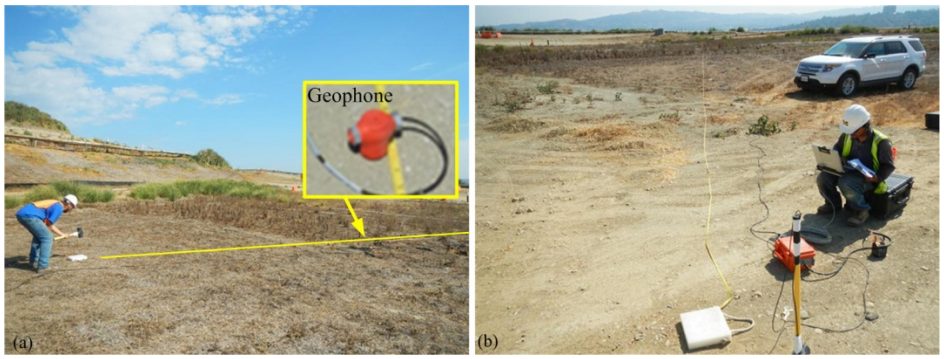

Figure 8.50 Surface wave testing at the BKK: (a) MASW and (b) MAM.

Figure 8.51 presents the theoretical and field combined dispersion curves from location 1 at the BKK. In this figure, raw dispersion curves from active and passive tests are also presented. Dispersion curve from location 1 had frequency content ranging from 3.8 Hz to 39 Hz that corresponded with Rayleigh wave or phase velocity (V_{ph}) of 300 m/s to 116 m/s. Figure 8.52 shows the corresponding V_s profiles in location 1 at the BKK. In general, near surface shear wave velocity was 156 m/s and increased to 340 m/s at depth of 27 m. Figure 8.51 also shows the shear wave velocities measured from downhole and crosshole seismic tests. Shear wave velocity profile from surface wave testing was in between shear wave velocities from downhole and crosshole seismic tests. It should be noted that downhole and crosshole seismic tests are more localized measurements than surface wave testing. Different results between those tests may occur, particularly in solid waste where waste variability could be high within a small area and at the scale and frequency range of the various methods. In location 1, the highest frequency in the dispersion curve corresponded with the shortest wavelength (λ) of 3 m. By assuming a

wavelength to depth of investigation conversion factor of 0.5 (Ballard 1964), the shallowest reliable depth of investigation was about 1.5 m. This resulted in uncertainty in the shear wave velocity for the top 1.5 m from the surface wave testing. Downhole and crosshole seismic tests were better to capture the localized shear wave velocity variability at depth shallower than 1.5 m.

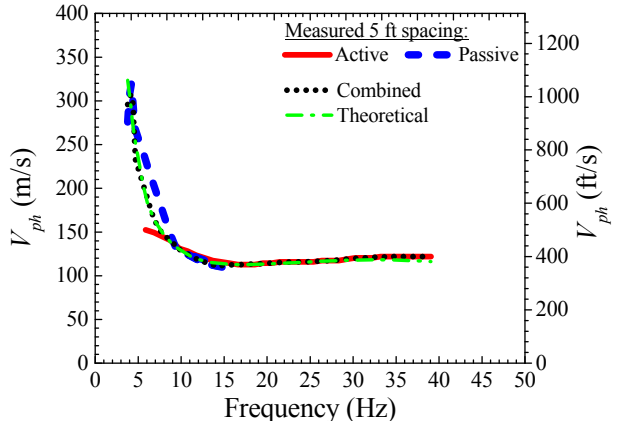

Figure 8.51 Dispersion curves from location 1 at the BKK.

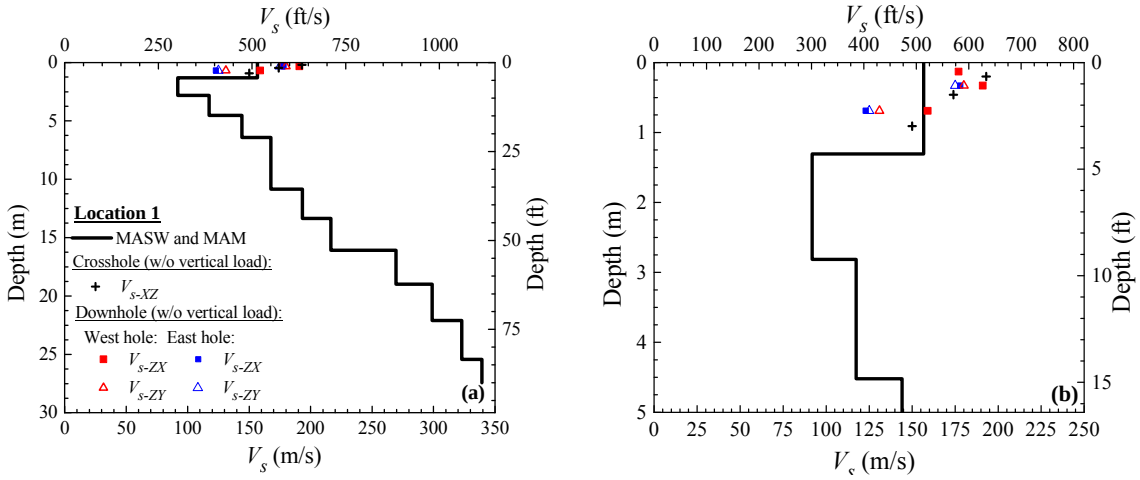

Figure 8.52 V_s profile in location 1 at the BKK: (a) up to 30 m and (b) up to 5 m.

The theoretical and field combined dispersion curves from location 2 at the BKK are presented in Figs. 8.53. Frequency content of this dispersion curve ranged from 3.5 Hz to 49 Hz that corresponded with V_{ph} of 179 m/s to 151 m/s. The V_s profiles in location 2 at the BKK are presented in Fig. 8.54. The shear wave velocity profiles varied from 165 m/s to 184 m/s from the

surface to depth of 17 m. The shear wave velocities from downhole and crosshole seismic testing are also presented in Fig. 8.54. In general, the shear wave velocities from downhole and crosshole seismic tests were relatively higher than those of surface wave testing. The highest frequency in the dispersion curve corresponded with the shortest λ of 3.1 m. Thus, the shallowest reliable depth of investigation from the surface wave testing was about 1.5 m. Downhole and crosshole seismic tests were better to identify the localized shear wave velocity variability at depth shallower than 1.5 m.

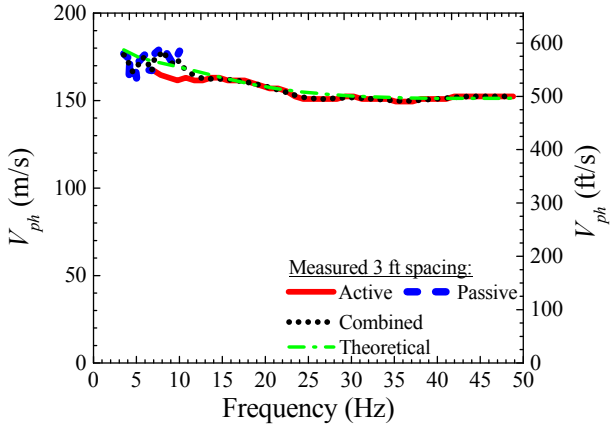

Figure 8.53 Dispersion curves from location 2 at the BKK.

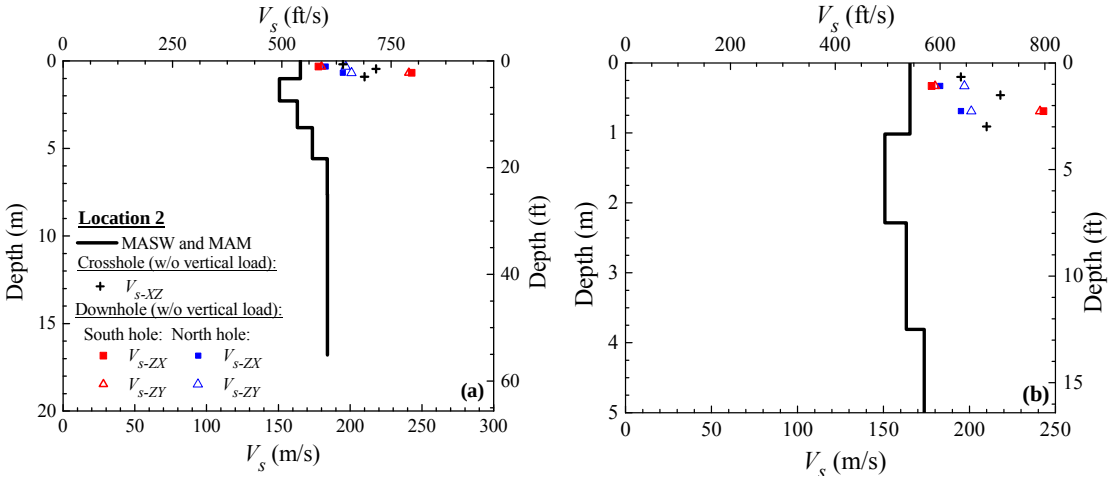

Figure 8.54 V_s profile in location 2 at the BKK: (a) up to 20 m and (b) up to 5 m.

Figure 8.55 presents the theoretical and field combined dispersion curves in location 3 at the BKK. Raw dispersion curve from active and passive tests are also shown in this figure. Dispersion curve from location 3 had frequency content ranging from 5 Hz to 15 Hz that corresponded with Rayleigh wave or phase velocity (V_{ph}) of 262 m/s to 161 m/s. Figure 8.56 shows the V_s profiles in location 3 at the BKK. In general, near surface shear wave velocity was 136 m/s and increased to 274 m/s at depth of 18 m. Generally, the shear wave velocities from downhole and crosshole seismic tests were relatively higher than those of surface wave testing test. In location 3, the highest frequency in the dispersion curve corresponded with the shortest λ of approximately 10 m. By assuming a wavelength to depth of investigation conversion factor of 0.5 (Ballard 1964), the reliable shallowest depth of investigation was about 5 m. This resulted in uncertainty in the shear wave velocity for the top 5 m from the surface wave testing.

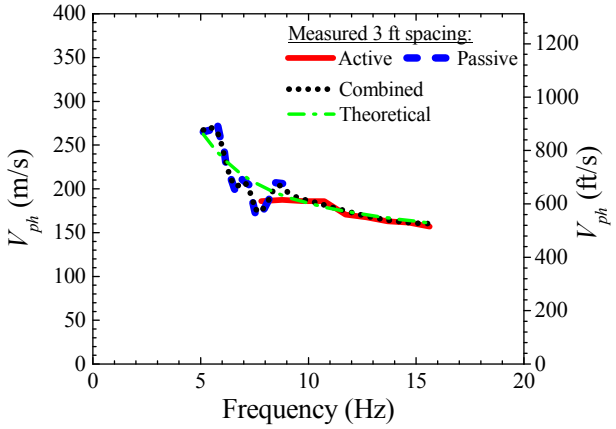

Figure 8.55 Dispersion curves from location 3 at the BKK.

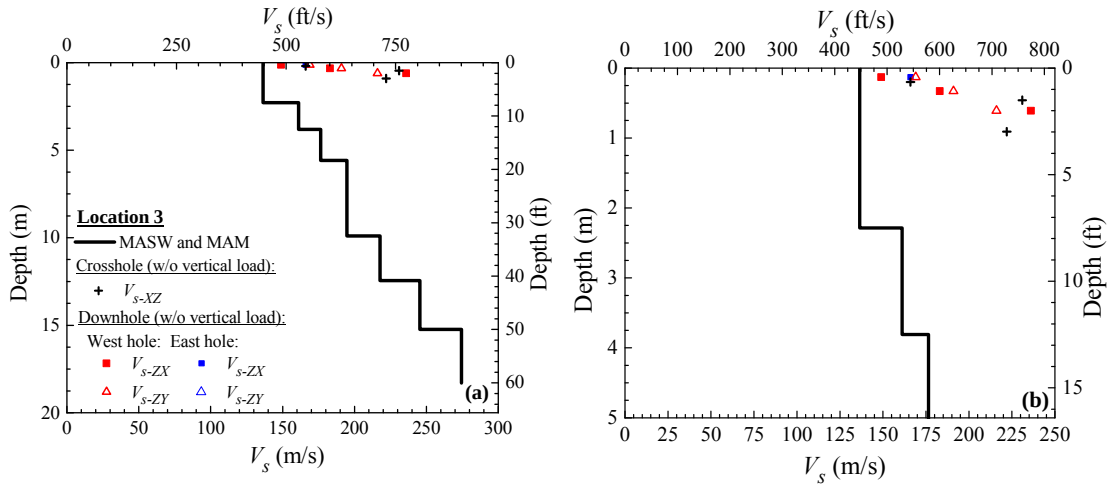

Figure 8.56 Surface wave testing result in location 3 at the BKK: (a) up to 20 m and (b) up to 5 m.

Figure 8.57 presents the statistical analysis results of 14 V_s profiles from surface wave testing at the BKK. On average, V_s value was about 188 m/s at the surface and increased up to 373 m/s at depth of 40 m. Coefficient of variance (COV) ranged from 0.11 to 0.25 with an average of 0.18.

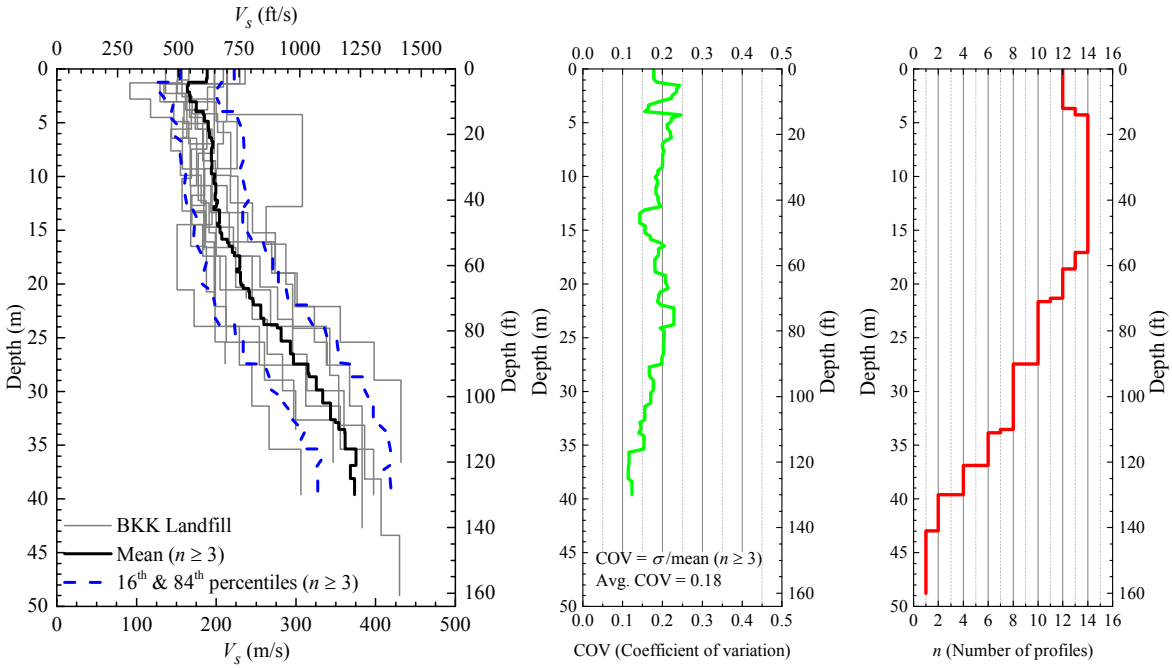

Figure 8.57 Statistical analysis of 14 V_s profiles from surface wave testing at the BKK.

8.9 **Steady-state Dynamic Testing**

Steady-state dynamic test using Thumper and T-Rex was conducted to study the relationship between shear modulus or normalized shear modulus and shearing strain at the BKK (Fig. 8.58). This test was performed at different static vertical load levels to study the effect of confining stress on the shear modulus and normalized shear modulus reduction curves. In each test location at the BKK, Thumper or T-Rex was used to impose static vertical loads of 18 kN, 36 kN, 71 kN, and 133 kN as illustrated in Fig. 8.10. Thumper was used for steady-state test with static vertical load up to 36 kN. At each vertical static load level, dynamic horizontal loads were applied from small to large amplitude. Chapter 4 describes the testing method of the steady-state dynamic testing as well as the limitations and uncertainties of this method. In this section, the results are presented.

Figure 8.58 Steady-state dynamic testing using (a) Thumper and (b) T-Rex at the BKK.

Figure 8.59 shows the quadrilateral elements for location 1 at the BKK. Elements A, D, and F were defined by four adjacent geophones. Element A was defined by the four sensors closest to the surface, element D was defined by the four intermediate sensors, and element F was defined by the four deepest sensors. Element C was defined by the two deepest and the two shallowest geophones. Figures 8.60 and 8.61 present the quadrilateral elements for locations 2

and 3 at the BKK, respectively. As mentioned earlier, sensor G9 in X axis in location 3 was damaged. Thus, in location 3, elements C and F that included sensor G9 were not analyzed.

Shear modulus was calculated using the shear wave velocity and mass density of solid waste or soil cover. Vertically propagating shear wave velocity was calculated using the phase difference in travel time as shown in Fig. 8.62(a). Mass density was obtained from in-situ unit weight measurements. The average of the shear modulus calculated from both arrays was used as the shear modulus of each element. It should be noted that the mass density may affect the accuracy in shear modulus calculation, but, does not affect the normalized shear modulus reduction curve. The 4-node displacement based method (Rathje et al. 2005) was used to calculate the shearing strain at the center of quadrilateral elements. Example of shearing strain time history calculated using the 4-node method is shown in Fig. 8.62(b). The analysis method to reduce data from the steady-state test is described in detail in Chapter 4. The results of normalized shear modulus reduction curves from this site were used to develop recommended G/G_{max} curves in Chapter 9.

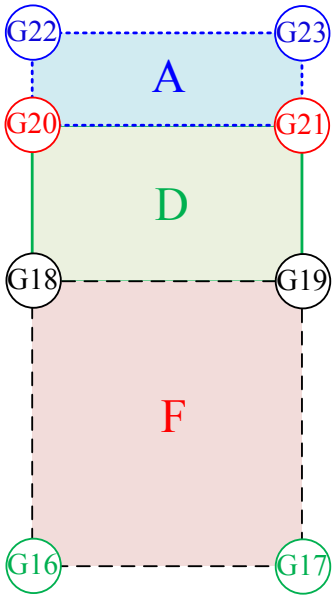

Element	Geophones/Nodes
A	G20, G21, G23, G22
D	G18, G19, G21, G20
F	G16, G17, G19, G18
C = A+D+F	G16, G17, G23, G22

Figure 8.59 Quadrilateral elements in location 1 at the BKK.

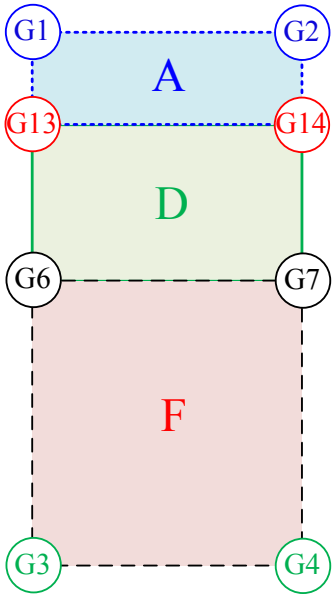

Element	Geophones/Nodes
A	G14, G13, G1, G2
D	G7, G6, G13, G14
F	G4, G3, G6, G7
C = A+D+F	G4, G3, G1, G2

Figure 8.60 Quadrilateral elements in location 2 at the BKK.

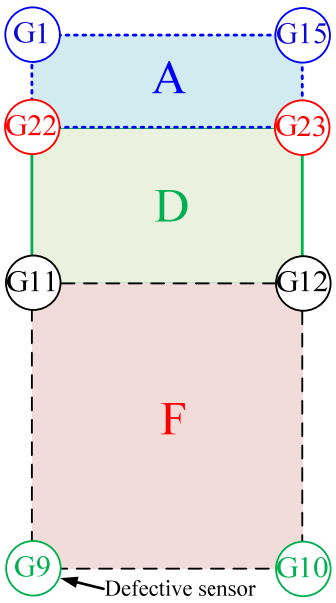

Element	Geophones/Nodes
A	G23, G22, G1, G15
D	G12, G11, G22, G23
F	G10, G9, G11, G12
C = A+D+F	G10, G9, G1, G15

Figure 8.61 Quadrilateral elements in location 3 at the BKK.

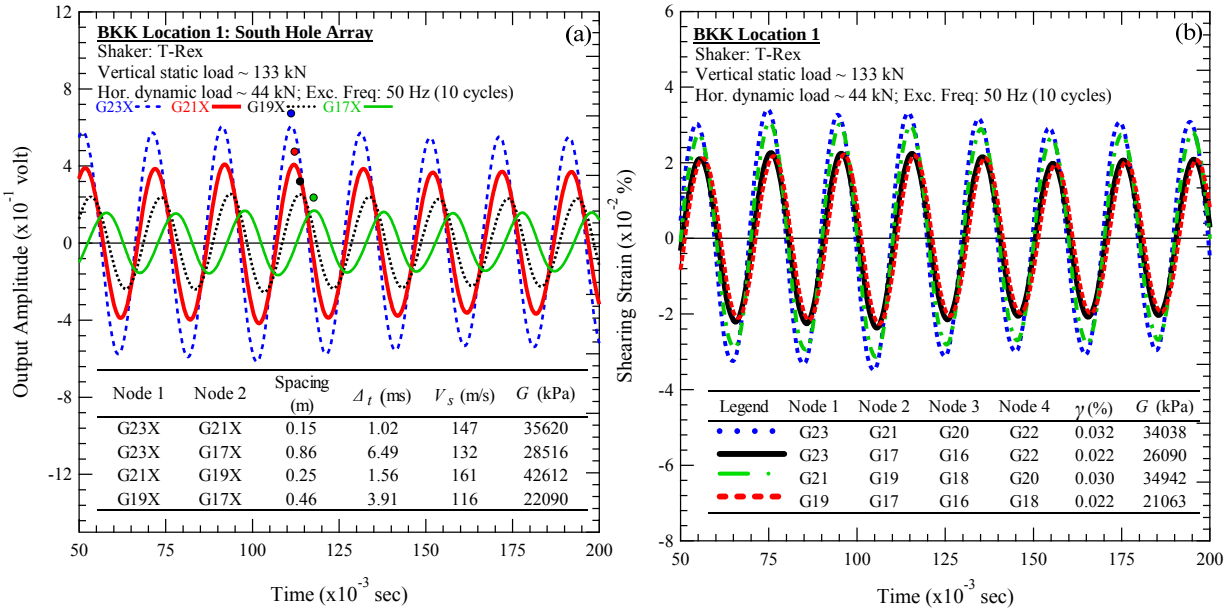

Figure 8.62 Examples of steady-state dynamic testing: (a) shear modulus calculation and (b) shearing strain time history at the BKK.

8.10 Shear Modulus and Normalized Shear Modulus Reduction Curves of Solid Waste in Location 1 at the BKK

The effect of confining stress on the shear modulus and the normalized shear modulus as a function of shearing strain could be evaluated by examining the same element at different confining stress. Examining the same element isolates the effect of waste composition when investigating the effect of confining stress. Then, by examining different elements at the same confining stress, the effect of waste composition can be investigated. It should be noted that data from steady-state dynamic test using vertical static load of 71 kN in location 1 at the BKK was not included in this manuscript due to relatively poor waveforms observed.

8.10.1 Effect of Confining Stress on Shear Modulus and Normalized Shear Modulus Reduction Curves in Location 1 at the BKK

The shear modulus and normalized shear modulus reduction curves for element A in location 1 are presented in Figs. 8.63(a) and 8.63(b), respectively. The center of this element was located at an effective depth of 0.13 m below the footing. The shear modulus was evaluated for shearing strain ranging from 0.0025% up to 0.15%. It should be noted that Element A was the shallowest element and exhibited the largest shearing strain. The effect of confining stress on the shear modulus curve is shown in Fig. 8.63(a). The small-strain shear modulus (G_{max}) increased from 24 MPa to 36 MPa, as mean confining stress increased from 22 kPa to 137 kPa. The normalized shear modulus reduction curves for element A are shown in Fig. 8.63(b). The $G/G_{\max}$ curves systematically moved to the right and exhibited a more linear response with increasing confining stress. These trends in the shear modulus and the normalized shear modulus reduction curves are consistent with laboratory studies on municipal solid waste (MSW) (Lee 2007, Zekkos et al. 2008, and Yuan et al. 2011) as well as on soils (e.g., Darendeli 2001).

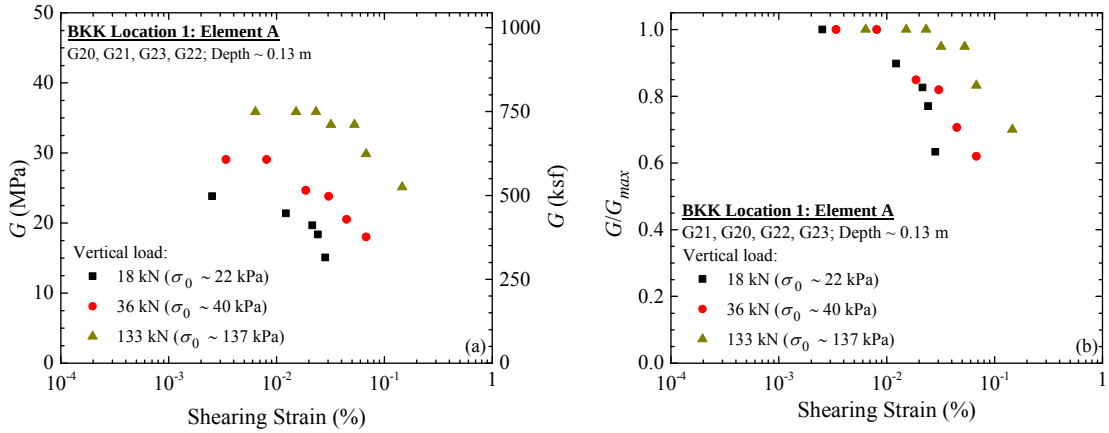

Figure 8.63 (a) Shear modulus and (b) normalized shear modulus reduction curves of element A in location 1 at the BKK.

Figures 8.64(a) and 8.64(b) presents the G-log γ and G/G_{max}-log γ relationship at different confining stresses for element D in location 1. The center of element D was located at an effective depth of 0.33 m below the footing. The steady-state dynamic test for element D was performed over shearing strain ranging from 0.0016% to 0.12%. It should be noted that reliable estimate of G_{max} for mean stress of 80 kPa was not obtained. The normalized shear modulus reduction curve for this mean stress was not included in Fig. 8.64(b).

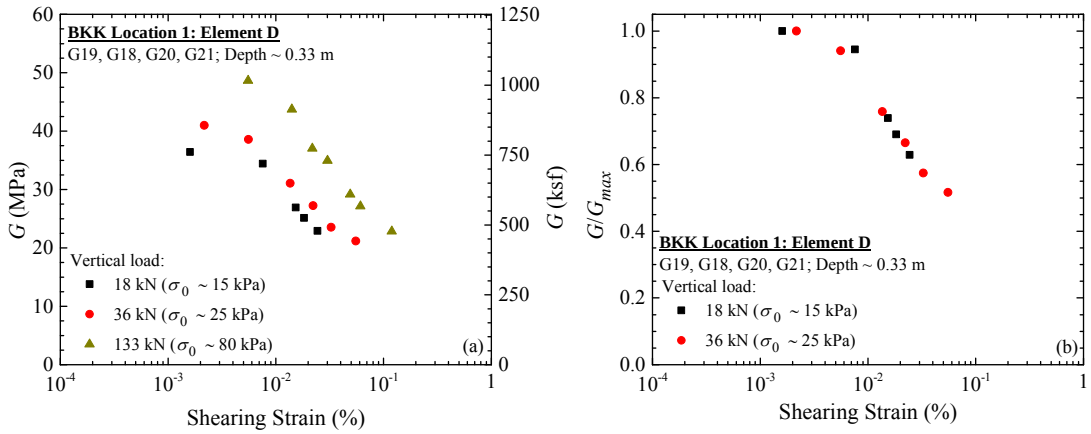

Figure 8.64 (a) Shear modulus and (b) normalized shear modulus reduction curves of element D in location 1 at the BKK.

The variation of shear modulus with shearing strain at different confining stresses for element F in location 1 is presented in Fig. 8.65(a). The center of element F was located at an effective depth of 0.69 m below the footing. As illustrated in Fig. 8.65(a), the shear modulus was successfully obtained from the field measurements over the strain range from 0.0005% to 0.087%. As shown in this figure, the small-strain shear modulus increased with increasing confining stress. The G_{max} increased from 19 MPa to 24 MPa, as mean confining stress increased from 12 kPa to 38 kPa. Figure 8.65(b) presents the normalized shear modulus reduction curves for element F. The normalized shear modulus became more linear with increasing confining stresses from 12 kPa to 38 kPa.

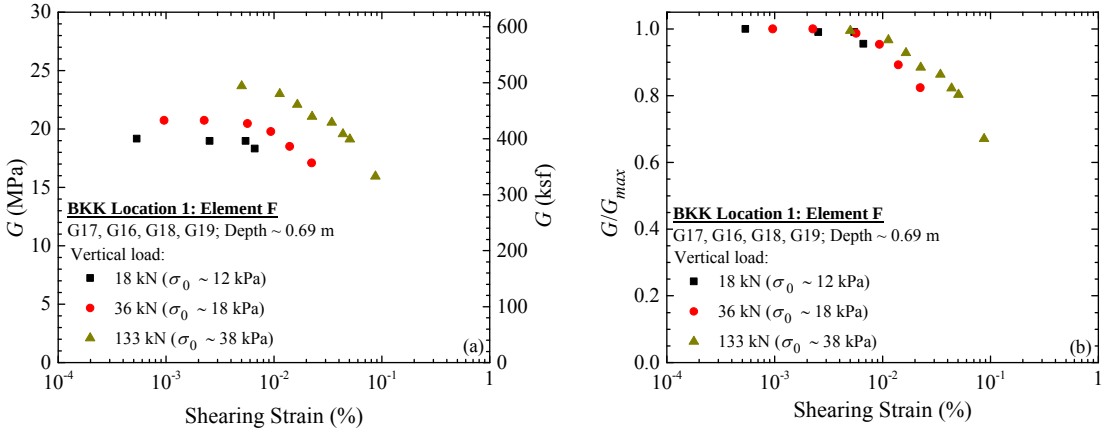

Figure 8.65 (a) Shear modulus and (b) normalized shear modulus reduction curves of element F in location 1 at the BKK.

The shear modulus and normalized shear modulus reduction curves for element C in location 1 are presented in Figs. 8.66(a) and 8.66(b), respectively. This element provided an average response of the other elements as it was defined by the shallowest and the deepest geophones. The center of this element was located at an effective depth of 0.48 m below the footing. The shear modulus was evaluated for shearing strain ranging from 0.0001% up to 0.091%. It should be noted that reliable estimate of G_{max} for mean stress of 54 kPa was not

clearly observed. The G/G_{max} value for this mean stress at shearing strain of $5x10^{-3}$ % was assumed on the basis of data series for mean stresses of 13 kPa and 19 kPa. As illustrated in Fig. 8.66(a), the small-strain shear modulus increased with confining stress. The G_{max} increased from 24 MPa to 31 MPa, as mean confining stress increased from 13 kPa to 54 kPa. The normalized shear modulus reduction curves for this element are presented in Fig. 8.66(b). With increasing confining stress, the normalized shear modulus became more linear.

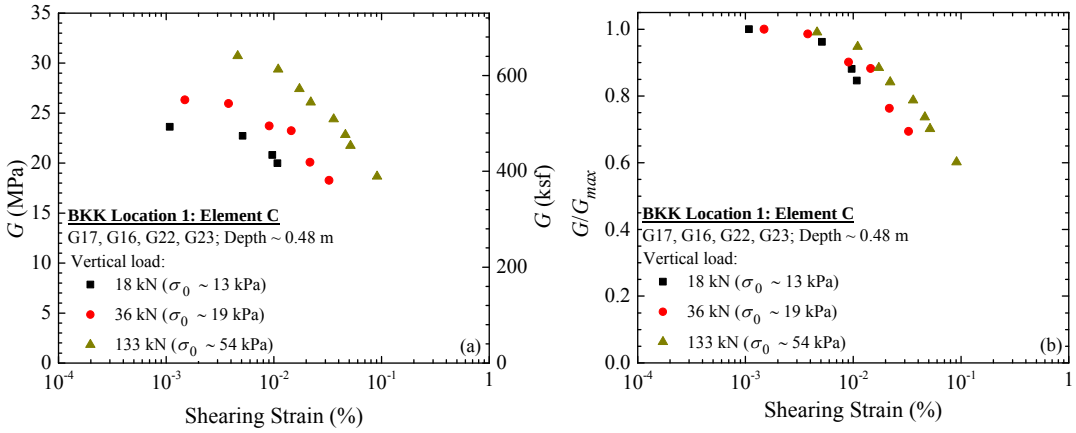

Figure 8.66 (a) Shear modulus and (b) normalized shear modulus reduction curves of element C in location 1 at the BKK.

8.10.2 Effect of Waste Composition on Shear Modulus and Normalized Shear Modulus Reduction Curves in Location 1 at the BKK

The effect of waste composition on the shear modulus and the normalized shear modulus reduction as a function of shearing strain could be evaluated using results from different sets of geophones that form elements. Figure 8.67 shows the effect of waste composition on the shear modulus and the normalized shear modulus curves from elements at nearly the same calculated confining stress that varied from 12 kPa to 22 kPa. As shown in Fig. 8.59, elements A, C, D and F were representatives of waste at different depths. It should be noted that element C represented the average of the other three elements. Figure 8.67(a) shows differences in shear modulus that

are attributed to waste variability. At this stress level, the small-strain shear modulus ranged from 19 MPa to 36 MPa. The corresponding normalized shear modulus reduction curves are shown in Fig. 8.67(b).

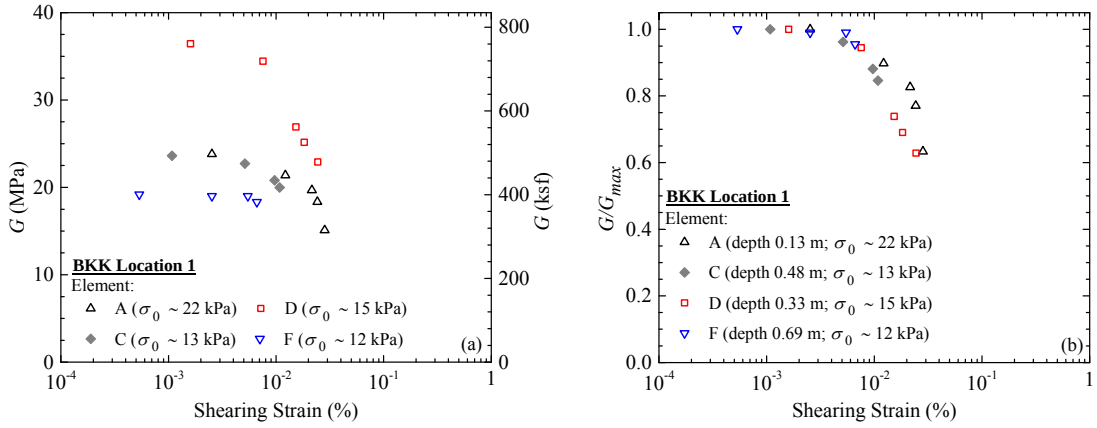

Figure 8.67 Waste composition effect on (a) shear modulus and (b) normalized shear modulus reduction curves in location 1 at the BKK.

8.11 **Shear Modulus and Normalized Shear Modulus Reduction Curves of Solid Waste in Location 2 at the BKK**

8.11.1 Effect of Confining Stress on Shear Modulus and Normalized Shear Modulus Reduction Curves in Location 2 at the BKK

The variation of shear modulus and normalized shear modulus with shearing strain at different confining stresses for element A in location 2 is presented in Figs. 8.68(a) and 8.68(b), respectively. The center of this element was located at an effective depth of 0.13 m below the footing. The shear modulus was evaluated for shearing strain ranging from 0.001% up to 0.19%. Element A was the shallowest element and exhibited the largest shearing strain. As shown in Fig. 8.68(a), the G_{max} increased from 26 MPa to 36 MPa, as mean confining stress increased from 22 kPa to 132 kPa. Note that reliable estimate of G_{max} was not obtained for mean stress of 72 kPa. The G/G_{max} at shearing strain of 9×10^{-3} % for mean stress of 72 kPa was assumed on the basis of

available data series for the other mean stresses. As shown in Fig. 8.68(b), the G/G_{max} curves moved to the right and exhibited a more linear response with increasing confining stress.

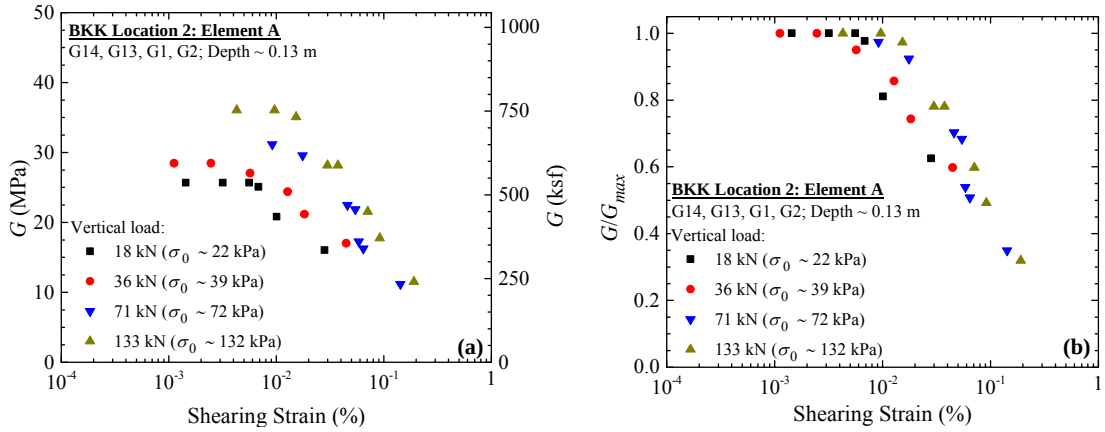

Figure 8.68 (a) Shear modulus and (b) normalized shear modulus reduction curves of element A in location 2 at the BKK.

The variation of shear modulus and normalized shear modulus with shearing strain at different confining stresses for element D in location 2 is presented in Figs. 8.69(a) and 8.69(b), respectively. The center of element D was located at an effective depth of 0.33 m below the footing. The shear modulus curves were successfully obtained from the field measurements over the shearing strain ranging from 0.0006% to 0.13% as presented in Fig. 8.69(a). In this figure, the small-strain shear modulus increased from 28 MPa to 40 MPa, as mean confining stress increased from 15 kPa to 79 kPa. Note that reliable estimate of G_{max} for mean stress of 45 kPa was not obtained. The G/G_{max} at shearing strain of $6\text{x}10^{-3}$ % for mean stress of 45 kPa was assumed on the basis of available data series in G-log γ and G/G_{max}-log γ curves for the other mean stresses. The normalized shear modulus reduction curves for element D are presented in Fig. 8.69(b). The normalized shear modulus reduction curves became more linear with confining stress increase from 15 kPa to 79 kPa.

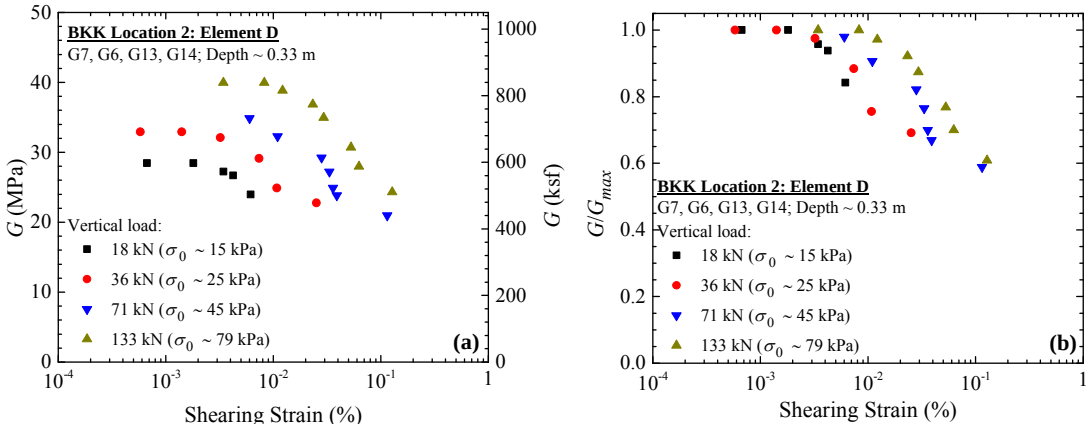

Figure 8.69 (a) Shear modulus and (b) normalized shear modulus reduction curves of element D in location 2 at the BKK.

The G-log γ and G/G_{max}-log γ relationships at different confining stresses for element F in location 2 are presented in Figs. 8.70(a) and 8.70(b), respectively. The center of element F was located at an effective depth of 0.69 m below the footing. The steady-state dynamic test for element F was performed over shearing strain ranging from 0.0003% to 0.03%. The small-strain shear modulus increased from 48 MPa to 59 MPa as mean confining stress increased from 12 kPa to 36 kPa [Fig. 8.70(a)]. Note that reliable estimate of G_{max} for mean stress of 23 kPa was not obtained. The G/G_{max} at shearing strain of $3\text{x}10^{-3}$ % for mean stress of 45 kPa was assumed on the basis of available data series for the other mean stresses. The normalized shear modulus reduction curves became more linear with increasing confining stress.

Figures 8.71(a) and 8.71(b) present the shear modulus and normalized shear modulus reduction curves for element C in location 2, respectively. Element C provided an average response of the tested waste mass as it was defined by the shallowest and the deepest geophones. The center of this element was located at an effective depth of 0.48 m below the footing. This element experienced shearing strain ranging from 0.0005% to 0.05% during steady-state dynamic tests. The G_{max} increased from 34 MPa to 45 MPa, as mean confining stress increased from 13 kPa to 52 kPa [Fig. 8.71(a)]. Note that reliable estimate of G_{max} for mean stress of 31

kPa was not obtained. The G/G_{max} at shearing strain of $5x10^{-3}$ % for mean stress of 31 kPa was assumed on the basis of available data series for the other mean stresses. As shown in Fig. 8.71(b), the normalized shear modulus reduction curves became more linear with increasing confining stress.

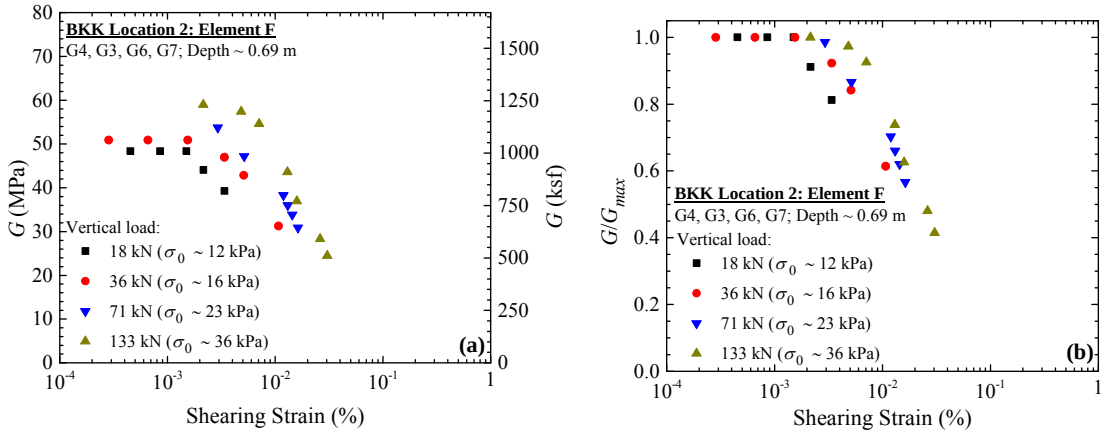

Figure 8.70 (a) Shear modulus and (b) normalized shear modulus curves of element F in location 2 at the BKK.

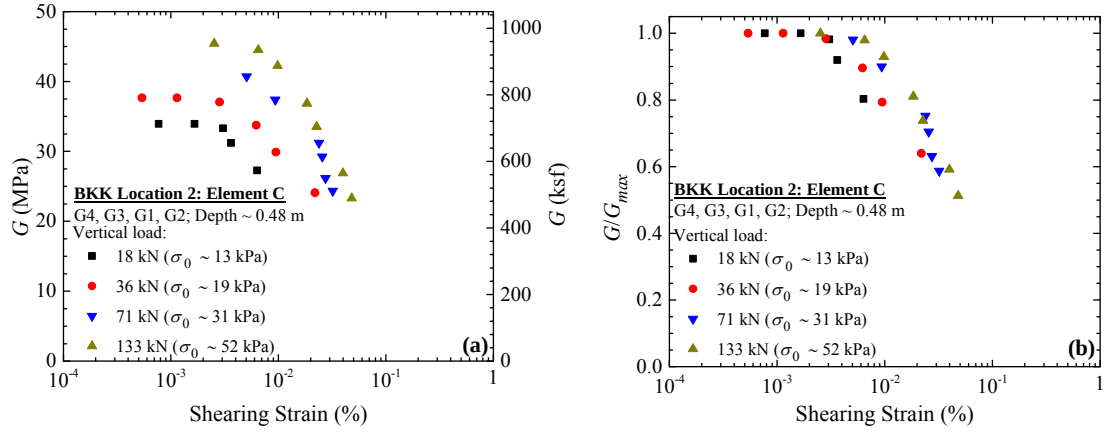

Figure 8.71 (a) Shear modulus and (b) normalized shear modulus reduction curves of element C in location 2 at the BKK.

8.11.2 Effect of Waste Composition on Shear Modulus and Normalized Shear Modulus Reduction Curves in Location 2 at the BKK

The effect of waste composition on G-log γ and G/G_{max}-log γ curves from location 2 at the BKK is presented in Figs. 8.72(a) and 8.72(b). All elements in these figures were at nearly the same calculated confining stress ranging from 12 kPa to 22 kPa. It can be observed that shear modulus from these elements ranging from 26 MPa to 48 MPa [Fig. 8.72(a)]. In this case, element F showed the highest shear modulus and the most nonlinearity in the G-log γ curve. The differences in shear modulus and the degree of nonlinearity could be attributed to the differences in waste composition in each element. The impact of waste composition on the relationship between G/G_{max} and shearing strain is demonstrated in Fig. 8.72(b).

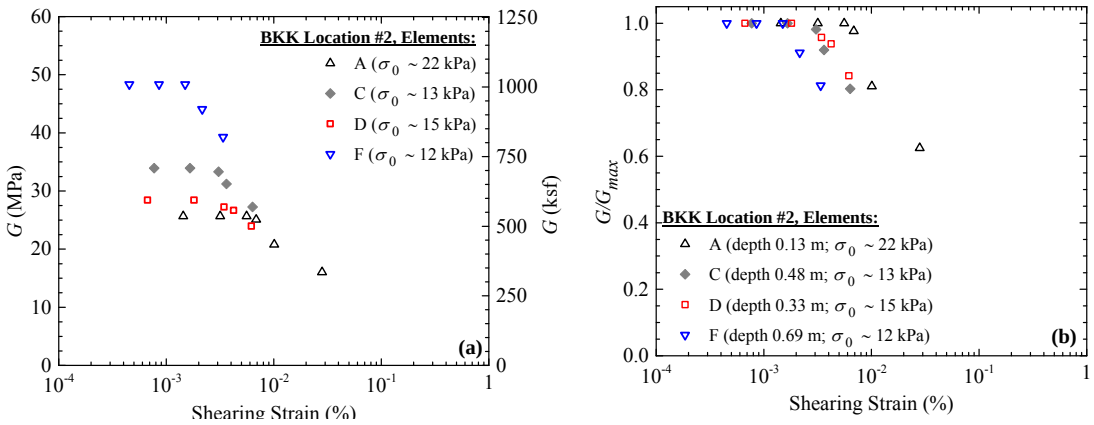

Figure 8.72 Waste composition effect on (a) shear modulus and (b) normalized shear modulus reduction curves in location 2 at the BKK.

8.12 **Shear Modulus and Normalized Shear Modulus Reduction Curves of Soil Cover in Location 3 at the BKK**

The shear modulus and normalized shear modulus reduction curves of soil cover for element A in location 3 are presented in Figs. 8.73(a) and 8.73(b). The center of this element was located at

an effective depth of 0.13 m below the footing. The shear modulus was evaluated for shearing strain ranging from 0.0006% up to 0.09%. Element A was the shallowest element and exhibited the largest shearing strain. As shown in Fig. 8.73(a), shear modulus increased with confining stress. It should be noted that reliable estimate of G_{max} for mean stresses of 72 kPa and 131 kPa were not obtained. The normalized shear modulus reduction curves for mean stresses of 72 kPa and 131 kPa were not included in Fig. 8.73(b).

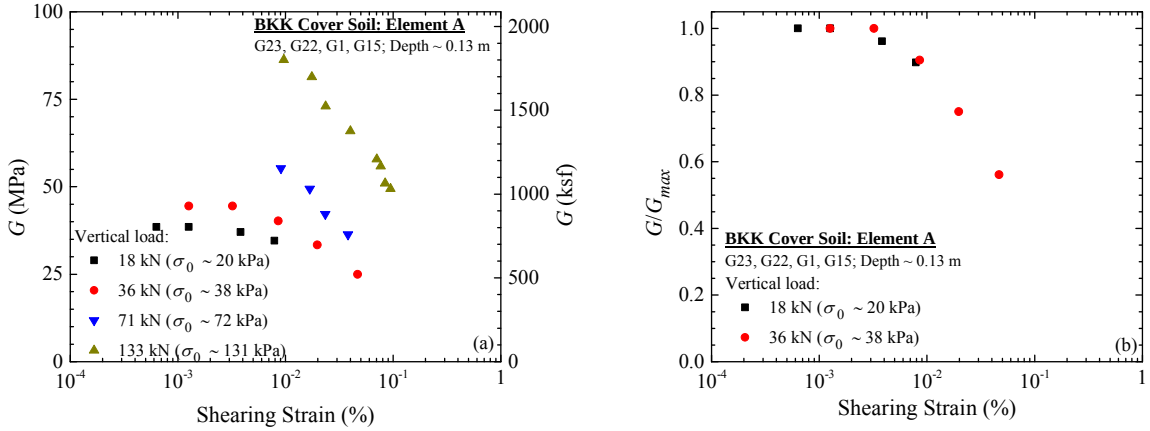

Figure 8.73 (a) Shear modulus and (b) normalized shear modulus reduction curves of element A in location 3 at the BKK.

Figures 8.74(a) and 8.74(b) present the G-log γ and G/G_{max}-log γ relationships at different confining stresses for element D in location 3, respectively. The center of element D was located at an effective depth of 0.33 m below the footing. The nonlinear behavior of element D is shown in Fig. 8.74(a). This element experienced shearing strain ranging from 0.0006% to 0.06% during the steady-state dynamic test. Figure 8.74(b) shows that small-strain shear modulus increased with confining stress. As shown in Fig. 8.74(b), the normalized shear modulus became more linear with increasing confining stresses from 15 kPa to 77 kPa.

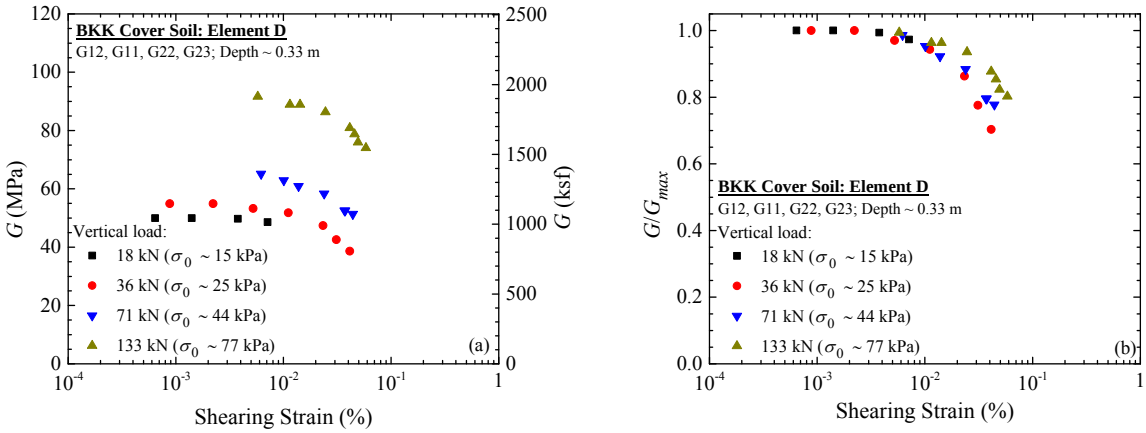

Figure 8.74 (a) Shear modulus and (b) normalized shear modulus curves of element D in location 3 at the BKK.

8.13 **Comparison of Normalized Shear Modulus Reduction Curves**

In this section, the variation of normalized shear modulus reduction curves as a function of shearing strain from two solid waste test locations at the BKK was compared. In addition, the field G/G_{max} data from the BKK was also compared with curves proposed by other studies in the literature. In this case, the comparison was made with results from laboratory testing and recorded ground motion back-calculation analysis.

The steady-state dynamic test results from two solid waste test locations at the BKK are presented in Fig. 8.75. Dataset from locations 1 and 2 are shown as black squares and red circles, respectively. In location 1, normalized shear modulus reduction curve was evaluated for shearing strains ranging from 0.0005% to 0.15%. In location 2, normalized shear modulus reduction curve was evaluated for shearing strains ranging from 0.0003% to 0.19%. In general, the normalized shear modulus reduction curves were consistent. Nevertheless, normalized shear modulus reduction at low mean confining stress in location 2 appeared to be slightly more nonlinear than that of location 1. At high confining stress, some data series from location 1 were more linear than that of location 2. The variation of normalized shear modulus reduction curves as a function

of shearing strain was likely attributed to variability in waste composition between the two locations as well as differences in confining stresses between quadrilateral elements.

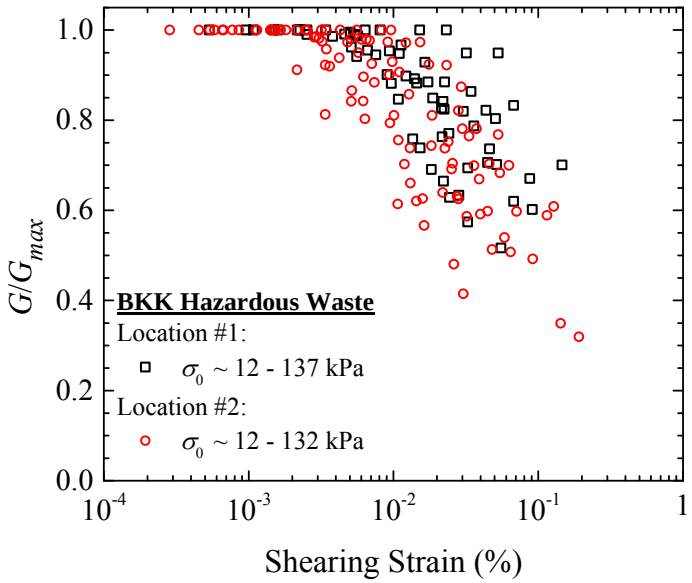

Figure 8.75 The normalized shear modulus reduction curves solid waste from testing locations 1 and 2 at the BKK.

Figure 8.76 shows the comparison between the field G/G_{max} data from the BKK and Zekkos et al. (2008) curves for mean stress < 125 kPa that were largely developed on the basis of testing at mean stress of 75 kPa. In general, the field G/G_{max} data from the BKK was generally more nonlinear than the recommended curves from Zekkos et al. (2008) and closer to the recommendation for 100% < 20 mm. It should be noted that Zekkos et al. (2008) curves was developed based on laboratory testing of MSW specimens.

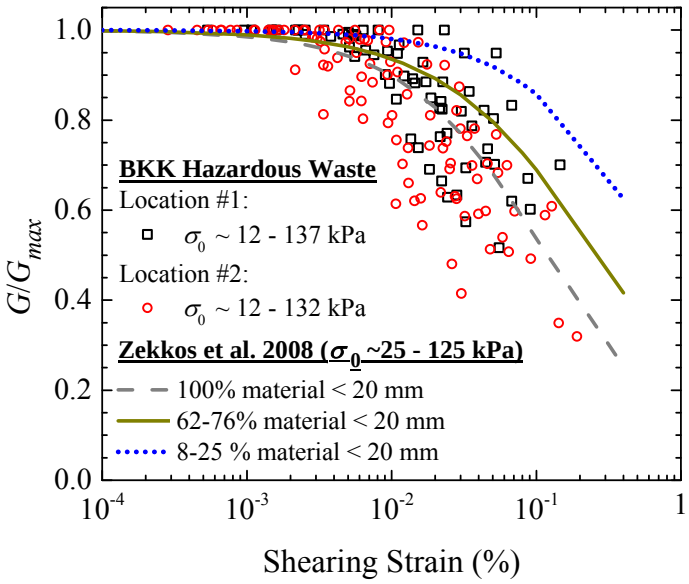

Figure 8.76 Comparison of the normalized shear modulus reduction curves with Zekkos et al. (2008) recommended curves.

Figure 8.77 presents the comparison between the normalized shear modulus reduction curves measured in situ at the BKK with curves proposed by other researchers. The normalized shear modulus reduction curves proposed by Idriss et al. (1995), Matasovic and Kavazanjian (1998), and Augello et al. (1998) were derived from back-calculation analyses using recorded ground motions at the surface of the OII landfill, California. In addition, Matasovic and Kavazanjian (1998) also performed cyclic simple shear testing to extend their curves to larger strain. Singh and Murphy (1990) proposed a curve that was developed using the shear modulus reduction curve of peat and clay. Singh and Murphy curve showed more significant shear modulus reduction below shearing strain of 0.001 % than the field G/G_{max} data from the BKK. Idriss et al. curve exhibited a relatively more nonlinear shear modulus reduction than the field G/G_{max} data from the BKK. Overall, the field G/G_{max} data from the BKK does not agree with Sing and Murphy and Idriss et al. curves. Augello et al. curve was generally more consistent with

the field G/G_{max} data. The recommended Matasovic and Kavanzanjian curve provided an approximate upper bound curve for the field G/G_{max} data from the BKK.

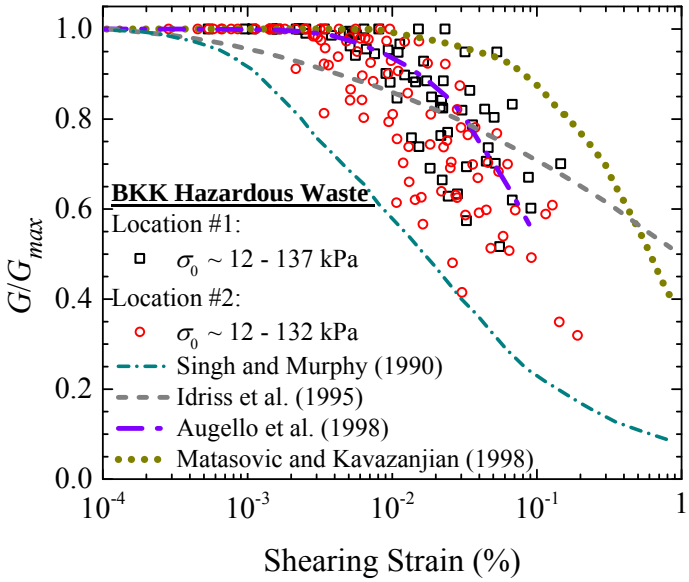

Figure 8.77 Comparison of the normalized shear modulus reduction curves with curves from other studies in the literature.

Figure 8.78 presents the comparison between the field G/G_{max} data of soil cover in location 3 at the BKK with curves recommended by Vucetic and Dobry (1991) for PI of 30% and 50%. As mentioned earlier, soil cover in location 3 had a PI of 43%. Some field G/G_{max} data series were beyond the bound defined by curves for PI of 30% and 50% as recommended by Vucetic and Dobry. It should be noted that the G/G_{max} curve is affected by many factors, including confining stress, and cannot be described only by the PI of soil.

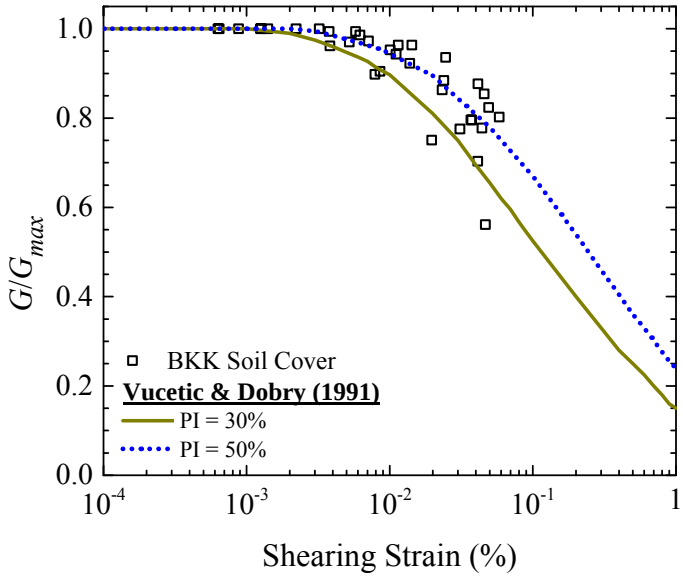

Figure 8.78 Comparison of the normalized shear modulus reduction curves of soil cover at the BKK with Vucetic and Dobry (1991) recommended curves.

8.14 **Summary**

A field investigation program was performed in three locations at the BKK hazardous landfill, West Covina, California, to investigate the dynamic properties of solid waste and soil cover in the linear and nonlinear strain range. Crosshole and downhole seismic tests were conducted to evaluate wave propagation velocities in solid waste and soil cover. Steady-state dynamic testing over a wide shear strain range was conducted at four different static vertical loads applied using Thumper and T-Rex. Two arrays of 3-D geophone sensors were embedded in the waste mass or soil cover and were used to capture the material response during dynamic testing. A combined MASW and MAM tests were also performed at the BKK to measure the shear wave velocity profile in 14 test locations. Additionally, load-settlement measurements were carried out. Pit excavation was performed at solid waste test locations to measure the in-situ unit weight, visually assess waste composition, and collect samples for waste characterization and laboratory testing. The results from small-strain testing were the wave propagation velocity profile and

wave propagation velocity-stress relationship. The study also generated in-situ data on shear modulus and normalized shear modulus reduction relationship as a function of shear strain. The results from field testing at the BKK will be synthesized with the results from field testing at other landfills to generate broad conclusions and recommendations in Chapter 9.

Crosshole and downhole seismic testing allowed for an assessment of $V_{p\text{-}X}$, $V_{p\text{-}Z}$, $V_{s\text{-}XZ}$, $V_{s\text{-}ZX}$, and $V_{s\text{-}ZY}$ as a function of waste composition and confining stress in solid waste. Crosshole and downhole seismic testing with different static vertical loads showed that wave propagation velocities in solid waste increased with stress. However, wave propagation velocities increases were generally small and indicated that the solid waste test locations were overconsolidated and remained so throughout the course of staged loading sequence. The results of crosshole and downhole seismic testing in soil cover at the BKK showed a bi-linearity in the relationship between wave propagation velocity and stress. This indicated that soil cover initially was in the OC regime and shifted to NC regime as the stress increased.

The wave propagation velocity measurements at the BKK were also used to assess anisotropy of waste and soil cover in term of waver propagation velocity ratio. For example, in solid waste, the ratio of $V_{p\text{-}Z}$ to $V_{p\text{-}X}$ ranged from 0.79 to 0.90 with a mean value of 0.85. The ratio of $V_{s\text{-}vertical}$ to $V_{s\text{-}horizontal}$ was found to be between 0.85 and 1.00 with an average value of 0.92. These average values indicated that the stiffness in the horizontal direction was generally higher than the stiffness in the vertical direction. The small-strain Poisson's ratio in solid waste test locations varied from 0.23 to 0.38. The small-strain Poisson's ratio in soil cover test location varied from 0.20 to 0.32.

The impact of solid waste variability and confining stress on the shear modulus was also assessed in situ. Shear modulus was found to increase with increasing confining stress and to be

affected by waste composition. The normalized shear modulus reduction curves were also affected by waste composition and confining stress. The normalized shear modulus became more linear as confining stress increased. At the same confining stress, the shear modulus and normalized shear modulus curves of the solid waste at different locations varied indicating the effect of waste composition on these nonlinear dynamic properties of solid waste.

CHAPTER 9. SYNTHESIS OF FIELD TESTING RESULTS

9.1 **Introduction**

This chapter synthesizes results from field investigations at the Austin Community Landfill (ACL), Lamb Canyon Sanitary Landfill (LCSL), Los Reales Landfill (LRL), and BKK Hazardous Landfill. In particular, this chapter presents an evaluation of anisotropy of solid waste, a synthesis of the downhole and crosshole seismic test results, an evaluation of Poisson's ratio of solid waste, and the development of recommended G/G_{max} curves for solid waste.

9.2 **Anisotropy of Solid Waste**

Figure 9.1(a) shows a comparison between P-wave and S-wave velocities propagating in the vertical direction (i.e. $V_{p\text{-}Z}$ and $V_{s\text{-}ZX}$) of municipal solid waste (MSW) in test locations at the ACL, LCSL, and LRL. The ratio of $V_{s\text{-}ZX}$ to $V_{p\text{-}Z}$ in test locations at the ACL ranged from 0.39 to 0.66. The ratio of $V_{s\text{-}ZX}$ to $V_{p\text{-}Z}$ in test locations at the LCSL varied from 0.42 to 0.61. The ratio of $V_{s\text{-}ZX}$ to $V_{p\text{-}Z}$ in test locations at the LRL varied from 0.44 to 0.67. The mean from all MSW test locations shows that the ratio of $V_{s\text{-}ZX}$ to $V_{p\text{-}Z}$ was 0.51. In addition, the ratio of $V_{s\text{-}ZX}$ to $V_{p\text{-}Z}$ for solid waste in test locations at the BKK varied from 0.44 to 0.59 with a mean value of 0.53. The ratio of $V_{s\text{-}ZX}$ to $V_{p\text{-}Z}$ for soil cover (i.e. fat clay) in test location at the BKK varied from 0.54 to 0.61 with a mean value of 0.58. For comparison, data from Stokoe et al. (1995) indicated that the ratio of $V_{s\text{-}ZX}$ to $V_{p\text{-}Z}$ for washed mortar sand varied from 0.61 to 0.69 with a mean value of 0.63. Based on these results, the ratios of $V_{s\text{-}ZX}$ to $V_{p\text{-}Z}$ of solid waste in this study had lower average than those of clayey soil cover and washed mortar sand. Statistics for the ratio of $V_{s\text{-}ZX}$ to $V_{p\text{-}Z}$, such as mean, maximum, minimum, and standard deviation (SD), is tabulated in Table 9.1.

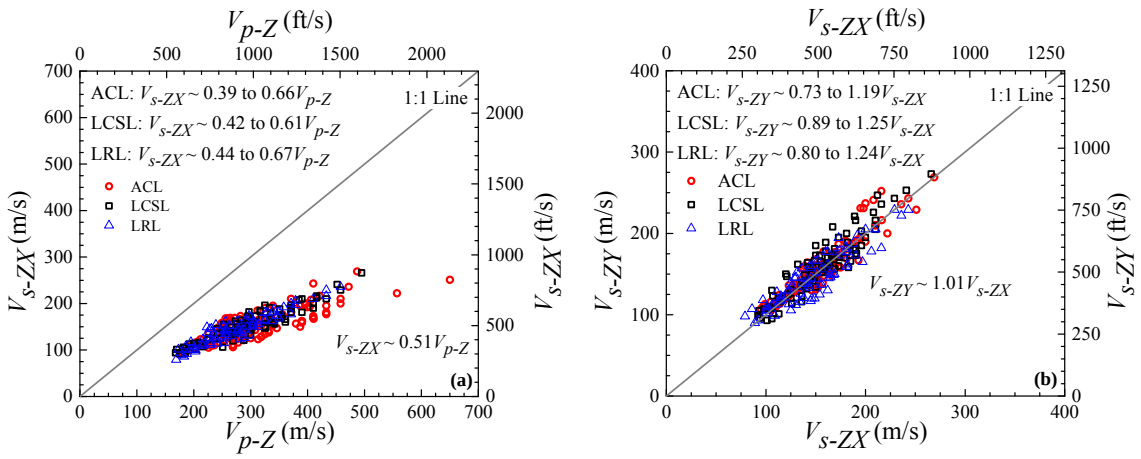

Figure 9.1 Comparison on (a) $V_{p\text{-}Z}$-$V_{s\text{-}ZX}$ and (b) $V_{s\text{-}ZX}$ -$V_{s\text{-}ZY}$ in test locations at the ACL, LCSL, and LRL.

Table 9.1 Statistics for ratio of $V_{s\text{-}ZX}$ to $V_{p\text{-}Z}$.

Location	$V_{s\text{-}ZX}/V_{p\text{-}Z}$			
	Mean	Max	Min	SD
ACL 1	0.53	0.66	0.39	0.07
ACL 2	0.48	0.60	0.39	0.07
LCSL 1	0.51	0.59	0.44	0.05
LCSL 2	0.53	0.61	0.42	0.05
LCSL 3	0.53	0.59	0.48	0.03
LRL 1	0.54	0.59	0.50	0.03
LRL 2	0.50	0.54	0.44	0.03
LRL 3	0.55	0.67	0.47	0.06
BKK 1 (solid waste)	0.56	0.59	0.52	0.02
BKK 2 (solid waste)	0.50	0.58	0.44	0.05
BKK 3 (soil cover)	0.58	0.61	0.54	0.03
Washed mortar sand	0.63	0.69	0.61	0.03

Figure 9.1(b) presents a comparison between the $V_{s\text{-}ZX}$ and the $V_{s\text{-}ZY}$. In test locations at the ACL, the ratio of $V_{s\text{-}ZY}$ to $V_{s\text{-}ZX}$ varied from 0.73 to 1.19. In test locations at the LCSL, the ratio of $V_{s\text{-}ZY}$ to $V_{s\text{-}ZX}$ ranged from 0.89 to 1.25. In test locations at the LRL, the ratio of $V_{s\text{-}ZY}$ to $V_{s\text{-}ZX}$ ranged from 0.80 to 1.24. The mean of this ratio from all MSW test locations was found to be 1.01. For comparison, the ratio of $V_{s\text{-}ZY}$ to $V_{s\text{-}ZX}$ from solid waste test locations at the BKK ranged from 0.82 to 1.13 with a mean value of 1.00. The ratio of $V_{s\text{-}ZY}$ to $V_{s\text{-}ZX}$ in soil cover test location at the BKK ranged from 0.89 to 1.13 with a mean value of 0.98. The averages of this

ratio from all solid waste and soil cover test locations were found to be close to 1 indicating practically no difference on average between S-wave propagation velocities in the YZ and the XZ plane. Statistics for the ratio of $V_{s\text{-}ZY}$ to $V_{s\text{-}ZX}$ is presented in Table 9.2.

Table 9.2 Statistics for ratio of $V_{s\text{-}ZY}$ to $V_{s\text{-}ZX}$.

Location	$V_{s\text{-}ZY}/V_{s\text{-}ZX}$			
	Mean	Max	Min	SD
ACL 1	1.03	1.19	0.87	0.10
ACL 2	0.96	1.06	0.73	0.09
LCSL 1	1.08	1.25	0.86	0.11
LCSL 2	1.04	1.23	0.94	0.08
LCSL 3	0.99	1.15	0.89	0.07
LRL 1	0.97	1.12	0.84	0.09
LRL 2	1.00	1.16	0.84	0.10
LRL 3	1.01	1.24	0.80	0.12
BKK 1 (solid waste)	0.94	1.04	0.82	0.07
BKK 2 (solid waste)	1.05	1.13	0.98	0.04
BKK 3 (soil cover)	1.00	1.13	0.89	0.07

Figure 9.2 shows a comparison between P-wave and S-wave velocities propagating in the horizontal direction (i.e. $V_{p\text{-}X}$ and $V_{s\text{-}XZ}$). In test locations at the ACL, the ratio of $V_{s\text{-}XZ}$ to $V_{p\text{-}X}$ ranged from 0.31 to 0.55. In test locations at the LCSL, $V_{s\text{-}XZ}$ to $V_{p\text{-}X}$ ratio varied from 0.40 to 0.59. In test locations at the LRL, $V_{s\text{-}XZ}$ to $V_{p\text{-}X}$ ratio varied from 0.31 to 0.58. In general, the ratio of $V_{s\text{-}XZ}$ to $V_{p\text{-}X}$ in test locations at the ACL, LCSL, and LRL ranged from 0.31 to 0.59 with a mean value of 0.45. For comparison, the ratio of $V_{s\text{-}XZ}$ to $V_{p\text{-}X}$ from solid waste test locations at the BKK ranged from 0.44 to 0.55 with a mean value of 0.48. The ratio of $V_{s\text{-}XZ}$ to $V_{p\text{-}X}$ of soil cover test location at the BKK ranged from 0.52 to 0.57 with a mean value of 0.55. In addition, data from Stokoe et al. (1995) indicated that the ratio of $V_{s\text{-}XZ}$ to $V_{p\text{-}X}$ for washed mortar sand varied from 0.58 to 0.66 with a mean value of 0.61. Based on these results, the ratios of $V_{s\text{-}XZ}$ to $V_{p\text{-}X}$ of solid waste in this study had lower average than those of clayey soil cover and washed mortar sand. Statistics for the ratio of $V_{s\text{-}XZ}$ to $V_{p\text{-}X}$ is summarized in Table 9.3.

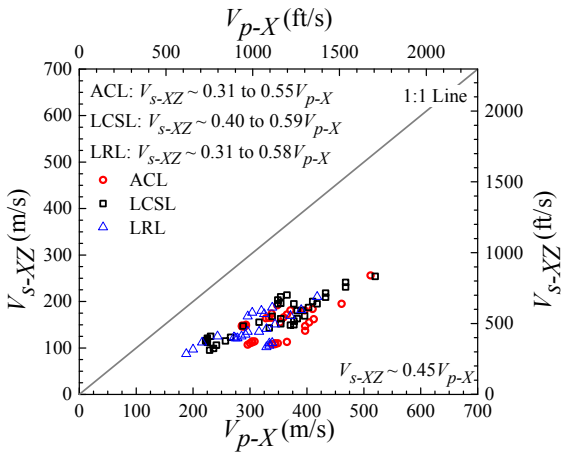

Figure 9.2 Comparison on $V_{p\text{-}X}$ and $V_{s\text{-}XZ}$ in in test locations at the ACL, LCSL, and LRL.

Table 9.3 Statistics for ratio of $V_{s\text{-}XZ}$ to $V_{p\text{-}X}$.

Location	$V_{s\text{-}XZ}/V_{p\text{-}X}$			
	Mean	Max	Min	SD
ACL 1	0.44	0.55	0.31	0.10
ACL 2	0.41	0.49	0.35	0.05
LCSL 1	0.51	0.59	0.46	0.05
LCSL 2	0.45	0.51	0.40	0.04
LCSL 3	0.48	0.54	0.41	0.05
LRL 1	0.53	0.58	0.43	0.07
LRL 2	0.46	0.53	0.44	0.03
LRL 3	0.40	0.52	0.31	0.09
BKK 1 (solid waste)	0.52	0.55	0.49	0.01
BKK 2 (solid waste)	0.47	0.49	0.44	0.01
BKK 3 (soil cover)	0.54	0.57	0.52	0.02
Washed mortar sand	0.61	0.66	0.58	0.03

Figure 9.3(a) shows a comparison between V_p propagating in the horizontal ($V_{p\text{-}X}$) and vertical ($V_{p\text{-}Z}$) directions. In test locations at the ACL, the ratios of $V_{p\text{-}Z}$ to $V_{p\text{-}X}$ varied from 0.69 to 0.89. In test locations at the LCSL, the ratios of $V_{p\text{-}Z}$ to $V_{p\text{-}X}$ varied from 0.77 to 0.93. In test locations at the LRL, the ratios of $V_{p\text{-}Z}$ to $V_{p\text{-}X}$ varied from 0.75 to 0.99. The ratio of $V_{p\text{-}Z}$ to $V_{p\text{-}X}$ from test locations at these landfills ranged from 0.69 to 0.99 with a mean value of 0.83. For comparison, the ratios of $V_{p\text{-}Z}$ to $V_{p\text{-}X}$ from solid waste test locations at the BKK varied from 0.79 to 0.90 with a mean value of 0.85. In soil cover test location at the BKK, the ratios of $V_{p\text{-}Z}$ to $V_{p\text{-}X}$ varied from 0.83 to 0.97 with a mean value of 0.90. In addition, data from Stokoe et al. (1995)

indicated that the ratio of $V_{p\text{-}Z}$ to $V_{p\text{-}X}$ for washed mortar sand varied from 0.88 to 0.94 with a mean value of 0.90. According to Stokoe et al. (1995), the ratio of $V_{p\text{-}Z}$ to $V_{p\text{-}X}$ is the best indicator of anisotropy. Statistics for the ratio of $V_{p\text{-}Z}$ to $V_{p\text{-}X}$ is presented in Table 9.4. Based on presented results, on average, MSW was slightly more anisotropic than BKK solid waste and MSW and BKK solid waste were more anisotropic than soil cover.

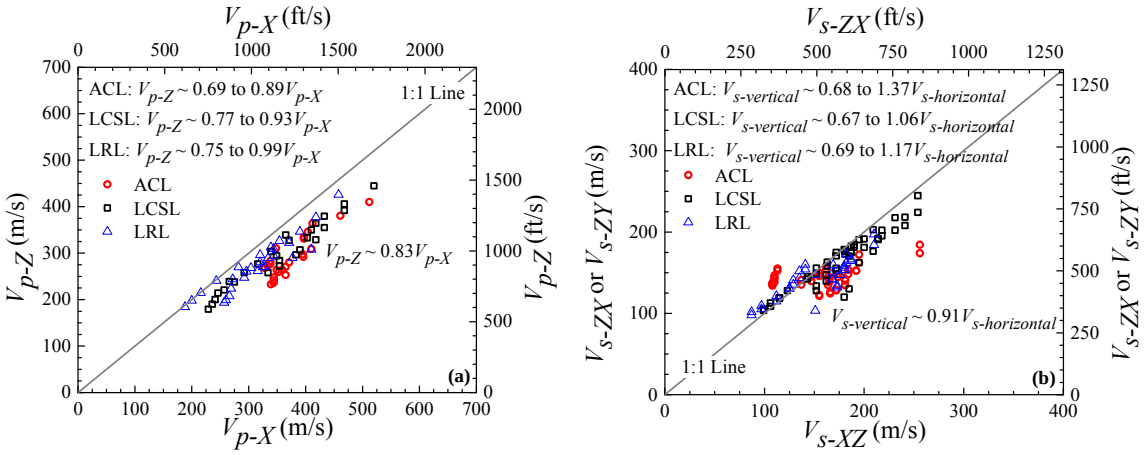

Figure 9.3 (a) Comparison on V_p propagating in the vertical and horizontal directions; and (b) V_s propagating in the vertical and horizontal directions in test locations at the ACL, LCSL, and LRL.

Table 9.4 Statistics for ratio of $V_{p\text{-}Z}$ to $V_{p\text{-}X}$.

Location	$V_{p\text{-}Z}/V_{p\text{-}X}$			
	Mean	Max	Min	SD
ACL 1	0.80	0.89	0.69	0.05
ACL 2	0.79	0.88	0.74	0.05
LCSL 1	0.83	0.88	0.77	0.04
LCSL 2	0.83	0.88	0.77	0.05
LCSL 3	0.86	0.93	0.78	0.04
LRL 1	0.85	0.93	0.75	0.06
LRL 2	0.88	0.93	0.83	0.03
LRL 3	0.89	0.99	0.75	0.10
BKK 1 (solid waste)	0.83	0.86	0.81	0.02
BKK 2 (solid waste)	0.86	0.90	0.79	0.03
BKK 3 (soil cover)	0.90	0.97	0.83	0.06
Washed mortar sand	0.90	0.94	0.88	0.03

The relationship between V_s propagating in the horizontal ($V_{s\text{-}horizontal}$: $V_{s\text{-}XZ}$) and vertical ($V_{s\text{-}vertical}$: $V_{s\text{-}ZX}$ and $V_{s\text{-}ZY}$) directions is shown in Figure 9.3(b). The ratios of $V_{s\text{-}vertical}$ to $V_{s\text{-}horizontal}$

in test locations at the ACL were found to be between 0.68 and 1.37. In test locations at the LCSL, the ratios of $V_{s\text{-}vertical}$ to $V_{s\text{-}horizontal}$ ranged from 0.67 to 1.06. In test locations at the LRL, the ratios of $V_{s\text{-}vertical}$ to $V_{s\text{-}horizontal}$ varied from 0.69 to 1.17. On average, the ratio of $V_{s\text{-}vertical}$ to $V_{s\text{-}horizontal}$ from all MSW test locations was found to be 0.91. For comparison, the ratios of $V_{s\text{-}vertical}$ to $V_{s\text{-}horizontal}$ from solid waste test locations at the BKK were found to be between 0.85 and 1.00 with an average value of 0.92. In soil cover test location at the BKK, the ratio $V_{s\text{-}vertical}$ to $V_{s\text{-}horizontal}$ were found to be between 0.86 and 1.09 with an average value of 0.95. Additionally, data from Stokoe et al. (1995) indicated that the ratio of $V_{s\text{-}vertical}$ to $V_{s\text{-}horizontal}$ for washed mortar sand varied from 0.93 to 0.97 with a mean value of 0.94. The ratio of $V_{s\text{-}vertical}$ to $V_{s\text{-}horizontal}$ for sandy silt of Po River Valley (Italia) varied from 0.85 to 1.11 with a mean value of 1.00 (Fioravante et al. 1998). Statistics for the ratio of $V_{s\text{-}vertical}$ to $V_{s\text{-}horizontal}$ are summarized in Table 9.5.

Table 9.5 Statistics for ratio of $V_{s\text{-}vertical}$ to $V_{s\text{-}horizontal}$.

Location	$V_{s\text{-}vertical}/V_{s\text{-}horizontal}$			
	Mean	Max	Min	SD
ACL 1	1.09	1.37	0.83	0.23
ACL 2	0.84	1.03	0.68	0.10
LCSL 1	0.91	0.99	0.67	0.07
LCSL 2	0.93	1.02	0.70	0.08
LCSL 3	1.04	1.06	1.02	0.01
LRL 1	0.95	1.13	0.84	0.12
LRL 2	0.87	0.98	0.69	0.10
LRL 3	1.09	1.17	1.02	0.05
BKK 1 (solid waste)	0.90	0.97	0.85	0.03
BKK 2 (solid waste)	0.93	1.00	0.88	0.03
BKK 3 (soil cover)	0.97	1.09	0.86	0.08
Washed mortar sand	0.94	0.97	0.93	0.02
Po River Valley sandy silt	1.00	1.12	0.85	0.08

In general, the data indicated that wave propagation in the vertical direction was slower than that in the horizontal direction, highlighting that solid waste is an anisotropic material. The average ratios of solid waste were also lower than those of soil cover, washed mortar sand, and Po River Valley sandy silt indicating solid waste was more anisotropic.

9.3 **Discussion on Crosshole and Downhole Seismic Testing Results**

The results from small-scale downhole and crosshole seismic tests were also used to establish the relationship between wave propagation velocities and stress states using power function in the overconsolidated (OC) and normally consolidated (NC) regimes. For convenience of the reader, the power functions for $V_{s\text{-}ZX}$, $V_{s\text{-}ZY}$, $V_{p\text{-}Z}$, $V_{s\text{-}XZ}$, and $V_{p\text{-}X}$ are presented again in Eqs. 9.1, 9.2, 9.3, 9.4, and 9.5, respectively.

$$V_{s-ZX} = A_{ZX} \cdot \left(\frac{\sigma_0}{P_a} \right)^{n_{ZX}} \tag{9.1}$$

$$V_{s-ZY} = A_{ZY} \cdot \left(\frac{\sigma_0}{P_a} \right)^{n_{ZY}} \tag{9.2}$$

$$V_{p-Z} = A_{pZ} \cdot \left(\frac{\sigma_v}{P_a} \right)^{n_{pZ}} \tag{9.3}$$

$$V_{s-XZ} = A_{XZ} \cdot \left(\frac{\sigma_0}{P_a} \right)^{n_{XZ}} \tag{9.4}$$

$$V_{p-X} = A_{pX} \cdot \left(\frac{\sigma_h}{P_a} \right)^{n_{pX}} \tag{9.5}$$

where σ_v is vertical stress, σ_h is horizontal stress, and σ_0 is mean confining stress, A_{ij} is an empirical constant that indicates corresponding wave propagation velocity at 1 atm, n_{ij} is an empirical constant that quantifies the effect of stress on the corresponding wave propagation velocity, and P_a is atmospheric pressure in kPa. As shown in the previous chapters, either linear or bi-linear relationship between wave propagation velocity and the state of stress in MSW and soil cover was observed in the log V_p-log σ_v, log V_p-log σ_h, and log V_s-log σ_0 spaces.

Fitting parameters for wave propagation velocity and stress relationship from crosshole and downhole seismic tests at the ACL are summarized in Table 9.6 to 9.8. Table 9.9 to 9.12 summarize fitting parameters for wave propagation velocity and stress relationship calculated from testing at the LCSL. Table 9.13 to 9.16 summarize fitting parameters for wave propagation velocity and stress relationship calculated from testing at the LRL. Fitting parameters for wave propagation velocity and stress relationship from in solid waste test locations at the BKK are tabulated in Table 9.17 to 9.20. Table 9.21 to 9.24 present fitting parameters for wave propagation velocity and stress relationship calculated from soil cover test location at the BKK. Statistics for A_{pX} and n_{pX} are presented in Table 9.25. Statistics for A_{XZ} and n_{XZ} are presented in Table 9.26. Table 9.27 summarizes statistics for A_{pZ} and n_{pZ}. Statistics for A_{ZX} and n_{ZX} are shown in Table 9.28. Statistics for A_{ZY} and n_{ZY} are presented in Table 9.29.

Table 9.6 Parameters of A_{pX}, n_{pX}, A_{XZ}, and n_{XZ} for test locations at the ACL.

ACL	Depth (m)	OC		NC		OC		NC	
		A_{pX}	n_{pX}	A_{pX}	n_{pX}	A_{XZ}	n_{XZ}	A_{XZ}	n_{XZ}
1	0.50	443	0.09	-	-	199	0.07	-	-
	0.72	402	0.05	-	-	115	0.02	-	-
	1.05	306	0.02	-	-	154	0.02	-	-
2	0.21	423	0.02	548	0.18	181	0.09	245	0.34
	0.36	447	0.08	-	-	194	0.07	-	-
	0.56	331	0.03	-	-	118	0.03	-	-

Table 9.7 Parameters of A_{ZX} and n_{ZX} for test locations at the ACL.

ACL	Depth (m)	West/South				East/North			
		OC		NC		OC		NC	
		A_{ZX}	n_{ZX}	A_{ZX}	n_{ZX}	A_{ZX}	n_{ZX}	A_{ZX}	n_{ZX}
1	0.32	182	0.05	213	0.21	156	0.06	183	0.21
	0.61	121	0.09	-	-	173	0.06	-	-
	0.89	237	0.08	-	-	191	0.05	-	-
2	0.13	205	0.03	260	0.23	202	0.07	241	0.18
	0.29	213	0.10	-	-	127	0.06	-	-
	0.46	134	0.09	-	-	130	0.05	-	-

Table 9.8 Parameters of A_{ZY} and n_{ZY} for test locations at the ACL.

ACL	Depth (m)	West/South				East/North			
		OC		NC		OC		NC	
		A_{ZY}	n_{ZY}	A_{ZY}	n_{ZY}	A_{ZY}	n_{ZY}	A_{ZY}	n_{ZY}
1	0.32	167	0.04	193	0.20	163	0.06	186	0.22
	0.61	131	0.07	-	-	154	0.06	-	-
	0.89	272	0.07	-	-	210	0.07	-	-
2	0.13	156	0.05	213	0.21	179	0.05	219	0.16
	0.29	196	0.07	-	-	133	0.07	-	-
	0.46	144	0.07	-	-	137	0.07	-	-

Table 9.9 Parameters of A_{pX}, n_{pX}, A_{XZ}, and n_{XZ} for test locations at the LCSL.

LCSL	Depth (m)	OC		NC		OC		NC	
		A_{pX}	n_{pX}	A_{pX}	n_{pX}	A_{XZ}	n_{XZ}	A_{XZ}	n_{XZ}
1	0.20	487	0.07	565	0.17	214	0.06	256	0.19
	0.41	473	0.06	601	0.18	222	0.08	277	0.26
	0.66	450	0.10	-	-	231	0.07	-	-
2	0.20	-	-	477	0.19	175	0.05	214	0.21
	0.41	452	0.10	-	-	185	0.09	227	0.29
	0.66	475	0.08	-	-	186	0.09	-	-
3	0.20	323	0.08	398	0.20	-	-	-	-
	0.41	281	0.07	364	0.21	117	0.08	144	0.25
	0.66	288	0.10	-	-	136	0.08	-	-

Table 9.10 Parameters of A_{pZ} and n_{pZ} for test locations at the LCSL.

LCSL	Depth (m)	West/South				East/North			
		OC		NC		OC		NC	
		A_{pZ}	n_{pZ}	A_{pZ}	n_{pZ}	A_{pZ}	n_{pZ}	A_{pZ}	n_{pZ}
1	0.13	364	0.10	398	0.24	324	0.07	361	0.21
	0.30	342	0.08	386	0	435	0.08	467	0.22
	0.53	372	0.09	-	-	348	0.07	-	-
2	0.13	296	0.08	336	0.21	318	0.09	342	0.25
	0.30	282	0.07	308	0.25	326	0.08	349	0.29
	0.53	301	0.07	-	-	309	0.07	-	-
3	0.13	318	0.09	377	0.29	299	0.06	361	0.33
	0.30	228	0.08	260	0.25	200	0.06	234	0.22
	0.53	232	0.08	-	-	206	0.09	-	-

Table 9.11 Parameters of A_{ZX} and n_{ZX} for test locations at the LCSL.

LCSL	Depth (m)	West/South				East/North			
		OC		NC		OC		NC	
		A_{ZX}	n_{ZX}	A_{ZX}	n_{ZX}	A_{ZX}	n_{ZX}	A_{ZX}	n_{ZX}
1	0.13	-	-	229	0.27	145	0.06	187	0.22
	0.30	180	0.06	241	0.28	240	0.07	297	0.24
	0.53	176	0.07	-	-	200	0.05	-	-
2	0.13	155	0.07	186	0.25	139	0.08	179	0.22
	0.30	177	0.06	218	0.21	175	0.09	224	0.26
	0.53	174	0.08	-	-	191	0.09	-	-
3	0.13	166	0.06	212	0.22	159	0.08	202	0.24
	0.30	122	0.09	161	0.29	122	0.06	158	0.26
	0.53	139	0.09	-	-	122	0.10	-	-

Table 9.12 Parameters of A_{ZY} and n_{ZY} for test locations at the LCSL.

LCSL	Depth (m)	West/South				East/North			
		OC		NC		OC		NC	
		A_{ZY}	n_{ZY}	A_{ZY}	n_{ZY}	A_{ZY}	n_{ZY}	A_{ZY}	n_{ZY}
1	0.13	207	0.07	238	0.20	175	0.05	207	0.20
	0.30	225	0.07	280	0.27	253	0.05	297	0.19
	0.53	189	0.09	-	-	190	0.07	-	-
2	0.13	155	0.08	181	0.25	167	0.08	201	0.23
	0.30	192	0.08	225	0.20	166	0.07	209	0.24
	0.53	199	0.10	-	-	192	0.10	-	-
3	0.13	155	0.09	203	0.27	142	0.04	197	0.23
	0.30	136	0.09	160	0.23	106	0.04	143	0.26
	0.53	142	0.09	-	-	122	0.08	-	-

Table 9.13 Parameters of A_{pX}, n_{pX}, A_{XZ}, and n_{XZ} for test locations at the LRL.

LRL	Depth (m)	OC		NC		OC		NC	
		A_{pX}	n_{pX}	A_{pX}	n_{pX}	A_{XZ}	n_{XZ}	A_{XZ}	n_{XZ}
1	0.20	363	0.06	472	0.21	147	0.04	-	-
	0.51	441	0.11	-	-	194	0.05	-	-
	0.91	-	-	-	-	177	0.07	-	-
2	0.23	435	0.06	533	0.20	195	0.08	248	0.26
	0.41	398	0.06	-	-	-	-	-	-
	0.61	400	0.11	-	-	138	0.05	-	-
3	0.20	221	0.04	343	0.28	111	0.08	140	0.20
	0.51	302	0.04	-	-	-	-	-	-
	0.91	441	0.09	-	-	128	0.10	-	-

Table 9.14 Parameters of A_{pZ} and n_{pZ} for test locations at the LRL.

LRL	Depth (m)	West/South				East/North			
		OC		NC		OC		NC	
		A_{pZ}	n_{pZ}	A_{pZ}	n_{pZ}	A_{pZ}	n_{pZ}	A_{pZ}	n_{pZ}
1	0.13	-	-	-	-	-	-	-	-
	0.36	332	0.08	-	-	259	0.08	-	-
	0.71	280	0.07	-	-	366	0.10	-	-
2	0.15	340	0.07	383	0.23	361	0.05	415	0.20
	0.32	366	0.08	405	0.29	345	0.08	364	0.17
	0.51	303	0.08	-	-	301	0.09	-	-
3	0.13	261	0.07	306	0.27	248	0.05	294	0.26
	0.36	206	0.07	245	0.33	212	0.07	234	0.25
	0.71	221	0.07	-	-	255	0.07	-	-

Table 9.15 Parameters of A_{ZX} and n_{ZX} for test locations at the LRL.

LRL	Depth (m)	West/South				East/North			
		OC		NC		OC		NC	
		A_{ZX}	n_{ZX}	A_{ZX}	n_{ZX}	A_{ZX}	n_{ZX}	A_{ZX}	n_{ZX}
1	0.13	199	0.05	239	0.23	-	-	-	-
	0.36	177	0.07	-	-	148	0.09	-	-
	0.71	179	0.09	-	-	212	0.08	-	-
2	0.15	174	0.07	231	0.22	176	0.05	242	0.28
	0.32	183	0.05	240	0.20	185	0.08	238	0.27
	0.51	164	0.10	-	-	139	0.07	-	-
3	0.13	103	0.09	127	0.25	155	0.07	185	0.23
	0.36	135	0.10	183	0.30	110	0.07	139	0.22
	0.71	133	0.11	-	-	175	0.08	-	-

Table 9.16 Parameters of A_{ZY} and n_{ZY} for test locations at the LRL.

LRL	Depth (m)	West/South				East/North			
		OC		NC		OC		NC	
		A_{ZY}	n_{ZY}	A_{ZY}	n_{ZY}	A_{ZY}	n_{ZY}	A_{ZY}	n_{ZY}
1	0.13	180	0.06	229	0.26	-	-	-	-
	0.36	220	0.08	-	-	133	0.08	-	-
	0.71	155	0.05	-	-	213	0.07	-	-
2	0.15	170	0.05	234	0.25	-	-	229	0.24
	0.32	161	0.05	204	0.21	160	0.06	198	0.21
	0.51	181	0.09	-	-	163	0.11	-	-
3	0.13	117	0.06	146	0.21	141	0.08	179	0.22
	0.36	136	0.08	182	0.25	113	0.08	148	0.30
	0.71	131	0.08	-	-	142	0.08	-	-

Table 9.17 Parameters of A_{pX}, n_{pX}, A_{XZ}, and n_{XZ} for solid waste test locations at the BKK.

BKK	Depth (m)	OC		NC		OC		NC	
		A_{pX}	n_{pX}	A_{pX}	n_{pX}	A_{XZ}	n_{XZ}	A_{XZ}	n_{XZ}
1	0.20	438	0.04	-	-	202	0.05	-	-
	0.46	408	0.06	-	-	199	0.06	-	-
	0.91	324	0.04	-	-	171	0.06	-	-
2	0.20	466	0.05	-	-	204	0.04	-	-
	0.46	541	0.06	-	-	228	0.05	-	-
	0.91	477	0.04	-	-	229	0.05	-	-

Table 9.18 Parameters of A_{pZ} and n_{pZ} for solid waste test locations at the BKK.

BKK	Depth (m)	West/South				East/North			
		OC		NC		OC		NC	
		A_{pZ}	n_{pZ}	A_{pZ}	n_{pZ}	A_{pZ}	n_{pZ}	A_{pZ}	n_{pZ}
1	0.13	364	0.06	-	-	-	-	-	-
	0.33	372	0.06	-	-	364	0.06	-	-
	0.69	297	0.05	-	-	250	0.06	-	-
2	0.13	-	-	-	-	-	-	-	-
	0.33	392	0.06	-	-	433	0.05	-	-
	0.69	459	0.05	-	-	447	0.04	-	-

Table 9.19 Parameters of A_{ZX} and n_{ZX} for solid waste test locations at the BKK.

BKK	Depth (m)	West/South				East/North			
		OC		NC		OC		NC	
		A_{ZX}	n_{ZX}	A_{ZX}	n_{ZX}	A_{ZX}	n_{ZX}	A_{ZX}	n_{ZX}
1	0.13	212	0.06	-	-	-	-	-	-
	0.33	222	0.05	-	-	206	0.05	-	-
	0.69	181	0.06	-	-	138	0.05	-	-
2	0.13	-	-	-	-	-	-	-	-
	0.33	204	0.05	-	-	201	0.04	-	-
	0.69	266	0.06	-	-	217	0.05	-	-

Table 9.20 Parameters of A_{ZY} and n_{ZY} for solid waste test locations at the BKK.

BKK	Depth (m)	West/South				East/North			
		OC		NC		OC		NC	
		A_{ZY}	n_{ZY}	A_{ZY}	n_{ZY}	A_{ZY}	n_{ZY}	A_{ZY}	n_{ZY}
1	0.13	-	-	-	-	-	-	-	-
	0.33	218	0.06	-	-	203	0.05	-	-
	0.69	151	0.06	-	-	145	0.06	-	-
2	0.13	-	-	-	-	-	-	-	-
	0.33	202	0.05	-	-	228	0.06	-	-
	0.69	277	0.05	-	-	235	0.06	-	-

Table 9.21 Parameters of A_{pX}, n_{pX}, A_{XZ}, and n_{XZ} for soil cover test locations at the BKK.

BKK	Depth (m)	OC		NC		OC		NC	
		A_{pX}	n_{pX}	A_{pX}	n_{pX}	A_{XZ}	n_{XZ}	A_{XZ}	n_{XZ}
3	0.20	371	0.04	489	0.21	199	0.06	247	0.25
	0.46	501	0.05	-	-	262	0.05	-	-
	0.91	-	-	-	-	261	0.07	-	-

Table 9.22 Parameters of A_{pZ} and n_{pZ} for soil cover test locations at the BKK.

BKK	Depth (m)	West				East			
		OC		NC		OC		NC	
		A_{pZ}	n_{pZ}	A_{pZ}	n_{pZ}	A_{pZ}	n_{pZ}	A_{pZ}	n_{pZ}
3	0.13	314	0.05	351	0.22	342	0.05	-	-
	0.33	374	0.05	385	0.23	357	0.06	375	0.22
	0.69	430	0.05	-	-	414	0.06	-	-

Table 9.23 Parameters of A_{ZX} and n_{ZX} for soil cover test locations at the BKK.

BKK	Depth (m)	West				East			
		OC		NC		OC		NC	
		A_{ZX}	n_{ZX}	A_{ZX}	n_{ZX}	A_{ZX}	n_{ZX}	A_{ZX}	n_{ZX}
3	0.13	186	0.07	233	0.26	191	0.05	229	0.21
	0.33	222	0.07	279	0.27	233	0.07	272	0.22
	0.69	272	0.05	-	-	-	-	-	-

Table 9.24 Parameters of A_{ZY} and n_{ZY} for soil cover test locations at the BKK.

BKK	Depth (m)	West				East			
		OC		NC		OC		NC	
		A_{ZY}	n_{ZY}	A_{ZY}	n_{ZY}	A_{ZY}	n_{ZY}	A_{ZY}	n_{ZY}
3	0.13	187	0.03	240	0.25	-	-	-	-
	0.33	241	0.08	285	0.24	233	0.09	268	0.23
	0.69	245	0.05	-	-	250	0.09	-	-

Table 9.25 Statistics for A_{pX} and n_{pX}.

Landfill	OC								NC							
	A_{pX}				n_{pX}				A_{pX}				n_{pX}			
	Mean	Max	Min	SD	Mean	Max	Min	SD	Mean	Max	Min	SD	Mean	Max	Min	SD
ACL	392	447	306	60	0.05	0.09	0.02	0.03	548	-	-	-	0.18	-	-	-
LCSL	404	487	281	90	0.08	0.10	0.06	0.01	481	601	364	102	0.19	0.21	0.17	0.02
LRL	375	441	221	78	0.07	0.11	0.04	0.03	449	533	343	97	0.23	0.28	0.20	0.05
ACL, LCSL, LRL	390	487	221	76	0.07	0.11	0.02	0.03	478	601	343	92	0.20	0.28	0.17	0.04
BKK solid waste	442	541	324	73	0.05	0.06	0.04	0.01	-	-	-	-	-	-	-	-
BKK soil cover	436	501	371	92	0.04	0.05	0.04	0.003	489	-	-	-	0.21	-	-	-

Table 9.26 Statistics for A_{XZ} and n_{XZ}.

Landfill	OC								NC							
	A_{XZ}				n_{XZ}				A_{XZ}				n_{XZ}			
	Mean	Max	Min	SD	Mean	Max	Min	SD	Mean	Max	Min	SD	Mean	Max	Min	SD
ACL	160	199	115	37	0.05	0.09	0.02	0.03	245	-	-	-	0.34	-	-	-
LCSL	183	231	117	40	0.07	0.09	0.05	0.02	224	277	144	51	0.24	0.29	0.19	0.04
LRL	155	195	111	33	0.07	0.10	0.04	0.02	194	248	140	76	0.23	0.26	0.20	0.04
ACL, LCSL, LRL	167	231	111	38	0.06	0.10	0.02	0.02	219	277	140	51	0.25	0.34	0.19	0.05
BKK solid waste	205	229	171	22	0.05	0.06	0.04	0.01	-	-	-	-	-	-	-	-
BKK soil cover	241	262	199	36	0.06	0.07	0.05	0.01	247	-	-	-	0.25	-	-	-

Table 9.27 Statistics for A_{pZ} and n_{pZ}.

Landfill	OC								NC							
	A_{pZ}				n_{pZ}				A_{pZ}				n_{pZ}			
	Mean	Max	Min	SD	Mean	Max	Min	SD	Mean	Max	Min	SD	Mean	Max	Min	SD
ACL	334	462	209	85	0.07	0.09	0.04	0.02	443	542	369	90	0.22	0.28	0.16	0.06
LCSL	306	435	200	60	0.08	0.10	0.06	0.01	348	467	234	62	0.25	0.33	0.21	0.04
LRL	291	366	206	56	0.07	0.10	0.05	0.01	331	415	234	71	0.25	0.33	0.17	0.05
ACL, LCSL, LRL	308	462	200	67	0.07	0.10	0.04	0.01	354	542	234	74	0.25	0.33	0.16	0.04
BKK solid waste	375	459	250	69	0.05	0.06	0.04	0.01	-	-	-	-	-	-	-	-
BKK soil cover	372	430	314	44	0.05	0.06	0.05	0.004	370	385	351	17	0.22	0.23	0.22	0.003

Table 9.28 Statistics for A_{ZX} and n_{ZX}.

Landfill	OC								NC							
	A_{ZX}				n_{ZX}				A_{ZX}				n_{ZX}			
	Mean	Max	Min	SD	Mean	Max	Min	SD	Mean	Max	Min	SD	Mean	Max	Min	SD
ACL	172	237	121	39	0.07	0.10	0.03	0.02	224	260	183	34	0.21	0.23	0.18	0.02
LCSL	164	240	122	31	0.07	0.10	0.05	0.02	208	297	158	39	0.25	0.29	0.21	0.03
LRL	162	212	103	30	0.08	0.11	0.05	0.02	203	242	127	46	0.24	0.30	0.20	0.03
ACL, LCSL, LRL	165	240	103	32	0.07	0.11	0.03	0.02	208	297	127	40	0.24	0.30	0.18	0.03
BKK solid waste	205	266	138	34	0.05	0.06	0.04	0.01	-	-	-	-	-	-	-	-
BKK soil cover	221	272	186	35	0.06	0.07	0.05	0.01	253	279	229	26	0.24	0.27	0.21	0.03

Table 9.29 Statistics for A_{ZY} and n_{ZY}.

Landfill	OC								NC							
	A_{ZY}				n_{ZY}				A_{ZY}				n_{ZY}			
	Mean	Max	Min	SD	Mean	Max	Min	SD	Mean	Max	Min	SD	Mean	Max	Min	SD
ACL	170	272	131	40	0.06	0.07	0.04	0.01	203	219	186	16	0.20	0.22	0.16	0.03
LCSL	173	253	106	37	0.07	0.10	0.04	0.02	212	297	143	44	0.23	0.27	0.19	0.03
LRL	157	220	113	31	0.07	0.11	0.05	0.02	194	234	146	33	0.24	0.30	0.21	0.03
ACL, LCSL, LRL	167	272	106	36	0.07	0.11	0.04	0.02	204	297	143	37	0.23	0.30	0.16	0.03
BKK solid waste	207	277	145	44	0.06	0.06	0.05	0.005	-	-	-	-	-	-	-	-
BKK soil cover	231	250	187	25	0.07	0.09	0.03	0.024	264	285	240	23	0.24	0.25	0.23	0.01

The relationship between wave propagation velocity and stress state of MSW in this study is in general agreement with field testing results reported by Zalachoris (2010) as well as Stokoe et al. (2011). In this study, the n_{ZX} for shear wave velocity from MSW testing locations ranged from 0.03 to 0.11 with an average of 0.07 in the OC regime. In the NC regime, the n_{ZX} ranged from 0.18 to 0.30 with an average of 0.24. Zalachoris performed similar measurements in 1 site and reported n_{ZX} for S-wave that ranged from 0.04 to 0.05 in the OC regime and increased to 0.31 in the NC regime. Stokoe et al. (2011) reported n_{ZX} for S-wave of 0.09 in the OC regime and 0.28 in the NC regime. Lee (2007), based on resonant column testing, reported that n_{ZX} for S-wave in the OC regime varied from 0.18 to 0.26. These n_{ZX}-OC values were relatively higher than those observed in field testing. Lee (2007) reported n_{ZX} in the NC regime that ranged from 0.31 to 0.36. It is interesting to see that n_{ZX}-NC values from field testing were in general agreement with n_{ZX} of 0.27 which was reported by Zekkos et al. (2013). In addition, the n_{ZX}-NC values from this study, Zalachoris (2010), and Stokoe et al. (2011) were relatively close to the n_{ZX} of 0.25 that has been traditionally recommended for soils (e.g., Hardin and Richart 1963; Hardin and Black 1968). In this study, the A_{ZX} for S-wave ranged from 103 m/s to 240 m/s with an average of 165 m/s in the OC regime. In the NC regime, the A_{ZX} varied from 127 m/s to 297 m/s with an average of 208 m/s. Zalachoris reported that A_{ZX} for S-wave ranged from 128 m/s to 146 m/s in the OC regime and A_{ZX} of 220 m/s in the NC regime. Stokoe et al. (2011) reported A_{ZX} of 157 m/s in the OC regime and A_{ZX} of 212 m/s in the NC regime. Lee (2007) reported that A_{ZX} ranged from 155 m/s to 200 m/s in the OC regime and varied from 167 m/s to 214 m/s in the OC regime.

In this study, the n_{pZ} for P-wave velocity from MSW test locations varied from 0.04 to 0.10 with an average of 0.07 in the OC regime. In the NC regime, n_{pZ} varied from 0.16 to 0.33

with an average of 0.25. Zalachoris reported the n_{pZ} for P-wave ranged from 0.05 to 0.11 in the OC regime, but, did not perform V_p measurements in the NC regime. In this study, the A_{pZ} for P-wave ranged from 200 m/s to 462 m/s with a mean of 308 m/s in the OC regime. In the NC regime, A_{pZ} varied from 234 m/s to 542 m/s with an average of 354 m/s. Zalachoris reported that A_{pZ} ranged from 291 m/s to 301 m/s in the OC regime.

The n_{ZX}-OC for S-wave velocity from solid waste testing locations at the BKK ranged from 0.04 to 0.06 with an average of 0.05. The A_{ZX} for S-wave ranged from 138 m/s to 266 m/s with a mean of 205 m/s in the OC regime. The n_{pZ}-OC for P-wave from solid waste testing locations ranged from 0.04 to 0.06 with a mean of 0.05. The A_{pZ} for P-wave from solid waste testing locations varied from 250 m/s to 459 m/s with an average of 375 m/s in the OC regime.

For soil cover at the BKK, the n_{ZX} for S-wave varied from 0.05 to 0.07 with an average of 0.06 in the OC regime. In the NC regime, the n_{ZX} varied from 0.21 to 0.27 with an average of 0.24. The A_{ZX} for S-wave ranged from 186 m/s to 272 m/s with an average of 221 m/s in the OC regime. In the NC regime, the A_{ZX} varied from 229 m/s to 279 m/s with average of 253 m/s. The n_{pZ} for P-wave ranged from 0.05 to 0.06 with an average of 0.05 in the OC regime. In the NC regime, n_{pZ} varied from 0.22 to 0.23 with an average of 0.22.

Results from this study show that the range of n_{ij} for S-wave and P-wave for MSW is generally broader than that of soil cover. For MSW, Lee (2007) did not find any systematic effect of waste composition on n_{ij} for S-wave. It should be noted that n_{ij} is not only affected by preconsolidation stress. The n_{ij} has also been related to contact stresses between particles (Santamarina et al. 2001) as well as anisotropy. In addition, a small n_{ij} value (i.e. < 0.1) for sandy soil may also be indicative of cementation (Stokoe et al. 2005).

9.4 **Discussion on Poisson's Ratio of Solid Waste and Soil Cover**

The V_p and V_s from downhole and crosshole seismic tests can be used to evaluate small-strain Poisson's ratio (v) using elasticity equation (Eq. 2.13). It should be noted that this equation was derived for homogeneous, isotropic, and elastic solid material. For anisotropic material, such as MSW, the meaning of Poisson's ratio can be very complex. Nevertheless, Eq. 2.13 was used to evaluate Poisson's ratio of MSW by Sharma et al. (1990), Houston et al. (1995), Matasovic and Kavazanjian (1998), and Zalachoris (2010). A robust anisotropic model was beyond the scope of this study and the Poisson's ratios calculated are referred as "pseudo" Poisson's ratios. In this study, "pseudo" Poisson's ratios v_{ZX}, v_{ZY}, and v_{XZ} were evaluated using Eqs. 9.6, 9.7, and 9.8. These equations are identic to Eq. 2.13.

$$v_{ZX} = \frac{0.5 \cdot \left(V_{s-ZX}/V_{p-Z}\right)^2 - 1}{\left(V_{s-ZX}/V_{p-Z}\right)^2 - 1} \tag{9.6}$$

$$v_{ZY} = \frac{0.5 \cdot \left(V_{s-ZY}/V_{p-Z}\right)^2 - 1}{\left(V_{s-ZY}/V_{p-Z}\right)^2 - 1} \tag{9.7}$$

$$v_{XZ} = \frac{0.5 \cdot \left(V_{s-XZ}/V_{p-X}\right)^2 - 1}{\left(V_{s-XZ}/V_{p-X}\right)^2 - 1} \tag{9.8}$$

The mean, maximum, minimum, and standard deviation of "pseudo" Poisson's ratios evaluated in each location at the ACL, LCSL, and LRL are summarized in Table 9.30. In this table, mean, maximum, minimum, and standard deviation values of Poisson's ratios for the three MSW landfills are also presented. Table 9.31 presents Poisson's ratios for solid waste and soil cover in test locations at the BKK.

Table 9.30 Poisson's ratio from MSW test locations.

Location	ν_{ZX}				ν_{ZY}				ν_{XZ}			
	mean	max	min	SD	mean	max	min	SD	mean	max	min	SD
ACL 1	0.29	0.41	0.12	0.08	0.27	0.41	0.06	0.10	0.37	0.45	0.31	0.06
ACL 2	0.34	0.41	0.22	0.07	0.35	0.43	0.23	0.06	0.40	0.43	0.34	0.03
LCSL 1	0.32	0.38	0.24	0.04	0.28	0.37	0.14	0.06	0.32	0.36	0.23	0.05
LCSL 2	0.30	0.39	0.20	0.05	0.28	0.36	0.13	0.07	0.37	0.41	0.37	0.03
LCSL 3	0.30	0.35	0.23	0.03	0.30	0.36	0.24	0.04	0.35	0.40	0.29	0.04
LRL 1	0.29	0.33	0.24	0.03	0.26	0.36	0.14	0.07	0.31	0.39	0.25	0.06
LRL 2	0.34	0.38	0.29	0.02	0.34	0.39	0.27	0.04	0.36	0.38	0.30	0.03
LRL 3	0.27	0.36	0.10	0.07	0.28	0.34	0.19	0.05	0.40	0.45	0.32	0.06
ACL, LCSL, LRL	0.31	0.41	0.10	0.06	0.30	0.43	0.06	0.07	0.36	0.45	0.23	0.05

Table 9.31 Poisson's ratio from solid waste and soil cover test locations at the BKK.

Location	ν_{ZX}				ν_{ZY}				ν_{XZ}			
	mean	max	min	SD	mean	max	min	SD	mean	max	min	SD
BKK 1 (solid waste)	0.27	0.31	0.23	0.03	0.30	0.36	0.26	0.03	0.32	0.34	0.29	0.01
BKK 2 (solid waste)	0.33	0.38	0.24	0.04	0.31	0.35	0.24	0.04	0.36	0.38	0.34	0.01
BKK 1 and 2	0.30	0.38	0.23	0.05	0.31	0.36	0.24	0.04	0.34	0.38	0.29	0.02
BKK 3 (soil cover)	0.24	0.29	0.20	0.03	0.25	0.30	0.20	0.04	0.29	0.32	0.26	0.02

Evaluation on small-strain Poisson's ratio at the ACL, LCSL, and LRL showed that v_{ZX} varied from 0.10 to 0.41 with an average of 0.31, v_{ZY} ranged from 0.06 to 0.43 with an average of 0.30, and v_{XZ} varied from 0.23 to 0.45 with a mean of 0.36. The average values of v_{ZX}, v_{ZY}, and v_{XZ} from the three MSW landfills are 0.31, 0.30, and 0.36, respectively. Evaluation on small-strain Poisson's ratio of solid waste in test locations at the BKK showed that v_{ZX} varied from 0.23 to 0.38 with an average of 0.30, v_{ZY} ranged from 0.24 to 0.36 with an average of 0.31, and v_{XZ} varied from 0.29 to 0.38 with a mean of 0.34. On average, v_{ZX}, v_{ZY}, and v_{XZ} from BKK solid waste test locations were similar to those of MSW test locations. Evaluation on small-strain Poisson's ratio of soil cover in test location at the BKK showed that v_{ZX} varied from 0.20 to 0.29 with an average of 0.24, v_{ZY} ranged from 0.20 to 0.30 with an average of 0.25, and v_{XZ} varied from 0.26 to 0.32 with a mean of 0.29. On average, v_{ZX} and v_{ZY} were similar for solid waste and

soil cover. The v_{XZ} was generally larger than v_{ZX} and v_{ZY}. In addition, v_{ZX}, v_{ZY}, and v_{XZ} of soil cover were generally lower than those of MSW and BKK solid waste.

Zalachoris (2010) performed in-situ measurements of v_{ZX} and reported that v_{ZX} of MSW varied from 0.19 to 0.40 with a mean value of 0.33, which is in general agreement with the average of v_{ZX} from this study. Zekkos (2005) performed a series of laboratory cyclic triaxial testing in mean confining stress ranging from 25 kPa to 90 kPa and reported that v for MSW with 100% < 20 mm fraction ranged from 0.28 to 0.44 and v for MSW that included material > 20 mm varied from 0.05 to 0.31. It should be noted that these laboratory results were Poisson's ratios that were measured in the shearing strain levels ranging from 0.0017% to 0.48% using the following equation:

$$\nu = -\frac{\varepsilon_r}{\varepsilon_\alpha} \tag{9.9}$$

where ε_r and ε_α are strain variation in the radial and axial direction. Small-strain or dynamic Poisson's ratios in this present study probably were measured in shearing strain level of about 10^{-4}% or even lower. It is not clear if Poisson's ratio of MSW change with shearing strain.

9.5 **Model for Normalized Shear Modulus Reduction Curves for MSW**

A model was developed to describe the normalized shear modulus reduction (G/G_{max}) relationship with shearing strain for MSW. Hardin and Drnevich (1972a and 1972b) were amongst the first who applied the hyperbolic model to describe the relationship of the normalized shear modulus with shearing strain of soils. The Hardin and Drnevich hyperbolic model is shown in Eq. 9.10.

$$G/G_{\max} = \frac{1}{1+\frac{\gamma}{\gamma_r}} \tag{9.10}$$

where γ is the shearing strain and γ_r is the reference strain at τ_{max}/G_{max}, and τ_{max} is the maximum shear stress. However, Eq. 9.10 may not model the G/G_{max} data accurately because the relationship of G/G_{max} and shearing strain may not be perfectly hyperbolic.

Stokoe et al. 1999 and Darendeli 2001 proposed a modified hyperbolic model (Eq. 9.11) to obtain a better fit to testing data.

$$G/G_{\max} = \frac{1}{1+\left(\frac{\gamma}{\gamma_r}\right)^{\alpha}} \tag{9.11}$$

where α is a curvature coefficient. As shown in Eq. 9.11, the modified hyperbolic model still includes γ_r, but, γ_r is re-defined as the shearing strain at $G/G_{max} = 0.5$. Recommended normalized shear modulus reduction curves in this study were developed using the modified hyperbolic model (Eq. 9.11).

Uncertainty in the recommended curves was quantified using standard deviation. This value is very important to estimate the effect of waste variability on the recommended curves. The standard deviations of the recommended normalized shear modulus curves (SD_G) were estimated using the point-estimate method (Rosenblueth 1975, 1981). Rosenblueth's point-estimate method is widely used in geotechnical analyses (Christian and Beacher 1999). For examples, Andrus et al. (2003) and Zhang et al. (2005) applied this method to estimate uncertainty in G/G_{max} curve model for South Carolina soils. The standard deviation of point-estimate method was calculated using the following equations:

$$SD_G^2(G/G_{max}) = X[(G/G_{max})^2] - [X(G/G_{max})]^2 \quad (9.12)$$

$$X(G/G_{max}) = \frac{1}{4} \cdot \left(\frac{1}{1+\left(\frac{\gamma}{\gamma_r + SD_{\gamma r}}\right)^{\alpha+SD_\alpha}} + \frac{1}{1+\left(\frac{\gamma}{\gamma_r - SD_{\gamma r}}\right)^{\alpha+SD_\alpha}} + \frac{1}{1+\left(\frac{\gamma}{\gamma_r + SD_{\gamma r}}\right)^{\alpha-SD_\alpha}} + \frac{1}{1+\left(\frac{\gamma}{\gamma_r - SD_{\gamma r}}\right)^{\alpha-SD_\alpha}} \right) \quad (9.13)$$

where $SD\gamma r$ and SD_α are standard deviations of reference strain and curvature coefficient.

9.5.1 Distribution Data as a Function of Mean Confining Stress

Distribution of mean confining stress from all quadrilateral elements in test locations at the ACL, LCLS, and LRL is presented in Fig. 9.4. As shown in this figure, the mean of the mean confining stress is 42 kPa. For convenience of the reader, an example of quadrilateral elements is illustrated again in Fig. 9.5. As shown in this figure, elements A, D, and F were the shallowest, middle, and deepest elements, respectively. Element C was an element that encompassed elements A, D, and F.

In order to develop models for normalized shear modulus curves, normalized shear modulus reduction data points from each landfill were sorted in mean confining stress bins of 20 kPa interval that ranged from 0 to 140 kPa. The data series in each bin were assigned to mean confining stress of 10 kPa, 30 kPa, 50 kPa, 70 kPa, 90, kPa, 110 kPa, and 130 kPa. It should be noted that each bin of confining stress contained data from a variety of quadrilateral elements or waste compositions. Thus, the developed models also inherently capture the variability of waste composition.

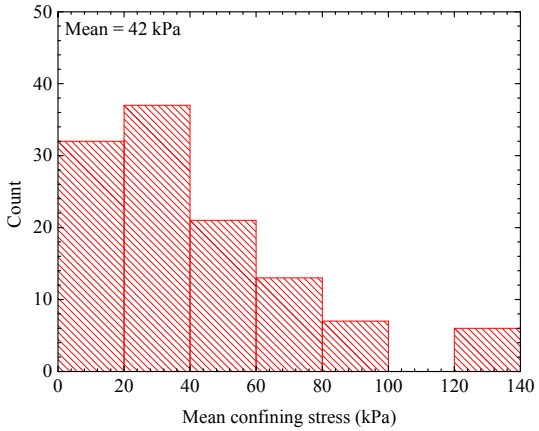

Figure 9.4 Mean confining stress distribution for normalized shear modulus reduction curves of elements A, C, D, and F at the ACL, LCSL, and LRL.

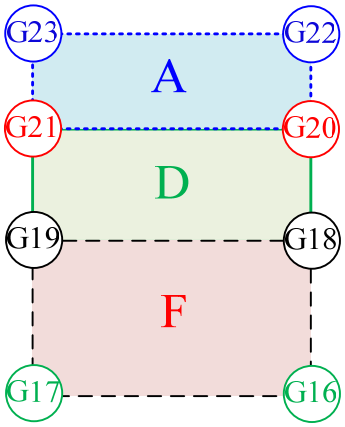

Element	Geophones/Nodes
A	G20, G21, G23, G22
D	G18, G19, G21, G20
F	G16, G17, G19, G18
C = A+D+F	G16, G17, G23, G22

Figure 9.5 Example of quadrilateral elements A, C, D, and F.

9.5.2 Recommended Normalized Shear Modulus Reduction Curves based on In-situ Test at the ACL

The normalized shear modulus reduction data series from in-situ testing at the ACL are presented in Fig. 9.6. Multiple regression analyses for each mean confining stress bin were performed to find γ_r and α. The γ_r and α from regression analysis are presented along with their standard deviations (SDγ_r and SDα), coefficient of determination (R^2), and coefficient of variation (*COV*) in Table 9.32. It should be noted that regression analysis was not performed for bin of 101-120 kPa as there was no data in this bin.

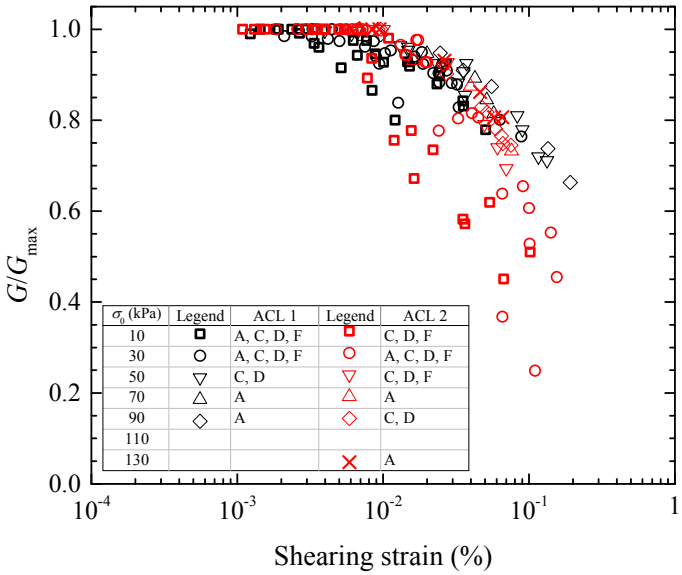

Figure 9.6 Field G/G_{max} data from the ACL.

Table 9.32 Regression analysis results on G/G_{max} data from the ACL.

Mean Confining Stress (kPa)	Number of G/G_{max} curves	Parameters						
		Mean		Standard deviaton (SD)		Coefficient of variation (COV)		R^2
		γ_r	α	$SD\gamma_r$	$SD\alpha$	$COV\gamma_r$	$COV\alpha$	
10	8	0.085	1.14	0.051	0.12	0.60	0.10	0.77
30	10	0.112	1.32	0.043	0.15	0.39	0.12	0.82
50	6	0.156	1.39	0.065	0.13	0.42	0.10	0.76
70	2	0.171	1.41	0.028	0.24	0.17	0.17	0.96
90	3	0.212	1.39	0.050	0.05	0.24	0.04	0.73
110	0	-	-	-	-	-	-	-
130*	1	0.13	2.55	-	-	-	-	-

*Fitting parameters for 130 kPa was derived based on single G/G_{max} data series

Regressed G/G_{max} curves and field G/G_{max} data from the ACL for mean confining stresses of 10 kPa, 30 kPa, 50 kPa, 70 kPa, and 90 kPa are presented in Figs. 9.7(a), 9.7(b), 9.8(a), 9.8(b), and 9.9, respectively. The mean recommended G/G_{max} curves for the ACL are shown in Fig. 9.10. The G/G_{max} calculated using the mean G/G_{max} model was compared with the field G/G_{max} data in Fig. 9.11. In this figure, data points are fairly evenly distributed about the 1:1 line.

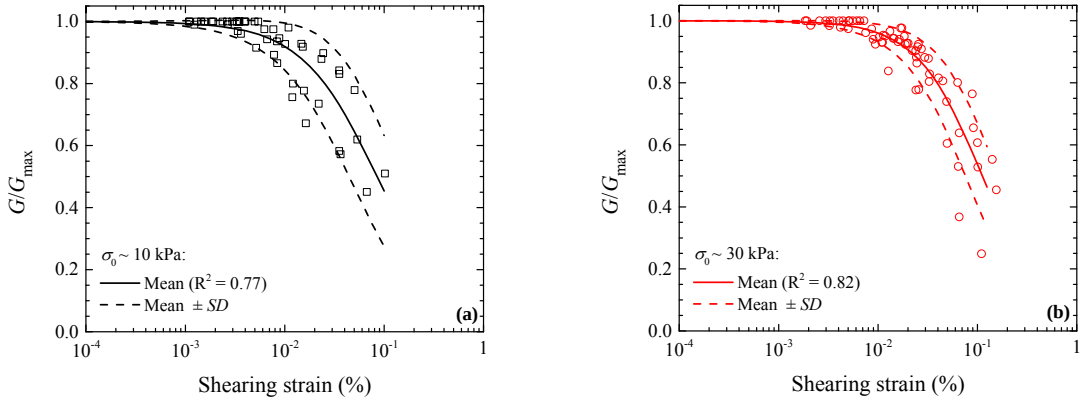

Figure 9.7 Regressed G/G_{max} curves for MSW at the ACL for mean confining stresses of (a) 10 kPa and (b) 30 kPa.

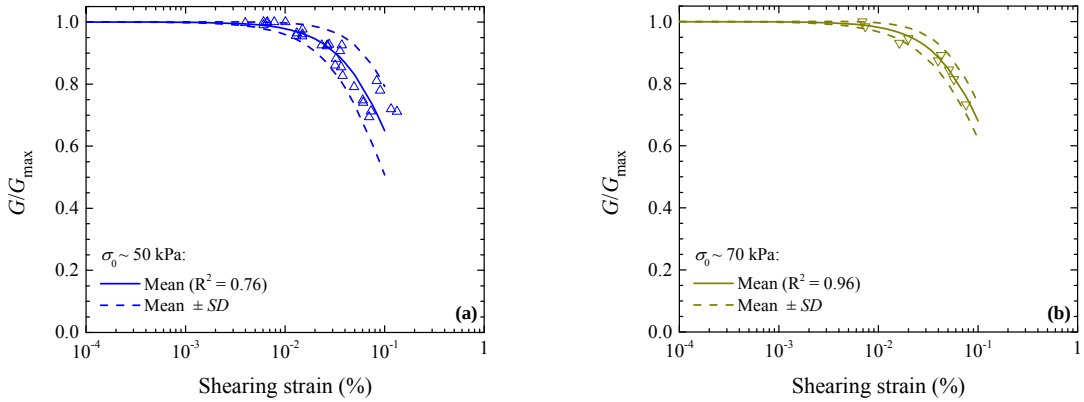

Figure 9.8 Regressed G/G_{max} curves for MSW at the ACL for mean confining stresses of (a) 50 kPa and (b) 70 kPa.

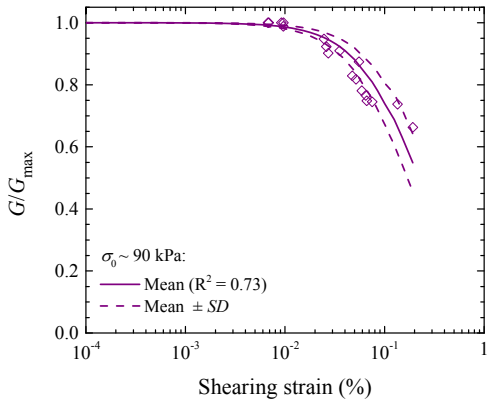

Figure 9.9 Regressed G/G_{max} curves for MSW at the ACL for mean confining stress of 90 kPa.

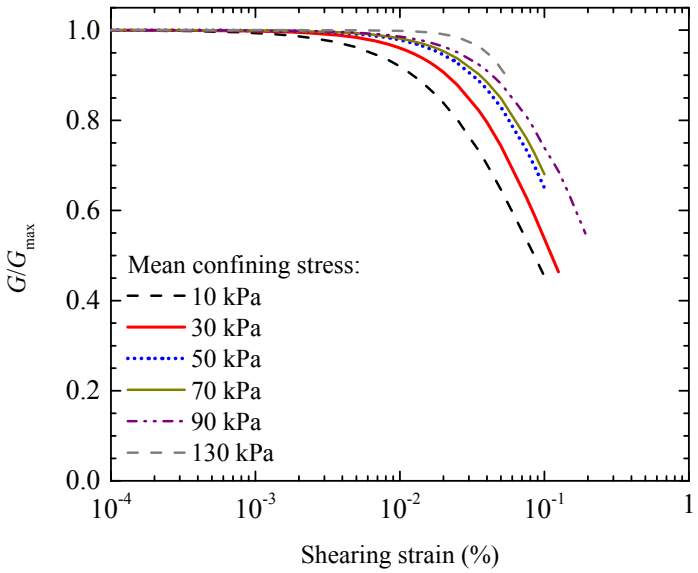

Figure 9.10 Regressed G/G_{max} curves for MSW at the ACL.

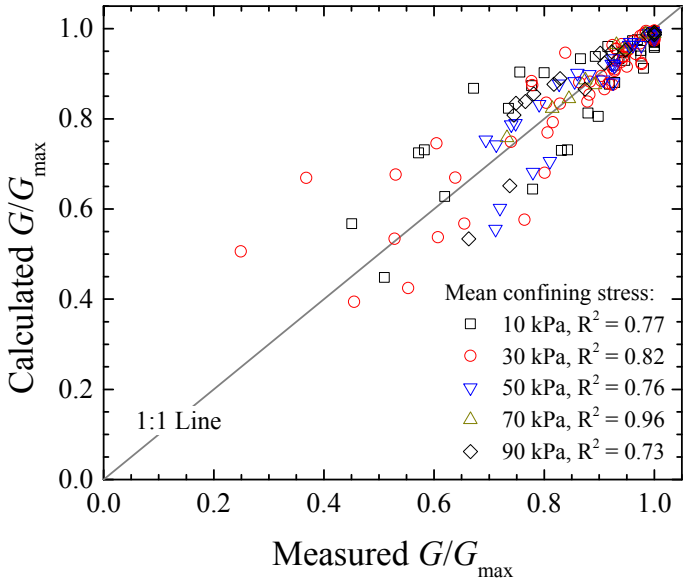

Figure 9.11 Comparison between calculated and measured G/G_{max} data from the ACL.

9.5.3 Recommended Normalized Shear Modulus Reduction Curves based on In-situ Test at the LCSL

Figure 9.12 shows the normalized shear modulus reduction data from field testing at the LCSL. The γ_r and α from regression analysis are presented along with SDγ_r and SDα, R^2, and *COV* in Table 9.33.

Regressed G/G_{max} curves and field G/G_{max} data from the LCSL for mean confining stresses of 10 kPa, 30 kPa, 50 kPa, 70 kPa, 90 kPa, and 130 kPa are presented in Figs. 9.13(a), 9.13(b), 9.14(a), 9.14(b), 9.15(a), and 9.15(b), respectively. The mean recommended G/G_{max} curves for MSW at the LCSL are shown in Fig. 9.16. The G/G_{max} calculated using the mean G/G_{max} model was compared with the field G/G_{max} data in Fig. 9.17.

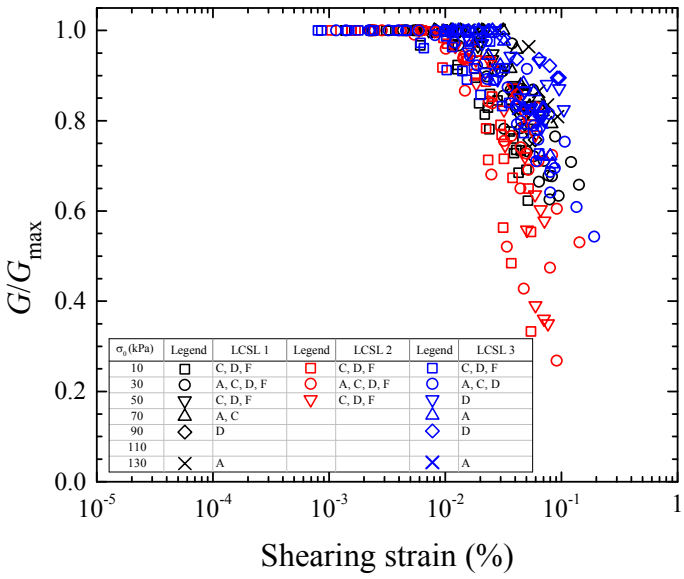

Figure 9.12 Field G/G_{max} data from the LCSL.

Table 9.33 Regression analysis results on G/G_{max} data from the LCSL.

Mean Confining Stress (kPa)	Number of G/G_{max} curves	Parameters						
		Mean		Standard deviaton (SD)		Coefficient of variation (COV)		R^2
		γ_r	α	$SD\gamma_r$	$SD\alpha$	$COV\gamma_r$	$COV\alpha$	
10	12	0.066	1.55	0.033	0.09	0.50	0.06	0.75
30	13	0.112	1.57	0.054	0.23	0.48	0.15	0.60
50	4	0.146	1.76	0.049	0.13	0.33	0.07	0.27
70	3	0.150	1.85	0.024	0.35	0.16	0.19	0.88
90	2	0.155	1.95	0.054	0.23	0.35	0.12	0.25
110	0	-	-	-	-	-	-	-
130	2	0.17	1.99	0.061	0.27	0.36	0.14	0.70

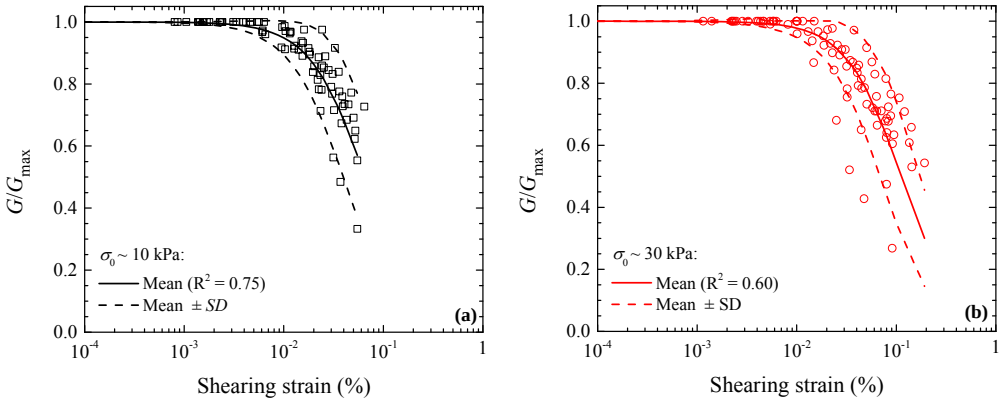

Figure 9.13 Regressed G/G_{max} curves for MSW at the LCSL for mean confining stresses of (a) 10 kPa and (b) 30 kPa.

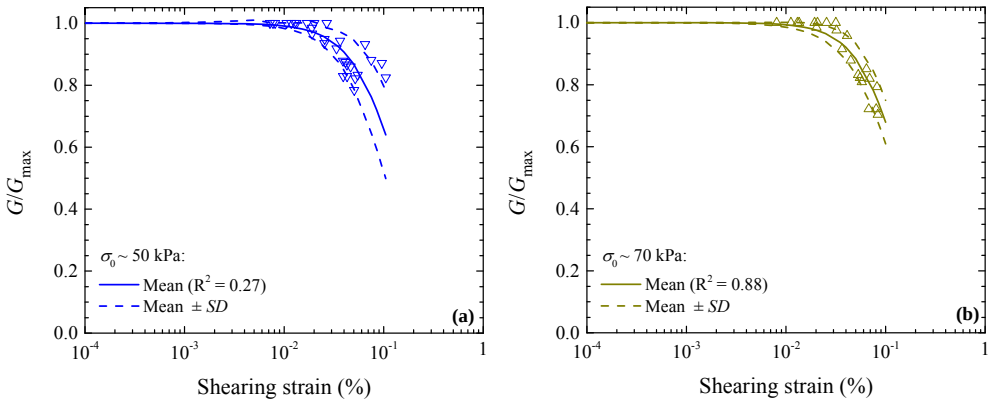

Figure 9.14 Regressed G/G_{max} curves for MSW at the LCSL for mean confining stresses of (a) 50 kPa and (b) 70 kPa.

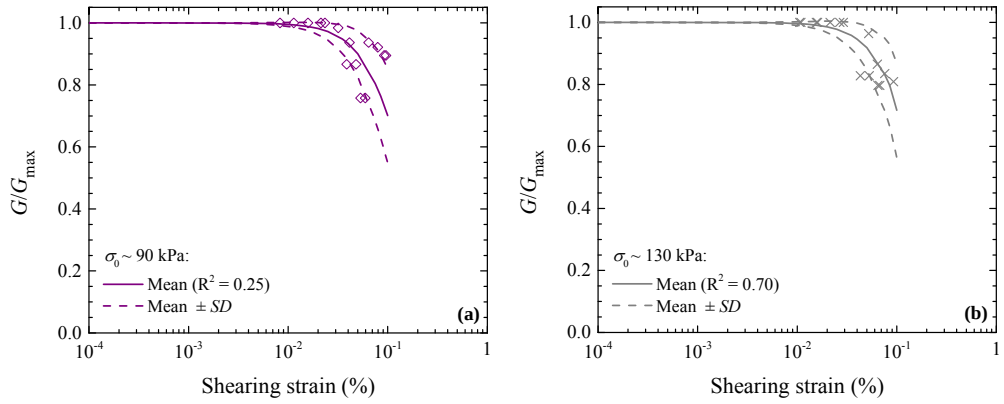

Figure 9.15 Regressed G/G_{max} curves for MSW at the LCSL for mean confining stresses of (a) 90 kPa and (b) 130 kPa.

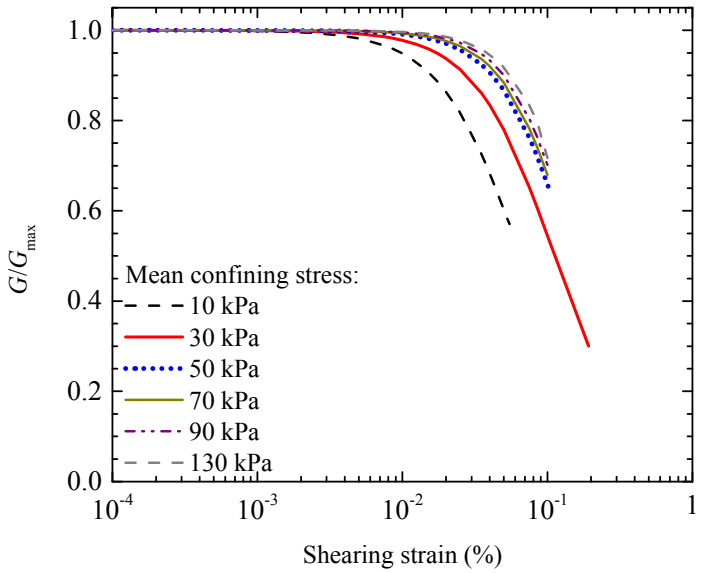

Figure 9.16 Regressed G/G_{max} curves for MSW at the LCSL.

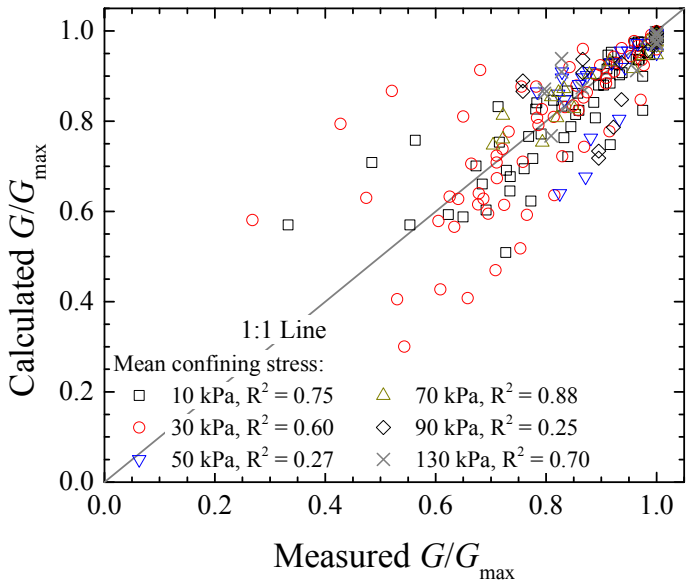

Figure 9.17 Comparison between calculated and measured G/G_{max} data from the LCSL.

9.5.4 Recommended Normalized Shear Modulus Reduction Curves based on In-situ Test at the LRL

The normalized shear modulus reduction data from field test at the LRL is presented in Fig. 9.18. The γ_r and α from regression analysis are presented along with SDγ_r and SDα, R^2, and *COV* in Table 9.34.

Regressed G/G_{max} curves and field G/G_{max} data from the LRL for mean confining stresses of 10 kPa, 30 kPa, 50 kPa, 70 kPa, and 130 kPa are presented in Figs. 9.19(a), 9.19(b), 9.20(a), 9.20(b), and 9.21, respectively. The mean recommended G/G_{max} curves for the LRL are shown in Fig. 9.22. Figure 9.23 shows a comparison between G/G_{max} calculated using the mean G/G_{max} model and the field G/G_{max}.

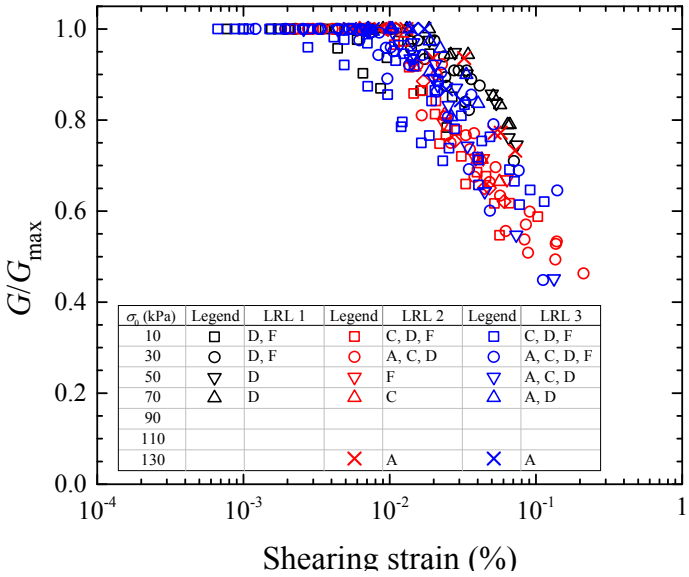

Figure 9.18 Field G/G_{max} data from the LRL.

Table 9.34 Regression analysis results on G/G_{max} data from the LRL.

Mean Confining Stress (kPa)	Number of G/G_{max} curves	Parameters						
		Mean		Standard deviaton (SD)		Coefficient of variation (COV)		R^2
		γ_r	α	$SD\gamma_r$	$SD\alpha$	$COV\gamma_r$	$COV\alpha$	
10	12	0.110	0.99	0.042	0.30	0.38	0.30	0.83
30	12	0.127	1.13	0.046	0.36	0.36	0.32	0.87
50	5	0.139	1.21	0.046	0.32	0.33	0.26	0.80
70	4	0.142	1.32	0.063	0.28	0.44	0.21	0.66
110	0	-	-	-	-	-	-	-
130	2	0.137	1.63	0.033	0.31	0.24	0.19	0.85

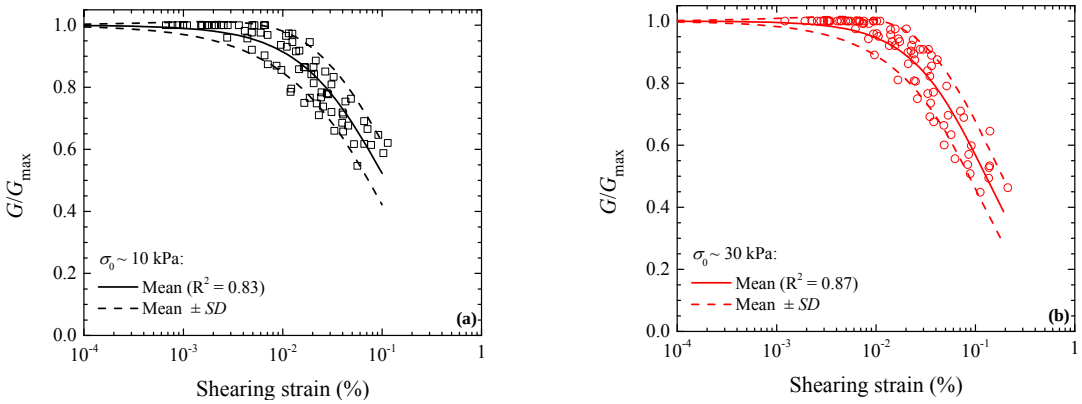

Figure 9.19 Regressed G/G_{max} curves for MSW at the LRL for mean confining stresses of (a) 10 kPa and (b) 30 kPa.

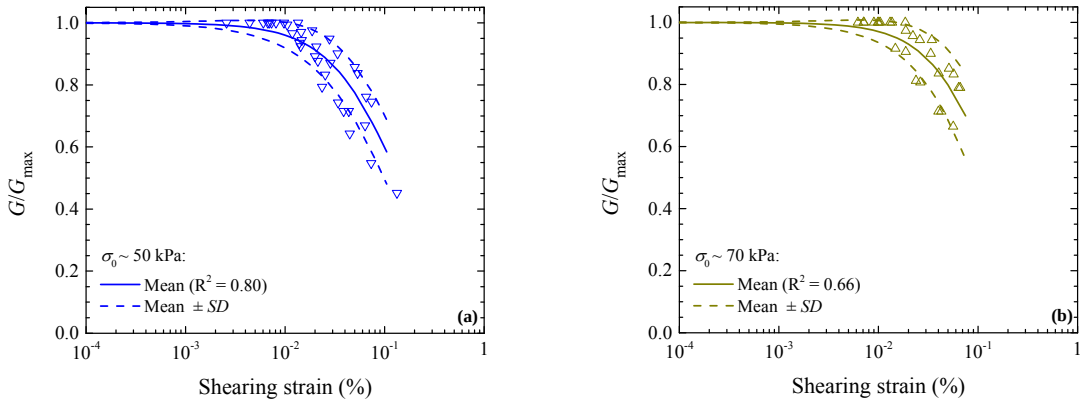

Figure 9.20 Regressed G/G_{max} curves for MSW at the LRL for mean confining stresses of (a) 50 kPa and (b) 70 kPa.

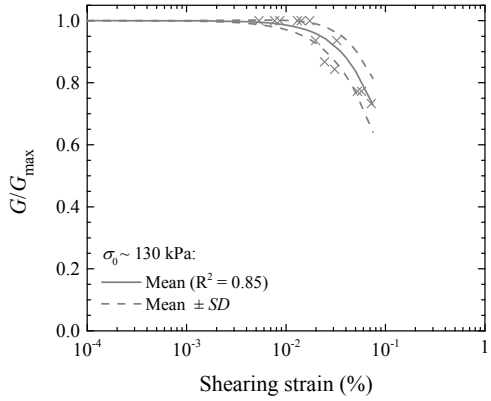

Figure 9.21 Regressed G/G_{max} curves for MSW at the LRL for mean confining stress of 130 kPa.

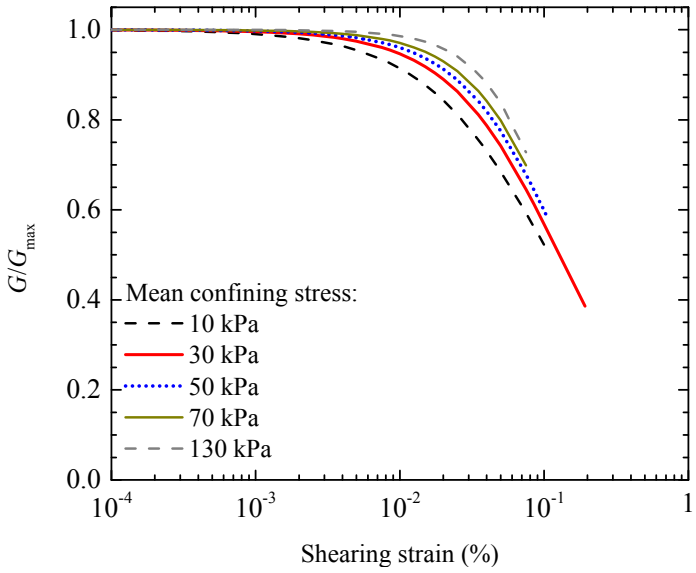

Figure 9.22 Regressed G/G_{max} curves for MSW at the LRL.

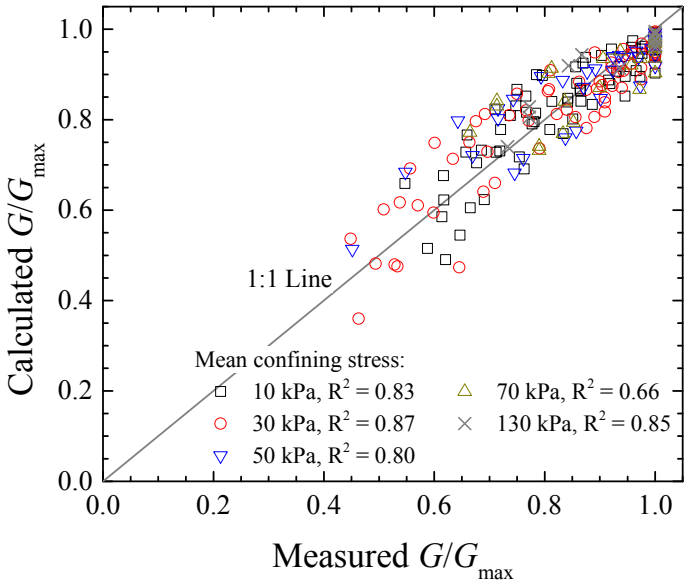

Figure 9.23 Comparison between calculated and measured G/G_{max} data from the LRL.

9.5.5 Recommended Normalized Shear Modulus Reduction Curves for MSW based on In-situ Test at the ACL, LCLS, and LRL

The normalized shear modulus reduction curves from in-situ test at the ACL, LCSL, and LRL are presented in Fig. 9.24. In order to generalize recommended normalized shear modulus curves for MSW, regression analysis was performed using field G/G_{max} data from the ACL, LCSL, and

LRL. The γ_r and α from regression analysis are presented along with SDγ_r and SDα, R^2, and *COV* in Table 9.35.

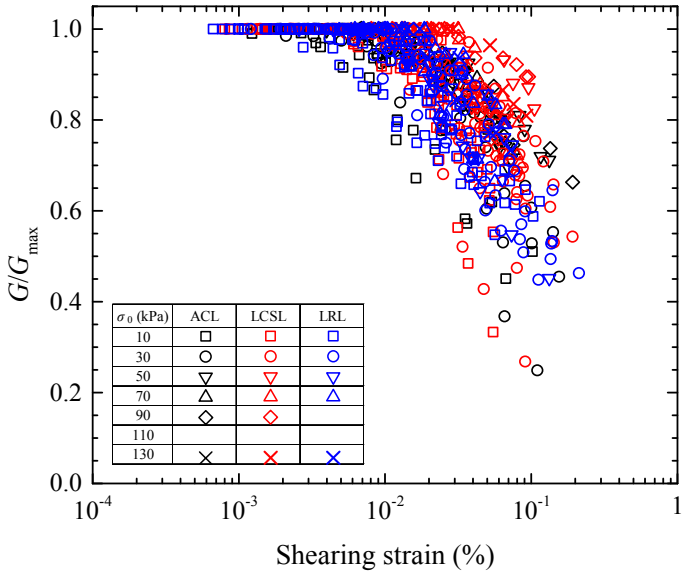

Figure 9.24 Field G/G_{max} data from the ACL, LCSL, and LRL.

Table 9.35 Regression analysis results on G/G_{max} data from the ACL, LCSL, and LRL.

Mean Confining Stress (kPa)	Number of G/G_{max} curves	Parameters						
		Mean		Standard deviaton (*SD*)		Coefficient of variation (*COV*)		R^2
		γ_r	α	$SD\gamma_r$	$SD\alpha$	$COV\gamma_r$	$COV\alpha$	
10	32	0.093	1.09	0.050	0.18	0.54	0.17	0.75
30	35	0.131	1.16	0.071	0.32	0.54	0.28	0.77
50	15	0.155	1.19	0.067	0.31	0.43	0.26	0.54
70	9	0.184	1.19	0.069	0.33	0.37	0.27	0.67
90	5	0.212	1.25	0.103	0.28	0.49	0.22	0.35
110	0	-	-	-	-	-	-	-
130	5	0.231	1.34	0.076	0.28	0.33	0.21	0.70

Regressed G/G_{max} curves and field G/G_{max} data for MSW for mean confining stresses of 10 kPa, 30 kPa, 50 kPa, 70 kPa, 90 kPa, and 130 kPa are presented in Figs. 9.25(a), 9.25(b), 9.26(a), 9.26(b), 9.27(a), and 9.27(b), respectively. The mean recommended G/G_{max} curves for MSW are shown in Fig. 9.28. The G/G_{max} calculated using hyperbolic model for mean G/G_{max}

curves was compared with the field G/G_{max} data in Fig. 9.29. This figure shows that data points are fairly evenly distributed about the 1:1 line.

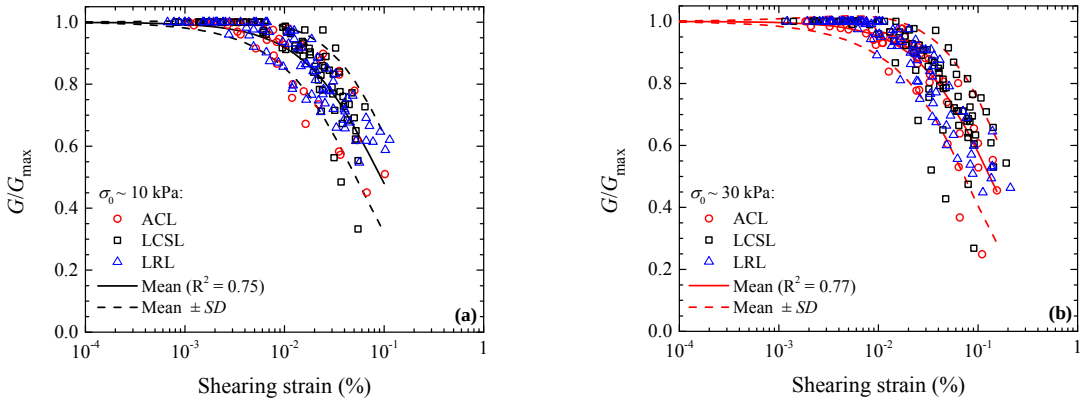

Figure 9.25 Regressed G/G_{max} curves for MSW for mean confining stresses of (a) 10 kPa and (b) 30 kPa.

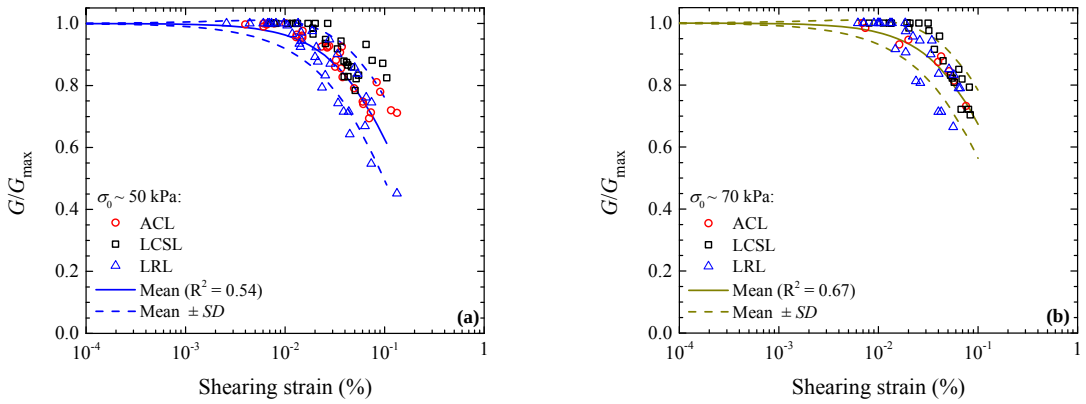

Figure 9.26 R Regressed G/G_{max} curves for MSW for mean confining stresses of (a) 50 kPa and (b) 70 kPa.

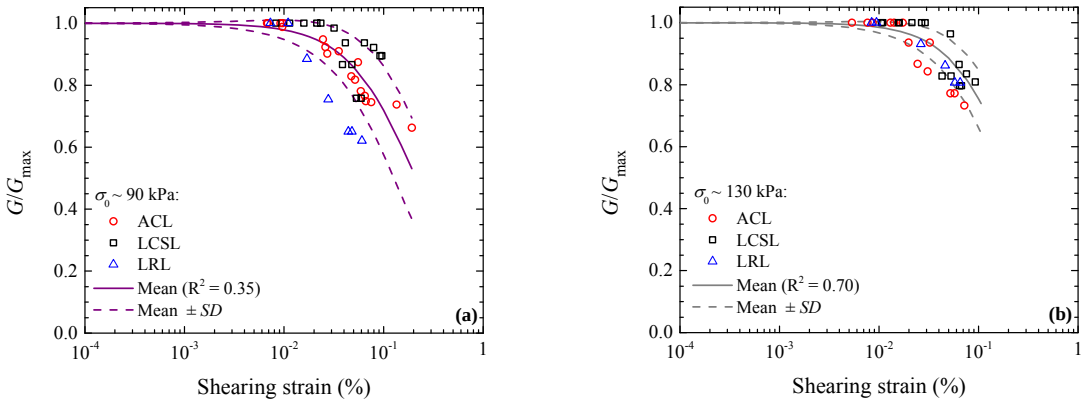

Figure 9.27 Regressed G/G_{max} curves for MSW for mean confining stresses of (a) 90 kPa and (b) 130 kPa.

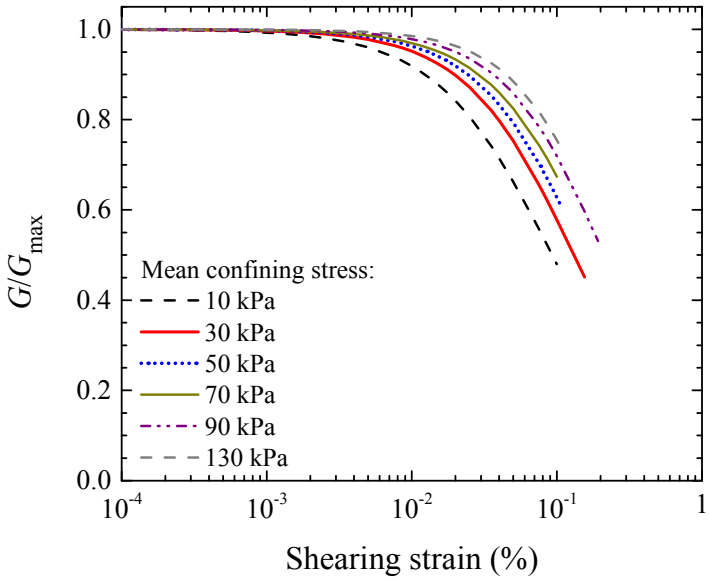

Figure 9.28 Regressed G/G_{max} curves for MSW.

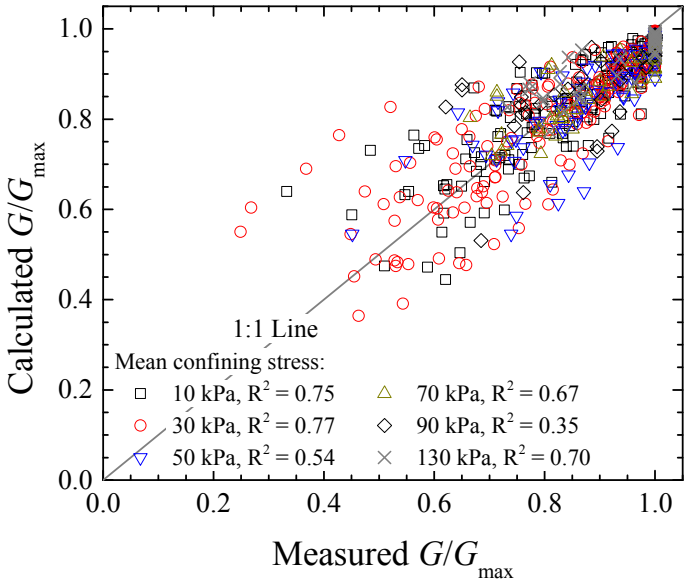

Figure 9.29 Comparison between calculated and measured G/G_{max} data from the ACL, LCSL, and LRL.

Based on regression results shown in Table 9.35, a generic relationship between γ_r and mean confining stress was established and is presented in Fig. 9.30(a). This relationship was modeled using a power function (Eq. 9.14). In addition, the relationship between fitting parameter α and mean confining stress was modeled using a linear function and is shown in Fig. 9.30(b) and Eq. 9.15. Error bars in these figures reflect the impact of waste variability on γ_r and α.

$$\gamma_r = 0.21 * \left(\sigma_0 / P_a\right)^{0.37} \tag{9.14}$$

$$\alpha = 0.20 * \left(\sigma_0 / P_a\right) + 1.08 \tag{9.15}$$

The G/G_{max} curves as a function of mean confining stress for MSW can be developed using Eqs. 9.14 and 9.15.

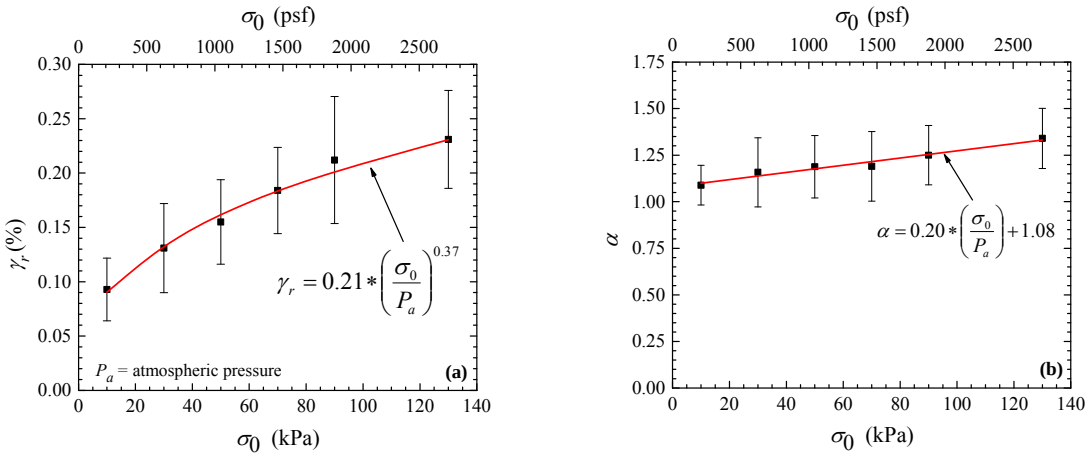

Figure 9.30 Relationship between confining stress with (a) γ_r and (b) α for recommended G/G_{max} curves for MSW.

9.6 **Recommended Normalized Shear Modulus Reduction Curves for Solid Waste at the BKK Hazardous Landfill**

A model for normalized shear modulus reduction curve for solid waste at the BKK was also developed in a similar way to that of MSW. The normalized shear modulus reduction curves from solid waste test locations at the BKK are presented in Fig. 9.31. Multiple regression analyses for each mean confining stress bin were performed to find γ_r and α parameters. Table 9.36 presents γ_r, α, SDγ_r , SDα, R^2, and *COV* for recommended normalized shear modulus model for solid waste at the BKK.

Regressed G/G_{max} curves and field G/G_{max} data for solid waste at the BKK for mean confining stresses of 10 kPa, 30 kPa, 50 kPa, 70 kPa, and 130 kPa are shown in Figs. 9.32(a), 9.32(b), 9.33(a), 9.33(b), and 9.34. The mean recommended G/G_{max} curves for solid waste at the BKK are shown in Fig. 9.35. Figure 9.36 shows a comparison between the mean G/G_{max} model and the field G/G_{max} data.

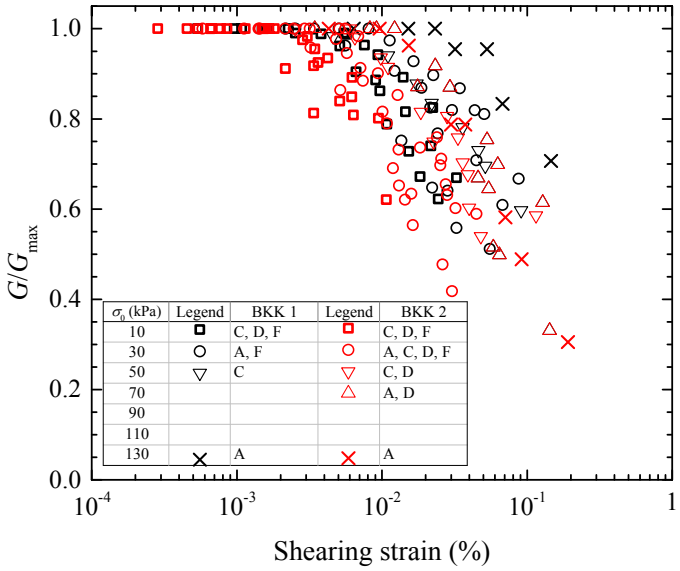

Figure 9.31 Field G/G_{max} data from solid waste test locations at the BKK.

Table 9.36 Regression analysis results on G/G_{max} from solid waste test locations at the BKK.

Mean Confining Stress (kPa)	Number of G/G_{max} curves	Parameters						
		Mean		Standard deviaton (SD)		Coefficient of variation (COV)		R^2
		γ_r	α	$SD\gamma_r$	$SD\alpha$	$COV\gamma_r$	$COV\alpha$	
10	10	0.048	1.10	0.025	0.25	0.52	0.23	0.71
30	10	0.069	1.14	0.038	0.21	0.55	0.19	0.50
50	4	0.088	1.18	0.030	0.05	0.34	0.04	0.73
70	2	0.108	1.24	0.038	0.16	0.35	0.13	0.83
90	0	-	-	-	-	-	-	-
110	0	-	-	-	-	-	-	-
130	2	0.16	1.28	0.088	0.16	0.55	0.12	0.60

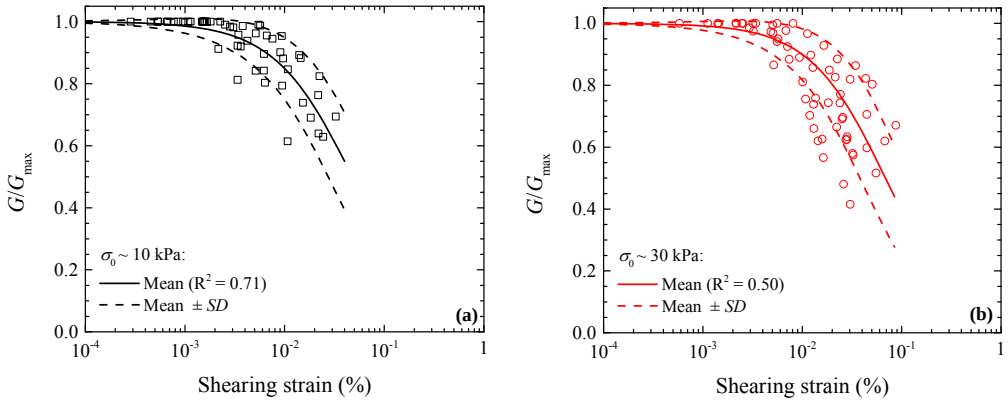

Figure 9.32 Regressed G/G_{max} curves for solid waste test locations at the BKK for mean confining stresses of (a) 10 kPa and (b) 30 kPa.

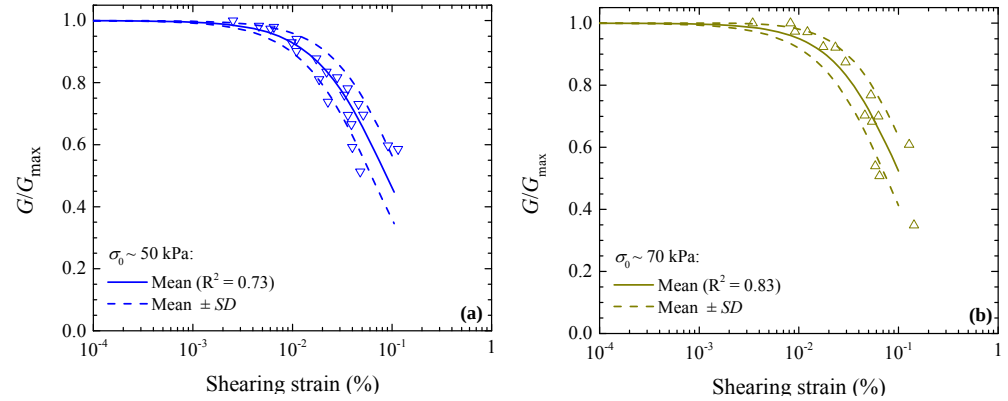

Figure 9.33 Regressed G/G_{max} curves for solid waste test locations at the BKK for mean confining stress of mean confining stresses of (a) 50 kPa and (b) 70 kPa.

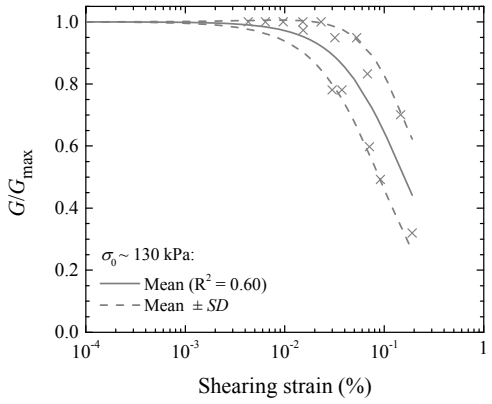

Figure 9.34 Regressed G/G_{max} curves for solid waste test locations at the BKK for mean confining stress of mean confining stress of 130 kPa.

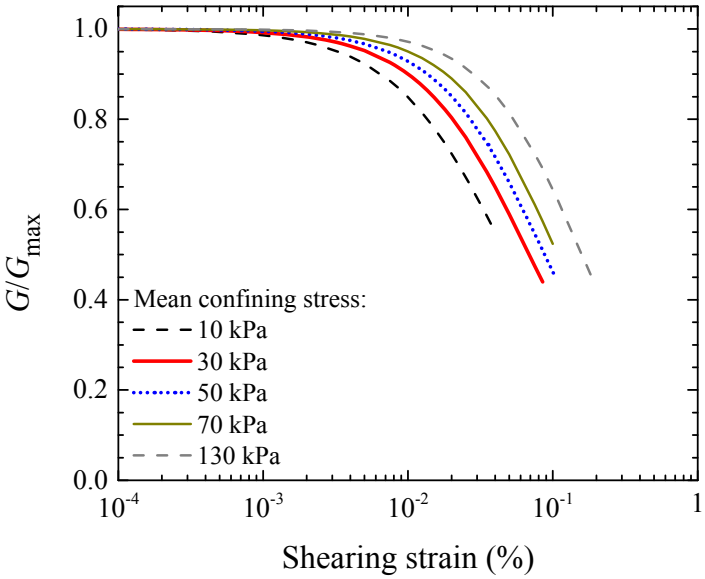

Figure 9.35 Regressed G/G_{max} curves for solid waste test locations at the BKK.

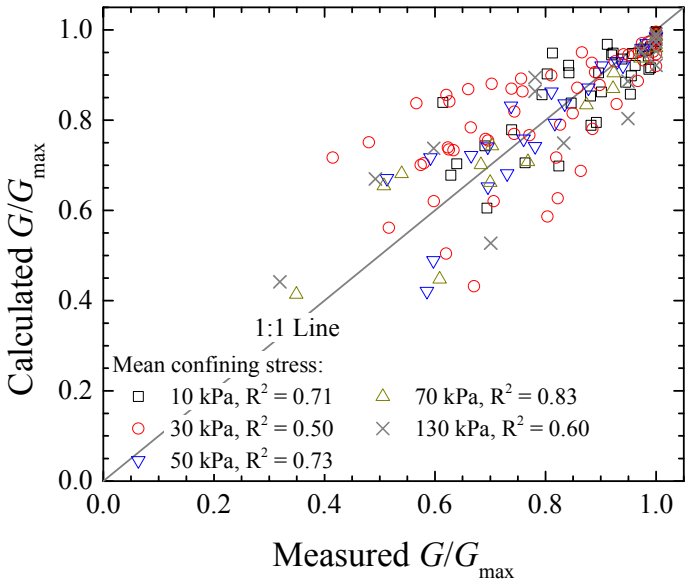

Figure 9.36 Comparison between calculated and measured G/G_{max} data from solid waste locations at the BKK.

The relationship between fitting parameter γ_r and mean confining stress was established based on regression results presented in Table 9.36. As shown in Fig. 9.37(a), this relationship was modeled using a power function (Eq. 9.16). Figure 9.37(b) shows the relationship between

fitting parameter α and mean confining stress that was modeled using a linear function (Eq. 9.17).

$$\gamma_r = 0.13 * \left(\sigma_0 / P_a\right)^{0.46} \tag{9.16}$$

$$\alpha = 0.15 * \left(\sigma_0 / P_a\right) + 1.09 \tag{9.17}$$

The G/G_{max} curves as a function of mean confining stress for solid waste at the BKK can be developed using Eqs. 9.16 and 9.17.

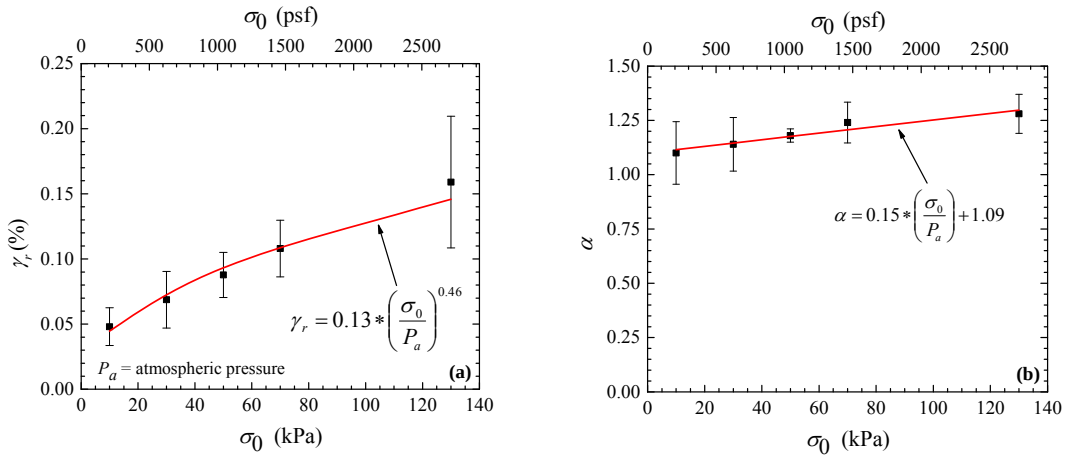

Figure 9.37 Relationship between confining stress with (a) γ_r and (b) α for recommended G/G_{max} curves for solid waste at the BKK.

9.7 **Recommended Normalized Shear Modulus Reduction Curves for Soil Cover from In-situ Test at BKK Landfills**

A recommended G/G_{max} curve for soil cover at the BKK was also developed for the limited data available. The normalized shear modulus reduction curves from in-situ test in soil cover location at the BKK are presented in Fig. 9.38. The γ_r and α from regression analysis are presented along with R^2 in Table 9.37.

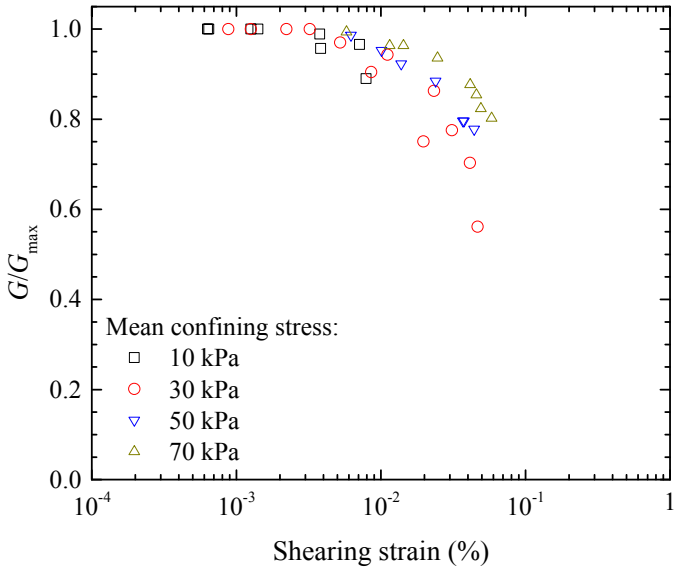

Figure 9.38 Field G/G_{max} data from soil cover test location at the BKK.

Table 9.37 Regression analysis results on G/G_{max} from soil cover waste test location at the BKK.

Mean confining stress (kPa)	γ_r	α	R^2
10	0.059	1.18	0.67
30	0.082	1.20	0.90
50	0.106	1.36	0.98
70	0.133	1.58	0.98

Regressed G/G_{max} curves and field G/G_{max} data for soil cover at the BKK for mean confining stresses of 10 kPa, 30 kPa, 50 kPa, and 70 kPa are shown in Figs. 9.39(a), 9.39(b), 9.40(a), and 9.40(b). The mean recommended G/G_{max} curves for soil cover at the BKK are shown in Fig. 9.41. Figure 9.42 shows a comparison between the mean G/G_{max} model and the field G/G_{max} data.

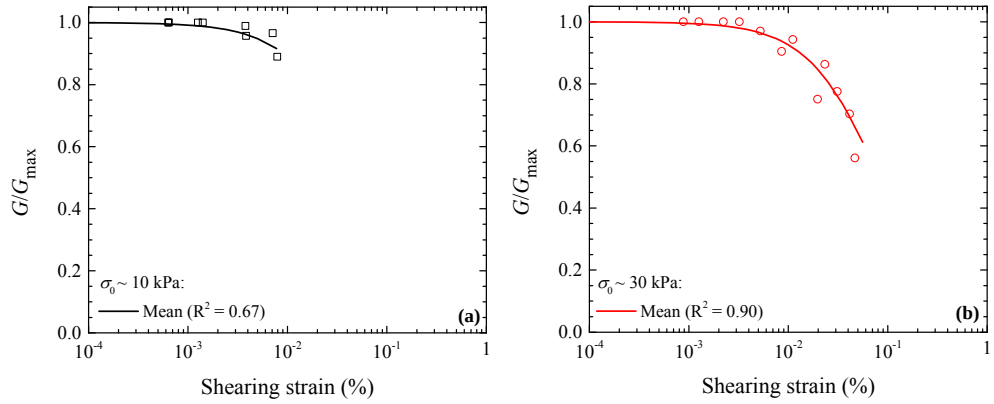

Figure 9.39 Regressed G/G_{max} curves for soil cover test location at the BKK for mean confining stresses of (a) 10 kPa and (b) 30 kPa.

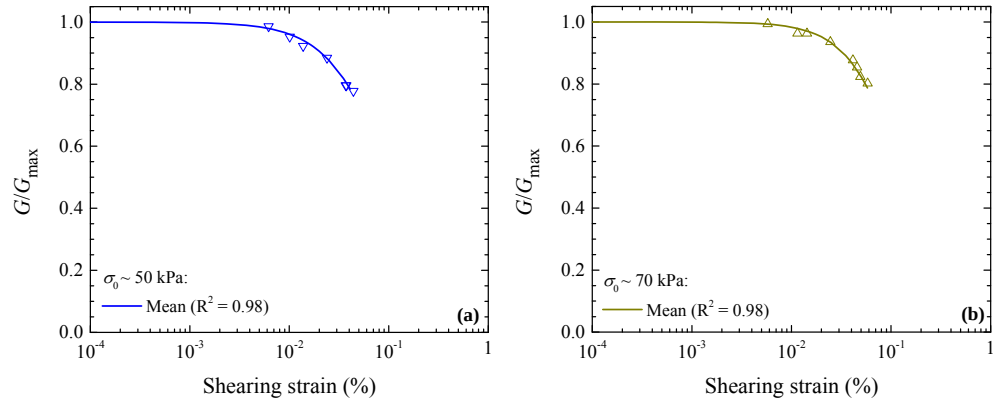

Figure 9.40 Regressed G/G_{max} curves for soil cover test location at the BKK for mean confining stresses of (a) 50 kPa and (b) 70 kPa.

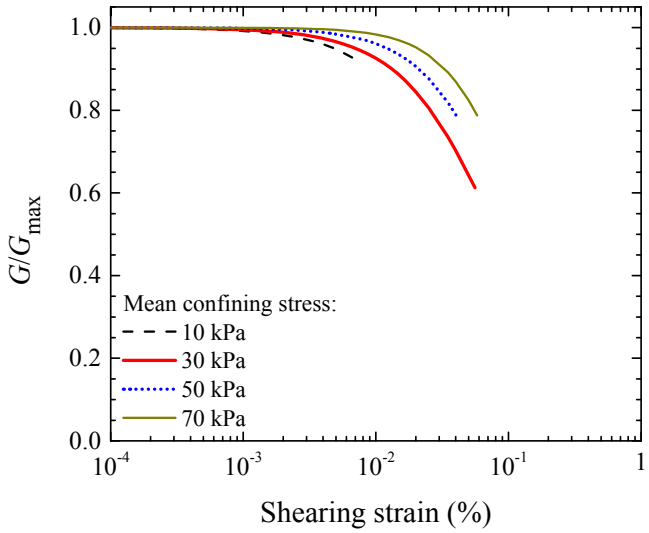

Figure 9.41 Regressed G/G_{max} curves for soil cover test location at the BKK.

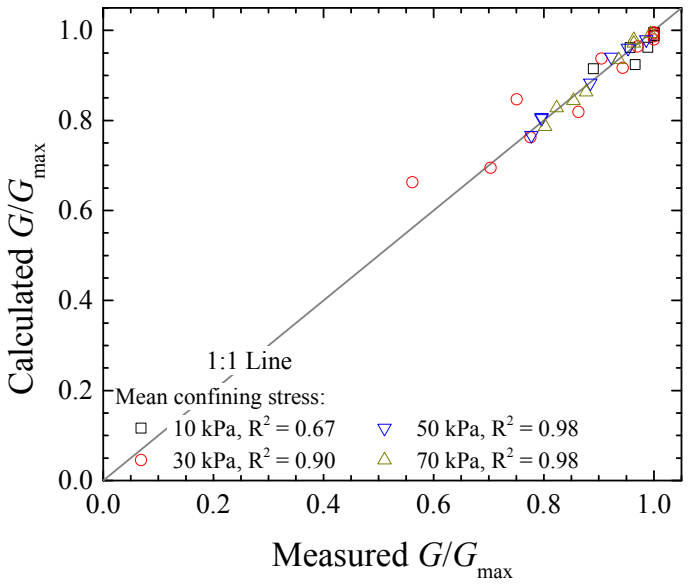

Figure 9.42 Comparison between calculated and measured G/G_{max} for soil cover at the BKK.

Based on regression results shown in Table 9.37, a relationship between γ_r and mean confining stress was established and is presented in Fig. 9.43(a). This relationship was modeled using a power function (9.18). In addition, the relationship between fitting parameter α and mean confining stress was modeled using a linear function and is shown in Fig. 9.43(b) and Eq. 9.19.

$$\gamma_r = 0.14 * (\sigma_0 / P_a)^{0.40} \tag{9.18}$$

$$\alpha = 0.68 * (\sigma_0 / P_a) + 1.06 \tag{9.19}$$

The G/G_{max} curves as a function of mean confining stress for soil cover can be developed using Eqs. 9.18 and 9.19.

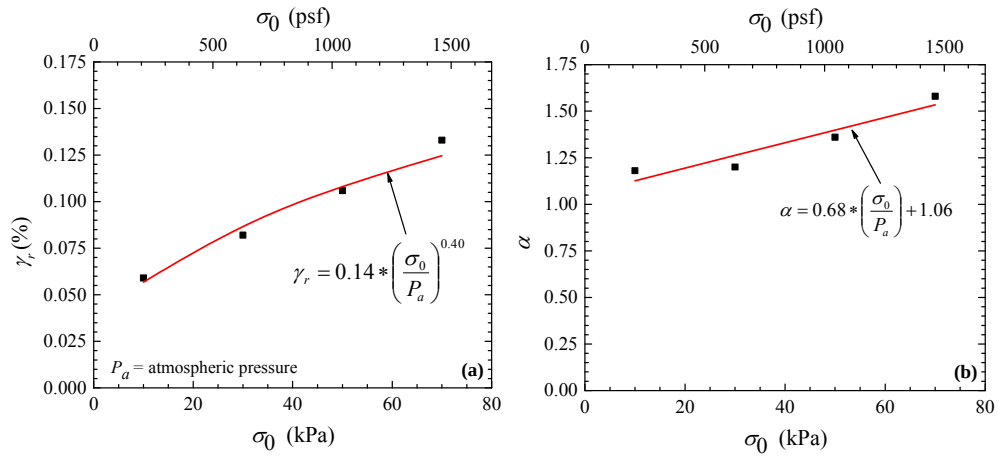

Figure 9.43 Relationship between confining stress with (a) γ_r and (b) α for recommended $G/G_{\max}$ curves for soil cover at the BKK.

9.8 **Summary**

In this chapter, field testing results from the ACL, LCSL, LRL, and BKK are summarized to generate generalized conclusions and recommendations. The main objectives of this chapter are presenting an assessment on anisotropy of solid waste, a synthesis of the downhole and crosshole seismic test results, an evaluation of Poisson's ratio of solid waste, and the development of recommended G/G_{max} curves for solid waste.

The experimental data highlighted that solid waste is an anisotropic material. Comparison of the ratio of wave propagation velocities of solid waste, soil cover, washed mortar sand, and Po River Valley sandy silt indicated the average wave propagation velocity ratios (e.g. the ratios of $V_{p\text{-}Z}$ to $V_{p\text{-}X}$) of solid waste were lower than those of soil cover, washed mortar sand, and Po River Valley sandy silt indicating solid waste was more anisotropic. In addition, the data indicated that wave propagation in the vertical direction was slower than that in the horizontal direction. Thus, the stiffness of solid waste in the horizontal direction was higher than the stiffness in the vertical direction. The average ratios of $V_{s\text{-}ZY}$ to $V_{s\text{-}ZX}$, for solid waste or soil cover,

had a mean close to 1 indicating no difference on average between S-wave propagation velocities in the YZ and the XZ plane.

The dependency of wave propagation velocity on the state of stress in solid waste and soil cover was modeled using a power function and showed a bi-linear relationship in the log V_p-log σ_v, log V_p-log σ_h, and log V_s-log σ_0 spaces. This relationship was described by a linear range in the OC regime, at low stresses, where wave propagation velocity was less dependent on stress that indicated by small power exponent ($n_{ij} \leq 0.11$). As the stress increased, there was a second linear range in the NC regime where the effect of the stress on wave propagation velocity was more important and the power exponent increased. The solid waste was overconsolidated due to compaction during placement in the landfill.

Evaluation on Poisson's ratio of municipal solid waste showed that the average values of v_{ZX}, v_{ZY}, and v_{XZ} from the ACL, LCSL, and LRL were 0.31, 0.30, and 0.36, respectively. For solid waste at the BKK, the average values of v_{ZX}, v_{ZY}, and v_{XZ} were 0.30, 0.31, and 0.34, respectively. On average, v_{ZX}, v_{ZY}, and v_{XZ} of MSW were similar with their counterparts for solid waste at the BKK. Evaluation of Poisson's ratio of soil cover showed that the average values of v_{ZX}, v_{ZY}, and v_{XZ} were 0.24, 0.25, and 0.29, respectively. On average, v_{ZX}, v_{ZY}, and v_{XZ} of solid waste were higher than their counterparts for soil cover. The ranges of v_{ZX}, v_{ZY}, and v_{XZ} of solid waste were generally broader than the corresponding Poisson's ratio of soil cover. Additionally, the v_{XZ} values for solid waste and soil cover were on average higher than their corresponding v_{ZX} and v_{ZY}.

Recommended G/G_{max} curves of MSW for the ACL, LCSL, and LRL were developed using the modified hyperbolic model. In addition, general recommended G/G_{max} curves of MSW were also developed by combining data from the three MSW landfills. The field G/G_{max} data

series from a variety of waste compositions or elements were sorted into their corresponding mean confining stress bins. The recommended G/G_{max} curves were developed for each mean confining stress bin. Point-estimate method was used to estimate uncertainties in the recommended G/G_{max} curves due to waste composition in each confining stress bin. Similarly, recommended G/G_{max} curves of solid waste at the BKK hazardous landfill were also developed. In addition, estimated G/G_{max} curves for soil cover were also presented.

CHAPTER 10. SUMMARY, CONCLUSIONS, AND RECOMMENDATIONS

10.1 Summary

Reliable dynamic properties of solid waste are critical to assess the seismic performance of landfills. However, a fundamental understanding of these properties is still lacking and is further exacerbated by the lack of a field performance record of modern landfills during earthquakes. The 1994 Northridge Earthquake demonstrated that landfills were seismically sensitive infrastructure systems (Matasovic et al. 1995). Excessive displacement during earthquake may cause stability failures as well as damage the landfill's components, such as the containment or cover system. Landfill failures have significant consequences, such as environmental and public health consequences, loss of life, and financial costs (e.g. Eid et al. 2000, Koelsch et al. 2005, and Merry et al. 2005). In this study, the dynamic properties of solid waste including shear wave velocity (V_s), primary wave velocity (V_p), small-strain shear modulus (G_{max}), and normalized shear modulus (G/G_{max}) reduction were investigated in situ. In addition, unit weight and Poisson's ratio were also measured.

The shear wave velocity variation with depth of municipal solid waste (MSW) was measured in situ using a surface wave based methodology that used a linear array of 16 geophones. Surface wave testing combined active measurements (Multichannel Analysis of Surface Wave/MASW) and passive measurements (Microtremor Analysis Method/MAM). The methodology was implemented in Arbor Hills, Oakland Heights, Sauk Trail Hills, and Carleton Farms landfills in southeast Michigan. Surface wave testing was also performed in the Lamb Canyon Sanitary Landfill and BKK Hazardous Landfill in California. Shear wave velocity

profiles generated in this study and from the literature were used in the development of models for shear wave velocity of MSW.

An experimental method to investigate the dynamic properties of solid waste in situ was also performed using The George E. Brown, Jr. Network for Earthquake Engineering Simulation (NEES) equipment available at the University of Texas, Austin, and eight 3-D geophone sensor units fabricated at the University of Michigan. This testing method included crosshole and downhole seismic testing in the small-strain range as well as steady-state dynamic testing in the nonlinear strain range. The field testing method is attractive to evaluate nonlinear dynamic properties of these materials, such as MSW, which are practically impossible to recover in an undisturbed manner and test in the laboratory. In addition, load-settlement tests and in-situ unit weight measurements were performed. The main results from this field testing method are: (1) wave propagation velocities in varying propagation and polarization directions, as well as their variation with stress state and (2) shear modulus-log shearing strain (γ) and normalized shear modulus-log shearing strain relationships as well as their variation with confining stresses. Field investigations were performed at the Austin Community Landfill (ACL) in Texas, Lamb Canyon Landfill (LCSL) in California, Los Reales Landfill (LRL) in Arizona, and BKK Hazardous Landfill in California.

10.2 **Conclusions**

The MASW and MAM were implemented to measure shear wave velocity profiles in 6 solid waste landfills. These methods are attractive as they are non-intrusive (i.e. no drilling required), efficient, and reliable. A combination of these methods has advantages compared to implementing MASW or MAM technique solely. It allowed an independent evaluation of the results using two techniques and increased the frequency range of the developed dispersion

curve. In addition, the agreement between measured dispersion curves from both techniques increased confidence in the results. The combination of these methods was capable of evaluating shear wave velocity profile of MSW up to 45 m depth in some cases without the aid of a high energy vibration source. Nevertheless, the combined method could not be used if the independently derived dispersion curves from the active and passive methods were not consistent. This inconsistency between the two methods was attributed to the sensitivity of the passive technique to background noise locations. Thus, if the dispersion curves from both methods did not agree, analysis was performed using the active dispersion curve only, reducing the depth of investigation. Three cases, where the dominant source of passive data was known, were used to evaluate the effect of the relative orientation of the background noise sources with respect to the geophone array. In cases where the linear array was aligned with the background noise source, or the background noise was truly omni-directional, the active and passive dispersion curves were consistent. When the linear array was perpendicular to the propagation direction of the background noise, the passive data yielded higher apparent phase velocities that were not reliable.

Semi-empirical and empirical models for the V_s of MSW were developed in this study. The semi-empirical model was a more comprehensive model that was based on similar models for soils. Its mathematical expression was formulated using data generated from large-scale laboratory studies on reconstituted MSW. The semi-empirical model independently captures the effect of waste unit weight, composition, and confining stress on the V_s of MSW. The empirical model has a simpler mathematical expression that only relates shear wave velocity and depth. The parameters of both models were derived by calibrating them against a total of 49 in situ

shear wave velocity profiles at 19 MSW landfills, including 13 V_s profiles from 4 landfills in southeast Michigan generated as part of this study.

The semi-empirical V_s model is described by the following equation:

$$V_S = \left(A_F + \frac{B_F \times \frac{\sigma_v'}{P_a}}{C_F + \frac{\sigma_v'}{P_a}} \right) \left(\frac{\gamma_t}{\gamma_w} \right)^{r_\gamma} \tag{10.1}$$

where A_F, B_F, C_F and r_γ are model fitting parameters, σ_v' is effective vertical stress, P_a is atmospheric pressure in kPa, γ_t is total unit weight of MSW, and γ_w is unit weight of water. Estimation of γ_t can be performed using the recommended unit weight profile by Zekkos et al. (2006a). Model fitting parameters are summarized in Table 10.1.

Table 10.1 Statistics of regressed A_F, B_F, C_F, r_γ, V_{si}, α_{Vs}, and β_{Vs} parameters.

Model	Parameter	Mean (μ)	Median	Standard Deviation (σ_{SD})	Max	Min
Semi-empirical (Eq. 10.1)	A_F (m/s)	83	80	15	120	50
	B_F (m/s)	124	130	56	255	40
	C_F [1]	1.3				
	r_γ [2]	0.6				
Fully empirical (Eq. 10.2)	V_{si} (m/s)	89	85	21	158	48
	α_{Vs} (s)	0.08	0.07	0.04	0.19	0.04
	β_{Vs} (s/m)	0.006	0.005	0.003	0.012	0.003

[1] C_F was determined based on laboratory data
[2] r_γ was determined based on regression analysis results

The empirical V_s model is formulated in Eq.10.2.

$$V_S = V_{si} + \frac{z}{\alpha_{Vs} + \beta_{Vs} \times z} \tag{10.2}$$

where V_{si} is the shear wave velocity at the surface (without considering the presence of the "crust") and α_{Vs} and β_{Vs} are hyperbolic model parameters. Fitting parameters for the empirical model are tabulated in Table 10.1.

The semi-empirical and empirical models for the V_s of MSW along with V_s profiles from the literature are presented in Fig 10.1. In this figure, low, typical, and high γ are MSW unit weight values per Zekkos et al. (2006a) that were used to develop the recommended profiles. The models can be used at existing MSW landfills for preliminary design purposes in the absence of site-specific data. The models are not intended to replace in-situ data and do not predict abrupt changes in the V_s profile due to changes in the type of disposed waste. In addition, the models are not intended to capture the crust or other special fill and soil materials disposed of at some landfill locations.

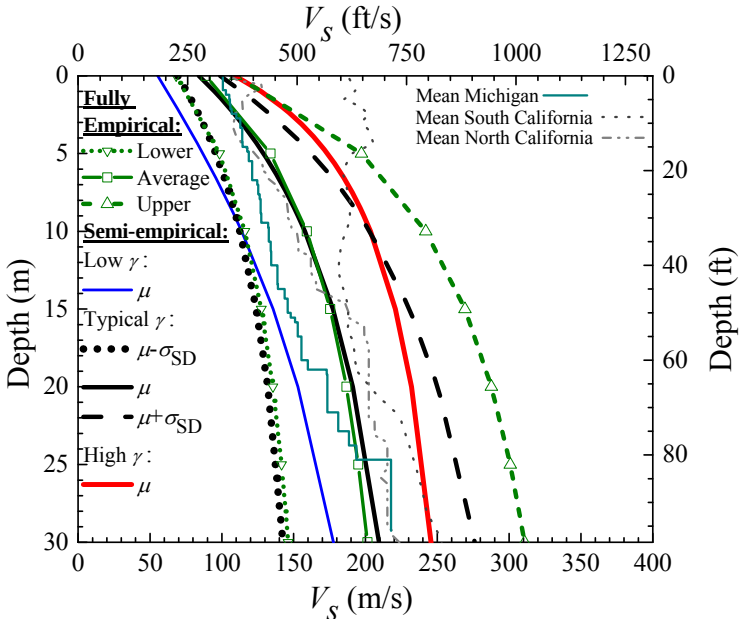

Figure 10.1 Semi-empirical and fully empirical V_s profile models.

The linear and nonlinear dynamic properties were evaluated in situ at the ACL, LCSL, LRL, and BKK. The crosshole and downhole seismic tests were successfully performed under different stress levels up to a confining stress of 140 kPa. Steady-state dynamic testing was successfully performed to evaluate G-log γ and G/G_{max}-log γ relationships in situ for shearing

strains ranging from $3x10^{-4}$% to 0.21%. The following conclusions were made based on the performance and evaluation of the results from field testing at these landfills:

- A staged vertical loading sequence was proven to be an effective way to measure the linear and nonlinear dynamic properties of solid waste and soil cover, and their variation with confining stress.
- The 3-D geophone sensor units fabricated in this study were capable of measuring the linear and nonlinear behavior of solid waste and soil cover over short measurement distances and in varying propagation directions and polarizations.
- In the steady-state dynamic tests, neither Thumper nor T-Rex was capable of generating purely horizontal dynamic loads due to rocking of the shakers' load plates. The 2-node displacement based (DB) method does not consider the vertical component of motion in shearing strain analysis. Thus, the 4-node DB method, which incorporates vertical motion, is recommended to analyze shearing strains in the steady-state dynamic test. At small shearing strain, the shearing strains calculated using the 2-node DB and 4-node DB were relatively similar. But, as the shearing strain increased, 2-node DB yielded lower shearing strain than that of 4-node DB.
- Spatial variability of V_s and V_p in solid waste over short measurement distances was observed and was attributed to the differences in waste composition at the testing scale.
- The relationship between wave propagation velocity and the stress state in solid waste and soil cover was modeled using a power function and showed generally a bi-linear relationship in the log V_p-log vertical stress and log V_s-log confining

stress spaces. Examples of the power functions are shown in the following equations.

$$V_{s-ZX} = A_{ZX} \cdot \left(\frac{\sigma_0}{P_a} \right)^{n_{ZX}} \tag{10.3}$$

$$V_{p-Z} = A_{pZ} \cdot \left(\frac{\sigma_v}{P_a} \right)^{n_{pZ}} \tag{10.4}$$

where $V_{s\text{-}ZX}$ is the velocity of vertically-propagating horizontally-polarized in the X-axis S-wave, $V_{p\text{-}Z}$ is the velocity of vertically propagating P-wave velocity, σ_0 is mean confining stress, σ_v is vertical stress, A_{ij} is an empirical constant that indicates corresponding wave propagation velocity at 1 atm, n_{ij} is an empirical constant that quantifies the effect of stress on the corresponding wave propagation velocity. Bi-linearity in the relationship was caused by oversonsolidation due to compaction. In the overconsolidated (OC) range, at lower stresses, wave propagation velocity was less dependent on stress as indicated by a lower power exponent. For example, n_{ij}-OC for V_s ranged from 0.02 to 0.11. As the stress increased, the waste was in the normally consolidated (NC) regime where the effect of stress on wave propagation velocity was more pronounced as indicated by an increase in n_{ij}. For example, the power exponent n_{ij}-NC for V_s varied from 0.16 to 0.34.

- Evaluation of anisotropy of wave propagation velocity in solid waste in this study highlighted that solid waste was an anisotropic material. The comparison was on the basis of the ratios of wave propagation velocity of solid waste and a soil cover site. Data indicated that wave propagation in the vertical direction was slower

than that in the horizontal direction indicating that the stiffness of solid waste in the horizontal direction was higher than the stiffness in the vertical direction. The average wave propagation velocity ratios of solid waste were lower than those of soil cover and of values reported in the literature for soils indicating that solid waste was more anisotropic. For example, the ratio of P-wave velocities propagating in the vertical and horizontal directions (i.e. $V_{p\text{-}Z}$ and $V_{p\text{-}X}$) from test locations at the ACL, LCSL, and LRL ranged from 0.69 to 0.99 with a mean value of 0.83. In the soil cover, $V_{p\text{-}Z}$ to $V_{p\text{-}X}$ varied from 0.83 to 0.97 with a mean value of 0.90.

- The average Poisson's ratios calculated using various pairs of V_s and V_p from the three MSW landfills and a hazardous landfill were similar. Additionally, Poisson's ratios calculated using crosshole seismic tests were, on average, higher than their corresponding Poisson's ratio calculated using downhole seismic tests. However, it should be noted that the evaluation of Poisson's ratios was performed using elastic equation for isotropic material.
- Steady-state dynamic test results showed that shear modulus increased with increasing confining stress. In addition, G/G_{max} curves generally moved to the right exhibiting a more linear response with increasing confining stress. These trends in G-log γ and G/G_{max}-log γ curves are consistent with laboratory studies on MSW and on soils.
- Normalized shear modulus reduction models were developed for solid waste and soil cover and are presented in Chapter 9. The models were developed using a hyperbolic model (Eq. 10.5).

$$G/G_{\max} = \frac{1}{1+\left(\frac{\gamma}{\gamma_r}\right)^{\alpha}} \tag{10.5}$$

where γ_r is a reference strain and α is a curvature coefficient. Uncertainties in the model due to variability in solid waste composition were assessed in term of standard deviation (SD_G) using point-estimate method as shown in Eqs. 10.6 and 10.7 (Rosenblueth 1975, 1981).

$$SD_G^2(G/G_{max}) = X[(G/G_{max})^2] - [X(G/G_{max})]^2 \tag{10.6}$$

$$X(G/G_{max}) = \frac{1}{4}\cdot\left(\frac{1}{1+\left(\frac{\gamma}{\gamma_r+SD_{\gamma_r}}\right)^{\alpha+SD_\alpha}} + \frac{1}{1+\left(\frac{\gamma}{\gamma_r-SD_{\gamma_r}}\right)^{\alpha+SD_\alpha}} + \frac{1}{1+\left(\frac{\gamma}{\gamma_r+SD_{\gamma_r}}\right)^{\alpha-SD_\alpha}} + \frac{1}{1+\left(\frac{\gamma}{\gamma_r-SD_{\gamma_r}}\right)^{\alpha-SD_\alpha}}\right) \tag{10.7}$$

where SD_G, $SD\gamma r$, and SD_α are standard deviations of shear modulus reduction curve, reference strain, and curvature coefficient, respectively. Field G/G_{max} data from the ACL, LCSL, and LRL were sorted into 20 kPa interval bins that ranged from 10 kPa to 130 kPa. The γ_r and α from regression analysis are presented along with their standard deviations, coefficient of determination (R^2), and coefficient of variation (*COV*) in Table 10.2. Figure 10.2 shows regressed G/G_{max} curves for MSW. The regression analysis results using G/G_{max} data from solid waste sites at the BKK is summarized in Table 10.3. Figure 10.3 presents regressed G/G_{max} curves for solid waste at the BKK sites. The regression analysis results using G/G_{max} data from soil cover location at the BKK is summarized in Table 10.4. It should be noted that the recommended G/G_{max} curve for soil cover was developed only for mean curves due to limited soil cover data series that could be sorted in

mean confining stress bins. Figure 10.4 presents regressed G/G_{max} curves for soil cover location at the BKK.

Table 10.2 Regression analysis results on G/G_{max} data from the ACL, LCSL, and LRL.

Mean Confining Stress (kPa)	Number of G/G_{max} curves	Parameters						
		Mean		Standard deviaton (SD)		Coefficient of variation (COV)		R^2
		γ_r	α	$SD\gamma_r$	$SD\alpha$	$COV\gamma_r$	$COV\alpha$	
10	32	0.093	1.09	0.050	0.18	0.54	0.17	0.75
30	35	0.131	1.16	0.071	0.32	0.54	0.28	0.77
50	15	0.155	1.19	0.067	0.31	0.43	0.26	0.54
70	9	0.184	1.19	0.069	0.33	0.37	0.27	0.67
90	5	0.212	1.25	0.103	0.28	0.49	0.22	0.35
110	0	-	-	-	-	-	-	-
130	5	0.231	1.34	0.076	0.28	0.33	0.21	0.70

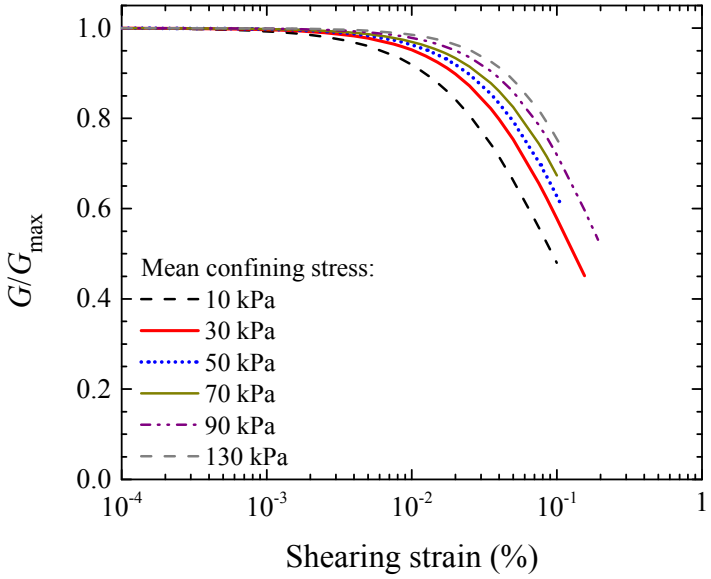

Figure 10.2 Regressed G/G_{max} curves for MSW.

Table 10.3 Regression analysis results on G/G_{max} from solid waste test locations at the BKK.

Mean Confining Stress (kPa)	Number of G/G_{max} curves	Parameters						
		Mean		Standard deviaton (SD)		Coefficient of variation (COV)		R^2
		γ_r	α	$SD\gamma_r$	$SD\alpha$	$COV\gamma_r$	$COV\alpha$	
10	10	0.048	1.10	0.025	0.25	0.52	0.23	0.71
30	10	0.069	1.14	0.038	0.21	0.55	0.19	0.50
50	4	0.088	1.18	0.030	0.05	0.34	0.04	0.73
70	2	0.108	1.24	0.038	0.16	0.35	0.13	0.83
90	0	-	-	-	-	-	-	-
110	0	-	-	-	-	-	-	-
130	2	0.16	1.28	0.088	0.16	0.55	0.12	0.60

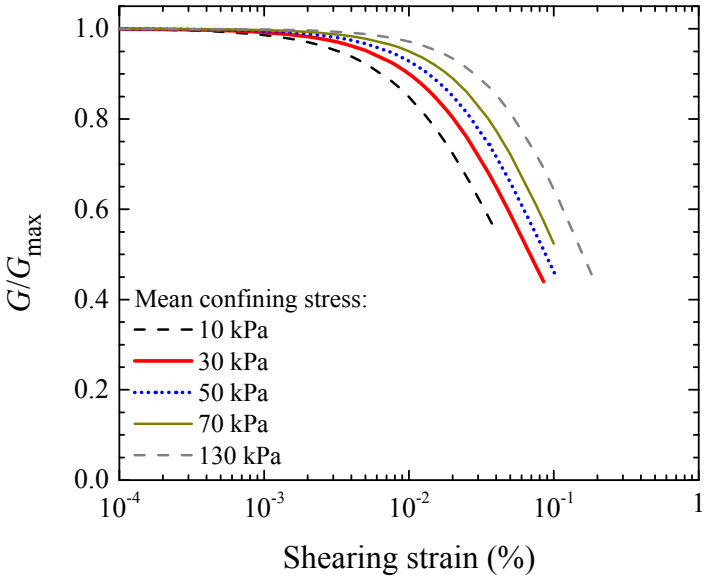

Figure 10.3 Regressed G/G_{max} curves for solid waste test locations at the BKK.

Table 10.4 Regression analysis results on G/G_{max} from soil cover location at the BKK.

Mean confining stress (kPa)	γ_r	α	R^2
10	0.059	1.18	0.67
30	0.082	1.20	0.90
50	0.106	1.36	0.98
70	0.133	1.58	0.98

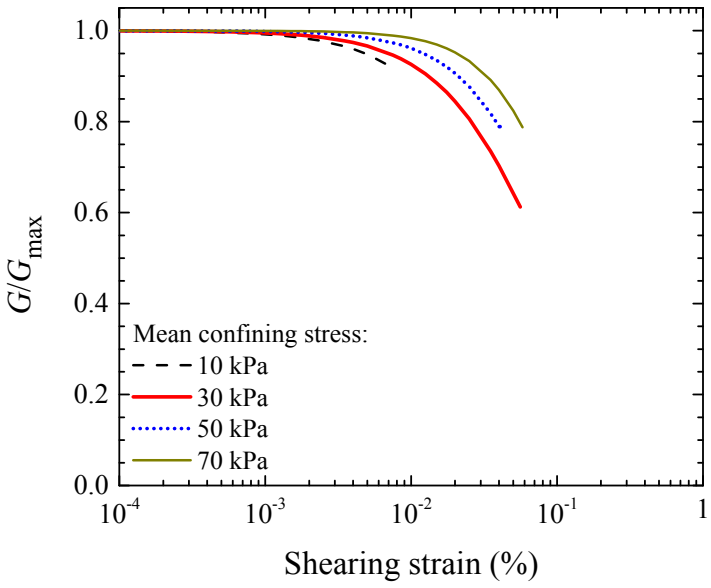

Figure 10.4 Regressed G/G_{max} curves for soil cover location at the BKK.

- The relationships between confining stress and modified hyperbolic fitting parameters (i.e. γ_r and α) for the recommended G/G_{max} curve models for MSW, solid waste at the BKK sites, and soil cover at the BKK are shown in Figs. 10.5, 10.6, and 10.7, respectively. The relationship between γ_r and confining stress was modeled using a power function. The relationship between α and confining stress was fitted using a linear function. Error bars in Figs 10.5 and 10.6 reflect the impact of waste variability on γ_r and α.

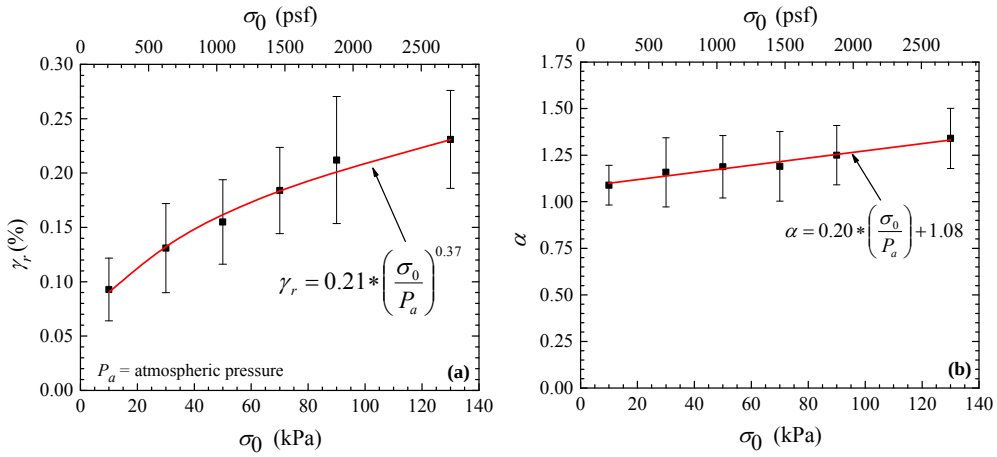

Figure 10.5 Relationship between confining stress with (a) γ_r and (b) α for recommended G/G_{max} curves for MSW.

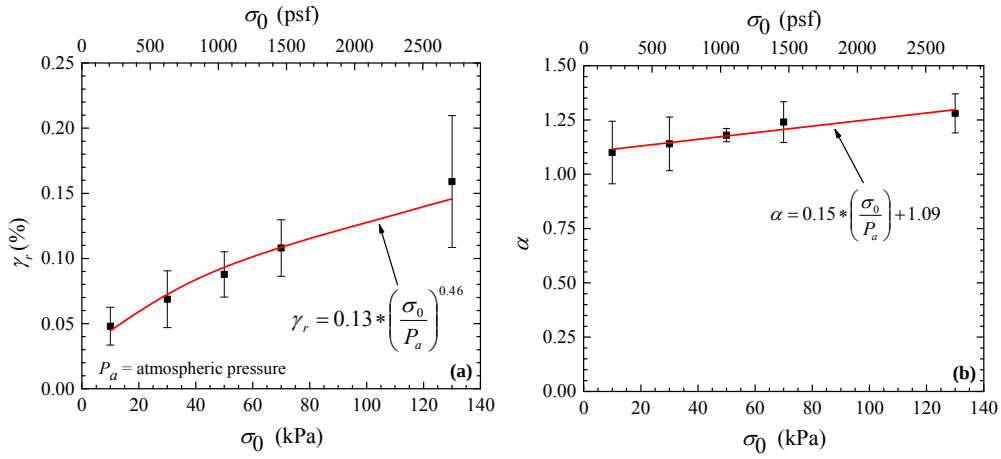

Figure 10.6 Relationship between confining stress with (a) γ_r and (b) α for recommended G/G_{max} curves for solid waste at the BKK hazardous landfill.

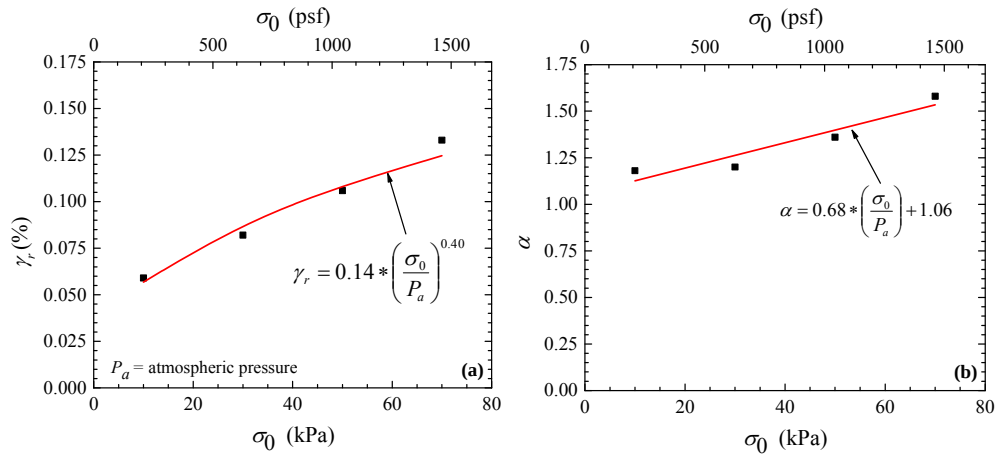

Figure 10.7 Relationship between confining stress with (a) γ_r and (b) α for recommended G/G_{max} curves for soil cover at the BKK hazardous landfill.

- The field G/G_{max} data from the ACL, LCSL, and LRL were generally consistent with Zekkos et al. (2008) G/G_{max} curves. The field G/G_{max} data from the ACL, LCSL, LRL, and BKK were significantly different from Singh and Murphy (1990) and Idriss et al. (1995) recommended curves. The recommended Augello et al. (1998) curve in general was close to the field G/G_{max} data from the ACL, LCSL, LRL, and BKK. The recommended Matasovic and Kavanzanjian (1998) curve was generally more linear than the field G/G_{max} data from the ACL, LCSL, LRL, and BKK.

10.3 **Recommendations for Future Research**

The following recommendations are made for further research.

- Although this testing has been successfully used to investigate the shear modulus and normalized shear modulus versus shearing strain, in-situ investigation of the corresponding material damping curve has yet to be resolved. An extensive amount of data that was generated in this field testing could be potentially used to investigate the material damping curve.

- Large-scale laboratory testing, such as CSS, should be performed to evaluate the dynamic properties of reconstituted MSW. Comparison between laboratory and field testing results can validate whether laboratory testing results are representative of field condition or not. In addition, the variation of damping as a function of shearing strain can be evaluated from laboratory testing.
- The exact waste composition between 3-D geophones cannot be known in the field testing. Thus, laboratory testing should be performed using specimens with variable waste composition to quantify the impact of waste variability on the dynamic properties of MSW.
- On the basis of new dataset from in-situ and laboratory evaluation of dynamic properties of MSW, numerical simulations are recommended to re-visit our understanding of the seismic response and stability of MSW landfills and provide reliable recommendations for use in landfill design.